Development of an integrated platform for multi-omics prototyping of Pseudomonas putida strains

Gurdo, Nicolas

Publication date:
2023

Document Version
Publisher's PDF, also known as Version of record

DTU

The Novo Nordisk Foundation
Center for Biosustainability

Development of an integrated platform for multi-omics prototyping of *Pseudomonas putida* strains

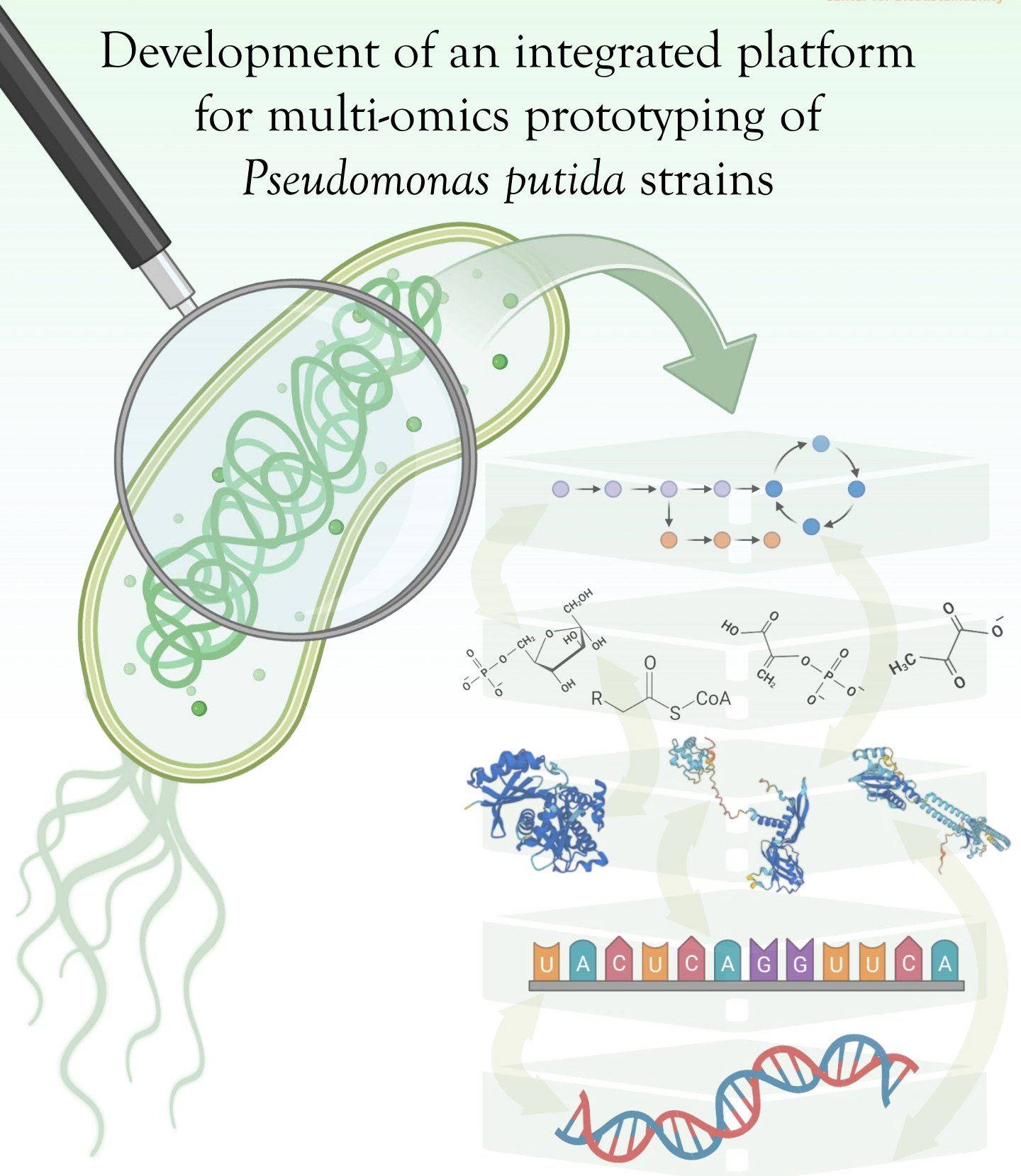

Ph.D. Thesis, Nicolás Gurdo

October 2023

Development of an integrated platform for multi-omics prototyping of *Pseudomonas putida* strains.

Ph.D. Thesis

Nicolás Gurdo

Novo Nordisk Foundation Center for Biosustainability
Technical University of Denmark

July 2023

Development of an integrated platform for multi-omics prototyping of *Pseudomonas putida* strains.

Ph.D. thesis written by Nicolás Gurdo.

Supervised by Professor Pablo Iván Nikel and co-supervised by Senior Researcher Daniel Christoph Volke.

"I have no special talents. I am only passionately curious."

“Look deep into nature, and then you will understand everything better.”

Albert Einstein.

“Your Ph.D. title is like the World Cup for Messi. Life owes it to you."

Dr. Manuel Nieto, Teams conversation.

Preface

This thesis is written as a partial fulfilment of the requirements to obtain a Ph.D. degree at the Technical University of Denmark. The work presented in this thesis was carried out between December 2019 and March 2023 at the Novo Nordisk Foundation Center for Biosustainability at the Technical University of Denmark (DTU Biosustain). It was supervised by Professor Pablo Iván Nikel and co-supervised by Senior Researcher Daniel Christoph Volke. Funding was provided by the Novo Nordisk Foundation through grants NNF20CC0035580, LiFe (NNF18OC0034818), and TARGET (NNF21OC0067996), the Danish Council for Independent Research (SWEET, DFF-Research Project 8021-00039B), the European Union's Horizon 2020 Research and Innovation Programme under grant agreement No. 814418 (SinFonia), and the Cystic Fibrosis Trust, Strategic Research Centre Award–2019–SRC017 to Prof. Nikel.

Nicolás Gurdo

Kgs. Lyngby, September 2023

Thesis summary

Cutting-edge, systems-level approaches to study the physiology and metabolism of microorganisms can bridge the gap between fundamental scientific knowledge and practical biotechnological applications. Such technologies utilize advanced methods and interdisciplinary strategies that integrate fields as diverse as synthetic and systems biology, multi-omics, big data, and computational biology. Through the application of these tools, researchers can gain a comprehensive understanding of a biological systems and their underlying mechanisms. This knowledge can then be translated into tangible solutions, including therapeutics, enhanced bioprocessing techniques, and sustainable biotechnological applications. In the intersection of fundamental and applied knowledge, systems biology and multi-omics analysis play a pivotal role in unraveling the complexity of biological systems. *Pseudomonas putida* is a robust microbial *chassis* endowed with metabolic versatility, adaptability, and genetic tractability, making it an ideal model organism for studying complex biological networks and developing biotechnological applications. Integrating systems biology and multi-omics approaches in *P. putida* research will provide valuable insights into cellular functions and will support the design of tailored metabolic engineering strategies for several biotechnological purposes. The work reported in this thesis builds on the versatile metabolism of *P. putida* and describes a multi-omics workflow developed to explore the physiology and metabolism of this model bacterium. Hence, a multi-omics platform was established to enable the analysis of the metabolome, proteome, and fluxome of *P. putida*. Furthermore, to extend the utility of the platform, a quantitative proteomic approach incorporating QconCATs was integrated into the workflow. This platform in combination with physiological analysis, adaptive laboratory evolution approaches and genomics was able to explore *P. putida* metabolism in multi-substrate environments (glycolytic and gluconeogenic), toxic conditions involving acetate, genetic perturbations in oxidative and phosphorylative pathways, and the introduction of novel functionalities—i.e. synthetic metabolic modules—to the system. Overall, this thesis deepens our understanding of central carbon metabolism in *P. putida*, and provides insights and tools for the development of robust microbial factories based on this bacterium.

Dansk resumé

Avancerede bioteknologiske tilgange udvikles for at formidle kløften mellem grundlæggende videnskabelig viden og praktiske anvendelser. Disse tilgange udnytter avancerede teknologier og tværfagligt samarbejde til at integrere områder som syntetisk og systembiologi, multi-omics, big data og beregningsbiologi. Ved hjælp af disse værktøjer kan forskere opnå en omfattende forståelse af biologiske systemer og deres underliggende mekanismer. Denne viden kan derefter omsættes til konkrete løsninger, herunder banebrydende terapier, forbedrede bioprocesseringsteknikker og bæredygtige bioteknologiske anvendelser.

I krydsfeltet mellem grundlæggende og anvendt viden spiller systembiologi og multi-omics-analyse en afgørende rolle i afklaringen af kompleksiteten i biologiske systemer. *Pseudomonas putida* er en robust mikrobiel chassis med metabolisk alsidighed, tilpasningsevne og genetisk håndterbarhed, hvilket gør det til en ideel modelorganisme til undersøgelse af komplekse biologiske netværk og udvikling af bioteknologiske anvendelser. Integration af systembiologi og multi-omics-tilgange i *P. putida*-forskning giver værdifulde indsigter i cellulære funktioner og hjælper med at designe skræddersyede metaboliske ingeniørstrategier til adskillige bioteknologiske formål.

Arbejdet, der rapporteres i denne afhandling, udnytter *P. putida* alsidige metabolisme ved at anvende en multi-omics-workflow udviklet inden for rammerne af denne undersøgelse. En multi-omics-platform blev etableret for at muliggøre analyse af *P. putida* metabolom, proteom og fluxomer. Ydermere blev en kvantitativ proteomisk tilgang med brug af QconCATs integreret for at forbedre platformens kapaciteter. Denne platform i kombination med fysiologisk analyse, adaptive laboratorieudviklingsmetoder og genetik var i stand til at udforske *P. putida* metabolisme i multisubstratmiljøer (glukose og citrat), toksiske betingelser med acetat, genetiske forstyrrelser i oxidagtige og phosphorylative veje samt indførelsen af nye funktionaliteter, f.eks. syntetiske moduler, til systemet.

Samlet set strækker denne afhandling grænserne for *P. putida* metabolisme for at dykke dybere ned i vores forståelse af central kulstofforbrænding med det formål at levere værdifulde indsigter og værktøjer til udviklingen af robuste mikrobielle fabrikker.

Acknowledgement

To my wife Carolina: I want to express my heartfelt gratitude for everything you did during my Ph.D. journey. You are more than just my partner in life; you are my confidant, my best friend, and the one who understands me like no one else. I cannot thank you enough for the countless sacrifices you make every day to ensure our happiness. Your unwavering strength, kindness, and patience inspire me every day. I feel blessed to have you in my life and cannot imagine navigating this world without you by my side. Your love is a constant source of comfort and joy, and I cherish every moment we spend together. I love you more than words can express, and I am forever grateful for the love and support you give me.

To my family: my dad Fabián, my mom Adriana and my two siblings Romina and Ludmila. My beloved grandparents Alberto, Tota and Héctor that are not physically present today with us and to my lovely grandmother Margot - I do not think I can ever express in words how grateful I am to have you all in my life. You have been my rock through the highs and lows of life. Your unwavering support and unconditional love have helped me through some of the toughest moments, and I am forever indebted to you. The memories we have created together are priceless, and I hold them dear to my heart. From the endless laughs we have shared, each moment has brought us closer and made us stronger. I want to thank you for being my family, for being my home, and for always believing in me. You have given me the courage to pursue my dreams, the confidence to overcome my fears, and the love to make it all worthwhile.

To the Argentinian gang Agus, Santi, Fede, Chris, Lucas, Cata, Agus Beis, Vale, Leo, Sami, Meli, Mati, Javi and Ariel - As I sit down to write this message, I am filled with a flood of emotions. Gratitude, love, and appreciation are just a few of the many feelings that come to mind when I think of you all. You have been my constant companions through thick and thin. The memories we have shared together are some of the most precious moments of my life. From the silly jokes and laughter to the deep conversations and heart-to-hearts, each moment has strengthened our bond and made us closer. You have taught me the true meaning of friendship and have shown me what it means to have people in your life who truly care for you. I look forward to many more adventures, laughter, and memories with you all.

To the SEMsters that were present during the entire Ph.D. project: Manu, Carlos, Patri, Rob, Justine, Antonin, Kate, María Gracia, Garret, Mariela, Filippo, Enrico, Stefano, Alberto, Óscar, Javi, Abou, Nienke, Kris and Lorena; I want to take a moment to express my deepest appreciation for all that you did. You were not merely individuals I worked with or collaborated with, but more importantly, you are my friends. Working alongside you has been an incredible journey filled with challenges, triumphs, and growth. I have learned so much from each one of you, and I am constantly inspired by your dedication, professionalism, and commitment to excellence. In the face of adversity, you have shown resilience, creativity, and adaptability. Your diligent efforts have played a crucial role in our achievements, and I deeply appreciate the opportunity to collaborate with such skilled and enthusiastic individuals. Most of all, I want to thank you for your kindness, understanding, and support. Your encouragement and empathy have been a source of comfort during difficult times, and I feel fortunate to be part of such a caring and supportive team. To my labmates, Cheers!

A *special mention* to the Nico´s cluster (Nico W and Nico K), you two have been like sparks of scientific inspiration, lighting up my path throughout our collaborative projects. Let's raise a glass to Manu and Carlos! You two turned my days from mundane to mind-blowingly amazing. I will remember those office beer nights after our never-ending journeys. Cheers to the memories we made and the tales we will tell when we are old and wise (or at least old)! María Gracia and Garret, you both deserve a standing ovation for your assistance with the final experiments. Your contributions were crucial in bringing my research to fruition, and I cannot thank you enough. And to Shannara, you are a proteomic powerhouse! Your support with the proteomic workflow was nothing short of amazing. It has been a pleasure collaborating with you on your projects too. Keep rocking those mass spectrometers! Massive thanks to Tommaso and Martina who bravely tackled their Master's theses under my supervision, and we had a blast along the way. We made memories, laughed till our sides hurt, and probably shed a few tears too (mostly out of joy, I swear). Also, Román and Fiorella who joined the group as part of their internships. Our journey together was nothing short of extraordinary, and having a dash of Argentinian spirit in the mix made it even more unforgettable.

To the Californian gang Chris and Phillip - thank you for joining me in the quest to unravel the mysteries of the California foliage. Our encounters with those affectionate hugging trees provided endless amusement and left us questioning the true nature of arboreal affection. Who knew trees had so much love to give? Oh, and let's not forget my infamous sense of distance! I would confidently declare that a place was "just around the corner" when it was actually light years away. My infamous "10 blocks, 20 minutes" catchphrase will forever be etched in our memories, serving as a reminder that my estimations deserve a good laugh. Chris and Phillip, thank you for being my comrades in these comical adventures. Our laughter-filled escapades and inside jokes made our time in California truly memorable.

To Berkeley Lab, Aindrila, Thomas, Abhi, Javi, Shwan, Russel, Shweta and Deepanwita for the great internship. Thank you for providing me with an opportunity to work in such a prestigious institution. The research facilities, resources, and collaborative atmosphere have been instrumental in broadening my scientific horizons and fostering a passion for innovation. The exposure to cutting-edge projects and the chance to contribute to groundbreaking research have been a privilege.

To DTU Biosustain - I am truly grateful for the resources, facilities, and collaborative environment the institute provided, which have greatly contributed to the success of my research. Thank you for your generosity and for fostering an environment of growth and innovation. Also, thank you the exceptional team in the Analytics Department, whose expertise and dedication have been vital to the success of my research. Your vast experience in running various analytical techniques, including HPLC, LC-MS/MS and GC-FID/MS, has provided invaluable insights and enriched the quality of my study. To each member of the Analytics Department, thank you for your dedication to achieving exceptional results. Your meticulous attention to detail, technical expertise, and tireless efforts in performing complex analyses have been instrumental in generating accurate and meaningful data for my research. Your ability to navigate sophisticated instrumentation and troubleshoot any challenges that arose throughout the process has been truly remarkable.

I am deeply grateful to my co-supervisor Daniel for their invaluable guidance and unwavering support throughout my Ph.D. journey. Your expertise, feedback, and encouragement have significantly shaped my research and improved the quality of the present thesis. I am honored to have had the privilege of working under their mentorship, and I appreciate their unwavering belief in my potential. Thank you for being an exceptional co-supervisor.

Lastly, I am immensely thankful to my supervisor Pablo, for its priceless mentorship during the Ph.D. studies. Your wealth of knowledge, insightful feedback, and constant encouragement have pushed me to surpass my own limits and strive for excellence. Your mentorship has not only expanded my understanding of the subject matter but also helped me develop critical thinking skills and research methodologies that will benefit me throughout my career. I am really grateful for your support, and collaborative spirit. Your valuable input, constructive criticism, and willingness to share your insights have significantly enriched my research. Your dedication to my academic growth and your commitment to fostering a collaborative and stimulating research environment have been truly inspiring. Also, thank you for giving this unique opportunity and bring me to this amazing country. Since 2017, we have been planning this scientific adventure, and for the next 2.5 years, you have been grilling away to make my dream a reality. Remember that great BBQ in Palermo where we fired up our plans? It is hilarious how it all came together, despite my failed CBP interviews. You reassured me, saying, "One way or another, I'll bring you to DK!" Thank you for having faith in me and for more mouthwatering BBQs together the SEM group. Let's keep the flame of scientific discovery burning, one meaty experiment at a time!

List of publications

1. **Gurdo, N.**, Taylor Parkins, S.K., Fricano, M., Wulff, T., Nielsen, L.K., and Nikel, P.I. (2023) Protocol for absolute quantification of proteins in Gram-negative bacteria based on QconCAT-based labeled peptides, STAR Protocols 4: 102060. https://doi.org/10.1016/j.xpro.2023.102060.
2. **Gurdo, N.,** Volke, D.C., McCloskey, D. & Nikel, P.I. Automating the design-build-test-learn cycle towards next-generation bacterial cell factories. *New Biotechnology* 74, 1-15 (2023). https://doi.org/10.1016/j.nbt.2023.01.002.
3. **Gurdo, N.**, Volke, D.C. & Nikel, P.I. Merging automation and fundamental discovery into the design–build–test–learn cycle of nontraditional microbes. *Trends in Biotechnology* (2022). https://doi.org/10.1016/j.tibtech.2022.03.004.
4. **Gurdo, N.**, Wirth, N., Volke, D.C., Donati, S., Wulff, T., & Nikel, P.I. A multi-omic platform for system level analysis of Gram-negative bacteria. *Manuscript in preparation*.
5. **Gurdo, N.**, Mohamed, E. T., Johnsen, J., Tagliani, T., O'Connell, G. W., Taylor Parkins, S.K., Nielsen, L.K., Feist, A. M., & Nikel, P. I. Understanding and engineering the native metabolism of *Pseudomonas putida* during adaptation to multi-substrate environments. *Manuscript in preparation*.
6. **Gurdo, N.,** Tagliani, T., O'Connell, G. W., Wirth, N., Donati, S., Johnsen, J., Srinivasan A., Eng T., Mukhopadhyay A., Feist, A. M., & Nikel, P. I. Elucidating acetate tolerance mechanism in a genome reduced *Pseudomonas putida* strain by multi-omics analysis. *Manuscript in preparation*.
7. **Gurdo, N.**, Wirth, N., Donati, S., Wulff, T., Volke, D.C., & Nikel, P. I. System-level analyses of *Pseudomonas putida* strains blocked in sugar phosphorylation and oxidation unveil adaptive mechanisms for restoring systemic equilibrium. *Manuscript in preparation*.
8. Sánchez-Pascuala A., **Gurdo, N.**, Fernández-Cabezón L., Turlin T., Wirth N., Johnsen J., Mohamed E. T., Sobral da Rocha A. C., Donati S., Taylor Parkins S. K., Lukassen M. V., Nielsen L., Fuhrer T., Feist A. M., Sauer U., de Lorenzo V., Nikel P. I. Systems-level analysis of an engineered *Pseudomonas putida* strain carrying a synthetic glycolysis. *Manuscript in preparation*.

Publications not included in this thesis

1. Gomez-Hinostroza ES, **Gurdo N**, Alvan Vargas MVG, Nikel PI, Guazzaroni M-E, Guaman LP, Castillo Cornejo DJ, Platero R and Barba-Ostria C (2023). Current landscape and future directions of synthetic biology in South America. Front. Bioeng. Biotechnol. 11:1069628. https://doi.org/10.3389/fbioe.2023.1069628.
2. Donati, S., Mattanovich, M., Hjort, P., **Gurdo, N.**, *et al*. An automated workflow for multi-omics screening of microbial model organisms. Syst Biol Appl 9, 14 (2023). https://doi.org/10.1038/s41540-023-00277-6.
3. Wirth, N.T., **Gurdo, N.**, Krink, N., Vidal-Verdú, À., Donati, S., Férnandez-Cabezón, L., et al. (2022) A synthetic C2 auxotroph of *Pseudomonas putida* for evolutionary engineering of alternative sugar catabolic routes, Metabolic Engineering 74: 83-97. https://doi.org/10.1016/j.ymben.2022.09.004.
4. Fernández-Cabezón, L., Rosich i Bosch, B., Kozaeva, E., **Gurdo, N.** & Nikel, P.I. Dynamic flux regulation for high-titer anthranilate production by plasmid-free, conditionally-auxotrophic strains of *Pseudomonas putida*. *Metabolic Engineering* **73**, 11-25 (2022). https://doi.org/10.1016/j.ymben.2022.05.008.
5. Calero, P., **Gurdo, N.**, and Nikel, P.I. (2022) Role of the CrcB transporter of *Pseudomonas putida* in the multi-level stress response elicited by mineral fluoride, Environmental Microbiology 24: 5082-5104. https://doi.org/10.1111/1462-2920.16110
6. B.H. Pedersen, **N. Gurdo**, H.K. Johansen, S. Molin, P.I. Nikel, R. La Rosa. High-throughput dilution-based growth method enables time-resolved exo-metabolomics of *Pseudomonas putida* and *Pseudomonas aeruginosa*. *Microbial Biotechnology* **14**, 2214-2226 (2021). https://doi.org/10.1111/1751-7915.13905.
7. Volke DC, **Gurdo N**, Milanesi R, Nikel PI. Time-resolved, deuterium-based fluxomics uncovers the hierarchy and dynamics of sugar processing by *Pseudomonas putida*. *Metab Eng.* 2023 Jul 14:S1096-7176(23)00110-6. https://doi.org/10.1016/j.ymben.2023.07.004. Epub ahead of print. PMID: 37454792.
8. Taylor Parkins, S.K., **Gurdo N.**, Wulff T., Nikel P. I., Nielsen L. K.. Automated data analysis for absolute quantitative proteomics – a benchmarking study in *Escherichia coli*. *Manuscript in preparation*.

9. **Gurdo, N.**, Ortíz, A.S., Wirth, N., Donati, S., Tune, W., Schmidt M., Pearson A., Deutschbauer A., Eng T., Mukhopadhyay A., Nikel, P.I. (2023). Elucidating fluoroacetate metabolism in *Pseudomonas putida* KT2440. *Manuscript in preparation*.

Table of Contents

Thesis outline

Systems biology has emerged as a promising discipline capable of disentangling intricate biological networks by integrating diverse types of data, including genomics, transcriptomics, proteomics, metabolomics, fluxomics and other "omics" approaches. Similarly, the combination of existing methodologies poses a substantial difficulty in terms of experimental complexity and data analysis. The vast volume of data and conditions that need to be tested in omics experiments can be complex to integrate and examine in a controllable manner. Adopting standardized methods, which involve a straightforward workflow starting from sample collection, processing and culminating in data analysis, integration, and visualization, can be a valuable resource in gaining a system biology perspective of the biological entity. The implementation of an appropriate workflow into the *Design-Build-Test-Learn* cycle (DBTLc) context has the potential to improve the development of novel products and technologies, accelerate the testing and validation of hypotheses, and facilitate the translation of research into practical applications.

The objective of this Ph.D. is to create a multi-omics platform that can be used to systematically study metabolic processes in the model bacterium *Pseudomonas putida* KT2440 under relevant conditions for biotechnology purposes. The ultimate goal is to provide valuable insights into the functioning of the microbial system from a systems biology perspective and identify potential biotechnological applications as well as expand the knowledge about bacterial physiology. On this background, the Ph.D. thesis is divided into the following eight chapters.

Chapter 1 furnishes a comprehensive overview of modern biotechnology, along with the tools that have been developed over the last two decades, forming the building blocks for a more sophisticated field. The chapter also encompasses an exposition of how these tools can be integrated into the DBTLc in a more standardized manner. A comprehensive examination of the metabolic profile of *Pseudomonas putida* concludes the chapter, elucidating its distinctive metabolic attributes that warrant deeper investigation through the implementation of a metabolism-centric methodology, exemplifying this approach in practice.

Chapter 2 introduces the multi-omics strategy and the experimental set-up implemented in this thesis. The methodological steps allow capturing the dynamic at different metabolic levels comprising metabolites, proteins and metabolic fluxes. This approach is combined with a synchronized sampling procedure, which ensures that data from each of the omics levels is collected at the same time. This multi-omics integration and synchronized sampling provide a more comprehensive and accurate understanding of the metabolic system under investigation. The chapter also describes the analytical techniques carried out to obtain the multi-omics data and it is demonstrated by performing an exploratory analysis of *P. putida* metabolism under glycolytic regimen.

Chapter 3 details the developed methodology for an absolute quantification of *P. putida* proteins enabling more precise quantitative measurements of central carbon metabolism proteins. This chapter provides a thorough description of the experimental procedures used to achieve this absolute quantification, including sample preparation, protein extraction, and mass spectrometry-based analysis.

Chapter 4 shows a comprehensive multi-omic analysis of *P. putida* while growing in a dual gluconeogenic-glycolytic regimen that utilizes citrate and glucose as carbon sources. To enhance the time-shift from the gluconeogenic substrate to the glycolytic, a fluctuating adaptive laboratory evolution approach was implemented to identify mutations that contributed to an improvement in the final phenotype. Whole-genome sequencing revealed the appearance of mutations in the RNA polymerase α and the regulatory subunit of the two-component system GacS/GacA. The identified mutations were retro engineered into the parental strain in order to analyze the effects at systems-level from a multi-omic perspective.

Chapter 5 highlights the potential of *P. putida* to tolerate high acetate concentrations and provides a detailed understanding of its metabolic capabilities for surmounting this stressful condition. Acetate metabolism was in depth studied applying TALE (Tolerance Adaptive Laboratory Evolution) approach coupled with an extensive multi-omic analysis in order to disentangle the metabolic dynamic under toxic concentration of the organic acid. The sequencing outcomes revealed a relevant mutation in the GacA two-component system and the FabB synthase of the fatty acid

synthesis II pathway. Through retro engineering, the strain exhibited an improved growth performance in high acetate concentrations compared to the non-evolved strain. Further analysis through proteomics and metabolic flux analysis revealed notable alterations in various metabolic processes at different levels. In addition, structure predictions offered valuable information about the conformation that resulted from the mutations examined in this section.

Chapter 6 presents a comprehensive investigation into the alterations observed in the central carbon metabolism of *P. putida*, triggered by genetic perturbation in the peripheral glucose pathway. The study specifically examines the impact on phosphorylation and oxidation processes, aiming to gain a deeper understanding of the global changes that emerge in the metabolic network**.** Several knock-outs were analyzed and the impact of the genetic disturbances were assessed using metabolomics, proteomics and metabolic flux analysis. This study exposes the metabolic flexibility and robustness of *P. putida* architecture, thus making it an ideal model for exploring complex biological networks.

Chapter 7 presents a systematic study of an *E. coli* linear glycolytic graft implanted in *P. putida* and its functional characterization at different metabolic levels under glucose as main carbon source. The methodology encompasses several key tools, namely adaptive laboratory evolution, genomics, physiological analysis, quantitative proteomics and fluxomics. Growth on glucose of the engineered strain was significantly improved after an adaptation process of the engineered and the evolved strain was analyzed as mentioned before. Sequencing results identified a key mutation in the topoisomerase I that was further analyzed from a systems biology point of view.

Chapter 8 presents the overall conclusions drawn from the research presented in the thesis, as well as offering a prospective outlook for potential future studies that could not only expand but also build upon the findings outlined in the current work.

Chapter 1 - Leading-edge biotechnology as a bridge between fundamental and applied knowledge

The following chapter is based on the review article and opinion letter:

1) **Gurdo, N.,** Volke, D.C., McCloskey, D. & Nikel, P.I. Automating the design-build-test-learn cycle towards next-generation bacterial cell factories. *New Biotechnology* 74, 1-15 (2023).

2) **Gurdo, N.**, Volke, D.C. & Nikel, P.I. Merging automation and fundamental discovery into the design–build–test–learn cycle of nontraditional microbes. *Trends in Biotechnology* 40, 1148-1159 (2022).

1.1 Unleashing the power of life: exploring the foundational pillars of modern biotechnology

Modern biotechnology has revolutionized the fields of medicine, agriculture, and environmental science, leading to significant advancements in various industries (Clark and Pazdernik, 2015). To expand the boundaries of science, biotechnology has laid down the foundational pillars that have transformed the way researchers approach scientific challenges. The fundamental aspect of modern biotechnology resides in the capability to manipulate and modify DNA, which serves as the primary basis for further advancements in the field. Techniques such as recombinant DNA technology, polymerase chain reaction (PCR), and gene editing have enabled scientists to modify genes in living organisms and even create entirely new organisms (Adrio and Demain, 2010). Along the same pillar, synthetic biology is a growing field, which involves the design and construction of biological systems from scratch using standardized biological parts and engineering principles (Benner and Sismour, 2005). The second pillar is the development of advanced analytical tools such as mass spectrometry and next-generation sequencing (NGS) that have allowed scientists to study and understand complex interactions between biological molecules in unprecedented detail (Wiechert, 2001, Domon and Aebersold, 2006, Dettmer, et al., 2007, Goodwin, et al., 2016). The third pillar is the field of bioinformatics, which

involves the use of computational methods to analyze and interpret large-scale biological data sets, enabling scientists to identify patterns and correlations that would be difficult to discern using traditional analytical methods (Kanehisa and Bork, 2003, Bansal, 2005). The fourth pillar is the development of high-throughput screening techniques that allow for the rapid screening of large numbers of compounds or molecules, facilitating drug discovery and development (Lee, et al., 2005, Zeng, et al., 2020). Lastly, the incorporation of machine learning and artificial intelligence (AI) into the core principles of modern biotechnology has facilitated the emergence of novel tools and methodologies for bioproduction. For example, machine learning algorithms have been developed to optimize fermentation processes, enabling the production of high-value compounds such as bioplastics and biofuels at lower costs and higher yields. AI algorithms have been developed to predict the performance of engineered biological systems, allowing for the rapid optimization of these systems for industrial and medical use. Together, these foundational pillars have paved the way for a new era in modern biotechnology, enabling scientists to tackle some of the most pressing challenges facing humanity, from developing new treatments for diseases to engineering sustainable solutions for food and energy production (**Figure 1.1**).

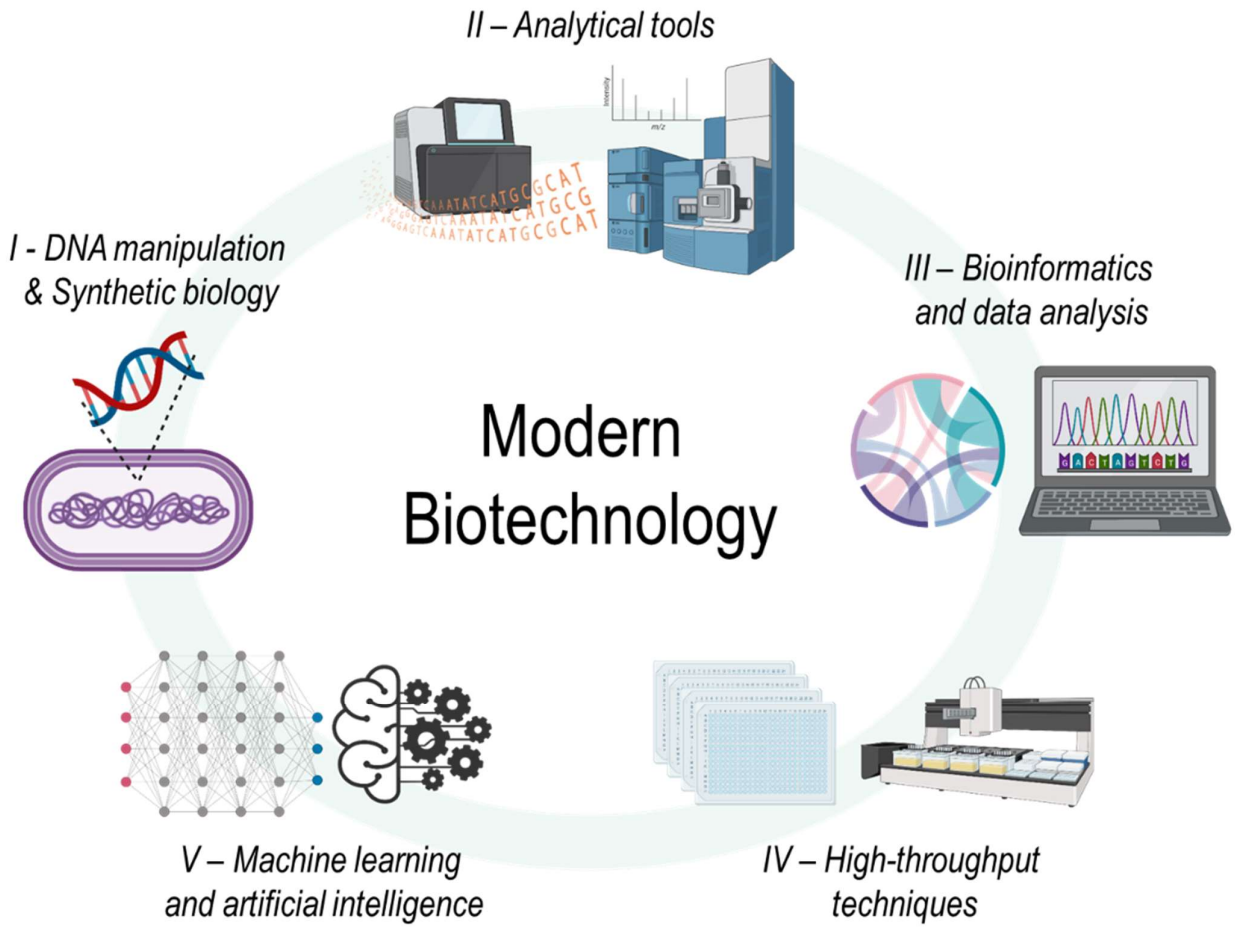

Figure 1.1. Foundational pillars in modern biotechnology. Building on the foundations of DNA manipulation and synthetic biology, modern biotechnology stands tall with the support of analytical tools, bioinformatics, high-throughput techniques, and the power of AI and machine learning.

1.2 The "knowledge wheel" in systems biotechnology: the Design-Build-Test-Learn cycle

In recent times, the scientific community has devised an innovative approach to seamlessly incorporate the cutting-edge tools offered by modern biotechnology into a streamlined and efficient workflow. The DBTL cycle, which stands for Design-Build-Test-Learn, is a systematic framework used in biotechnology, synthetic and systems biology. The integration of software tools, high-throughput DNA sequencing, omics technologies, and ML approaches has propelled the frontiers of the field, surpassing conventional boundaries and fostering unprecedented progress (Carbonell, et al.,

2018, Gurdo, et al., 2023). The methodologies employed as part of the DBTL cycle are exposed in **Figure 1.2**. The upcoming sections illustrate the core phases of the DBTL cycle, encompassing the design of cell factories, followed by the implementation of genetic circuits in suitable hosts as the building phase. After the candidate strain undergoes rigorous testing, the subsequent phase involves extracting valuable insights from the data accumulated in the preceding stage, thereby facilitating the learning process.

Design

Computational tools play a crucial role in generating novel designs for metabolic pathways (Wang, et al., 2017). Repository databases are useful for selecting and assembling pathways of interest, with KEGG, BRENDA, and MetaCyc among the most prominent examples (Kanehisa and Goto, Karp, 2002, Schomburg, et al., 2002). Specialized software packages such as OptKnock, RetroPath, and Selenzyme help identify feasible metabolic designs by applying different strategies and algorithms (Burgard, et al., 2003, Carbonell, et al., 2014, Maia, et al., 2016, Carbonell, et al., 2018). EnzymeMiner provides computational solutions for acquiring suitable unmapped enzyme sequences for biocatalysis (Hon, et al., 2020). Various software packages have been developed for the efficient design and synthesis of DNA in metabolic engineering. GeneDesigner allows for fast design of synthetic DNA, including the addition, editing, and combination of structural and regulatory elements (Villalobos, et al., 2006). Standardization efforts, such as BioBricks and SEVA, enable the modular assembly of DNA parts with standardized functions (Knight, 2003, Silva-Rocha, et al., 2013, Martínez-García, et al., 2022). Tools like RBS Calculator aid in optimizing protein production by predicting translation initiation rates and optimizing ribosome binding sites (Salis, et al., 2009). SBOL serves as a standardized language for representing and visualizing synthetic biology designs, while CELLO provides a hardware description language for designing complex genetic circuits (Galdzicki, et al., 2012, Nielsen, et al., 2016, Madsen, et al., 2019).

Build

Building microbial cell factories require efficient and versatile incorporation of novel functions into the host of choice (Ko, et al., 2020, Luo and Lee, 2020). In the least two decades, the conventional approach for modifying a biological *chassis* has involved the utilization of plug-in and plug-out genetic elements. For example, one of the strategies for gene disruption in *E. coli* utilizes λ Red recombinase functions with PCR products containing an antibiotic marker (Datsenko and Wanner, 2000). Alongside the same line, DNA fragment insertion in *E. coli* could also employ homologous recombination (Zhang, et al., 2000). The KEIO collection is an *E. coli* knock-out library with mutants for 303 genes, enabling large-scale loss-of-function phenotype studies (Baba, et al., 2006, Yamamoto, et al., 2009). Oligonucleotide-based λ Red recombination can be combined with multiplex automated genome engineering (MAGE) to enhance recombination efficiency (Court, et al., 2002, Wang, et al., 2009). A breakthrough in molecular biology has been the discovery of clustered regularly interspaced short palindromic repeats (CRISPR) and associated Cas proteins, repurposed for gene and genome editing protocols (Jinek, et al., 2012). Multiplex-editing techniques enable simultaneous engineering of multiple sites in eukaryotic genomes (Cong, et al., 2013). The same principles were combined with recombineering or homologous recombination to adapt CRISPR/Cas methodologies in prokaryotes (Hoang, et al., 1998), lacking non-homologous end joining (Pyne, et al., 2015, Ronda, et al., 2016, Garst, et al., 2017, Blombach, et al., 2021). Base-editors based on CRISPR/Cas allow precise single-base manipulations (Komor, et al., 2016, Gaudelli, et al., 2017, Volke, et al., 2022) while synthetic small regulatory RNAs can control gene expression by inhibiting translation (Na, et al., 2013). Other CRISPR variations encompasses: CRISPR interference (CRISPRi) that blocks gene transcription as well as CRISPR activation (CRISPRa) which boosts gene expression (Cong, et al., 2013, Qi, et al., 2013, Jakočiūnas, et al., 2017, Batianis, et al., 2020). Numerous additional enhanced CRISPR/Cas procedures are consistently arising, and novel approaches for DNA assembly that are more effective have been devised (Vo, et al., 2021). USER cloning incorporates deoxyuridine and excision for seamless assembly (Geu-Flores, et al., 2007). Gibson assembly synthesizes DNA blocks using exonuclease, DNA polymerase, and ligase in a single step (Gibson, et al., 2008). Ligase chain reaction (LCR) and Golden Gate assembly enable high-throughput assembly of DNA

constructs (Engler, et al., 2008, Kok, et al., 2014). These advancements have paved the way for automation and large-scale DNA molecule construction (Smanski, et al., 2014).

Test

The advent of multi-omics methodologies has brought about a revolutionary transformation in the analysis of regulatory layers within cellular systems (Becker and Wittmann, 2018). The integration of whole genome sequencing, cellular metabolite measurements, and the identification of interconnections between regulatory levels is of utmost importance in the field of systems metabolic engineering.

Genomics

Next-generation sequencing (NGS) technologies, such as Sanger sequencing and pyrosequencing, have played a pivotal role in genomics, improving throughput, coverage, and accuracy (Sanger, et al., 1977, Margulies, et al., 2005, Bentley, et al., 2008, Rothberg, et al., 2011, Goodwin, et al., 2016). NanoPore sequencing has also provided an advanced and robust technology, offering high-throughput, real-time, long-read, and large-scale DNA sequencing (Cherf, et al., 2012).

Transcriptomics

Transcriptomics emerged alongside DNA microarrays for studying gene expression changes (Taub E, et al., 1983). It enabled the investigation of global mRNA abundance changes, such as in *E. coli* under different stresses (Khodursky, et al., 2000). RNA sequencing (RNA-Seq) subsequently emerged as a deep-sequencing approach to deduce and quantify the transcriptome (Bainbridge, et al., 2006, Nagalakshmi, et al., 2008, Wang, et al., 2009). These methodologies find applications in ensuring the quality control of DNA designs, engineered pathways, and strains. However, it is important to note that continuous mRNA decay can introduce distortions in quantification and differential expression transcriptome analyses (Robles, et al., 2012, Herzel, et al., 2022). High-resolution transcriptomic profiling can combine RNA-Seq and DNA microarrays (Kogenaru, et al., 2012). Recent studies employed poly(A)-independent single-cell RNA sequencing to capture growth-dependent expression

patterns in individual bacteria across all RNA classes and genomic regions (Imdahl, et al., 2020).

Proteomics

In proteomics, mass spectrometry (MS) has greatly improved protein detection and quantification (Aebersold and Mann, 2003, Silva, et al., 2006). Targeted proteomics, employing selected- and multiple-reaction monitoring (SRM/MRM) after liquid chromatography (LC) separation, enables absolute protein quantification (Picotti, et al., 2009, Redding-Johanson, et al., 2011, Picotti and Aebersold, 2012). Data-dependent analysis (DDA) and data-independent acquisition (DIA) have been used for effective spectra acquisition, with DIA providing higher sensitivity and reproducibility (Stahl, et al., 1996, Venable, et al., 2004). OpenSWATH utilizes Sequential Window Acquisition of All Theoretical Mass Spectra (SWATH-MS) for automated and high-throughput analysis (Gillet, et al., 2012). Deep neural networks combined with DIA enhance peptide identification and coverage when paired with rapid chromatographic methods (Demichev, et al., 2020). Single-cell proteomics has emerged as an attractive development in transcriptomics; however, it faces limited sensitivity (Kelly, 2020). To address this, novel approaches with higher sensitivity and multiplexing capacity have been proposed for single-cell proteomic analysis. A pioneering study explored the single-cell transcriptome and proteome of *E. coli*, demonstrating the applicability of these approaches (Taniguchi, et al., 2010). These methods can also be applied to more complex systems, as demonstrated by mapping query datasets onto a reference proteome atlas (Lotfollahi, et al., 2022).

Metabolomics

Metabolomics provides essential information about overall physiology, including metabolite accumulation and depletion in response to genetic and environmental perturbations. Historically, high-pressure liquid chromatography (HPLC) has replaced thin-layer chromatography (TLC), and tandem MS has replaced ultraviolet and flame-ionization detection, driving advancements in metabolomics (Brotherton and Yost, 1983). Improvements in LC and MS technologies have led to faster separation, higher sensitivity, resolution, and dynamic detection ranges (Miggiels, et al., 2019). Dedicated methodologies, such as LC, hydrophilic interaction LC, reversed-phase ion pairing chromatography, gas chromatography (GC) coupled to MS, nuclear

magnetic resonance (NMR), and flow-injection MS, are used to measure the metabolome space (Bajad, et al., 2006, Coulier, et al., 2006, Wishart, 2008, Fuhrer, et al., 2011, Koek, et al., 2011, Beale, et al., 2018). Metabolomics can be targeted or non-targeted, each with advantages and disadvantages. Non-targeted metabolomics detects all measurable metabolites but generates complex datasets, while targeted metabolomics selects analytes of interest for higher sensitivity and precision (Ribbenstedt, et al., 2018). Technical advances in high-resolution tandem MS (HRMS) have enabled the integration of target and non-targeted metabolomics, facilitating metabolite discovery, identification, and quantification (Ramanathan, et al., 2011, Zhou, et al., 2016). Big data repositories and improved algorithms have also aided identification in untargeted metabolomics (Haug, et al., 2013, Teoh, et al., 2015, Blaženović, et al., 2018). The combination of metabolomics methodologies accelerate the DBTL cycle by providing fundamental information about the host metabolome landscape and its response to perturbations (Calero, et al., 2022).

Fluxomics

Metabolic fluxes cannot be measured directly, but they can be assessed through changes in metabolite concentrations or by detecting isotope distribution upon feeding isotopic labeled precursors (e.g. ^{13}C-labelled substrates). Fluxomics, based on the same detection methods as metabolomics, involves quantifying isotopologues. Flux balance analysis (FBA) and isotope tracer experiments have contributed to the development of fluxomics (Varma and Palsson, 1994, Marx, et al., 1996, Vallino and Stephanopoulos, 2000). Access to fluxomics protocols has been facilitated by publicly-available software, leading to wider implementation (Antoniewicz, et al., 2007, Zamboni, et al., 2009, Young, 2014). High-throughput approaches have been made possible through automated and downscaled fluxomics (Heux, et al., 2014). Fluxomics has the potential to become a central analytical approach for exploring cell factory performance in the DBTLc (Kohlstedt, et al., 2010). **Figure 1.2** (Test) provides an overview of the main technologies developed in the omics field.

Learn

SynBio utilizes both mechanistic and ML models to analyze omics data and enhance strain engineering in the DBTLc. Mechanistic models represent biological components

and interactions, promoting interpretability and transparency. ML techniques identify differentiating features among strains and conditions, improving the accuracy of mechanistic models by addressing missing or inaccurate components. They also assist in experimental design based on data, model topology, and simulations. While ML models may lack interpretability and complete explainability, they aid in understanding omics data and advancing biological knowledge. **Figure 1.2** (Learn) provides a visual summary of key advancements in mechanistic modeling and ML in SynBio. The inclusion of enzyme production costs in mass balance calculations enhances the accuracy of pathway utilization predictions, but it also presents computational challenges. Metabolic flux analysis derives fluxes from isotope labeling experiments, guiding engineering strategies. Recent advancements in MFA include enhanced analytics, model reduction, and genome-wide atom transfer prediction algorithms (Zamboni, et al., 2005, Ravikirthi, et al., 2011, Crown and Antoniewicz, 2012, Buescher, et al., 2015, McCloskey, et al., 2016).

DBTLc was developed as part of the bio-based industry's efforts to expedite the development of cell factories. The primary objective of this methodological framework, both in industry and academia, is to optimize workflows for creating efficient and robust microbial platforms capable of sustainable chemical production. Additionally, the process of reprogramming cells not only provides valuable insights into the intricacies of living systems but also stimulates subsequent cycles of engineering. This approach aims to establish overarching principles for biodesign, applicable across different organisms, enabling the reprogramming of cells for various biotechnological and biomedical applications.

On the other hand, this cycle offers an incredible capability of generating fundamental knowledge that can be employed to improve and establish novel cell factories. However, a significant constraint arises as this knowledge is not directly transferred into the final prototype. There is a need for a more rational integration process to ensure coherence within the different datasets, particularly when the final phenotype relies on a faithful representation of the system-level interconnections among various cellular layers. The field of systems biology offers promising approaches to bridge the gap between the knowledge gathered, for instance, in the DBTLc and, the practical biological application. Based on the latter fact, we decided to develop an integrative

platform for system-biology analysis (**Chapter 2** and **Chapter 3**) which aims to provide a comprehensive understanding of biological systems, thereby enhancing the DBTLc workflow and facilitating the translation of this knowledge into practical applications.

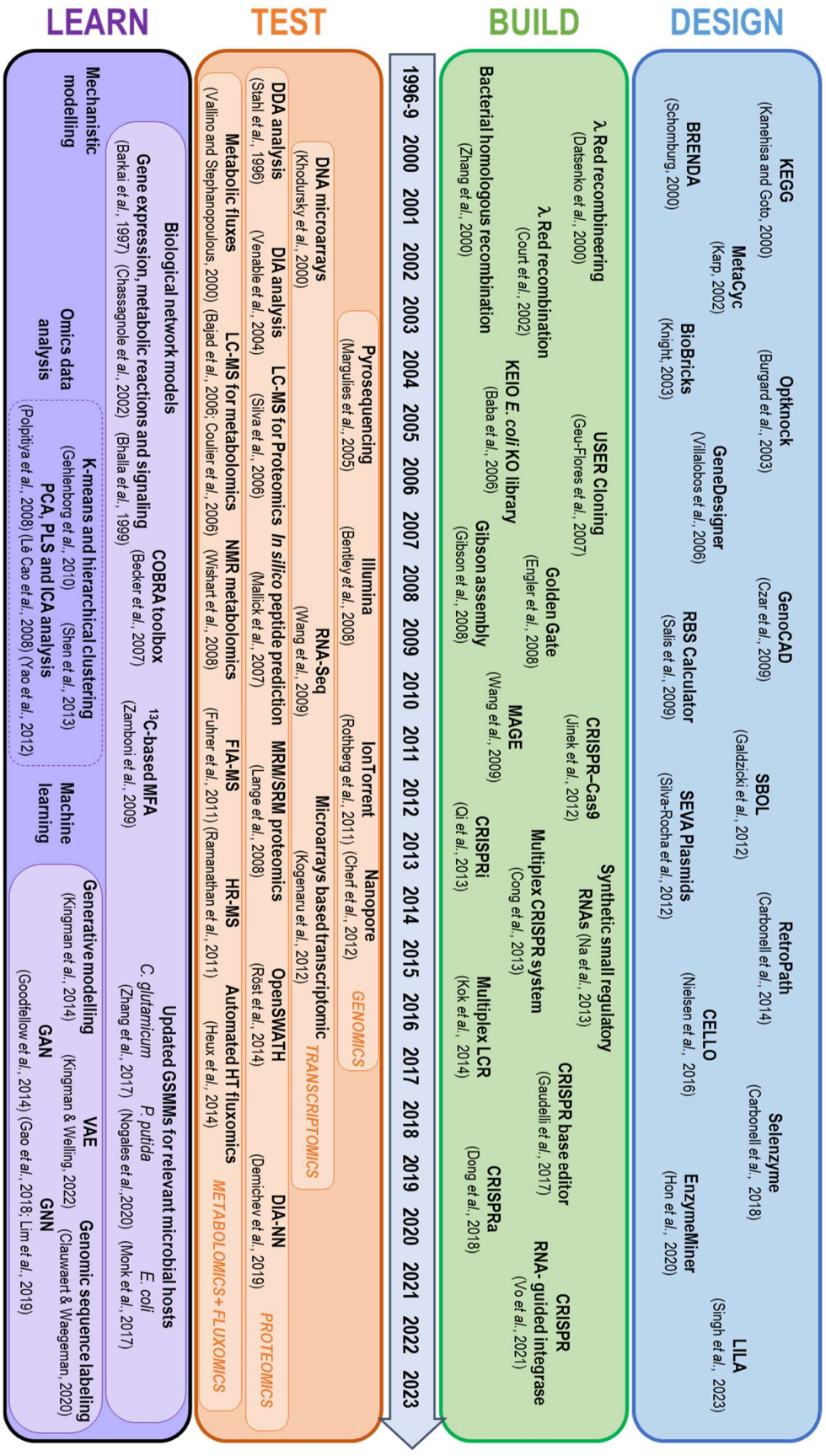
DESIGN
BUILD
TEST
LEARN
KEGG (Kanehisa and Goto, 2000)
MetaCyc (Karp, 2002)
BRENDA (Schomburg, 2000)
BioBricks (Knight, 2003)
Optknock (Burgard et al., 2003)
GeneDesigner (Villalobos et al., 2006)
GenoCAD (Czar et al., 2009)
RBS Calculator (Salis et al., 2009)
SBOL (Galdzicki et al., 2012)
SEVA Plasmids (Silva-Rocha et al., 2012)
RetroPath (Carbonell et al., 2014)
CELLO (Nielsen et al., 2016)
Selenzyme (Carbonell et al., 2018)
EnzymeMiner (Hon et al., 2020)
LILA (Singh et al., 2023)
λ Red recombineering (Datsenko et al., 2000)
λ Red recombination (Court et al., 2002)
Bacterial homologous recombination (Zhang et al., 2000)
USER Cloning (Geu-Flores et al., 2007)
KEIO E. coli KO library (Baba et al., 2006)
Golden Gate (Engler et al., 2008)
Gibson assembly (Gibson et al., 2008)
CRISPR-Cas9 (Jinek et al., 2012)
MAGE (Wang et al., 2009)
Synthetic small regulatory RNAs (Na et al., 2013)
Multiplex CRISPR system (Cong et al., 2013)
CRISPRi (Qi et al., 2013)
CRISPR base editor (Gaudelli et al., 2017)
Multiplex LCR (Kok et al., 2014)
CRISPR-guided integrase (Vo et al., 2021)
CRISPRa (Dong et al., 2018)
1996-9 2000 2001 2002 2003 2004 2005 2006 2007 2008 2009 2010 2011 2012 2013 2014 2015 2016 2017 2018 2019 2020 2021 2022 2023
Pyrosequencing (Margulies et al., 2005)
Illumina (Bentley et al., 2008)
IonTorrent (Rothberg et al., 2011)
Nanopore (Cherf et al., 2012)
GENOMICS
DNA microarrays (Khodursky et al., 2000)
RNA-Seq (Wang et al., 2009)
Microarrays based transcriptomic (Kogenaru et al., 2012)
TRANSCRIPTOMICS
DDA analysis (Stahl et al., 1996)
DIA analysis (Venable et al., 2004)
LC-MS for Proteomics (Silva et al., 2006)
In silico peptide prediction (Mallick et al., 2007)
MRM/SRM proteomics (Lange et al., 2008)
OpenSWATH (Röst et al., 2014)
DIA-NN (Demichev et al., 2019)
PROTEOMICS
Metabolic fluxes (Vallino and Stephanopoulous, 2000)
LC-MS for metabolomics (Bajad et al., 2006; Coulier et al., 2006)
NMR metabolomics (Wishart et al., 2008)
FIA-MS (Fuhrer et al., 2011)
HR-MS (Ramanathan et al., 2011)
Automated HT fluxomics (Heux et al., 2014)
METABOLOMICS+ FLUXOMICS
Biological network models
Gene expression, metabolic reactions and signaling (Barkai et al., 1997)
COBRA toolbox (Becker et al., 2007)
13C-based MFA (Zamboni et al., 2009)
Updated GSMMs for relevant microbial hosts
C. glutamicum (Zhang et al., 2017)
P. putida (Nogales et al.,2020)
E. coli (Monk et al., 2017)
Mechanistic modelling
Omics data analysis
K-means and hierarchical clustering (Chassagnole et al., 2002)
(Gehlenborg et al., 2010)
PCA, PLS and ICA analysis (Bhalla et al., 1999)
(Shen et al., 2013)
(Polpitiya et al., 2008) (Lê Cao et al., 2008) (Yao et al., 2012)
Machine learning
Generative modelling
(Kingman et al., 2014)
VAE (Kingman & Welling, 2022)
Genomic sequence labeling (Clauwaert & Waegeman, 2020)
GAN (Goodfellow et al., 2014)
GNN (Gao et al., 2018; Lim et al., 2019)

Figure 1.2. DBTL cycle timeline. Selected technologies and approaches developed in the design-build-test-learn cycle of Synthetic Biology over the past 30 years (from left to right). The diagram illustrates some key breakthroughs in each stage of the design-build-test-learn cycle (DBTLc): Design (blue), Build (green), Test (orange) and Learn (purple). Each methodology is referred to (and explained in detail) in the text. Note that the list of examples is non-exhaustive due to space constraints; abbreviations are provided in the text.

1.3 Metabolism-centric approach concept as an integral component of the DBTLc

Expanding our understanding of microbial metabolism is crucial to broaden the range of microbial organisms that can be effectively utilized as cell factories. Many questions surrounding the impact of DNA modifications on phenotype and the intricate interactions within metabolic networks across different regulatory levels remain unresolved for most nontraditional microorganisms. To unravel the relationships between genotype and phenotype, two essential approaches are required.
Firstly, the utilization of synthetic biology tools that enable deliberate and targeted DNA modifications is necessary. Secondly, a comprehensive exploration of the dynamic behavior of metabolism is needed to establish links between physicochemical or biochemical disturbances and resulting changes in phenotype.

Currently, the primary focus of addressing these challenges lies in the development of innovative tools for engineering non-model microorganisms (Riley and Guss, 2021). There is a growing momentum in employing in-depth multi-omic analysis for microbial prototyping in model organisms, enabling the exploration of multiple layers of regulation within the cell with unprecedented detail (Robinson, et al., 2021). While these strategies are indispensable, they often fall short in fully investigating the potential of nontraditional microorganisms as platforms for bioproduction due to the lack of a comprehensive understanding of the entire biological system (Roy, et al., 2021).

Hence, a smart combination of rational design, integration of multi-omic data, predictive models, and automation is pivotal in constructing efficient cell factories while simultaneously expanding our fundamental knowledge while providing guidance for metabolic engineering endeavors.

Nontraditional hosts have emerged as viable alternatives for microbial candidates due to their unique or additional advantageous properties. These hosts exhibit improved performance in the production of specific compounds or demonstrate resilience in the face of harsh conditions commonly encountered in industrial-scale production. In **Chapter 5** of this thesis, we delved into the utilization of acetate as a carbon source by *Pseudomonas putida* under toxic conditions, investigating the mechanisms employed by this bacterium to overcome the challenges posed by this organic acid. Through this study, significant insights were gained into the metabolic response to acetate, thereby contributing to the fundamental understanding of its adaptive strategies in the face of acetate-induced stress.

Furthermore, nontraditional hosts offer the advantage of utilizing a wide range of conventional carbon sources, as glucose, xylose, fructose, lactose, cellobiose, acetate or alternative feedstocks, such as C1 compounds like CO_2 (Dvořák and de Lorenzo, 2018, Liew, et al., 2022), thereby avoiding competition with other industrial processes and food production. Among the numerous promising microorganisms, several bacterial species including *Streptomyces coelicolor*, *Clostridium acetobutylicum*, *Bacillus subtilis*, *Corynebacterium glutamicum*, and *Rhodococcus spp.*, as well as eukaryotes such as *Aspergillus sp.* and *Rhodotorula toruloides*, can be classified within the broad category of nontraditional bioproduction platforms.

The primary challenge in utilizing non-model organisms as *chassis* for bioproduction lies not only in the limited availability of genetic engineering tools but also in the lack of comprehensive information regarding their metabolic architectures and regulatory mechanisms. Therefore, in-depth analysis of metabolism under various environmental conditions, including genetic or chemical perturbations, is essential to gain insights into these metabolic architectures and their regulation. This information can then be used to determine the feasible metabolic landscape relevant to biotechnology applications.

Similar to how automation and synthetic biology synergistically enhance the speed and efficiency of constructing cell factories, the combination of automation and multi-omics analysis can significantly expand our knowledge of metabolic networks (Amer and Baidoo, 2021). Substantial progress has been achieved in the field of multi-omics as was explained in the previous Section 1.2. **Figure 1.3** illustrates the central concept of **metabolism-centric analysis** which couple accelerated genome engineering, multi-omics analysis, and automation to drive the DBTL (Design-Build-Test-Learn) cycle while addressing fundamental questions regarding microbial metabolism. This type of comprehensive multi-omic analysis is exemplified in certain applications that adopt a metabolism-centric view in different microorganisms. Notably, *Pseudomonas putida* has been employed as an ideal example in two cases. These examples involve a multi-omic exploration of (i) the utilization of δ-valerolactam (piperidin-2-one) as the sole carbon source and the catabolism of ε-caprolactam (azepan-2-one), and (ii) the intricate metabolism of fatty acids and alcohols (Thompson, et al., 2019, Thompson, et al., 2020).

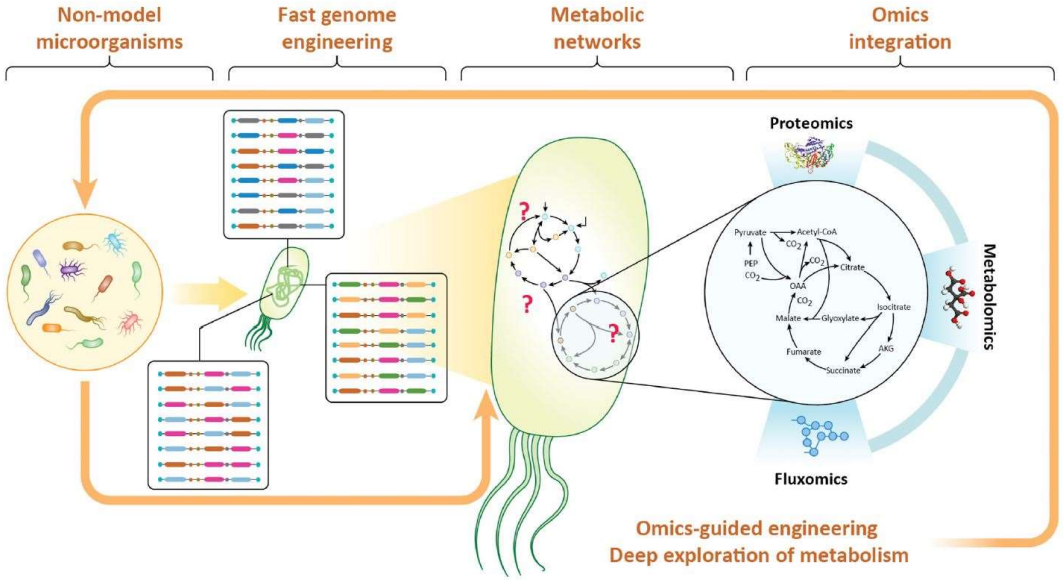

Figure 1.3. Metabolism-centric approach to the design–build–test–learn cycle of synthetic biology as supported by deep multi-omic analysis. The illustration depicts – from left to right – the general strategy to guide engineering steps while exploring fundamental aspects of metabolic architectures in nontraditional hosts as supported by fast genome engineering, multi-omics analyses, and automation.

1.4 *Pseudomonas putida*: Metabolic architecture and carbon metabolism

Given the increasing demand of more complex bioproducts as well as the appearance of novel microbial cell platforms with unique functionalities, there is a necessity to gather scientific insights and explore the metabolic capabilities of the host. This will enable the development of a systematic and well-organized approach for the efficient bioproduction of desired compounds. One example of these platforms, is the non-traditional Gram-negative host *Pseudomonas putida*, which is acknowledged for its adaptable and complex metabolic capabilities. Its unique cyclic core metabolism, regulated by redox demand, plays a crucial role in enabling high metabolic activity and tolerance (Nikel, et al., 2015). The core metabolic pathways of this microorganism have recently come under investigation, revealing its potential for the synthesis of new-to-nature compounds (Wirth and Nikel, 2021). A brief overview of the *P. putida´*s central carbon metabolism is presented, providing a general outline of its metabolic processes when consuming glucose as carbon source (**Figure 1.4).**

Glucose is transported into the cytoplasm or oxidized in the periplasm, leading to the formation of gluconate (Glnc) and 2-ketogluconate (2-KGA). These organic acids can enter the cytoplasm and be phosphorylated to form 6-phosphogluconate (6PG) and 6-phospho-2-ketogluconate (2-KGA-6P), which converge into 6PG (Castillo, et al., 2007). These oxidation pathways allow *P. putida* to bypass direct glucose uptake and partially decouple ATP production from NADH formation. Each oxidation step releases two electrons, coupled to ATP generation (Ebert, et al., 2011). When cells grown on glucose, it is observed that there is an excess production of ATP, wherein the oxidation pathway plays a substantial role in this process. *P. putida* has an incomplete glycolysis pathway due to the absence of 6-phosphofructo-1-kinase (Pfk). The central intermediate, 6PG, is mainly metabolized through the Entner-Doudoroff (ED) pathway, resulting in pyruvate (Pyr) and glyceraldehyde-3-P (G3P). A portion of pyruvate is recycled back to hexoses through the gluconeogenic EMP pathway, forming the EDEMP cycle. Hence, cyclic sugar catabolism in *P. putida* leads to a slight surplus generation of NADPH in cultures utilizing glucose as the carbon source. Although most of the studies on the EDEMP cycle has been conducted using model

carbon sources, it serves as the intrinsic metabolic hub in *P. putida*, being essential for the hierarchical consumption of sugars and aromatic substrates.

The most relevant characteristics of *P. putida* where exploited in this thesis and are summarized as follows:

a) *P. putida* exhibits rapid growth, high biomass yields, minimal to no secretion of by-products, and low maintenance demands. Moreover, the bacterium naturally maintains an excess production of ATP and high rates of NAD(P)H regeneration through the EDEMP (Entner-Doudoroff, Embden-Meyerhof-Parnas and PP pathways) overflow metabolism on hexoses. Furthermore, metabolic pathways can be rewired to support the EDEMP cycle and enable NAD(P)H overproduction from other gluconeogenic substrates, such as glycerol.

b) *P. putida* exhibits a regulatory system that endows it with remarkable adaptability to promptly react to dynamic circumstances, including external environmental factors or internal perturbations. As studied in **Chapter 6**, physiological analysis combined with fluxomics, metabolomics and proteomics elucidated a regulatory mechanism governing the perturbation in energy metabolism resulting from genetic disruptions in glucose phosphorylation and oxidation peripheral pathways. This integrative analysis provides valuable insights into the regulatory networks that orchestrate and modulate the impact of genetic disturbances on energy metabolism, shedding light on the underlying mechanisms that govern these processes. In **Chapter 7** of this thesis, we introduced a glycolytic module from *E. coli* into *P. putida* to reshape the bacterium metabolic *identity*. Through the utilization of adaptive laboratory evolution and systems biology methodologies, the rewiring of the central carbon metabolism (CCM) in the bacterium was comprehensively investigated. We showed how *P. putida* successfully accommodated the artificially implanted glycolytic device by regulating the level of CCM´s proteins and metabolic fluxes.

c) It exhibits a versatile catabolism of carbon sources: the substrate range of *P. putida* has been successfully expanded including sucrose, L-arabinose, D-cellobiose, D-xylose, phenol, ethylene glycol, and C1 compounds such as formate and CO_2, among others. In **Chapter 4** of this thesis, we conducted an in-depth investigation into the mechanism that leads to the diauxic shift phenomenon resulting from the exposure of bacteria to two distinct carbon sources: glucose, representing a glycolytic substrate, and citrate, representing a gluconeogenic substrate. Through this comprehensive

exploration, we enhanced our understanding of the metabolic pathways and mechanisms employed by the bacteria for the utilization of these two substrates.

d) *P. putida* demonstrates high tolerance to physicochemical stresses, chemical stresses (e.g., heavy metals and organic acids), solvents, and oxidative stress. This tolerance is attributed to an efficient regulatory machinery, secretion systems, trans-isomerization of the cell membrane. In **Chapter 5,** we focused our attention in the organic acid acetate where we explored how the bacterium can overcome the toxicity effects after being exposure upon high concentration of the C_2-molecule. Once again, a systems biology approach was adopted to unravel the underlying mechanisms of tolerance.

e) Lastly, *P. putida* naturally possesses an elevated GC content (~62%), making it suitable for the heterologous expression of genes from GC-rich microbes that harbor gene clusters responsible for secondary metabolite biosynthesis, such as Actinobacteria and Myxobacteria. In summary, owing to its numerous characteristics, *P. putida* is considered an excellent microbial host for industrial biotechnology applications.

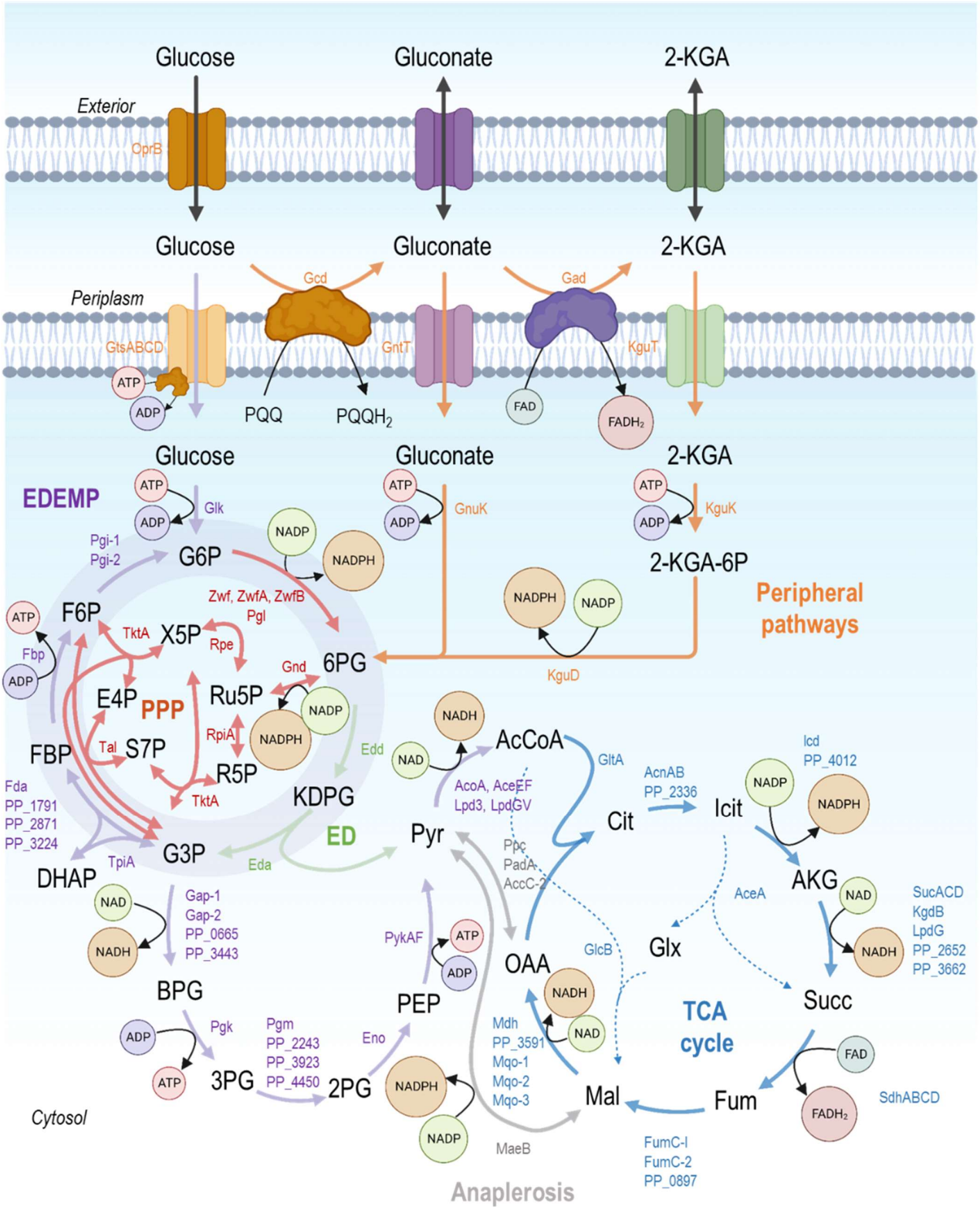
Glucose
Gluconate
2-KGA
Exterior
OprB
Periplasm
GtsABCD
ATP
ADP
Gcd
PQQ
PQQH2
GntT
Gad
FAD
FADH2
KguT
EDEMP
Glk
GnuK
KguK
2-KGA-6P
Peripheral pathways
KguD
G6P
Pgi-1
Pgi-2
NADP
NADPH
Zwf, ZwfA, ZwfB
Pgl
F6P
Fbp
TktA
X5P
Rpe
6PG
Gnd
E4P
PPP
Ru5P
RpiA
FBP
Tal
S7P
R5P
Edd
KDPG
ED
Fda
PP_1791
PP_2871
PP_3224
G3P
TpiA
Eda
DHAP
Gap-1
Gap-2
PP_0665
PP_3443
NAD
NADH
BPG
Pgk
3PG
Pgm
PP_2243
PP_3923
PP_4450
2PG
Eno
PEP
PykAF
Pyr
AcCoA
AcoA, AceEF
Lpd3, LpdGV
GltA
Cit
AcnAB
PP_2336
Icit
Icd
PP_4012
Ppc
PadA
AccC-2
AceA
AKG
SucACD
KgdB
LpdG
PP_2652
PP_3662
Glx
GlcB
OAA
Mdh
PP_3591
Mqo-1
Mqo-2
Mqo-3
TCA cycle
Succ
Mal
Fum
FumC-I
FumC-2
PP_0897
SdhABCD
MaeB
Anaplerosis
Cytosol

Figure 1.4. Architecture of *Pseudomonas putida* KT2440 central carbon metabolism. Metabolic blocks are identified using different colors: Peripheral pathways (Orange), EDEMP (Purple), PPP-Pentose Phosphate Pathway (Vermillion), ED-Entner-Doudoroff Pathway (Green), TCA cycle (Blue) and Anaplerosis (Grey). Abbreviation of metabolites are as follows: G6P, glucose-6-P; F6P, fructose-6-P; FBP, fructose-1,6-P2; DHAP, dihydroxyacetone-P; 6PG, 6-phosphogluconate; KDPG, 2-keto-3-deoxy-6-phosphogluconate; Ru5P, ribulose-5-P; R5P, ribose-5-P; Xu5P, xylulose-5-P; S7P, sedoheptulose-7-P; E4P, erythrose-4-P; G3P, glyceraldehyde-3-P; 2PG, glycerate-2-P; PEP, phosphoenolpyruvate; Pyr, pyruvate; AcCoA, acetyl-coenzyme A; OAA, oxaloacetate; 2-KGA-6P, 2-ketogluconate-6-phosphate; Cit, citrate; Icit, isocitrate; AKG, 2-oxoglutarate; Succ, succinate; Fum, fumarate; Mal, malate; Glx, glyoxylate. Abbreviations for enzymes: EDEMP enzymes: Glucose kinase (Glk); Glucose-6-*P* isomerase-1 (Pgi-1); Glucose-6-*P* isomerase-2 (Pgi-2); 6-phosphogluconate dehydratase (Edd); 2-dehydro-3-deoxy-6-phosphogluconate aldolase (Eda); Fructose-1,6-*P2* phosphatase (Fbp); Fructose-1,6-P_2 aldolase (Fda); Triosephosphate isomerase (TpiA); Glyceraldehyde-3-P dehydrogenase-1 (Gap-1); Glyceraldehyde-3-P dehydrogenase-2 (Gap-2); Phosphoglycerate kinase (Pgk); Phosphoglycerate mutase (Pgm); Enolase (Eno); Pyruvate kinase (PykA); Pyruvate kinase complex (PykAF). PP pathway enzymes: Glucose-6-*P* dehydrogenase-1 (Zwf); Glucose-6-*P* dehydrogenase-2 (ZwfA); Glucose-6-*P* dehydrogenase-3 (ZwfB); Phosphogluconolactonase (Pgl); Phosphogluconate dehydrogenase (Gnd); Ribose-5-P isomerase (Rpi); Ribulose-5-P 3-epimerase (Rpe); Transketolase (Tkt); Transaldolase (Tal). TCA cycle enzymes: AceF, Acetyltransferase component of pyruvate dehydrogenase complex; Lpd, Dihydrolipoyl dehydrogenase; AceE, Pyruvate dehydrogenase E1 component; LpdG, Dihydrolipoyl dehydrogenase G; GltA, Citrate synthase; AcnA-I, Aconitate hydratase I; AcnA-II, Aconitate hydratase II; AcnB, Aconitate hydratase B; Icd, Isocitrate dehydrogenase [NADP]; SucA, Oxoglutarate dehydrogenase (succinyl-transferring); SucC, Succinate-CoA ligase [ADP-forming] subunit beta; SucD, Succinate-CoA ligase [ADP-forming] subunit alpha; SdhA, Succinate dehydrogenase flavoprotein subunit; SdhB, Succinate dehydrogenase iron-sulfur subunit; FumC, Fumarate hydratase class II; Mqo-1, Malate:quinone oxidoreductase 1; Mqo-2, Malate:quinone oxidoreductase 2; Mqo-3, Malate:quinone oxidoreductase 3; AceA, Isocitrase; GlcB, Malate synthase. Adapted from (Nikel, et al., 2015).

References Chapter 1

Adrio, J.-L., and Demain, A.L. (2010) Recombinant organisms for production of industrial products, *Bioengineered bugs* **1**: 116-131.

Aebersold, R., and Mann, M. (2003) Mass spectrometry-based proteomics, *Nature* **422**: 198-207.

Amer, B., and Baidoo, E.E.K. (2021) Omics-Driven Biotechnology for Industrial Applications, *Frontiers in Bioengineering and Biotechnology* **9**: 613307.

Antoniewicz, M.R., Kelleher, J.K., and Stephanopoulos, G. (2007) Elementary metabolite units (EMU): A novel framework for modeling isotopic distributions, *Metabolic Engineering* **9**: 68-86.

Baba, T., Ara, T., Hasegawa, M., Takai, Y., Okumura, Y., Baba, M., et al. (2006) Construction of *Escherichia coli* K-12 in-frame, single-gene knockout mutants: the Keio collection, *Molecular Systems Biology* **2**: 2006.0008.

Bainbridge, M.N., Warren, R.L., Hirst, M., Romanuik, T., Zeng, T., Go, A., et al. (2006) Analysis of the prostate cancer cell line LNCaP transcriptome using a sequencing-by-synthesis approach, *BMC Genomics* **7**: 246.

Bajad, S.U., Lu, W., Kimball, E.H., Yuan, J., Peterson, C., and Rabinowitz, J.D. (2006) Separation and quantitation of water soluble cellular metabolites by hydrophilic interaction chromatography-tandem mass spectrometry, *Journal of Chromatography A* **1125**: 76-88.

Bansal, A.K. (2005) Bioinformatics in microbial biotechnology–a mini review, *Microbial Cell Factories* **4**: 1-11.

Batianis, C., Kozaeva, E., Damalas, S.G., Martín-Pascual, M., Volke, D.C., Nikel, P.I., and Martins dos Santos, V.A.P. (2020) An expanded CRISPRi toolbox for tunable control of gene expression in *Pseudomonas putida*, *Microbial Biotechnology* **13**: 368-385.

Beale, D.J., Pinu, F.R., Kouremenos, K.A., Poojary, M.M., Narayana, V.K., Boughton, B.A., et al. (2018) Review of recent developments in GC–MS approaches to metabolomics-based research, *Metabolomics* **14**: 152-152.

Becker, J., and Wittmann, C. (2018) From systems biology to metabolically engineered cells — an omics perspective on the development of industrial microbes, *Current Opinion in Microbiology* **45**: 180-188.

Benner, S.A., and Sismour, A.M. (2005) Synthetic biology, *Nature reviews genetics* **6**: 533-543.

Bentley, D.R., Balasubramanian, S., Swerdlow, H.P., Smith, G.P., Milton, J., Brown, C.G., et al. (2008) Accurate whole human genome sequencing using reversible terminator chemistry, *Nature* **456**: 53-59.

Blaženović, I., Kind, T., Ji, J., and Fiehn, O. (2018) Software Tools and Approaches for Compound Identification of LC-MS/MS Data in Metabolomics, *Metabolites* **8(2):31**.

Blombach, B., Grünberger, A., Centler, F., Wierckx, N., and Schmid, J. (2021) Exploiting unconventional prokaryotic hosts for industrial biotechnology, *Trends in Biotechnology*.

Brotherton, H.O., and Yost, R.A. (1983) Determination of drugs in blood serum by mass spectrometry/mass spectrometry, *Analytical chemistry* **55**: 549-553.

Buescher, J.M., Antoniewicz, M.R., Boros, L.G., Burgess, S.C., Brunengraber, H., Clish, C.B., et al. (2015) A roadmap for interpreting 13C metabolite labeling patterns from cells, *Current Opinion in Biotechnology* **34**: 189-201.

Burgard, A.P., Pharkya, P., and Maranas, C.D. (2003) Optknock: A bilevel programming framework for identifying gene knockout strategies for microbial strain optimization, *Biotechnology and Bioengineering* **84**: 647-657.

Calero, P., Gurdo, N., and Nikel, P.I. (2022) Role of the CrcB transporter of *Pseudomonas putida* in the multi-level stress response elicited by mineral fluoride, *Environmental Microbiology* **24**: 5082-5104.

Carbonell, P., Jervis, A.J., Robinson, C.J., Yan, C., Dunstan, M., Swainston, N., et al. (2018) An automated Design-Build-Test-Learn pipeline for enhanced microbial production of fine chemicals, *Communications Biology* **1**: 66-66.

Carbonell, P., Parutto, P., Baudier, C., Junot, C., and Faulon, J.-L. (2014) Retropath: Automated Pipeline for Embedded Metabolic Circuits, *ACS Synthetic Biology* **3**: 565-577.

Carbonell, P., Wong, J., Swainston, N., Takano, E., Turner, N.J., Scrutton, N.S., et al. (2018) Selenzyme: enzyme selection tool for pathway design, *Bioinformatics* **34**: 2153-2154.

Castillo, T.d., Ramos, J.L., Rodríguez-Herva, J.J., Fuhrer, T., Sauer, U., and Duque, E. (2007) Convergent Peripheral Pathways Catalyze Initial Glucose Catabolism in *Pseudomonas putida*: Genomic and Flux Analysis, *Journal of Bacteriology* **189**: 5142-5152.

Cherf, G.M., Lieberman, K.R., Rashid, H., Lam, C.E., Karplus, K., and Akeson, M. (2012) Automated forward and reverse ratcheting of DNA in a nanopore at 5-Å precision, *Nature Biotechnology* **30**: 344-348.

Clark, D.P., and Pazdernik, N.J. (2015) *Biotechnology*: Newnes.

Cong, L., Ran, F.A., Cox, D., Lin, S., Barretto, R., Habib, N., et al. (2013) Multiplex Genome Engineering Using CRISPR/Cas Systems, *Science* **339**: 819-823.

Coulier, L., Bas, R., Jespersen, S., Verheij, E., van der Werf, M.J., and Hankemeier, T. (2006) Simultaneous quantitative analysis of metabolites using ion-pair liquid chromatography− electrospray ionization mass spectrometry, *Analytical chemistry* **78**: 6573-6582.

Court, D.L., Sawitzke, J.A., and Thomason, L.C. (2002) Genetic Engineering Using Homologous Recombination, *Annual Review of Genetics* **36**: 361-388.

Crown, S.B., and Antoniewicz, M.R. (2012) Selection of tracers for 13C-Metabolic Flux Analysis using Elementary Metabolite Units (EMU) basis vector methodology, *Metabolic Engineering* **14**: 150-161.

Datsenko, K.A., and Wanner, B.L. (2000) One-step inactivation of chromosomal genes in Escherichia coli K-12 using PCR products, *Proceedings of the National Academy of Sciences* **97**: 6640-6645.

Demichev, V., Messner, C.B., Vernardis, S.I., Lilley, K.S., and Ralser, M. (2020) DIA-NN: neural networks and interference correction enable deep proteome coverage in high throughput, *Nature Methods* **17**: 41-44.

Dettmer, K., Aronov, P.A., and Hammock, B.D. (2007) Mass spectrometry-based metabolomics, *Mass spectrometry reviews* **26**: 51-78.

Domon, B., and Aebersold, R. (2006) Mass spectrometry and protein analysis, *science* **312**: 212-217.

Dvořák, P., and de Lorenzo, V. (2018) Refactoring the upper sugar metabolism of *Pseudomonas putida* for co-utilization of cellobiose, xylose, and glucose, *Metabolic Engineering* **48**: 94-108.

Ebert, B.E., Kurth, F., Grund, M., Blank, L.M., and Schmid, A. (2011) Response of *Pseudomonas putida* KT2440 to increased NADH and ATP demand, *Appl Environ Microbiol* **77**: 6597-6605.

Engler, C., Kandzia, R., and Marillonnet, S. (2008) A One Pot, One Step, Precision Cloning Method with High Throughput Capability, *PLoS ONE* **3**: e3647-e3647.

Fuhrer, T., Heer, D., Begemann, B., and Zamboni, N. (2011) High-Throughput, Accurate Mass Metabolome Profiling of Cellular Extracts by Flow Injection–Time-of-Flight Mass Spectrometry, *Analytical Chemistry* **83**: 7074-7080.

Galdzicki, M., Wilson, M., Rodriguez, C.A., Pocock, M.R., Oberortner, E., Adam, L., et al. (2012) Synthetic biology open language (SBOL) version 1.1. 0.

Garst, A.D., Bassalo, M.C., Pines, G., Lynch, S.A., Halweg-Edwards, A.L., Liu, R., et al. (2017) Genome-wide mapping of mutations at single-nucleotide resolution for protein, metabolic and genome engineering, *Nature Biotechnology* **35**: 48-55.

Gaudelli, N.M., Komor, A.C., Rees, H.A., Packer, M.S., Badran, A.H., Bryson, D.I., and Liu, D.R. (2017) Programmable base editing of A•T to G•C in genomic DNA without DNA cleavage, *Nature* **551**: 464-471.

Geu-Flores, F., Nour-Eldin, H.H., Nielsen, M.T., and Halkier, B.A. (2007) USER fusion: a rapid and efficient method for simultaneous fusion and cloning of multiple PCR products, *Nucleic Acids Research* **35**: e55-e55.

Gibson, D.G., Benders, G.A., Axelrod, K.C., Zaveri, J., Algire, M.A., Moodie, M., et al. (2008) One-step assembly in yeast of 25 overlapping DNA fragments to form a complete synthetic *Mycoplasma genitalium* genome, *Proceedings of the National Academy of Sciences* **105**: 20404-20409.

Gillet, L.C., Navarro, P., Tate, S., Röst, H., Selevsek, N., Reiter, L., et al. (2012) Targeted data extraction of the MS/MS spectra generated by data-independent acquisition: a new concept for consistent and accurate proteome analysis, *Molecular & Cellular Proteomics* **11**.

Goodwin, S., McPherson, J.D., and McCombie, W.R. (2016) Coming of age: ten years of next-generation sequencing technologies, *Nature Reviews Genetics* **17**: 333-351.

Gurdo, N., Volke, D.C., McCloskey, D., and Nikel, P.I. (2023) Automating the design-build-test-learn cycle towards next-generation bacterial cell factories, *New Biotechnology* **74**: 1-15.

Haug, K., Salek, R.M., Conesa, P., Hastings, J., de Matos, P., Rijnbeek, M., et al. (2013) MetaboLights--an open-access general-purpose repository for metabolomics studies and associated meta-data, *Nucleic acids research* **41**: D781-D786.

Herzel, L., Stanley, J.A., Yao, C.-C., and Li, G.-W. (2022) Ubiquitous mRNA decay fragments in *E. coli* redefine the functional transcriptome, *Nucleic Acids Research* **50**: 5029-5046.

Heux, S., Poinot, J., Massou, S., Sokol, S., and Portais, J.-C. (2014) A novel platform for automated high-throughput fluxome profiling of metabolic variants, *Metabolic Engineering* **25**: 8-19.

Hoang, T.T., Karkhoff-Schweizer, R.R., Kutchma, A.J., and Schweizer, H.P. (1998) A broad-host-range Flp-FRT recombination system for site-specific excision of chromosomally-located DNA sequences: application for isolation of unmarked Pseudomonas aeruginosa mutants, *Gene* **212**: 77-86.

Hon, J., Borko, S., Stourac, J., Prokop, Z., Zendulka, J., Bednar, D., et al. (2020) EnzymeMiner: automated mining of soluble enzymes with diverse structures, catalytic properties and stabilities, *Nucleic Acids Research* **48**: W104-W109.

Imdahl, F., Vafadarnejad, E., Homberger, C., Saliba, A.-E., and Vogel, J. (2020) Single-cell RNA-sequencing reports growth-condition-specific global transcriptomes of individual bacteria, *Nature Microbiology* **5**: 1202-1206.

Jakočiūnas, T., Jensen, M.K., and Keasling, J.D. (2017) System-level perturbations of cell metabolism using CRISPR/Cas9, *Current Opinion in Biotechnology* **46**: 134-140.

Jinek, M., Chylinski, K., Fonfara, I., Hauer, M., Doudna, J.A., and Charpentier, E. (2012) A Programmable Dual-RNA-Guided DNA Endonuclease in Adaptive Bacterial Immunity, *Science* **337**: 816-821.

Kanehisa, M., and Bork, P. (2003) Bioinformatics in the post-sequence era, *Nature genetics* **33**: 305-310.

Kanehisa, M., and Goto, S. KEGG: Kyoto Encyclopedia of Genes and Genomes: 4-4.

Karp, P.D. (2002) The MetaCyc Database, *Nucleic Acids Research* **30**: 59-61.

Kelly, R.T. (2020) Single-cell proteomics: progress and prospects, *Molecular & Cellular Proteomics* **19**: 1739-1748.

Khodursky, A.B., Peter, B.J., Cozzarelli, N.R., Botstein, D., Brown, P.O., and Yanofsky, C. (2000) DNA microarray analysis of gene expression in response to physiological and genetic changes that affect tryptophan metabolism in *Escherichia coli*, *Proceedings of the National Academy of Sciences* **97**: 12170-12175.

Knight, T. (2003) Idempotent Vector Design for Standard Assembly of Biobricks. Fort Belvoir, VA: Defense Technical Information Center.

Ko, Y.-S., Kim, J.W., Lee, J.A., Han, T., Kim, G.B., Park, J.E., and Lee, S.Y. (2020) Tools and strategies of systems metabolic engineering for the development of microbial cell factories for chemical production, *Chemical Society Reviews* **49**: 4615-4636.

Koek, M.M., Jellema, R.H., van der Greef, J., Tas, A.C., and Hankemeier, T. (2011) Quantitative metabolomics based on gas chromatography mass spectrometry: status and perspectives, *Metabolomics* **7**: 307-328.

Kogenaru, S., Qing, Y., Guo, Y., and Wang, N. (2012) RNA-seq and microarray complement each other in transcriptome profiling, *BMC Genomics* **13**: 629-629.

Kohlstedt, M., Becker, J., and Wittmann, C. (2010) Metabolic fluxes and beyond—systems biology understanding and engineering of microbial metabolism, *Applied Microbiology and Biotechnology* **88**: 1065-1075.

Kok, S.d., Stanton, L.H., Slaby, T., Durot, M., Holmes, V.F., Patel, K.G., et al. (2014) Rapid and Reliable DNA Assembly *via* Ligase Cycling Reaction, *ACS Synthetic Biology* **3**: 97-106.

Komor, A.C., Kim, Y.B., Packer, M.S., Zuris, J.A., and Liu, D.R. (2016) Programmable editing of a target base in genomic DNA without double-stranded DNA cleavage, *Nature* **533**: 420-424.

Lee, S.Y., Lee, D.-Y., and Kim, T.Y. (2005) Systems biotechnology for strain improvement, *Trends in Biotechnology* **23**: 349-358.

Liew, F.E., Nogle, R., Abdalla, T., Rasor, B.J., Canter, C., Jensen, R.O., et al. (2022) Carbon-negative production of acetone and isopropanol by gas fermentation at industrial pilot scale, *Nature Biotechnology* **40**: 335-344.

Lotfollahi, M., Naghipourfar, M., Luecken, M.D., Khajavi, M., Büttner, M., Wagenstetter, M., et al. (2022) Mapping single-cell data to reference atlases by transfer learning, *Nature Biotechnology* **40**: 121-130.

Luo, Z.W., and Lee, S.Y. (2020) Metabolic engineering of *Escherichia coli* for the production of benzoic acid from glucose, *Metabolic Engineering* **62**: 298-311.

Madsen, C., Goñi Moreno, A., P, U., Palchick, Z., Roehner, N., Atallah, C., et al. (2019) Synthetic Biology Open Language (SBOL) Version 2.3, *Journal of Integrative Bioinformatics* **16**.

Maia, P., Rocha, M., and Rocha, I. (2016) *In Silico* Constraint-Based Strain Optimization Methods: the Quest for Optimal Cell Factories, *Microbiology and Molecular Biology Reviews* **80**: 45-67.

Margulies, M., Egholm, M., Altman, W.E., Attiya, S., Bader, J.S., Bemben, L.A., et al. (2005) Genome sequencing in microfabricated high-density picolitre reactors, *Nature* **437**: 376-380.

Martínez-García, E., Fraile, S., Algar, E., Aparicio, T., Velázquez, E., Calles, B., et al. (2022) SEVA 4.0: an update of the Standard European Vector Architecture database for advanced analysis and programming of bacterial phenotypes, *Nucleic Acids Research* **51**: D1558-D1567.

Marx, A., de Graaf, A.A., Wiechert, W., Eggeling, L., and Sahm, H. (1996) Determination of the fluxes in the central metabolism of *Corynebacterium glutamicum* by nuclear magnetic resonance spectroscopy combined with metabolite balancing, *Biotechnology and Bioengineering* **49**: 111-129.

McCloskey, D., Young, J.D., Xu, S., Palsson, B.O., and Feist, A.M. (2016) MID Max: LC–MS/MS Method for Measuring the Precursor and Product Mass Isotopomer Distributions of Metabolic Intermediates and Cofactors for Metabolic Flux Analysis Applications, *Anal. Chem.*: 9-9.

Miggiels, P., Wouters, B., van Westen, G.J., Dubbelman, A.-C., and Hankemeier, T. (2019) Novel technologies for metabolomics: More for less, *TrAC Trends in Analytical Chemistry* **120**: 115323.

Na, D., Yoo, S.M., Chung, H., Park, H., Park, J.H., and Lee, S.Y. (2013) Metabolic engineering of *Escherichia coli* using synthetic small regulatory RNAs, *Nature Biotechnology* **31**: 170-174.

Nagalakshmi, U., Wang, Z., Waern, K., Shou, C., Raha, D., Gerstein, M., and Snyder, M. (2008) The Transcriptional Landscape of the Yeast Genome Defined by RNA Sequencing, *Science* **320**: 1344-1349.

Nielsen, A.A.K., Der, B.S., Shin, J., Vaidyanathan, P., Paralanov, V., Strychalski, E.A., et al. (2016) Genetic circuit design automation, *Science* **352**: aac7341.

Nikel, P.I., Chavarría, M., Fuhrer, T., Sauer, U., and de Lorenzo, V. (2015) *Pseudomonas putida* KT2440 Strain Metabolizes Glucose through a Cycle Formed by Enzymes of the Entner-Doudoroff, Embden-Meyerhof-Parnas, and Pentose Phosphate Pathways, *J Biol Chem* **290**: 25920-25932.

Picotti, P., and Aebersold, R. (2012) Selected reaction monitoring–based proteomics: workflows, potential, pitfalls and future directions, *Nature Methods* **9**: 555-566.

Picotti, P., Bodenmiller, B., Mueller, L.N., Domon, B., and Aebersold, R. (2009) Full Dynamic Range Proteome Analysis of S. cerevisiae by Targeted Proteomics, *Cell* **138**: 795-806.

Pyne, M.E., Moo-Young, M., Chung, D.A., and Chou, C.P. (2015) Coupling the CRISPR/Cas9 System with Lambda Red Recombineering Enables Simplified Chromosomal Gene Replacement in *Escherichia coli*, *Applied and Environmental Microbiology* **81**: 5103 LP-5114.

Qi, Lei S., Larson, Matthew H., Gilbert, Luke A., Doudna, Jennifer A., Weissman, Jonathan S., Arkin, Adam P., and Lim, Wendell A. (2013) Repurposing CRISPR as an RNA-Guided Platform for Sequence-Specific Control of Gene Expression, *Cell* **152**: 1173-1183.

Ramanathan, R., Jemal, M., Ramagiri, S., Xia, Y.-Q., Humpreys, W.G., Olah, T., and Korfmacher, W.A. (2011) It is time for a paradigm shift in drug discovery bioanalysis: from SRM to HRMS, *Journal of Mass Spectrometry* **46**: 595-601.

Ravikirthi, P., Suthers, P.F., and Maranas, C.D. (2011) Construction of an *E. coli* genome-scale atom mapping model for MFA calculations, *Biotechnology and Bioengineering* **108**: 1372-1382.

Redding-Johanson, A.M., Batth, T.S., Chan, R., Krupa, R., Szmidt, H.L., Adams, P.D., et al. (2011) Targeted proteomics for metabolic pathway optimization: Application to terpene production, *Metabolic Engineering* **13**: 194-203.

Ribbenstedt, A., Ziarrusta, H., and Benskin, J.P. (2018) Development, characterization and comparisons of targeted and non-targeted metabolomics methods, *PLoS One* **13**: e0207082-e0207082.

Riley, L.A., and Guss, A.M. (2021) Approaches to genetic tool development for rapid domestication of non-model microorganisms, *Biotechnology for Biofuels* **14**: 30.

Robinson, C.J., Tellechea-Luzardo, J., Carbonell, P., Jervis, A.J., Yan, C., Hollywood, K.A., et al. (2021) Prototyping of microbial chassis for the biomanufacturing of high-value chemical targets, *Biochemical Society Transactions* **49**: 1055-1063.

Robles, J.A., Qureshi, S.E., Stephen, S.J., Wilson, S.R., Burden, C.J., and Taylor, J.M. (2012) Efficient experimental design and analysis strategies for the detection of differential expression using RNA-Sequencing, *BMC Genomics* **13**: 484.

Ronda, C., Pedersen, L.E., Sommer, M.O.A., and Nielsen, A.T. (2016) CRMAGE: CRISPR Optimized MAGE Recombineering, *Scientific Reports* **6**: 19452-19452.

Rothberg, J.M., Hinz, W., Rearick, T.M., Schultz, J., Mileski, W., Davey, M., et al. (2011) An integrated semiconductor device enabling non-optical genome sequencing, *Nature* **475**: 348-352.

Roy, S., Radivojevic, T., Forrer, M., Marti, J.M., Jonnalagadda, V., Backman, T., et al. (2021) Multiomics Data Collection, Visualization, and Utilization for Guiding Metabolic Engineering, *Frontiers in Bioengineering and Biotechnology* **9**.

Salis, H.M., Mirsky, E.A., and Voigt, C.A. (2009) Automated design of synthetic ribosome binding sites to control protein expression, *Nature Biotechnology* **27**: 946-950.

Sanger, F., Nicklen, S., and Coulson, A.R. (1977) DNA sequencing with chain-terminating inhibitors, *Proceedings of the National Academy of Sciences* **74**: 5463-5467.

Schomburg, I., Chang, A., and Schomburg, D. (2002) BRENDA, enzyme data and metabolic information, *Nucleic Acids Res* **30**: 47-49.

Silva-Rocha, R., Martínez-García, E., Calles, B., Chavarría, M., Arce-Rodríguez, A., de las Heras, A., et al. (2013) The Standard European Vector Architecture (SEVA): a coherent platform for the analysis and deployment of complex prokaryotic phenotypes, *Nucleic Acids Research* **41**: D666-D675.

Silva, J.C., Denny, R., Dorschel, C., Gorenstein, M.V., Li, G.-Z., Richardson, K., et al. (2006) Simultaneous Qualitative and Quantitative Analysis of the *Escherichia coli* Proteome: A Sweet Tale, *Molecular & Cellular Proteomics* **5**: 589-607.

Smanski, M.J., Bhatia, S., Zhao, D., Park, Y., B A Woodruff, L., Giannoukos, G., et al. (2014) Functional optimization of gene clusters by combinatorial design and assembly, *Nature Biotechnology* **32**: 1241-1249.

Stahl, D.C., Swiderek, K.M., Davis, M.T., and Lee, T.D. (1996) Data-controlled automation of liquid chromatography/tandem mass spectrometry analysis of peptide mixtures, *Journal of the American Society for Mass Spectrometry* **7**: 532-540.

Taniguchi, Y., Choi, P.J., Li, G.-W., Chen, H., Babu, M., Hearn, J., et al. (2010) Quantifying *E. coli* Proteome and Transcriptome with Single-Molecule Sensitivity in Single Cells, *Science* **329**: 533-538.

Taub E, F., DeLeo, J.M., and Thompson, E.B. (1983) Sequential comparative hybridizations analyzed by computerized image processing can identify and quantitate regulated RNAs, *Dna* **2**: 309-327.

Teoh, S.T., Putri, S., Mukai, Y., Bamba, T., and Fukusaki, E. (2015) A metabolomics-based strategy for identification of gene targets for phenotype improvement and its application to 1-butanol tolerance in *Saccharomyces cerevisiae*, *Biotechnology for Biofuels* **8**: 144-144.

Thompson, M.G., Incha, M.R., Pearson, A.N., Schmidt, M., Sharpless, W.A., Eiben, C.B., et al. (2020) Fatty Acid and Alcohol Metabolism in *Pseudomonas putida*: Functional Analysis Using Random Barcode Transposon Sequencing, *Applied and environmental microbiology* **86**: e01665-01620.

Thompson, M.G., Valencia, L.E., Blake-Hedges, J.M., Cruz-Morales, P., Velasquez, A.E., Pearson, A.N., et al. (2019) Omics-driven identification and elimination of

valerolactam catabolism in *Pseudomonas putida* KT2440 for increased product titer, *Metabolic Engineering Communications* **9**: e00098.

Vallino, J.J., and Stephanopoulos, G. (2000) Metabolic flux distributions in *Corynebacterium glutamicum* during growth and lysine overproduction. Reprinted from Biotechnology and Bioengineering, Vol. 41, Pp 633-646 (1993), *Biotechnology and bioengineering* **67**: 872-885.

Varma, A., and Palsson, B.O. (1994) Stoichiometric flux balance models quantitatively predict growth and metabolic by-product secretion in wild-type *Escherichia coli* W3110, *Applied and environmental microbiology* **60**: 3724-3731.

Venable, J.D., Dong, M.-Q., Wohlschlegel, J., Dillin, A., and Yates, J.R. (2004) Automated approach for quantitative analysis of complex peptide mixtures from tandem mass spectra, *Nature Methods* **1**: 39-45.

Villalobos, A., Ness, J.E., Gustafsson, C., Minshull, J., and Govindarajan, S. (2006) Gene Designer: a synthetic biology tool for constructing artificial DNA segments, *BMC bioinformatics* **7**: 1-8.

Vo, P.L.H., Ronda, C., Klompe, S.E., Chen, E.E., Acree, C., Wang, H.H., and Sternberg, S.H. (2021) CRISPR RNA-guided integrases for high-efficiency, multiplexed bacterial genome engineering, *Nature Biotechnology* **39**: 480-489.

Volke, D.C., Martino, R.A., Kozaeva, E., Smania, A.M., and Nikel, P.I. (2022) Modular (de)construction of complex bacterial phenotypes by CRISPR/nCas9-assisted, multiplex cytidine base-editing, *Nature Communications* **13**: 3026.

Wang, H.H., Isaacs, F.J., Carr, P.A., Sun, Z.Z., Xu, G., Forest, C.R., and Church, G.M. (2009) Programming cells by multiplex genome engineering and accelerated evolution, *Nature* **460**: 894-898.

Wang, L., Dash, S., Ng, C.Y., and Maranas, C.D. (2017) A review of computational tools for design and reconstruction of metabolic pathways, *Synthetic and Systems Biotechnology* **2**: 243-252.

Wang, Z., Gerstein, M., and Snyder, M. (2009) RNA-Seq: a revolutionary tool for transcriptomics, *Nature Reviews Genetics* **10**: 57-63.

Wiechert, W. (2001) 13C metabolic flux analysis, *Metabolic engineering* **3**: 195-206.

Wirth, N.T., and Nikel, P.I. (2021) Combinatorial pathway balancing provides biosynthetic access to 2-fluoro-cis,cis-muconate in engineered *Pseudomonas putida*, *Chem Catalysis* **1**: 1234-1259.

Wishart, D.S. (2008) Quantitative metabolomics using NMR, *TrAC trends in analytical chemistry* **27**: 228-237.

Yamamoto, N., Nakahigashi, K., Nakamichi, T., Yoshino, M., Takai, Y., Touda, Y., et al. (2009) Update on the Keio collection of *Escherichia coli* single-gene deletion mutants, *Molecular Systems Biology* **5**: 335.

Young, J.D. (2014) INCA: a computational platform for isotopically non-stationary metabolic flux analysis, *Bioinformatics (Oxford, England)* **30**: 1333-1335.

Zamboni, N., Fendt, S.-M., Rühl, M., and Sauer, U. (2009) ^{13}C-based metabolic flux analysis, *Nature protocols* **4**: 878.

Zamboni, N., Fischer, E., and Sauer, U. (2005) FiatFlux – a software for metabolic flux analysis from 13C-glucose experiments, *BMC Bioinformatics* **6**: 209-209.

Zeng, W., Guo, L., Xu, S., Chen, J., and Zhou, J. (2020) High-throughput screening technology in industrial biotechnology, *Trends in biotechnology* **38**: 888-906.

Zhang, Y., Muyrers, J.P.P., Testa, G., and Stewart, A.F. (2000) DNA cloning by homologous recombination in *Escherichia coli*, *Nature Biotechnology* **18**: 1314-1317.

Zhou, J., Liu, H., Liu, Y., Liu, J., Zhao, X., and Yin, Y. (2016) Development and Evaluation of a Parallel Reaction Monitoring Strategy for Large-Scale Targeted Metabolomics Quantification, *Analytical Chemistry* **88**: 4478-4486.

Chapter 2 - An integrated multi-omics workflow for metabolic profiling of *Pseudomonas*

This chapter is mainly composed of results from the following publication in preparation: **N. Gurdo**[a], N. Wirth[a], D. C. Volke[a], S. Donati[a], T. Wulff[a], & P. I. Nikel[a] (2023). An integrated multi-omics workflow for metabolic profiling of *Pseudomonas*, *Manuscript in preparation*.

[a]The Novo Nordisk Foundation Center for Biosustainability, Technical University of Denmark, 2800 Kongens Lyngby, Denmark.

* Correspondence to:
Pablo I. Nikel (pabnik@biosustain.dtu.dk)
The Novo Nordisk Foundation Center for Biosustainability,
Technical University of Denmark
Lyngby, Denmark
Tel: (+45 93) 51 19 18

Here, we described a step-by-step methodology to perform -omic experiments in a standardized manner, combined with a novel visual framework for metabolic flux analysis. The strategies were applied to investigate glucose metabolism in *Pseudomonas putida* KT2440 to a degree of detail that surpasses previous studies. The multi-omic platform is implemented from **Chapter 4** to **Chapter 7**, with specific modifications according the goals and aims of the topic under study.

Abstract

Multi-omics strategies integrate diverse data sets from different omics experiments for a comprehensive understanding of biological systems. A key challenge in multi-omics analysis is the integration of large datasets. To overcome this, computational methods such as correlation-based approaches, network analysis, and machine learning techniques have been developed. Nevertheless, researchers may possess limited knowledge or experience regarding the use of these complex techniques employed in the analysis of microbial metabolism. The analysis can also lead to data misinterpretation and require significant time and resources. For that, in this chapter, we described a versatile, robust and user-friendly workflow that facilitates running multi-omics experiments, data analysis and interpretations as well as visualization across three omic levels (i.e. metabolomics, proteomics and fluxomics). The experimental set-up has been standardized to enable precise sampling for the different analysis. In addition, the pipeline was complemented with a visualization framework that permit to represent the changes of metabolites, proteins and metabolic fluxes. Using this methodology, we captured metabolites, proteins and fluxes changes during two different time-points showing a rigid upper glycolytic pathway, PP pathway and active TCA cycle to support growth. The utility of the procedure developed in this chapter is illustrated by using the Gram-negative bacterium *Pseudomonas putida* KT2440, a versatile microbial cell factory with great biotechnological potential.

2.1 Introduction

2.1.1 Multi-omics analysis to explore metabolism at the systems scale

Microbial metabolism involves a complex network of biochemical reactions that are tightly regulated in time and space. In accordance with the central dogma of molecular biology, the metabolic complexity is the manifestation of how genetic information flows from the genome across the different information layers which lead to the observable characteristics of the microorganism (Cobb, 2017). Several methods have been developed in order to unravel the interconnected network of the final phenotype. By utilizing a set of techniques collectively known as multi-omics methods, scientist can track the information from the genome (genomics) through the transcriptome (transcriptomics), the proteome (proteomics), the metabolome (metabolomics), and ultimately the fluxome (fluxomics) (Veenstra, 2021, Gurdo, et al., 2023). For instance, these techniques allow researchers to examine how microbes adapt their metabolism in response to different conditions (Zhang, et al., 2010). Many studies have demonstrated the usefulness of omics analyses as a tool to guide metabolic engineering efforts or expand the knowledge about the system under study. **Table 2.1** presents several examples conducted over the past two decades, illustrating the application of these methodologies in studying microbial platforms including *Pseudomonas putida*, *Escherichia coli*, *Corynebacterium glutamicum*, *Bacillus subtilis*, *Bacillus licheniformis* as well as human pathogens as *Pseudomonas aeruginosa*.

In particular, these system biology approaches provide data from various biological levels, including genetic information, transcript levels, protein and metabolite abundances or concentrations, as well as measurements of metabolic fluxes, serving as experimental outputs (De Keersmaecker, et al., 2006, Oldiges, et al., 2007, Kanani, et al., 2008). The study of transcriptomics can provide valuable insights into the gene structures and RNA-mediated control mechanisms in any living organism (Sorek and Cossart, 2010). Proteomics based-mass spectrometry helps on understanding how cells functions at a global level by analyzing proteome dynamics (Graham, et al., 2007, Altelaar, et al., 2013, Vranakis, et al., 2014). Metabolomics enables the precise detection and quantification of a large number of metabolites in numerous samples, enabling the investigation of dynamic metabolomic networks and yielding findings that cannot

be obtained through traditional methods (Weckwerth, 2003). Finally, the quantification of intracellular fluxes is also a major objective in Systems Biology, and metabolic flux analysis (^{13}C–MFA) constitutes a key tool for this purpose (Wiechert, 2001). This type of analysis uses isotopic labeling experiments to determine the distribution of intracellular fluxes across key metabolic pathways. To obtain the final flux distribution, *in vivo* experiments and *in silico* simulations must be compared using an iterative computation process (Driouch, et al., 2012). Next, the resulting estimated fluxes can be visualized using metabolic network diagrams.

However, multi-omics research presents several challenges, such as experimental design, data integration and visualization (Gehlenborg, et al., 2010). The reason for this is that multi-omics experiments were originally developed to study individual layers separately, making it hard to obtain data under the same metabolic conditions. Consequently, challenges arise from the complexity of the data sets and the heterogeneity between data sources (López de Maturana, et al., 2019). Also, another primary obstacle faced by both users and developers of visualization tools in the field of systems biology is how to take advantage of the vast amounts of available data without becoming overwhelmed by it. In practical terms, this means finding ways to present the data in a coherent, informative way that strikes the right balance between level of detail and comprehensibility. Nevertheless, to get a clear understanding of phenotypes and allow reliable interpretations, it is crucial to gather high-quality data from various cellular components in an integrated experimental set-up.

Table 2.1. A list of different examples of –omic approaches applied to explore several features of microbial metabolism.

Organisms	Purpose	-omic approach	Ref.
Pseudomonas putida	Investigating metabolism of valerolactam and caprolactam degradation	RB-TnSeq and shotgun proteomics	(Thompson, et al., 2019)
	Improving heterologous indigoidine production	^{13}C–Metabolic flux analysis and metabolomics	(Czajka, et al., 2022)
	Understanding activation of mcl-PHA biosynthesis and genetic target identification for polymer accumulation.	RNA sequencing (RNAseq) and proteomics (1D-LC-MS)	(Fu, et al., 2015)
Pseudomonas aeruginosa	Studying and tracking mechanism of persistence in CF condition	Sequencing and genotyping	(Bartell, et al., 2021)
	Analyzing growth and survival on n-alkenes	RNA sequencing (RNAseq) and microarray analysis, ribosome profiling, proteomics, metabolomics	(Grady, et al., 2017)
Pseudomonas pseudoalcaligenes	Exploring response to cyanide	Genomics, transcriptomics and proteomics	(Luque-Almagro, et al., 2015, Cabello, et al., 2018)
Escherichia coli	Elucidating the complex interplay between synthetic and endogenous *E. coli* metabolism	Metabolomics, proteomics, transcriptomics and fluxomics data	(Kim, et al., 2016)
	Deciphering genotype-phenotype relationship in *E.coli* strains.	Transcriptomics and proteomics and genome scale metabolic models	(Yoon, et al., 2012)
Corynebacterium glutamicum	Interpreting cellular global regulatory mechanisms and physiological events related to L-arginine synthesis	Genomics and transcriptomics	(Zhao, et al., 2022)
Lactococcus lactis	Comprehending metabolic regulations during multi-substrate growth	Transcriptomics and proteomics	(Lahtvee, et al., 2011)
Bacillus licheniformis	Investigating the physiological response to cadmium	Transcriptomics, metabolomics and proteomics	(Sun, et al., 2015)
Bacillus subtilis	Examining physiological adaptations to grow in a sustained high-salinity environment that is simultaneously limited for carbon supply	Transcriptomic, mass spectrometry-based proteomic, metabolomics and ^{13}C-fluxomic	(Kohlstedt, et al., 2014)
Streptococcus mutans and ***Candida albicans***	Exploring cross-kingdom interaction and sugar metabolism	Transcriptomics and quantitative proteomics	(Ellepola, et al., 2019)

2.1.2 Capturing the dynamics of metabolism by visualizing multi-omic data

Visualization enables portraying different data sets according to metabolite pools, protein abundances, and metabolic flux changes within cells in a given metabolic network. There are various visualization methods available today (Neuweger, et al., 2008, Wiklund, et al., 2008, Xia and Wishart, 2010, Hartmann and Jozefowicz, 2018). Nonetheless, the large number of metabolites and proteins in a metabolic network, as well as the wide range of concentrations, from *fmol* to several *mmol*, make it difficult to directly compare different conditions. Consequently, a transformation into biological relevant values, i.e., metabolite concentrations or protein fold changes, has to be compulsory by peak area integration. Another challenge in the realm of visualization lies in the lack of a standardized methodology to effectively display and integrate the vast amount of data generated from a singular experiment.

Several software tools are accessible to facilitate the visualization of complex metabolic networks and the integration of omics datasets, including Omix (Droste, et al., 2011), MiBIOmics (Zoppi, et al., 2021) and MicrobioSee (Li, et al., 2022). While software tools are capable of presenting data from various perspectives, they may require significant computational resources or come at a cost, which can restrict their accessibility. As a result, researchers have historically relied on custom-built tools to analyze, interpret, integrate, and visualize -omics data which, can lead to perplexing outcomes that present difficulties in comprehension and interpretation. More recently, the field has become simpler with the advent of new and improved software. Nevertheless, until now, only a limited number of investigations have integrated microbial physiology with more than two -omics experiments. These studies have conventionally relied on the information derived from one or two biological layers.

2.1.3 The environmental bacterium *Pseudomonas putida* as a model organism for multi-omics analysis

A way to delve into metabolic architectures involves the exploration of the microbial metabolism by applying multi-omics strategies, as was mentioned in **Section 2.1.1**. *Pseudomonas putida*, a versatile bacterium renowned for its robustness and metabolic

flexibility, serves as an excellent candidate for such investigations. This Gram-negative bacterium can survive and grow in a variety of harsh conditions, such as high salt concentrations and toxic compounds. *P. putida* is known for its ability to use a wide variety of carbon sources, such as aromatic compounds, fatty acids, and amino acids (Weimer, et al., 2020).

Numerous research studies have investigated the adaptability of *P. putida*'s metabolism. The following examples serve as compelling evidence: i) *Refactoring metabolic pathway for co-utilization of a wide range of sugars: P. putida* has been engineered to enable the simultaneous use of a wide range of sugars. This includes the ability to efficiently grow on cellobiose and co-metabolize it with glucose and xylose. This demonstrates not only an expansion in the bacterium's metabolic capability to use novel substrates but also highlights *P. putida* as a viable platform for integrating novel biochemical pathways that utilize carbohydrate mixtures from lignocellulose sources (Dvořák and de Lorenzo, 2018). ii) *Tolerance to toxic compounds: P. putida* has been shown to have a high tolerance to toxic compounds such as organic solvents. *P. putida* butanol tolerance was found to be primarily linked to classic solvent defense mechanisms, such as efflux pumps, membrane modifications and control of redox state (Cuenca, et al., 2016). iii) *Segregated metabolic pathways:* a study on simultaneous carbon substrate uptake has demonstrated the ability to co-utilize glucose and benzoate in *P. putida*. The multi-omic strategy revealed metabolic segregation on the substrate carbons providing new insights into the metabolic architecture of this bacteria (Kukurugya, et al., 2019). iv) S*tress response mechanisms:* finally, a study by Bojanovic and colleagues (2019) delved into the stress response mechanisms of *P. putida* and discovered that it can endure high salt concentrations and oxidative stress by activating specific stress response pathways (Bojanovič, et al., 2017). This metabolic flexibility is due to the presence of multiple catabolic pathways and regulatory systems that enable *P. putida* to efficiently utilize different carbon sources or withstand several environmental conditions. The main strength of this bacterium is its robust but complex metabolic architecture. *P. putida* central carbon metabolism (CCM) has four main pathways that direct carbons towards biosynthetic building blocks. These pathways are the Entner-Doudoroff (ED) pathway, the pentose-phosphate pathway (PPP), the upper Embden-Meyerhof-Parnas (EMP) pathway, and the TCA cycle.

Glucose catabolism is used to direct glucose-derived carbons towards the ED and PP pathways. This can be achieved through direct glucose phosphorylation to glucose-6-phosphate (G6P) or by oxidizing glucose to gluconate (Glcn) and 2-ketogluconate (2-KGA) in the periplasm, followed by phosphorylation to 6-phosphogluconate (6PG) (Sudarsan, et al., 2014, Nikel, et al., 2015, Sasnow, et al., 2016). Given that *Pseudomonas putida* KT2440 is a microorganism that possesses a complex metabolic architecture and considering that it has the ability to strongly rewire its metabolism upon internal or external perturbations, we decided to create an integrated multi-omics to: i) standardize the different strategies; ii) provide an experimental, data integration and visualization framework and; iii) capture relevant metabolic information in *Pseudomonas putida* KT2440.

2.2 Results

2.2.1 Setting up a multi-omics workflow for physiological characterization, metabolomics, proteomics and fluxomics analyses

The use of standardized multi-omic protocols for sample collection, data integration, and visualization can result in improved reproducibility, reduced experimental variability, and more accurate conclusions (Quinn, et al., 2016). To fully harness the potential of different -omics methodologies, a systematic and integrated workflow was developed to obtain an overall perspective on the metabolic status (**Figure 2.1**). This strategy involves conducting multiple -omics experiments in parallel, all executed under the same, reproducible conditions. The goal is to integrate different data sets coming from metabolomics, proteomics, and fluxomics assays in a meaningful way. By running the experiments under uniform conditions, it becomes easier to compare and integrate the results from different -omics approaches (**Figure 2.2**). In the study, we adopted *Pseudomonas putida* KT2440 as model organism to display how the workflow can be used to explore its unique metabolic properties and robust metabolism. The framework provides a simple and straightforward approach for the analysis and interpretation of the obtained data, improving the understanding of the cellular metabolic state. The experimental and analytical workflow was complemented by a set of custom R scripts assembled into the package *VisomX* (www.github.com/Nicwir/VisomX) to facilitate user-friendly and comprehensive

omics data analysis. The included visualization functions aim to overcome the challenges faced in integrating a large amount of data generated from multi-omics experiments, making it easier for biologists to comprehend the results and draw valid conclusions.

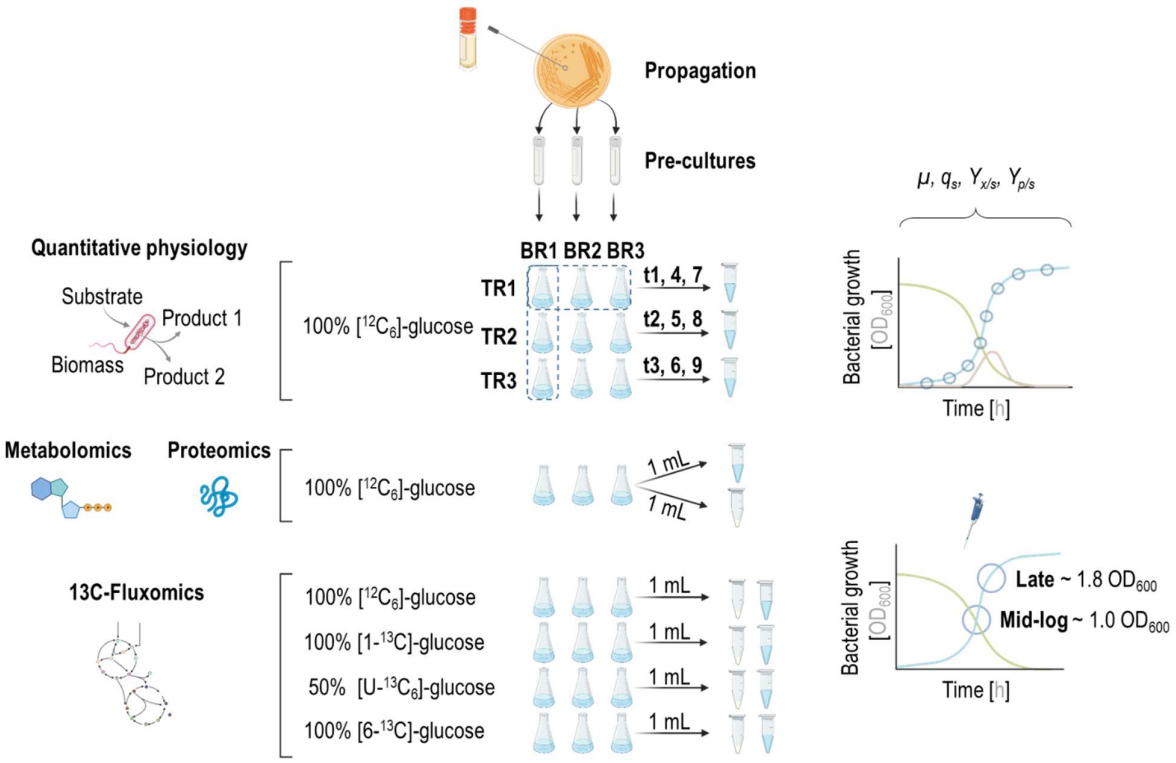

Figure 2.1. Experimental set-up for multi-omics analysis in this study. The diagram represents the set of experiments to carry out. The analysis involves four main strategies: quantitative physiology analysis, metabolomics, proteomics, and fluxomics. Cultivations are performed using the corresponding labelling (^{12}C or ^{13}C Glucose). At least three biological replicates per set of experiment. μ: Specific growth rate (h^{-1}), qs: substrate uptake rate (mmol g_{CDW}^{-1} h^{-1}), Yx/s: biomass yield (g biomass produced × g substrate consumed^{-1}), Yp/s (g product produced × g substrate consumed^{-1}). BR1,2,3: Biological replicate 1, 2 and 3. TR1, 2, 3: Technical replicates 1, 2 and 3. t1, …, t9 represent different sampling time points (in h).

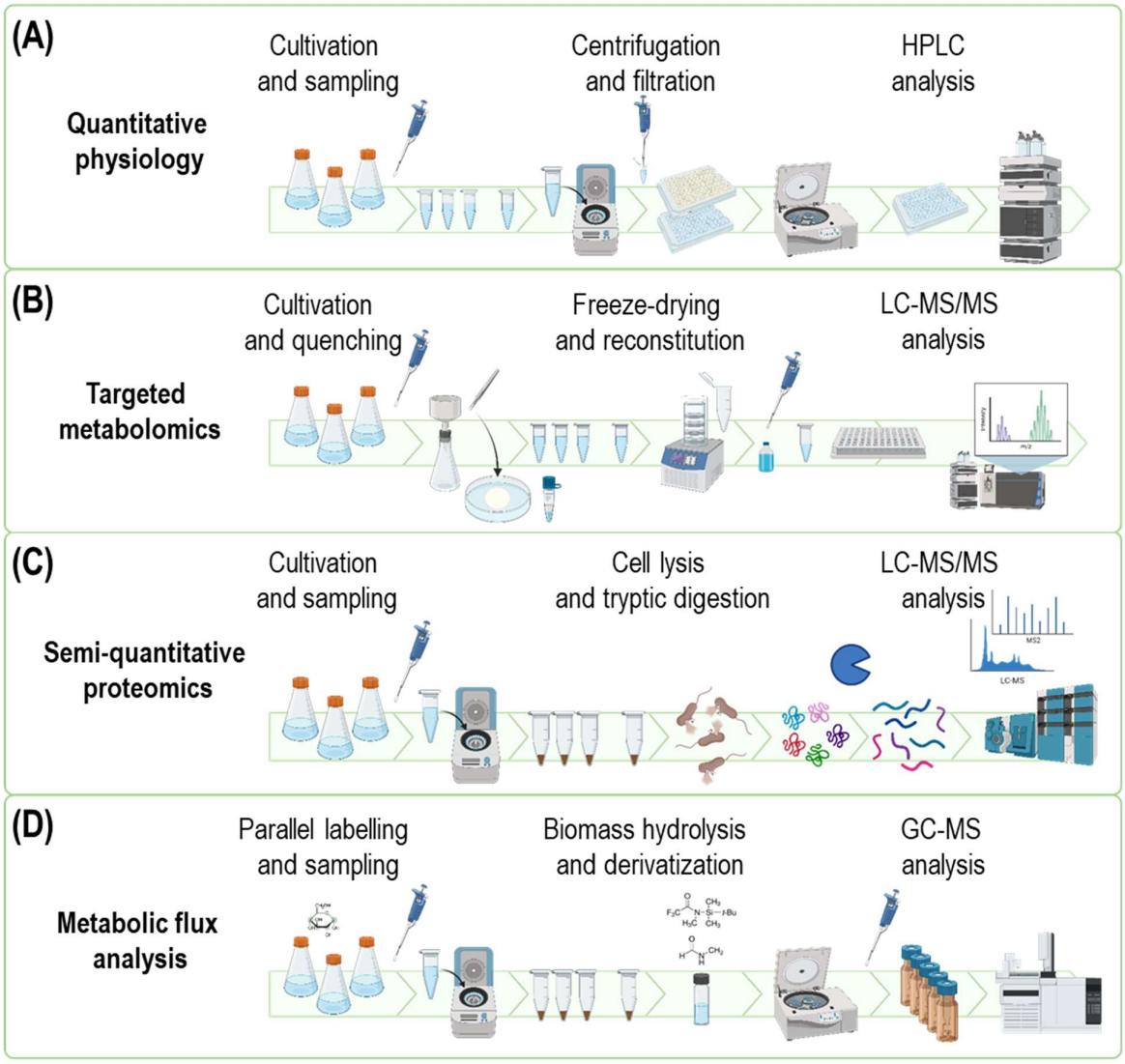

Figure 2.2. Description of the main methodologies for quantitative physiology and –omics analysis. Overall, the first step is common for all the strategies consisting on culturing the strains in non-labeled glucose or, in the case of metabolic flux analysis, labeled glucose. For quantitative physiology analysis **(A)**, the steps involve sampling, optical density measurement and supernatant analysis by HPLC. For targeted metabolomics **(B)**, the samples are quenched, lyophilized and reconstituted for LC-MS/MS analysis. In semi-quantitative proteomics **(C)**, the pellet is lysed, digested and prepared for LC-MS/MS analysis. Finally, for metabolic flux analysis **(D)**, the harvested biomass is hydrolyzed, derivatized and analysed by GC-MS.

To bring the efforts to fruition, the initial stage involved cultivating *Pseudomonas putida* KT2440 in $DBMG_{2g/L}$ to gather quantitative information on its physiology. **Figure 2.3A** shows a typical growth curve (with the biomass concentration estimated as the optical density measured at 600 nm, OD_{600}), as well as the extracellular concentrations for glucose, gluconate, and 2-ketogluconate—the three forms of sugars utilized and processed by *P. putida*. The calculated specific growth rate (μ) of *P. putida* KT2440 was 0.61 h^{-1}, with a maximum optical density (OD_{600max}) of 2.42 or 1.02 g_{CDW} L^{-1}. The glucose uptake rate was 7.08 ± 0.22 mmol g_{CDW}^{-1} h^{-1} ($q_{Glucose}$) and the biomass yield was 0.42 ± 0.03 g_{CDW} $g_{glucose}^{-1}$ ($Y_{X/S}$) (**Figure 2.3B**). The rate of gluconate secretion was determined to be 16.96 ± 3.56 mmol g_{CDW}^{-1} h^{-1} ($q^{Sec}_{Gluconate}$) during the initial 2-hour period of cultivation. From hour 3 to 8, the uptake rate of gluconate was found to be 0.83 ± 0.08 mmol g_{CDW}^{-1} h^{-1} ($q^{Upt}_{Gluconate}$). In the case of 2-KGA, the secretion rate was estimated to be 4.65 ± 0.16 mmol g_{CDW}^{-1} h^{-1} ($q^{Sec}_{2\text{-}KGA}$) within the first 4 hours of cultivation. Subsequently, from hours 4 to 6, the uptake rate of 2-KGA was observed to be 2.08 ± 0.09 mmol g_{CDW}^{-1} h^{-1} ($q^{Upt}_{2\text{-}KGA}$). These results were consistent with previous findings (Nikel, et al., 2015). Glucose was first oxidized into gluconate and, in a second oxidation step, gluconate was converted into 2-ketogluconate. As soon as they were secreted into the extracellular space, both organic acids were progressively consumed along the cultivation. **Figure 2.3A** shows the specific time intervals during which we collected samples for -omic analysis while maintaining a constant specific growth rate and glucose uptake rate: 1) at *Mid-log phase*, which indicates the cultures reached OD_{600}~1.0 and; 2) *Late phase,* at OD_{600}~1.8. Based on the specific time points indicated in **Figure 2.3A**, we conducted metabolomics and proteomics analyses, as well as metabolic flux analysis. These procedures were performed following the general methodology outlined in **Figure 2.2**, which provided a framework for the overall experimental design and analytical approach.

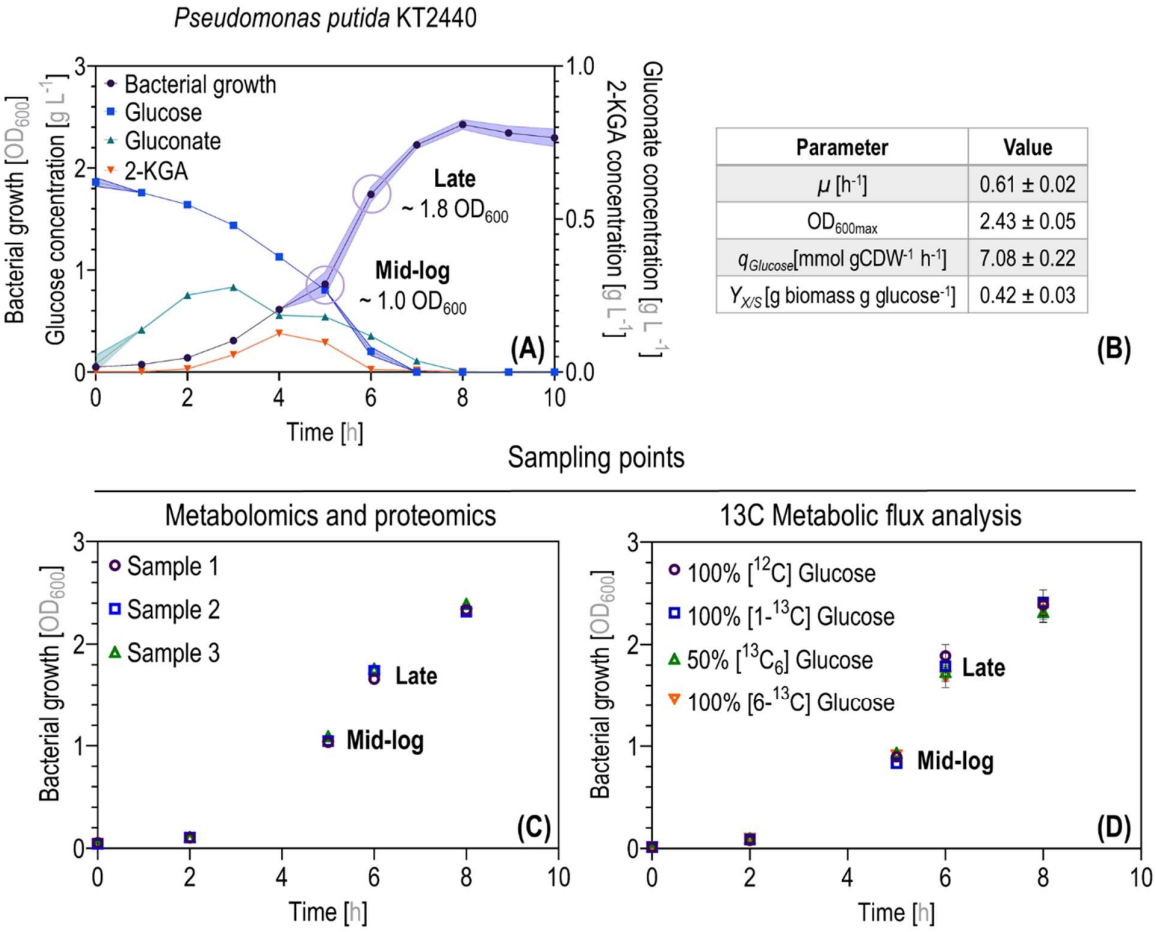

Figure 2.3. Physiological characterization of *Pseudomonas putida* KT2440. (A) Growth curve showing bacterial growth (OD_{600}, purple circles), glucose (blue squares), gluconate (green up triangles) and 2-ketogluconate (orange down triangles) concentration in g L^{-1} in the supernatant. Points denote average of three biological replicates while shading area represents standard deviation. **(B)** Calculated parameters are shown in the table on the left: specific growth rate (μ), maximum optical density (OD_{600max}), glucose uptake rate ($q_{Glucose}$) and biomass yield ($Y_{X/S}$). **(C)** Symbols indicate where the aliquot for metabolomics and proteomics were taken as well as in **(D)** for the case of ^{13}C metabolic flux analysis.

2.2.2 Visualization of omic datasets generated in this study

To simplify the analysis and integration of various types of omics data, we developed several "dummies" template maps representing the central carbon metabolism of *Pseudomonas putida* KT2440 (shown in **Figure 2.4**) (Nikel, et al., 2015). These maps enabled us to easily assign information from our -omics analyses. The data sets consisted on normalized absolute concentrations (metabolomics) and relative protein abundances (proteomics). The metabolic fluxes were expressed as relative values, provided as percentages and incorporated into the template.

In order to visualize metabolite concentrations and protein relative changes, we used sizable circles (**Figure 2.4A**) and squares (**Figure 2.4B**), which were colored using a specific color palette (see below). Moreover, it was also possible to provide further details regarding the energy levels of cells by indicating the concentrations of energy and redox molecules such as ATP, NAD^+, NADH, $NADP^+$ and NAD(P)H. Finally, to represent metabolic fluxes, we varied the arrow intensity color to indicate the magnitude of the flux (**Figure 2.4C**). The data set of omics was created during the course of this study by conducting the experiments illustrated in **Figure 2.2**, which included targeted metabolomics, semi-quantitative proteomics, and ^{13}C fluxomics.

With the aim of visualizing the collected data in the dummies maps, we allocated the previous metabolites data, protein abundances and metabolic fluxes. Metabolites were indicated with a yellow-to-violet color gradient and varying size, proportional to their measured concentrations. Small yellow circles indicate metabolites with the lowest concentrations while big violet circles correspond to metabolites with the highest concentrations. As the metabolite concentrations can span several orders of magnitude, logarithmic transformation (base 4) was applied to the metabolite concentrations before applying the color gradient and calculating circle radio. The purpose of applying a logarithmic transformation was to effectively capture and highlight visual distinctions arising from variations in metabolite concentrations. Metabolites not measured are shown by leaving their name on the metabolic map (**Figure 2.5**).

For proteomics data visualization, log_2 fold-changes were depicted in squared boxes beside the flux arrows within the metabolic network map. For isozymes, the squares are placed horizontally and labeled with letters (e.g. ZwfA, ZwfB and ZwfC), while for enzymes complexes, they were arranged vertically and labeled with numbers (e.g. pyruvate dehydrogenase complex where, 1, 2 and 3 are components I, II and III respectively). We applied a palette color ranging from blue (downregulated proteins), over white (no change), to red (overregulated proteins). Furthermore, the limits of the color gradient were set at -2 and 2 in order to capture all the changes in the interval (**Figure 2.6**).

For fluxomics, the flux values (%) were depicted on the metabolic map by adjusting the blue intensity in the arrows. The darker blue color indicated a 100% flux (which was the glucose uptake rate), while light gray dashed lines represented the absence of flux. The directionality of every arrow indicates the direction of each flux. In addition, the network model includes three compartmentalized sections showing metabolite pools in the extracellular, periplasmic or cytosolic space (**Figure 2.7**).

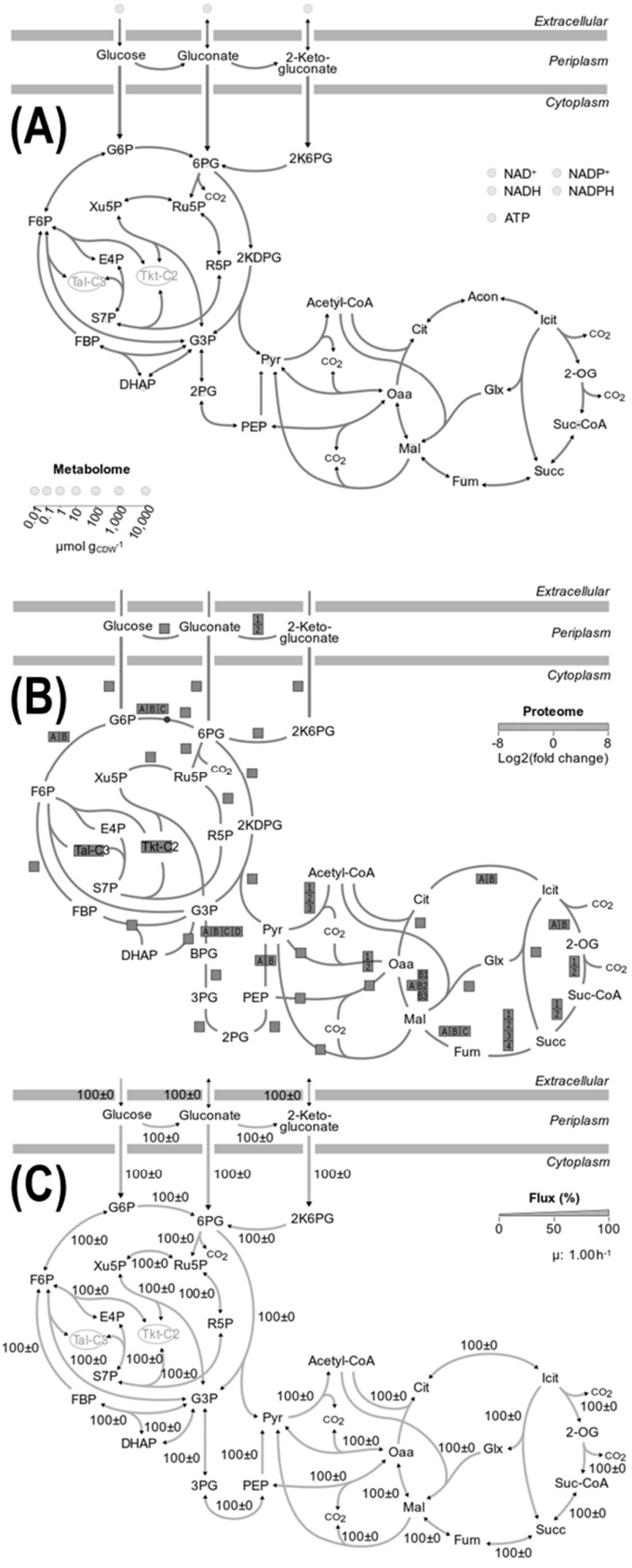
(A)
Extracellular
Periplasm
Cytoplasm
Glucose
Gluconate
2-Keto-gluconate
G6P
6PG
2K6PG
NAD+
NADP+
NADH
NADPH
ATP
Xu5P
Ru5P
CO2
F6P
E4P
R5P
2KDPG
Tal-C3
Tkt-C2
S7P
FBP
G3P
DHAP
2PG
PEP
Pyr
Acetyl-CoA
Cit
Acon
Icit
2-OG
Glx
Suc-CoA
Mal
Fum
Succ
Metabolome
0.01
0.1
1
10
100
1,000
10,000
µmol gCDW-1
(B)
Proteome
-8
0
8
Log2(fold change)
BPG
3PG
(C)
Flux (%)
0
50
100
µ: 1.00h-1
100±0

Figure 2.4. Templates used to visualize metabolome, proteome and fluxome in central carbon metabolism of *Pseudomonas putida* KT2440. (A) Map containing the normalized concentration (μmol g_{CDW}^{-1}) of the different metabolites. Gray circles represent the specific metabolites. **(B)** Template showing the Log_2(fold change) of proteins involve in CCM. Squares symbolize the enzyme(s) acting in the metabolic steps. **(C)** Template map including metabolic fluxes calculated after 13C–MFA. Arrows denote direction and the value (%) is the relative flux versus total carbon uptake. Abbreviations are as follows: G6P, glucose-6-P; F6P, fructose-6-P; F1,6P_2, fructose-1,6-P2; DHAP, dihydroxyacetone-P; 6PG, 6-phosphogluconate; 2KDPG, 2-keto-3-deoxy-6-phosphogluconate; Ru5P, ribulose-5-P; R5P, ribose-5-P; Xu5P, xylulose-5-P; S7P, sedoheptulose-7-P; E4P, erythrose-4-P; G3P, glyceraldehyde-3-P; 2PG, glycerate-2-P; PEP, phosphoenolpyruvate; Pyr, pyruvate; Acetyl-CoA, acetyl-coenzyme A; Oaa, oxaloacetate; 2K6PG, 2-ketogluconate-6-phosphate; Cit, citrate; Acon, aconitate; Icit, isocitrate; 2-OG, 2-oxoglutarate; SucCoa, succinyl-CoA; Succ, succinate; Fum, fumarate; Mal, malate; Glx, glyoxylate; CO_2, carbon dioxide.

2.2.3 Quantitative comparison of metabolome, proteome and fluxome dataset

With the aim of exposing the main variations in comparative -omics analyses, we created five visualization maps: two for *Mid-log* and *Late* metabolomics (**Figure 2.5A** and **Figure 2.5B**)**,** two for *Mid-log* and *Late* fluxomics (**Figure 2.7A** and **Figure 2.7B**), and one for proteomics (**Figure 2.6**). The data included in the proteomic map used the *Mid-log* phase data as a reference point for calculating log_2(fold change). By utilizing the *met_to_map()*, *prot_to_map()*, and *flux_to_map()* functions in the R package VisomX, we were able to simultaneously process, analyze, and visualize the data set obtained from the three omics experiments. All our analyses were performed by comparing the data obtained from the *Mid-log* phase with that from the *Late* phase. In order to capture the metabolic dynamics between the two different cellular states (*Mid-log* and *Late*), we first represented the calculated metabolite concentration data in the metabolic map. As specified in material and methods, measured concentration data were pre-processed before visualization in the reaction network. The first processing step was the normalization of the concentrations in μmol g_{CDW}^{-1} by using the optical density (OD_{600}) and its correlation with cell dry weight at the harvesting time point.

In this study, we have examined the most commonly used sampling techniques in the field of metabolomics (Bolten, et al., 2007). This methods involved cell separation by fast filtration and quenching using cold methanol at -20°C. We were able to achieve reasonable concentrations of intermediates from glycolysis, PP pathway, and TCA

cycle ranging from 0 to around 400 μmol g_{CDW}^{-1} (**Table S2.1**). As previously stated, this approach has been shown to have strong consistency and reproducibility across both biological and technical replicates (Wordofa, et al., 2017). We observed that during the *Mid-log* phase, there was an increased concentration of all metabolites across the different metabolic pathways compared to the *Late* phase, indicating a high level of metabolic activity during this phase.

Concerning metabolic flux analysis, **Figure 2.8** shows a typical flux distribution of *Pseudomonas putida* KT2440 grown on glucose. The calculated relative fluxes are listed in **Table S2.1**. In both phases (*Mid-log* and *Late*), more than 90% of the input substrate is metabolized via periplasmic oxidation to gluconate and 2-ketogluconate. Assimilation of these two sugar acids converges at 6-phosphogluconate, which is further metabolized through the ED pathway. It should be noted that the exact split ratio between the gluconate uptake branch and the 2-ketogluconate uptake branch cannot be resolved based on carbon transitions utilizing this experimental set up. A different tracer strategy employing deuterated sugar substrates, known as *D-fluxomics*, should be employed in order to follow the fate of glucose in the upper sugar processing routes (Volke, et al., 2023). At the output node of the ED pathway, specifically at the convergent G3P metabolic hub, approximately 20% of the carbon is recycled back through the EMP pathway to form hexose phosphates (F6P and G6P). The observed net fluxes through ED pathway and lower glycolysis corroborated earlier outcomes proposed for pseudomonads, where the ED pathway is the core pathway for glucose processing (Vicente and Cánovas, 1973, Fuhrer, et al., 2005, del Castillo, et al., 2007, Ebert, et al., 2011, Sudarsan, et al., 2014, Nikel, et al., 2015). In addition, previous *in silico* analysis and experimental results in glucose-grown cells have demonstrated that the flux through the PP pathway is low in *P. putida* KT2440 (Tokic, et al., 2020, Wirth, et al., 2022), which is optimized for providing the necessary biomass precursors.

Regarding proteomics, the analysis provided a global overview of the proteome allocation when cells grew on glucose as carbon source. As shown in **Figure 2.6**, most of the proteomic changes were centered on peripheral reactions (gluconate oxidation into 2-KGA as well as 2-KGA into 2K6PG), G6P dehydrogenase (Zwf) and 6PG

dehydrogenase (Gnd) and TCA cycle. When comparing *Late* phase against *Mid-log*, the enzymes responsible for the oxidation of gluconate (Gad) or the phosphorylation of 2-KGA (KguK) were downregulated. This observation is consistent with the fact that in *Late* phase gluconate is not further processed into 2-KGA (**Figure 2.3A**), yet one must bear in mind that the proteomics methodology employed in this study is not optimized for the extraction and analysis of membrane-bound proteins, such as Gad (Tan, et al., 2008).

In addition, it was expected that the protein levels of all PPP enzymes, except for transketolase (Tkt) and transaldolase (Tal), would be low in the two tested conditions. Tkt and Tal are responsible for interconverting PPP metabolites, rearrange carbon skeletons and act on two substrates simultaneously, F6P and E4P (Stincone, et al., 2015). The enzymatic reactions mediated by Tkt and Tal involve the transfer of two- and three-carbon fragments (Tal-C and Tkt-C in **Figure 2.4A**) from a ketose donor to an aldose acceptor. Tkt facilitates the transfer of glycolaldehyde (C_2 skeleton) utilizing tightly bound thiamine pyrophosphate (TPP) as a cofactor. Within TPP, the second carbon atom of the thiazole ring possesses a propensity for ionization, resulting in the formation of a carbanion. This carbanion readily reacts with the carbonyl group of the ketose substrates, namely xylulose 5-phosphate (X5P), fructose 6-phosphate (F6P), or sedoheptulose 7-phosphate (S7P). The phosphorylated portion of the ketose substrate is cleaved, resulting in a negatively charged C_2 atom bound to TPP. Through resonance forms, the glycolaldehyde moiety remains attached to TPP until an appropriate acceptor molecule, such as ribose 5-phosphate (R5P), erythrose 4-phosphate (E4P), or glyceraldehyde 3-phosphate (G3P), is encountered. In contrast to Tkt, Tal lacks a prosthetic group and instead relies on the formation of a Schiff base. This occurs between the carbonyl group of the ketose substrate (F6P, S7P) and the ε-amino group of a lysine residue within the enzyme's active site. This interaction results in the production of either G3P or E4P, with the bound dihydroxyacetone (C_3 skeleton) remaining. Similar to the nitrogen atom within the thiazole ring of Tkt, the nitrogen atom within the Schiff base stabilizes the dihydroxyacetone unit through resonance forms until an appropriate aldose acceptor (G3P, E4P) becomes bound (Kleijn, et al., 2005).

The overall control over the flux of these reactions is likely exerted at the metabolite level. These reactions can only occur if the remaining PP pathway reactions can provide the required substrates. Having elevated levels of Tkt and Tal as a baseline, in this case in *Mid-log* phase, could enable a faster adaptation to alterations in the flux distribution in the EDEMP network. Also, in order to compensate the lack of reducing equivalents in the upper glycolysis and TCA cycle at the end of the *Late* phase, the cell increases the activity of Zwf, Gnd, isocitrate dehydrogenase (Icd), succinate dehydrogenase (SdhD), and malate dehydrogenase (Mdh) enzymes to extract energy from the remaining glucose and gluconate before entering in stationary phase.

Summarizing, the whole analysis of comparative metabolome, proteome, and fluxome data in biochemical network diagrams is a powerful tool that allows for a comprehensive understanding of the metabolic state of a system. By analyzing the data in this manner, we can gain critical insights into the system, such as identifying key regulatory points, determining the impact of genetic mutations or environmental changes, and understanding how changes within the network affect the entire system. Overall, this systematic visualization approach is a powerful tool for advancing our understanding of metabolism and its regulation in biological systems.

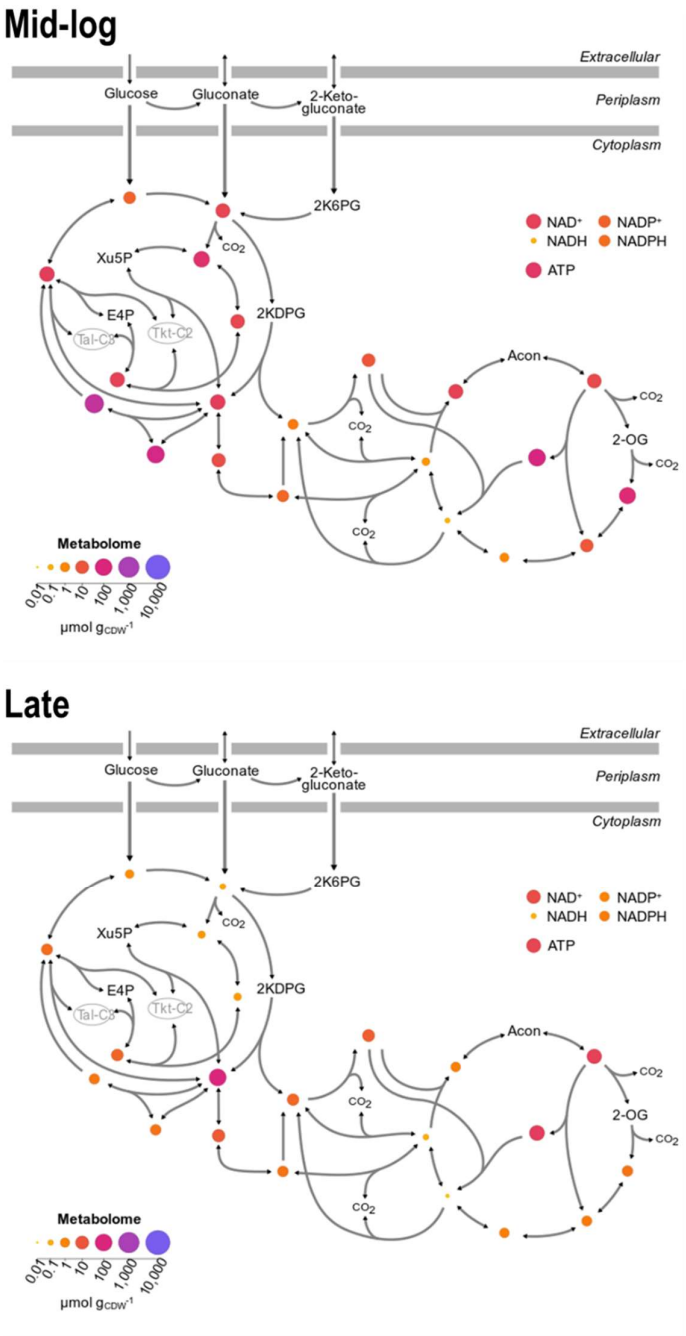

Figure 2.5. Visualization of central carbon metabolites in *Mid-log* and *Late* phases. Metabolite concentrations are depicted and colored according the palette reference on the left down corner of each graph. Abbreviations can be found in the legend to **Figure 2.4**. Smaller and yellow circles represent lowest concentration (0.01 µmol g_{CDW}^{-1}) while bigger and purple circles the highest concentration (10,000 µmol g_{CDW}^{-1})

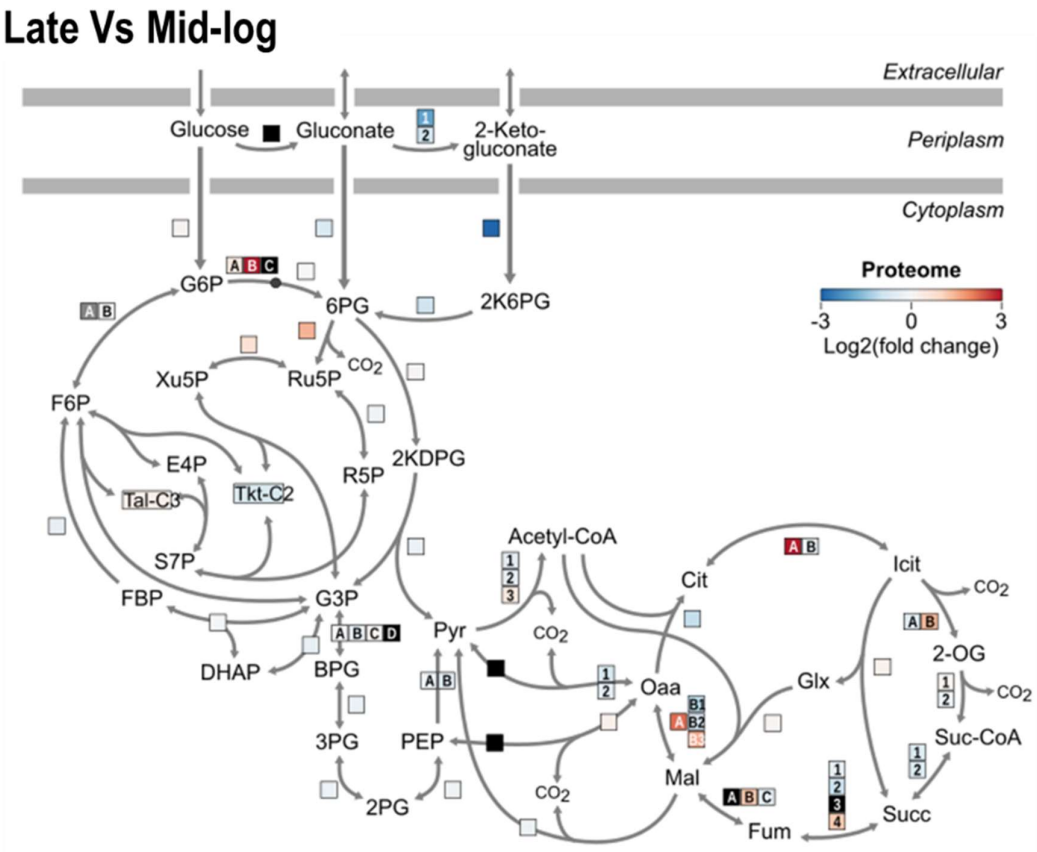

Figure 2.6. Visualization of proteins in *Pseudomonas putida* KT2440 central carbon metabolism during *Mid-log* in comparison to *Late* phase. Protein fold change are symbolize in squared boxes according the color bar on the right upper corner. Log_2(fold change) covers from -2 (blue), 0 (white) to 2 (red). Black boxes represent that the corresponding protein has not been detected. Abbreviations can be found in **Figure 2.4.**

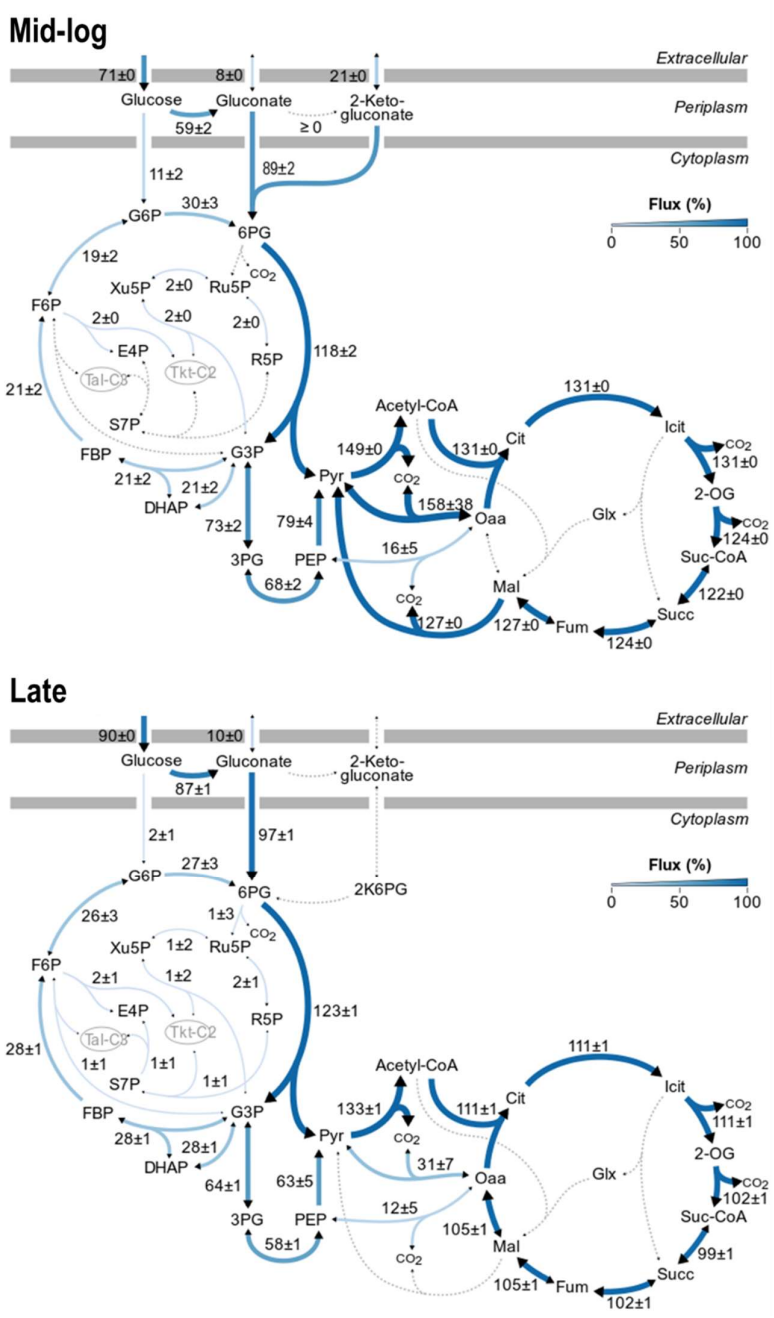

Figure 2.7. Visualization of metabolic fluxes during *Mid-Log* and *Late* phases. All fluxes were normalized to the specific glucose uptake rate (arbitrarily set to 100), and the intensity of each arrow correlates proportionally to the relative flux percentage. Dashed lines indicate that no significant flux through the corresponding biochemical step was detected under the experimental conditions tested. Abbreviations can be referred in **Figure 2.5**.

2.3 Discussion

Several bioinformatics tools have been previously developed for multi-omics analysis. (Gomez-Cabrero, et al., 2014, Yugi, et al., 2016, Hasin, et al., 2017, Argelaguet, et al., 2018). However, researchers typically create customized pipelines that incorporate some of these available tools, as each multi-omics dataset is unique. Although this approach is common, we assert that a general framework is crucial for gaining knowledge and conducting an optimized integrated research analysis in the future. Here, we first presented an experimental strategy to gather comparable –omic data sets for metabolomics, proteomics and fluxomics in *Pseudomonas putida* KT2440 under glycolytic regime.

We also developed an intuitive framework to capture the system-wide changes in the metabolism. Together with this, we were able to visualize and compare the information collected in the –omic experiments. This flexible framework allowed allocating the cellular components in a pre-designed metabolic network. Thus, we could examine and integrate the different cellular components being able to acquire an overview picture of the metabolism. The current design is suitable to incorporate, for example, transcriptomic data (in form of fold-changes), which can expand the information about the system. This visual framework is adaptable to the necessities of numerous application fields in Systems Biology. Frameworks like the one presented in this study, as well as other complementary tools (Rohart et al., 2017), are becoming more and more essential with the increasing volume of multi-omics data, especially in the field of multi-omics (Pinu, et al., 2019).

By utilizing the approach developed in this study, it becomes feasible to identify metabolic bottlenecks and acquire fundamental understanding about molecular mechanisms that are associated with a particular trait or phenotype. The workflow outlined in this study enables a wide audience of scientists to easily explore, integrate, and analyze multi-omics datasets. Ultimately, the entire pipeline can be implemented, scaled-down or –up, and applied in Biofoundries with the aim of increasing the throughput and conditions to be tested. Forthcoming work will focus on the integration and automated analysis of –Omic datasets by incorporating R-based statistical tools. In connection to this, another objective is to include a high-resolution

time-course set up allowing detecting temporal changes in relevant condition for biotechnological purposes (Xia, et al., 2011).

The future of multi-omics integration in system biology looks promising. With the development of new technologies, such as single-cell omics, high-throughput sequencing, machine learning and artificial intelligence (AI) researchers will be able to generate and analyze even larger and more complex datasets. This will enable the development of more accurate predictive models and the identification of new drug targets and diagnostic biomarkers (Lee, et al., 2020).

2.4 Material and Methods

2.4.1 Experiment design and platform set up for multi-omics analysis

The experimental design involves four sets of experiments: quantitative physiology, targeted metabolomics, semi-quantitative proteomics, and fluxomics. Regarding the quantitative physiological analysis, three biological replicates—named as BR1, BR2, and BR3—with their corresponding technical replicates—TR1, TR2, and TR3 were run in this experiment. In total, nine flasks were required for this first initial experimental set. For *Pseudomonas putida* KT2440, ten time points were harvested to analyze the entire growth curve in de Bont medium with 2 g L^{-1} glucose ($DBMG_{2g/L}$). In case of using a different strain or condition, is important to adjust the sampling time along the cultivation. In order to collect different aliquots (700 µl each), the sampling sequence was done as follows: for TR1 (BR1, BR2 and BR3) three samples were harvested at t1, 4, and 7 (hours 1, 4, and 7), TR2 (BR1, BR2, and BR3), at t2, 5 and8 (hour 2, 5, and 8), and TR3 (BR1, BR2, and BR3) at t3, 6 and 9 (hours 3, 6 and 9). The sampling sequence was carried out as previously mentioned in order to prevent the removal of over 10% of the flask volume (~2.0 mL). Once the strain was characterized in terms of growth, the sampling window was selected in order to harvest at *Mid-log* (OD_{600}~1.0) and *Late* (OD_{600}~1.8) phases. On the following day, metabolomics and proteomics were carried out by culturing the strain in three different flask (biological replicates). Within the same experimental set, samples for metabolomics were taken first according *Metabolomics sample processing and analysis* and later, proteomics samples as is indicated in *Semi-quantitative proteomics analysis*.

2.4.2 Culture conditions

Throughout the experiments conducted in this study, *Pseudomonas putida* KT2440 was grown at a temperature of 30°C. For propagation and storage, cells were grown in lysogeny broth (LB) medium (10 g L^{-1} tryptone, 7.5 g L^{-1} yeast extract, and 10 g L^{-1} NaCl). Pre-cultures as well as cultures were performed using de Bont medium (1.55 g L^{-1} K_2HPO_4, 0.85 g L^{-1} NaH_2PO_4, 2.0 g L^{-1} $(NH_4)_2SO_4$,0.1 g L^{-1} $MgCl_2$, 10 mg L^{-1} EDTA, 2 mg L^{-1} $ZnSO_4$, 1 mg L^{-1} $CaCl_2$, 5 mg L^{-1} $FeSO_4$, 0.2 mg L^{-1} Na_2MoO_4, 0.2 mg L^{-1} $CuSO_4$, 0.4 mg L^{-1} $CoCl_2$, and 1 mg L^{-1} $MnCl_2$) containing 2 g L^{-1} glucose (Hartmans, et al.,

1989). Solid culture media contained 15 g L^{-1} agar. Pre-cultures were set in 12-mL plastic tubes with 3 mL of $DBMG_{2g/L}$. Cultures were done in sterile 100-mL shaken flasks covered with aluminum foil and filled with 20 mL of $DBMG_{2gL}$. All liquid pre-cultures were agitated at 250 rpm (MaxQ™8000 incubator; ThermoFisher Scientific, Waltham, MA, USA) while the cultures were agitated at 200 rpm (New Brunswick™ Innova® 42/42R Shaker, sticky pad). Solid culture media contained 15 g L^{-1} agar.

2.4.3 Growth and uptake/secretion rates determination

Bacterial growth, uptake and secretion rates were calculated according (Long and Antoniewicz, 2019). Briefly, inoculum and cultures were done as explained in section *Culture conditions.* During the cultivation, nine samples per replicate were taken along the entire growth curve covering from the *lag* phase until stationary phase. Optical density was followed at 600nm (OD_{600}) and supernatants were collected by centrifugation at 10,000 *g* for 5 min at 4°C. Supernatants were stored at -20°C until further analysis. Glucose, gluconate and 2-ketogluconate consumption were determined as is described in section *High-performance Liquid Chromatography (HPLC) metabolite analysis*. Specific growth rates (h^{-1}) as well as uptake and secretion rates (mmol g_{CDW}^{-1} h^{-1}) were determined by plotting the natural logarithm ln(OD_{600}) versus time (hours) and external concentration (mM) versus OD_{600}, respectively. Biomass concentration was calculated transforming OD values in grams of cell dry weight per liter (g_{CDW} L^{-1}) using a conversion factor of 0.42 g_{CDW} L^{-1} OD_{600}^{-1}.

2.4.4 High-performance Liquid Chromatography (HPLC) metabolite analysis

The quantification of glucose, gluconate, and 2-ketogluconate was carried out using a Dionex Ultimate 3000 HPLC with an Aminex® HPX-87X Ion Exclusion (300 x 7.8 mm) column from BioRad, Hercules, CA. Detection was achieved using a combination of refractive index (RI-150) and UV detectors set to 260, 277, 304, and 210 nm. For analysis, the temperature column was maintained at 30°C and 5 mM H_2SO_4 solution was used as mobile phase with a flow rate of 0.5 mL min^{-1}. Chromeleon 7.1.3 software (Thermo Fisher Scientific®) was used to process and analyze chromatograms,

compound concentrations were calculated from peak areas using calibration curves with six different standard concentrations (Standard range for glucose was 0-4 g L^{-1}, sodium gluconate 0-1 g L^{-1} and 2-Keto-D-gluconic acid hemicalcium salt hydrate 0-1 g L^{-1}).

2.4.5 Multiomic analysis - Experimental set up and sampling

The experimental design is described in **Figure 1**. For all the experiments, pre-cultures were inoculated by taking one colony per replicate from a fresh LB plate (< 7 days) and incubated overnight for ~16 h. For fluxomics experiments, three biological replicates were used while for metabolomics and proteomics analysis four replicates were utilized. Each biological replicate pre-culture was used to inoculate the corresponding shaken flask with an initial OD_{600} of 0.05 as it is indicated in section *Culture conditions*. Prior to inoculation, the aliquots were centrifuged at 5,000 *g* for 5 min and washed once with de Bont minimal medium without carbon source. Then, the biomass pellet was resuspended in $DBMG_{2g/L}$ to initiate the different cultures. In all the experiments, once the culture reached an optical density of one (OD_{600} ~ 1.0), one milliliter was taken from the culture for fluxomics analysis and two milliliters for metabolomics and proteomics. The samples were processed according the procedures in *Metabolomic Analysis*, *Semi-quantitative proteomics* and *Fluxomics Analysis*.

2.4.6 Metabolomics sample processing and analysis

The cultivation for the metabolomics analysis was carried out as it is indicated in section *Culture conditions*. When the cultures reached *Mid-Log* or *Late* phase, 1 mL per replicate was taken. Each sample was rapidly filtrated in MF Millipore™ membrane filter (0.45-μm pore size; Sigma-Aldrich Co.). Later, the filter containing the bacterial biomass was placed onto a mini-Petri dish with 1 mL of quenching solution [40% (vol vol^{-1}) acetonitrile, 40% (vol vol^{-1}) methanol and 100 mM formic acid] precooled to -20°C. The solution containing the quenched biomass was transferred into a 2-mL tube; the filter was rinsed with an extra 1 mL of quenching solution and collected in a 2-mL Eppendorf tube. Samples were promptly placed in a dry ice bath and kept under these conditions for 30 min.

Next, the samples were thawed and centrifuged at 13,000 *g* for 5 min and the supernatants were transferred to a clean 2-mL Eppendorf tube, where the solvent was evaporated in a SpeedVac centrifuge for ca. 2 h at 45°C until they were fully dried. Finally, the samples were stored at -80°C until analysis. Just prior to metabolite analysis, the samples were resuspended in 100 µl of LC–MS grade water. Chromatographic separation of metabolites was done with an ACQUITY UPLC™ high-strength silica T3 column (1.8 µm × 2.1 mm × 30 mm, Agilent Technologies Inc.) in an HPLC apparatus (Shimadzu; Columbia, MD, USA). A gradient of eluent A [10 mM acetic acid, 5% (vol vol^{-1}) methanol, 10 mM tributylamine and 2% (vol vol^{-1}) 2-propanol] and 2-propanol was implemented for metabolite separation as previously described (McCloskey, et al., 2018). The flow rate was set to 0.5 ml min^{-1} with a total run time of 4.4 min; the autosampler was kept at 10°C and the column oven was set at 40°C with an injection volume of 10 µl. For metabolite identification and determination, a mass spectrometer (QTrap™ AB SCIEX mass spectrometer 5500) was operated in negative ion mode with the following settings: ionization set, −4,500; temperature, 500°C; curtain gas, 45; collision gas, high; ion source gas, 1; and ion source gas pressure, 250 pound square $inch^{-1}$.

2.4.7 Semi-quantitative proteomics analysis

For proteomics analysis, please refer to (Gurdo, et al., 2023) for a detailed step-by-step. Briefly, the samples were obtained from the same shaken flask where metabolomics samples were taken. Cells were harvested by centrifugation at 17,000 *g* for 2 minutes at 4°C. After removal of the supernatant, the cell pellets were frozen at −80°C until further analysis. Thawing of the cells was done on ice, and any remaining supernatant was removed after centrifugation at 15,000 *g* for 10 min. While kept on ice, two 3-mm zirconium oxide beads (Glen Mills, NJ, USA) were added to the samples. Immediately after removing the samples from ice, 100 µl of a solution containing 6 M Guanidinium hydrochloride (GuHCl), 5 mM tris(2-carboxyethyl)phosphine (TCEP), 10 mM chloroacetamide (CAA), and 100 mM Tris–HCl pH 8.5 heated at 95°C was added to the samples. The cells were disrupted in a Mixer Mill (MM 400 Retsch, Haan, Germany) set at 25 Hz for 5 min at room temperature, followed by 10 min in a thermal

mixer at 95°C and 2,000 rpm. Any cell debris was removed by centrifugation at 15,000 *g* for 10 min, after which 50 µl of supernatant was collected and diluted with 50 µl of 50 mM ammonium bicarbonate. Based on protein concentration quantification [via the Bradford method with BSA concentration standards (He, 2011)], 100 µg of protein was used for tryptic digestion. Tryptic digestion was carried out at constant shaking (400 rpm) for 8 h, after which 10 µl of 10% trifluoroacetic acid (TFA) was added, and samples were ready for StageTipping, using C18 as resin (Empore, 3M, USA).

For sample analysis, a CapLC system (Thermo Scientific) coupled to an Orbitrap Q exactive HF-X mass spectrometer (Thermo Scientific) was used. First, samples were captured at a flow rate of 10 µl min^{-1} on a pre-column (µ-precolumn C18 PepMap 100, 5 µm, 100Å). Subsequently, the peptides were separated in a 15 cm C18 easy spray column (PepMap RSLC C18 2µm, 100Å, 150 µmx15cm) at a flow rate of 1.2 µl min^{-1}, with an applied gradient from 4% (v v^{-1}) acetonitrile in water to 76% (v v^{-1}) over a total of 60 minutes. While spraying the samples into the mass spectrometer, the instrument operated in data-dependent mode using the following settings: MS-level scans were performed with Orbitrap resolution set to 60,000; AGC Target 3.0e6; maximum injection time 50 ms; intensity threshold 5.0e3; dynamic exclusion 25 s. Data-dependent MS2 selection was performed in Top 20 Speed mode with HCD collision energy set to 28% (AGC target 1.0e4, maximum injection time 22 ms, Isolation window 1.2 m z^{-1}).

For analysis of the thermo raw files, Proteome discoverer 2.4 was used with the following settings: Fixed modifications: Carbamidomethyl (C); Variable modifications: oxidation of methionine residues; First search mass tolerance: 20 ppm; MS/MS tolerance: 20 ppm; Trypsin as enzyme, allowing one missing cleavage; the false-discovery rate (FDR) was set at 0.1%; the match-between-runs window was set to 0.7 min. Only unique peptides were considered for quantification. To assign the detected peptides to their functions, a protein database consisting of the *Pseudomonas putida* reference proteome (UP000000556) was used, supplemented with heterologously expressed proteins.

2.4.8 Fluxomics Analysis

For parallel isotopic labeling experiment, *Pseudomonas putida* KT2440 was pre-grown in $DBMG_{2gL}$ with unlabeled $^{12}C_6$ glucose. The pre-cultures containing non-labeled biomass were used to inoculate the flask containing labeled substrate. In this case, three different isotopic tracers were used as carbon source: (i) 99% [1–^{13}C] glucose, (ii) 99% [6–^{13}C] glucose, and (iii) a 50:50% mixture of naturally labelled ^{12}C and 99% [U-$^{13}C_6$] glucose. Labeled glucose was acquired in Cambridge Isotope Laboratories, Inc. (Teddington, Middlesex, United Kingdom). Prior to the flux experiments, *P. putida* KT2440 cells from a cryovials were streaked onto a LB agar plate and grown overnight (~18 hours). All experiments were comprised of three biological replicates and two technical replicates.

2.4.9 GC-MS labeling analysis of aminoacids

For the analysis of proteinogenic amino acids, one absorbance unit at 600 nm (OD_{600} ~ 1.0 or 0.42 g_{CDW} L^{-1}) was harvested in a refrigerated (4°C) centrifuge at 10,000 *g* for 5 min. After removing the supernatant, pellets were re-suspended in 200 μL of 6 M HCl and incubated at 105°C for 16-24 hours in order to hydrolyze the biomass (Zamboni, et al., 2009). Hydrolyzed samples were then filtered on a 96-filter plate (MultiScreenHTS, HV Filter Plate 0.45 μm, hydrophilic, clear, non-sterile, Millipore, Catalogue number MSHVN45) by centrifugation at 1,500 *g* for 2 min, and dried for 4 h at 30°C using a vacuum concentrator (SAVANT, SpeedVac, Thermo Fisher Scientific, San Diego, CA, USA). Then, dried samples were derivatized in a two-step reaction: 1) by re-suspending the hydrolysate with 50 μL dimethylformamide (DMF) until it turns brownish and; 2) by adding the previous solution into a glass vial with 50 μL of N-tertbutyldimethylsilyl-N-methyltrifluoroacetamide with 1% (wt wt^{-1}) tertbutyldimethyl-chlorosilane (TBDMSTFA) and incubating it at 85°C for 1 hour. The derivatized samples were aliquoted in glass vials with inlets for GC-MS analysis within 12 h from derivatization.

The samples were injected on a single quadrupole Agilent 5977 GC-MS system with an Agilent DB-5ms capillary column (30m, inner diameter of 0.25 mm, film thickness of 0.25 μm). Samples were measured in full-scan mode, using a 1:100 split ratio, with

the following gradient: start at 160°C, hold for 1 min, ramp to 310°C at 20°C min^{-1}, hold for 1 min. Raw chromatographic data was integrated using SmartPeak (Kutuzova, et al., 2020). Processed data was further corrected for the natural abundance of isotopes in the derivatization agents used for GC-MS analysis using INCA software (Young, 2014).

Altogether, 12 amino acids yielded ion clusters with clean mass isotopomer distributions (MIDs), which were considered as inputs for flux estimation: alanine (m/z 232, m/z 260), glycine (m/z 218, m/z 246), valine (m/z 260, m/z 288), leucine (m/z 274), isoleucine (m/z 274), proline (m/z 258), serine (m/z 362, m/z 390), threonine (m/z 376, m/z 404), phenylalanine (m/z 302, m/z 308, m/z 336), aspartate (m/z 390, m/z 418), glutamate (m/z 330, m/z 432), lysine (m/z 329, m/z 431), and tyrosine (m/z 302).

These fragments have been previously demonstrated to be suitable for 13C flux studies of Pseudomonads (Kohlstedt and Wittmann, 2019). Glutamate and aspartate also reflected the pools of glutamine and asparagine, which underwent deamination during protein hydrolysis. The proteinogenic amino acids cysteine, methionine and tryptophan were not detected due to their degradation in the hydrolysis process (Wittmann, 2007).

2.4.10 GC-MS labeling analysis of sugars

For the analysis of cellular sugars, one absorbance unit at 600 nm (OD_{600} ~ 1.0 or 0.42 g_{CDW} L^{-1}) was harvested by centrifugation (5 min, 4°C, 10,000 *g*) and pellets were hydrolyzed in 250 µL 2 M HCl for 2 h at 100°C (Kiefer, et al., 2004). Afterwards, cell debris was removed by filtration using a 96-filter plate (MultiScreenHTS, HV Filter Plate 0.45 µm, hydrophilic, clear, and non-sterile, Millipore, Catalogue number MSHVN45). Subsequently, the hydrolysate was dried in a vacuum concentrator (SAVANT, SpeedVac, Thermo Fisher Scientific, San Diego, CA, USA). Analytes contained in the dried residue were incubated in 100 µL methoxylamine 2 % m v^{-1} in pyridine at 80°C for 1 h. The obtained O-methyl oxime forms of the analytes were silylated at 80°C for 30 min into trimethylsilyl (TMS) derivatives in a second step using N,O-bis-trimethylsilyl-trifluoroacetamide (BSTFA, Macherey-Nagel). The derivatized

analytes were quantified by GC-MS as it is described in *GC-MS labeling analysis of aminoacids*. The fragments considered for ^{13}C–MFA were: glucose (m/z 319, m/z 554) and glucosamine (m/z 319, m/z 553).

2.4.11 Data manipulation and visualization

2.4.11.1 Targeted metabolomics based on LC-MS/MS

Peak intensities for metabolites within central carbon metabolism were obtained from this analysis by processing the raw mass spectrometry data through the SmartPeak workflow (Kutuzova, et al., 2020, Kozaeva, et al., 2021). Metabolomics data analysis was carried out in Excel and the analysed data—metabolite fold change (FC)—was used as input to visualize it on a map by utilizing the R package *fluctuator*.

2.4.11.2 Semi-quantitative proteomics

Proteomics data, acquired as described above, were analyzed using a customized R script in RStudio (version 2022.12.0). The abundance values were $\log_2$-transformed and normalized via variance stabilization normalization using the *vsn* package (Huber, et al., 2002). Next, missing values were imputed by replacing them with the lowest observations of each sample (Liu and Dongre, 2021). A differential enrichment test was performed for each contrast in the dataset based on protein-wise linear models and empirical Bayes statistics using *limma* (Ritchie, et al., 2015). *P-values* were adjusted using *fdrtool* with the Benjamini-Hochberg method (Strimmer, 2008). The adjusted *P-value* threshold for significant observations was set at a value of 0.05. The $\log_2$(fold change) values of proteins in central metabolism were visualized on a map by using functions of the package *fluctuator*.

2.4.11.3 Reaction network for metabolic flux analysis

The metabolic networks of *Pseudomonas putida* KT2440 was built using the last genome scale metabolic model published: iJN1463 (Nogales, et al., 2020). In total, 79 reactions were included as part of the central carbon metabolism in *P. putida* KT2440. The full

list containing the whole compendium of reactions as well as the carbon atom transition are listed in Supplementary Information (**Table S2.2**).

2.4.11.4 Flux estimation using INCA software

For ^{13}C–metabolic flux analysis (^{13}C–MFA) and flux estimation, INCA software package was implemented to analyze the metabolic network (Young, 2014). Growth rates, glucose, gluconate and 2-KGA uptake/secretion rates were used to constrain the MFA model. The biomass equation was derived from biomass yield that represents the normalized precursor drainage to calculate the experimental growth rates (Czajka, et al., 2022). Also, ATP and NAD(P)H maintenance rates were converted into relative fluxes and included as fixed parameters in the model according (Zobel, et al., 2017). The uptake rates used to constrain the model were normalized using the sum of the uptake rates (100% = sum of glucose + gluconate and 2-KGA uptake rates). The relative intracellular fluxes (%) were calculated by minimizing the sum-of-squared residuals (SSR) between computationally simulated and experimentally determined measurements (MDVs or mass distribution vectors for each fragment analyzed).

References Chapter 2

Altelaar, A.F.M., Munoz, J., and Heck, A.J.R. (2013) Next-generation proteomics: towards an integrative view of proteome dynamics, *Nature Reviews Genetics* **14**: 35-48.
Argelaguet, R., Velten, B., Arnol, D., Dietrich, S., Zenz, T., Marioni, J.C., et al. (2018) Multi-Omics Factor Analysis—a framework for unsupervised integration of multi-omics data sets, *Molecular Systems Biology* **14**: e8124.
Bartell, J.A., Sommer, L.M., Marvig, R.L., Skov, M., Pressler, T., Molin, S., and Johansen, H.K. (2021) Omics-based tracking of *Pseudomonas aeruginosa* persistence in "eradicated" cystic fibrosis patients, *European Respiratory Journal* **57**: 2000512.
Bojanovič, K., D'Arrigo, I., and Long, K.S. (2017) Global Transcriptional Responses to Osmotic, Oxidative, and Imipenem Stress Conditions in *Pseudomonas putida*, *Appl Environ Microbiol* **83**: e03236-03216.
Bolten, C.J., Kiefer, P., Letisse, F., Portais, J.-C., and Wittmann, C. (2007) Sampling for Metabolome Analysis of Microorganisms, *Analytical Chemistry* **79**: 3843-3849.
Cabello, P., Luque-Almagro, V.M., Olaya-Abril, A., Sáez, L.P., Moreno-Vivián, C., and Roldán, M.D. (2018) Assimilation of cyanide and cyano-derivatives by *Pseudomonas pseudoalcaligenes* CECT5344: from omic approaches to biotechnological applications, *FEMS Microbiology Letters* **365**: fny032.
Cobb, M. (2017) 60 years ago, Francis Crick changed the logic of biology, *PLoS Biol* **15**: e2003243.
Cuenca, M.d.S., Roca, A., Molina-Santiago, C., Duque, E., Armengaud, J., Gómez-Garcia, M.R., and Ramos, J.L. (2016) Understanding butanol tolerance and assimilation in *Pseudomonas putida* BIRD-1: an integrated omics approach, *Microbial Biotechnology* **9**: 100-115.
Czajka, J.J., Banerjee, D., Eng, T., Menasalvas, J., Yan, C., Munoz, N.M., et al. (2022) Tuning a high performing multiplexed-CRISPRi *Pseudomonas putida* strain to further enhance indigoidine production, *Metabolic Engineering Communications* **15**: e00206.
De Keersmaecker, S.C.J., Thijs, I.M.V., Vanderleyden, J., and Marchal, K. (2006) Integration of omics data: how well does it work for bacteria?, *Molecular Microbiology* **62**: 1239-1250.
del Castillo, T., Ramos, J.L., Rodríguez-Herva, J.J., Fuhrer, T., Sauer, U., and Duque, E. (2007) Convergent peripheral pathways catalyze initial glucose catabolism in *Pseudomonas putida*: genomic and flux analysis, *J Bacteriol* **189**: 5142-5152.
Driouch, H., Melzer, G., and Wittmann, C. (2012) Integration of *in vivo* and *in silico* metabolic fluxes for improvement of recombinant protein production, *Metabolic Engineering* **14**: 47-58.

Droste, P., Miebach, S., Niedenführ, S., Wiechert, W., and Nöh, K. (2011) Visualizing multi-omics data in metabolic networks with the software Omix—A case study, *Biosystems* **105**: 154-161.

Dvořák, P., and de Lorenzo, V. (2018) Refactoring the upper sugar metabolism of *Pseudomonas putida* for co-utilization of cellobiose, xylose, and glucose, *Metabolic Engineering* **48**: 94-108.

Ebert, B.E., Kurth, F., Grund, M., Blank, L.M., and Schmid, A. (2011) Response of *Pseudomonas putida* KT2440 to increased NADH and ATP demand, *Appl Environ Microbiol* **77**: 6597-6605.

Ellepola, K., Truong, T., Liu, Y., Lin, Q., Lim, T.K., Lee, Y.M., et al. (2019) Multi-omics Analyses Reveal Synergistic Carbohydrate Metabolism in *Streptococcus mutans-Candida albicans* Mixed-Species Biofilms, *Infect Immun* **87**: :e00339-00319.

Fu, J., Sharma, P., Spicer, V., Krokhin, O.V., Zhang, X., Fristensky, B., et al. (2015) Quantitative 'omics analyses of medium chain length polyhydroxyalkanaote metabolism in *Pseudomonas putida* LS46 cultured with waste glycerol and waste fatty acids, *PLoS One* **10**: e0142322.

Fuhrer, T., Fischer, E., and Sauer, U. (2005) Experimental identification and quantification of glucose metabolism in seven bacterial species, *J Bacteriol* **187**: 1581-1590.

Gehlenborg, N., O'donoghue, S.I., Baliga, N.S., Goesmann, A., Hibbs, M.A., Kitano, H., et al. (2010) Visualization of omics data for systems biology, *Nature methods* **7**: S56-S68.

Gomez-Cabrero, D., Abugessaisa, I., Maier, D., Teschendorff, A., Merkenschlager, M., Gisel, A., et al. (2014) Data integration in the era of omics: current and future challenges, *BMC Systems Biology* **8**: I1.

Grady, S.L., Malfatti, S.A., Gunasekera, T.S., Dalley, B.K., Lyman, M.G., Striebich, R.C., et al. (2017) A comprehensive multi-omics approach uncovers adaptations for growth and survival of *Pseudomonas aeruginosa* on n-alkanes, *BMC Genomics* **18**: 334.

Graham, R.L.J., Graham, C., and McMullan, G. (2007) Microbial proteomics: a mass spectrometry primer for biologists, *Microbial Cell Factories* **6**: 26.

Gurdo, N., Taylor Parkins, S.K., Fricano, M., Wulff, T., Nielsen, L.K., and Nikel, P.I. (2023) Protocol for absolute quantification of proteins in Gram-negative bacteria based on QconCAT-based labeled peptides, *STAR Protocols* **4**: 102060.

Gurdo, N., Volke, D.C., McCloskey, D., and Nikel, P.I. (2023) Automating the design-build-test-learn cycle towards next-generation bacterial cell factories, *New Biotechnology* **74**: 1-15.

Hartmann, A., and Jozefowicz, A.M. (2018) VANTED: A Tool for Integrative Visualization and Analysis of -Omics Data. In: *Plant Membrane Proteomics: Methods and Protocols*. Mock, H.-P., Matros, A., and Witzel, K. (eds). New York, NY: Springer New York. 261-278.

Hartmans, S., Smits, J.P., van der Werf, M.J., Volkering, F., and de Bont, J.A. (1989) Metabolism of Styrene Oxide and 2-Phenylethanol in the Styrene-Degrading *Xanthobacter Strain* 124X, *Appl Environ Microbiol* **55**: 2850-2855.

Hasin, Y., Seldin, M., and Lusis, A. (2017) Multi-omics approaches to disease, *Genome Biology* **18**: 83.

He, F. (2011) Bradford protein assay, *Bio-protocol*: e45-e45.

Huber, W., von Heydebreck, A., Sültmann, H., Poustka, A., and Vingron, M. (2002) Variance stabilization applied to microarray data calibration and to the quantification of differential expression, *Bioinformatics* **18 Suppl 1**: S96-104.

Kanani, H., Chrysanthopoulos, P.K., and Klapa, M.I. (2008) Standardizing GC–MS metabolomics, *Journal of Chromatography B* **871**: 191-201.

Kiefer, P., Heinzle, E., Zelder, O., and Wittmann, C. (2004) Comparative metabolic flux analysis of lysine-producing *Corynebacterium glutamicum* cultured on glucose or fructose, *Applied and Environmental Microbiology* **70**: 229-239.

Kim, M., Rai, N., Zorraquino, V., and Tagkopoulos, I. (2016) Multi-omics integration accurately predicts cellular state in unexplored conditions for *Escherichia coli*, *Nature Communications* **7**: 13090.

Kleijn, R.J., van Winden, W.A., van Gulik, W.M., and Heijnen, J.J. (2005) Revisiting the 13C-label distribution of the non-oxidative branch of the pentose phosphate pathway based upon kinetic and genetic evidence, *The FEBS Journal* **272**: 4970-4982.

Kohlstedt, M., Sappa, P.K., Meyer, H., Maaß, S., Zaprasis, A., Hoffmann, T., et al. (2014) Adaptation of *Bacillus subtilis* carbon core metabolism to simultaneous nutrient limitation and osmotic challenge: a multi-omics perspective, *Environmental Microbiology* **16**: 1898-1917.

Kohlstedt, M., and Wittmann, C. (2019) GC-MS-based ^{13}C metabolic flux analysis resolves the parallel and cyclic glucose metabolism of *Pseudomonas putida* KT2440 and *Pseudomonas aeruginosa* PAO1, *Metabolic Engineering* **54**: 35-53.

Kozaeva, E., Volkova, S., Matos, M.R.A., Mezzina, M.P., Wulff, T., Volke, D.C., et al. (2021) Model-guided dynamic control of essential metabolic nodes boosts acetyl-coenzyme A–dependent bioproduction in rewired *Pseudomonas putida*, *Metabolic Engineering* **67**: 373-386.

Kukurugya, M.A., Mendonca, C.M., Solhtalab, M., Wilkes, R.A., Thannhauser, T.W., and Aristilde, L. (2019) Multi-omics analysis unravels a segregated metabolic flux

network that tunes co-utilization of sugar and aromatic carbons in *Pseudomonas putida*, *J Biol Chem* **294**: 8464-8479.

Kutuzova, S., Colaianni, P., Rost, H., Sachsenberg, T., Alka, O., Kohlbacher, O., et al. (2020) SmartPeak automates targeted and quantitative metabolomics data processing, *Analytical chemistry* **92**: 15968-15974.

Lahtvee, P.-J., Adamberg, K., Arike, L., Nahku, R., Aller, K., and Vilu, R. (2011) Multi-omics approach to study the growth efficiency and amino acid metabolism in *Lactococcus lactis* at various specific growth rates, *Microbial Cell Factories* **10**: 12.

Lee, J., Hyeon, D.Y., and Hwang, D. (2020) Single-cell multiomics: technologies and data analysis methods, *Experimental & Molecular Medicine* **52**: 1428-1442.

Li, J., Sang, Y., Zeng, S., Mo, S., Zhang, Z., He, S., et al. (2022) MicrobioSee: A Web-Based Visualization Toolkit for Multi-Omics of Microbiology, *Frontiers in Genetics* **13**: 853612.

Liu, M., and Dongre, A. (2021) Proper imputation of missing values in proteomics datasets for differential expression analysis, *Brief Bioinform* **22**.

Long, C.P., and Antoniewicz, M.R. (2019) High-resolution ^{13}C metabolic flux analysis, *Nature Protocols* **14**: 2856-2877.

López de Maturana, E., Alonso, L., Alarcón, P., Martín-Antoniano, I.A., Pineda, S., Piorno, L., et al. (2019) Challenges in the integration of omics and non-omics Data, *Genes (Basel)* **10**.

Luque-Almagro, V.M., Escribano, M.P., Manso, I., Sáez, L.P., Cabello, P., Moreno-Vivián, C., and Roldán, M.D. (2015) DNA microarray analysis of the cyanotroph *Pseudomonas pseudoalcaligenes* CECT5344 in response to nitrogen starvation, cyanide and a jewelry wastewater, *Journal of Biotechnology* **214**: 171-181.

McCloskey, D., Xu, J., Schrübbers, L., Christensen, H.B., and Herrgård, M.J. (2018) RapidRIP quantifies the intracellular metabolome of 7 industrial strains of *E. coli*, *Metabolic Engineering* **47**: 383-392.

Neuweger, H., Albaum, S.P., Dondrup, M., Persicke, M., Watt, T., Niehaus, K., et al. (2008) MeltDB: a software platform for the analysis and integration of metabolomics experiment data, *Bioinformatics* **24**: 2726-2732.

Nikel, P.I., Chavarría, M., Fuhrer, T., Sauer, U., and de Lorenzo, V. (2015) *Pseudomonas putida* KT2440 Strain Metabolizes Glucose through a Cycle Formed by Enzymes of the Entner-Doudoroff, Embden-Meyerhof-Parnas, and Pentose Phosphate Pathways, *J Biol Chem* **290**: 25920-25932.

Nogales, J., Mueller, J., Gudmundsson, S., Canalejo, F.J., Duque, E., Monk, J., et al. (2020) High-quality genome-scale metabolic modelling of *Pseudomonas putida* highlights its broad metabolic capabilities, *Environmental Microbiology* **22**: 255-269.

Oldiges, M., Lütz, S., Pflug, S., Schroer, K., Stein, N., and Wiendahl, C. (2007) Metabolomics: current state and evolving methodologies and tools, *Applied Microbiology and Biotechnology* **76**: 495-511.

Pinu, F.R., Beale, D.J., Paten, A.M., Kouremenos, K., Swarup, S., Schirra, H.J., and Wishart, D. (2019) Systems Biology and Multi-Omics Integration: Viewpoints from the Metabolomics Research Community, *Metabolites* **9**: 76.

Quinn, R.A., Navas-Molina, J.A., Hyde, E.R., Song, S.J., Vázquez-Baeza, Y., Humphrey, G., et al. (2016) From Sample to Multi-Omics Conclusions in under 48 Hours, *mSystems* **1**: e00038-00016.

Ritchie, M.E., Phipson, B., Wu, D., Hu, Y., Law, C.W., Shi, W., and Smyth, G.K. (2015) limma powers differential expression analyses for RNA-sequencing and microarray studies, *Nucleic Acids Res* **43**: e47.

Sasnow, S.S., Wei, H., and Aristilde, L. (2016) Bypasses in intracellular glucose metabolism in iron-limited *Pseudomonas putida*, *Microbiologyopen* **5**: 3-20.

Sorek, R., and Cossart, P. (2010) Prokaryotic transcriptomics: a new view on regulation, physiology and pathogenicity, *Nature Reviews Genetics* **11**: 9-16.

Stincone, A., Prigione, A., Cramer, T., Wamelink, M.M., Campbell, K., Cheung, E., et al. (2015) The return of metabolism: biochemistry and physiology of the pentose phosphate pathway, *Biological Reviews* **90**: 927-963.

Strimmer, K. (2008) fdrtool: a versatile R package for estimating local and tail area-based false discovery rates, *Bioinformatics* **24**: 1461-1462.

Sudarsan, S., Dethlefsen, S., Blank, L.M., Siemann-Herzberg, M., and Schmid, A. (2014) The Functional Structure of Central Carbon Metabolism in *Pseudomonas putida* KT2440, *Applied and Environmental Microbiology* **80**: 5292-5303.

Sun, J., Zhou, J., Wang, Z., He, W., Zhang, D., Tong, Q., and Su, X. (2015) Multi-omics based changes in response to cadmium toxicity in *Bacillus licheniformis* A, *RSC advances* **5**: 7330-7339.

Tan, S., Tan, H.T., and Chung, M.C. (2008) Membrane proteins and membrane proteomics, *Proteomics* **8**: 3924-3932.

Thompson, M.G., Valencia, L.E., Blake-Hedges, J.M., Cruz-Morales, P., Velasquez, A.E., Pearson, A.N., et al. (2019) Omics-driven identification and elimination of valerolactam catabolism in *Pseudomonas putida* KT2440 for increased product titer, *Metabolic Engineering Communications* **9**: e00098.

Tokic, M., Hatzimanikatis, V., and Miskovic, L. (2020) Large-scale kinetic metabolic models of *Pseudomonas putida* KT2440 for consistent design of metabolic engineering strategies, *Biotechnology for Biofuels* **13**: 33.

Veenstra, T.D. (2021) Omics in Systems Biology: Current Progress and Future Outlook, *PROTEOMICS* **21**: 2000235.

Vicente, M., and Cánovas, J.L. (1973) Glucolysis in *Pseudomonas putida*: physiological role of alternative routes from the analysis of defective mutants, *J Bacteriol* **116**: 908-914.

Volke, D.C., Gurdo, N., Milanesi, R., and Nikel, P.I. (2023) Time-resolved, deuterium-based fluxomics uncovers the hierarchy and dynamics of sugar processing by *Pseudomonas putida*, *Metabolic Engineering*.

Vranakis, I., Goniotakis, I., Psaroulaki, A., Sandalakis, V., Tselentis, Y., Gevaert, K., and Tsiotis, G. (2014) Proteome studies of bacterial antibiotic resistance mechanisms, *Journal of Proteomics* **97**: 88-99.

Weckwerth, W. (2003) Metabolomics in Systems Biology, *Annual Review of Plant Biology* **54**: 669-689.

Weimer, A., Kohlstedt, M., Volke, D.C., Nikel, P.I., and Wittmann, C. (2020) Industrial biotechnology of *Pseudomonas putida*: advances and prospects, *Applied Microbiology and Biotechnology* **104**: 7745-7766.

Wiechert, W. (2001) 13C metabolic flux analysis, *Metab Eng* **3**: 195-206.

Wiklund, S., Johansson, E., Sjöström, L., Mellerowicz, E.J., Edlund, U., Shockcor, J.P., et al. (2008) Visualization of GC/TOF-MS-based metabolomics data for identification of biochemically interesting compounds using OPLS class models, *Anal Chem* **80**: 115-122.

Wirth, N.T., Gurdo, N., Krink, N., Vidal-Verdú, À., Donati, S., Férnandez-Cabezón, L., et al. (2022) A synthetic C2 auxotroph of *Pseudomonas putida* for evolutionary engineering of alternative sugar catabolic routes, *Metabolic Engineering* **74**: 83-97.

Wittmann, C. (2007) Fluxome analysis using GC-MS, *Microbial Cell Factories* **6**: 6.

Wordofa, G.G., Kristensen, M., Schrübbers, L., McCloskey, D., Forster, J., and Schneider, K. (2017) Quantifying the Metabolome of *Pseudomonas taiwanensis* VLB120: Evaluation of Hot and Cold Combined Quenching/Extraction Approaches, *Analytical Chemistry* **89**: 8738-8747.

Xia, J., Sinelnikov, I.V., and Wishart, D.S. (2011) MetATT: a web-based metabolomics tool for analyzing time-series and two-factor datasets, *Bioinformatics* **27**: 2455-2456.

Xia, J., and Wishart, D.S. (2010) MSEA: a web-based tool to identify biologically meaningful patterns in quantitative metabolomic data, *Nucleic Acids Res* **38**: W71-77.

Yoon, S.H., Han, M.-J., Jeong, H., Lee, C.H., Xia, X.-X., Lee, D.-H., et al. (2012) Comparative multi-omics systems analysis of *Escherichia coli* strains B and K-12, *Genome Biology* **13**: R37.

Young, J.D. (2014) INCA: a computational platform for isotopically non-stationary metabolic flux analysis, *Bioinformatics (Oxford, England)* **30**: 1333-1335.

Yugi, K., Kubota, H., Hatano, A., and Kuroda, S. (2016) Trans-Omics: How To Reconstruct Biochemical Networks Across Multiple 'Omic' Layers, *Trends in Biotechnology* **34**: 276-290.

Zamboni, N., Fendt, S.-M., Rühl, M., and Sauer, U. (2009) ^{13}C-based metabolic flux analysis, *Nature protocols* **4**: 878.

Zhang, W., Li, F., and Nie, L. (2010) Integrating multiple 'omics' analysis for microbial biology: application and methodologies, *Microbiology* **156**: 287-301.

Zhao, Z., Cai, M., Liu, Y., Hu, M., Yang, F., Zhu, R., et al. (2022) Genomics and transcriptomics-guided metabolic engineering *Corynebacterium glutamicum* for l-arginine production, *Bioresource Technology* **364**: 128054.

Zobel, S., Kuepper, J., Ebert, B., Wierckx, N., and Blank, L.M. (2017) Metabolic response of Pseudomonas putida to increased NADH regeneration rates, *Engineering in Life Sciences* **17**: 47-57.

Zoppi, J., Guillaume, J.-F., Neunlist, M., and Chaffron, S. (2021) MiBiOmics: an interactive web application for multi-omics data exploration and integration, *BMC Bioinformatics* **22**: 6.

Chapter 3 - Protocol for absolute quantification of proteins in Gram-negative bacteria based on QconCAT-based labeled peptides

This chapter represents a protocol paper published in STAR protocol as follows:

Gurdo, N., Taylor Parkins, S.K., Fricano, M., Wulff, T., Nielsen, L.K., and Nikel, P.I. (2023) Protocol for absolute quantification of proteins in Gram-negative bacteria based on QconCAT-based labeled peptides, STAR Protocols 4: 102060. https://doi.org/10.1016/j.xpro.2023.102060.

Abstract

Mass-spectrometry-based absolute protein quantification uses labeled quantification concatamer (QconCAT) as internal standards (ISs). To calculate the amount of protein(s), the ion intensity ratio between the analyte and its cognate IS is compared in each biological sample. The present protocol describes a systematic workflow to design, produce, and purify QconCATs and to quantify soluble proteins in *Pseudomonas putida* KT2440. Our methodology enables the quantification of detectable peptide and serves as a versatile platform to produce ISs for different biological systems.

STAR Protocols

CellPress
OPEN ACCESS

Protocol

Protocol for absolute quantification of proteins in Gram-negative bacteria based on QconCAT-based labeled peptides

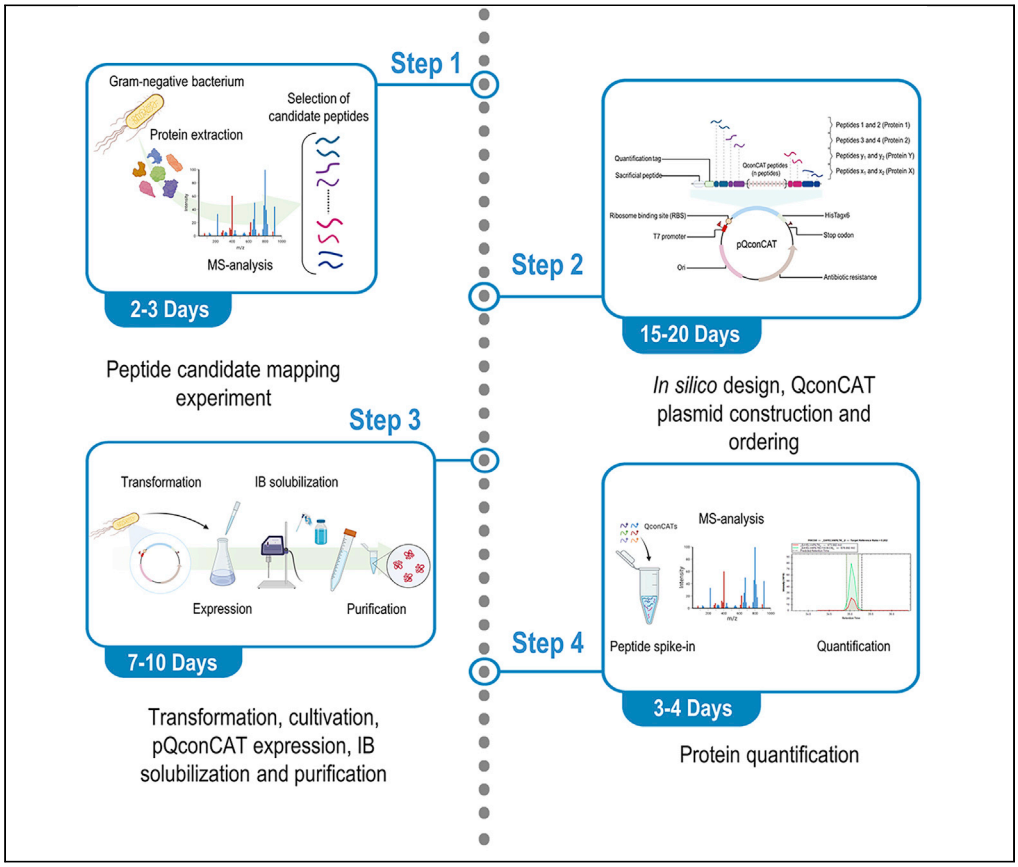

Mass-spectrometry-based absolute protein quantification uses labeled quantification concatamer (QconCAT) as internal standards (ISs). To calculate the amount of protein(s), the ion intensity ratio between the analyte and its cognate IS is compared in each biological sample. The present protocol describes a systematic workflow to design, produce, and purify QconCATs and to quantify soluble proteins in *Pseudomonas putida* KT2440. Our methodology enables the quantification of detectable peptide and serves as a versatile platform to produce ISs for different biological systems.

Publisher's note: Undertaking any experimental protocol requires adherence to local institutional guidelines for laboratory safety and ethics.

Nicolás Gurdo, Shannara Kayleigh Taylor Parkins, Martina Fricano, Tune Wulff, Lars Keld Nielsen, Pablo Iván Nikel

pabnik@biosustain.dtu.dk

Highlights

The workflow includes the expression and purification of peptide concatamers (QconCATs)

Systematic protocol for the selection of unique peptides

Mass spectrometry was used for quantitative sample analysis

Absolute quantification of proteins using a customized Python script

Gurdo et al., STAR Protocols 4, 102060
March 17, 2023
https://doi.org/10.1016/j.xpro.2023.102060

STAR Protocols

CellPress
OPEN ACCESS

Protocol

Protocol for absolute quantification of proteins in Gram-negative bacteria based on QconCAT-based labeled peptides

Nicolás Gurdo,[1,3] Shannara Kayleigh Taylor Parkins,[1] Martina Fricano,[1] Tune Wulff,[1] Lars Keld Nielsen,[1,2] and Pablo Iván Nikel[1,3,4,*]

[1]The Novo Nordisk Foundation Center for Biosustainability, Technical University of Denmark, 2800 Kongens Lyngby, Denmark

[2]Australian Institute for Bioengineering and Nanotechnology, The University of Queensland, Brisbane, QLD 4072, Australia

[3]Technical contact: nicrdo@biosustain.dtu.dk

[4]Lead contact

*Correspondence: pabnik@biosustain.dtu.dk
https://doi.org/10.1016/j.xpro.2023.102060

SUMMARY

Mass-spectrometry-based absolute protein quantification uses labeled quantification concatamer (QconCAT) as internal standards (ISs). To calculate the amount of protein(s), the ion intensity ratio between the analyte and its cognate IS is compared in each biological sample. The present protocol describes a systematic workflow to design, produce, and purify QconCATs and to quantify soluble proteins in *Pseudomonas putida* KT2440. Our methodology enables the quantification of detectable peptide and serves as a versatile platform to produce ISs for different biological systems.

BEFORE YOU BEGIN

The protocol below describes the steps needed to conduct an integral, quantitative proteomics analysis of the model soil bacterium *Pseudomonas putida* KT2440.[1–4] This workflow (Figure 1) can be likewise applied to different Gram-negative bacteria to quantify the protein content in the bacterial biomass. Regardless of the microbial host selected, an effective method for protein extraction is required to isolate the greatest number of proteins possible[5,6]—subjected to the specific experimental conditions employed.[7,8] In the last two decades, most of the studies developed to this end have applied qualitative strategies to explore the total bacterial proteome under different conditions (often, through direct comparison to a reference sample) by calculating relative ratios or fold changes in protein content.[9–11] This methodology, however, could potentially lead to biases due to the fact that relative quantification cannot explicitly provide the actual polypeptide concentrations, given that proteins are present at contents that vary in orders of magnitude (e.g., femto-, pico-, nano- or micromoles of protein per gram/number of cells).[12] To address this challenge, the asymmetrical distribution of protein concentrations in the cell could be quantified by targeted proteomics methods, capable of accurately determining the amount of specific proteins.[13] Here, quantification can be accomplished by incorporating labeled proteotryptic peptides—adopted as internal standards—in the samples, allowing the user to calculate the absolute concentration of a selected set of proteins.

Reagent preparation

Timing: 6–8 h

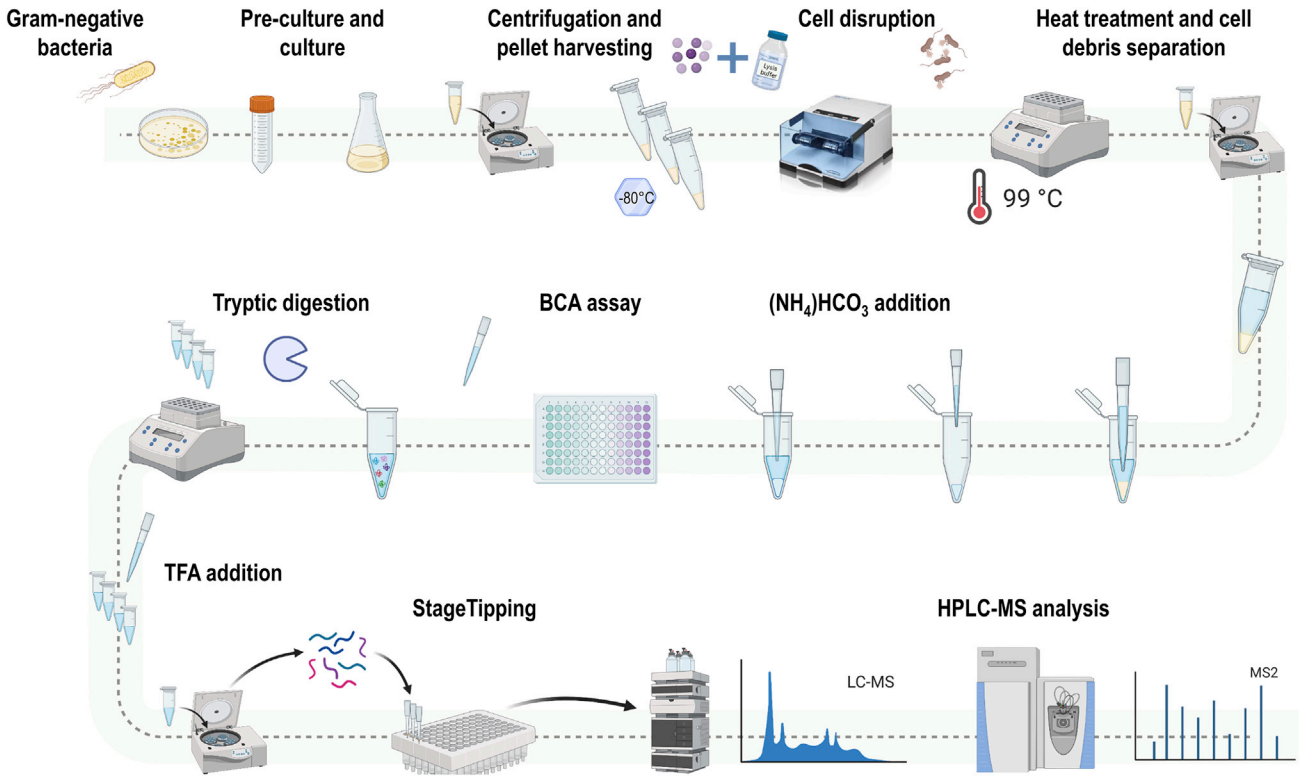

Figure 1. Workflow for the selection of candidate peptides

The scheme represents a detailed step-by-step procedure to obtain peptide candidates used in the design of the pQconCAT plasmid.

Note: This protocol has been used to express and purify unique peptides (i.e., peptides that are present in only one protein of a proteome of interest) from *Pseudomonas putida* (in this protocol, strain KT2440)[14,15] in *Escherichia coli* BL21(DE3) Δ*lysA* Δ*argH*. This strain is an L-lysine and L-arginine auxotroph derivative of *E. coli* BL21(DE3), commonly used for protein production,[16] and will only grow in a minimal medium when the corresponding amino acids are supplemented to the cultures.

The day before the "peptide candidate mapping experiment":

1. Prepare the following media: 2×YT and LB agar plates (with and without antibiotics as needed).
2. Make antibiotic and IPTG stock solutions.
3. Prepare lysis buffer, ammonium bicarbonate solution, resuspension buffer, Ni-resin equilibration buffer, elution buffer, phosphate buffer, SDS-PAGE buffer and [Glu1]-fibrinopeptide B solution.

KEY RESOURCES TABLE

REAGENT or RESOURCE	SOURCE	IDENTIFIER
Critical commercial assays		
Bicinchoninic acid (BCA) assay kit	VWR	Cat#89167-792
Bacteria strains		
Escherichia coli BL21 DE3 Δ*lysA* Δ*argH*	Denmark Technical University, The Novo Nordisk Foundation Center for Biosustainability	This work
Pseudomonas putida KT2440	ATCC	Cat#47054

(*Continued on next page*)

Continued

REAGENT or RESOURCE	SOURCE	IDENTIFIER
Chemicals, peptides, and recombinant proteins		
Yeast extract	Sigma-Aldrich	CAS# 8013-01-2
Bacto yeast extract	Thermo Fisher	Cat#212750
Tryptone	Sigma-Aldrich	CAS# 91079-40-2
Bacto tryptone	Thermo Fisher	Cat#211705
NaCl	Sigma-Aldrich	CAS# 7647-14-5
Calcium chloride dihydrate ($CaCl_2 \cdot H_2O$)	Sigma-Aldrich	CAS# 10043-52-4
Magnesium sulfate heptahydrate ($MgSO_4 \cdot 7H_2O$)	Sigma-Aldrich	CAS# 10034-99-8
Pyridoxine hydrochloride	Sigma-Aldrich	CAS# 58-56-0
Thiamine hydrochloride	Sigma-Aldrich	CAS# 67-03-8
Riboflavin	Sigma-Aldrich	CAS# 83-88-5
Nicotinic acid	Sigma-Aldrich	CAS# 59-67-6
Calcium D-(+)-pantothenate	Sigma-Aldrich	CAS# 137-08-6
p-Aminobenzoic acid	Sigma-Aldrich	CAS# 150-13-0
Thioctic acid	Sigma-Aldrich	CAS# 1077-28-7
Biotin	Sigma-Aldrich	CAS# 58-85-5
Folic acid	Sigma-Aldrich	CAS# 59-30-3
Vitamin B12	Sigma-Aldrich	CAS# 68-19-9
Disodium EDTA	Sigma-Aldrich	CAS# 6381-92-6
Zinc sulfate heptahydrate ($ZnSO_4 \cdot 7H_2O$)	Sigma-Aldrich	CAS# 7446-20-0
Manganese chloride tetrahydrate ($MnCl_2 \cdot 4H_2O$)	Sigma-Aldrich	CAS# 13446-34-9
Cobalt(II) chloride hexahydrate ($CoCl_2 \cdot 6H_2O$)	Sigma-Aldrich	CAS# 7791-13-1
Copper(II) chloride dehydrate ($CuCl_2 \cdot 2H_2O$)	Sigma-Aldrich	CAS# 10125-13-0
Disodium molybdate dehydrate ($Na_2MoO_4 \cdot 2H_2O$)	Sigma-Aldrich	CAS# 10102-40-6
Iron sulfate heptahydrate ($FeSO_4 \cdot 7H_2O$)	Sigma-Aldrich	CAS# 7782-63-0
Boric acid (H_3BO_3)	Sigma-Aldrich	CAS# 10043-35-3
Potassium iodide (KI)	Sigma-Aldrich	CAS# 7681-11-0
Disodium hydrogen phosphate (Na_2HPO_4)	Sigma-Aldrich	CAS# 7558-79-4
Potassium phosphate, monobasic (KH_2PO_4)	Sigma-Aldrich	CAS# 7778-77-0
Ammonium chloride (NH_4Cl)	Sigma-Aldrich	CAS# 12125-02-9
Agar	Sigma-Aldrich	CAS# 9002-18-0
Kanamycin monosulfate	Sigma-Aldrich	CAS# 25389-94-0
Guanidinium hydrochloride (GuHCl)	Sigma-Aldrich	CAS# 50-01-1
Tris(2-carboxyethyl)phosphine hydrochloride (TCEP)	Sigma-Aldrich	CAS# 51805-45-9
2-Chloroacetamide (CAA)	Sigma-Aldrich	CAS# 79-07-2
Tris(hydroxymethyl)aminomethane hydrochloride (Tris·HCl)	Sigma-Aldrich	CAS# 1185-53-1
Ammonium bicarbonate (NH_4HCO_3)	Sigma-Aldrich	CAS# 1066-33-7
Trifluoroacetic acid (TFA)	Sigma-Aldrich	CAS# 76-05-1
Isopropyl β-D-1-thiogalactopyranoside (IPTG)	Sigma-Aldrich	CAS# 367-93-1
Ethylenediaminetetraacetic acid (EDTA)	Sigma-Aldrich	CAS# 60-00-4
D,L-Dithiothreitol (DTT)	Sigma-Aldrich	CAS# 3483-12-3
Urea	Sigma-Aldrich	CAS# 57-13-6
Sodium phosphate dibasic heptahydrate ($Na_2HPO_4.7H_2O$)	Sigma-Aldrich	CAS# 7782-85-6
Sodium dihydrogen phosphate monohydrate ($NaH_2PO_4.H_2O$)	Sigma-Aldrich	CAS# 10049-21-5

(*Continued on next page*)

Continued

REAGENT or RESOURCE	SOURCE	IDENTIFIER
Imidazole	Sigma-Aldrich	CAS# 288-32-4
Trypsin and LysC digestion mix	Thermo Fischer	Cat#A40007
Pierce™ Universal Nuclease for Cell Lysis	Thermo Fischer	Cat#88700
4× Laemmli sample buffer	Bio-Rad	Cat#1610747
4× 2-Mercaptoethanol	Sigma-Aldrich	CAS# 60-24-2
2-Amino-2-(hydroxymethyl)-1, 3-propanediol (Tris base)	Sigma-Aldrich	CAS# 77-86-1
Glycine	Sigma-Aldrich	CAS# 56-40-6
Sodium dodecyl sulfate (SDS)	Sigma-Aldrich	CAS# 151-21-3
Page Ruler Plus Prestained Protein Ladder, 10–250 kDa	Thermo Fischer	Cat#26619
Instant Blue staining	Abcam	ab119211
[Glu1]-Fibrinopeptide B	Sigma-Aldrich	CAS# 103213-49-6
Water for chromatography (LC-MS Grade) LiChrosolv®	Sigma-Aldrich	CAS# 7732-18-5
Deposited data		
Pseudomonas putida KT2440 soluble protein quantification	This paper	https://github.com/biosustain/QconCATquantSTAR
Recombinant DNA		
pQconCAT plasmid	This paper	N/A
Software and algorithms		
Proteome Discoverer	Thermo Fisher	https://www.thermofisher.com/us/en/home/industrial/mass-spectrometry/liquid-chromatography-mass-spectrometry-lc-ms/lc-ms-software/multi-omics-data-analysis/proteome-discoverer-software.html v2.4
Python version 3.10.5	Python Software Foundation	https://www.python.org
Other		
3 mm zirconium oxide beads	Glen Mills	Cat#7361-003000
2 mm solid-glass beads	Sigma-Aldrich	SKU 1040140500
Mixer Mill	Retsch	MM400
ThermoMixer	Eppendorf	Cat#5382000023
C18 resin	Empore	Cat#13-110-018
Dionex UltiMate 3000	Thermo Fisher	Cat#IQLAAAGABHFAPBMBFD
Orbitrap Exploris 480	Thermo Fisher	Cat#BRE725533
Thermal Mixer with 24 × 2 mL microtube block Eppendorf shaker	Thermo Fisher	Cat#13687717
250 mL Nalgene™ plastic bottle	Sigma-Aldrich	SKU B1033-4EA
Vibra-Cell sonicator	Sonic & Material Instrument	Model VCX 130
Waving shaker	VWR	Cat#10811-240
HisPur™ Ni-NTA Resin	Thermo Fisher	Cat#88222
Pierce™ Disposable Columns, 10 mL	Thermo Fisher	Cat#29924
Amicon Ultra centrifugal filters (50 mL)	Millipore	Cat#UFC901096
NanoDrop 2000 spectrophotometer	Thermo Fisher	Cat#ND-2000
PCR tube	Thermo Fisher	Cat#14-230-210
Spin microcentrifuge	VWR	Cat#521-2844
Mini-PROTEAN TGX 4%–20% resolving gel	Bio-Rad	Cat#4561096
Mini-PROTEAN tetra cell vertical gel electrophoresis system	Bio-Rad	Cat#1658004
Spatula or Knife Gel	Thermo Fisher	Cat#EI9010

MATERIALS AND EQUIPMENT

LB agar plates containing kanamycin (or any other selected antibiotic)		
Reagent	Final concentration	Amount
Yeast extract	5 g/L	5 g
Tryptone	10 g/L	10 g
NaCl	10 g/L	10 g
Agar	15 g/L	15 g
Kanamycin (1,000×)	50 μg/mL (1×)	1 mL
Deionized water	Not applicable (N/A)	Up to 1 L
Total	**N/A**	**1 L**

Note: Autoclave LB agar medium at 15 psi, 121°C–124°C for 20 min and cool down to 45°C–50°C before adding kanamycin or the selected antibiotic. These can be stored at 4°C for ~1 month.

2×YT broth		
Reagent	Final concentration	Amount
Yeast extract	10 g/L	10 g
Tryptone	16 g/L	16 g
NaCl	5 g/L	5 g
Deionized water	N/A	Up to 1 L
Total	**N/A**	**1 L**

Note: This medium can be autoclaved (at 15 psi, 121°C–124°C for 20 min) and stored at 23°C for ~6 months.

M9 medium glucose		
Reagent	Final concentration	Amount
Calcium chloride ($CaCl_2$) solution	0.1 mM	0.1 mL
Magnesium sulfate ($MgSO_4$) solution	2 mM	1 mL
Wolfe's vitamin solution (1,000×)	1×	1 mL
Trace element solution (2,000×)	1×	0.5 mL
M9 medium salts (10×)	1×	100 mL
Glucose monohydrate	40 mM	7.2 g
Double deionized water	N/A	Up to 1 L
Total	**N/A**	**1 L**

Note: This medium can be stored at 23°C for ~6 months.

Calcium chloride solution		
Reagent	Final concentration	Amount
Calcium chloride ($CaCl_2$) dihydrate	1 M	147.01 g
Double deionized water	N/A	Up to 1 L
Total	**N/A**	**1 L**

Note: This medium can be stored at 23°C for ~12 months.

Magnesium sulfate solution		
Reagent	Final concentration	Amount
Magnesium sulfate ($MgSO_4$) heptahydrate	2 M	240.73 g
Double deionized water	N/A	Up to 1 L
Total	**N/A**	**1 L**

Note: This medium can be stored at 23°C for ~12 months.

Wolfe's vitamin solution (1,000×)		
Reagent	Final concentration	Amount
Pyridoxine hydrochloride	10.0 mg/L	10.0
Thiamine hydrochloride	5.0 mg/L	5.0
Riboflavin	5.0 mg/L	5.0
Nicotinic acid	5.0 mg/L	5.0
Calcium D-(+)-pantothenate	5.0 mg/L	5.0
p-Aminobenzoic acid	5.0 mg/L	5.0
Thioctic (α-lipoic) acid	5.0 mg/L	5.0
Biotin	2.0 mg/L	2.0
Folic Acid	2.0 mg/L	2.0
Vitamin B12	1.0 mg/L	1.0
Double deionized water	N/A	Up to 1 L
Total	**N/A**	**1 L**

Note: First, dissolve all compounds in 500 mL MQ water. Add double deionized water to a final volume of 1 L. Filter sterilize. Store the sterile solution at 4°C in the dark for ~12 months.

Trace element solution (2,000×)		
Reagent	Final concentration	Amount
Disodium EDTA	15 g/L	15
Zinc sulfate ($ZnSO_4$) heptahydrate	4.5 g/L	4.5
Manganese chloride ($MnSO_4$) tetrahydrate	0.7 g/L	0.7
Cobalt(II) chloride ($CoCl_2$) hexadrate	0.3 g/L	0.3
Copper(II) chloride ($CuCl_2$) dihydrate	0.2 g/L	0.2
Disodium molybdate (Na_2MoO_4) dihydrate	0.4 g/L	0.4
Calcium chloride ($CaCl_2$) dihydrate	4.5 g/L	4.5
Iron(II) sulfate ($FeSO_4$) heptahydrate	3.0 g/L	3.0
Boric acid (H_3BO_3)	1.0 g/L	1.0
Potassium iodide (KI)	0.1 g/L	0.1
Double deionized water	N/A	Up to 1 L
Total	**N/A**	**1 L**

Note: First, dissolve EDTA and $ZnSO_4 \cdot 7H_2O$ in 0.75 L of double deionized water and set the pH to 6.0 with 1 M NaOH. Whilst maintaining the pH at 6.0, dissolve in the other compounds one by one. When ready, set the pH to 4.0 with 1 M HCl and adjust the volume to 1.0 L. Sterilize by autoclaving (15 psi, 121°C–124°C for 20 min). Store the sterile solution at 4°C in the dark for ~12 months.

M9 medium salts (10×)		
Reagent	Final concentration	Amount
Disodium hydrogen phosphate (Na_2HPO_4)	68 g/L	10 g

(*Continued on next page*)

Continued		
Reagent	Final concentration	Amount
Potassium phosphate monobasic (KH_2PO_4)	30 g/L	16 g
Sodium chloride (NaCl)	5 g/L	5 g
Ammonium chloride (NH_4Cl)	10 g/L	10 g
Double deionized water	N/A	Up to 1 L
Total	**N/A**	**1 L**

Note: This medium can be stored at 23°C for ~12 months.

Buffer A – Inclusion bodies solubilization		
Reagent	Final concentration	Amount
Tris·HCl (pH = 8.0)	20 mM	242.3 mg
EDTA	1 mM	29.2 mg
DTT	5 mM	77.1 mg
Double deionized water	N/A	Up to 100 mL
Total	**N/A**	**100 mL**

⚠ CRITICAL: D,L-Dithiothreitol (DTT) is a reducing agent that can cause skin, eye and respiratory irritation. It is highly recommended to wear appropriate protective equipment and work under the chemical hood.

Note: Buffer A can be stored at 4°C for ~12 months.

Buffer B – Inclusion bodies solubilization		
Reagent	Final concentration	Amount
Tris·HCl (pH = 8.0)	20 mM	242.3 mg
EDTA	1 mM	29.2 mg
DTT	5 mM	77.1 mg
Urea	8 M	48.05 g
Double deionized water	N/A	Up to 100 mL
Total	**N/A**	**100 mL**

⚠ CRITICAL: Urea can cause irritation to the skin, eyes, and respiratory tract. Urea is harmful if swallowed or inhaled.

Note: Buffer B can be stored at 4°C for ~12 months.

Phosphate buffer (pH = 7.4)		
Reagent	Final concentration	Amount
Sodium phosphate dibasic heptahydrate ($Na_2HPO_4 \cdot 7H_2O$)	1 M	20.21 g
Sodium dihydrogen phosphate monohydrate ($NaH_2PO_4 \cdot H_2O$)	1 M	3.39 g
Double deionized water	N/A	Up to 100 mL
Total	**N/A**	**100 mL**

Note: Phosphate buffer can be stored for at least 2 years at 23°C.

Resuspension buffer		
Reagent	Final concentration	Amount
1 M phosphate buffer (pH = 7.4)	20 mM	2 mL
NaCl	300 mM	1.75 g
Imidazole	20 mM	0.136 g
Double deionized water	N/A	Up to 100 mL
Total	**N/A**	**100 mL**

Note: Resuspension buffer can be stored for at least 2 years at 4°C protected from light.

⚠ CRITICAL: Imidazole may form combustible dust concentrations in the air. It is harmful if swallowed and can cause severe skin burns and eye damage; it may also cause respiratory irritation. Personal protective equipment (e.g., goggles, laboratory coat and gloves) must be used when handling this compound.

Equilibration buffer Ni-resin		
Reagent	Final concentration	Amount
1 M phosphate buffer (pH = 7.4)	20 mM	2 mL
NaCl	300 mM	1.75 g
Imidazole	20 mM	0.136 g
Urea	8 M	48.05 g
Double deionized water	N/A	Up to 100 mL
Total	**N/A**	**100 mL**

Note: Equilibration buffer Ni-resin can be stored for at least 2 years at 4°C protected from light.

Elution buffer Ni-resin		
Reagent	Final concentration	Amount
1 M phosphate buffer (pH = 7.4)	20 mM	1 mL
NaCl	300 mM	0.825 g
Imidazole	500 mM	1.7 g
Urea	8 M	24.02 g
Double deionized water	N/A	Up to 50 mL
Total	**N/A**	**50 mL**

Note: Elution buffer Ni-resin can be stored for at least 2 years at 4°C protected from light.

Sample exchange buffer		
Reagent	Final concentration	Amount
1 M phosphate buffer (pH = 7.4)	20 mM	2 mL
Double deionized water	N/A	Up to 1 L
Total	**N/A**	**1 L**

Note: Sample exchange buffer can be stored for at least 2 years at 23°C.

SDS-PAGE buffer 10×		
Reagent	Final concentration	Amount
Tris base	30.3 g/L	30.3 g
Glycine	144.4 g/L	144.4 g
SDS	10 g/L	10 g
Double deionized water	N/A	Up to 1 L
Total	**N/A**	**1 L**

Note: SDS is a detergent, do not shake the mixture to avoid formation of foam.

⚠ CRITICAL: Sodium dodecyl sulfate (SDS) can cause skin, eye, and respiratory irritation. Avoid inhalation of dusts, substance contact, and keep away from heat and sources of ignition. Personal protective equipment (e.g., goggles, laboratory coat and gloves) must be used when handling this compound.

Note: This medium can be stored at 23°C for ~12 months.

[Glu1]-Fibrinopeptide B solution		
Reagent	Final concentration	Amount
[Glu1]-Fibrinopeptide (EGVNDNEEGFFSAR)	0.1 μg/μL	100 μg
LC-MS grade water	N/A	Up to 1 mL
Total	**N/A**	**1 mL**

Note: [Glu1]-Fibrinopeptide B solution must be stored at –20°C. Storage time ~2 years.

Ammonium bicarbonate solution		
Reagent	Final concentration	Amount
Ammonium bicarbonate (NH_4HCO_3)	50 mM	198 mg
LC-MS grade water	N/A	Up to 50 mL
Total	**N/A**	**50 mL**

Note: The ammonium bicarbonate solution can be stored for at least 2 years at 23°C.

Tris·HCl buffer (pH = 8.5)		
Reagent	Final concentration	Amount
Tris·HCl	1 M	7.88 g
LC-MS grade water	N/A	Up to 50 mL
Total	**N/A**	**50 mL**

Note: Adjust the pH of the solution to 8.5 with 5 M NaOH. The solution can be stored at 23°C for at least 2 years.

Lysis buffer		
Reagent	Final concentration	Amount
Gu·HCl	6 M	28.66 g

(*Continued on next page*)

Continued

Reagent	Final concentration	Amount
TCEP	5 mM	71.7 mg
CAA	10 mM	46.7 mg
Tris·HCl (pH = 8.5)	100 mM	5 mL
LC-MS grade water	N/A	Up to 50 mL
Total	**N/A**	**50 mL**

⚠ CRITICAL: Guanidinium hydrochloride (Gu·HCl) is harmful if swallowed. It can also cause eye and skin irritation. Tris(2-carboxyethyl)phosphine hydrochloride (TCEP) is corrosive and can cause severe skin and eye burns. 2-Chloroacetamide (CAA) is toxic upon ingestion and may cause an allergic skin reaction. Use appropriate protective personal equipment (e.g., goggles, laboratory coat and gloves) when working with these substances.

Note: This medium can be stored at 4°C for ~6 months.

Alternatives: Chemical compounds produced by manufacturers other than the ones specified in the key resources table are adequate substitutes, where and whenever are of highest purity, sequence grade, and LC-MS grade. The enzymes used in this protocol (Trypsin/LysC digestion mix and Pierce™ Universal Nuclease for Cell Lysis) should be purchased using the same vendor to ensure workflow reproducibility.

HPLC-MS and data analysis settings

For sample analysis, utilize a Dionex UltiMate 3000 coupled to an Orbitrap Exploris 480. Capture the sample on a pre-column (μ-precolumn C18 PepMap 100, 5 μm, 100 Å) at a flow rate of 10 μL/min. Separate the peptides on a 15 cm C18 easy spray column (PepMap RSLC C18 2 μm, 100 Å, 150 μm × 15 cm) at a flow rate of 1.2 μL/min, with an applied gradient from 4% (v/v) acetonitrile in water with 0.1%–76% (v/v) formic acid over a total of 60 min. Operate the instrument in data-dependent mode using the following settings: MS-level scans performed with resolution set to 120,000; AGC target of 3.0×10^6; maximum injection time of 50 ms; intensity threshold of 5.0×10^3; and dynamic exclusion at 25 s. Perform data-dependent MS2 selection in Top 20 Speed mode with HCD collision energy set to 28% (AGC target 1.0×10^4; maximum injection time of 22 ms; and isolation window 1.2 m/*z* with a resolution of 30,000).

For analysis of the .RAW files, run Proteome Discoverer v2.4 (Thermo Fisher Scientific, Waltham, MA, USA) with the following settings. Dynamic modifications: carbamidomethyl of cysteine residues and oxidation of methionine residues; label ^{13}C(6) in arginine and lysine residues; precursor mass tolerance set to 10 ppm; fragment mass tolerance at 0.02 Da; trypsin (full) as digestion enzyme, allowing for a maximum of two missed cleavages; minimum peptide length of 6; maximum peptide length of 144; and the false-discovery rate (FDR) set at 0.1%.

STEP-BY-STEP METHOD DETAILS

The first part of the protocol involves the selection of several unique peptides used in the design of the quantification concatamers (QconCATs) for absolute protein determination. QconCATs are implemented to precisely quantify the content of desired proteins not only in bacteria but also in any biological system by slightly adjusting the protein extraction procedure. The presented protocol includes all the necessary steps—from the *in silico* design to the calculation of the *in vivo* protein concentrations—to carry out an end-to-end workflow in Gram-negative bacteria (e.g., *P. putida* or *E. coli*).

Peptide candidate mapping experiment

Timing: 2–3 days

1. Grow the pre-culture of the selected Gram-negative bacterial strain for ~16 h at its optimal growth condition in a 50-mL Falcon tube containing 10 mL of 2×YT medium. Use colonies from a freshly-inoculated LB agar plate.

   Note: *E. coli* should be grown at 37°C and *P. putida* cultures are incubated at 30°C.

2. Re-inoculate a 250-mL Erlenmeyer flask containing 50 mL of 2×YT medium by diluting the pre-culture 100× (500 µL).
3. When the culture reaches mid-exponential phase (roughly equal to $0.5 \times OD_{600}^{max}$, i.e., half the maximum optical density measured at 600 nm) or ~0.4–0.5 mg of total cell dry weight.
4. Harvest 1 mL of the suspension by centrifugation at 10,000 g for 10 min at 4°C.
5. Remove the supernatant and freeze the cell pellets at –80°C until sample preparation.
6. Thaw the cell pellets on ice. Add two 3-mm zirconium oxide beads to each sample, and 100 µL of lysis buffer (6 M Gu·HCl [guanidinium hydrochloride], 5 mM TCEP [tris(2-carboxyethyl)phosphine], 10 mM CAA [2-chloroacetamide] and 100 mM Tris·HCl, pH = 8.5) to the samples.
7. Disrupt the cell suspension in a Mixer Mill set at 25 Hz for 5 min at ~20°C. Heat the sample for 10 min in a ThermoMixer at 99°C and 1,800 rpm.
8. Remove the cell debris by centrifugation at 15,000 *g* for 10 min at 23°C and collect 50 µL of supernatant into a new Eppendorf tube. Dilute the cell extract with 50 µL of 50 mM $(NH_4)HCO_3$ (ammonium bicarbonate).
9. Quantify protein concentration *via* the bicinchoninic acid (BCA) assay[4,17] and take 20 µg of protein for tryptic digestion into a new Eppendorf tube.
10. Dilute the tryptic digestion to reach a total volume of 100 µL by using the appropriate amount of 50 mM $(NH_4)HCO_3$ solution.

    Note: The expected protein concentration might vary according to the organism under study, carbon source and culture conditions. For a typical bacterial culture at OD_{600} = 1.0, the estimated protein concentration is ~2 µg/µL.

11. Add 20 µL of 0.1 µg/µL trypsin and LysC digestion mix (ratio 1:1). Initiate the tryptic digestion at constant shaking (400 rpm) for 8 h and 37°C.

    Note: Ensure at least a 4× dilution to avoid interferences between the Gu·HCl present in the lysis buffer and the digestion enzymes.

12. Add 10 µL of 10% (w/v) trifluoroacetic acid (TFA) to stop the tryptic digestion. Vortex and centrifuge the samples at 15,000 *g* for 15 min at 23°C (See problem 3 in troubleshooting).
13. Perform StageTipping, using C18 resin (solid phase extraction disk) to desalt the samples prior to HPLC-MS analysis. For a detailed explanation on StegeTipping desalting process, please refer to Rappsilber et al.[18] for further details.
14. HPLC-MS analysis of the samples is performed using a Dionex UltiMate 3000 coupled to an Orbitrap Exploris 480 operated using data-dependent acquisition. The data analysis of the .RAW files is executed using Proteome Discoverer. Further details on HPLC-MS and data analysis can be found in the materials and equipment section; please also refer to Wirth et al.[19] and Kozaeva et al.[20] for details.

The experimental workflow to build the peptide list is shown in Figure 2.

Note: Only consider unique peptides for quantification. Assign the detected peptides to their functions using a protein database consisting of the reference Gram-negative bacteria proteome. If necessary, supplement heterologously expressed proteins by adding those proteins and sequences to the FASTA file obtained from the database.

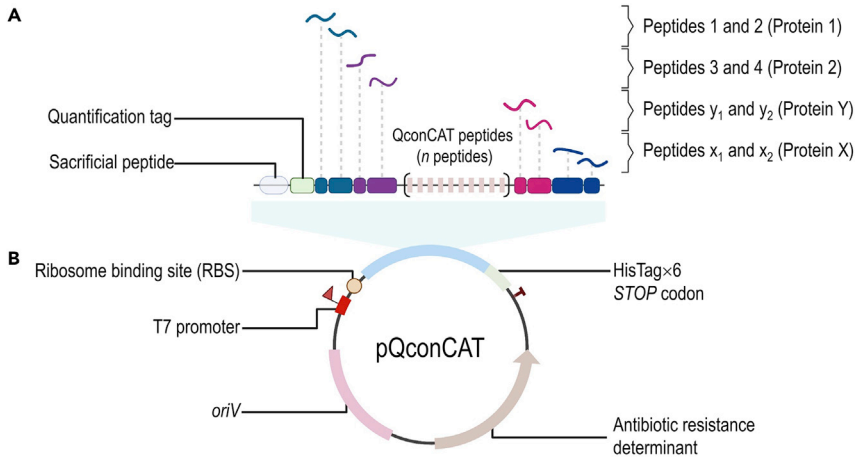

Figure 2. Standard design of the inducible pQconCAT plasmid to produce labeled peptides for absolute protein quantification

(A and B) The plasmid encompasses different parts that allow the production of the desired protein: (A) concatenated peptides (*n* peptides) selected in "peptide candidate mapping experiment" and (B) a T7 RNA polymerase promoter region, ribosome binding site (RBS), quantification tag (e.g., [Glu1]-fibrinopeptide B), sacrificial peptide, hexahistidine purification tag (HisTag×6), stop codon, antibiotic resistance determinant and origin of vegetative replication (*oriV*). This design allows for the production of an equimolar (1:1) amount of QconCAT peptides, which can be added in known quantities to the sample. Then, the amount of each represented peptide standard can be calculated based on the [Glu1]-fibrinopeptide B, serving as a reference to accurately quantify proteins.

15. From the peptide candidate list obtained, select the peptides using the following criteria:
    a. Mass peptide: select peptides ranging 350–5,000 Da in mass.

Avoid proline (P) residues on the carboxyl side of the cleavage site (RP or KP) as well as acidic residues—aspartate (D) and glutamate (E)—on either side of the cleavage site due to the lower rate of hydrolysis.

16. Pick two or more proteotyptic peptides per protein with the highest fragment intensity. Please refer to Calderón-Celis et al.[21] for details.

In silico QconCAT plasmid design (pQconCAT)

Timing: 15–20 days

17. *In silico* design of pQconCAT vectors.
    a. The plasmid design should contain the following structure:
        i. T7 RNA polymerase promoter region;
        ii. Ribosome binding site;
        iii. Quantification tag (e.g., [Glu1]-fibrinopeptide B);
        iv. Sacrificial peptide;
        v. Concatenated peptides (*n* peptides) selected in "peptide candidate mapping experiment";
        vi. Hexahistidine purification tag (HisTag×6);
        vii. *STOP* codon;
        viii. Antibiotic resistance determinant;
        ix. Origin of vegetative replication (*oriV*).

        The general structure of plasmid pQconCAT is depicted in Figure 2.

Note: Optimize (optional) the QconCAT gene for codon usage in *E. coli* to facilitate production of the concatamers.

b. Order the plasmid previously designed (typical synthesis time: 15 days).

QconCAT transformation and expression

Timing: 7–10 days

18. Competent cells for pQconCAT transformation.
    a. Grow for ~16 h a pre-culture of *E. coli* BL21(DE3) Δ*lysA* Δ*argH* in 5 mL of LB medium at 37°C in a shaker at 250 rpm.
    b. Inoculate 50 mL of fresh LB medium, placed in a 250-mL Erlenmeyer flask, with 0.5 mL of the pre-culture to yield an OD_{600} ~0.05.
    c. Grow cells at 37°C in a shaker at 250 rpm until the culture reaches OD_{600} ~0.5 (~2–3 h).
    d. Place the Erlenmeyer flask to ice to prevent further bacterial growth.

    Note: From now on, steps e-k should be performed at 4°C, maintaining cells on an ice bath and using chilled tubes.

    e. Transfer the cells to a pre-chilled 50-mL Falcon conical tube.
    f. Harvest the cells in a pre-cooled centrifuge at 4°C for 10 min and 4,500 *g*. Discard the supernatant.
    g. Resuspend the pellet in 1-mL chilled, filter-sterile 10% (v/v) glycerol solution and transfer to a chilled 1.5-mL Eppendorf tube.
    h. Centrifuge for 1 min at 11,000 *g* and 4°C. Discard supernatant.
    i. Repeat steps g and h at least twice.

    Note: The pellet will become softer with every wash round. Be careful when removing the supernatant.

    j. Resuspend the cell pellet in 10% (v/v) glycerol to 1:100 volume of initial culture (i.e., 500 µL). Culture volumes can be scaled down accordingly if only a few transformations will be performed.
    k. Transfer 30–50 µL aliquots to chilled 1.5-mL Eppendorf tubes.

    Note: Cells can be flash-frozen and maintained at –80°C until transformation or used directly for electroporation.

19. pQconCAT transformation.
    a. Take competent cells *E. coli* BL21(DE3) Δ*lysA* Δ*argH* from –80°C and place them on ice.
    b. Prepare the plasmid suspension by diluting it in the tube to a concentration of 100 ng/µL using MQ water.
    c. Add ~25–50 ng of the plasmid into the cell tubes and vortex quickly one time.
    d. Put the cells and the plasmid on ice for 30 min.
    e. Place the tube into the water bath at 42°C for 60 s. After that, place them back on ice for 2 min.
    f. Add 1 mL of LB medium (without antibiotics), transfer the cells into a 2-mL Eppendorf tube and incubate the bacterial suspension for 1 h at 37°C in a Thermal Mixer with a 24 × 2 mL microtube block Eppendorf shaker at 800 rpm.
    g. Plate 50 µL of the cell suspension on LB agar plates (with the corresponding antibiotic) using pre-sterilized 2-mm glass beads.

Note: The antibiotic to be added to the plates depends on the selection marker in the plasmid used for the protein expression. Prepare a 1,000× antibiotic stock solution and dilute to 1×.

h. Centrifuge the tube containing the remaining cells at 10,000 *g* for 5 min and discard most of the medium (~900 µL). Resuspend the cells in the remainder liquid.
i. Plate the cell suspension on LB agar plates (with the corresponding antibiotic) using 2-mm glass beads and incubate the plates for ~16 h in an incubator at 37°C.
j. Pick the colonies, confirm presence of the plasmid by mini-prep and sequencing, and prepare glycerol stocks of the selected clones.

20. QconCAT expression.
    a. Inoculate pre-cultures in 50-mL Falcon tubes containing 10 mL of M9 minimal medium with 40 mM glucose, 0.1 mg/mL U^{13}C-L-lysine, 0.1 mg/mL U^{13}C-L-arginine + the selected antibiotic (1× final concentration, see above) at 37°C at 200 rpm for ~16 h (see problem 1 in troubleshooting).
    b. Dilute the pre-culture 1:100 in 100 mL of the same medium described in 3.a. placed in 500-mL Erlenmeyer flask, and incubate the culture at 37°C.
    c. When the culture reaches OD_{600} ~ 0.5–0.6, cool down the flask (in ice or cold room) until it reaches approximately ~23°C.
    d. Induce the expression of the construct borne by plasmid pQconCAT by adding IPTG to a final concentration of 1 mM and incubate for 24 h at 30°C and 200 rpm (see problem 2 in troubleshooting).

Note: The concatamer polypeptide tends to form inclusion bodies (IBs) when using this IPTG concentration to induce the expression of the construct. It is possible to optimize the IPTG concentration for different polypeptides if needed. In case that no information is available, a low IPTG concentration (e.g., 0.2 mM) is a good starting point. Please refer to Lozano Terol et al.[22] for further information.

    e. Centrifuge the culture at 3,000 *g* and 4°C for 20 min in a 250-mL Nalgene™ plastic bottle.
    f. Freeze the bacterial pellets at –20°C for 1 h to weaken the cell membrane.

Pause point: It is possible to store the pellets at –20°C gor ~16 h and continue with the rest of the procedure the next day.

21. Cell disruption, inclusion bodies solubilization and pQconCAT purification.
    a. Cell disruption:
        i. Thaw the frozen pellets and resuspend the biomass in 25 mL of resuspension buffer by vortexing. Pour the suspended pellet solution in a 50-mL Falcon tube.
        ii. Sonicate the samples using a Vibra-Cell sonicator at 65% intensity for 10 min with ON-OFF cycles of 30 s.

Note: The samples should be maintained at 4°C during the sonication.

        iii. Incubate the lysate with 2 µL of Pierce™ Universal Nuclease for Cell Lysis for at least 30 min at 23°C to digest DNA and reduce the viscosity of the sample.
        iv. Centrifuge lysates for 20 min at 16,000 *g* in a cooled centrifuge (4°C).

⚠ CRITICAL: At this point, the soluble proteins should be present in the supernatant. However, because of the nature of the polypeptide, the QconCAT will be typically recovered from IBs. These IBs will be present in the pellet (insoluble fraction) of the sample, with a negligible amount of QconCATs in the supernatant.

        v. Recover the pellet and use it in the next step for IB solubilization.

Note: The supernatant should be stored at 4°C in case that no protein is detected in the IB fraction (pellet); if this is the case, filter the supernatant using a 0.45 μm and then a 0.22 μm membrane. Continue to step 5.a. if the protein of interest is in the soluble fraction.

Pause point: The pellet can be stored at –20°C in case you need to pause the process.

⚠ CRITICAL: The solubilization buffers A and B must be prepared immediately before this step.

b. IBs solubilization:
   i. Resuspend the pellet in 2 mL of buffer A by pipetting up and down until the protein pellet is completely dissolved. Place the dissolved protein in a new 2-mL Eppendorf tube.
   ii. Centrifuge for 60 min at 4°C and 15,000 *g*. Remove the supernatant and proceed with pellet solubilization.
   iii. Solubilize the protein by adding 5–10 mL of buffer B.

Note: Do not add the whole volume of buffer B directly to the pellet; rather add 1-mL aliquots at a time to gradually dissolve the materials. Repeat this procedure until dissolving the whole insoluble fraction. Do not use more than 10 mL of the solubilization solution. Place the solution in a 15-mL Falcon tube.

   iv. Stir gently for 1 h at 4°C in a waving shaker with an inclination of 30°C.

Note: In case the pellet is not completely dissolved, it is recommended to leave the sample for ~16 h at the conditions mentioned above to complete the solubilization of the polypeptide.

   v. Centrifuge for 15 min at 4°C and 15,000 *g* to eliminate insoluble debris. Store the supernatant containing the solubilized protein. Continue to the purification step.

c. QconCAT purification:
   i. Assemble the purification Pierce™ Disposable Column by placing a filter disc in the bottom, cap the column tip and add 2 mL of HisPur™ Ni-NTA resin.

Note: Mix the resin vigorously to form a homogenous solution before adding it to the column.

   ii. Allow the resin to drain without becoming completely dry by removing the cap. Once the resin is drained, recap the column.

Note: To drain buffers/solution, remove the cap and recap once the column is drained. Place several 50-mL Falcon tubes under the column during the different intermediate steps in order to collect the fractions.

   iii. To wash and equilibrate the column, add 2 mL of equilibration buffer (no need to be gentle with the resin) and let the resin drain. Place the cap on the tip.
   iv. Load the solution containing the QconCATs on top of the resin. Collect the flow-through and repeat this step twice to increase protein recovery.

Note: It is important to keep the fraction containing the QconCATs at 4°C.

   v. Wash the resin twice with 10 mL of equilibration buffer Ni-resin.
   vi. Elute twice with 2 mL of elution buffer.
   vii. Load the eluent in a 50-mL Amicon Ultra centrifugal filters (with a cut-off of at least 10 kDa below the size of the polypeptide of interest) and proceed to exchange the buffer.

viii. Centrifuge at 4,000–7,000 *g* for 10 min at 4°C and refill the column with 4 mL of sample exchange buffer (see problem 4 in troubleshooting).
ix. Repeat the step above 3–4 times to properly exchange the buffer. Then, recover the purified proteins in a final volume of 1 mL of the buffer by pipetting up and down. Centrifuge the sample again in case that more than 1 mL is obtained.
x. Measure the protein concentration by using NanoDrop 2000 spectrophotometer. Absorbance ratio at 260 nm over 280 nm (A_{260}/A_{280}) should be around 0.6.
The schematic representation of pQconCAT transformation, pQconCAT expression, cell disruption, and inclusion bodies solubilization is presented in Figure 3. The QconCAT purification workflow is illustrated in Figure 4.

22. SDS-PAGE of purified proteins.
a. Prepare your protein samples in a 0.2-mL PCR tube by mixing the components listed in Table 1:

Note: Load ~0.2–1 μg of the purified protein in the polyacrylamide gel to get clear bands. Bigger protein amounts can lead to streaked bands, while lower a mass below 0.2 μg can result in the absence of noticeable bands in the gel.

⚠ CRITICAL: 4× 2-Mercaptoethanol is a 600 mM solution (in water); work in the chemical fume hood when preparing and handling this solution.

b. Incubate the samples at 95°C for 5 min and spin them down in a spin microcentrifuge.
c. Take a Mini-PROTEAN TGX 4%–20% resolving gel and remove the comb carefully to avoid damaging the wells. Remove the green tape at the bottom of the gel and insert it in a Mini-PROTEAN tetra cell vertical gel electrophoresis system.
d. Place the cell in the suitable position of the tank buffer. Use the 1× SDS-PAGE buffer to fill the cell volume completely and the rest of the buffer tank up to the appropriate level mark.
e. Load 10 μL of the suspension sample. Include at least one well with 2–3 μL of Page Ruler Plus Prestained Protein Ladder, 10–250 kDa.
f. Run the SDS-PAGE at 200 V for approximately 25 min.

Note: Recycle the buffer outside the electrophoresis cell as long as the dye inside the precast cell has not escaped through the bottom of the gel.

g. Open the precast gel using a spatula or gel knife, wash it with distilled water and incubate it in ~15–20 mL of Instant Blue staining (enough volume to cover the gel) with gently shaking at 23°C. Bands will be visible after 15 min and completely stained after 1 h.
h. Wash the gel to remove the dye by washing it with 30 mL of distilled water for 5 min. Repeat this step three times.

Quantification of the QconCAT

Timing: 2 days

23. For each purified QconCAT from step 21.c.x, add 10 μL to a new Eppendorf tube. Next, add 60 μL of 0.1 μg/μL quantification tag peptide [Glu1]-fibrinopeptide B as internal standard.
24. Perform tryptic digestion, StageTipping, HPLC-MS and data analysis as described in steps 6–14 of Section "peptide candidate mapping experiment".
25. Using the sequence of the quantification tag peptide and the Proteome Discoverer results file containing the "Peptide Groups", the abundance of the spiked-in quantification tag (light peptide) and the abundance of the ^{13}C-labeled quantification tag from the QconCAT (heavy peptide) can be determined. Next, the concentration of each QconCAT is calculated as shown in Equation 1:

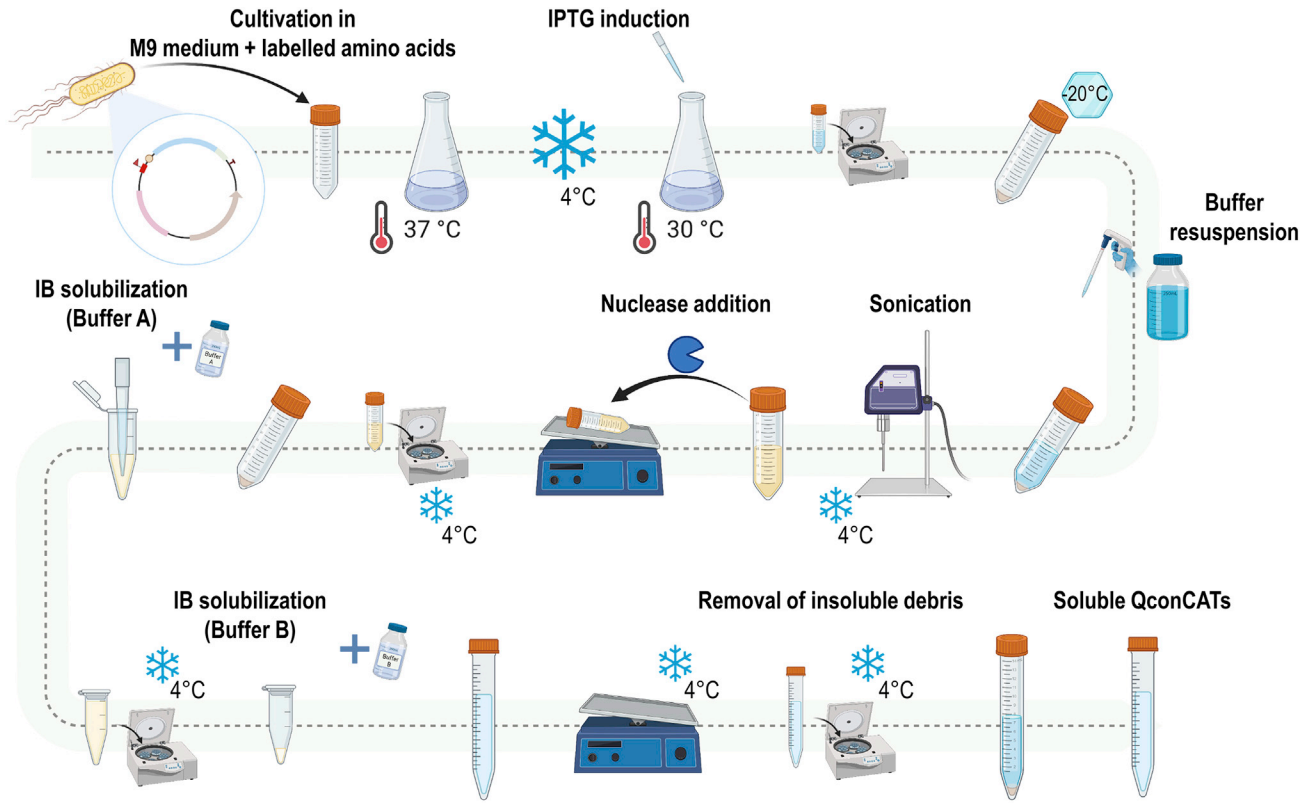

Figure 3. Cultivation procedures and expression of pQconCAT and inclusion bodies (IB) solubilization
The workflow lists the most important steps to obtain the final protein before the purification.

$$c_{QconCAT}\left(\frac{\mu g}{\mu L}\right) = c_{Qtag,light}\left(\frac{\mu g}{\mu L}\right) \cdot \frac{A_{Qtag,heavy}}{A_{Qtag,light}} \cdot \frac{MW_{QconCAT}\left(\frac{g}{mol}\right)}{MW_{Qtag,light}\left(\frac{g}{mol}\right)} \quad \text{(Equation 1)}$$

where $c_{QconCAT}$ is the concentration of the QconCAT, $c_{Qtag,light}$ is the concentration of the quantification tag peptide solution (i.e., 0.1 µg/µL in this example), $A_{Qtag,light}$ is the abundance of the spiked-in quantification tag (light peptide), $A_{Qtag,heavy}$ is the abundance of the ^{13}C-labeled quantification tag from the QconCAT (heavy peptide), $MW_{QconCAT}$ is the molecular weight of the QconCAT protein, and $MW_{Qtag,light}$ is the molecular weight of the spiked-in quantification tag, assuming equimolar concentrations of the ^{13}C-labeled quantification tag (heavy peptide) and the QconCAT protein (see problem 5 in troubleshooting).

Quantification of samples and expected results

Timing: 2 days

26. A biological sample from any experimental condition can be used for protein quantification using the QconCAT standards. Ensure that the samples (cell pellets, as described in step 1 of Section "peptide candidate mapping experiment") correspond to a total OD_{600} ranging from 1 to 2.
27. Perform cell lysis and total protein quantification following steps 6–9 of Section "peptide candidate mapping experiment".
28. Add an amount of each QconCAT protein to the samples that corresponds to approximately the mass of the endogenous proteins per 20 µg of total protein. These are the spiked-in concentrations of the QconCATs, which are required for quantification.

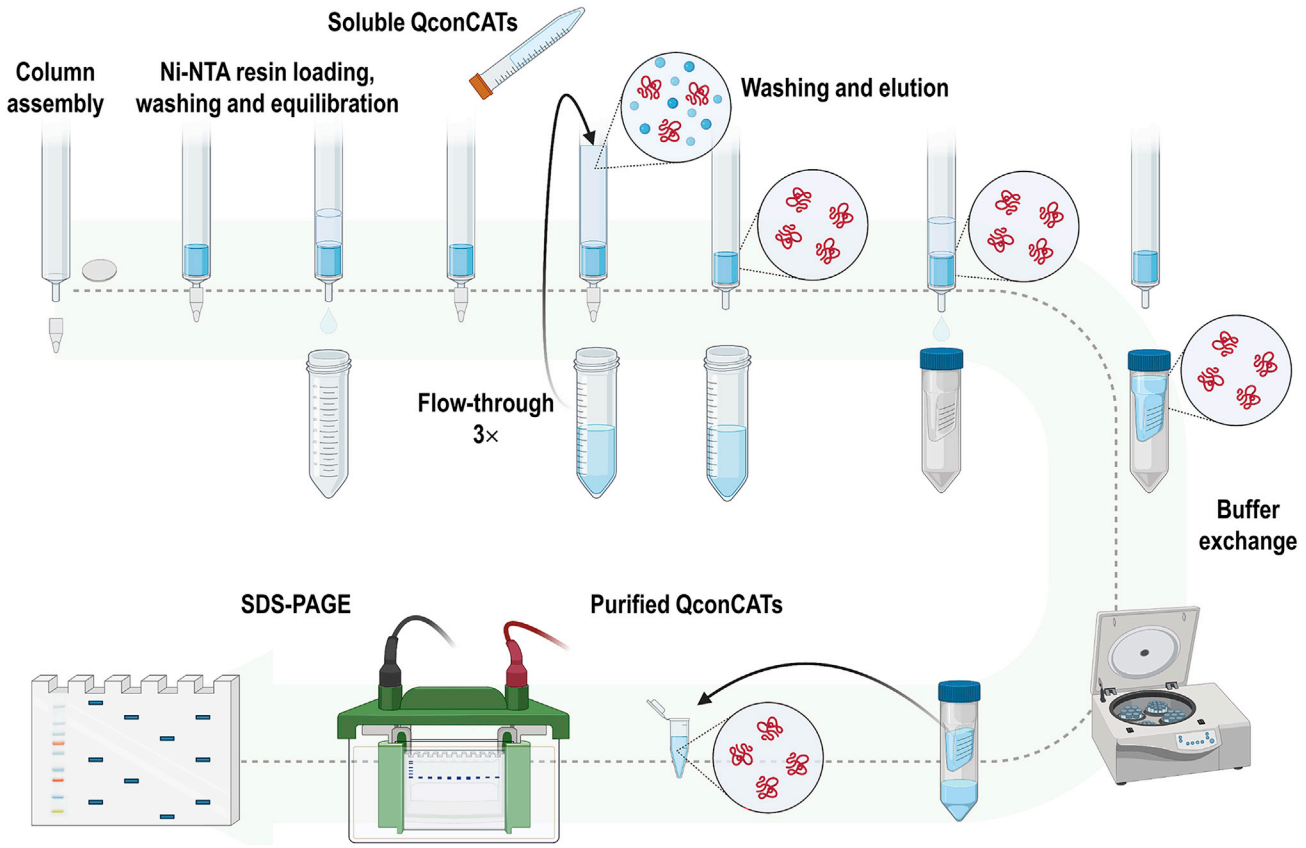

Figure 4. QconCAT purification using HisPur™ Ni-NTA Resin

Systematic procedure for QconCAT purification based on the HisTag technology.

Note: The endogenous protein quantity can be estimated from previous studies.[23] Usually, 200 fmol/μg total protein is a reasonable start point; this means that if 20 μg of protein are taken for the digestion, 4,000 fmol will be present in the sample. Hence, the QconCAT amount to spike-in would be around 4,000 fmol.

29. Perform tryptic digestion, StageTipping, HPLC-MS and data analysis as described in steps 6–8 of Section "peptide candidate mapping experiment".
30. Using the Proteome Discoverer results file containing the "Peptide Groups", the abundance of each QconCAT peptide (heavy peptide) and of each corresponding endogenous peptide (light peptide) can be determined. The concentration of the endogenous peptides, for which a QconCAT protein was constructed, are calculated as shown in Equation 2:

$$c_{pep,end} = \frac{A_{pep,end}}{A_{pep,QconCAT}} \cdot c_{pep,QconCAT} = c_{prot,end} \text{ or } c_{prot,end} = \frac{\sum c_{pep,end}}{\#\ end\ pep} \quad \text{(Equation 2)}$$

where $c_{pep,end}$ is the concentration of the endogenous peptide, $A_{pep,end}$ is the abundance of the endogenous peptide (light peptide), $A_{pep,QconCAT}$ is the abundance of the ^{13}C-labeled QconCAT peptide (heavy peptide), $c_{pep,QconCAT}$ is the concentration of the QconCAT peptide, $c_{prot,end}$ is the concentration of the corresponding endogenous protein, and $\#\ end\ pep$ is the number of endogenous peptides for which a ^{13}C-labeled QconCAT peptide was constructed, for a particular endogenous protein. The concentration of the endogenous peptide will have the same unit as the concentration of the QconCAT peptide, e.g., fmol/μg total protein. The concentration of the endogenous protein is either the same as the molar concentration of the corresponding

Table 1. Composition of protein samples for SDS-PAGE analysis

Component	Volume [μL]
Protein sample	Up to 6
4× Laemmli sample buffer	3
4× 2-Mercaptoethanol	3
Water	As needed
Final volume	12

endogenous peptide (due to equimolar concentrations of peptide and protein), or an average of the endogenous peptide concentrations when multiple peptides per endogenous protein where present in the QconCAT protein standard.

Please refer to the following repository https://github.com/biosustain/QconCATquantSTAR to calculate the peptide concentrations. Use the Python script (QconCATquantSTAR.py) to calculate those concentrations in the samples. See the *Pseudomonas putida* dataset example in the repository for a detailed outcome.

EXPECTED OUTCOMES

This protocol enables the production of labeled peptide concatamers to be used as internal standard. Following this protocol, it is possible to obtain pure QconCATs for absolute quantification of proteins in Gram-negative bacteria. Refer to Figure 5 to see the expected outcomes of the SDS-PAGE analysis of purified QconCATs.

LIMITATIONS

The main limitation is the unknown nature of the QconCAT produced in a biological (bacterial) system. As it is a construction of several peptides (chimeric protein), it is almost impossible to predict if the protein of interest will be produced in the form of soluble or insoluble protein (Inclusion body). Another limitation is that it is sometimes impossible to select two or three unique or signature peptides for each protein of interest.

TROUBLESHOOTING

Problem 1

Slow growth of the strain in minimal medium containing the labeled amino acids after 24 h (step 3.d).

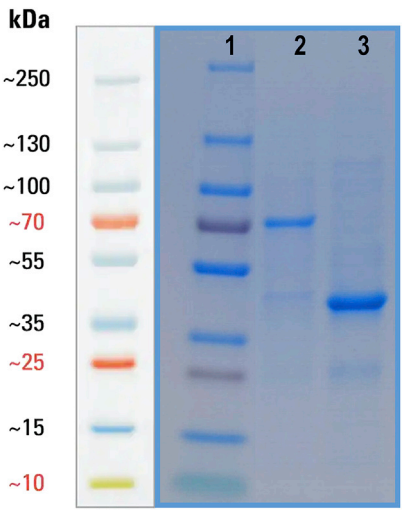

Figure 5. SDS-PAGE analysis of QconCATs

Line 1 corresponds to the Page Ruler Plus Prestained Protein Ladder, 10–250 kDa. Line 2 and 3 shows two examples of purified QconCAT proteins produced by applying this protocol.

Potential solution

Leave the culture for another 24 h and track the changes in OD_{600} of the culture; it should reach maximum OD_{600} after 48 h.

Problem 2

Poor expression of the QconCAT plasmid. This problem can be caused by (i) protein instability and/or (ii) protein toxicity.

Potential solution

In the case of (i), vary expression conditions such as temperature, aeration and induction time. For protein toxicity issues (ii), test different *E. coli* strains [e.g., BL21(DE3) pLysS or BL21(DE3) pLysE].[24]

Problem 3

Incomplete QconCAT digestion.

Potential solution

Increase amount of trypsin and modify digestion conditions in order to ensure complete proteolysis.

Problem 4

Filter blocked due to insoluble debris (step 21.c.viii.).

Potential solution

Resuspend the solution inside the filter and transfer it to a 15-mL Falcon tube. Centrifuge at 5,000 *g* for 10 min and repeat the buffer exchange from step 21.c.vii.

Problem 5

GluFib (or other tag) are not detected or identified in the analysis.

Potential solution

Repeat the analysis adding more QconCAT in the sample.

RESOURCE AVAILABILITY

Lead contact

Further information and requests for resources and reagents should be directed to and will be fulfilled by the lead contact, Pablo Iván Nikel (pabnik@biosustain.dtu.dk).

Materials availability

Further information and requests for resources and reagents should be directed to and will be fulfilled by the lead contact, Pablo Iván Nikel (pabnik@biosustain.dtu.dk).

Data and code availability

The published article includes figures, code and datasets generated with this protocol. The code and datasets are available on GitHub (https://github.com/biosustain/QconCATquantSTAR) and also on Zenodo (https://doi.org/10.5281/zenodo.7330244).

ACKNOWLEDGMENTS

The financial support from the Novo Nordisk Foundation through grants NNF14OC0009473, NNF20CC0035580, *LiFe* (NNF18OC0034818), and *TARGET* (NNF21OC0067996), the Danish Council for Independent Research (SWEET, DFF-Research Project 8021-00039B), the European Union's Horizon 2020 Research and Innovation Programme under grant agreement No. 814418 (*SinFonia*), and the Cystic Fibrosis Trust, Strategic Research Centre Award–2019–SRC017 to P.I.N. is gratefully acknowledged. L.K.N. is supported by the Novo Nordisk Foundation (grants NNF14OC0009473 and NNF20CC0035580) and the Australian Research Council (grant IC160100027).

AUTHOR CONTRIBUTIONS

N.G. developed, executed, optimized the protocol, and drafted the manuscript. S.K.T.P. performed sample preparation and data analysis and drafted the manuscript. M.F. executed and optimized the methodology. T.W. performed data analysis and optimized the protocol. L.K.N. and P.I.N. provided supervision and funding and contextualized and finalized the manuscript.

DECLARATION OF INTERESTS

The authors declare no competing interests.

REFERENCES

1. Weimer, A., Kohlstedt, M., Volke, D.C., Nikel, P.I., and Wittmann, C. (2020). Industrial biotechnology of *Pseudomonas putida*: advances and prospects. Appl. Microbiol. Biotechnol. *104*, 7745–7766. https://doi.org/10.1007/s00253-020-10811-9.

2. Nikel, P.I., and de Lorenzo, V. (2018). *Pseudomonas putida* as a functional *chassis* for industrial biocatalysis: from native biochemistry to *trans*-metabolism. Metab. Eng. *50*, 142–155. https://doi.org/10.1016/j.ymben.2018.05.005.

3. Nikel, P.I., Martínez-García, E., and de Lorenzo, V. (2014). Biotechnological domestication of pseudomonads using synthetic biology. Nat. Rev. Microbiol. *12*, 368–379. https://doi.org/10.1038/nrmicro3253.

4. Nikel, P.I., Pérez-Pantoja, D., and de Lorenzo, V. (2016). Pyridine nucleotide transhydrogenases enable redox balance of *Pseudomonas putida* during biodegradation of aromatic compounds. Environ. Microbiol. *18*, 3565–3582. https://doi.org/10.1111/1462-2920.13434.

5. Maaß, S., and Becher, D. (2016). Methods and applications of absolute protein quantification in microbial systems. J. Proteomics *136*, 222–233. https://doi.org/10.1016/j.jprot.2016.01.015.

6. Wiśniewski, J.R., and Rakus, D. (2014). Multi-enzyme digestion FASP and the 'Total Protein Approach'-based absolute quantification of the *Escherichia coli* proteome. J. Proteomics *109*, 322–331. https://doi.org/10.1016/j.jprot.2014.07.012.

7. Grabski, A.C. (2009). Advances in preparation of biological extracts for protein purification. Methods Enzymol. *463*, 285–303. https://doi.org/10.1016/S0076-6879(09)63018-4.

8. Ishihama, Y., Schmidt, T., Rappsilber, J., Mann, M., Hartl, F.U., Kerner, M.J., and Frishman, D. (2008). Protein abundance profiling of the *Escherichia coli* cytosol. BMC Genom. *9*, 102. https://doi.org/10.1186/1471-2164-9-102.

9. Messana, I., Cabras, T., Iavarone, F., Vincenzoni, F., Urbani, A., and Castagnola, M. (2013). Unraveling the different proteomic platforms. J. Sep. Sci. *36*, 128–139. https://doi.org/10.1002/jssc.201200830.

10. Hui, S., Silverman, J.M., Chen, S.S., Erickson, D.W., Basan, M., Wang, J., Hwa, T., and Williamson, J.R. (2015). Quantitative proteomic analysis reveals a simple strategy of global resource allocation in bacteria. Mol. Syst. Biol. *11*, 784. https://doi.org/10.15252/msb.20145697.

11. Mori, M., Zhang, Z., Banaei-Esfahani, A., Lalanne, J.B., Okano, H., Collins, B.C., Schmidt, A., Schubert, O.T., Lee, D.S., Li, G.W., et al. (2021). From coarse to fine: the absolute *Escherichia coli* proteome under diverse growth conditions. Mol. Syst. Biol. *17*, e9536. https://doi.org/10.15252/msb.20209536.

12. Schmidt, A., Kochanowski, K., Vedelaar, S., Ahrné, E., Volkmer, B., Callipo, L., Knoops, K., Bauer, M., Aebersold, R., and Heinemann, M. (2016). The quantitative and condition-dependent *Escherichia coli* proteome. Nat. Biotechnol. *34*, 104–110. https://doi.org/10.1038/nbt.3418.

13. Ong, S.E., and Mann, M. (2005). Mass spectrometry–based proteomics turns quantitative. Nat. Chem. Biol. *1*, 252–262. https://doi.org/10.1038/nchembio736.

14. Belda, E., van Heck, R.G.A., José Lopez-Sanchez, M., Cruveiller, S., Barbe, V., Fraser, C., Klenk, H.P., Petersen, J., Morgat, A., Nikel, P.I., et al. (2016). The revisited genome of *Pseudomonas putida* KT2440 enlightens its value as a robust metabolic *chassis*. Environ. Microbiol. *18*, 3403–3424. https://doi.org/10.1111/1462-2920.13230.

15. Volke, D.C., Calero, P., and Nikel, P.I. (2020). *Pseudomonas putida*. Trends Microbiol. *28*, 512–513. https://doi.org/10.1016/j.tim.2020.02.015.

16. Jeong, H., Kim, H.J., and Lee, S.J. (2015). Complete genome sequence of *Escherichia coli* strain BL21. Genome Announc. *3*, e00134-15. https://doi.org/10.1128/genomeA.00134-15.

17. Volke, D.C., Turlin, J., Mol, V., and Nikel, P.I. (2020). Physical decoupling of XylS/*Pm* regulatory elements and conditional proteolysis enable precise control of gene expression in *Pseudomonas putida*. Microb. Biotechnol. *13*, 222–232. https://doi.org/10.1111/1751-7915.13383.

18. Rappsilber, J., Mann, M., and Ishihama, Y. (2007). Protocol for micro-purification, enrichment, pre-fractionation and storage of peptides for proteomics using StageTips. Nat. Protoc. *2*, 1896–1906. https://doi.org/10.1038/nprot.2007.261.

19. Wirth, N.T., Gurdo, N., Krink, N., Vidal-Verdú, À., Donati, S., Férnandez-Cabezón, L., Wulff, T., and Nikel, P.I. (2022). A synthetic C2 auxotroph of *Pseudomonas putida* for evolutionary engineering of alternative sugar catabolic routes. Metab. Eng. *74*, 83–97. https://doi.org/10.1016/j.ymben.2022.09.004.

20. Kozaeva, E., Volkova, S., Matos, M.R.A., Mezzina, M.P., Wulff, T., Volke, D.C., Nielsen, L.K., and Nikel, P.I. (2021). Model-guided dynamic control of essential metabolic nodes boosts acetyl-coenzyme A–dependent bioproduction in rewired *Pseudomonas putida*. Metab. Eng. *67*, 373–386. https://doi.org/10.1016/j.ymben.2021.07.014.

21. Calderón-Celis, F., Encinar, J.R., and Sanz-Medel, A. (2018). Standardization approaches in absolute quantitative proteomics with mass spectrometry. Mass Spectrom. Rev. *37*, 715–737. https://doi.org/10.1002/mas.21542.

22. Lozano Terol, G., Gallego-Jara, J., Sola Martínez, R.A., Martínez Vivancos, A., Cánovas Díaz, M., and de Diego Puente, T. (2021). Impact of the expression system on recombinant protein production in *Escherichia coli* BL21. Front. Microbiol. *12*, 682001. https://doi.org/10.3389/fmicb.2021.682001.

23. Gao, Y., Fillmore, T.L., Munoz, N., Bentley, G.J., Johnson, C.W., Kim, J., Meadows, J.A., Zucker, J.D., Burnet, M.C., Lipton, A.K., et al. (2020). High-throughput large-scale targeted proteomics assays for quantifying pathway proteins in *Pseudomonas putida* KT2440. Front. Bioeng. Biotechnol. *8*, 603488. https://doi.org/10.3389/fbioe.2020.603488.

24. Volke, D.C., Friis, L., Wirth, N.T., Turlin, J., and Nikel, P.I. (2020). Synthetic control of plasmid replication enables target- and self-curing of vectors and expedites genome engineering of *Pseudomonas putida*. Metab. Eng. Commun. *10*, e00126. https://doi.org/10.1016/j.mec.2020.e00126.

Chapter 4 – Understanding and engineering the native metabolism of *Pseudomonas putida* during adaptation to multi-substrate environments

This chapter is mainly composed of results from the following publication in preparation:

Gurdo, N., Tagliani, T., O'Connell, G. W., Taylor Parkins, S.K., Mohamed, E. T., Johnsen, J., Nielsen, L.K., Feist, A. M., & Nikel, P. I. Engineering the native metabolism of *Pseudomonas putida* for adaptation to multi-substrate environments. *Manuscript in preparation*.

Summary

The environmental bacterium *Pseudomonas putida* thrives in complex habitats that necessitate adaptation to fluctuating conditions. For instance, when exposed to a mixture of two sugars, these bacteria demonstrate a distinct sequential utilization pattern by initially consuming the preferred sugar, followed by metabolic utilization of the second sugar. Subsequent to the initial phase of rapid growth, a transient period of stasis, known as the *diauxie* lag phase, ensues. This phase is a critical interval during which the bacteria undergo specific preparatory processes, enabling them to effectively harness and metabolize the second sugar. However, the mechanism behind this complex process is not widely understood. Here, we provided a systematic analysis using a fluctuating adaptive laboratory evolution strategy between glucose and citrate, retroengineering of identified mutations coupled with targeted metabolomics and proteomics for multi-omics analysis. Our results showed that evolved clones showing absent of diauxic shift contained key mutations in *rpoA* (RNA polymerase α subunit) and *gacA* (encoding the regulatory subunit GacA of the two-component system GacS/GacA). Metabolomic profiling revealed shifts in the hexose phosphates, PP pathway, and the tricarboxylic acid (TCA) cycle. Concurrently, proteomic analysis detected significant changes in the glyoxylate-pyruvate nodes and the EDEMP cycle. Taken together, our findings provide a comprehensive understanding of the mechanisms underlying adaptation in multi-substrate environments at a systems-level.

4.1 Introduction

4.1.1 Exploring bacterial metabolism in multi-substrate environments

In their natural surroundings, bacteria encounter a range of environmental perturbations, including changes in nutrient availability, as well as biotic or abiotic stressors, which may vary over time (Aertsen and Michiels, 2004). The existence of multiple environmental conditions can prompt a distinct metabolic response in bacteria, which facilitates the allocation of vital resources required for their survival in a specific niche. This response highlights the complex and multifaceted nature of bacterial metabolism, illustrating the sophisticated mechanisms through which various microorganisms interact with their environment. For instance, when bacterial cells are exposed to multiple carbon sources (e.g. organic acids and sugars), a particular response is triggered that allows them to adapt and flourish in their ecological habitat.

It is well-established that bacteria do not metabolize all carbon sources simultaneously; rather, there is a structured hierarchy in the utilization of specific carbon sources (Görke and Stülke, 2008). This behavior is usually interpreted as an adaptation to maximize population-level growth in multi-nutrient environments. In general, bacterial cells first metabolize the most-preferred carbon source and; later, when it is depleted, switch to the less-preferred one. Between this carbon source shifts, there is a period of time which the cell seems to stop growing. However, it is implicit that cells need to invest resources in order to produce the proper enzymes—required for each carbon source—to switch from one substrate to another (Stanier, 1951). This phenomenon was described by Jacques Monod as “diauxie” (Monod, 1949). Several studies have provided evidence that *E. coli* exhibits a preference for the utilization of glycolytic substrates over gluconeogenic substrates (e.g. organic acids). As an illustrative example, when exposed to a combination of glucose and acetate, *E. coli* initially exhibits growth on glucose followed by growth on acetate (Enjalbert, et al., 2013). Interestingly, certain microorganisms display an alternative preference for carbon sources, presenting a "reverse" diauxic effect consuming first gluconeogenic over glycolytic carbon sources, as in many *Pseudomonas spp.* (McGill, et al., 2021). Traditionally, diauxic shift has been known as part of a catabolite repression process,

wherein the depletion of the preferred substrate releases the repression of specific genes for metabolizing the second substrate resulting in a significant reprogramming of central carbon metabolism (Haurie, et al., 2001, Solopova, et al., 2014, Perrin, et al., 2020). Stated differently, a persistent and adaptable metabolic reprogramming must be active to facilitate the sequential or simultaneous uptake of desired compounds from the external environment (Fondi, et al., 2016). Surprisingly, this aspect has not received sufficient attention, despite its potential significance in comprehending the dynamics of nutrient exchange on a micro-scale. In this context, the soil bacterium *Pseudomonas putida* serves as an example of the challenges faced by microorganisms in effectively and expeditiously utilizing complex nutritional inputs.

In the particular case of *P. putida* KT2440, it prioritizes the consumption of organic acids such as citrate, succinate or pyruvate over glycolytic substrates like glucose or fructose (**Figure 4.1**). A fundamental requirement for the establishment of a microbial *chassis* is the microorganism's capacity to seamlessly transition between diverse carbon sources and efficiently metabolize multiple carbon substrates. Among the next generation of microbial platforms, *P. putida* KT2440 occupies a privileged place for the development of biotechnological applications including the production of a vast plethora of biochemicals (Weimer, et al., 2020), and bioremediation of contaminants in the environment (Wasi, et al., 2013). Gaining an insight on the molecular mechanism during transitions between carbon sources can assist the design of genetic strategies for further strain improvement (Siegal, 2015).

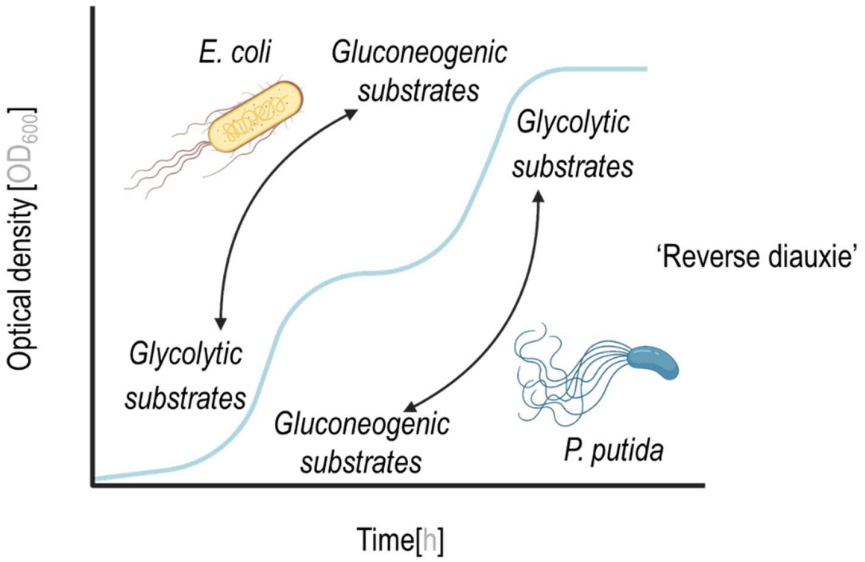

Figure 4.1. Comparison between diauxic shifts in *Escherichia coli* and *Pseudomonas putida*.

4.1.2 Exploring and engineering the phenotype of *Pseudomonas putida* in dynamic growth environments using ALE and multi-omic analyses.

Adaptive laboratory evolution (ALE) is a valuable approach for detecting crucial mutations in evolved phenotype that are difficult to anticipate beforehand. This is particularly useful to capture genetic changes that occur during evolution in alternating carbon sources (Dragosits and Mattanovich, 2013). ALE can be customized to different setups to closely simulate the natural environment where microorganisms thrive opening up a number of experimental possibilities. For example, incremental tolerance to specific chemicals can result in optimized bioproduction strains (Mohamed, et al., 2017), or by rapidly altering the growth environment, strains with desirable diauxic phenotypes can be obtained (Karve, et al., 2015, Sandberg, et al., 2017). The use of -omics analyses in conjunction with ALE techniques can enhance the exploration of intrinsic biochemical capabilities in bacteria, providing valuable insights. This integration can improve the effectiveness of ALE methods to better understand the metabolic potential of microorganisms (Wu, et al., 2022). The information gathered in these studies can assist the development of novel microbial chassis that requires an in-depth and wide understanding of the cellular metabolism. However, much of the research to date focuses on phenotypic characterization,

mutation identification and evaluation in the parental strain to corroborate the effect of such mutation (LaCroix, et al., 2015). A deeper analysis supported by –omics analysis is needed to expand the knowledge behind the microorganism physiology (Gurdo, et al., 2022).

In this study, we combined Fluctuating Logarithmic Iterative Growth in High Throughput Adaptive Laboratory Evolution (FLIGHT ALE) alternating the carbon sources citrate (gluconeogenic) and glucose (glycolytic). The methodology generated clones capable of erasing the diauxic shift in the dual condition with glycolytic and gluconeogenic substrates. Some evolved clones showed an improved growth rate versus the parental strain, and mutations were identified having an effect in the enhanced phenotype. Reverse engineering of *rpoA* (encoding a DNA-directed RNA polymerase subunit α) and *gacA* (the two-component system GacS/GacA, regulatory subunit), both contributed to the enhanced final phenotype. Time-course targeted metabolomics and proteomics were used to study the dynamic reshaping of metabolism during diauxic shift. The evolved and double mutant strain exhibited a faster protein allocation response in the TCA cycle, anaplerotic reactions, and EDEMP enzymes, effectively utilizing glucose and citrate. Protein analysis revealed that the T300A substitution in RpoA had no impact on its structure. However, the GacA mutation, specifically the T66I residue replacement, could potentially disrupt catalytic phosphorylation activation and downstream reactions, possibly contributing to the observed phenotype improvement. Overall, the mutations identified in this work are promising targets for future improvement of *Pseudomonas putida* in multi-substrate conditions.

4.2 Results

4.2.1 Evolution of *Pseudomonas putida* Δ*gcd* to erase diauxic shift on minimal medium with citrate and glucose and candidate selection

ALE was employed to adapt *Pseudomonas putida* Δ*gcd* to an environment with constantly alternating carbon growth substrates citrate and glucose. When subjected to citrate and glucose as carbon sources, this strain exhibits a diauxic growth pattern characterized by the sequential consumption of citrate as the primary substrate, followed by glucose. Generally, the utilization of carbon sources in *P. putida* follows a hierarchical pattern, characterized by distinct diauxic lag phases during growth on mixed carbon sources (Bloxham, et al., 2022). *P. putida* is known to display a preference for tricarboxylic acid cycle intermediates and amino acids as its primary carbon sources (Kukurugya, et al., 2019, McGill, et al., 2021). Interestingly, unlike many enteric bacteria, glucose does not hold a particularly favored status in the metabolic preferences of *P. putida*. Upon this background, the general strategy adopted in this study to erase the diauxic lag is described in **Figure 4.2.** FLIGHT ALE experiments were performed by culturing six independent parallel replicates (evolved lineages or populations) in M9 minimal medium alternating between medium containing 1.5 g L^{-1} sodium citrate and 1.5 g L^{-1} glucose.

The alternation between both carbon sources was designed to shorten the diauxic lag between the two carbon sources. The FLIGHT ALE experiments were ran for a total of 20 days, corresponding to around 400 generations. During the evolution, growth rates were used to assess phenotypic improvements. The number of generations achieved for each individual replicate, together with the growth rate improvements on each carbon source is presented in **Figure 4.3B**. The final growth rate was calculated separately for each replicate as the average of the growth rate in the three last batch of the evolution experiment with each respective carbon source. For glucose, the improvement measured in change percentage (%) compared to the parental strain increased from 17 to 33% while; for citrate, it was between 18 and 25% (**Figure 4.3B**). Fitness trajectories of the six evolved replicates of the Δ*gcd* strain are presented in **Figure 4.3A**. At the end of the experiment, a PCR confirmation was done to confirm the deletion of the correct strain for each replicate. We next proceeded to select clones

from the evolved end populations by picking five colonies with different sizes. Then, we evaluated the growth of the chosen clones in 10 mL of M9 minimal medium with 1 g L^{-1} sodium citrate and 2 g L^{-1} glucose in 50-mL Falcon tubes (**Figure 4.3C-H**). *P. putida* Δ*gcd* showed a diauxic shift behavior between hours 5 to 7 while, most of the selected clones significantly decreased the diauxic lag time. Clone 5.5 (from now on Δgcd^{evo}) showed almost complete reduction of the diauxic shift in this condition (**Figure 4.4**E). Likewise, given that Δgcd^{evo} had the best performance in two independent replicates among all the selected clones, additional clones were not analyzed.

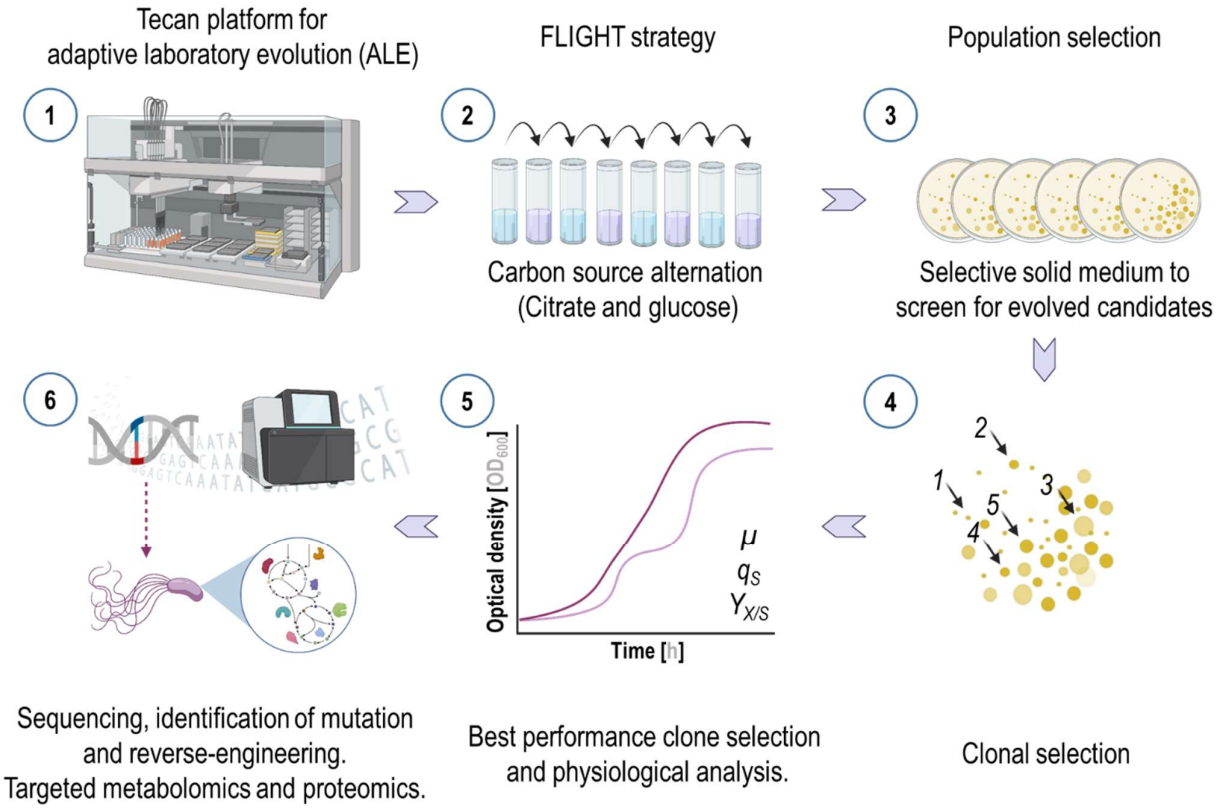

Figure 4.2. Overview workflow of the main steps carried out in this study. 1) Automated platform for adaptive laboratory evolution. 2) FLIGHT strategy using alternating carbon sources. 3) End-populations selection in selective minimal medium. 4) Colony picking and selection of clone candidates. 5) Evaluation of best performing candidates and physiological analysis in Falcon tubes. 6) Sequencing, mutational analysis and reverse-engineering of the selected mutation into the parental strain. Targeted metabolomics and proteomics in the evolved, mutant and parental strain.

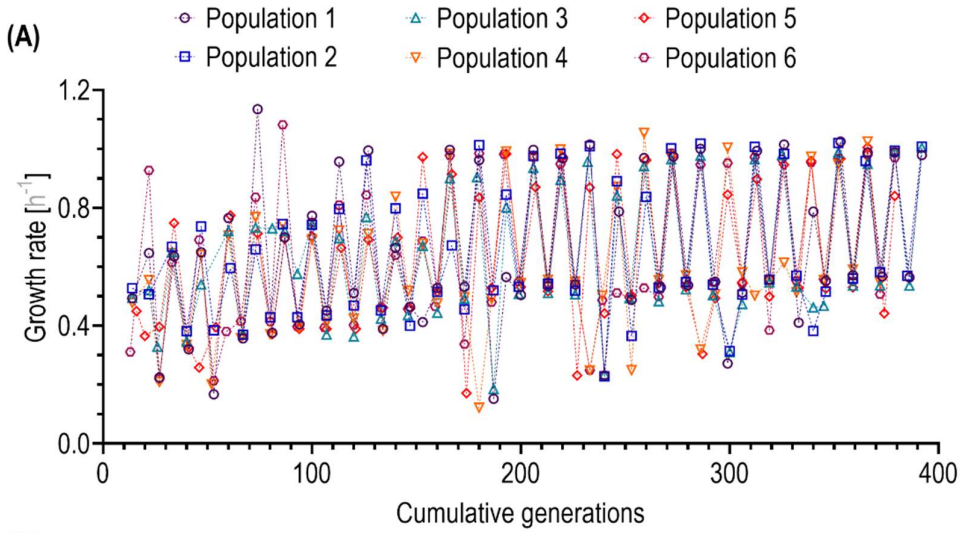

(B)

Rep.	N° of Gen.	Glucose – Growth rate [h^{-1}]			Citrate – Growth rate [h^{-1}]		
		Initial	Final	Change	Initial	Final	Change
1	400	0.43 ± 0.02	0.57 ± 0.01	32%	0.79 ± 0.06	0.98 ± 0.01	24%
2	400		0.57 ± 0.01	33%		0.99 ± 0.02	25%
3	400		0.54 ± 0.01	25%		0.98 ± 0.02	24%
4	385		0.56 ± 0.02	32%		0.99 ± 0.03	25%
5	387		0.50 ± 0.04	17%		0.94 ± 0.06	18%
6	379		0.54 ± 0.02	26%		0.97 ± 0.01	23%

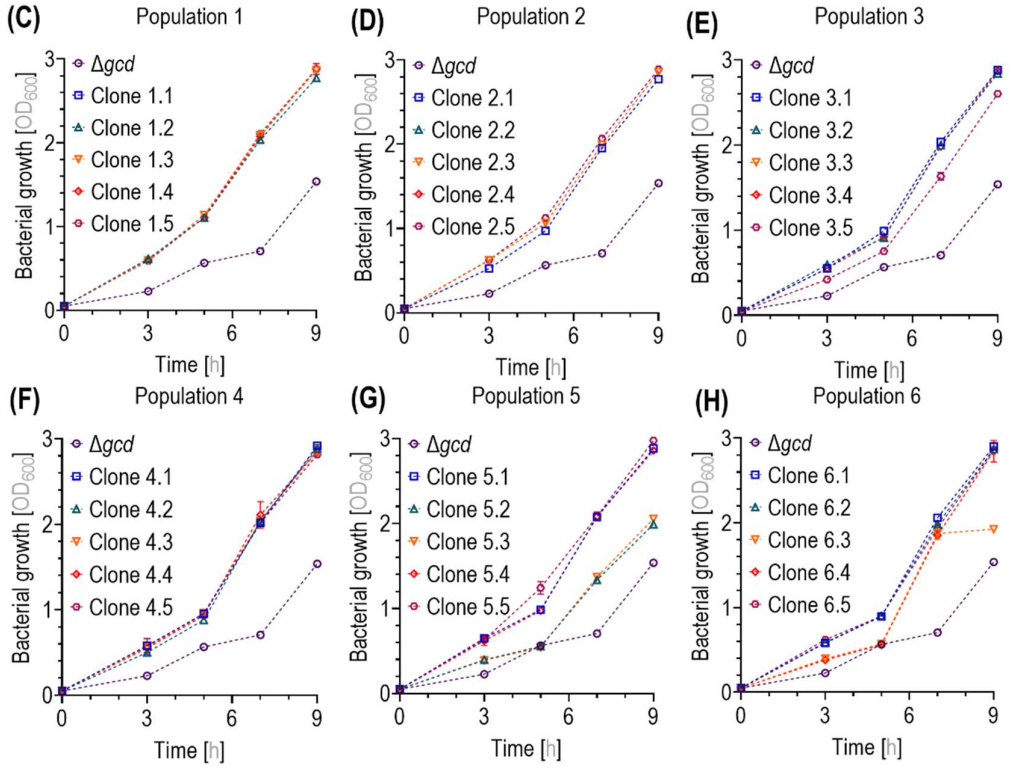

Figure 4.3. Comparison of evolved populations and growth analysis of the clones selected from the evolved end populations. (A) Fitness trajectories of the Δ*gcd* Glucose-citrate FLIGHT ALE experiments. Population's growth rate [h^{-1}] plotted against the number of batches for each replicate. **(B)** Resulting phenotypic changes for each evolved population (replicates) in the Glucose/Citrate FLIGHT ALE experiments; number of generations, growth rate improvements on glucose and citrate are given. For growth analysis, cells were cultivated in Falcon® tubes in M9 minimal media supplemented with 1.5 g L^{-1} sodium citrate and 1.5 g L^{-1} glucose. Growth curves of **(C)** population 1, **(D)** population 2, **(E)** population 3, **(F)** population 4, **(G)** population 5 and **(H)** population 6. Dashed lines represents the course of bacterial growth [OD_{600}] along the cultivation. Error bars indicate the standard deviation from two biological replicates.

4.2.2 Physiological characterization of evolved clones in shaken-flask cultures

In order to characterize Δgcd^{evo} from a physiological point of view, we analyzed growth, substrate consumption and yields on M9 containing: A) 2 g L^{-1} glucose, B) 1 g L^{-1} sodium citrate plus 2 g L^{-1} glucose, and C) 2 g L^{-1} sodium citrate using 250-mL shaken-flasks (**Figure 4.4**). By analyzing the physiological parameters, we found that in glucose as only carbon source, the evolved strain displayed a significant improvement from 0.48 to 0.57 h^{-1} and 0.43 to 0.63 g_{CDW} g $glucose^{-1}$ in terms of growth rates and biomass yields, respectively (**Figure 4.4A and 4.4D**). This indicates that most of the beneficial mutations were acquired during the evolution in glucose. Also, the evolved strain was more efficient in converting the carbon sources into biomass because of its higher yields while keeping equal uptakes rates. On the other hand, in the condition with citrate, growth rates and yields exhibited a slightly increase in the evolved strain compared to the parental strain (**Figure 4.4C**).

Finally, when citrate and glucose were present in the medium, we observed that citrate was consumed primarily as the preferred carbon source after 4 hours of cultivation. Later, for the parental strain Δ*gcd*, a diauxic lag of 2 h was observed between 4 and 6 h while; for Δgcd^{evo}, it was practically omitted. As soon as citrate was completely depleted in the medium, cells started to consume glucose. Here, the evolved strain metabolized glucose faster than the parental strain (**Figure 4.4B**). This isolated clone and parental strain were then subjected to DNA sequencing to examine and compare their genetic basis, with the goal of better understanding the genotype responsible for the observed increase in fitness.

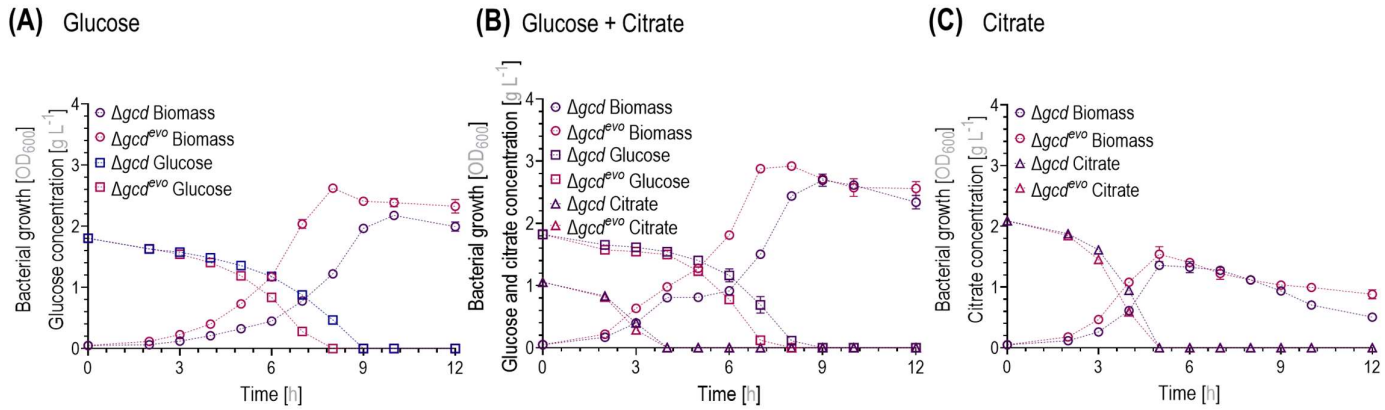

(D)

Pseudomonas putida Strain	Carbon source		Specific growth rate [h^{-1}]		Uptake rate [mmol g_{CDW}^{-1} h^{-1}]		$Y_{X/S}$ [g_{CDW} g glucose^{-1}, g_{CDW} g citrate^{-1}]	
Δ*gcd*	Glucose		0.48 ± 0.01		5.32 ± 0.15		0.43 ± 0.01	
	Citrate	Glucose	0.70 ± 0.01	0.49 ± 0.01	8.57 ± 0.28	4.06 ± 0.55	0.31 ± 0.01	0.60 ± 0.03
	Citrate		0.83 ± 0.02		11.55 ± 0.39		0.27 ± 0.01	
Δ*gcd*^{evo}	Glucose		0.57 ± 0.01		4.86 ± 0.06		0.63 ± 0.01	
	Citrate	Glucose	0.77 ± 0.01	0.41 ± 0.02	7.81 ± 0.13	3.66 ± 0.20	0.38 ± 0.01	0.59 ± 0.01
	Citrate		0.90 ± 0.04		11.05 ± 0.55		0.31 ± 0.02	

Figure 4.4. Physiological characterization in 250-mL shaken-flask of Δ*gcd*^{evo} versus *Pseudomonas putida* Δ*gcd*. Cells were grown on M9 minimal medium containing on glucose **(A)**, glucose complemented with citrate **(B)** and citrate **(C)**. Calculated physiological parameters (specific growth rate, uptake rate and biomass yields) **(D)** for the Δ*gcd*^{evo} and parental strain on M9 minimal medium with glucose, glucose and citrate and citrate.

4.2.3 Whole genome sequencing and mutation analysis in the parental strain and its Δ*gcd*^{evo} derivative

Whole-genome sequencing was applied to determine the genetic basis of the improved fitness phenotype of the evolved *Pseudomonas putida* Δ*gcd*^{evo} on glucose-citrate M9 minimal medium. Overall, two genes were identified having unique mutations in the selected clone (**Figure 4.5A**). Δ*gcd*^{evo} exhibited two important mutations, specifically in the genes for DNA-directed RNA polymerase α subunit *rpoA* and the regulatory subunit GacA of the two-component system GacS/GacA (**Figure 5B**). Regarding the first key mutation, a single nucleotide polymorphism (SNP) A→G occurred in the amino acid residue 300 (ACT→GCT) where the amino acid L-threonine was substituted by an L-alanine residue (Simpson, 1979, Ross, et al.,

1993). This polymerase catalyzes the transcription of DNA into RNA using the four-ribonucleoside triphosphates as substrates (Ishihama, 1992). Specific mutations in *rpoA* were identified in *E. coli* affecting central metabolic pathways when growing on different carbon sources (Conrad, et al., 2010, Rajaraman, et al., 2016, Utrilla, et al., 2016). Also, mutations in *rpoA* and *rpoB* genes conferred higher stress resistance to different conditions: temperature (Igarashi, et al., 1990), rifampicin (Alifano, et al., 2015) and organic acids (Lennen, et al., 2023). Surprisingly, there are few evidences to date showing that *rpoA* has a beneficial effect in the phenotype fitness in *Pseudomonas spp*. A study revealed that mutations in *rpoB* bestowed higher tolerance to the organic acid 4-hydroxybenzoate (4HBA) (Hosokawa, et al., 2002). The second important mutation corresponds to the regulatory subunit *gacA* in the GacS-GacA complex (Song, et al., 2023). This two-component system has a critical role in recognizing signaling molecules and regulating physiological responses as an adaptation to the environment (Stock, et al., 2000, Gao, et al., 2007). Previous studies in *Escherichia coli* have demonstrated that disrupting the BarA-UvrY complex (GacS-GacA two component system in *Pseudomonas spp.*) impairs the bacterial capability to switch between two different carbon sources or compete for glycolytic substrates (Tomenius, et al., 2006). With this contextual knowledge, we decided to explore the effects of these mutations in the central carbon metabolism using the strain *Pseudomonas putida* Δ*gcd* as genetic background.

(A)

Reference Seq	Position	Mutation Type	Sequence Change	Gene	Product	Details
AE015451	563,815	SNP	A > G	*rpoA*	DNA-directed RNA polymerase (α subunit)	T300A (ACT→GCT)
	4,635,559	SNP	G > A	*gacA*	Two-component system GacA-GacS - regulatory subunit	T66I (ACC→ATC)

(B)

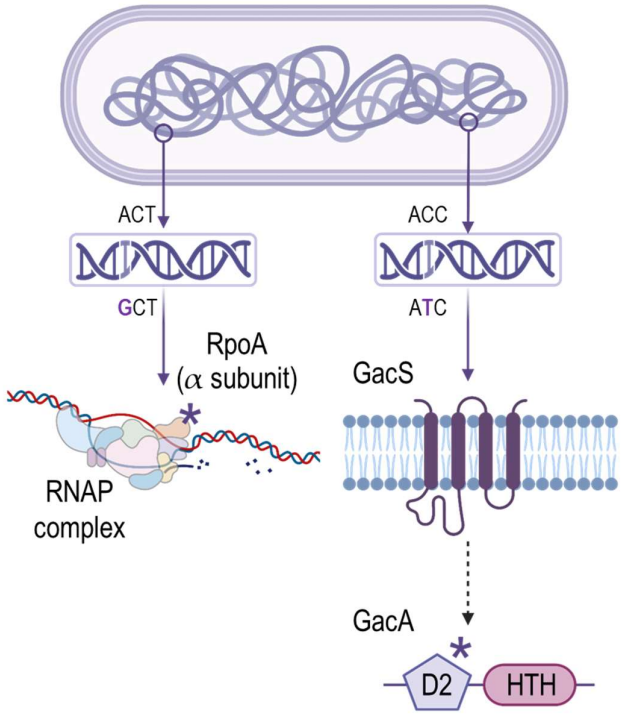

Figure 4.5. Mutational analysis in *Pseudomonas putida* Δ*gcd*^{evo}. (A) Relevant mutations found after evolution in glucose and citrate. The analysis was made utilizing the reference sequence AEO15451; genomic position is indicated, along with the type of mutation and specific amino acid change. Gene name, product and aminoacids modification are also shown. **(B)** Schematic representation of the mutations in the corresponding gene and protein product. RNAP (RNA polymerase) complex shows the different subunits in multicolor. α subunit is depicted in orange. The domain composition of GacS/GacA: GacS contains the sensing domain and GacA is a typical response regulator composed of the N-terminal REC (D2) and C-terminal helix-turn-helix (HTH). Asterisks points out where the mutations occurred.

4.2.4 Reverse engineering to validate mutational effect

In order to examine how mutations affect the diauxic shift in *Pseudomonas putida* KT2440, we generated three different strains containing the following mutations: 1) *rpoA* [T300A (ACT→GCT)], *gacA* [T66I (ACC→ATC)] and the combination of both *rpoA* and *gacA*. Fitness analyses were performed in parallel on M9 medium supplemented with both sodium citrate (1 g L^{-1}) and glucose (2 g L^{-1}). Mutations were evaluated and compared for improved fitness by analyzing growth rates in this condition (**Figure 4.6**)**.** The comparative analysis of reverse engineered strains exhibited that the mutated genes *rpoA* and *gacA* identified in this FLIGHT ALE experiment conferred a fitness advantage over the parental strain allowing to mostly rescue the diauxic lag phenotype. The analysis also showed that the mutation at amino acid 66 of RpoA shortened the shifting time from citrate to glucose in approximately 50% in comparison to the parental strain Δ*gcd*.

It is also worth noting that the single mutant *rpoA* not only reached a higher biomass density but also enhanced specific growth rate in comparison to the single mutant *gacA*. Along the same line, we observed that introducing the mutation in *gacA*, the growth rate on citrate phase increased from 0.59 to 0.71 h^{-1}. Finally, when the double mutation was introduced in the parental genetic background, both mutation acted sinergically where *gacA* improved growth on citrate and *rpoA* accelerated the shift into glucose. To summarize, the non-evolved strain with the double point mutation was able to replicate the fitness of the final phenotype to a great extent, as it significantly shortened the diauxic phase and exhibited growth similar to the evolved strain.

(A)

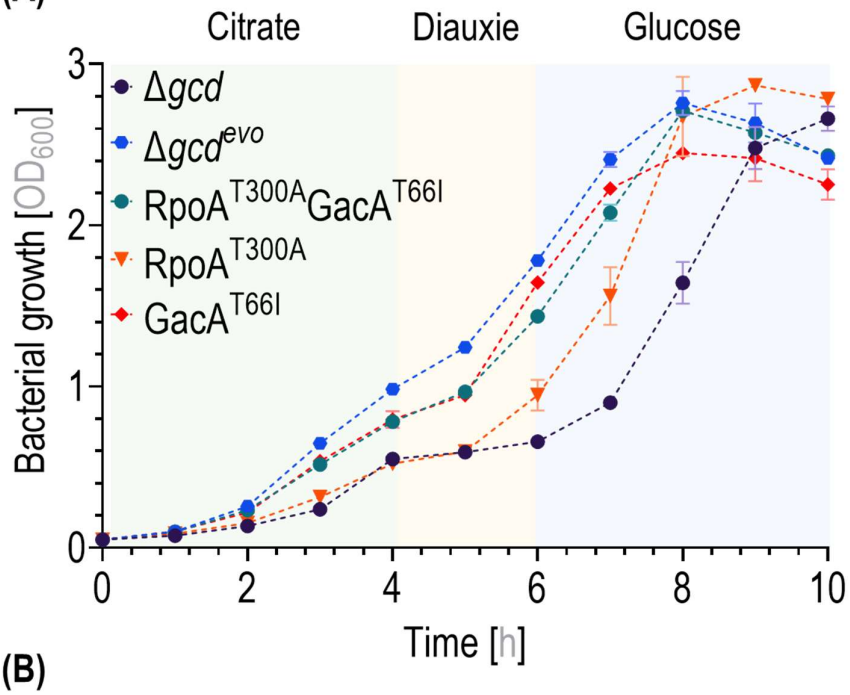

(B)

Pseudomonas putida Strain	Specific growth rate [h^{-1}]	
	Citrate	Glucose
Δ*gcd*	0.59 ± 0.01	0.46 ± 0.02
Δ*gcd*^{evo}	0.78 ± 0.01	0.33 ± 0.02
RpoA^{T300A}GacA^{T66I}	0.71 ± 0.01	0.35 ± 0.01
RpoA^{T300A}	0.60 ± 0.01	0.52 ± 0.01
GacA^{T66I}	0.71 ± 0.01	0.43 ± 0.02

Figure 4.6. Reverse-engineered strain analysis. (A) Evaluation of retro-engineered strains in shaken-flask cultivations. Growth curves were done in M9 minimal medium with citrate and glucose as carbon sources. Optical density at 600 nm was measured every hour until the cultures reached stationary phase. **(B)** The table shows calculated specific growth rates of the different mutants for each substrate.

4.2.5 Targeted metabolomics reveals temporal organization of gluconeogenic-glycolytic shift in *Pseudomonas putida* Δ*gcd*

As mentioned in **Chapter 1**, *P. putida* KT2440 exhibits a cyclic glycolytic metabolism, encompassing the catabolic and anabolic activities of the Entner-Doudoroff pathway and the Embden-Meyerhof-Parnas (EMP) pathway (in a gluconeogenic manner), alongside the pentose phosphate (PP) pathway. This metabolic framework, known as the EDEMP cycle, facilitates the regeneration of hexose phosphates and promotes catabolic NAD(P)H production. The concentration of metabolites within the EDEMP and tricarboxylic acid (TCA) cycles was analyzed to gain insights into the metabolic dynamics (**Figure 4.7A**). In order to disentangle the physiological changes that cells undergo during the diauxic shift, we first captured the dynamics of 15 intracellular metabolites from central carbon metabolism (EDEMP, PPP and TCA cycle). The data gathered in this analysis was normalized using the cell dry weight previously estimated for *P. putida* KT2440. We plotted normalized concentrations along the different stages from 0-3 hours (pre-shift, citrate phase), 3-5 hours (diauxic shift) to 5-7 hours (post-shift, glucose) within (**Figure 4.7B**). Overall, the data revealed the conventional dynamic of intracellular metabolite concentrations upon glycolytic-gluconeogenic regimen. The levels of TCA cycle metabolites including citrate, glyoxylate, 2-OG and succinate remained high at 3 h when cells were exposed to citrate, but decreased continuously during the diauxic phase (time points 4, 5, and 6) as well as during the glucose phase (7 and 8 h). However, there was an exception for citrate, which started to increase again during hours 6 and 7, specifically during the glycolytic phase.

In contrast, PP pathway metabolites R5P, Ru5P and S7P as well as DHAP operated in contraposition to the TCA cycle where, metabolite levels stayed at low concentrations within citrate phase and raised up to 3-fold in glucose condition. Hexose phosphates F6P, G6P and 6PG remained stable across the cultivation in the wild-type strain while double mutant showed an increase in F6P and G6P during the diauxic lag (hour 5) and; both Δ*gcd*^{evo} and double mutant experienced a significant overproduction of the two previous metabolites upon glycolytic regimen. These results indicate that the TCA cycle is the predominant catabolic route for citrate under a gluconeogenic regime (Zampar, et al., 2013). In addition and particularly for the double mutant, pentose

phosphate pathway metabolites exhibited a higher metabolite activity during the diauxic lag phase, in comparison with the wild-type, indicating that this metabolic block is also critical to rapidly switch from citrate to glucose. Overall, these measurements showed a specific pattern in the concentrations of intracellular metabolites based on the pathways in which they participate.

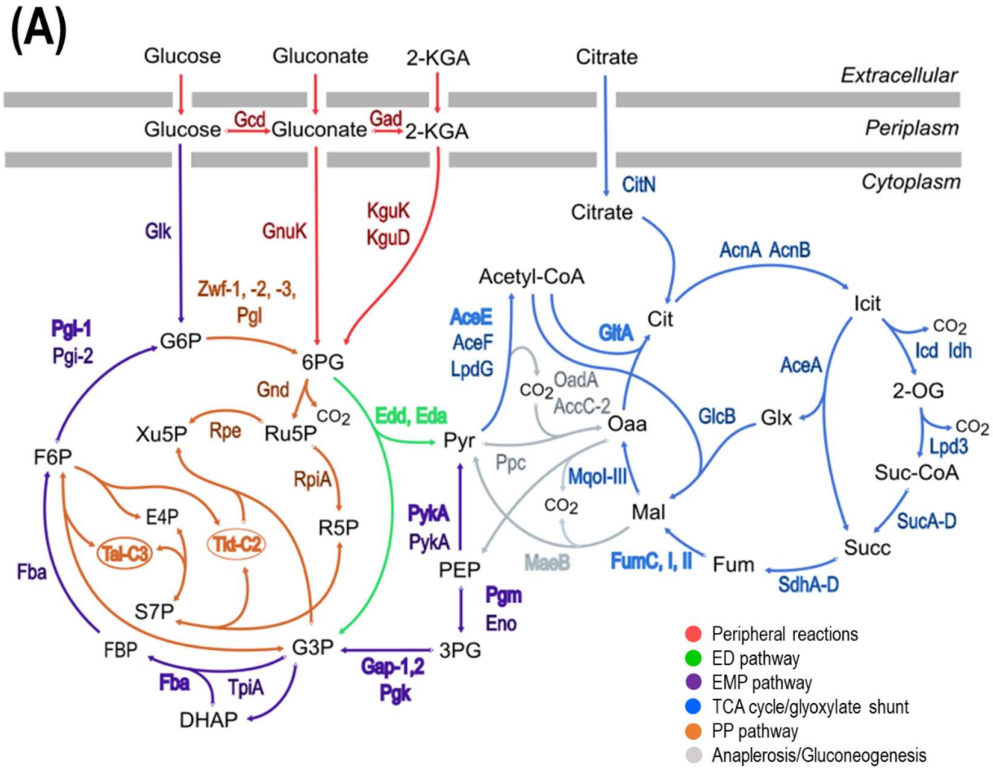

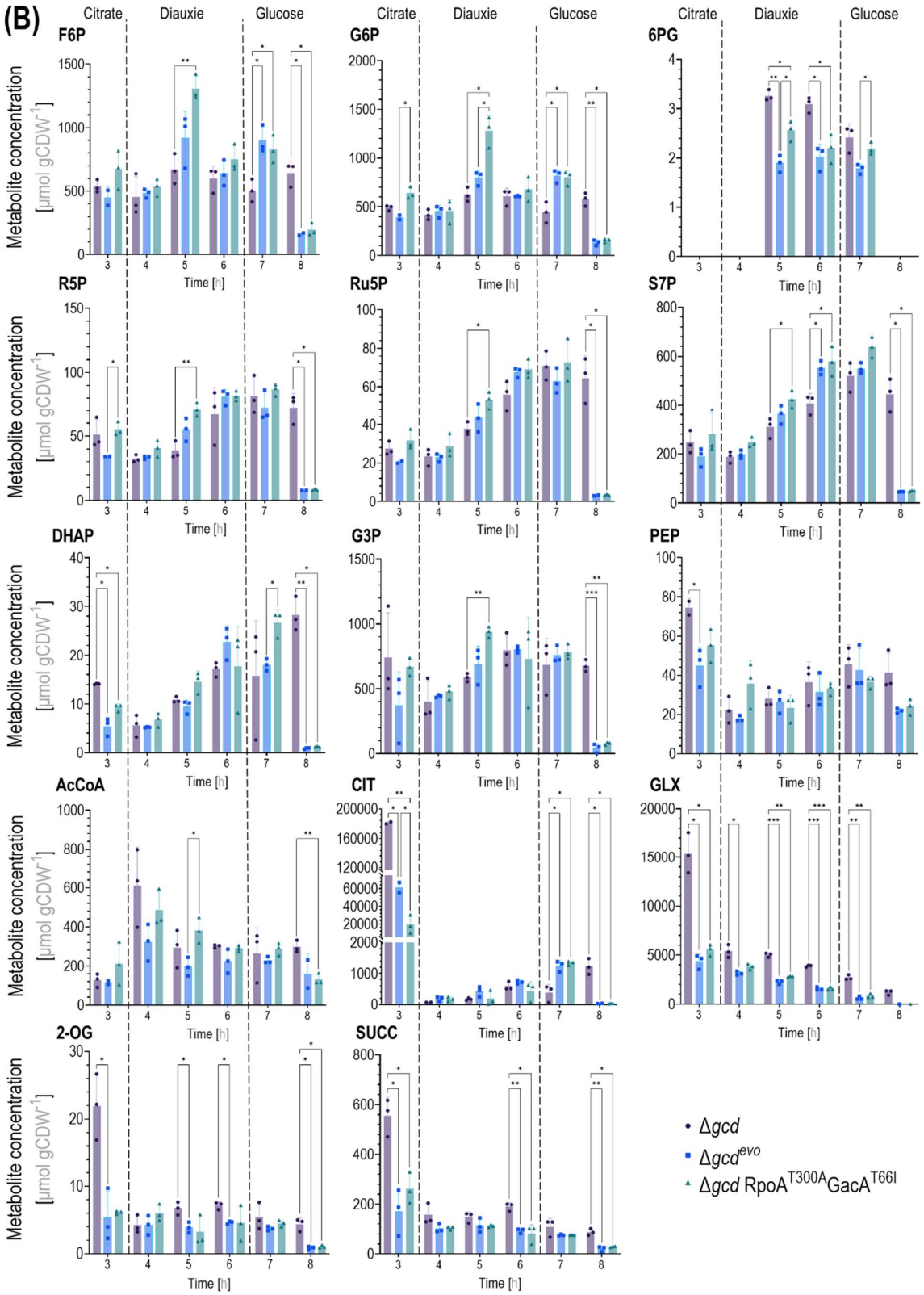
(B)
Citrate
Diauxie
Glucose
F6P
G6P
6PG
R5P
Ru5P
S7P
DHAP
G3P
PEP
AcCoA
CIT
GLX
2-OG
SUCC
Metabolite concentration [µmol gCDW⁻¹]
Time [h]
Δgcd
Δgcd^evo
Δgcd RpoA^T300A GacA^T66I

Figure 4.7. Targeted metabolomics in M9 medium glucose and sodium citrate for wild-type strain and Δ*gcd*^{evo} and double mutant. (A) Simplified metabolic map of central metabolism in *P. putida* KT2440. Peripheral reactions of glucose processing are highlighted in red while and the Entner–Doudoroff pathway in green; reactions within the pentose phosphate (PP) pathway are shown in orange. Purple arrows identify the incomplete Embden–Meyerhof–Parnas (EMP) pathway, and blue arrows are used for reactions within the tricarboxylic acid (TCA) cycle. Proteins that show a concentration difference in the presence either on citrate or glucose are pinpointed in bold face. Abbreviations for enzymes: EDEMP enzymes: Glucose kinase (Glk); Glucose-6-P isomerase-1 (Pgi-1); Glucose-6-P isomerase-2 (Pgi-2); 6-phosphogluconate dehydratase (Edd); 2-dehydro-3-deoxy-6-phosphogluconate aldolase (Eda); Fructose-1,6-P2 phosphatase (Fbp); Fructose-1,6-P2 aldolase (Fda); Triosephosphate isomerase (TpiA); Glyceraldehyde-3-P dehydrogenase-1 (Gap-1); Glyceraldehyde-3-P dehydrogenase-2 (Gap-2); Phosphoglycerate kinase (Pgk); Phosphoglycerate mutase (Pgm); Enolase (Eno); Pyruvate kinase (PykA); Pyruvate kinase complex (PykAF). PP pathway enzymes: Glucose-6-P dehydrogenase-1 (Zwf-1); Glucose-6-P dehydrogenase-2 (Zwf-2); Glucose-6-P dehydrogenase-3 (Zwf-3); Phosphogluconolactonase (Pgl); Phosphogluconate dehydrogenase (Gnd); Ribose-5-P isomerase (Rpi); Ribulose-5-P 3-epimerase (Rpe); Transketolase (Tkt); Transaldolase (Tal). Citrate transport and TCA cycle enzymes: CitN, Citrate transporter; AceF, Acetyltransferase component of pyruvate dehydrogenase complex; Lpd, Dihydrolipoyl dehydrogenase; AceE, Pyruvate dehydrogenase E1 component; LpdG, Dihydrolipoyl dehydrogenase G; GltA, Citrate synthase; AcnA-I, Aconitate hydratase I; AcnA-II, Aconitate hydratase II; AcnB, Aconitate hydratase B; Icd, Isocitrate dehydrogenase [NADP]; SucA, Oxoglutarate dehydrogenase (succinyl-transferring); SucC, Succinate-CoA ligase [ADP-forming] subunit beta; SucD, Succinate-CoA ligase [ADP-forming] subunit alpha; SdhA, Succinate dehydrogenase flavoprotein subunit; SdhB, Succinate dehydrogenase iron-sulfur subunit; FumC, Fumarate hydratase class II; Mqo-1, Malate:quinone oxidoreductase 1; Mqo-2, Malate:quinone oxidoreductase 2; Mqo-3, Malate:quinone oxidoreductase 3; AceA, Isocitrase; GlcB, Malate synthase. **(B)** Normalized intracellular concentrations (*y-axis*) of metabolites participating in glycolysis, TCA/glyoxylate cycle and PP pathway during growth on citrate and glucose from 3 to 8 hours (*x*-axis). Purple, blue and green bars represent wild-type strain Δ*gcd*, Δ*gcd*^{evo} and double mutant respectively. The concentrations of each metabolite were normalized using cell dry weight (g_{CDW}). Average data is represented from 3 biological replicates. Statistical analysis was performed using two-way ANOVA analysis. * p<0.05, ** p<0.01, *** p<0.001. Abbreviations are as follows: F6P, fructose-6-phospahte; G6P, glucose-6-phosphate; 6PG, 6-phosphogluconate; R5P, ribose-5-P; Ru5P, ribulose-5-P; S7P, sedoheptulose-7-P; DHAP, dihydroxyacetone-P; G3P, glyceraldehyde-3-P; PEP, phosphoenolpyruvate; AcCoA, acetyl-coenzyme A; CIT, citrate; GLX, glyoxylate; 2-OG, 2-oxoglutarate; SUCC, succinate.

4.2.6 Protein allocation in the glyoxylate-pyruvate nodes and the EDEMP cycle facilitates metabolic transitions from citrate to glucose in evolved *Pseudomonas putida*

The crucial role of proteins in shaping microbial phenotypes is widely acknowledged in the academic community. Given the constraints of limited cellular resources and space, it is essential for microbes to efficiently allocate proteins in order to achieve maximum proliferation rates, while also being able to adapt to changing environmental conditions such as diauxic shift. The phenomenon of diauxic shift has

been previously investigated in cultures of *P. aeruginosa* using systems biology approaches such as genomics, exo-metabolomics and label-free proteomics (Yung, et al., 2019, McGill, et al., 2021). However, to the best of our knowledge, there is no explicit description of this diauxic phenotype in *P. putida* using targeted proteomics methods. Accurately assessing the diauxic phenotype in *P. putida* within a dual environmental context is a fundamental requirement for gaining insight into the nutrient and energy fluxes that govern energy metabolism, growth, and adaptation at the cellular level. As part of our study, we analyzed the diauxic shift dynamic at proteome level in the three strains. To accomplish this, we collected samples in the same manner as we did for metabolomics, and subsequently processed them using the methodology outlined in the materials and methods section. Proteomic data typically provides a more reliable representation of how cellular resources are utilized and offers stronger insights into cell function compared to relying solely on transcriptomic or genomic data (Veenstra, 2021). The final phenotypes were studied using quantitative proteomics with mass spectrometry (MS) using QconCAT peptides added on whole-cell lysates taken in pre-diauxic shift (3 h), in the diauxic shift (5 h) and post-shift (7 h) (Gurdo, et al., 2023). The utilization of this approach was based on its ability to precisely measure the levels of targeted CCM proteins in *P. putida*. Additionally, it exhibits superior accuracy compared to alternative methods such as label-free strategies. Moreover, it enables direct quantification of protein expression levels across different samples, conditions, or time points, thereby providing a comprehensive understanding of the dynamic changes within the bacterial proteome (Neilson, et al., 2011). The data obtained from proteomic analysis was examined in order to identify the proteins involve in central carbon metabolism and the transition between gluconeogenic (citrate) to glycolytic regimen (glucose). When analyzing the data in TCA cycle, we observed a significant upregulation of the acetyl-CoA synthetase II (AcsA-II), citrate synthase (GltA), pyruvate dehydrogenase E1 component (AceA), FumC-II (**Figure 4.8A**) and the malic enzyme (MaeB) corresponding to the pyruvate shunt in the Δ*gcd*^{evo} and Δ*gcd*RpoA^{T300A}GacA^{T66I} when compared to the parental strain, during the diauxic shift (5 h) (**Figure 4.8B**). Moreover, there is a clear change in the concentration of certain protein when citrate is depleted, namely AcnA-I, Icd and FumC-II (which are only significantly active during the glucose phase). This data suggests that during growth on citrate, TCA enzymes could

supply more energy, reducing power and precursors for many important metabolites in the Δ*gcd*^{evo} and Δ*gcd* RpoA^{T300A} GacA^{T66I} strains as compared with the parental *P. putida*, leading to a better performance in this condition.

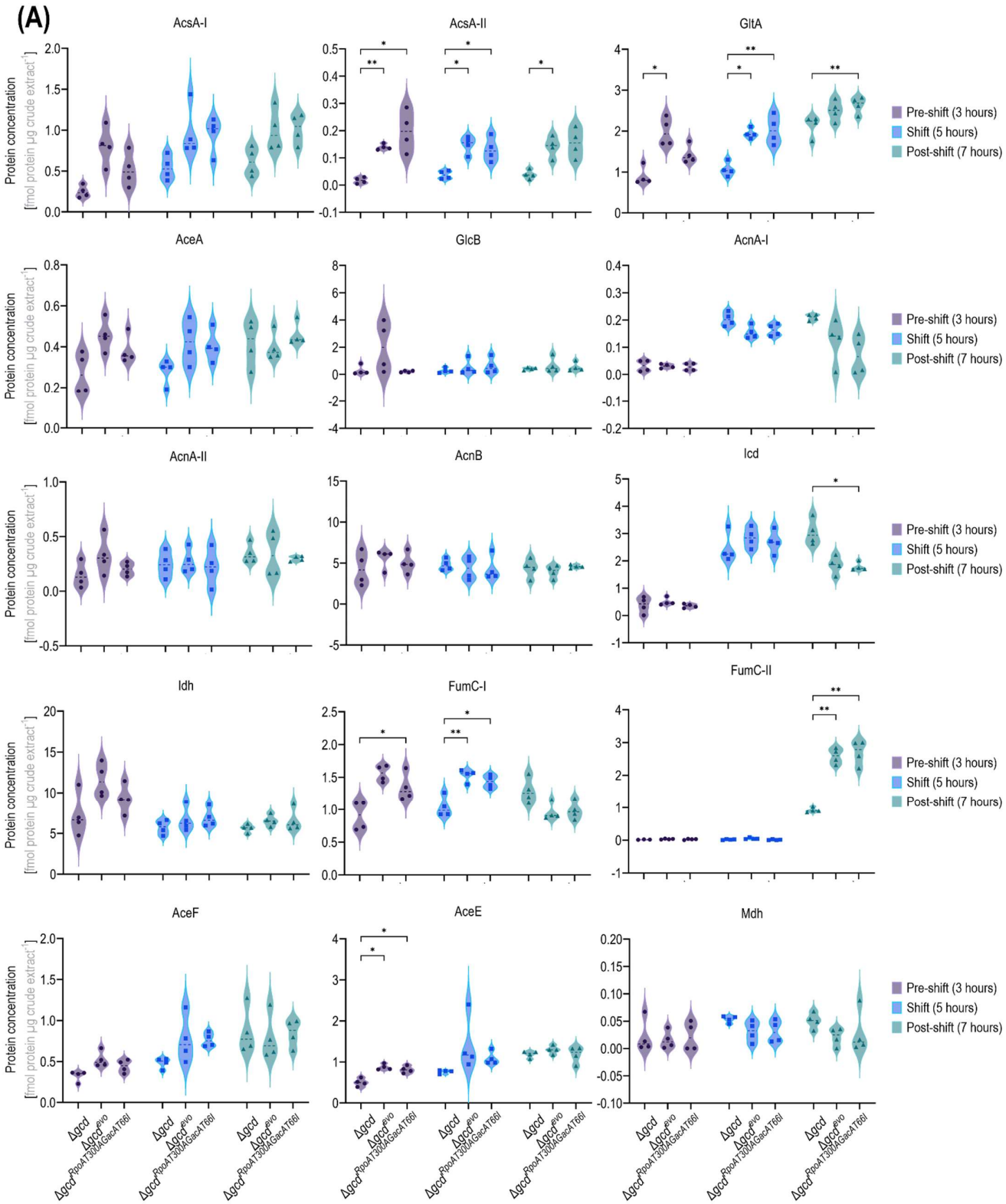
(A)
AcsA-I
AcsA-II
GltA
AceA
GlcB
AcnA-I
AcnA-II
AcnB
Icd
Idh
FumC-I
FumC-II
AceF
AceE
Mdh
Protein concentration
[fmol protein µg crude extract-1]
Pre-shift (3 hours)
Shift (5 hours)
Post-shift (7 hours)
Δgcd
Δgcd evo
Δgcd RpoA T300A GacA T66I

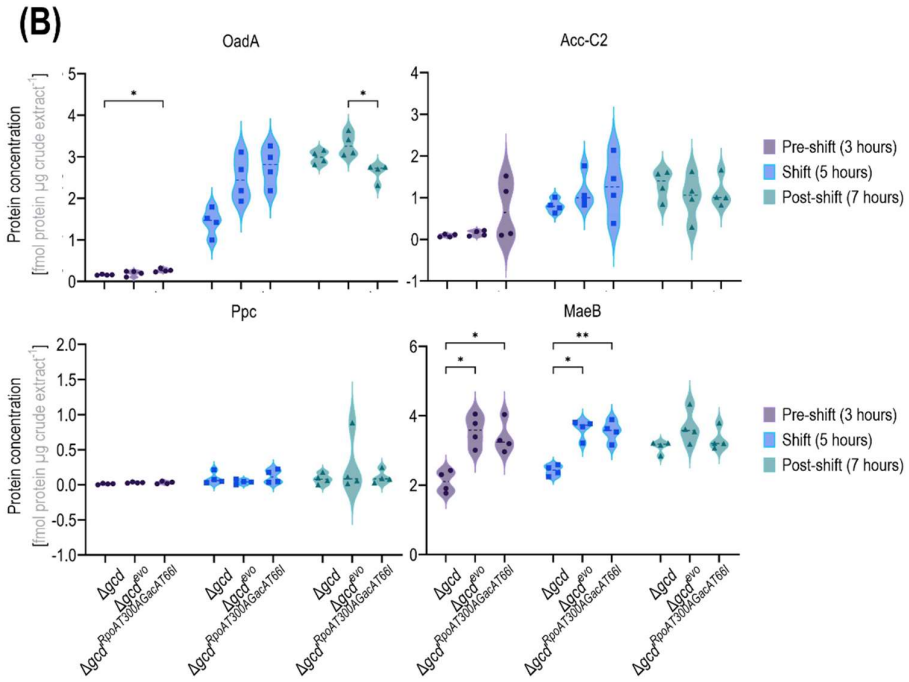

Figure 4.8. Protein quantification of TCA cycle during pre-shift (3 hours), shift (5 hours) and post-shift (7 hours). The strains were grown in M9 medium containing sodium citrate (1 g L^{-1}) and glucose (2 g L^{-1}) as carbon sources and were harvested at different time points. Violin graph were depicted to visualize four biological replicates per strain. The horizontal line inside the violin area represents the median. The area around the dots is a kernel density estimation showing the distribution shape of the data. Wider sections of the violin plot represent a higher probability that members of the population will take on the given value; the skinnier sections represent a lower probability. Statistical analysis was performed using two-way ANOVA analysis. *p<0.05, **p<0.01, ***p<0.001. Abbreviations are as follows: **(A)** TCA cycle: Acetyl-CoA synthetase-I (AcsA-I); Acetyl-CoA synthetase-I (AcsA-II); Citrate synthase (GltA); Isocitrate lyase (AceA); Malate synthase (GlcB); Aconitate hydratase I (AcnA-I); Aconitate hydratase II (AcnA-II); Aconitate hydratase B (AcnB); Isocitrate dehydrogenase [NADP] (Icd); Isocitrate dehydrogenase isozyme (Idh); Fumarate hydratase class II (FumC-I); Fumarate hydratase class II (FumC-II); Acetyltransferase component of pyruvate dehydrogenase complex (AceF); Pyruvate dehydrogenase E1 component (AceE) and Malate dehydrogenase (Mdh). **(B)** Anaplerotic reactions: Pyruvate carboxylase subunit A (PycA); Pyruvate carboxylase subunit B (PycB); Phosphoenolpyruvate carboxylase (Ppc) and Malic enzyme (MaeB).

With respect to the EDEMP cycle proteins (**Figure 4.9A**), notable changes were detected in Pgi-1 protein—responsible for converting fructose-6-P into glucose-6-P through an isomerization reaction—whereby the strains Δ*gcd*^{evo} and Δ*gcd*RpoA^{T300A}GacA^{T66I} exhibited reduced protein levels in the upper metabolism when compared to the parental strain. This observation implies that these strains exhibit less preference towards this particular step of the EDEMP cycle. Then, we also noticed a higher concentration of the Entner–Doudoroff (ED) enzymes 6PG dehydratase (Edd) and KDPG aldolase (Eda) in the Δ*gcd*^{evo} and Δ*gcd*RpoA^{T300A}GacA^{T66I} not only during the gluconeogenic phase (citrate as only carbon source) but also during the diauxic shift. Earlier studies have suggested that deactivation of GacA may result in substantial alterations in gene transcription by negatively regulating the expression of the secretory systems (Hassan, et al., 2010), reducing biofilm formation (Parkins, et al., 2001) as well as the production of secondary metabolites and extracellular enzymes (Wei, et al., 2013). However, it is not clear its effect in primary metabolism in the presence (with or without mutations) or absence of this gene. Here, we believe that the mutated protein could be acting at transcriptional level activating several transcription factors, which affect the expression of central carbon metabolism enzymes. During growth on citrate and in the transition into glucose consumption (diauxic shift), it was observed that enzymes associated with the lower glycolysis pathway, including PykA, Pgm, Pgk, Gap-1/Gap-2 and Fda were significantly higher in Δ*gcd*^{evo} and Δ*gcd*RpoA^{T300A}GacA^{T66I} in comparison to the parental strain. This indicates that certain enzymes may be subjected to transcriptional derepression, resulting in increased transcript levels that are subsequently translated into greater amounts of enzyme content. This, in turn, could enhance the metabolic efficiency of Embden-Meyerhof-Parnas (EMP) pathway. As a general trend, a higher protein content in EDEMP enzymes is evident when comparing the complete time-course profile of the strain with its parental counterpart.

Concerning PP pathway, transketolase (TktA) and transaldolase (Tal) exhibited a significantly higher concentration during the citrate phase, and Tal was the sole enzyme with increased concentration during the diauxic shift when comparing Δ*gcd*^{evo} and Δ*gcd*^{evo}RpoA^{T300A}GacA^{T66I} against the parental strain. Transketolase mediates two crucial reactions that occur in opposite directions within two different pathways. The

initial step of the non-oxidative pentose phosphate pathway involves transketolase, which utilizes thiamine diphosphate as a cofactor. In this reaction, transketolase accepts a 2-carbon fragment from D-xylulose-5-P (X5P), a 5-carbon ketose, and then transfers this fragment to D-ribose-5-P (R5P), a 5-carbon aldose, producing sedoheptulose-7-P (S7P), a 7-carbon ketose. The removal of two carbons from X5P results in the formation of glyceraldehyde-3-P (G3P), a 3-carbon aldose. The second reaction involves the transfer of a 2-carbon fragment from X5P to an aldose, namely, erythrose-4-phosphate (E4P), via thiamine diphosphate. This reaction leads to the production of fructose 6-phosphate (F6P) and glyceraldehyde-3-P (G3P). On the other hand, transaldolase (Tal) facilitates the reversible transfer of a three-carbon ketol unit from S7P to G3P, leading to the production of E4P and F6P. The up-regulation of PP pathway enzymes, as Tal and Tkt, specifically in the non-oxidative phase, may indicate metabolic adaptations to rearrange carbon skeletons to meet the demands of cellular anabolism. This can be a strategic mechanism employed by the bacteria to optimize the allocation of resources and maintain efficient growth and survival in various environmental conditions (Rytter, et al., 2021). On the other hand, even though no significant difference where observed within the strains, isozymes Zwf-2 and Zwf-3 were found at very low concentrations. However, Zwf-1 appeared to be functional and the amount of protein increased along the culture, having the highest concentration during post-shift (glucose phase) which was consistent with prior findings (Volke, et al., 2021). Pgl and Gnd behaved similarly than Zwf-1, as their concentration escalated throughout the cultivation process, which corroborates earlier findings indicating that these enzymes are upregulated under glycolytic substrates (**Figure 4.9B**) (Nikel, et al., 2015).

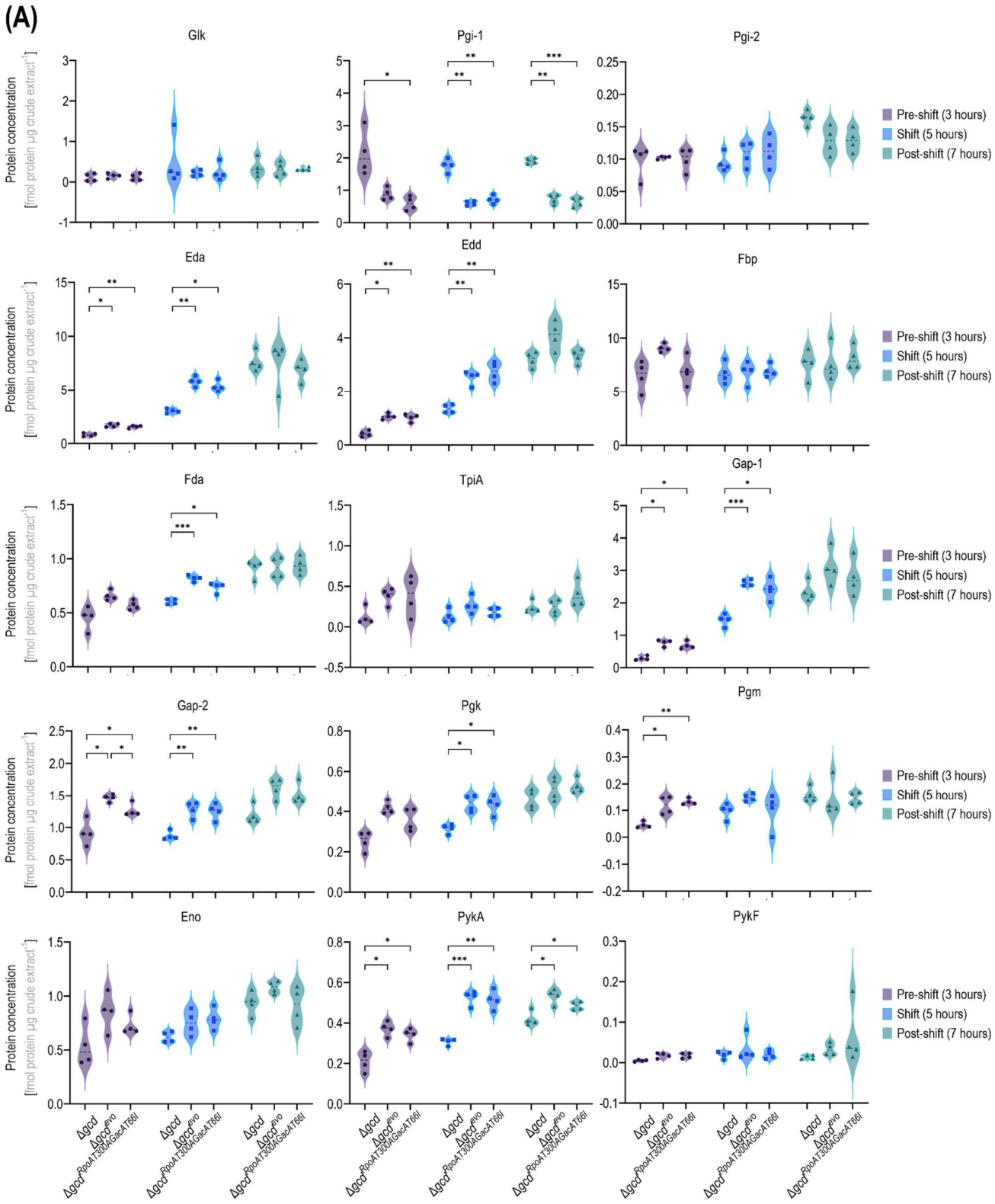
(A)
Glk
Pgi-1
Pgi-2
Eda
Edd
Fbp
Fda
TpiA
Gap-1
Gap-2
Pgk
Pgm
Eno
PykA
PykF
Protein concentration
[fmol protein µg crude extract⁻¹]
Pre-shift (3 hours)
Shift (5 hours)
Post-shift (7 hours)
Δgcd
Δgcd^evo
Δgcd^RpoAT300AGacAT66I

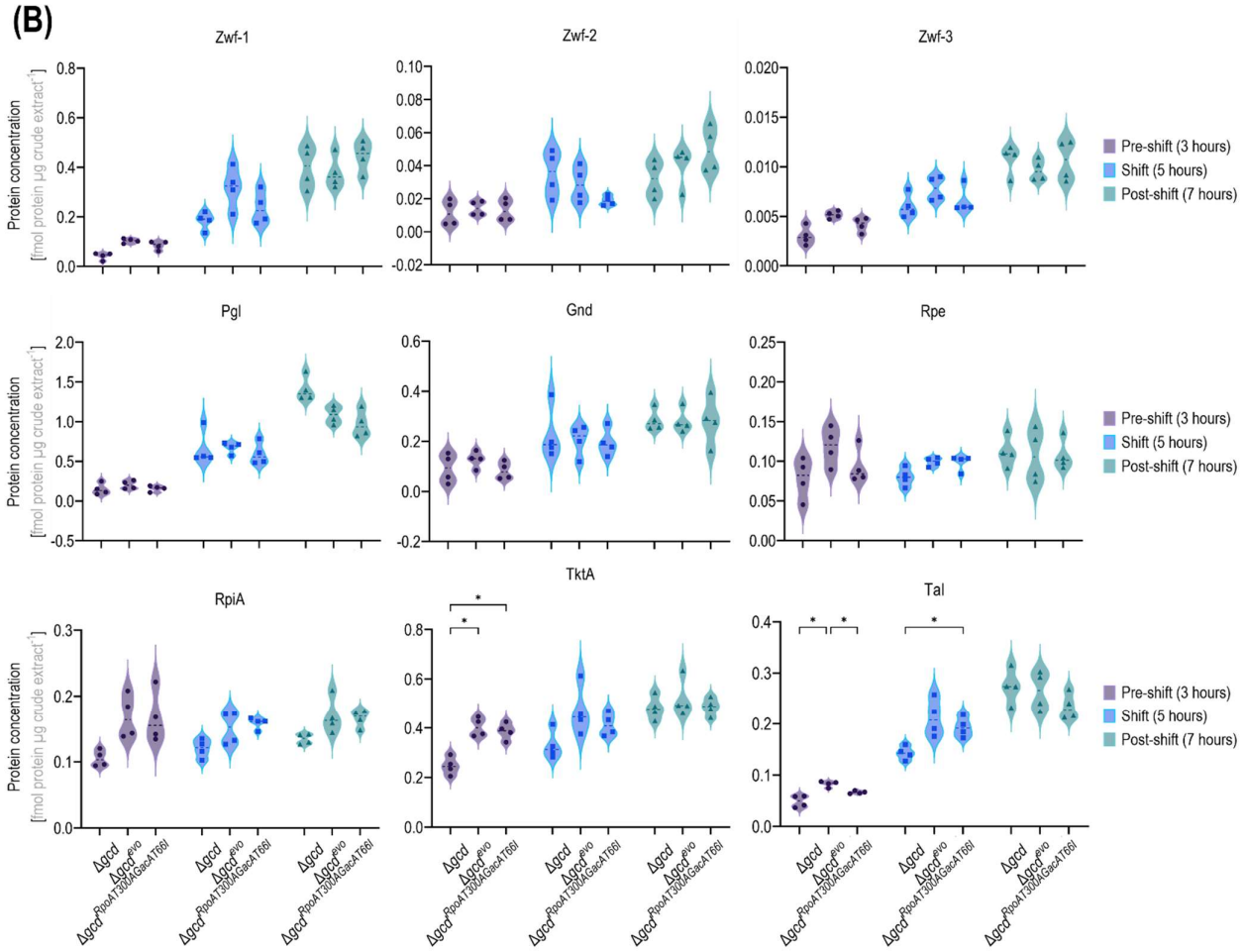

Figure 4.9. Protein quantification of during pre-shift (3 hours), shift (5 hours) and post-shift (7 hours). The strains were grown in M9 medium containing sodium citrate (1 g L^{-1}) and glucose (2 g L^{-1}) as carbon sources and were harvested at different time points. Violin graph were depicted to visualize four biological replicates per strain. The horizontal line inside the violin area represents the median. The area around the dots is a kernel density estimation showing the distribution shape of the data. Wider sections of the violin plot represent a higher probability that members of the population will take on the given value; the skinnier sections represent a lower probability. Statistical analysis was performed using two-way ANOVA analysis. * $p<0.05$, ** $p<0.01$, *** $p<0.001$. Abbreviations are as follows: **(A)** EDEMP proteins: Glucose kinase (Glk); Glucose-6-*P* isomerase-1 (Pgi-1); Glucose-6-*P* isomerase-2 (Pgi-2); 6-phosphogluconate dehydratase (Edd); 2-dehydro-3-deoxy-6-phosphogluconate aldolase (Eda); Fructose-1,6-*P2* phosphatase (Fbp); Fructose-1,6-P_2 aldolase (Fda); Phosphogluconate dehydrogenase (Gnd); Triosephosphate isomerase (TpiA); Glyceraldehyde-3-P dehydrogenase-1 (Gap-1); Glyceraldehyde-3-P dehydrogenase-2 (Gap-2); Phosphoglycerate kinase (Pgk); Phosphoglycerate mutase (Pgm); Enolase (Eno); Pyruvate kinase (PykA); Pyruvate kinase (PykF). **(B)** PP pathway enzymes: Glucose-6-*P* dehydrogenase-1 (Zwf-1); Glucose-6-*P* dehydrogenase-2 (Zwf-2); Glucose-6-*P* dehydrogenase-3 (Zwf-3); Phosphogluconolactonase (Pgl); Ribose-5-P isomerase (Rpi); Ribulose-5-P 3-epimerase (Rpe); Transketolase (Tkt); Transaldolase (Tal).

4.2.7 Protein analysis and AlphaFold predictions

Based on the knowledge gained through our proteomic study and considering the current background information about the effects of mutations on RpoA and GacA, we decided to investigate in more detail the structural consequences of these specific mutations and determine if these changes could potentially result in an implicit impact on genomic regulation, thereby influencing protein synthesis and resource allocation. We utilized PyMOL software and AlphaFold to examine the impact of the mutation on RpoA and GacA proteins.

4.2.7.1 $RpoA^{T300A}$

In *Escherichia coli,* the gene *rpoA* encodes the α subunit of DNA-direct RNA polymerase (RNAP). This subunit is responsible for activating several operons controlled by transcriptional regulators such as OxyR, OmpR, UhpA, MetR, CatR (Jafri, et al., 1995, Tao, et al., 1995). Studies have shown that in *E. coli*, the N-terminal region of the α subunit RNAP, also known as αNTD, is involved in the formation of the core enzyme ($\alpha_2\beta\beta'$). Additionally, the C-terminal region, or αCTD, plays a critical role in interacting with transcriptional activators, binding to specific DNA sequences, and dimerizing with αRNAP. Biochemical data indicates that there is a flexible linker connecting αCTD and αNTD, and this linkage could potentially play a role in transcriptional activation. In *Pseudomonas putida*, *rpoA* gene was generally used as an endogenous reference to compensate inter-PCR variations (Martínez-García, et al., 2015). The protein that received the most in-depth examination was a variant of the transcriptional activator SoxS (R93A/S101A), which has the ability to be fused to a CRISPR-Cas DNA binding domain that can be programmed to activate gene expression in *E. coli*. SoxS interacts with an interface on the α-subunit of RNA polymerase (RpoA) that is widely conserved throughout bacterial species, including *P. putida*, suggesting that the CRISPRa system developed in *E. coli* should also be effective in *P. putida* and other bacteria. Since there are no available RpoA structure for *P. putida*, AlphaFold was implemented to predict the structure and; later, the analysis was extended to one of the closest relative of *P. putida*—in this case *Pseudomonas aeruginosa* homologous. We also continued following the relative

distances of its genetic tree to the other members of the proteobacteria phylum to conduct a more in-depth analysis. After predicting the RpoA protein structure using AlphaFold (Varadi, et al., 2021), we ranked different structure model predictions (**Figure 4.10A**). To assess model quality, we utilized the Local Distance Difference Test (lDDT) which is a superposition-free score that evaluates local distance differences of all atoms in a model. Score of 60 or greater is considered a reasonable model and scores above 80 are robust models (Mariani, et al., 2013). The model yielded five predictions being "rank_1" the one with the highest score (**Figure 4.10B**). For our analysis, we searched for structural and functional homologs in *Pseudomonas* genus. Then, we used rank_1 model to make different superpositions analysis among the homologs. We assessed two homologs in *Pseudomonas aeruginosa* that contain a 96.4% sequence similarity. Specifically, we focused on the α subunit of the RNAP sigma S holoenzyme complex which was positioned alongside the transcription factors SutA (**Figure 4.11C**) and AlpA (not shown) (He, et al., 2022, Wen, et al., 2022).

Despite the disordered state of the C-Terminal domain of the α subunit in SutA, the superposition results were satisfactory. Our prediction of RpoA showed a nearly flawless alignment with chain C of SutA's α subunit in the model, except for the lower quality segment between amino acid position 150 and 170 as well as the C-terminal domain from amino acid 230 and 333, which were not included. Additionally, there is no corresponding model in SutA available for superposing the C-terminal domain of RpoA. We were interested in the C-terminal domain of RpoA because it contains the mutation we aimed to investigate, specifically T300 (marked by pink dots enclosed in white dashed circles). The location of the C-terminal domain in the predicted RpoA suggests that there is a possibility of a direct interaction with the transcriptional regulation region of a particular DNA sequence as has been studied in *E. coli* (Jafri, et al., 1995). Conversely, the prediction scores indicate that the linker domain of RpoA has a low IDDT score, indicating either instability of the domain or inaccuracies in the model. The previously stated observations are also applicable to the transcriptional regulator AlpA. Additionally, it can be noticed that DNA can bind to the complex in various ways, depending on the transcription factors involved. This suggests that the flexibility of the C-terminal domain of RpoA is potentially associated with the bendability of DNA (Russo and Silhavy, 1992, Gourse, et al., 2000). This complexity

makes it exceedingly challenging to obtain a three-dimensional illustration of RpoA, due to its highly conjectured flexibility and diverse functions.

We also decided to broaden our analysis of the C-terminal domain by comparing the segment that contains the mutation of interest in *Pseudomonas* genus. Firstly, we searched for homologs in the very last portion of the C-terminal domain. Specifically, we performed a BLAST search on the last amino acid sequence (F251-A333) [ILLRPVDDLELTVRSANCLKAENIYYIGDLIQRTEVELLKTPNLGKKSLTEIKDVLA SRGLSLGMRLDNWPPASLKKDDKATA] of several *Pseudomonas* species that we marked with pink dots in the illustration (**Figure 4.11D**). BLASTP results demonstrated that this domain is highly conserved among the *Pseudomonas* genus (not shown). In the next step, we excluded the *Pseudomonas* genus from the query in order to investigate how the domain was conserved in different phyla. Indeed, the BLASTP analysis indicated that this domain was also entirely and highly conserved in numerous gammaproteobacteria phyla (**Supplementary Figure S4.2**). For instance, our Threonine residue (T300) corresponds to the conserved residue T301 in *E. coli*. Prior investigations in the latter have evaluated an alanine library to assess the influence of different mutations on 2 UP elements (α recognition element), which revealed that T301A does not have a significant impact on their activity (Ross, et al., 2003). Conversely, in a separate study, the alanine substitution T301A resulted in a 2-fold impairment of UP elements, while the proline substitution (T301P) caused an 8-fold reduction in the before mention UP elements (Krishnan, 1996).

Ultimately, we conducted an analysis on RpoA from distantly related microorganisms by superposing their structures. It can be noticed that our residue T300 is included in a relatively high conserved domain, but specifically T300 is not at all conserved among different life domains (Murakami, et al., 1996). We identified the C-terminal domain structure of RpoA in *H. pylori* and *B. subtilis* as an example of closely related RpoA without a conserved T300, and included one from *E. coli* in our analysis (**Figure 4.10E**, **Figure 4.10F** and **Figure 4.10G**). The superposition of these structures was highly accurate, suggesting a conserved structure-function relationship. However, our investigation also indicated that the T300 residue might be specific to a particular phylum and that it is not evolutionarily significant. In the context of this particular

mutation, the protein structure remained conserved across the various bacteria examined. This suggests that the structural integrity of the protein is not affected by the mutation. However, it is plausible that this mutation might still play a role in influencing the protein's function and regulation.

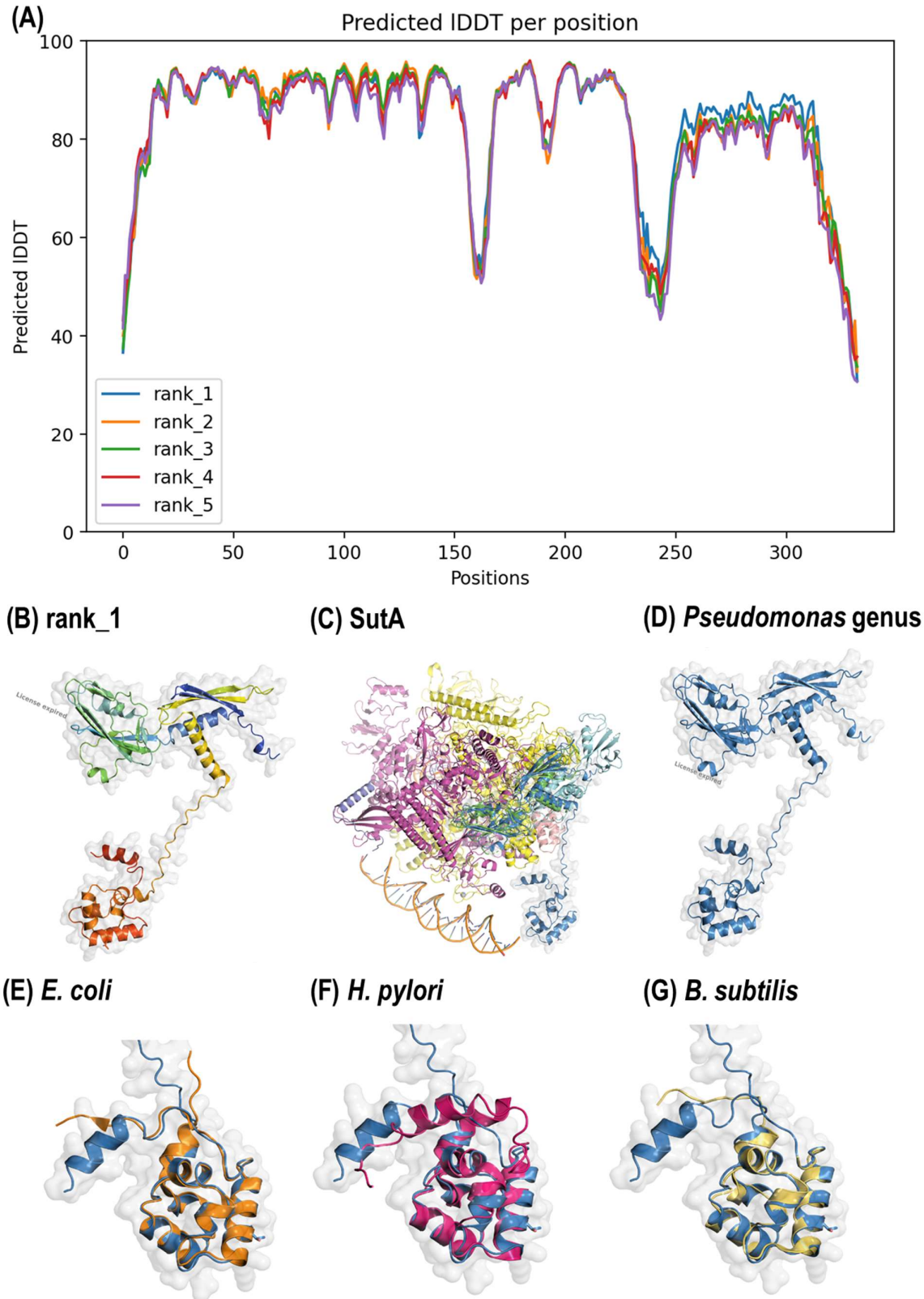
(A)
Predicted lDDT per position
Predicted lDDT
Positions
rank_1
rank_2
rank_3
rank_4
rank_5
(B) rank_1
(C) SutA
(D) Pseudomonas genus
(E) E. coli
(F) H. pylori
(G) B. subtilis

Figure 11. AlphaFold α subunit RpoA protein predictions and superimpositions. (A) Protein prediction of *Pseudomonas putida* KT2440 RpoA protein. **(B)** Selected predictive α subunit RpoA protein for comparison with other structures. Superimposition analysis of *Pseudomonas putida* α subunit RpoA protein with **(C)** *P. aeruginosa* RNAP holoenzyme complexed with DNA (transcription factors are removed from the pics). **(D)** C-terminal domain analysis using BLASTP on several species of *Pseudomonas* genus. *Pseudomonas* genus C-terminal domain superimposed with the predicted α subunit RpoA protein. C-terminal domain structure superimposition of RpoA in *E.coli* **(E)**, *H. pylori* **(F)** and *B. subtilis* **(G).**

4.2.7.2 GacA^{T66I}

The GacS/GacA system, classified as a two-component system (TCS), exhibits the capacity for regulating global gene expression that is linked to environmental traits (Yan, et al., 2018, Latour, 2020). The conventional method of signal transduction employed by Two-Component Systems (TCS) is characterized by a stimulus-response coupling mechanism (Buschiazzo and Trajtenberg, 2019). Typically, the process involves the transfer of a phosphoryl group between two conserved components: a histidine kinase protein (HK), which possesses a kinase core, and a response regulatory protein (RR), which features a regulatory domain (Gao and Stock, 2009). The sensor kinase GacS and response regulator GacA, or their equivalent counterparts, are prevalent in multiple Gram-negative bacterial species, including *Pseudomonas*, *Salmonella* and *Vibrio*. These components have a notable impact, for instance, on the virulence and pathogenicity of these microorganisms (Gooderham and Hancock, 2009). The primary mechanism by which GacS/GacA controls various physiological processes in bacteria is through the Gac/Rsm signaling cascade pathway (Ferreiro and Gallegos, 2021). The Two-Component System (TCS) serves as a bridge between bacteria sensing environmental signals and the intrinsic regulation of the physiological behavior (Zschiedrich, et al., 2016). The principal stages for TCS recognition and regulation involve the autophosphorylation of HK and the phosphorylation of RR.

In this study, we identified a mutation (SNP) which caused an aminoacid residue substitution in the residue Threonine at position 66 for Isoleucine (T66I). The mutation was located within the N-terminal Response Regulator Domain of GacA, which interacts with the histidine protein kinase (HK) and catalyzes the transfer of a

phosphoryl group to one of its own Asp residues as well as its own autodephosphorylation. The RR domain has a doubly wound five-stranded α/β fold consisting of about 125 residues. The structure of this fold is composed of a core five-stranded parallel β sheet, surrounded by ten amphipathic α helices. In all RR domains, there are specific residues that are conserved and concentrated in two areas: one being an active-site cleft that is formed by extensions from the C-terminal ends of β strands 1, 3 and 5, and the other being a pair of residues that form a diagonal pathway across the molecule from the active site. The active site itself is a consistent acidic pocket containing the phosphorylable aspartate residue (Stock, et al., 2000). Given this background information, we conducted a structural analysis to examine the impact of our mutation on the protein in question. Our analysis revealed that the polar amino acid T66 may act as a helix coordinator, forming polar contacts with Glycine at position 62 (G62) and situated in a position that allows for interactions with nearby amino acids of the front-facing β-sheet that terminates in the essential catalytic residue Glutamate at position 54 (D54) (**Figure 4.11A**). Protein mutagenesis analysis showed that the more hindered and hydrophobic residue I66 could potentially disrupt this coordination due to its lack of polar coordination and the presence of repulsive interactions with the hydrophobic residues MET-53, VAL-78, and LEU-93 could interfere with the mechanism for catalytic phosphorylation activation (**Figure 4.11B**).

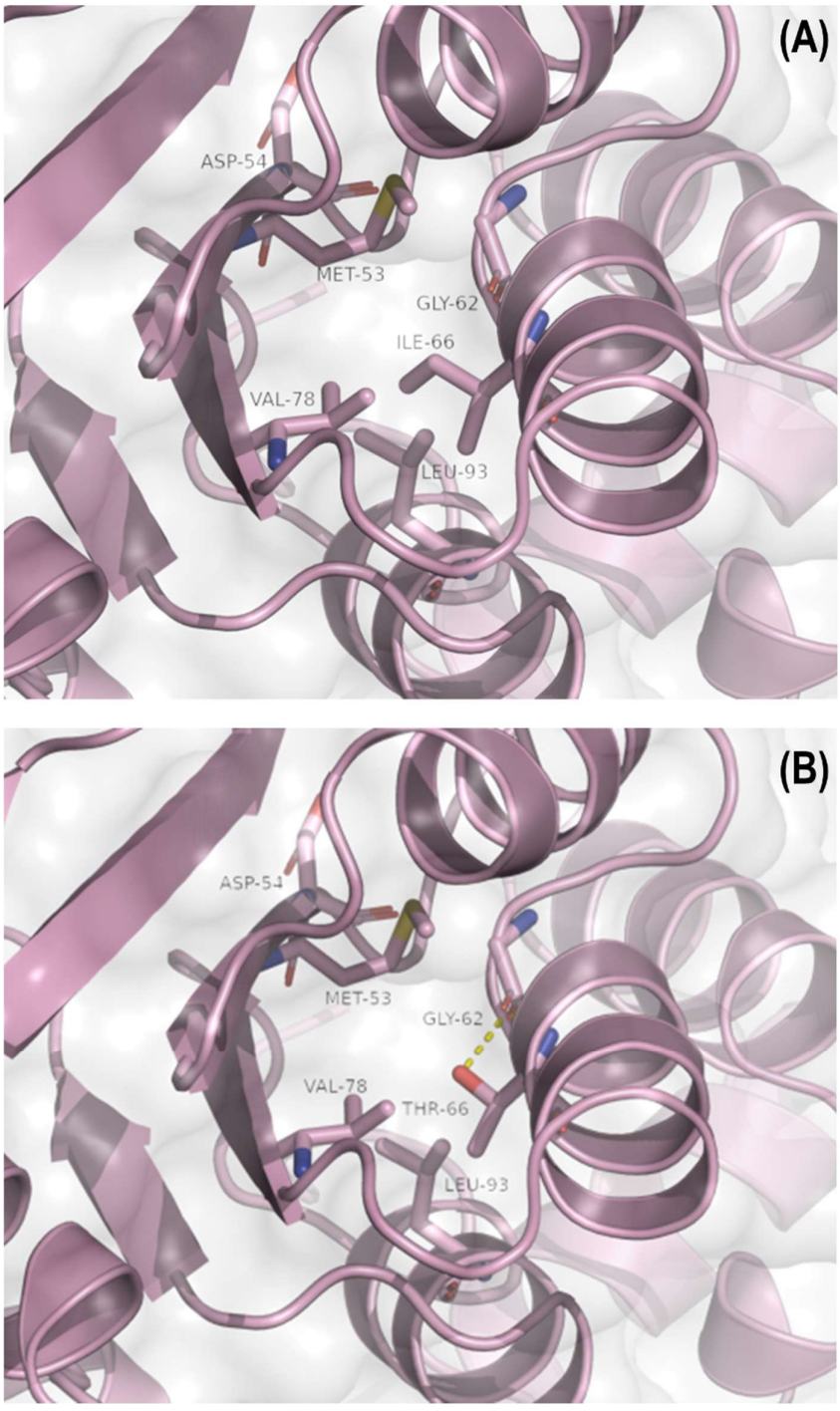

Figure 4.11. Mutational analysis of wild-type protein GacA (A) and mutant GacA^{T66I} (B). View centered on the mutation under analysis surrounded by neighbor amino acids. The picture were drawn using PYMOL software. Residues: Met53, Asp54, Gly62, Thr66/Ile66, Leu93 and Val78.

4.3 Outlook

In this study, we investigated the metabolic adaptation of *Pseudomonas putida* Δ*gcd* in dual-substrate conditions containing citrate and glucose as carbon sources, with the goal of gaining insight into the mechanism of diauxic shift. Through adaptive laboratory evolution in alternating conditions, we were able to significantly reduce the diauxic lag in the final evolved population. Our analysis revealed two critical mutations in the genes *rpoA* (encoding the DNA-directed RNA polymerase α subunit) and gacA (encoding the regulatory subunit GacA of the two-component system GacS/GacA), which could mostly explain the contribution to the final phenotype. After reverse engineering the non-evolved strain, we achieved a significant improvement in the double mutant strain with respect the parental strain. The results showed that GacA acted during the citrate phase and RpoA improve the growth on glucose. More interestingly, both mutations operated sinergically to the extent that the diauxic lag was practically erased in the double mutant strains as it was for the evolved one.

Through our work, we untangled the temporal organization of the diauxic shift at metabolome and proteome level within the central carbon metabolism. These analyses showed a particular pattern of metabolites and proteins during glycolytic and gluconeogenic regimen which changed according the different cultivations phases (pre-shift, diauxic shift and post-shift).

We also evaluated the effect of the different mutations on the protein structures and if these had a structural consequence that might affect transcription or downstream reactions. We found that the *rpoA* mutation did not have any structural chances and the mutation seemed to be particularly associated with the Pseudomonadotas phylum and that it is not evolutionarily significant. Even though this seems to be the case, we believe that this mutation has an effect at transcriptional level. On the other side, GacA exposed a modification close to the phosphorylation-autophosphorylation site which can provoke considerable effect in the metabolism, such as secondary metabolism, nutrient homeostasis and cellular motility. The current study has the potential to provide important insights in comprehending the mechanism of carbon source regulation that governs the transition from gluconeogenesis to glycolysis. This

understanding can then be utilized to develop innovative approaches aimed at enhancing the production of biotechnological products through the use of multi-carbon substrates.

4.4 Materials and Methods

Table 4.2. Strains used and constructed in this study.

Strain name	Description	Reference or source
Escherichia coli		
DH5α λpir	Cloning host; F⁻ λ⁻ *endA1 glnX44*(AS) *thiE1 recA1 relA1 spoT1 gyrA96*(Nal^R) *rfbC1 deoR nupG* Φ80(*lacZ*ΔM15) Δ(*argF-lac*)*U169 hsdR17*(r_K^- m_K^+), λ pir lysogen	Platt et al., 2000
Pseudomonas		
KT2440	Wild-type strain, derived from *P. putida* mt-2 (Worsey and Williams, 1975) cured of the TOL plasmid pWW0	Bagdasarian, et al. (1981)
Δ*gcd*	*Pseudomonas putida* with *gcd* (PP1444) deleted	
Δ*gcd rpoA*^{T300A}	*Pseudomonas putida* carrying the T300A substitution in *rpoA*	This work
Δ*gcd gacA*^{T66I}	*Pseudomonas putida* carrying the T66I substitution in *gacA*	This work
Δ*gcd rpoA*^{T300A} *gacA*^{T66I}	*Pseudomonas putida* carrying T300A substitution in *rpoA* and T66I substitution in *gacA*	This work

Table 4.3. Plasmids used and constructed in this study.

Plasmid Name	Description	Source
pSNW2	Derivative of vector pGNW2 (Wirth et al., 2020) with P14g(BCD2)→msfGFP; KmR	Volke et al., 2020
pSNW::*rpoA*T300A	Derivative of vector pSNW2 carrying homology regions to introduce the T300A substitution in *rpoA* (PP_0479); KmR	This work
pSNW::*uvrY*T66I	Derivative of vector pSNW2 carrying homology regions to introduce the T66I substitution in *urvY* (PP_4099); KmR	This work
pQURE6·H	Derivative of vector pJBSD1 carrying XylS/Pm→I-SceI and P14g(BCD2) →mRFP; GmR	Volke et al., 2020

Table 4.4. Primers used in this study.

Primer name	Nucleotide sequence (5′ to 3′)	Usage
pSNW2_U_F	aggatc**U**ggtaccgagctcgaattcagattaccc	pSNW2 linerization
pSNW2_U_R	agtcgacc**U**cagggtaatccggcgtaatcatggt	
23_pEMG_seq_F	tgtaaaacgacggccagt	Plasmid sequencing
24_pEMG_seq_R	ctttacactttatgcttccggc	
479_*rpoA*_B_U_R	aggtcgac**U**agaaataaacaatagatgtataaacaaaaaaccgggc	pSNW::*rpoA*^{T300A} construction
480_*rpoA*_A_U_F	agatcc**U**gtccgactacggcacccag	
481_*rpoA*_A_U_R	agggac**U**tcttacccaggttaggagtctt	
482_*rpoA*_B_U_F	agtccc**U**ggctgaaatcaaggacgtt	
483_*rpoA*-chk-1F	gcccgtgttgaacagcgtacca	Sequencing
484_*rpoA*-chk-1R	cgtaacgcttgcccaggtcgtt	
485_*gacA*_B_U_R	aggtcgac**U**ggccgggtgcggttgg	pSNW::*gacA*^{T66I} construction
486_ *gacA* _A_U_F	agatcc**U**ggcgggcagcccgtac	
487_ *gacA* _A_U_R	atggcc**U**ccaggccgccg	
488_ *gacA* _B_U_F	aggcca**U**ccgcaaactgctgc	
489_*gacA* -chk-1F	ggatccaatcgccctgctgacg	Sequencing
490_ *gacA* -chk-1R	caaggcctgcacccttggtcag	

4.4.1 Bacterial strains and culture conditions

The bacterial strains and plasmids employed in this study are listed in **Table 4.2** and **Table 4.3**, respectively. *Escherichia coli* and *Pseudomonas putida* KT2440 strains were incubated at 37°C and 30°C, respectively. For cell propagation and storage, routine cloning and genome engineering manipulations, cells were grown in lysogeny broth (LB) medium (10 g L^{-1} tryptone, 5 g L^{-1} yeast extract, and 10 g L^{-1} NaCl). Unless otherwise indicated, liquid pre-cultures were performed keeping the ratio medium volume:flask volume 1:5. In this case, we used 50-mL Falcon® centrifuge tubes with a medium volume of 10 mL or; for culture, 250-mL Erlenmeyer flask containing 50 mL of medium. All liquid pre-cultures were agitated at 250 rpm (MaxQ™8000 incubator;

ThermoFisher Scientific, Waltham, MA, USA) while cultures were incubated at 200 rpm (New Brunswick™ Innova® 42/42R Shaker, sticky pad). Solid culture media contained an additional 15 g L^{-1} agar. Selection of plasmid-harboring cells was achieved by adding kanamycin (Km) or gentamicin (Gm), when required at 50 μg mL^{-1} and 10 μg mL^{-1}, respectively.

For adaptive laboratory evolution (ALE) experiments, clone screening, phenotypic characterizations as well as targeted metabolomics and proteomics analyses in shaken flasks, the experiments were performed in M9 medium: 1x M9 salts, 2 mM $MgSO_4$, 100 μM $CaCl_2$ and 1x trace elements and Wolfe's vitamin solution. Stock 10x M9 salts solution contained 68 g L^{-1} Na_2HPO_4 anhydrous, 30 g L^{-1} KH_2PO_4, 5 g L^{-1} NaCl, and 10 g L^{-1} NH_4Cl dissolved in Milli-Q filtered water. 2000x M9 trace elements solution was prepared as follows: 3.0 g L^{-1} $FeSO_4{\cdot}7H_2O$, 4.5 g L^{-1} $ZnSO_4{\cdot}7H_2O$, 0.3 g L^{-1} $CoCl_2{\cdot}6H_2O$, 0.4 g L^{-1} $Na_2MoO_4{\cdot}2H_2O$, 4.5 g L^{-1} $CaCl_2{\cdot}H_2O$, 0.2 g L^{-1} $CuSO_4{\cdot}2H_2O$, 1.0 g L^{-1} H_3BO_3, 15 g L^{-1} disodium ethylene-diamine-tetra-acetate, 0.1 g L^{-1} KI, 0.7 g L^{-1} $MnCl_2{\cdot}4H_2O$ and concentrated HCl dissolved in Milli-Q filtered water. The pH of the medium was adjusted at 7.0 and supplemented with 1 g L^{-1} sodium citrate and 2 g L^{-1} glucose. For all experiments, the pre-culture media were identical to those used for the experiment. The pre-cultures were harvested by centrifugation at 8,000 *g* for 5 min, washed with M9 medium without the addition of any carbon source, and resuspended in the final media of the experiment at the desired start-optical density at 600 nm (OD_{600}). Bacterial growth was followed spectrophotometrically by measuring the absorbance at 600 nm.

4.4.2 Adaptive Laboratory Evolution (ALE)

Pseudomonas putida KT2440 Δ*gcd* was evolved in an automated platform monitoring growth and performing serial passaging at late exponential phase, as described previously [1–3]. Six evolution experiments were carried out in parallel giving, as final outcome, six different populations. Cultures were kept well mixed and aerated at 1200 rpm with magnetic stirring at 30°C in 15 mL M9 minimal medium (See composition in **Bacterial strains and culture conditions**). When the cultures reached

approximately an OD_{600} of 0.3 (Tecan Sunrise OD plate reader, equal to approximately OD 1 benchtop 1cm), 150 μL were passed into the next tube with fresh media. The M9 minimal medium contained either citrate (1.5 g L^{-1}) or glucose (1.5 g L^{-1}) were alternating between the two carbon sources, i.e., one transfer in M9 with glucose and the next in M9 medium citrate for FLIGHT experiment.

4.4.3 Clone screening from populations and candidate selection

For clone screening, the six resulting populations from the ALE experiment were streaked out onto selective condition in minimal medium M9 containing 1.5 g L^{-1} sodium citrate and 1.5 g L^{-1} glucose. Five clones per population with different colony sizes were selected with a sterile toothpick and, were individually inoculated in the same selected condition as mentioned above. The clones were storage at -80°C in 2-mL cryotubes with cryopreservation solution until further characterization. The cryopreservation solution consists of 50% vol vol^{-1} glycerol (of the highest purity available), 0.1 M $MgSO_4$, and 50 mM Tris·HCl (pH = 8.0). For candidate selection, the screened clones were subjected to a rapid analysis in 50-mL Falcon tubes. Briefly, 10 mL of minimal medium M9 were inoculated with an initial OD_{600} of 0.05 and 4/5 samples were taken from the culture. The clone that suppressed the diauxic shift was chosen () for a detailed phenotypic characterization in 250-mL shaking flask.

4.4.4 Phenotypic characterization of selected clone

The selected clone 5.5 and Δ*gcd* strain were phenotypically analyzed in 250-mL shaking flask with baffles by measuring optical density at 600nm, sodium citrate and glucose consumption. The shaking flasks were inoculated at an initial OD_{600} of 0.05 and incubated at 30°C with an agitation of 200 rpm. In total, 10 samples were collected along the cultures (one sample per hour). The samples were measured spectrophotometrically at 600nm, the supernatants were collected by centrifugation (10,000 *g* for 5 min at 4°C) and storage at -20°C for HPLC analysis.

4.4.5 Whole genome sequencing and mutational analysis

Genomic DNA was extracted from the cultures using PureLink Genomic DNA Mini Kit. Sequencing libraries were prepared using Plexwell, and the sequencing was performed on Nextseq500 using Illumina Nextseq mid output kit, 300 cycles. The sequenced samples were analyzed using the in-house mutation calling pipeline [4], using the reference genome with GenBank accession number AE015451. The average coverage for the clonal and the population samples was approximately 60x. For population samples, mutations with frequencies less than 0.50 were excluded from the analysis in order to filter out artifacts in the mutation callings and focus on causal mutations.

4.4.6 Retroengineering of relevant mutations into *Pseudomonas putida* Δ*gcd*: USER cloning and plasmid construction

In order to re-introduce the mutations obtained from ALE experiments, plasmids were constructed for homologous recombination mediate gene replacement (**Table 3**). In brief, primers were designed to include the substitution of interest and cloning was performed with Uracil-excision (USER). To begin, the AMUSER web tool (Genee, et al., 2015) was used to generate three fragments, two containing the substitution of interest and 500 bp up or downstream the gene of interest and linearized pSNW2. DNA fragments were produced using Phusion™ U high-fidelity DNA polymerase (ThermoFisher Scientific®), gel-purified with a NucleoSpin™ gel purification kit (Macherey-Nagel, Germany), digested with USER enzyme (New England BioLabs, Ipswich, MA, USA) and transformed into chemically competent E. coli DH5*α* *λ*pir.

Homologous recombination was performed following established protocols (Martínez-García and de Lorenzo, 2011, Volke, et al., 2020, Wirth, et al., 2020). In brief, up to 500 ng of modified pSNW2 plasmid was transformed into, 0.3 M sucrose washed, *Pseudomonas putida* Δ*gcd* via electroporation. Green colonies resistant to kanamycin were grown in liquid media and electroporated with up to 100 ng

pQURE6·H. Then, the cells were directly recovered overnight in LB with gentamicin and 5 mM 3-methylbenzoate (3mBz). The following day, up to 10 μL of liquid media was streak on solid LB media with gentamicin. Red colonies, capable of growing on gentamicin but not kanamycin, were screened via colony PCR with sequencing primers and the resulting fragment sent for Sanger sequencing (Eurofins Genomics, Ebersberg, Germany) with the same primers. Colonies with successful gene replacement were grown in non-selective media, screened for gentamicin sensitivity and preserved in cryostock solution at -80°C.

4.4.7 Time-course targeted metabolomics

For time-course metabolomics, six samples per flask were taken across the cultivation at 3, 4, 5, 6, 7 and 8 hours covering the diauxic shift. Each sample was immediately filtrated in MF Millipore™ membrane filter (0.45-μm pore size; Sigma-Aldrich Co.) and the filter containing the bacterial biomass was instantly quenched with 1 ml of 40% vol. $vol.^{-1}$ acetonitrile, 40% vol. $vol.^{-1}$ methanol and 100 mM formic acid at −20°C. The resulting solution was transferred into a sterile 2-ml Eppendorf tube; the filter was rinsed with an additional 1-ml of quenching solution and collected in the same tube. Samples were placed in a dry ice bath for 30 min. Later, the samples were thawed and centrifuged at 13,000 *g* for 5 min. and the supernatants were transferred to a new tube to evaporate the solvent in a SpeedVac centrifuge (2 h at 45°C). Finally, the samples were stored at −80°C until prior analysis.

Samples at -80°C were thawed on ice and prepared for injection. Prior to the LC-MS/MS analysis, the samples were resuspended in 100 μl of LC–MS grade water. Chromatographic separation of metabolites was done with an ACQUITY UPLC™ high-strength silica T3 column (XP, XSelect HSS 2.5 μm, 2.1×150 mm from Waters) in an HPLC apparatus (Shimadzu; Columbia, MD, USA). A gradient of eluent A [5% vol. $vol.^{-1}$ methanol, 2% vol. $vol.^{-1}$ 2-propanol, 10 mM tributylamine (TBA) and 10 mM acetic acid in H_2O] and 2-propanol was implemented for metabolite separation

(McCloskey, et al., 2016). The flow rate was set to 0.4 ml min^{-1} with a total run time of 33 min.; the autosampler was kept at 10°C and the column oven was set at 40°C with an injection volume of 10 µl. For metabolite identification as well as determination, a mass spectrometer (QTrap™ AB SCIEX mass spectrometer 5500) was operated in negative ion mode with the following settings: ionization set, −4500; temperature, 500°C; curtain gas, 45; collision gas, high; ion source gas, 1; and ion source gas pressure, 250 pound square inch−1. Metabolomics data analysis was carried out in Excel and the analysed data—metabolite fold change (FC)—were used as input to visualize the data in line graphs using GraphPad Prism® 9.5.0.

4.4.8 Targeted proteomics by mass spectrometry (MS)

Sample preparation for proteomic analysis was performed as described previously by (Gurdo, et al., 2023) and any modifications are mentioned below. Briefly, cell pellets of either *Pseudomonas putida* strains were lysed in 6 M Gu·HCl [guanidinium hydrochloride], 5 mM TCEP [tris(2-carboxyethyl)phosphine], 10 mM CAA [2-chloroacetamide] and 100 mM Tris·HCl, pH = 8.5, disrupted mechanically and heated to 99°C. After centrifugation, the cell-free lysates were diluted with 50 mM ammonium bicarbonate and subjected to bicinchoninic acid (BCA) assay to estimate protein concentrations. Trypsin and LysC digestion mix (Promega) was added to 20 µg protein of each sample and incubated for 8 hours. Trifluoroacetic acid was added to halt digestion and the samples were desalted using C18 resin (Empore, 3M) before HPLC-MS analysis. QconCAT proteins of central carbon metabolism of *Pseudomonas putida* as well as the proteins contained in the GlucoBrick were used as internal standard (**Table S3**).

All SIL QconCAT proteins were expressed, purified and quantified as previously described by Gurdo et al. (2023). The QconCAT proteins were labelled with ^{13}C-L-arginine and ^{13}C-L-lysine to ensure solely SIL QconCAT peptides after tryptic digestion. During sample preparation, QconCAT proteins in varied amounts were added to the samples preceding digestion (see SUP) subsection HPLC-MS analysis.

4.4.9 HPLC-MS acquisition settings

HPLC-MS analysis of the samples was performed on the Orbitrap Exploris 480 instrument (Thermo Fisher Scientific) prefaced by the EASY-nLC 1200 HPLC system (Thermo Fisher Scientific). For each sample, 500 ng of peptides was captured on a 2cm C18 trap column (Thermo Fisher 164946) and subsequently separated using a 70 minute gradient from 8\% (v v^{-1}) to 48% (v v^{-1}) of acetonitrile in 0.1% (v v^{-1}) formic acid on a 15 cm C18 reverse-phase analytical column (Thermo EasySpray ES904) at a flow rate of 250 nL min^{-1}. The mass spectrometer was operated in data-independent acquisition mode with the specific settings listed below subsubsection DIA For data-independent acquisition, the mass spectrometer was run with the HRMS1 method as previously described (Xuan 2020) prefaced by the FAIMS Pro Interface (Thermo Fisher Scientific) with CV of -45 V, and any modifications are mentioned below. Full MS1 spectra were collected at a resolution of 120,000 and scan range of 400-1000 m/z, with an AGC target of 300 or the maximum injection time set to auto. MS2 spectra were obtained at a resolution of 60,000, with an AGC target of 1000 or the maximum injection time set to auto, and the collision energy set to 32. Each cycle consisted of three DIA experiments each covering a range of 200 m/z with a window size of 6 m/z and a 1 m/z overlap, while a full MS scan was obtained in between experiments.

All the experiments reported were independently repeated at least twice (as indicated in the corresponding figure or table legend), and the mean value of the corresponding parameter ± standard deviation is presented. In some cases, the level of significance of the differences when comparing results was evaluated by means of the Student's t test with $\alpha = 0.05$.

4.4.10 Statistical analysis of metabolomics and proteomics data

GraphPad Prism 9 ® was used to analyze the two datasets from metabolomics and proteomics. Two-way ANOVA was carried out to assess the main effects and interactions between the two independent variables (strains and time) on the dependent variable (metabolite or protein concentrations). The significance level was set at $\alpha = 0.05$ to determine the statistical significance of the observed effects.

4.4.11 Metabolite analyses via HPLC

Glucose and sodium citrate were analyzed using a Dionex Ultimate 3000 HPLC with an Aminex® HPX-87X Ion Exclusion (300 x 7.8 mm) column (BioRad, Hercules, CA) as well as RI-150 refractive index and UV (260, 277, 304 and 210 nm) detectors. For analysis, the column was maintained at 45°C and a 5 mM H_2SO_4 solution was used as mobile phase at a flowrate of 0.6 mL min^{-1}. HPLC data were processed using the Chromeleon 7.1.3 software (Thermo Fisher Scientific), and compound concentrations were calculated from peak areas using calibration curves with five different standard concentrations.

4.5 Supplementary Material

Table S4.1. Peptides belonging to the central carbon metabolism that were used for targeted and quantitative proteomics.

Enzyme name	Protein name and PP number (s)	Peptide sequence	Entry	QconCAT plasmid
Glucose dehydrogenase	Gcd (PP1444)	LLALDPDTGAEIWR	Q88MX4	1
Gluconate 2-dehydrogenase cytochrome c subunit	PP3382	LSDQEVAEVVNFIR	Q88HH6	1
Gluconate kinase	GnuK (PP3416)	GEPLTLALDATQPIEALAE AVDHWLK	Q88HE4	1
2-Ketogluconate kinase	KguK (PP3378)	VVDTVGAGDAFAVGVLSA LLEGRPVAEAVAR	Q88HH9	1
2-Ketogluconate 6-P reductase	KguD (PP3376)	GAGLDVFVHEPLPIDSPLL QLDNVVATPHIGSATEETR	Q88HI1	1
6-Phosphogluconate dehydratase	Edd (PP1010)	MAFSPAEQGASAFTSALEH LK	Q88P43	1
2-Keto-3-deoxi-6-phosphogluconate aldolase	Eda (PP1024)	EEDILPLADALAAGGIR	Q88P29	1
Glucose-6-P 1-dehydrogenase	ZwfA	ALAPITGDGLSTSVVR	Q88P31	1
	Zwf	WAGVPFYLR	Q88C32	1
6-Phosphoglucolactonase	Pgl (PP1023)	LASEHLDWAK	Q88P30	1
6-Phosphogluconate dehydrogenase	Gnd (PP4043)	DAITGLEGEGAQGAHDLG ALVQK	Q88FP6	1
Ribulose-5-P-3-Epimerase	Rpe (PP0415)	MQPYAIAPSILSADFAR	Q88QS3	1
Ribose-5-P isomerase	RpiA (PP5150)	LVPVLGAFPLPVEVIPMAR	Q88CN0	1
Transketolase	TktA (PP4965)	STPNLDTWRPADAVESAVS WK	Q88D62	1
TransaldolaseB	Tal (PP2168)	LKPVDATTNPSLLLK	Q88KX1	1
Glucokinase	Glk (PP1011)	ALPGEGGHVDLPVGNAR	Q88P42	1
Fructose-1,6-bisphosphate aldolase	Fda (PP4960)	QMLDHAAEFGYGVPAFNV NNLEQMR	Q88D67	1
Fructose-1,6-bisphosphatase	Fbp (PP5040)	YVGELLAGETGPLKK	Q88CY9	1
Glucose-6-P Isomerase 1	Pgi-1 (PP1808)	TPHDVTALPAWK	Q88LW9	1
Glucose-6-P Isomerase 2	Pgi-2 (PP4701)	TPHDVTALPAWQALQK	Q88DW7	1
Triose phosphate isomerase	TpiA (PP4715)	VQLLYGGSVK	Q88DV4	1

Glyceraldehyde-3-P-dehydrogenase 1	Gap-1 (PP1009)	GADATVVYGVNHDILR	Q88P44	1
	Gap-2 (PP2149)	EELADVVGQQNASAR	Q88KZ0	1
Phosphoglyceratekinase	Pgk (PP4963)	VSVPLPVDVVVAK	Q88D64	1
Phosphoglycerate mutase	Pgm (PP5056)	EGGVLADVAPTMLK	Q88CX4	1
Phosphopyruvate hydrolase	Eno (PP1612)	FNQIGSLTETLEAIQMAK	Q88MF9	1
Pyruvate kinase	PykA (PP1362)	IVATLGPASNSPEVIEQLILAGLDVAR	Q88N54	1
Acetyltransferase component of pyruvate dehydrogenase complex	AceF (PP0338)	LMLPLSLSYDHR	Q88QZ6	1
Pyruvate dehydrogenase E1 component	AceE (PP0339)	AMVEDLSDEEIWK	Q88QZ5	1
Citrate Synthase	GltA (PP4194)	LEEIALTDPYFIER	Q88FA4	2
Aconitate Hydratase	AcnA (PP2112)	AIGSADLTVASVLSGNR	Q88L24	2
	AcnB (PP2339)	VQTGSTVVSTSTR	Q88KF1	2
	acnA-II (PP2336)	LAPNITATDLVLALTEFLR	Q88KF4	2
Isocitrate dehydrogenase	Icd (PP4011)	LVSSSGFGDEMIK	Q88FS2	2
	Idh (PP4012)	VLANTLDQATGK	Q88FS1	2
2-Ketoglutarate dehydrogenase	KgdB (PP4188)	LGFMSFFVK	Q88FB0	2
	SucA (PP4189)	LLELPEGFVVQR	Q88FA9	2
Succinyl CoA synthetase	SucD (PP4185)	FAALQDAGVK	Q88FB3	2
	SucC (PP4186)	VLAESGLNIIAATSLTDAAQQVVK	Q88FB2	2
Succinate dehydrogenase	SdhA (PP4191)	IEALELQNLLEVAEATAIAAEAR	Q88FA7	2
	SdhB (PP4190)	LASLDDPFSVFR	Q88FA8	2
	SdhC (PP4193)	SQRPVNLDLR	Q88FA5	2
	SdhD (PP4192)	VTNVTNLSR	Q88FA6	2
Fumarate hydratase	FumC-1 (PP0944)	AVDNFPISGQR	Q88PA6	2
	FumC-2 (PP1755)	LLPAVTELSSGLAELSMR	Q88M20	2
	FumC (PP0897)	MAMLNPSDSIVDWVLK	Q88PF3	2
Malate dehydrogenase	Mdh (PP0654)	IIELPLDAQEQAMFDHSADQVAR	Q88Q44	2
	DpkA (PP3591)	VDAAGGFAQPALAAAR	Q88GX6	2
Malate:quinone oxidoreductase	Mqo-1 (PP0751)	TLATDAALYHK	Q88PU7	2

	Mqo-2 (PP1251)	AYGIASTGAPPMSVPHLDTR	Q88NF9	2
	Mqo-3 (PP2925)	LGTEVVTSR	Q88IS4	2
Isocitrate lyase	AceA (PP4116)	LAADVSGVPTIILAR	Q88FI0	2
Malate synthase	GlcB (PP0356)	FALNAANAR	Q88QX8	2
Pyruvate carboxylase	OadA (PP5346)	VDITGVGVK	Q88C37	2
	AccC-2 (PP5347)	SGQFNTSFVESHPELTNYSIK	Q88C36	2
Phosphoenolpyruvate carboxylase	Ppc (PP1505)	QQHGDAFLQK	Q88MR4	2
Malic enzyme	MaeB (PP5085)	SDYPNQVNNVLGFPFIFR	Q88CU5	2

Table S4.2. BLASTP analysis in gammaproteobacteria phyla.

Description	Scientific Name	Max Score	Total Score	Query Cover	E value	Per. ident	Acc. Len	Accession
DNA-directed RNA polymerase subunit alpha [Enterobacter hormaechei]	*Enterobacter hormaechei*	167	167	1	1E-51	100	115	MCE1776939.1
DNA-directed RNA polymerase subunit alpha [Klebsiella pneumoniae]	*Klebsiella pneumoniae*	167	167	1	2E-51	100	131	HBQ8682308.1
DNA-directed RNA polymerase subunit alpha [Gammaproteobacteria bacterium]	*Gammaproteobacteria bacterium*	168	168	1	2E-51	100	149	MBU1861264.1
DNA-directed RNA polymerase subunit alpha [Pseudomonadales bacterium 32-61-5]	*Pseudomonadales bacterium 32-61-5*	168	168	1	2E-51	100	152	OYW86933.1
DNA-directed RNA polymerase subunit alpha [Mycobacterium tuberculosis]	*Mycobacterium tuberculosis*	167	167	1	2E-51	100	149	CNJ68737.1
DNA-directed RNA polymerase subunit alpha C-terminal domain-containing protein [Leclercia adecarboxylata]	*Leclercia adecarboxylata*	168	168	1	3E-51	100	160	WP_272713920.1
DNA-directed RNA polymerase subunit alpha [Eggerthia catenaformis]	*Eggerthia catenaformis*	168	168	1	3E-51	100	162	OUC50534.1
DNA-directed RNA polymerase subunit alpha [Gammaproteobacteria bacterium]	*Gammaproteobacteria bacterium*	169	169	1	1E-50	100	233	MBU0882341.1
DNA-directed RNA polymerase subunit alpha [Gammaproteobacteria bacterium]	*Gammaproteobacteria bacterium*	169	169	1	1E-50	100	241	MBU0565710.1
DNA-directed RNA polymerase subunit alpha [Gammaproteobacteria bacterium]	*Gammaproteobacteria bacterium*	169	169	1	1E-50	100	240	MBU2333823.1
DNA-directed RNA polymerase subunit alpha [Gammaproteobacteria bacterium]	*Gammaproteobacteria bacterium*	169	169	1	2E-50	100	248	MBU2011334.1
DNA-directed RNA polymerase subunit alpha [Gammaproteobacteria bacterium]	*Gammaproteobacteria bacterium*	169	169	1	6E-50	100	302	MBU2255663.1
DNA-directed RNA polymerase subunit alpha [Klebsiella pneumoniae]	*Klebsiella pneumoniae*	169	169	1	9E-50	100	333	SVJ63247.1
DNA-directed RNA polymerase subunit alpha [Azomonas agilis]	*Azomonas agilis*	169	169	1	9E-50	100	333	WP_144572999.1
DNA-directed RNA polymerase subunit alpha [Pseudomonadales bacterium RIFCSPHIGHO2_02_FULL_60_43]	*Pseudomonadales bacterium*	169	169	1	9E-50	100	333	OHC29687.1

DNA-directed RNA polymerase subunit alpha [Gammaproteobacteria bacterium]	*Gammaproteobacteria bacterium*	169	169	1	1E-49	100	333	MBU0807032.1
DNA-directed RNA polymerase subunit alpha [Pseudomonas sp. ADP]	*Pseudomonas sp. ADP*	169	169	1	1E-49	100	333	KSW25962.1
DNA-directed RNA polymerase subunit alpha [Enterobacter cloacae]	*Enterobacter cloacae*	169	169	1	1E-49	100	333	SAJ31530.1
DNA-directed RNA polymerase subunit alpha [Stutzerimonas stutzeri subgroup]	*Stutzerimonas stutzeri subgroup*	169	169	1	1E-49	100	333	WP_003281807.1
DNA-directed RNA polymerase subunit alpha [Stutzerimonas stutzeri]	*Stutzerimonas stutzeri*	169	169	1	1E-49	100	333	WP_102824663.1
DNA-directed RNA polymerase subunit alpha [Pseudomonadaceae]	*Pseudomonadaceae*	169	169	1	1E-49	100	333	WP_003289187.1
DNA-directed RNA polymerase subunit alpha [Stutzerimonas stutzeri]	*Stutzerimonas stutzeri*	169	169	1	1E-49	100	333	WP_181082232.1
DNA-directed RNA polymerase subunit alpha [Azotobacter vinelandii]	*Azotobacter vinelandii*	169	169	1	1E-49	100	333	WP_012699326.1
DNA-directed RNA polymerase subunit alpha [Pseudomonadales bacterium RIFCSPLOWO2_02_FULL_63_210]	*Pseudomonadales bacterium*	169	169	1	1E-49	100	333	OHC47757.1
DNA-directed RNA polymerase subunit alpha [Mesorhizobium sp.]	*Mesorhizobium sp.*	169	169	1	1E-49	100	333	TIR55146.1
DNA-directed RNA polymerase subunit alpha [Pseudomonadaceae]	*Pseudomonadaceae*	169	169	1	1E-49	100	333	WP_014854205.1
DNA-directed RNA polymerase subunit alpha [Stutzerimonas kirkiae]	*Stutzerimonas kirkiae*	169	169	1	1E-49	100	333	WP_131186015.1
DNA-directed RNA polymerase subunit alpha [Stutzerimonas stutzeri]	*Stutzerimonas stutzeri*	169	169	1	1E-49	100	333	AZO84817.1
DNA-directed RNA polymerase subunit alpha [Pseudomonadaceae bacterium]	*Pseudomonadaceae bacterium*	169	169	1	1E-49	100	333	MBQ54681.1
DNA-directed RNA polymerase subunit alpha [Pseudomonadales bacterium]	*Pseudomonadales bacterium*	169	169	1	1E-49	100	333	MBH1969047.1
DNA-directed RNA polymerase subunit alpha [Stutzerimonas]	*Stutzerimonas*	169	169	1	1E-49	100	333	WP_138408828.1
DNA-directed RNA polymerase subunit alpha [Stutzerimonas stutzeri]	*Stutzerimonas stutzeri*	169	169	1	1E-49	100	333	WP_181079260.1
DNA-directed RNA polymerase subunit alpha [Pseudomonadaceae]	*Pseudomonadaceae*	169	169	1	1E-49	100	333	WP_003293045.1
DNA-directed RNA polymerase subunit alpha [Stutzerimonas stutzeri]	*Stutzerimonas stutzeri*	169	169	1	1E-49	100	333	MCF6783845.1
DNA-directed RNA polymerase subunit alpha [[Pseudomonas] nosocomialis]	*[Pseudomonas] nosocomialis*	169	169	1	1E-49	100	333	WP_138411267.1
DNA-directed RNA polymerase subunit alpha [Pseudomonas cremoris]	*Pseudomonas cremoris*	169	169	1	1E-49	100	333	MBC2385459.1
DNA-directed RNA polymerase subunit alpha [Pseudomonadales bacterium GWC2_63_15]	*Pseudomonadales bacterium GWC2_63_15*	169	169	1	1E-49	100	333	OHC13905.1
DNA-directed RNA polymerase subunit alpha [Gammaproteobacteria]	*Gammaproteobacteria*	169	169	1	1E-49	100	333	WP_003255452.1
DNA-directed RNA polymerase subunit alpha [Stutzerimonas stutzeri]	*Stutzerimonas stutzeri*	169	169	1	1E-49	100	333	NIM33434.1

DNA-directed RNA polymerase subunit alpha [Pseudomonadaceae bacterium]	*Pseudomonadaceae bacterium*	169	169	1	1E-49	100	333	MAB97142.1
DNA-directed RNA polymerase subunit alpha [Stutzerimonas kunmingensis]	*Stutzerimonas kunmingensis*	169	169	1	1E-49	100	333	WP_102832133.1
DNA-directed RNA polymerase subunit alpha [Pseudomonadales bacterium GWC1_66_9]	*Pseudomonadales bacterium*	169	169	1	1E-49	100	333	OHC11062.1
DNA-directed RNA polymerase subunit alpha [Stutzerimonas azotifigens]	*Stutzerimonas azotifigens*	169	169	1	1E-49	100	333	WP_028238743.1
DNA-directed RNA polymerase subunit alpha [Pseudomonadaceae]	*Pseudomonadaceae*	169	169	1	1E-49	100	333	WP_014821626.1
DNA-directed RNA polymerase subunit alpha [Pseudomonadaceae]	*Pseudomonadaceae*	169	169	1	1E-49	100	333	WP_019339960.1
DNA-directed RNA polymerase subunit alpha [Gammaproteobacteria bacterium]	*Gammaproteobacteria bacterium*	169	169	1	1E-49	100	333	MBO2510897.1
DNA-directed RNA polymerase subunit alpha [Pseudomonas typographi]	*Pseudomonas typographi*	169	169	1	1E-49	100	333	MBD1553034.1
DNA-directed RNA polymerase subunit alpha [[Pseudomonas] urumqiensis]	*[Pseudomonas] urumqiensis*	169	169	1	1E-49	100	333	WP_120997533.1
DNA-directed RNA polymerase subunit alpha [Azotobacter beijerinckii]	*Azotobacter beijerinckii*	169	169	1	1E-49	100	333	WP_090625029.1
DNA-directed RNA polymerase subunit alpha [Pseudomonadaceae]	*Pseudomonadaceae*	169	169	1	1E-49	100	333	WP_090350159.1
DNA-directed RNA polymerase subunit alpha [Pseudomonadales bacterium]	*Pseudomonadales bacterium*	169	169	1	1E-49	100	333	TNF09516.1
DNA-directed RNA polymerase subunit alpha [Azotobacter chroococcum]	*Azotobacter chroococcum*	169	169	1	1E-49	100	333	WP_089169342.1
DNA-directed RNA polymerase subunit alpha [Stutzerimonas chloritidismutans]	*Stutzerimonas chloritidismutans*	169	169	1	1E-49	100	333	WP_023445631.1
DNA-directed RNA polymerase subunit alpha [Stutzerimonas stutzeri]	*Stutzerimonas stutzeri*	169	169	1	1E-49	100	333	WP_256073801.1
DNA-directed RNA polymerase subunit alpha [Azotobacter salinestris]	*Azotobacter salinestris*	169	169	1	1E-49	100	333	WP_152388475.1
DNA-directed RNA polymerase subunit alpha [Azotobacter chroococcum]	*Azotobacter chroococcum*	169	169	1	1E-49	100	333	WP_039806100.1
DNA-directed RNA polymerase subunit alpha [Pseudomonadaceae]	*Pseudomonadaceae*	169	169	1	2E-49	100	333	WP_041110249.1
DNA-directed RNA polymerase subunit alpha [Azomonas macrocytogenes]	*Azomonas macrocytogenes*	169	169	1	2E-49	100	333	WP_183165833.1

References Chapter 4

Aertsen, A., and Michiels, C.W. (2004) Stress and how bacteria cope with death and survival, *Critical reviews in microbiology* **30**: 263-273.

Alifano, P., Palumbo, C., Pasanisi, D., and Talà, A. (2015) Rifampicin-resistance, rpoB polymorphism and RNA polymerase genetic engineering, *Journal of biotechnology* **202**: 60-77.

Bagdasarian, M., Lurz, R., Rückert, B., Franklin, F.C.H., Bagdasarian, M.M., Frey, J., and Timmis, K.N. (1981) Specific purpose plasmid cloning vectors. II. Broad host range, high copy number, RSF1010-derived vectors, and a host-vector system for gene cloning in *Pseudomonas*, *Gene* **16**: 237-247.

Bloxham, B., Lee, H., and Gore, J. (2022) Diauxic lags explain unexpected coexistence in multi-resource environments, *Molecular Systems Biology* **18**: e10630.

Buschiazzo, A., and Trajtenberg, F. (2019) Two-component sensing and regulation: how do histidine kinases talk with response regulators at the molecular level?, *Annual review of microbiology* **73**: 507-528.

Conrad, T.M., Frazier, M., Joyce, A.R., Cho, B.K., Knight, E.M., Lewis, N.E., et al. (2010) RNA polymerase mutants found through adaptive evolution reprogram *Escherichia coli* for optimal growth in minimal media, *Proc Natl Acad Sci U S A* **107**: 20500-20505.

Dragosits, M., and Mattanovich, D. (2013) Adaptive laboratory evolution – principles and applications for biotechnology, *Microbial Cell Factories* **12**: 64.

Enjalbert, B., Letisse, F., and Portais, J.-C. (2013) Physiological and molecular timing of the glucose to acetate transition in *Escherichia coli*, *Metabolites* **3**: 820-837.

Ferreiro, M.D., and Gallegos, M.T. (2021) Distinctive features of the Gac-Rsm pathway in plant-associated Pseudomonas, *Environmental Microbiology* **23**: 5670-5689.

Fondi, M., Bosi, E., Presta, L., Natoli, D., and Fani, R. (2016) Modelling microbial metabolic rewiring during growth in a complex medium, *Bmc Genomics* **17**: 1-17.

Gao, R., Mack, T.R., and Stock, A.M. (2007) Bacterial response regulators: versatile regulatory strategies from common domains, *Trends Biochem Sci* **32**: 225-234.

Gao, R., and Stock, A.M. (2009) Biological insights from structures of two-component proteins, *Annual review of microbiology* **63**: 133-154.

Genee, H.J., Bonde, M.T., Bagger, F.O., Jespersen, J.B., Sommer, M.O., Wernersson, R., and Olsen, L.R. (2015) Software-supported USER cloning strategies for site-directed mutagenesis and DNA assembly, *ACS Synthetic Biology* **4**: 342-349.

Gooderham, W.J., and Hancock, R.E. (2009) Regulation of virulence and antibiotic resistance by two-component regulatory systems in *Pseudomonas aeruginosa*, *FEMS microbiology reviews* **33**: 279-294.

Gourse, R.L., Ross, W., and Gaal, T. (2000) UPs and downs in bacterial transcription initiation: the role of the alpha subunit of RNA polymerase in promoter recognition, *Molecular Microbiology* **37**: 687-695.
Gurdo, N., Taylor Parkins, S.K., Fricano, M., Wulff, T., Nielsen, L.K., and Nikel, P.I. (2023) Protocol for absolute quantification of proteins in Gram-negative bacteria based on QconCAT-based labeled peptides, *STAR Protocols* **4**: 102060.
Gurdo, N., Volke, D.C., and Nikel, P.I. (2022) Merging automation and fundamental discovery into the design–build–test–learn cycle of nontraditional microbes, *Trends in Biotechnology* **40**: 1148-1159.
Görke, B., and Stülke, J. (2008) Carbon catabolite repression in bacteria: many ways to make the most out of nutrients, *Nature Reviews Microbiology* **6**: 613-624.
Hassan, K.A., Johnson, A., Shaffer, B.T., Ren, Q., Kidarsa, T.A., Elbourne, L.D.H., et al. (2010) Inactivation of the GacA response regulator in *Pseudomonas fluorescens* Pf-5 has far-reaching transcriptomic consequences, *Environmental Microbiology* **12**: 899-915.
Haurie, V., Perrot, M., Mini, T., Jenö, P., Sagliocco, F., and Boucherie, H. (2001) The transcriptional activator Cat8p provides a major contribution to the reprogramming of carbon metabolism during the diauxic shift in *Saccharomyces cerevisiae*, *Journal of Biological Chemistry* **276**: 76-85.
He, D., You, L., Wu, X., Shi, J., Wen, A., Yan, Z., et al. (2022) *Pseudomonas aeruginosa* SutA wedges RNAP lobe domain open to facilitate promoter DNA unwinding, *Nat Commun* **13**: 4204.
Hosokawa, K., Park, N.-H., Inaoka, T., Itoh, Y., and Ochi, K. (2002) Streptomycin-resistant (rpsL) or rifampicin-resistant (rpoB) mutation in *Pseudomonas putida* KH146-2 confers enhanced tolerance to organic chemicals, *Environmental Microbiology* **4**: 703-712.
Igarashi, K., Fujita, N., and Ishihama, A. (1990) Sequence analysis of two temperature-sensitive mutations in the alpha subunit gene (rpoA) of *Escherichia coli* RNA polymerase, *Nucleic Acids Research* **18**: 5945-5948.
Ishihama, A. (1992) Role of the RNA polymerase α subunit in transcription activation, *Molecular microbiology* **6**: 3283-3288.
Jafri, S., Urbanowski, M.L., and Stauffer, G.V. (1995) A mutation in the rpoA gene encoding the alpha subunit of RNA polymerase that affects metE-metR transcription in *Escherichia coli*, *J Bacteriol* **177**: 524-529.
Karve, S.M., Daniel, S., Chavhan, Y.D., Anand, A., Kharola, S.S., and Dey, S. (2015) *Escherichia coli* populations in unpredictably fluctuating environments evolve to face novel stresses through enhanced efflux activity, *Journal of evolutionary biology* **28**: 1131-1143.

Krishnan, V. (1996) DNA-binding determinants of the alpha subunit of RNA polymerase: novel DNA-binding domain architecture, *Genes & development* **10**: 16-26.
Kukurugya, M.A., Mendonca, C.M., Solhtalab, M., Wilkes, R.A., Thannhauser, T.W., and Aristilde, L. (2019) Multi-omics analysis unravels a segregated metabolic flux network that tunes co-utilization of sugar and aromatic carbons in *Pseudomonas putida*, *J Biol Chem* **294**: 8464-8479.
LaCroix, R.A., Sandberg, T.E., O'Brien, E.J., Utrilla, J., Ebrahim, A., Guzman, G.I., et al. (2015) Use of adaptive laboratory evolution to discover key mutations enabling rapid growth of *Escherichia coli* K-12 MG1655 on glucose minimal medium, *Applied and environmental microbiology* **81**: 17-30.
Latour, X. (2020) The evanescent GacS signal, *Microorganisms* **8**: 1746.
Lennen, R.M., Lim, H.G., Jensen, K., Mohammed, E.T., Phaneuf, P.V., Noh, M.H., et al. (2023) Laboratory evolution reveals general and specific tolerance mechanisms for commodity chemicals, *Metabolic Engineering* **76**: 179-192.
Mariani, V., Biasini, M., Barbato, A., and Schwede, T. (2013) lDDT: a local superposition-free score for comparing protein structures and models using distance difference tests, *Bioinformatics* **29**: 2722-2728.
Martínez-García, E., Jatsenko, T., Kivisaar, M., and de Lorenzo, V. (2015) Freeing *Pseudomonas putida* KT2440 of its proviral load strengthens endurance to environmental stresses, *Environmental Microbiology* **17**: 76-90.
Martínez-García, E., and de Lorenzo, V. (2011) Engineering multiple genomic deletions in Gram-negative bacteria: analysis of the multi-resistant antibiotic profile of *Pseudomonas putida* KT2440, *Environmental microbiology* **13**: 2702-2716.
McCloskey, D., Young, J.D., Xu, S., Palsson, B.O., and Feist, A.M. (2016) MID Max: LC–MS/MS Method for Measuring the Precursor and Product Mass Isotopomer Distributions of Metabolic Intermediates and Cofactors for Metabolic Flux Analysis Applications, *Analytical Chemistry* **88**: 1362-1370.
McGill, S.L., Yung, Y., Hunt, K.A., Henson, M.A., Hanley, L., and Carlson, R.P. (2021) *Pseudomonas aeruginosa* reverse diauxie is a multidimensional, optimized, resource utilization strategy, *Scientific reports* **11**: 1-16.
Mohamed, E.T., Wang, S., Lennen, R.M., Herrgård, M.J., Simmons, B.A., Singer, S.W., and Feist, A.M. (2017) Generation of a platform strain for ionic liquid tolerance using adaptive laboratory evolution, *Microbial cell factories* **16**: 1-15.
Monod, J. (1949) The growth of bacterial cultures, *Annual review of microbiology* **3**: 371-394.

Murakami, K., Fujita, N., and Ishihama, A. (1996) Transcription factor recognition surface on the RNA polymerase alpha subunit is involved in contact with the DNA enhancer element, *Embo j* **15**: 4358-4367.
Neilson, K.A., Ali, N.A., Muralidharan, S., Mirzaei, M., Mariani, M., Assadourian, G., et al. (2011) Less label, more free: Approaches in label-free quantitative mass spectrometry, *PROTEOMICS* **11**: 535-553.
Nikel, P.I., Chavarría, M., Fuhrer, T., Sauer, U., and de Lorenzo, V. (2015) *Pseudomonas putida* KT2440 Strain Metabolizes Glucose through a Cycle Formed by Enzymes of the Entner-Doudoroff, Embden-Meyerhof-Parnas, and Pentose Phosphate Pathways, *J Biol Chem* **290**: 25920-25932.
Parkins, M.D., Ceri, H., and Storey, D.G. (2001) *Pseudomonas aeruginosa* GacA, a factor in multihost virulence, is also essential for biofilm formation, *Molecular microbiology* **40**: 1215-1226.
Perrin, E., Ghini, V., Giovannini, M., Di Patti, F., Cardazzo, B., Carraro, L., et al. (2020) Diauxie and co-utilization of carbon sources can coexist during bacterial growth in nutritionally complex environments, *Nature Communications* **11**: 3135.
Rajaraman, E., Agarwal, A., Crigler, J., Seipelt-Thiemann, R., Altman, E., and Eiteman, M.A. (2016) Transcriptional analysis and adaptive evolution of *Escherichia coli* strains growing on acetate, *Applied Microbiology and Biotechnology* **100**: 7777-7785.
Ross, W., Gosink, K.K., Salomon, J., Igarashi, K., Zou, C., Ishihama, A., et al. (1993) A third recognition element in bacterial promoters: DNA binding by the alpha subunit of RNA polymerase, *Science* **262**: 1407-1413.
Ross, W., Schneider, D.A., Paul, B.J., Mertens, A., and Gourse, R.L. (2003) An intersubunit contact stimulating transcription initiation by *E. coli* RNA polymerase: interaction of the alpha C-terminal domain and sigma region 4, *Genes Dev* **17**: 1293-1307.
Russo, F.D., and Silhavy, T.J. (1992) Alpha: the Cinderella subunit of RNA polymerase, *J Biol Chem* **267**: 14515-14518.
Rytter, H., Jamet, A., Ziveri, J., Ramond, E., Coureuil, M., Lagouge-Roussey, P., et al. (2021) The pentose phosphate pathway constitutes a major metabolic hub in pathogenic Francisella, *PLoS Pathogens* **17**: e1009326.
Sandberg, T.E., Lloyd, C.J., Palsson, B.O., and Feist, A.M. (2017) Laboratory Evolution to Alternating Substrate Environments Yields Distinct Phenotypic and Genetic Adaptive Strategies, *Applied and Environmental Microbiology* **83**: e00410-00417.
Siegal, M.L. (2015) Shifting sugars and shifting paradigms, *PLoS biology* **13**: e1002068.
Simpson, R.B. (1979) The molecular topography of rna polymerase-promoter interaction, *Cell* **18**: 277-285.

Solopova, A., Van Gestel, J., Weissing, F.J., Bachmann, H., Teusink, B., Kok, J., and Kuipers, O.P. (2014) Bet-hedging during bacterial diauxic shift, *Proceedings of the National Academy of Sciences* **111**: 7427-7432.

Song, H., Li, Y., and Wang, Y. (2023) Two-component system GacS/GacA, a global response regulator of bacterial physiological behaviors, *Engineering Microbiology* **3**: 100051.

Stanier, R. (1951) Enzymatic adaptation in bacteria, *Annual review of microbiology* **5**: 35-56.

Stock, A.M., Robinson, V.L., and Goudreau, P.N. (2000) Two-component signal transduction, *Annu Rev Biochem* **69**: 183-215.

Tao, K., Zou, C., Fujita, N., and Ishihama, A. (1995) Mapping of the OxyR protein contact site in the C-terminal region of RNA polymerase alpha subunit, *Journal of bacteriology* **177**: 6740-6744.

Tomenius, H., Pernestig, A.-K., Jonas, K., Georgellis, D., Möllby, R., Normark, S., and Melefors, Ö. (2006) The *Escherichia coli* BarA-UvrY two-component system is a virulence determinant in the urinary tract, *BMC Microbiology* **6**: 27.

Utrilla, J., O'Brien, Edward J., Chen, K., McCloskey, D., Cheung, J., Wang, H., et al. (2016) Global Rebalancing of Cellular Resources by Pleiotropic Point Mutations Illustrates a Multi-scale Mechanism of Adaptive Evolution, *Cell Systems* **2**: 260-271.

Varadi, M., Anyango, S., Deshpande, M., Nair, S., Natassia, C., Yordanova, G., et al. (2021) AlphaFold Protein Structure Database: massively expanding the structural coverage of protein-sequence space with high-accuracy models, *Nucleic Acids Research* **50**: D439-D444.

Veenstra, T.D. (2021) Omics in Systems Biology: Current Progress and Future Outlook, *PROTEOMICS* **21**: 2000235.

Volke, D.C., Friis, L., Wirth, N.T., Turlin, J., and Nikel, P.I. (2020) Synthetic control of plasmid replication enables target- and self-curing of vectors and expedites genome engineering of *Pseudomonas putida*, *Metabolic Engineering Communications* **10**: e00126.

Volke, D.C., Olavarría, K., and Nikel, P.I. (2021) Cofactor Specificity of Glucose-6-Phosphate Dehydrogenase Isozymes in *Pseudomonas putida* Reveals a General Principle Underlying Glycolytic Strategies in Bacteria, *mSystems* **6**: e00014-00021.

Wasi, S., Tabrez, S., and Ahmad, M. (2013) Use of *Pseudomonas spp*. for the bioremediation of environmental pollutants: a review, *Environmental monitoring and assessment* **185**: 8147-8155.

Wei, X., Huang, X., Tang, L., Wu, D., and Xu, Y. (2013) Global control of GacA in secondary metabolism, primary metabolism, secretion systems, and motility in the rhizobacterium *Pseudomonas aeruginosa* M18, *Journal of bacteriology* **195**: 3387-3400.

Weimer, A., Kohlstedt, M., Volke, D.C., Nikel, P.I., and Wittmann, C. (2020) Industrial biotechnology of *Pseudomonas putida*: advances and prospects, *Applied Microbiology and Biotechnology* **104**: 7745-7766.

Wen, A., Zhao, M., Jin, S., Lu, Y.-Q., and Feng, Y. (2022) Structural basis of AlpA-dependent transcription antitermination, *Nucleic Acids Research* **50**: 8321-8330.

Wirth, N.T., Kozaeva, E., and Nikel, P.I. (2020) Accelerated genome engineering of *Pseudomonas putida* by I-SceI-mediated recombination and CRISPR-Cas9 counterselection, *Microbial biotechnology* **13**: 233-249.

Worsey, M.J., and Williams, P.A. (1975) Metabolism of toluene and xylenes by *Pseudomonas putida* (*arvilla*) mt-2: evidence for a new function of the TOL plasmid, *Journal of Bacteriology* **124**: 7-13.

Wu, Y., Jameel, A., Xing, X.-H., and Zhang, C. (2022) Advanced strategies and tools to facilitate and streamline microbial adaptive laboratory evolution, *Trends in Biotechnology* **40**: 38-59.

Yan, Q., Lopes, L.D., Shaffer, B.T., Kidarsa, T.A., Vining, O., Philmus, B., et al. (2018) Secondary metabolism and interspecific competition affect accumulation of spontaneous mutants in the GacS-GacA regulatory system in *Pseudomonas protegens*, *MBio* **9**: e01845-01817.

Yung, Y.P., McGill, S.L., Chen, H., Park, H., Carlson, R.P., and Hanley, L. (2019) Reverse diauxie phenotype in *Pseudomonas aeruginosa* biofilm revealed by exometabolomics and label-free proteomics, *npj Biofilms and Microbiomes* **5**: 31.

Zampar, G.G., Kümmel, A., Ewald, J., Jol, S., Niebel, B., Picotti, P., et al. (2013) Temporal system-level organization of the switch from glycolytic to gluconeogenic operation in yeast, *Mol Syst Biol* **9**: 651.

Zschiedrich, C.P., Keidel, V., and Szurmant, H. (2016) Molecular mechanisms of two-component signal transduction, *Journal of molecular biology* **428**: 3752-3775.

Chapter 5 - Dissecting tolerance acetate metabolism in genome–reduced *Pseudomonas putida* via adaptive laboratory evolution and multi-omic strategies.

This chapter is mainly composed of results from the following publication in preparation:

Gurdo, N., Tagliani, T., O'Connell, G. W., Alvan Vargas M.V.G, Wirth, N., Volke, D.C., Johnsen, J., Srinivasan A., Eng T., Mukhopadhyay A., Feist, A. M., & Nikel, P. I. Dissecting tolerance acetate metabolism in genome–reduced *Pseudomonas putida* via adaptive laboratory evolution and multi-omic strategies. *Manuscript in preparation*.

Summary

Pseudomonas putida is a robust microbial *chassis* suitable for biomanufacturing, exhibiting the ability to assimilate a wide range of substrates while simultaneously tolerating unfavorable environmental conditions. Of particular interest among these substrates is acetate, which holds promise for eco-friendly production of significant biotechnological products. Acetate, a C2 substrate, can be derived from various renewable sources like CO_2 electrolysis and lignocellulosic biomass hydrolysis. However, the acetate levels in the medium often reach inhibitory concentrations, negatively impacting bacterial metabolism. To enhance the strength and stability of biotechnological processes constrained by the toxic effects of acatate, deeper insights into its underlying toxicity mechanisms are vital. In this study, we employed adaptive laboratory evolution to obtain tolerant clones to the organic acid and conducted whole-genome sequencing (WGS) to identify mutations arising from the evolutionary process. Our approach uncovered two point mutations: one in *gacA* gene, encoding the regulatory subunit of the GacS/GacA two-component system, and the other in *fabB* gene, encoding 3-oxoacyl-[acyl-carrier-protein] synthase I. To assess the effects of these mutations in the presence of high acetate concentrations from a systems biology perspective, we retro-engineered them into the parental strain and analyzed these strains by applying proteomics and ^{13}C-acetate fluxomics. The strain harboring the double mutation exhibited a spectrum of adaptive responses, including metabolic flux reconfiguration towards NAD(P)H-generating reactions, rewiring of methionine

biosynthesis, activation of detoxifying enzymes, and facilitation of extracellular iron uptake through the pyoverdine system.

5.1 Introduction

5.1.1 Acetate as a non-conventional carbon source for biotechnology

In recent decades, there has been a substantial interest in utilizing non-traditional carbon sources to develop innovative bioprocesses in order to produce a diverse array of biochemicals. This may include, for example, the production of biofuels, biopolymers, and other high-value products (Wendisch, et al., 2016). Moreover, in response to the rising demand for bio-based products, there has been a concerted effort to engineer microbial cell factories that can metabolize a wide range of non-conventional carbon sources (Schrader, et al., 2009, Dürre and Eikmanns, 2015, Kim, et al., 2021). Among them, C1 compounds such as carbon dioxide/monoxide, syngas, formate, methanol and methane as well as C2 substrates such as acetate can be used to produce alcohol and lipids (Klasson, et al., 1992, Henstra, et al., 2007, Lagoa-Costa, et al., 2017), lactic acid and 2,3-butanediol (McAnulty, et al., 2017, Hwang, et al., 2018, Nguyen, et al., 2018) and polymers (Khosravi-Darani, et al., 2013).

Acetate is a promising alternative to traditional sugar feedstock for the production of biochemicals, owing to several advantages. One of the primary benefits of acetate is its low cost, which makes it an attractive option for large-scale production. Additionally, acetate can be derived from renewable sources, further increasing its appeal as a sustainable feedstock. Nowadays, acetate can be generated from chemical and biological approaches, encompassing chemical catalysis (CC; for instance, methanol carbonylation, acetaldehyde oxidation), lignocellulose biomass hydrolysis (LBH), microbial electrosynthesis (MES), syngas fermentation (SF), anaerobic digestion (AD) (Novak and Pflügl, 2018, Kiefer, et al., 2021, Kim, et al., 2021).

5.1.2 Biological conversion of acetate into high-added products

Numerous microorganisms have the ability to assimilate acetate into their metabolic pathways, making it a versatile and widely applicable substrate for bioprocesses. Regarding acetate metabolism in bacteria, the process begins with acetate passing through the cellular cytoplasm using the acetate permease ActP, which is a cation/acetate symporter (although part of the protonated form, acetic acid, may permeate directly). Next, the acetyl-CoA synthetase I (AcsA-I) transforms acetate into acetyl-coenzyme A (CoA) being utilized in the TCA cycle to generate energy and form building blocks for biomass or biotechnologically relevant biomolecules.

It was previously demonstrated that acetate can be biologically converted into organic acids (succinic and itaconic acid), alcohol (isobutanol) free fatty acids, and recombinant proteins (Leone, et al., 2015, Huang, et al., 2018, Noh, et al., 2018, Song, et al., 2018). Some example of microorganism that can metabolize acetate include *Pseudomonas sp.*, *Escherichia coli*, *Corynebacterium glutamicum*, *Saccharomyces cerevisiae*, *Rhodotorula toruloides*, *Yarrowia lipolytica* and *Aspergillus oryzae*. Among these microbial platforms, *Escherichia coli* have been widely exploited to produce high-added chemical from acetate (Xiao, et al., 2013, Li, et al., 2016, Chen, et al., 2018, Jo, et al., 2019, Yang, et al., 2019). However, this two-carbon molecule is not a preferred carbon source for most bacteria, and it exerts a toxic effect in *E. coli* growth.

Different strategies have been applied to improve acetate utilization in this Gram-negative by modifying endogenous metabolic pathways (glyoxylate shunt) or several regulation points across TCA cycle, for example modulating the activity of the isocitrate lyase enzyme (Roe, et al., 2002, Díaz-Guerra, et al., 2006, Pinhal, et al., 2019). Although the before mentioned studies have achieved their desired outcomes, acetate toxicity has been observed to hinder the production of the specific product where production rates, yield and titer are far from profitable industrial values. Thus, resistant microorganisms, such as *Pseudomonas putida,* have emerged as robust microbial *chassis* that can tolerate higher concentrations of toxic compounds and;

particularly, it can naturally use organic acids as a preferred carbon source over glycolytic substrates. Recent studies have showed the potential of *P. putida* to convert acetate into valuable products—e.g. *mcl*-polyhydroxyalkanoates (Yang, et al., 2019). Along the same line, the dynamic of acetate metabolism, not only in *E. coli* but also in *P. putida*, was only partially explored to date. Hence, more efforts are required in order to decipher the molecular basis for acetate utilization.

5.1.3 Adaptive laboratory evolution to improve acetate tolerance

Adaptive laboratory evolution (ALE) is commonly utilized in biology to better understand the fundamental mechanisms of molecular evolution, as well as the adaptive modifications that occur within microbial populations over prolonged periods of selection under specific growth conditions (Dragosits and Mattanovich, 2013). Moreover, ALE is also an effective strategy employed to adapt microorganisms to toxic or stressful conditions (Sandberg, et al., 2019). ALE involves growing microorganisms under specific and well-defined conditions for a prolonged period ranging from weeks to years, enabling the selection of improved phenotypes. Microbial cells are particularly advantageous for ALE studies due to several factors: (a) their simple nutrient requirements, (b) their ease of cultivation in a laboratory setting, and (c) their rapid growth rate, allowing for several hundred generations to be cultured within a matter of weeks or months.

Rational approaches have been applied to optimize specific growth rate (Pfeifer, et al., 2017), increase tolerance to toxic compounds or stressful conditions (Wallace-Salinas and Gorwa-Grauslund, 2013), boost yield/titer (von Kamp and Klamt, 2017), substrate uptake (Latif, et al., 2015) and general discovery to determine the genetic basis (Long, et al., 2018). Regarding the last application, ALE has been applied to study fundamental aspect of biology such as metabolic regulation in response to stressors. In order to deeply analyze the underlying mechanisms of an adapted microorganisms at system-level, ALE can be combined with –omics analysis which allow capturing the

crosstalk between the different layers of information (Horinouchi and Furusawa, 2020). The process of metabolic adaptation induces alterations in both the metabolic state and through the genome, transcriptome, metabolome and proteome. To gain insights into the molecular mechanisms underlying metabolic adaptation, it is crucial to examine the "trans-omics" network, which refers to the interactions occurring among molecules across multiple layers within the cell (Yugi, et al., 2016, Yugi and Kuroda, 2018).

On the background exposed above, in this work we evolved the genome-reduced *Pseudomonas putida* strain SEM1.4 through ALE in increasing acetate concentration to enhance tolerance against this C2-carboxylic acid aiming to elucidate the molecular mechanism underlying acetate toxicity at genome, proteome and fluxomes levels. Systematic genomics and phenotypic analysis of the evolved clone and the reverse-engineered strain revealed that the two point mutations in *gacA* and *fabB* genes significantly contributed to the final tolerized phenotype. Proteomics unveiled substantial alterations in the pathways associated with methionine metabolism, motility, oxidative stress response, biofilm formation, and amino acid synthesis. Moreover, analysis of metabolic flux distribution revealed modifications in both the EDEMP and PP pathways. The outcomes of this research study indicated that individual mutations in the *gacA* and *fabB* genes played a crucial role in granting resistance to acetate, given their extensive influence on the proteome. These findings underscored the remarkable adaptability and flexibility exhibited by the metabolic processes of *P. putida*.

5.2 Results

5.2.1 Adaptive laboratory evolution enhanced resistance of *Pseudomonas putida* SEM1.4 to acetate

Acetate is a weak C2-organic acid that exerts a toxic effect in the cytoplasm of bacterial cells. One of the most dramatic consequences is that the undissociated acid molecule can permeate through the highly lipophilic cell membrane by passive diffusion and dissociate inside the cytosol into the anion acetate. When acetic acid dissociates, it gives rise to the accumulation of protons causing a significant decrease of the cytosolic pH together with the disruption of the electrochemical gradient across the cell membrane. Not only protons generate a toxic effect, but also acetate itself can cause pleiotropic damages on cell physiology (Trček, et al., 2015). An increase in the internal acetate concentration disturbs amino acid homeostasis, mainly glutamate and methionine biosynthesis pathways (Roe, et al., 1998, Roe, et al., 2002). Microorganisms possess protective mechanism against acetate toxicity, for instance, regulation of membrane transporters to pump the acetate anion out to the extracellular space (Steiner and Sauer, 2001, Nakano, et al., 2006), modification of the membrane composition (e.g. increasing phosphatidylglycerol content in the lipid bilayer) (Trcek, et al., 2007), formation of extracellular polysaccharides (Deeraksa, et al., 2005) and overexpression of genes encoding heat shock proteins (Andrés-Barrao, et al., 2012), among others.

Aiming to overcome acetate toxicity towards identifying acetate-resistance mechanisms in the Gram-negative bacteria *P. putida* SEM1.4, we first evolved the parental strain by gradually increasing the acetate concentration in de Bont minimal medium starting from 20 until 180 mM. The evolution process was stopped after 130 days and ten colonies were selected from the evolved population by placing them in de Bont minimal medium agar plates containing 180 mM potassium acetate, which allowed for the identification of potential candidates while maintaining a strong selective pressure (**Figure 5.1A**). After selecting the candidates, a physiological

characterization was carried out to analyze the behavior of each clone at high acetate concentration. The clones were then subjected to whole-genome sequencing (WGS) to investigate the genetic alterations that occurred during the evolution. Specific mutations were reintroduced into the parental strain and evaluated through multi-omic analyses, including genomic, proteomic, and fluxomics assessments, in order to uncover the molecular mechanism behind this stress, as shown in **Figure 5.1B**.

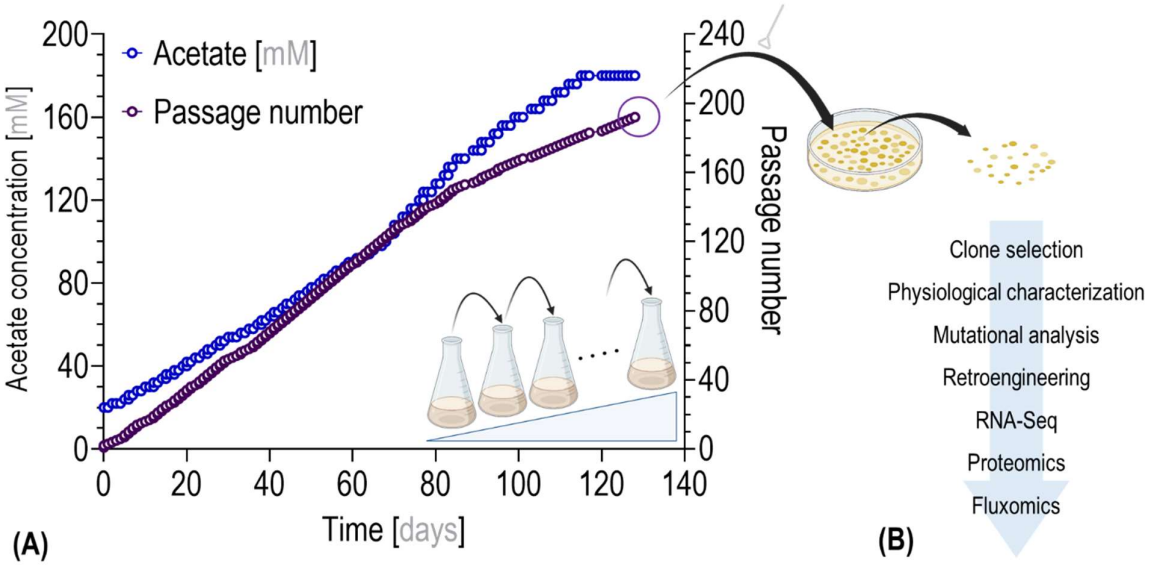

Figure 5.1. Overall workflow to explore acetate toxicity in *Pseudomonas putida* SEM1.4 (A) Adaptive laboratory evolution strategy adopted to increase tolerance to high concentrations of potassium acetate. **(B)** Steps for physiological and metabolic characterization of selected clones.

Later, we tested the selected clones against the parental strain in different concentrations of potassium acetate: 20, 60, 100, 140 and 180 mM for 48 h. The performance of the selected clones was superior in all the conditions tested in comparison with the wild-type strain. The clones and parental strain displayed similar behavior at 20 mM, except that the clones reached higher final OD_{600} after 10 h of cultivation (**Figure 5.2A**). A reduction of 50% in the lag phase was observed for 60 and 100 mM in most of the clones (**Figure 5.2B** and **Figure 5.2C**). When the cells were exposed to 140 mM acetate, the parental strain was not able to growth after 48 h while the tolerized clones reached OD_{600}~2.5 (**Figure 5.2D**). Finally, at the highest

concentration tested (180 mM), cells could not overcome acetate toxicity. The findings obtained in this section demonstrate the effective enhancement of tolerance to potassium acetate through the implementation of the adaptive laboratory evolution (ALE) strategy. Subsequently, the set of ten clones were subjected to further characterization by analyzing the genetic background as first step.

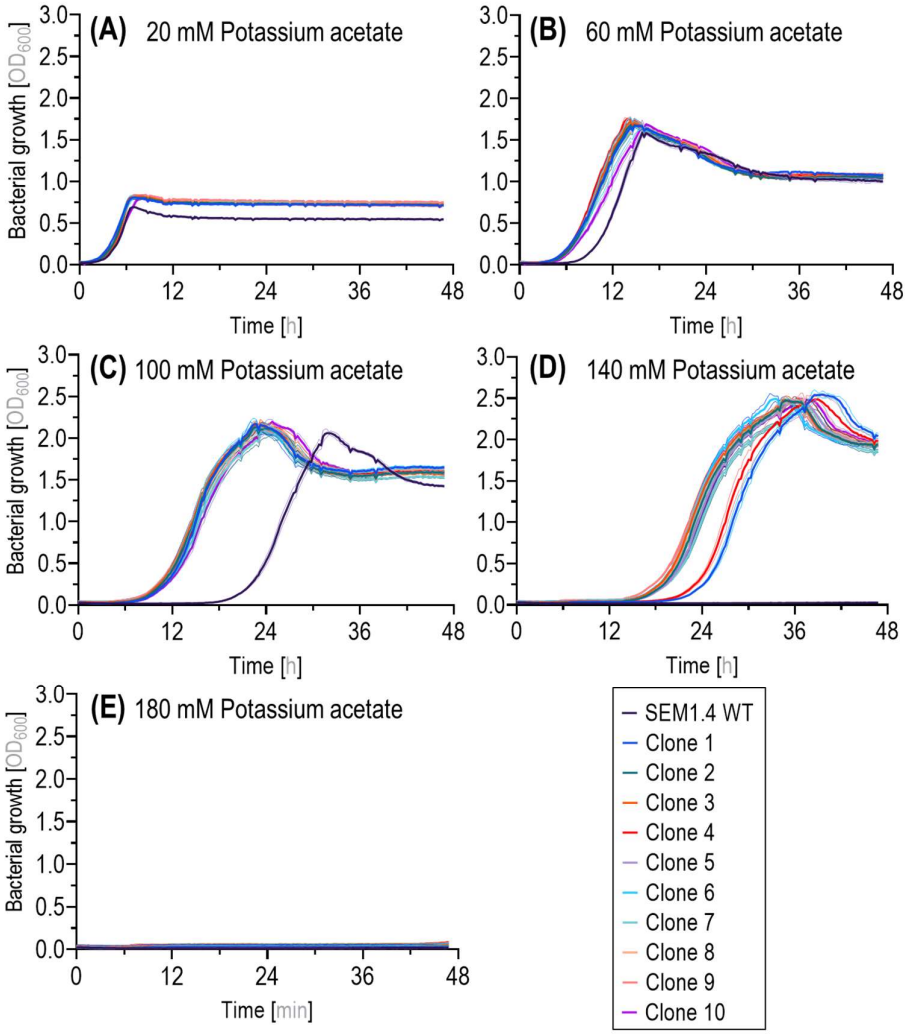

Figure 5.2. Evaluating acetate tolerance in selected clones and wild type strain in 96-microtiter wells. Growth profiles of the ten clones in de Bont minimal medium with 5 g L^{-1} MOPS supplemented with different concentrations of potassium acetate: **(a)** 20 mM, **(b)** 60 mM, **(c)** 100 mM and **(d)** 140 mM. Solid lines represent the optical density average and the shaded area surrounded the average line correspond to the standard deviation of four biological replicates.

5.2.2 Mutational analysis exposed key mutations associated to global regulation and fatty acid metabolism

To identify mutations associated with acetate tolerance, the selected clones were investigated using WGS. With the aim of identifying key point mutations, we focused our analysis in unique mutations appearing in most of the clones and within the gene sequence. Using this criterion, we identified mutations in four genes with regulatory functions, namely, *rsmY* (*PP0371,* transcriptional regulator—LysR family), *gacA* (*PP4099*, two-component system GacS/GacA, regulatory subunit), *hupB* (*PP2303*, DNA binding regulator, β subunit) and *fabB* (*PP4175*, 3-oxoacyl-[acyl-carrier-protein] synthase I involved in fatty acid metabolism) (**Table 5.1**). It was previously reported that RsmY has a relevant role in carbon and secondary metabolism and acts as a central node; its transcription being strictly dependent on GacA (Valverde, et al., 2003). In connection to this and, most crucially, the two-component system GacS/GacA mediates bacterial adaptation to environmental perturbations and, mutations on their genes can cause global rearrangements in various metabolic pathways (mainly central carbon and secondary metabolism, quorum sensing and biofilm formation) (Song, et al., 2023). In addition, *hupB* was also associated with essential metabolic functions in growth homeostasis and stress responses (Griego, et al., 2022). Lastly, *fabB* catalyzes the Claisen condensation of acyl-ACP (acyl carrier protein) and malonyl-ACP via an acyl-enzyme intermediate to elongate fatty acid chains (Yadrykhins' ky, et al., 2021). In *Escherichia coli*, FabB is implicated in the production of unsaturated fatty acids relevant for the formation of the bacterial membrane (Feng and Cronan, 2009). To evaluate the effect of the arisen mutations after the adaptive process, we decided to individually incorporate those point mutations back in the parental strain by reversed engineering. The selection criteria was based on the presence of the specific mutations in the majority of the isolated clones (>50%).

Table 5.1. Mutational analysis of selected clones after the evolution on acetate. Single nucleotide polymorphisms (SNPs) found in the isolated clones after whole-genome sequencing (WGS).

Position	Mutation Type	Sequence Change	Gene name (Locus ID)[a]	Gene annotation(s)[b]	Details	Clones									
						1	2	3	4	5	6	7	8	9	10
451,043	SNP	C > T	*PP0371, rsmY*	Transcriptional regulator, LysR family	R277H (CGC > CAC)	1	1	1	1	1	1	1	1	1	1
4,635,167	SNP	C > T	*gacA*	Two-component system GacS/GacA, regulatory subunit	E197K (GAA > AAA)	1	1	1	1	1	1	1	1	1	1
4,717,665	SNP	T > C	*fabB*	3-oxoacyl-[acyl-carrier-protein] synthase 1	L77P (CTG > CCG)	1	1	1	1	1	1	1	1	1	
2,633,188	SNP	C > T	*hupB*	DNA binding regulator, beta subunit B	A35V (GCC > GTC)	1	1		1	1	1		1		
2,633,230	SNP	C > T	*hupB*	DNA binding regulator, beta subunit B	T49I (ACC > ATC)									1	
2,633,326	SNP	C > T	*hupB*	DNA binding regulator, beta subunit B	A81V (GCC > GTC)										1
4,717,483	SNP	C > T	*fabB*	3-oxoacyl-[acyl-carrier-protein] synthase 1	G16G (GGC > GGT)										1

[a]Locus identifiers (IDs) are provided from the NCBI Prokaryotic Genome Annotation Pipeline Version 4.10 (Oct. 2019).

[a]Annotations assigned from NCBI Reference Genome NC_002947.4.

We first generated a group of individual mutants and we incorporated the following mutations on *P. putida* SEM1.4 by Uracil-excision (USER) cloning and recombination mediated by I-*SceI* (Wirth, et al., 2020): $rsmY^{R277H}$, $gacA^{E197K}$, $fabB^{L77P}$ and $hupB^{A35V}$. Later, we assessed the tolerance of the mutants at increasing concentration of potassium acetate (**Figure 5.3**). In control conditions (i.e. with 20 mM potassium acetate), no significant differences were observed within the strains (**Figure 5.3A**). We observed that the evolved strain SEM1.4 as well as single mutants $gacA^{E197K}$, $fabB^{L77P}$ and $hupB^{A35V}$, exhibited a dramatic reduction in lag phase times in the conditions where acetate concentration was higher than 60 mM against the wild-type strain. The reduction observed in the duration of the lag phase varied from 14% in the case of $gacA^{E197K}$ at 60 mM, to a substantial 77% in the SEM1.4^{evo} strain at a concentration of 100 mM (**Table 5.2**). Most importantly, no growth was detected in the parental strain when was cultivated at 120 and 140 mM after 72 h (**Figure 5.3F** and **Figure 5.3G**). In addition, the strain carrying the $rsmY^{R277H}$ mutation presented an impaired growth in all the condition and against each strain, so we decided to set this strain aside for further characterization. Our observation revealed that among the selected mutations, two mutants, namely $gacA^{E197K}$ and $fabB^{L77P}$, demonstrated superior performance. This

finding led us to question whether the combination of these mutations could result in a synergistic effect on the final phenotype. Based on this, we decided to build the double mutant strain *P. putida* SEM1.4 $gacA^{E197K}$ $fabB^{L77P}$ and we challenged the mutant with increasing acetate concentrations as it was previously done with the single mutants. Surprisingly, the double mutant strain behaved similarly to the evolved strain SEM1.4^{evo}, in most condition, suggesting that the combination of both point mutations might act in cooperation to overcome acetate toxicity (**Figure 5.3**). Then, we decided to characterize the three strain in shaken-flask cultivations to capture relevant physiological parameters (e.g. growth rates, lag phase times and acetate consumption rates) as well as to determine sampling times for omics experiments. Overall, the double mutant achieved to recapitulate around the 50% of the phenotype obtained in the evolved strain.

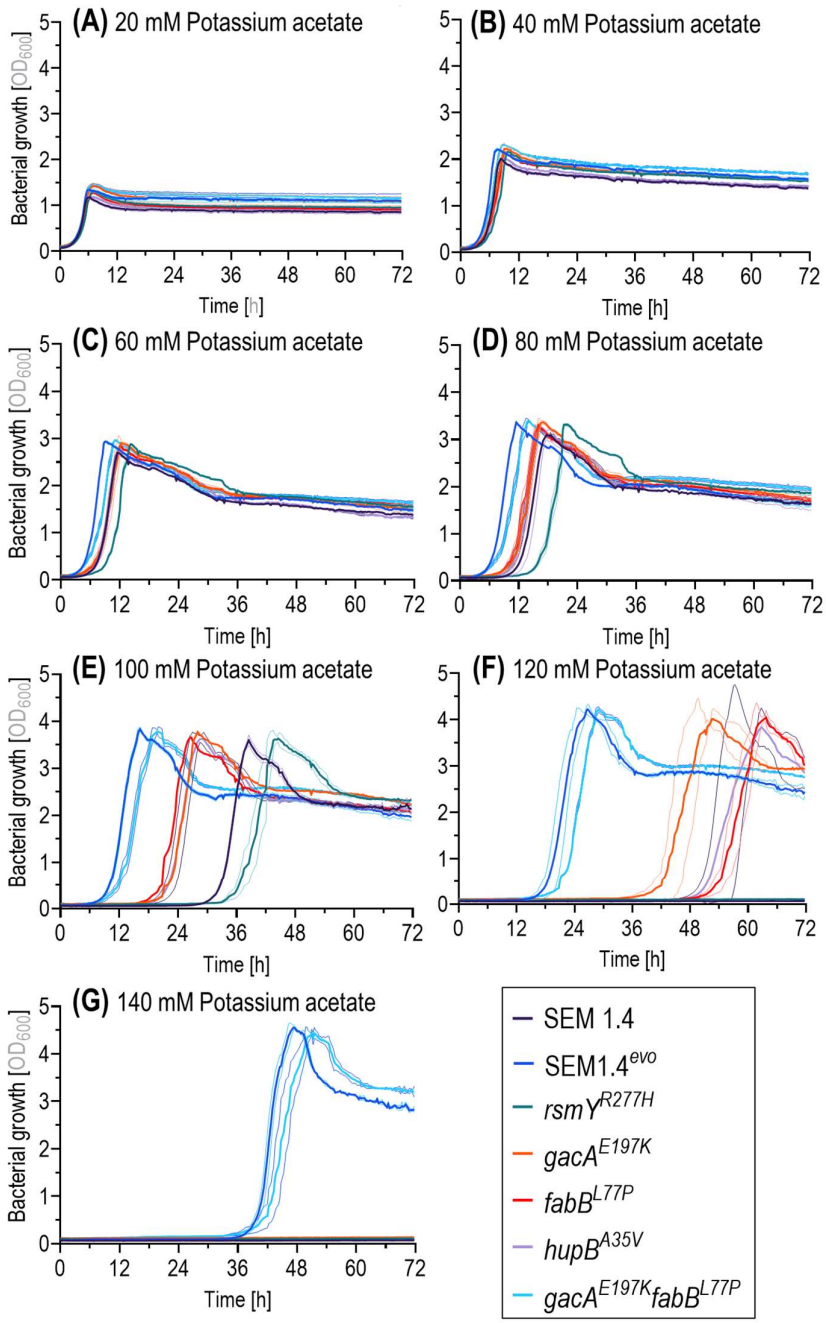

Figure 5.3. Evaluation of the different mutants containing the identified single nucleotide polymorphisms (SNPs) in high acetate concentration. Mutant (*rsmY*^{R277H}, *gacA*^{E197K}, *fabB*^{L77P}, *hupB*^{A35V} and *gacA*^{E197K}*fabB*^{L77P}) were tested in de Bont minimal medium with **(A)** 20 mM, **(B)** 60 mM, **(C)** 80 mM, **(D)** 100 mM, **(E)** 120 mM **and (F)** 140 mM of potassium acetate. Solid lines represent the average and the surrounding shading area correspond to the standard deviation of four biological replicates.

Table 5.2. Growth parameters of *Pseudomonas putida* SEM1.4, SEM1.4^{evo} and reverse-engineered strains grown in increasing concentration of potassium acetate (20-140 mM). Specific growth rates and lag phase times were calculated using the package QurvE (https://github.com/NicWir/QurvE/)

Acetate concentration [mM]	Strains						
	SEM1.4	SEM1.4^{evo}	*rsmY*^{R277H}	*gacA*^{E197K}	*fabB*^{L77P}	*hupB*^{A35V}	*gacA*^{E197K} *fabB*^{L77P}
	Specific growth rate (μ) [h^{-1}]						
	Avg. ± SD	Avg. ± SD	Avg. ± SD	Avg. ± SD	Avg. ± SD	Avg. ± SD	Avg. ± SD
20	0.78 ± 0.03	0.75 ± 0.02	0.72 ± 0.02	0.72 ± 0.02	0.73 ± 0.01	0.73 ± 0.02	0.69 ± 0.02
60	0.62 ± 0.01	0.66 ± 0.03	0.62 ± 0.01	0.57 ± 0.01	0.60 ± 0.02	0.58 ± 0.01	0.54 ± 0.01
80	0.58 ± 0.01	0.59 ± 0.01	0.59 ± 0.01	0.53 ± 0.02	0.55 ± 0.01	0.53 ± 0.01	0.50 ± 0.02
100	0.52 ± 0.01	0.54 ± 0.01	0.52 ± 0.01	0.49 ± 0.02	0.51 ± 0.01	0.50 ± 0.01	0.47 ± 0.02
120	N/A	0.53 ± 0.02	N/A	0.44 ± 0.01	0.43 ± 0.05	0.38 ± 0.10	0.45 ± 0.02
140	N/A	0.49 ± 0.01	N/A	0.44 ± 0.01	N/A	N/A	0.42 ± 0.01
	Lag phase time (λ) [h]						
20	1.7 ± 0.2	1.6 ± 0.1	1.9 ± 0.1	1.8 ± 0.1	1.7 ± 0.2	1.7 ± 0.1	1.4 ± 0.1
60	4.3 ± 0.1	2.2 ± 0.1	5.5 ± 0.1	3.7 ± 0.4	3.2 ± 0.3	4.0 ± 0.1	2.2 ± 0.2
80	8.9 ± 0.6	3.1 ± 0.1	11.3 ± 0.2	6.3 ± 0.5	5.4 ± 0.5	7.5 ± 0.1	3.3 ± 0.1
100	26.7 ± 2.6	6.2 ± 0.3	29.1 ± 0.8	15.8 ± 0.6	13.6 ± 0.9	19.2 ± 0.6	6.6 ± 0.4
120	N/A	14.8 ± 1.0	N/A	36.8 ± 5.7	40.3 ± 4.1	63.4 ± 3.2	15.0 ± 0.2
140	N/A	33.3 ± 4.1	N/A	N/A	N/A	N/A	32.2 ± 1.3

5.2.3 Physiological characterization in shaken-flasks and sampling determination for proteomics and fluxomics.

With the objective of analyzing the physiological parameters of *P. putida* SEM1.4, SEM1.4^{evo} and the double mutant *gacA*^{E197K}*fabB*^{L77P}, we performed a growth characterization in shaken-flasks to calculate specific growth rate, lag phase, acetate uptake rate and yield. In addition, the sampling time window for each strain was selected in order to execute a consistent and reproducible –Omics experiments. Therefore, the strains were cultured in de Bont minimal medium containing 5 g L^{-1} MOPS supplemented with 100 mM of potassium acetate because it was the concentration where substantial differences were observed among the strains in the previous analysis (**Figure 5.3D**). We determined that the ideal sampling point for each strain was approximately at OD_{600} ~1.0 after 13, 19 and 29 hours for the evolved, double mutant and parental strains, respectively. Afterwards, physiological parameters were individually calculated for the strains under study. As expected, lag phases were significantly shorter both in the evolved (9 hours) and double mutant (15 hours) in comparison with the parental strain (22 hours) (**Figure 5.4A**). Along the same line,

acetate consumption mirrored growth with a specific acetate uptake rate of ca. 25.8 ± 0.8 mmol g_{CDW}^{-1} h^{-1} for the evolved strain, 23.8 ± 1.6 mmol g_{CDW}^{-1} h^{-1} while, the parental strain reached ca. 34.1 ± 4.7 mmol g_{CDW}^{-1} h^{-1} (**Figure 5.4B** and **Figure 5.4C**). In this condition, specific growth rates were improved by around 20% and biomass yields were increased by 60% in both strains (**Figure 5.4C**). Based on this results, we confirmed that the evolved strain as well the double mutant, improved their fitness upon acetate toxicity where cells grew faster (reduced lag phase and higher specific growth rate) as well as were able to transform acetate into biomass more efficiently than the parental strain. Having these preliminary results at hand, we expected the possibility that large metabolic rewiring might be caused due to acetate toxicity. Thus, we considered exploring the dynamics at proteome and fluxome level to identify global changes in acetate metabolism.

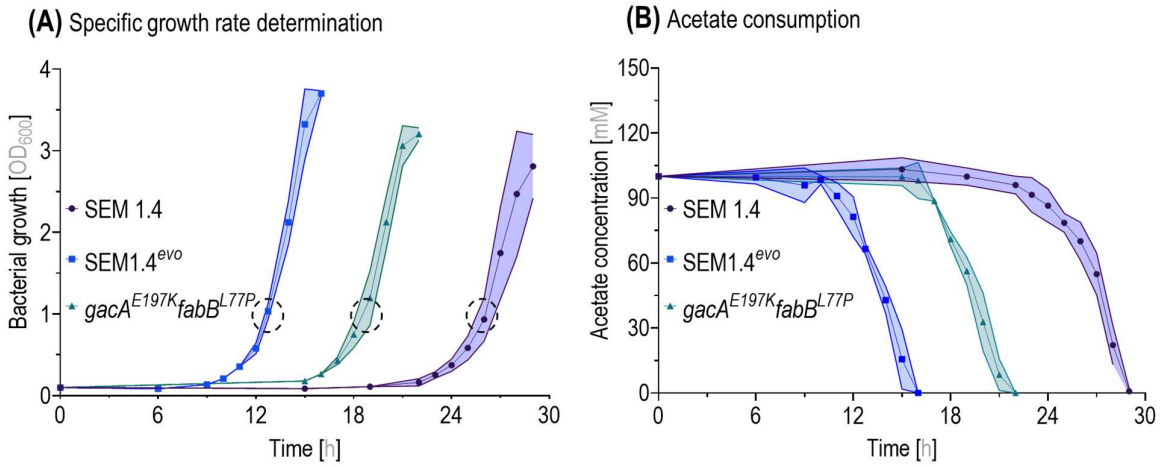

(C) Physiological parameters

Pseudomonas putida SEM1.4 Strains	Specific growth rate [h^{-1}]	Acetate uptake rate, q_s [mmol g_{CDW}^{-1} h^{-1}]	$Y_{X/S}$ [g_{CDW} g acetate consumed^{-1}]
Wild-type	0.44 ± 0.02	34.1 ± 4.7	0.13 ± 0.02
SEM1.4^{evo}	0.55 ± 0.01	25.9 ± 0.8	0.21 ± 0.01
gacA^{E197K} *fabB*^{L77P}	0.50 ± 0.03	23.8 ± 1.6	0.22 ± 0.02

Figure 5.4. Physiological parameter determination in shaken-flask cultivations. *Pseudomonas putida* SEM1.4, SEM1.4^{evo} and *gacA*^{E197K}*fabB*^{L77P} were grown in 100 mM of potassium acetate to evaluate **(A)** growth **(B)** acetate consumption. Specific growth rates, acetate uptake rate and yields are displayed in **(C).** Solid lines represent the average and the shading area correspond to the standard deviation of three biological replicates.

5.2.4 Network-wide proteomics analysis reveals major adaptive mechanisms upon acetate toxicity in *Pseudomonas putida*

P. putida SEM1.4, SEM1.4^{evo} and *gacA*^{E197K}*fabB*^{L77P} were cultivated in the presence of 100 mM of potassium acetate and harvested in mid-exponential phase (OD_{600}~1.0) as was determined previously. As a first step, protein changes, $\log_2$(fold-changes) were analyzed by LC-MS/MS. For data visualization, three volcano plots were created to help identify proteins that were expressed differently by plotting on the X-axis the $\log_2$(fold-change) of proteins against their statistical significance on the Y-axis [represented by the negative $\log_{10}$(*p-value*)] (**Figure 5A**, **Figure 5.5B** and **Figure 5.5C**). The absolute fold-change values are represented in the supplementary **Table S5.1**, **Table S5.2** and **Table S5.3**. The results showed that there were 23 proteins up regulated and 259 down regulated when the SEM1.4^{evo} was compared to the wild type. Similarly, when comparing the double mutant to the wild type, 29 proteins were up regulated and 198 down regulated. Lastly, only 9 proteins were significantly up regulated and 3 were down regulated when comparing the SEM1.4^{evo} strain to the double mutant under high acetate concentration growth conditions. In general, the SEM1.4^{evo} strain and double mutant exhibited comparable volcano plots, suggesting that the mutations that were previously incorporated significantly rewired the cellular proteome.

Subsequently, based on the proteomics analysis, we investigated which protein groups or pathways were impacted by the presence of elevated acetate concentrations. We observed substantial alterations in methionine metabolism of both the SEM1.4^{evo} and double mutant strains. Methionine transport system ATP-binding protein (MetN1) and sulfate permeate (CysZ) were significantly upregulated by a $\log_2$(fold-change) of 8.5 and 7.3, respectively. Also, related to sulfur metabolism, alkanesulfonate monooxygenase (SsuD), the organosulfonate utilization protein (SsuF) together with thiosulfate sulfurtransferase (GlpE) were significantly downregulated with a $\log_2$(fold-change) of -9. In addition, the enzyme that convert O-acetylhomoserine and sulfide into L-homocysteine, O-acetylhomoserine sulfhydrylase (MetY) was downregulated (Kulikova, et al., 2019). These findings are in agreement with earlier research, which suggested two key points. Firstly, that the addition of methionine shields *E. coli* from the damaging effects of acetate. Secondly,

homocysteine obstructs the enzymes that are responsible for generating methionine (Roe, et al., 2002). It is assumed that providing additional methionine protects against the negative effects of homocysteine by triggering a regulatory mechanism that suppress methionine production, preventing homocysteine accumulation. Methionine and cysteine biosynthesis were also studied in *Pseudomonas putida* S-313 and *Pseudomonas aeruginosa* PAO1. Both these organisms use direct sulfhydrylation of O-succinylhomoserine for the synthesis of methionine but also, contained substantial levels of O-acetylserine sulfhydrylase (cysteine synthase) activity which could support the cell to obtain extracellular sulfate by transcriptionally activating genes related to sulfate transport, activation and reduction in order to boost methionine production (Vermeij and Kertesz, 1999, Campanini, et al., 2015).

We also noticed an increase in the relative amount of SucC (Succinyl-CoA ligase [ADP-forming] subunit beta) and SucD (Succinyl-CoA ligase [ADP-forming] subunit alpha). The activity of these two enzymes been provide to increase during acetate oxidation phase (Saeki, et al., 1999). The findings indicate that *P. putida* might utilize this system in the TCA cycle as an additional mechanism to detoxify the acetate within the cell. This process involves directing acetate through the TCA cycle to neutralize its harmful effects (Mullins, et al., 2008).

Moreover, we also identified enzymes that are involved in several mechanisms to fight oxidative stress and avoid the imbalance of ROS (reactive oxygen species) levels that lead to cell toxicity. From these, the presence of scavenging enzymes that consume ROS (superoxide dismutases, catalases and peroxidases) are critical in self-defense mechanisms against oxidative stress in bacteria. Among them, we observed that glutathione S-transferase protein (*PP1821* and *PP2536*), thiol peroxidase (Tpx), catalase-peroxidase (KatG), superoxide dismutase (SodB) and cytochrome C (*PP1659* and *PP3822*) were down regulated in the evolved and double mutant strain in comparison with the wild type. This indicates that wild-type strain is more susceptible to oxidative stress as indicated the relative changes in abundance of detoxifying enzymes. It is known that glutathione reductases maintain and regulate redox homeostasis in the cell (Couto, et al., 2016) and together with the combined action of superoxide dismutases, catalases and thiol peroxidases can degrade superoxide (O_2^{-})

and hydrogen peroxide (H_2O_2) and thus, withstand the ROS effect (Fridovich, 1974, Mishra and Imlay, 2012, Somprasong, et al., 2012, Kim and Park, 2014, Gurdo, et al., 2018). Also, cytochrome C may also contribute to ROS defense mechanisms in bacteria catalyzing the four-electron reduction of O_2 to $2H_2O$ using quinol or cytochrome c as the electron donor (Malatesta, et al., 1995, Melo and Teixeira, 2016). In connection to oxidative stress, we noticed that pyoverdine synthetase (PvdL), the non-ribosomal peptide synthase (PvdI and *PP3788*) and L-Ornithine N5-oxygenase (PvdA) (Visca, et al., 1994) were significantly down regulated in the evolved and double mutant strain against the wild type. Pyoverdine (PvdI) has been previously reported to act as a siderophore for scavenging iron, a key nutrient in *Pseudomonas spp.* metabolism (Chimiak, et al., 1984, Leoni, et al., 1996, Ganne, et al., 2017, Ringel and Brüser, 2018). If there is oxidative stress, the Fe^{+2} is converted to Fe^{+3}, which stimulates the production of oxidative stress proteins via ROS molecules generated by the activation of the Fenton reaction through Fe^{+3} (Touati, 2000), which seem to be the case to greater extent for the non-evolved strain.

We also observed a general down regulation in the OmpA proteins (*PP3090*, *PP4669* and *PP1502*) in the evolved in comparison to the wild-type strain (Wang, 2002, Sainz, et al., 2005). Previous reports have demonstrated that the OmpA protein is associated with cell turgor maintenance and cellular size (Chevalier, et al., 2017). In *Acinetobacter baumannii,* this protein family are crucial in regulating outer membrane vesicles (OMVs) and formation of biofilm (Gaddy, et al., 2009, Moon, et al., 2012), both of which are vital for the survival of bacteria during stressful situations (Hall-Stoodley, et al., 2004, Schwechheimer and Kuehn, 2015). Cell morphology was also reported to be altered in response to the presence of acetate. Increasing the size of the cells is another cellular strategy to counteract its effects. This leads to a reduction in the relative area responsible for the passive diffusion of the carboxylic acid into the cell, providing an additional line of defense against acetate toxicity (Trcek, et al., 2007).

Another significant finding was that the enzymes responsible for β-oxidation FadE (*PP1893*) and fatty acid metabolism [acyl-CoA dehydrogenases (*PP0360*, *PP3638*, *PP3670*) and cyclopropane-fatty-acyl-phospholipid synthase (*PP5365*)] were down regulated in the evolved and double mutant strains in comparison with the wild-type

(Thompson, et al., 2020). This showed that the wild-type strain had higher levels of the proteins involved in the biosynthesis and degradation of fatty acids which may lead to changes in the lipidic membrane composition (Willdigg and Helmann, 2021). Finally, we noted a significant decrease in GacA abundance in both SEM1.4^{evo} and the double mutant. This suggests that the mutation could cause a loss of function, decreased activity, or reduced ability to bind to the DNA region. Earlier studies demonstrated that GacA had a negative impact on numerous genes responsible for iron uptake in *Pseudomonas fluorescens* Pf-5 when grown in culture. Our proteomic analysis supports previous experimental results which showed an increase in the production of siderophore after the loss of GacA/GacS signalling in a closely related *Pseudomonas fluorescens* strain called CHA0 (SCHMIDLI-SACHERER, et al., 1997, Duffy and Défago, 2000, Hassan, et al., 2010).

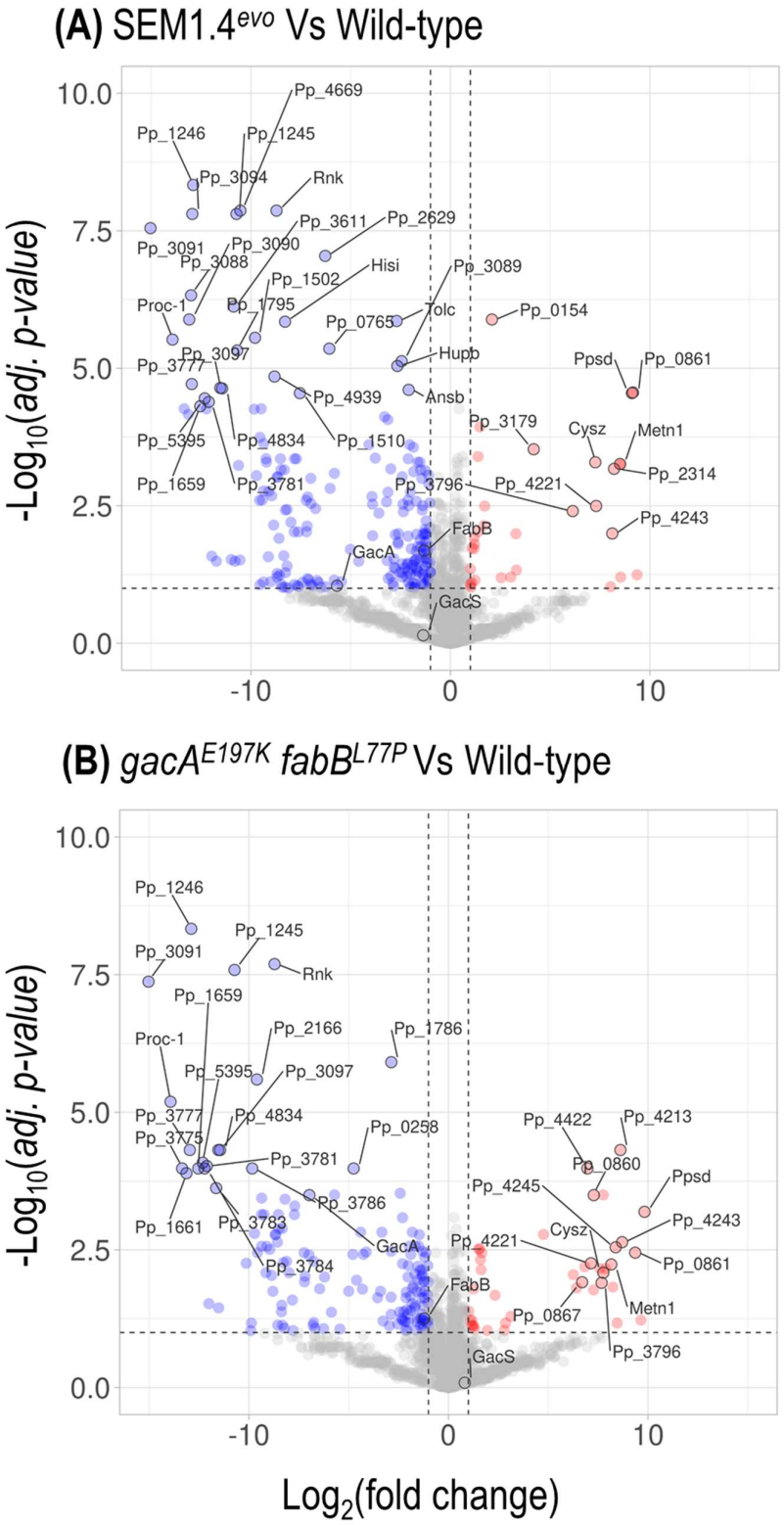
(A) SEM1.4evo Vs Wild-type
-Log10(adj. p-value)
10.0
7.5
5.0
2.5
0.0
-10
0
10
Pp_4669
Pp_1246
Pp_1245
Pp_3094
Rnk
Pp_3611
Pp_2629
Pp_3091
Pp_3090
Pp_3088
Hisi
Pp_3089
Pp_1502
Proc-1
Pp_1795
Tolc
Pp_0154
Pp_0765
Pp_3097
Hupb
Ppsd
Pp_0861
Pp_3777
Pp_4939
Ansb
Pp_3179
Cysz
Metn1
Pp_5395
Pp_4834
Pp_1510
Pp_2314
Pp_1659
Pp_3781
Pp_3796
Pp_4221
Pp_4243
FabB
GacA
GacS
(B) gacAE197K fabBL77P Vs Wild-type
-Log10(adj. p-value)
Log2(fold change)
Pp_1246
Pp_1245
Pp_3091
Rnk
Pp_1659
Pp_2166
Pp_1786
Proc-1
Pp_5395
Pp_3097
Pp_3777
Pp_4834
Pp_4422
Pp_4213
Pp_3775
Pp_0258
Pp_0860
Pp_3781
Ppsd
Pp_4245
Pp_3786
Pp_4243
Pp_1661
Pp_3783
Cysz
GacA
Pp_4221
Pp_3784
Pp_0861
FabB
Metn1
Pp_0867
GacS
Pp_3796

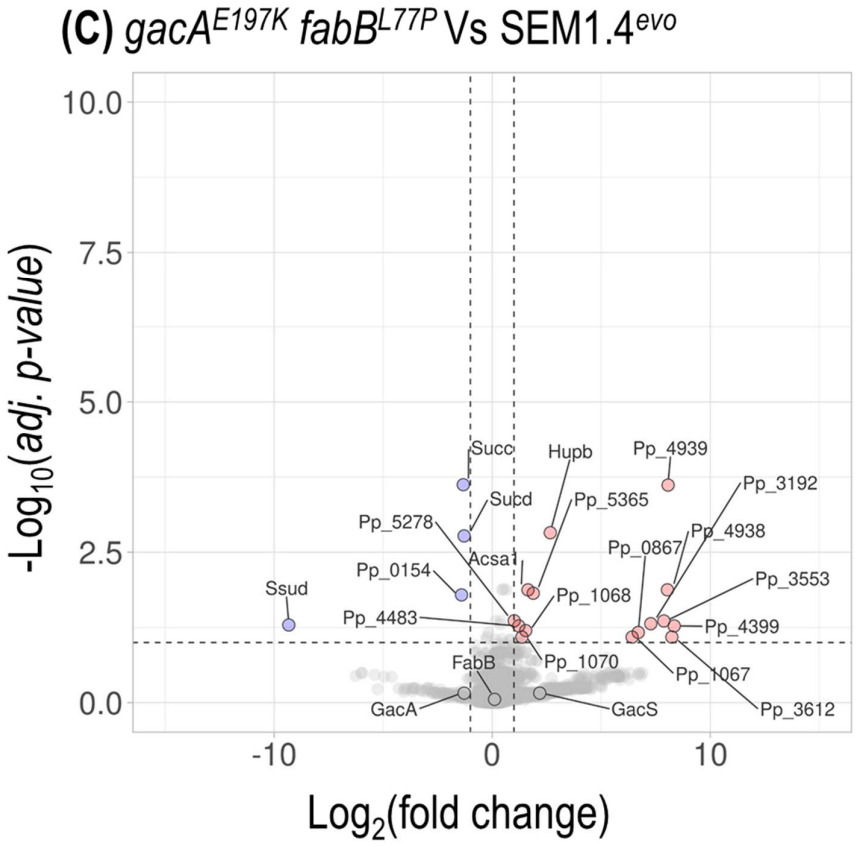

Figure 5.5. Volcano plot of mass spectrometry results showing differentially expressed proteins comparing the proteome profile within *Pseudomonas putida* SEM1.4 (A), evolved (B) and the double mutant *gacA*^{E197K}*fabB*^{L77P} strain (C). Four biological replicates were grown in de Bont minimal medium supplemented with 100 mM acetate harvested in the mid-exponential phase to measure the entire protein content of biomass. Each point in the plot represents an individual protein. The horizontal and vertical intersections were set at a 1.

5.2.5 Acetate toxicity exposes rewiring of metabolic fluxes in the EDEMP cycle to counteract oxidative stress

As previously mentioned, high levels of acetate induce oxidative stress in several microorganisms. Bacteria can adapt their metabolism to overcome adverse conditions by producing detoxifying enzymes such as superoxide dismutases, catalase, and glutathione/glutaredoxin recycling systems (Imlay, 2013). In *P. putida*, adjusting the central carbon metabolism is one of the tactics employed to counteract sub-lethal oxidative stress (Nikel, et al., 2021). In order to capture the metabolic effects of acetate

toxicity in *P. putida* strain used in this study, we carried out a ^{13}C fluxome analysis where the cells were exposed to high acetate concentration in de Bont minimal medium. We implemented a parallel labelling strategy ([1-$^{13}C_1$]-, [2-$^{13}C_1$]- and [50% U-$^{13}C_6$]-acetate) to resolve the relative contribution of TCA cycle, EDEMP, PP, and ED pathway. Samples were collected at mid-exponential phase to assess proteinogenic aminoacids and sugar monomers (glucose and glucosamine). The calculated relative fluxes for the three strains cultured on labeled acetate are shown in **Figure 5.6**. Also, the calculated flux distributions, carbon atom transition for each reaction and upper and lower boundaries of the flux estimates are provided in **Figure S5.1**.

Carbon fluxes in cultures grown on acetate varied greatly among the wild type strain SEM1.4 in comparison to the SEM1.4^{evo} and the double mutant strain. Initially, we first observed a distinct pattern in the wild type strain compared to the other two strains. Specifically, while the wild type strain had significant net flux through the EDEMP and PP pathways, there was almost absent flux in SEM1.4^{evo} and double mutant strains. The flux pattern in the wild type strain correlates with previous results where, under oxidative stress, increased cyclic operation in EDEMP and PP pathway was observed, especially in the oxidative segment of this metabolic pathway (Nikel, et al., 2021). Our flux analysis revealed that no carbon is utilized by the NAD(P)H-generating steps of the ED pathway during acetate growth, which suggests that this phenomenon may be regulated at the transcriptional level. Previous studies have shown that during growth on acetate, both Cra and CRP are activated to modulate the expression of key enzymes involved in glycolysis, but in opposing ways. Cra is known to down regulate the expression of most of the enzymes in the glycolysis pathway, with the exception of two genes, *fbp* and *ppsA*, which redirect flux towards gluconeogenesis and are up regulated to supply 5- or 6-carbon precursor molecules (Son, et al., 2011). Similarly, the fact that there is no flux in EDEMP and PP pathway of SEM1.4^{evo} and double mutant strains correlates to the results observed under non-toxic acetate conditions, indicating that these strains are capable of withstanding the effects of acetate within the cell (Dolan, et al., 2020). Moreover, during steady-state growth on acetate, we observed that the glyoxylate shunt received approximately 50% of the carbon reaching the acetyl-CoA node in the wild type strain, while this value was around 60% in SEM1.4^{evo} and double mutant strains.

The primary function of the glyoxylate shunt is to produce malate, which is then converted to oxaloacetate, a precursor to gluconeogenesis, through the catalytic action of malate:quinone oxidoreductase (MqoB). Also, malate dehydrogenase (MaeB) contributes to the NAD(P)H supply in these strains by converting malate into oxaloacetate. Hypothetically, high levels of oxaloacetate, which could be accumulated in response to limited NAD(P)H supply for anabolism, might stimulate the activity of one of the isozymes of isocitrate dehydrogenase, IDH. This forms an elegant feedback loop that restores the flux through the TCA cycle (Crousilles, et al., 2018). In addition, the evolved and double mutant strains exhibited around 50% increase in the carbon cycling through the pyruvate shunt compared to the wild type strain. Given that NAD(P)H is produced via the latter reaction, this observation suggests that the reaction may act as an additional energy source in the cell helping to cope with the stress induced by acetate (Blank, et al., 2008). Our analysis of flux data revealed that, in SEM1.4^{evo} and double mutant strains, the metabolic pathways of EDEMP and PP were shut down, whereas in the wild type strain, these pathways were highly active. Until now, our evaluation of these observations were mostly centered on the necessity of NAD(P)H to neutralize the oxidative stress that results from elevated levels of acetate.

(A) *Pseudomonas putida* acetate map

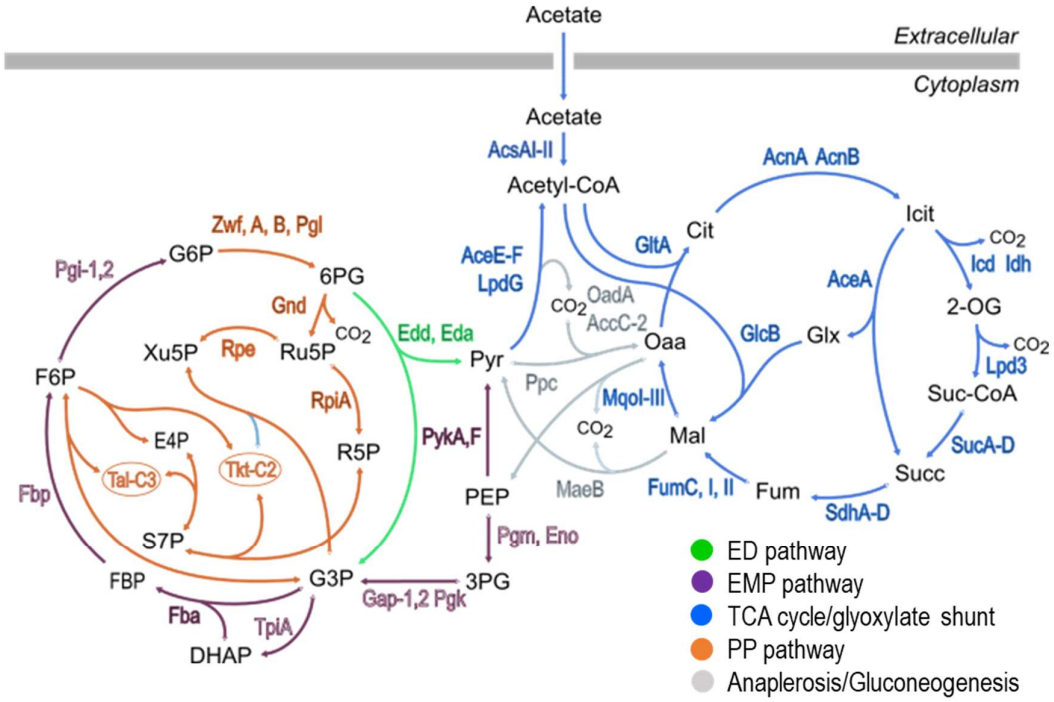

(B) *Pseudomonas putida* SEM1.4

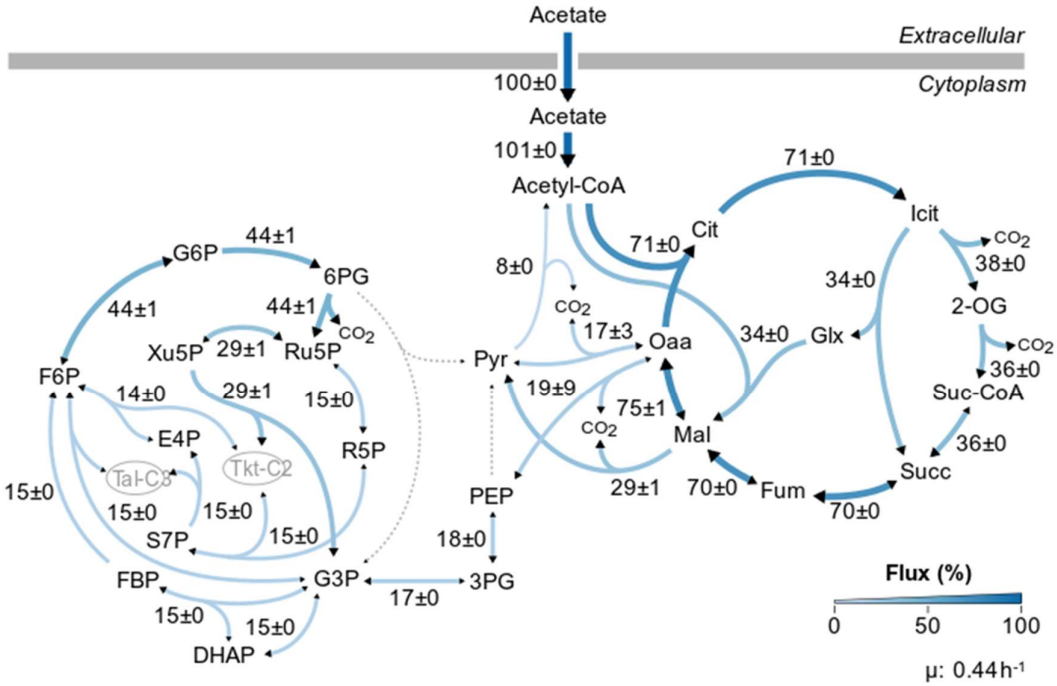

(C) *Pseudomonas putida* SEM1.4 evolved

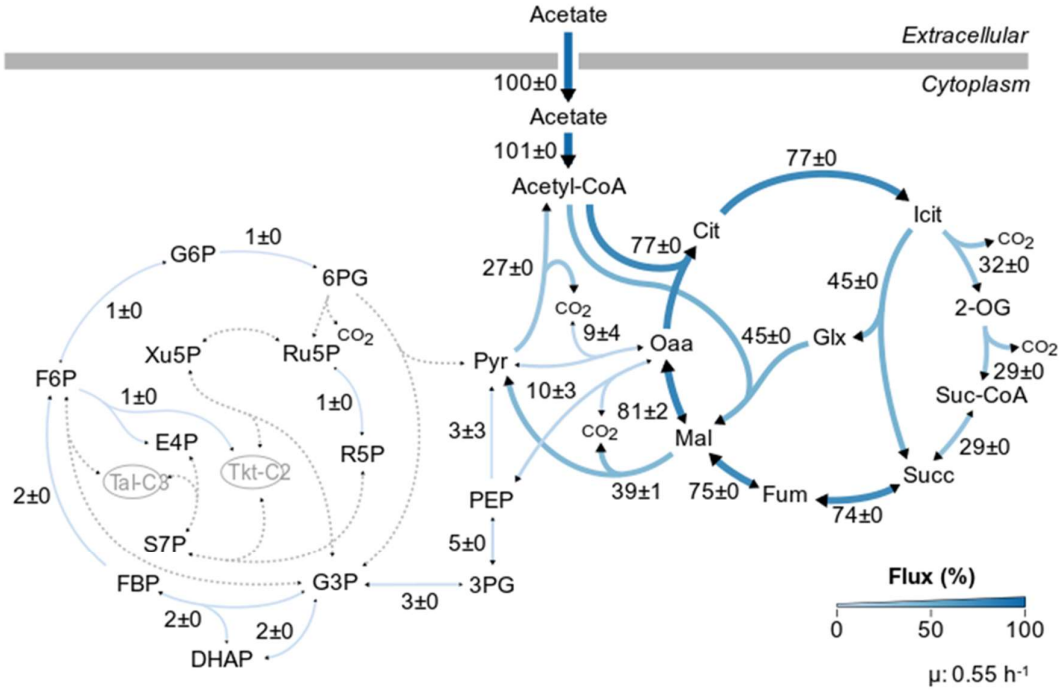

(D) *Pseudomonas putida* SEM1.4 *gacA*^{E197K} *fabB*^{L77P}

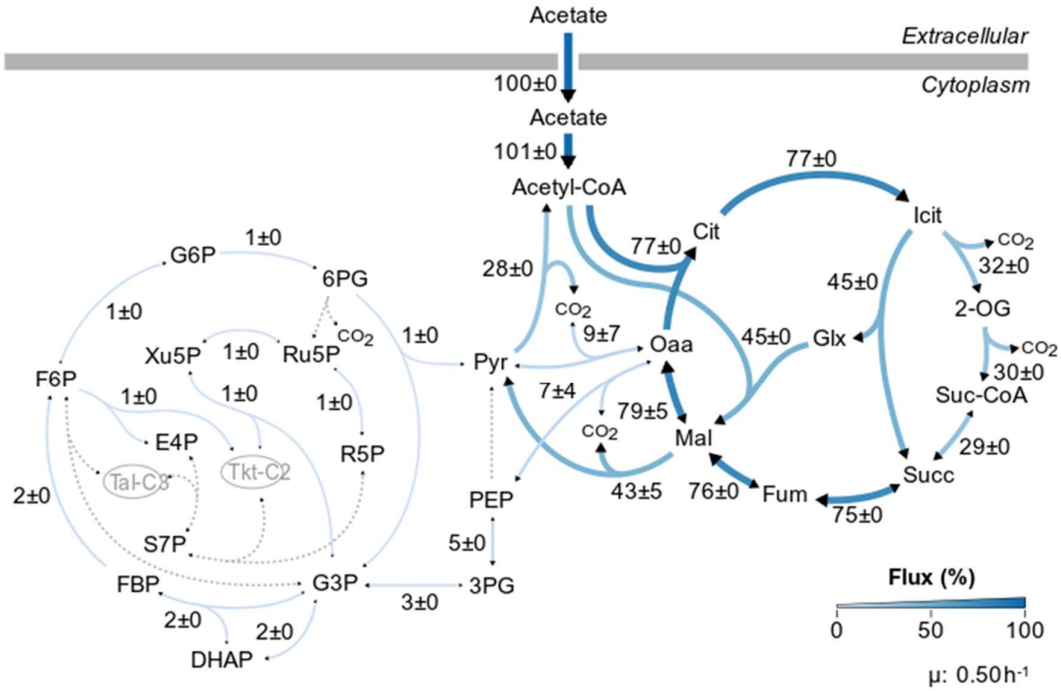

Figure 5.6. Acetate metabolism and proteins associated in *P. putida* KT2440 (A). *In vivo* carbon flux distributions in central metabolism of *P. putida* SEM1.4 (B), SEM1.4^{evo} (C), *gacA*^{E197K} *fabB*^{L77P}(D) during growth on acetate as unique carbon source. Fluxes are expressed as a molar percentage of the average acetate uptake rate, calculated from the individual rates in **Figure 5.4C**. Fluxes were expressed as a molar percentage of the average acetate (34.1, 25.9 and 23.8 mmol g_{CDW}^{-1} h^{-1} for wild type, SEM1.4^{evo} and double mutant, respectively) uptake rate, calculated from the individual rates in **Figure 5**. The inaccuracies assigned to each flux indicate the respective 95% confidence intervals. The fluxes were represented graphically by coloring the arrows in the flux map using a blue scale, where high fluxes were depicted as dark blue and no fluxes were shown as white.

5.2.6 Mutagenesis analysis in GacA^{E197K} evidences a bond disruption when it interacts with the DNA

Drawing on the knowledge of proteomics, and considering the current background information about the effects of mutations on GacA, we decided to investigate in more detail the structural consequences of this specific mutation. We utilized PyMOL software to investigate the impact of the mutation on GacA and the adjacent residues. Upon conducting the analysis, we discovered that the mutation was located in the C-terminal domain of LuxR-type HTH. This domain is a helix-turn-helix (HTH) DNA-binding domain that spans around 65 amino acids, and it is present in transcriptional regulators belonging to the LuxR/FixJ family of response regulators (Kahn and Ditta, 1991, Sitnikov, et al., 1995). According to the results of the structural analysis, glutamate-197 (E197), which carries a negative charge, appears to be capable of coordinating with either the polar threonine-193 (Thr-193) within the same chain, or more distantly with the positively charged lysine-164 (Lys-194) and/or glutamine-163 (Gln-163) (**Figure 5.7A**). The spatial separation between the amino acids could indicate the presence of an ion-coordinated bond or a similar type of interaction. In the unlikely event that the amino acid in question fails to form bonds with any other molecule or structure, its negative charge may still have an indirect impact on maintaining a delicate balance of charge. This possibility is supported by the examination of the neighboring amino acids mentioned above. Therefore, switching from the negatively charged glutamate (E) to the positively charged lysine (K) could significantly influence the coordination of dimerization, resulting in altered transcriptional regulation (**Figure 5.7B)**. This hypothesis is supported by experimental evidence

demonstrating that the inactivation of either *gacS* or *gacA* genes in *P. putida* or *Pseudomonas stutzeri* leads to significant fitness improvements (Eng, et al., 2021). These findings suggest that the E197K mutation may be detrimental for GacA, potentially diminishing or disrupting its regulatory function. Our analysis of mutagenesis provides further evidence to support the observations outlined above.

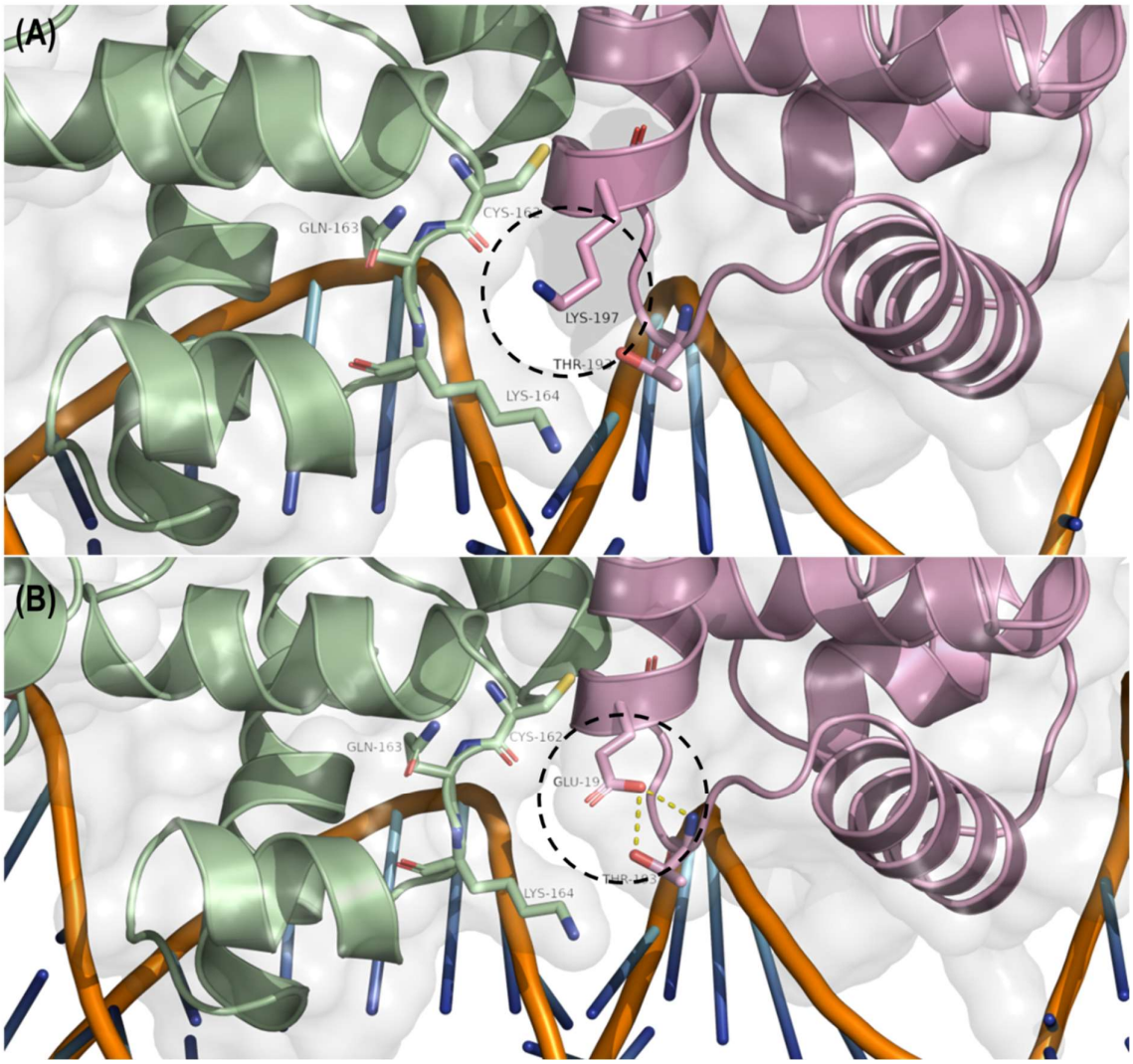

Figure 5.7. Mutational analysis in *Pseudomonas putida* mutant GacA^{E197K} (A) and wild-type GacA protein (B). View centered on the mutation under analysis surrounded by neighbor amino acids. The picture were drawn using PYMOL software. Residues: Cys162, Gln163, Lys164, Thr193 and Glu197/Lys197. The amino acid residues selected for mutational analysis is indicated with white dashed boxes.

5.3 Discussion

Understanding bacterial metabolism is the way forward to tackle metabolic bottlenecks as well as to comprehend the interaction between environment and cellular processes (Nicholson and Wilson, 2003, Vilchez-Vargas, et al., 2010). The focus of our investigation was to examine how *P. putida* SEM1.4 copes with acetate toxicity by studying its tolerance mechanisms applying –Omics methodologies (genomics, proteomics and fluxomics). Over time, *P. putida* has proven to be a robust host for bioproduction because of its ability to thrive in diverse environmental conditions. This characteristic is complemented by its high level of resilience to oxidative stress and toxic substances (Calero and Nikel, 2019). Despite having a versatile metabolism that enables it to metabolize a wide range of carbon sources, there is a dearth of knowledge about the fundamental mechanisms responsible for such biochemical activities. By combining systems-level analysis with multi-omics techniques, it is possible to conduct an in-depth examination of the entire metabolism across a range of environmental conditions (Gurdo, et al., 2022).

In this study, we employed the genome-reduced strain SEM1.4, derived from *P. putida* EM42 (Martínez-García, et al., 2014), for evolution experiments in order to increase the resistant to the dicarboxylic acid, acetate. After a long-term evolution in increasing acetate concentration, a tolerant population was isolated and several clones were screened for further analysis. We examined different clones from a physiological perspective and found that their fitness had improved significantly due to the accumulation of genetic mutations in its genome. Two single nucleotide polymorphism mutations were identified with relevant role in *Pseudomonas* metabolism: i) *gacA* gene, encoding the response regulator of the GacS/GacA two-component system and (Song, et al., 2023); ii) *fabB* gene, encoding the 3-oxoacyl-[acyl-carrier-protein] synthase that is involved in fatty acid metabolism (McNaught, et al., 2023). Once the mutations were reintroduced into the original strains, the impact of these two mutations was assessed in terms of their effects on the proteome and fluxome.

Global proteome analysis allowed capturing the changes at different levels including iron homeostasis, stress response (detoxifying enzymes), methionine biosynthesis,

osmotic maintenance systems as well as fatty acid β-oxidation regulation. ^{13}C-metabolic flux analysis showed a significant rewiring in the parental strain through the EDEM and PP pathway which might provide NAD(P)H and other anabolic routes to counteract the toxic effect of acetate. The results obtained from the comparison of a double mutant strain with an evolved strain in Volcano plot yielded significant insights into the effects of genetic modifications and evolutionary processes on the phenotype and performance of the organism.

Taken together, these experimental findings suggest that the metabolic modifications resulting from ALE allowed the organism to withstand the harmful effects of acetate. The outcomes of this study demonstrate that the mutations in *gacA* and *fabB* genes contributed significantly to the development of the observed phenotype, as revealed by the analyses of proteomes and fluxomes. Our results are supported and supplemented by earlier research on acetate tolerance (Trček, et al., 2015), and hence, it enriches the understanding of *Pseudomonas putida*'s strategies for overcoming acetate toxicity. This knowledge could be utilized to develop more effective bioproduction processes, thereby making acetate bioeconomy an attainable reality in the near future. The increasing interest in non-conventional carbon sources reflects a growing awareness of the need to develop more sustainable and environmentally friendly bioprocesses, while also exploring new and innovative solutions to meet the ever-growing demand for bio-based products.

5.4 Materials and Methods

Table 5.3. Strains used and constructed in this study.

Strain name	Description	Reference or source
Escherichia coli		
DH5α λpir	Cloning host; F⁻ λ⁻ *endA1 glnX44*(AS) *thiE1 recA1 relA1 spoT1 gyrA96*(Nal^R) *rfbC1 deoR nupG* Φ80(*lacZ*ΔM15) Δ(*argF-lac*)*U169 hsdR17*(r_K^- m_K^+), λ pir lysogen	(Platt, et al., 2000)
Pseudomonas		
P. putida KT2440	Wild-type strain, derived from *P. putida* mt-2 (Worsey and Williams, 1975) cured of the TOL plasmid pWW0	(Bagdasarian, et al., 1981)
P. putida EM42	Reduced-genome derivative of *P. putida* KT2440; Δ*PP4329-PP4397* (flagellar operon) Δ*PP3849-PP3920* (prophage I) Δ*PP3026-PP3066* (prophage II) Δ*PP2266-PP2297* (prophage III) Δ*PP1532-PP1586* (prophage IV) ΔTn*7* Δ*endA-1* Δ*endA-2* Δ*hsdRMS* Δ*Tn4652*	(Martínez-García et al., 2014)
***P. putida* SEM1.4**	Reduced genome derivative of EM42; Δ*PP5003-5008* (Δ*phaC1ZC2DFI*), Δ*PP3161-3164* (Δ*benABCD*), Δ*PP1408* (Δ*phaG*)	(Mezzina et al., not published)
***P. putida* evoSEM1.4**	ALE derivative of *P. putida* SEM1.4 with increased acetate tolerance of up to 180 mM Potassium acetate	This work
SEM1.4 *hupB*T49I	*P. putida* SEM1.4 *hupB*^{T49I}	This work
SEM1.4 *hupB*A35V	*P. putida* SEM1.4 *hupB*^{A35V}	This work
SEM1.4 *fabB*L77P	*P. putida* SEM1.4 *fabB*^{L77P}	This work
SEM1.4 *PP_0371*R277H	*P. putida* SEM1.4 *PP0371*^{R277H}	This work
SEM1.4 *uvrY*E197K	*P. putida* SEM1.4 *uvrY*^{E197K}	This work
SEM1.4 *uvrY*E197K *fabB*L77P	*P. putida* SEM1.4 *uvrY*^{E197K} *fabB*^{L77P}	This work

Table 5.4. Plasmids used in this study.

Plasmid Name	Description	Source
pSNW2	Derivative of vector pGNW2 (Wirth et al., 2020) with *P14g(BCD2)* → *msfGFP*; Km^R	(Volke et al., 2020)
pSNW::*uvrY*E197K	Derivative of vector pSNW2 carrying Homologous Regions (HRs) to introduce the E197K substitution in *uvrY*; Km^R	This work
pSNW::*hupB*T49I	Derivative of vector pSNW2 carrying HRs to introduce the T49I substitution in *hupB*; Km^R	This work
pSNW::*hupB*A35V	Derivative of vector pSNW2 carrying HRs to introduce the A35V substitution in *hupB*; Km^R	This work
pSNW::*PP0371*R277H	Derivative of vector pSNW2 carrying HRs to introduce the R277H substitution in *PP_0371*; Km^R	This work
pSNW::*fabB*L77P	Derivative of vector pSNW2 carrying HRs to introduce the L77P substitution in *fabB*; Km^R	This work
pQURE6·H	Conditionally-replicating vector; derivative of vector pJBSD1 carrying XylS/*Pm*→*I-SceI* and *P14g(BCD2)*→*mRFP*; Gm^R	(Volke et al., 2020)

Table 5.5. Primers used in this study.

Primer name	Nucleotide sequence (5′ to 3′)	Usage
491_UvrYE197K_A_U_F	agatcctGGCGGGCAGCCCGTAC	USER adaptors for mutagenesis of UvrYE197K
492_UvrYE197K_A_U_R	AGTTTGACGTCGCTGGTGACC	
493_UvrYE197K_B_U_F	ACGTCAAACTGACCTTGCTGGC	
494_UvrYE197K_B_U_R	aggtcgactGGCCGGGTGCGGTTGG	
495_UvrYE197K_chk-F	CTGACCAAGGGTGCAGGCCTTG	495_UvrYE197K_chk-F 496_UvrYE197K_chk-R
496_UvrYE197K_chk-R	TGGCCTTGCCCACGTAAAGCAG	495_UvrYE197K_chk-F 496_UvrYE197K_chk-R
497_HupBT49A_A_U_F	agatcctGTGTCGGCGCTGACGCA	USER adaptors for mutagenesis of hupBT49A
498_HupBT49A_A_U_R	AGAAGATACCAAAGCCAACCAGTACCAC	
499_HupBT49A_B_U_F	ATCTTCTCGGTCAAGGAGCGC	
500_HupBT49A_B_U_R	aggtcgactTGGCATCCTCAGCACCTTGCA	

501_HupBT49A-chk-F	CCATGCCTCCCAGCACACGTTT	sequencing for *hupB*
502_HupBT49A-chk-R	AAACGGCTGTACCACTGCGTCG	
503_HupBA35V_A_U_F	agatcctGTGTCGGCGCTGACGCA	USER adaptors for mutagenesis of HupBA35V
504_HupBA35V_A_U_R	ACGCCGGTGACGGATTCG	
505_HupBA35V_B_U_F	ACCGGCGTCCTGAAGCAAG	
506_HupBA35V_B_U_R	aggtcgactTGGCATCCTCAGCACCTTGCA	
507_PP_0371R277H_A_U_F	agatcctGAGCCCGGGTTGATCAACGC	USER adaptors for mutagenesis of PP_0371R277H
508_PP_0371R277H_A_U_R	AGGCCTGCTGGTGCTGGG	
509_PP_0371R277H_B_U_F	AGCAGGCCTCTGTGGAGCTG	
510_PP_0371R277H_B_U_R	aggtcgactGGCGGCGCTGGCG	
511_PP_0371R277H-chk-F	TGATGCTGGGCGAGGAGTTCCA	sequencing for PP_0371
512_PP_0371R277H-chk-R	CGGGGTTTTCTTTGCGTGCGTG	
513_FabBL77P_A_U_F	agatcctGAAGACCTGCTGCGCTGCA	USER adaptors for mutagenesis of FabBL77P
514_FabBL77P_A_U_R	ATGGCCGGGTAGGCGTAGG	
515_FabBL77P_B_U_F	ACCCGGCCATGCAGGAC	
516_FabBL77P_B_U_R	aggtcgactTACGCGATTCATCTGGGCGC	
517_FabBL77P-chk-F	GTCGGCGTGTTCACCTCCACTG	sequencing for *fabB*
518_FabBL77P-chk-R	AGGGTGTCCAGCGCTTCCATCT	

5.4.1 Bacterial strains and culture conditions

Escherichia coli and *Pseudomonas putida* KT2440 strains employed in this study are listed in **Table 5.2**. The strains were incubated at 37°C and 30°C, respectively. To perform cell propagation and storage as well as routine cloning and genome engineering manipulations, cells were grown in lysogeny broth (LB) medium (10 g L^{-1} tryptone, 5 g L^{-1} yeast extract, and 10 g L^{-1} NaCl). Liquid pre-cultures were done in 50-mL Falcon® centrifuge tubes with a medium volume of 10 mL or; for cultures, 250-mL Erlenmeyer flask containing 50 mL of medium. All liquid pre-cultures were agitated at 250 rpm (MaxQ™8000 incubator; ThermoFisher Scientific, Waltham, MA, USA) while cultures were incubated at 200 rpm (New Brunswick™ Innova® 42/42R Shaker, sticky pad). Solid culture media contained an additional 15 g L^{-1} agar. Selection of plasmid-

harboring cells was achieved by adding kanamycin (Km) or gentamicin (Gm), when required at 50 μg mL^{-1} and 10 μg mL^{-1}, respectively.

For adaptive laboratory evolution (ALE) experiments, clone screening, phenotypic characterizations as well as targeted metabolomics and proteomics analyses in shaken flasks, the experiments were performed in de Bont minimal medium additionally buffered with 5 g L^{-1} 3-(N-morpholino)propane sulfonic acid (MOPS) at pH 7.0 and supplemented with different concentrations of potassium acetate as explained later in the next sections. To inoculate the cultures, the aliquot taken from the pre-cultures were harvested by centrifugation at 8,000 *g* for 5 min, washed with de Bont medium without the addition of any carbon source, and resuspended in the final media of the experiment at the desired start-optical density at 600 nm (OD_{600}).

5.4.2 Adaptive Laboratory Evolution (ALE) in acetate

Pseudomonas putida SEM1.4 was evolved in 250-mL shaken baffled flask containing increasing concentrations of potassium acetate pH 7.0. The strain was streaked out onto a LB plate from the glycerol stock and it was incubated overnight. Several colonies were selected, pooled and inoculated in a 250-mL Erlenmeyer baffled flask containing 50 mL of minimal medium with an initial potassium acetate concentration of 20 mM. Cultures were kept well mixed and aerated at 200 rpm at 30°C in. When the culture reached stationary phase, 500 μL were passed into the next 250-mL Erlenmeyer baffled flask with fresh media. Three consecutive passages were performed within the same concentration prior the inoculation of the following Erlenmeyer with higher concentration. Concentrations in the flask were gradually increased a lag phase of 12 hours was observed.

5.4.3 Clone screening from populations and candidate evaluation

For clone screening, the cultures from the last Erlenmeyer was streaked out onto selective condition in minimal medium de Bont containing 180 mM of potassium acetate. Ten clones with different colony sizes were selected with a sterile toothpick and, were individually inoculated in the same selected condition as mentioned above.

The clones were stored at -80°C in 2-mL cryotubes with cryopreservation solution until further characterization. The cryopreservation solution consists of 50% vol vol^{-1} glycerol (of the highest purity available), 0.1 M $MgSO_4$, and 50 mM Tris·HCl (pH = 8.0).

The selected clones were evaluated in Growth Profiler 960 (System Duetz, Enzyscreen, Heemstede, The Netherlands) using 96-squared well microtiter plates sealed with a gas permeable sandwich cover (Enzyscreen, Heemstede, The Netherlands). Briefly, 300 µL of de Bont minimal medium with several concentrations of potassium acetate (20, 60, 100 and 140 mM) were inoculated with an initial OD_{600} of 0.1. Bacterial growth was followed every 15 min by optimal image scanning through the Growth Profiler 960. G-values (integrated green values) taken from each scan and well were transformed into equivalent OD_{600} values to determine microbial growth. This was determined by means of calibration values fitted to a Monod function:

$$\mathrm{G-value} = \frac{\mathrm{a} * \mathrm{OD}_{600}}{\mathrm{b} + \mathrm{OD}_{600}} \quad \text{(Equation 1)}$$

; with *a* and *b* parameters determined by non-linear regression, where the optical density of a culture at different dilutions was measured *a priori* in a UV-1600PC spectrophotometer (VWR, Radnor, USA) and the corresponding images of the culture were taken in the Growth Profiler 960.

5.4.4 Whole genome sequencing and mutational analysis

Genomic DNA (gDNA) was extracted from the cultures using PureLink® Genomic DNA Mini Kit. Sequencing libraries were prepared using Plexwell, and the sequencing was performed on Nextseq500 using Illumina Nextseq mid output kit, 300 cycles. The sequencing files were analyzed using a previously described in-house script (Phaneuf, et al., 2019) based on bowties2 (Deatherage and Barrick, 2014), using the reference genome with GenBank accession number AE015451. The average coverage for the clonal and the population samples was approximately 60x. For population samples, mutations with frequencies less than 0.50 were excluded from

the analysis in order to filter out artifacts in the mutation callings and focus on causal mutations.

5.4.5 Retro engineering of relevant mutations into *Pseudomonas putida* SEM1.4: USER cloning and plasmid construction

In order to re-introduce the mutations obtained from ALE experiments, plasmids were constructed for homologous recombination mediate gene replacement. Uracil-excision (USER) cloning (Nisson, et al., 1991, Cavaleiro, et al., 2015) was used for the construction of all plasmids. In order to build the plasmids for gene substitution by homology recombination, USER primers were designed with AMUSER (Genee, et al., 2015), containing the targeted single-nucleotide mutations. **Table 3** and **Table 4** shows the strains and plasmids used and generated in this study, respectively. **Table 5** describes the designed primers. Phusion™ U high-fidelity DNA polymerase (ThermoFisher Scientific) was used for PCR amplification, mutagenesis, and USER adaptors construction, in a one-step reaction. PCR products were then run on 1% agarose gel for confirmation and purified with NucleoSpin™ gel purification kit (Macherey-Nagel, Germany). The purified amplicons were ligated into pSNW2 vector with USER enzyme (New England BioLabs, Ipswich, MA, USA), following manufacturer's specifications, and transformed in *Escherichia coli* by heat shock for cryostock storage.

To perform gene substitution by homology recombination, I-*SceI*-mediated recombination engineering strategy (Martínez-García and de Lorenzo, 2011, Wirth, et al., 2020) was followed, with the addition of inducible self-curing vectors (Volke, et al., 2020). Briefly, the protocol of Wirth et al. (2020) was implemented for genomic integration and confirmed by green fluorescence (i.e. GFP) of individual colonies and colony PCR of selected amplicons. Positive colonies were grown in LB medium. Cultures were then washed with 0.3 M sucrose and transformed by electroporation with the self-curing plasmid (i.e. pQURE6·H). Cells were recovered overnight in LB medium containing 5 mM 3mBz, and then streaked onto LB medium agar with 10 μL mL^{-1} Gm and incubated overnight. Correct gene substitutions were confirmed by red fluorescence (i.e. mRFP) of individual colonies, colony PCR of selected amplicons and

sequencing. Single colonies were then inoculated and grown in LB, for plasmid curing. Eventually, the cultures were streaked onto solid media and non-fluorescent colonies were selected: the loss of the plasmid was confirmed by colony PCR, parallel plating in LB and Gm, and DNA sequencing. To store the positive mutants, single colonies were grown in LB and preserved as cryostocks.

5.4.6 Phenotypic characterization of retro engineered strains

The evolved, double mutant *P. putida* SEM1.4 *uvrY*^{E197K} *fabB*^{L77P} and reduced genome SEM1.4 strains were phenotypically characterized in 250-mL shaking baffled flask with 50 mL of de Bont minimal medium containing 100 mM of potassium acetate supplemented and 5 g L^{-1} MOPS. Optical density at 600 (OD_{600}) was measured and potassium acetate consumption (mmol g_{CDW}^{-1} h^{-1}) was determined. The shaking flasks were inoculated at an initial OD_{600} of 0.1 and incubated at 30°C with an agitation of 200 rpm. When appropriated, samples were collected along the cultures; the supernatants were collected by centrifugation (10,000 *g* for 5 min at 4°C) and storage at -20°C for HPLC analysis. Cell dry weight (CDW) was determined by growing the cells in the same conditions as is mentioned before. At different cultivation times, six samples (two per replicate) of 10 mL each were collected per strain in pre-weighted 15-mL Falcon® tubes. Optical density at 600nm was measured and the collected samples were centrifuged at 8,000 *g* for 10 min at 4°C, washed twice with de Bont minimal medium without carbon sources. The tubes containing the biomass were frozen at -20°C and lyophilized under vacuum until constant weight.

5.4.7 Metabolite analyses via HPLC

Potassium acetate consumption was analyzed using a Dionex Ultimate 3000 HPLC with an Aminex® HPX-87X Ion Exclusion (300 x 7.8 mm) column (BioRad, Hercules, CA) as well as RI-150 refractive index and UV (260, 277, 304 and 210 nm) detectors. For analysis, the column was maintained at 45°C and a 5 mM H_2SO_4 solution was used as mobile phase at a flowrate of 0.6 mL min^{-1}. HPLC data were processed using the Chromeleon 7.1.3 software (Thermo Fisher Scientific), and compound concentrations

were calculated from peak areas using calibration curves with six different standard concentrations covering the range from 0 to 250 mM.

5.4.8 Semi-quantitative proteomics by mass spectrometry (MS)

Pseudomonas putida strains were pre-cultured overnight in de Bont minimal medium supplemented with 20 mM potassium acetate. Experimental cultures were done in flasks containing de Bont minimal medium with 100 mM potassium acetate inoculated at an initial OD_{600} of 0.1. Samples were taken in the mid-log phase, and the cells were harvested by centrifugation at 10,000 *g* for 5 minutes at 4°C. Then, the supernatant was removed and the cell pellet were frozen at −80°C until the processing of samples. Samples were desalted and isolated using a variation of a previously-described chloroform/methanol extraction protocol (Flügge and Wessel, 1984). Cell pellets were first thawed at 4°C and resuspended in 100 μL HPLC water. Then, 400 μL of HPLC grade methanol, 100 μL of HPLC grade chloroform, 300 μL of HPLC grade water were added to each sample in sequential order with thorough vortexing after each addition. Later, samples were centrifuged for 60 sec at ~21,000 g to promote phase separation. The top layer (water and methanol) was discarded by centrifugation leaving on the protein pellet the chloroform layer remaining. Additional 300 μL of HPLC grade methanol was added, the samples were vortexed and centrifuged for 2 min at ~21,000 *g*. The remaining liquid was discarded and the cell pellets were dried in a fume hood for 5 min. Then, protein pellets were resuspended in freshly-prepared 100 mM ammonium bicarbonate buffer in HPLC water containing 20% (v v^{-1}) methanol HPLC grade.

Protein concentrations in the resuspended samples were quantified using a DC Protein Assay Kit (Bio-Rad Laboratories, Hercules, CA). In total, 100 μg of protein was transferred to a PCR strip and tris(2-carboxyethyl)phosphine (TCEP) was added until a final concentration of 5 mM. Samples were incubated at 22°C for 30 min and; subsequently, iodoacetamide (IAA) was added until a final concentration of 10 mM. Again, samples were incubated at 22°C in the dark for 30 min. Finally, trypsin was added to a final ratio of 1:25 w w^{-1} trypsin:sample, and samples were incubated at 37°C

for 5–8 h in order to digest the proteins prior being placed into a conical LC vials for LC-MS analysis.

For shotgun proteomic experiments, peptides were analyzed by using an Agilent 6550 iFunnel Q-TOF mass spectrometer (Agilent Technologies, Santa Clara, CA) coupled to an Agilent 1290 UHPLC system as described previously (González Fernández-Niño, et al., 2015). 20 μg of peptides were separated on a Sigma–Aldrich Ascentis Peptides ES-C18 column (2.1 mm × 100 mm, 2.7 μm particle size, operated at 60°C) at a 0.400 mL min^{-1} flow rate and eluted using following gradient: 98% solvent A (0.1% formic acid v v^{-1}) and 2% solvent B (99.9% v v^{-1} acetonitrile, 0.1% formic acid v v^{-1}). Solvent B was increased to 35% over 30 min, and then increased to 80% over 2 min, then was constant for 6 min, followed by a ramp back down to 2% Solvent B over 1 min where it was kept constant for 4 min in order to re-equilibrate the column to original conditions.

Peptides were introduced to the mass spectrometer from the LC by using a Jet Stream source (Agilent Technologies) operating in positive-ion mode (3500 V). Source parameters employed gas temp (250 C), drying gas (14 L min^{-1}), nebulizer (35 psig), sheath gas temp (250°C), sheath gas flow (11 L min^{-1}), VCap (3500 V), fragmentor (180 V), OCT 1 RF Vpp (750 V). Agilent MassHunter Workstation Software was used to acquire the data, LC/MS Data Acquisition B.06.01 operating in Auto MS/MS mode whereby the 20 most intense ions (charge states, 2–5) within 300–1400 m/z mass range above a threshold of 1500 counts were selected for MS/MS analysis. The quadrupole was set to "Medium" resolution in order to collect MS/MS spectra (100–1700 m/z) and were acquired until 45,000 total counts were collected or for a maximum accumulation time of 333 ms. Former parent ions were excluded for 0.1 min following MS/MS acquisition. The acquired data were exported as .mgf files and searched against the latest *Pseudomonas putida* KT2440 protein database with Mascot search engine version 2.3.02 (Matrix Science). The resulting search results were filtered and analyzed by Scaffold v 4.3.0 (Proteome Software Inc.).

5.4.9 Statistical analysis of proteomics data

The data from proteomics was examined using a customized R script in RStudio (version 1.3.1093), which was developed as part of the thesis. Only proteins that were detected in all samples were considered. The abundance values were normalized using quantile normalization through the R-package *qsmooth*. A Student's t-test was then conducted using the built-in *dt()* function. The data was $\log_2$-transformed for fold-change comparison between groups, and volcano plots were generated using VolcaNoseR online tool (Goedhart and Luijsterburg, 2020). Proteins that showed a $\log_2$-fold change of 1.0 in abundance and a –log10(*adj. p-value*) more than or equal to 1.0 were considered to be differentially expressed.

5.4.10 ^{13}C metabolic flux analysis using labeled acetate

Pre-cultures were initially inoculated with a loop of freshly plated evolved, double mutant *P. putida* SEM1.4 *uvrY*^{E197K} *fabB*^{L77P} and reduced genome SEM1.4 strains in de Bont minimal medium supplemented with 20 mM non-labeled potassium acetate and 5 g L^{-1} MOPS. Prior inoculation into the experimental culture, cells were centrifuged at 10,000 *g* for 5 min and washed twice using de Bont minimal medium without carbon source. Then, cells were separately inoculated with an initial OD_{600} of 0.02 in 100 mL shaken flask containing 20 mL of de Bont medium with 100 mM of the following labeled carbon sources: 99% [1–^{13}C] sodium acetate or [2–^{13}C] sodium acetate or a molar 1:1 mixture of [U-$^{13}C_2$] sodium acetate. The inoculum level of the cultures with ^{13}C-labeled tracer was kept below 1% (initial OD of <0.02) of the final sampled cell concentration. This was done to exclude potential interference of non-labeled inoculum with subsequent calculations of flux (Wittmann, 2007). All experiments were performed in two biological replicates and two technical replicates, and samples were harvested once the cultures reached OD_{600}~2.0 for the analysis of either proteinogenic amino acids or cellular sugars. The samples were centrifuged at 10,000 *g* for 5 min, the supernatant was removed and the pellet was frozen at -80°C until further processing.

5.4.11 GC-MS labeling analysis of proteinogenic aminoacids

Pellets were thawed on ice at 4°C and re-suspended in 200 μL of 6 M HCl and incubated at 105°C for 16-24 hours in order to hydrolyze the biomass (Zamboni, et al., 2009). Hydrolyzed samples were then filtered on a 96-filter plate (MultiScreenHTS, HV Filter Plate 0.45 μm, hydrophilic, clear, non-sterile, Millipore, Catalogue number MSHVN45) by centrifugation at 1,500 *g* for 2 min and were freeze dried and stored at –80ºC. Then, dried samples were derivatized in a two-step reaction: 1) by re-suspending the hydrolysate with 50 μL dimethylformamide (DMF) until it turns brownish and; 2) by adding the previous solution into a glass vial with 50 μL of N-tertbutyldimethylsilyl-N-methyltrifluoroacetamide with 1% (wt wt^{-1}) tertbutyldimethyl-chlorosilane (TBDMSTFA) and incubating it at 85°C for 1 hour. The derivatized samples were aliquoted in glass vials with inlets for GC-MS analysis within 12 h from derivatization. The samples were injected on a Agilent 7890A GC-MS system with an Agilent HP-5ms capillary column (30m, inner diameter of 0.25 mm, film thickness of 0.25 μm). Samples were measured in full-scan mode with the following gradient: start at 120°C, hold for 1 min (Initial step); ramp to 160°C at 4°C min^{-1}, hold for 5 min (Ramp 1); ramp to 270°C at 4°C min^{-1}, hold for 3 min (Ramp 2); ramp to 310°C at 20°C min^{-1} (Ramp 3), hold for 1 min and; ramp to 120°C at 60°C min^{-1} (Ramp 4).

5.4.12 GC-MS labeling analysis of sugar monomers

For cellular monomers analysis (glucose and glucosamine) pellets were hydrolyzed in 250 μL 2M HCl for 2 h at 100°C (Kiefer, et al., 2004). Next, cell debris was removed by filtration using a 96-filter plate (MultiScreenHTS, HV Filter Plate 0.45 μm, hydrophilic, clear, non-sterile, Millipore, Catalogue number MSHVN45). Subsequently, the hydrolysate were freeze dried and stored at –80ºC. Analytes contained in the dried residue were incubated in 100 μL methoxylamine 2 % m v^{-1} in pyridine at 80 °C for 1 h. The obtained O-methyl oxime forms of the analytes were silylated at 80 °C for 30 min into trimethylsilyl (TMS) derivatives in a second step using N,O-bis-trimethylsilyl-trifluoroacetamide (BSTFA, Macherey-Nagel). The derivatized analytes were quantified by GC-MS using an Agilent 7890A GC-MS system with an Agilent HP-5ms capillary column (30m, inner diameter of 0.25 mm, film thickness of 0.25 μm).

Samples were measured in full-scan mode with the following gradient: start at 120°C, hold for 2 min (Initial step); ramp to 280°C at 10°C min^{-1}, hold for 12 min (Ramp 1) and; ramp to 300°C at 10°C min^{-1}, hold for 0 min (Ramp 2).

5.4.13 GC-MS chromatographic data analysis

Raw chromatographic data was integrated using SmartPeak (Kutuzova S. et al., 2020). Processed data was further corrected for the natural abundance of isotopes in the derivatization agents used for GC-MS analysis using INCA software (Young, 2014). Altogether, 14 amino acids yielded ion clusters with clean mass isotopomer distributions (MIDs), which were considered as inputs for flux estimation: alanine (m/z 232, m/z 260), aspartate (m/z 302, m/z 390, m/z 418), glutamate (m/z 330, m/z 432), glycine (m/z 218, m/z 246), histidine (m/z 338, m/z 440), isoleucine (m/z 274), leucine (m/z 274), lysine (m/z 329, m/z 431), methionine (m/z 218, m/z 320), phenylalanine (m/z 302, m/z 308, m/z 336), proline (m/z 258), serine (m/z 362, m/z 390), threonine (m/z 376, m/z 404), tyrosine (m/z 302) and valine (m/z 260, m/z 288). These fragments have been previously demonstrated to be suitable for ^{13}C metabolic flux analysis in *Pseudomonas spp.* (Kohlstedt and Wittmann, 2019)Glutamate and aspartate also reflected the pools of glutamine and asparagine, which underwent deamination during protein hydrolysis. The proteinogenic amino acids cysteine and tryptophan were not detected due to their degradation in the hydrolysis process (Wittmann, 2007). For sugar analysis, the fragments considered for ^{13}C–MFA were: glucose (m/z 319, m/z 554) and glucosamine (m/z 319, m/z 553) as previously reported (Kohlstedt and Wittmann, 2019).

5.4.14 Reaction network and computational design for flux estimation

The metabolic networks of *Pseudomonas putida* SEM1.4 strains were built based on the most recent genome-scale metabolic model (Nogales, et al., 2020). In total, 72 reactions were included as part of the central carbon metabolism. All included reactions, as well as the carbon atom transitions, are listed in **Table S4**. The INCA software package was utilized for 13C-metabolic flux analysis (^{13}C-MFA) (Young, 2014). Specific growth rates, and uptake or secretion rates for acetate were used to constrain the MFA model.

The biomass equation was taken from (Czajka, et al., 2022). To estimate the relative intracellular fluxes, a weighted sum-of-squared-residuals (SSR) was minimized through iterative analysis of simulated and experimental labeling data for various molecules, including proteinogenic amino acids, extracellular sugars and sugar acids, glycogen, and glucosamine. . To ensure the most accurate results, the flux estimation was repeated at least 20 times with random initial values until convergence. To assess the goodness-of-fit, a $\chi 2$ test was applied, and precise 95% confidence intervals were calculated by determining the sensitivity of the sum of squared residuals to flux parameter variations (Antoniewicz, et al., 2006). The resulting flux results, including best fits, standard deviations, and upper and lower bounds of the 95% confidence intervals for all fluxes, can be found in **Table S4**. To visualize the flux distributions of different strains, computed flux values were mapped onto custom metabolic maps using the R package *fluctuator*.

5.4.15 Alphafold prediction and structure characterization

The 3D structure prediction of GacA were created with AlphaFold 2.0 with default settings (Jumper, et al., 2021). The tertiary structure fold of the 5 highest ranking predictions were analysed and validated with Local Distance Difference Test (lDDT), SPServer (Aguirre-Plans, et al., 2021) and ProSa-Web (Wiederstein and Sippl, 2007). Visualization, superimposition analysis and mutagenesis were performed with PyMOL v.2.3.4 [The PyMOL Molecular Graphics System, Version 2.3.4 Schrödinger, LLC.].

Original sequences were obtained from *Pseudomonas* Database (Winsor, et al., 2016) and protein homologs investigation was performed and analysed with AlphaFold's templates search algorithm in PDB, NCBI BLASTP (https://www.ncbi.nlm.nih.gov/), InterPro server (Paysan-Lafosse, et al., 2022) and with JalView v2.11 (Waterhouse, et al., 2009).

5.5 Supplementary Material

Table S5.1. Differentially expressed protein in SEM1.4^{evo} against Wild-type strain. The table shows protein ID (PP_number or protein name), protein description and Log$_2$(fold-change).

Protein ID	Protein description	Log$_2$(fold-change)
	SEM1.4^{evo} Vs Wild-type	
Pp_0861	Outer membrane ferric siderophore receptor	9.15
Ppsd	Non-ribosomal siderophore peptide synthetase	9.10
Pp_0371 (RsmY)	Transcriptional regulator, LysR family	8.55
Metn1	Methionine import ATP-binding protein MetN 1	8.50
Pp_2314	Class I SAM-dependent methyltransferase	8.20
Pp_4243	Pyoverdine synthetase (PvdL)	8.11
Pp_4221	Non-ribosomal peptide synthetase (PvdI)	7.31
Cysz	Sulfate transporter CysZ	7.26
Pp_3796	L-ornithine N5-oxygenase (PvdA)	6.13
Pp_3179	Transcriptional regulator, LysR family	4.18
Pp_4223	Diaminobutyrate-2-oxoglutarate transaminase	3.31
Pp_4421	Aminotransferase, class III	3.28
Pp_0154	Propionyl-CoA:succinate CoA transferase	2.08
Pp_0566	Translation initiation factor SUI1 (yciH)	1.72
Mmsa-1	Methylmalonate-semialdehyde dehydrogenase	1.68
Succ	Succinyl-CoA ligase [ADP-forming] subunit beta	1.48
Sucd	Succinyl-CoA ligase [ADP-forming] subunit alpha	1.39
Fpva	Outer membrane ferripyoverdine receptor	1.39
Pp_1078	ABC transporter, ATP-binding protein, putative (Iron transporter)	1.21
Ndh	NADH dehydrogenase	1.19
Pp_2474	Glutathione S-transferase family protein	1.19
Exbb	Ferric siderophore transport system protein ExbB	1.08
Waap	Lipopolysaccharide core heptose(I) kinase	1.00
Pp_3091	ImcF-like family protein	-15.03
Proc-1	Pyrroline-5-carboxylate reductase	-13.93
Pp_3775	Sarcosine oxidase, putative	-13.35
Pp_1661	Dehydrogenase subunit, putative	-13.13
Pp_3090	OmpA domain protein	-13.09
Pp_3088	ImpA_N domain-containing protein	-13.00
Pp_3777	Methyltranfer_dom domain-containing protein	-12.96
Pp_3094	Type VI secretion system lipoprotein TssJ	-12.94
Pp_1246	Conserved domain protein	-12.89
Pp_1659	Cytochrome C	-12.54

Pp_5395	BpsA_C domain-containing protein	-12.32
Pp_3784	Conserved domain protein (Endoribonuclease L-PSP)	-12.22
Pp_3781	Oxygen-independent Coproporphyrinogen III oxidase family protein	-12.11
Pp_3092	DotU domain-containing protein	-11.96
Pp_3108	Rhs-related protein (Related to secretion system)	-11.73
Pp_3097	ImpG (Type VI secretion system baseplate subunit TssF)	-11.53
Pp_4834	SPFH domain/Band 7 family protein	-11.44
Pp_3100	Type VI secretion system contractile sheath small subunit	-10.99
Pp_3611	Exported protein	-10.87
Pp_3691	DNA helicase-related protein	-10.80
Pp_1245	SH3b domain-containing protein	-10.72
Pp_1795	DUF4438 domain-containing protein	-10.69
Glgb	1,4-alpha-glucan branching enzyme GlgB	-10.62
Pp_0570	Extracellular protein, putative (Alpha-2-macroglobulin)	-10.55
Pp_4669	OmpA family protein (Related to cell turgor maintenance (Chevalier et al., 2017) and acting as non-specific transporters of ionic species (Nestorovich et al., 2006)	-10.53
Pp_3786	Aminotransferase	-9.84
Pp_1502	OmpA family protein	-9.79
Malq	4-alpha-glucanotransferase	-9.72
Pp_3638	Acyl-CoA dehydrogenase, putative	-9.57
Pp_2536	Glutathione S-transferase family protein	-9.55
Glpe	Thiosulfate sulfurtransferase GlpE	-9.48
Pp_0824	Phosphate ABC transporter, periplasmic phosphate-binding protein, putative	-9.43
Pp_2007	P-47-related protein	-9.37
Pp_1726	ABC transporter, periplasmic binding protein	-9.36
Eco (Pp_3072)	Ecotin	-9.24
Pp_4053	Glycosyl hydrolase, putative (Maltooligosyl trehalose synthase, TreY)	-9.22
Pp_4981	UPF0312 protein PP_4981	-9.13
Glga	Glycogen synthase	-9.10
Pp_1790	Acylneuraminate cytidylyltransferase, putative	-8.96
Pp_3680	Uncharacterized protein (ATP-dependent endonuclease)	-8.86
Pp_4939	Glycosyltransferase family 2 protein	-8.82
Rnk	Nucleoside diphosphate kinase regulator	-8.72
Pp_3087	Excinuclease ABC, A subunit, putative	-8.68
Pp_1793	Glycosyl transferase, group 2 family protein	-8.67
Ppra	Alginate biosynthesis protein PprA	-8.59
Pp_2853	Uncharacterized protein (Transporter)	-8.52
Pp_0203	Tabtoxinine-beta-lactam limiting dipeptidase, putative	-8.50

Pp_3785	Uncharacterized protein (related to Non-hame Fe2+, alpha-ketoglutarate-dependent halogenase; Syringomycin biosynthesis enzyme 2)	-8.35
Pp_3788	Non-ribosomal peptide synthetase, putative	-8.33
Hisi	Phosphoribosyl-AMP cyclohydrolase	-8.29
Pp_1660	Uncharacterized protein (related to the putitive cluster dehydrogenase)	-8.27
Pp_3127	Exopolysaccharide transport protein, putative	-8.19
Sela	L-seryl-tRNA(Sec) selenium transferase	-8.19
Glge	Alpha-1,4-glucan:maltose-1-phosphate maltosyltransferase	-7.99
Pp_3099	Uncharacterized protein (Uricase/urate oxidase)	-7.83
Pp_1663	Uncharacterized protein (Dehydrogenase)	-7.82
Pp_3822	Cytochrome c family protein	-7.72
Pp_4938	Glycosyl transferase, putative	-7.62
Pp_1510	Carboxyvinyl-carboxyphosphonate phosphorylmutase, putative	-7.54
Pp_4100	Transcriptional regulator, Cro/CI family	-7.23
Pp_4051	Malto-oligosyltrehalose trehalohydrolase	-7.21
Pp_2258	Sensory box protein	-7.18
Coae	Dephospho-CoA kinase	-7.16
Pp_4448	Uncharacterized protein (Helicase HerA central domain-containing protein)	-7.00
Pp_3128	Exopolysaccharide biosynthesis/transport protein, putative	-6.99
Dapf-1	Diaminopimelate epimerase	-6.76
Pp_2629	Uncharacterized protein (Not found in UniProt)	-6.28
Pp_0765	Uncharacterized protein (Adhesin)	-6.07
Pp_3095	Chaperone-associated ATPase, putative	-6.03
Mety	O-acetylhomoserine sulfhydrylase	-5.82
Pp_3988	Uncharacterized protein (related to DNA)	-5.01
Pp_1791	Aldolase/synthase, putative	-4.60
Pp_0766	Uncharacterized protein (DUF1329 domain-containing protein)	-4.08
Pp_0258	LysM domain protein	-3.93
Algc	Phosphomannomutase/phosphoglucomutase	-3.90
Pp_1893	Acyl-CoA dehydrogenase, putative (FadE) a long-chain 2,3-saturated fatty acyl-CoA + H+ + oxidized [electron-transfer flavoprotein] = a long-chain (2E)-enoyl-CoA + reduced [electron-transfer flavoprotein]	-3.90
Pp_1230	Uncharacterized protein (DUF945 domain-containing protein)	-3.77
Mine	Cell division topological specificity factor	-3.58
Pp_5365	Cyclopropane-fatty-acyl-phospholipid synthase, putative	-3.30
Acna	Aconitate hydratase	-3.20

Rmla	Glucose-1-phosphate thymidylyltransferase	-3.17
Pp_3106	Uncharacterized protein (Gp5/Type VI secretion system Vgr protein OB-fold domain-containing protein)	-3.13
Pp_0397	Uncharacterized protein (Protein kinase YeaG)	-3.13
Pp_1786	Glycosyl transferase, putative	-2.99
Ohr	Organic hydroperoxide resistance protein	-2.84
Pp_2132	Universal stress protein	-2.83
Pp_0396	UPF0229 protein PP_0396	-2.76
Pp_5182	Aminotransferase, class III	-2.75
Tolc	Agglutination protein	-2.69
Hupb	DNA-binding protein HU-beta	-2.66
Icd	Isocitrate dehydrogenase [NADP]	-2.63
Biod	ATP-dependent dethiobiotin synthetase BioD	-2.62
Glgp	Alpha-1,4 glucan phosphorylase	-2.60
Pp_3089	Uncharacterized protein (Type VI secretion system tube protein Hcp)	-2.45
Fumc	Fumarate hydratase class II	-2.42
Tpx	Probable thiol peroxidase	-2.40
Pp_0886	Uncharacterized protein (DUF541 domain-containing protein)	-2.38
Pp_0893	ThiJ/PfpI family protein	-2.36
Pp_5156	Uncharacterized protein (DUF4399 domain-containing protein)	-2.29
Pp_1071	Amino acid ABC transporter, periplasmic amino acid-binding protein	-2.16
Pp_5303	Endoribonuclease	-2.13
Pp_1752	Uncharacterized protein (Polyphosphate kinase-2-related domain-containing protein)	-2.12
Pp_4802	UPF0250 protein PP_4802	-2.12
Pp_0679	Uncharacterized protein DUF	-2.11
Pp_2648	Universal stress protein family	-2.11
Ansb	Glutaminase-asparaginase	-2.09
Pp_1908	Peptidase, putative	-2.09
Rpos	RNA polymerase sigma factor RpoS	-2.04
Gcd	Glucose dehydrogenase (Pyrroloquinoline-quinone)	-2.01
Pp_4570	Uncharacterized protein	-1.97
Glnd	Bifunctional uridylyltransferase/uridylyl-removing enzyme	-1.93
Pp_0859	Carbon-nitrogen hydrolase family protein	-1.89
Pp_2105	Uncharacterized protein (Aspartyl/asparaginy/proline hydroxylase domain-containing protein)	-1.85
Pp_3754	Beta-ketothiolase	-1.84
Phop	Transcriptional regulatory protein PhoP	-1.82
Pp_5234	Nitrogen regulatory protein P-II	-1.75
Trx-2	Thioredoxin	-1.71

Pp_0370	Acyl-CoA dehydrogenase family protein (Related to FadB)	-1.70
Acpp	Acyl carrier protein	-1.70
Pp_0541	Acetyltransferase, GNAT family	-1.69
Efp	Elongation factor P	-1.69
Ppib	Peptidyl-prolyl cis-trans isomerase	-1.69
Pp_2189	Uncharacterized protein (DUF)	-1.65
Dksa	RNA polymerase-binding transcription factor DksA	-1.64
Pp_4067 (MmcA)	Acetyl-CoA carboxylase, biotin carboxylase, putative (Methylcrotonyl-CoA carboxylase biotin-containing subunit alpha)	-1.56
Anr	Transcriptional regulator Anr	-1.52
Pp_1695	Sodium-solute symporter/sensory box histidine kinase/response regulator, putative	-1.51
Pp_0368	Acyl-CoA dehydrogenase, putative (Related to FadB)	-1.49
Pp_1056	Iron-chelator utilization protein, putative	-1.48
Ppc	Phosphoenolpyruvate carboxylase	-1.43
Pp_1488	Methyl-accepting chemotaxis transducer	-1.41
Pp_4034	N-carbamoyl-beta-alanine amidohydrolase, putative	-1.39
Acsa1	Acetyl-coenzyme A synthetase 1	-1.38
Cspa-2	Cold shock protein CspA	-1.35
Hpf	Ribosome hibernation promoting factor	-1.33
FabB	3-oxoacyl-(Acyl-carrier-protein) synthase I	-1.32
Csta	Carbon starvation protein CstA	-1.29
Pp_0985	Cold-shock domain family protein	-1.28
Katg	Catalase-peroxidase	-1.28
Mind	Site-determining protein	-1.28
Rmlb	dTDP-glucose 4,6-dehydratase	-1.27
Pp_1478	Xenobiotic reductase, putative	-1.26
Oprq	Outer membrane protein OprE3	-1.25
Ivd	Isovaleryl-CoA dehydrogenase	-1.22
Pp_0545	Aldehyde dehydrogenase family protein	-1.22
Ompr-1	DNA-binding response regulator OmpR	-1.21
Pp_1481	Betaine aldehyde dehydrogenase, putative	-1.20
Pp_0086	Uncharacterized protein	-1.20
Pp_2806	Transcriptional regulator, TetR family	-1.18
Mmsb	3-hydroxyisobutyrate dehydrogenase	-1.16
Pp_5309	Transcriptional regulator, LysR family	-1.16
Pp_1787	Uncharacterized protein (Oxidative and nitrosative stress transcriptional dual regulator, OxyR)	-1.10
Fadb1x	Enoyl-CoA hydratase/isomerase FadB1x	-1.09
Fadax	3-ketoacyl-CoA thiolase	-1.03
Glmu	Bifunctional protein GlmU	-1.03
Pp_4760	Alcohol dehydrogenase, zinc-containing	-1.03
Pp_1993	Uncharacterized protein (Putative motility protein fimV)	-1.01

Table S5.2. Differentially expressed protein in double mutant *gacA fabB* against Wild-type strain. The table shows protein ID (PP_number or protein name), protein description and Log_2(fold-change).

Protein	Protein description	Log_2(fold change)
	***gacA fabB* Vs Wild-type**	
Ppsd	Non-ribosomal siderophore peptide synthetase	9.83
Pp_0861	Outer membrane ferric siderophore receptor	9.36
Pp_4243	Pyoverdine synthetase	8.71
Pp_4213	Dipeptidase, putative	8.62
Pp_4245	Siderophore biosynthesis protein, putative	8.38
Pp_3612	TonB-dependent receptor, putative	8.24
Metn1	Methionine import ATP-binding protein MetN 1	8.16
Pp_3553	AMP-binding domain protein	7.87
Cysz	Sulfate transporter CysZ	7.77
Arop	Aromatic amino acid transporter	7.76
Pp_3796	L-ornithine N5-oxygenase	7.68
Pp_4214	Aminotransferase, class V	7.58
Pp_0860	Sulfite reductase, flavoprotein component, putative	7.29
Pp_1125	Helicase, putative	7.28
Pp_4221	Non-ribosomal peptide synthetase	7.15
Pp_4422	Succinate-semialdehyde dehydrogenase, putative	6.97
Pp_3599	5-dehydro-4-deoxyglucarate dehydratase	6.84
Pp_0867	FecA-like outer membrane receptor	6.70
Pp_1067	Histidine kinase	6.42
Pp_0862	PKHD-type hydroxylase PP_0862	6.26
Pp_3179	Transcriptional regulator, LysR family	4.76
Pp_4421	Aminotransferase, class III	2.34
Exbd	Ferric siderophore transport system, inner membrane protein ExbD	1.67
Ndh	NADH dehydrogenase	1.64
Pp_0566	Translation initiation factor SUI1	1.61
Fpva	Outer membrane ferripyoverdine receptor	1.56
Exbb	Ferric siderophore transport system protein ExbB	1.51
Pp_1078	ABC transporter, ATP-binding protein, putative	1.26
Prfc	Peptide chain release factor 3	1.02
Pp_3091	Uncharacterized protein (Imv protein, related to secretion)	-15.03
Proc-1	Pyrroline-5-carboxylate reductase	-13.93
Pp_3775	Sarcosine oxidase, putative	-13.35
Pp_1661	Dehydrogenase subunit, putative	-13.13
Pp_3777	Methyltranfer_dom domain-containing protein	-12.96
Pp_1246	Conserved domain protein	-12.89
Pp_1659	Cytochrome C	-12.54

Pp_5395	BpsA_C domain-containing protein (N(4)-bis(aminopropyl)spermidine synthase C-terminal domain-containing protein)	-12.32
Pp_3784	Conserved domain protein	-12.22
Pp_3781	Oxygen-independent Coproporphyrinogen III oxidase family protein	-12.11
Pp_3092	DotU domain-containing protein	-12.01
Pp_3783	Syringomycin biosynthesis enzyme 2, syrB	-11.64
Pp_3097	ImpG (Type VI secretion system baseplate subunit TssF)	-11.53
Pp_3094	Type VI secretion system lipoprotein TssJ	-11.52
Pp_4834	SPFH domain/Band 7 family protein	-11.44
Pp_1245	SH3b domain-containing protein	-10.72
Pp_3096	Type VI secretion system baseplate subunit TssG	-10.13
Pp_3786	Aminotransferase	-9.84
Malq	4-alpha-glucanotransferase	-9.72
Pp_2166	Anti-anti-sigma factor	-9.60
Pp_3638	Acyl-CoA dehydrogenase, putative	-9.57
Pp_1821	Glutathione S-transferase family protein	-9.37
Pp_2007	P-47-related protein	-9.37
Pp_1726	ABC transporter, periplasmic binding protein	-9.36
Eco	Ecotin	-9.24
Ssud	Alkanesulfonate monooxygenase	-9.15
Glga	Glycogen synthase	-9.10
Pp_1790	Acylneuraminate cytidylyltransferase, putative	-8.96
Pp_3680	Uncharacterized protein (atp-dependent endonuclease)	-8.86
Rhda-2	Sulfurtransferase	-8.80
Rnk	Nucleoside diphosphate kinase regulator	-8.72
Pp_3087	Excinuclease ABC, A subunit, putative	-8.68
Pp_1793	Glycosyl transferase, group 2 family protein	-8.67
Pp_0586	Heavy metal translocating P-type ATPase	-8.57
Pp_2853	Uncharacterized protein (Transporter)	-8.52
Pp_0203	Tabtoxinine-beta-lactam limiting dipeptidase, putative	-8.50
Pp_2536	Glutathione S-transferase family protein	-8.37
Pp_3785	Uncharacterized protein (related toNon-haem fe2+, alpha-ketoglutarate-dependent halogenase; Syringomycin biosynthesis enzyme 2;)	-8.35
Pp_3788	Non-ribosomal peptide synthetase, putative	-8.33
Pp_1660	Uncharacterized protein (related to the putitive cluster dehydrogenase)	-8.27
Ssuf	Organosulfonate utilization protein SsuF	-8.19
Pp_0142	ABC transporter, permease protein, putative	-8.11
Glge	Alpha-1,4-glucan:maltose-1-phosphate maltosyltransferase	-7.99
Wbpz	Glycosyl transferase WbpZ	-7.82
Pp_3822	Cytochrome c family protein	-7.72

Pp_0570	Extracellular protein, putative	-7.71
Pp_4100	Transcriptional regulator, Cro/CI family	-7.23
Pp_4051	Malto-oligosyltrehalose trehalohydrolase	-7.21
Pp_2258	Sensory box protein	-7.18
Pp_3128	Exopolysaccharide biosynthesis/transport protein, putative	-6.99
GacA	DNA-binding response regulator GacA	-6.97
Dapf-1	Diaminopimelate epimerase	-6.76
Pp_3108	Rhs-related protein	-6.45
Pp_3100	Type VI secretion system contractile sheath small subunit	-6.21
Mety	O-acetylhomoserine sulfhydrylase	-5.86
Pp_3093	Type VI secretion system baseplate subunit TssK	-5.71
Pp_3691	DNA helicase-related protein	-5.00
Pp_3095	Chaperone-associated ATPase, putative	-4.79
Pp_0258	LysM domain protein	-4.75
Pp_3761	Sensor histidine kinase/response regulator	-4.61
Pp_4054	Uncharacterized protein (DUF)	-4.40
Pp_1893	Acyl-CoA dehydrogenase, putative (FadE) a long-chain 2,3-saturated fatty acyl-CoA + H+ + oxidized [electron-transfer flavoprotein] = a long-chain (2E)-enoyl-CoA + reduced [electron-transfer flavoprotein]	-4.31
Pp_3988	Uncharacterized protein (related to DNA)	-4.26
Pp_0765	Uncharacterized protein (Adhesin)	-4.12
Pp_4981	UPF0312 protein PP_4981	-3.55
Trpc	Indole-3-glycerol phosphate synthase	-3.40
Pp_1230	Uncharacterized protein DUF	-3.33
Pp_1791	Aldolase/synthase, putative	-2.88
Pp_0766	Uncharacterized protein DUF	-2.87
Pp_0428	HIT family protein	-2.87
Pp_1786	Glycosyl transferase, putative	-2.86
Csra	Carbon storage regulator homolog	-2.45
Rmla	Glucose-1-phosphate thymidylyltransferase	-2.42
Pp_1314	Oxidoreductase, aldo/keto reductase family	-2.30
Tolc	Agglutination protein	-2.30
Pp_0165	GGDEF domain protein	-2.24
Pp_4138	Chromate reductase	-2.13
Pp_0396	UPF0229 protein PP_0396	-2.12
Pp_2648	Universal stress protein family	-2.10
Pp_5156	Uncharacterized protein DUF	-2.03
Pp_0893	ThiJ/PfpI family protein	-2.02
Pp_3089	Uncharacterized protein (Type VI secretion system tube protein Hcp)	-2.01
Fumc	Fumarate hydratase class II	-1.97
Pp_1752	(Polyphosphate kinase-2-related domain-containing protein)	-1.90

Ppic-2	Peptidyl-prolyl cis-trans isomerase C	-1.89
Ohr	Organic hydroperoxide resistance protein	-1.88
Cmk	Cytidylate kinase	-1.81
Pp_0679	Uncharacterized protein DUF	-1.81
Sodb	Superoxide dismutase [Fe]	-1.80
Pp_0397	Uncharacterized protein (Protein kinase YeaG)	-1.75
Pp_5234	Nitrogen regulatory protein P-II	-1.68
Pp_5303	Endoribonuclease	-1.68
Brac	Branched-chain amino acid ABC transporter, periplasmic amino acid-binding protein	-1.66
Pp_2105	(Aspartyl/asparaginy/proline hydroxylase domain-containing protein)	-1.66
Trpa	Tryptophan synthase alpha chain	-1.58
Rpos	RNA polymerase sigma factor RpoS	-1.53
Pp_0202	CBS domain protein	-1.53
Pp_3754	Beta-ketothiolase	-1.49
Pp_2189	Uncharacterized protein (DUF)	-1.46
Pp_5365	Cyclopropane-fatty-acyl-phospholipid synthase, putative	-1.42
Phop	Transcriptional regulatory protein PhoP	-1.36
Tpx	Probable thiol peroxidase	-1.33
Anr	Transcriptional regulator Anr	-1.33
Adk	Adenylate kinase	-1.32
Pp_0592	Oxidoreductase, short chain dehydrogenase/reductase family	-1.31
Efp	Elongation factor P	-1.30
Trx-2	Thioredoxin	-1.29
Acpp	Acyl carrier protein	-1.26
Pp_0985	Cold-shock domain family protein	-1.25
Pp_0545	Aldehyde dehydrogenase family protein	-1.21
Pp_1056	Iron-chelator utilization protein, putative	-1.20
Pp_1895	ABC transporter, ATP-binding protein	-1.20
Rmld	dTDP-4-dehydrorhamnose reductase	-1.18
Ppib	Peptidyl-prolyl cis-trans isomerase	-1.14
Pp_1787	Uncharacterized protein (Oxidative and nitrosative stress transcriptional dual regulator, OxyR)	-1.05
Pp_1291	PhoH family protein	-1.03
Pp_1478	Xenobiotic reductase, putative	-1.02
Gnd	6-phosphogluconate dehydrogenase	-1.01

Table S5.3. Differentially expressed protein in double mutant *gacA fabB* against SEM1.4^{evo} strain. The table shows protein ID (PP_number or protein name), protein description and Log$_2$(fold-change).

Protein	Protein description	Log$_2$(fold change)
	***gacA fabB* Vs SEM1.4^{evo}**	
Pp_4939	Glycosyltransferase family 2 protein	**8.07**
Pp_4938	Glycosyl transferase, putative	**8.04**
Pp_3192	Transcriptional regulator DauR	**7.27**
Pp_3553	AMP-binding domain protein	**7.87**
Hupb	DNA-binding protein HU-beta	**2.67**
Acsa1	Acetyl-coenzyme A synthetase 1	**1.64**
Pp_5278	Aldehyde dehydrogenase family protein	**1.01**
Pp_5365	Cyclopropane-fatty-acyl-phospholipid synthase, putative	**1.88**
Pp_0154	Acetyl-CoA hydrolase/transferase family protein	**-1.41**
Succ	Succinyl-CoA ligase [ADP-forming] subunit beta	**-1.33**
Sucd	Succinyl-CoA ligase [ADP-forming] subunit alpha	**-1.29**

Table S5.4. Relative net fluxes determined by ^{13}C-MFA in the *Pseudomonas putida* SEM1.4 model. Relative mean values (%) are net fluxes relative to acetate uptake rate of 100% (uptake rates were estimated for each strain and those mean values are reported in Table 2). Mean parameter estimates and 95% confidence bounds using INCA's parameter continuation method are shown below for SEM1.4, SEM1.4 Evolved and SEM1.4 *uvrY*^{E197K} *fabB*^{L77P}.

Reaction ID	Equation	*Pseudomonas putida* SEM1.4				*Pseudomonas putida* SEM1.4 Evolved				*Pseudomonas putida* SEM1.4 *uvrY*^{E197K} *fabB*^{L77P}			
		Value (%)	SD	Lower bond	Upper bond	Value (%)	SD	Lower bond	Upper bond	Value (%)	SD	Lower bond	Upper bond
1	Ac.ext -> Ac	100.0	0.0	100.0	100.0	100.0	0.0	100.0	100.0	100.0	0.0	100.0	100.0
2	Ac + 2*ATP -> AcCoA	100.7	0.0	100.7	100.7	101.1	0.0	101.1	101.1	101.1	0.0	101.1	101.1
3	OAA + AcCoA -> Cit	71.3	0.4	70.9	71.6	76.6	0.0	76.5	76.6	77.4	0.2	77.3	77.4
4	Cit <-> ICit	71.3	0.4	70.9	71.6	76.6	0.0	76.5	76.6	77.4	0.2	77.3	77.4
5	ICit -> Suc + Glyox	33.7	0.3	33.2	34.2	44.8	0.3	44.3	45.3	45.1	0.3	44.7	45.6
6	Glyox + AcCoA -> Mal	33.7	0.3	33.2	34.2	44.8	0.3	44.3	45.3	45.1	0.3	44.7	45.6
7	ICit -> AKG + CO2 + NADPH	37.7	0.5	37.0	37.9	31.8	0.3	31.2	32.3	32.3	0.5	31.8	32.6
8	AKG -> SucCoA + CO2 + NADH	36.2	0.5	35.5	36.4	29.3	0.3	28.7	29.8	29.8	0.5	29.4	30.2
9	SucCoA <-> Suc + ATP	35.8	0.5	35.1	36.0	28.6	0.3	28.1	29.1	29.2	0.5	28.8	29.6
10	Suc -> Fum + FADH2	69.8	0.4	69.3	70.1	74.0	0.0	74.0	74.1	74.9	0.2	74.9	75.0
11	Fum <-> Mal	70.5	0.4	70.0	70.7	75.1	0.0	75.0	75.1	75.9	0.2	75.9	76.0
12	Mal -> OAA + FADH2	75.3	1.0	69.6	81.2	81.1	1.6	74.4	84.4	78.5	5.0	75.5	80.7
13	Pyr + CO2 + ATP -> OAA	17.2	2.5	12.3	26.8	8.8	2.9	4.5	14.9	9.5	6.0	7.9	13.4
14	Pyr -> AcCoA + CO2 + NADH	7.9	0.4	7.1	8.7	26.7	0.3	26.2	27.3	27.7	0.5	27.3	28.2
15	OAA -> Pyr + CO2	0.0	1.3	0.0	15.5	0.0	2.7	0.0	11.9	0.0	3.5	0.0	6.0
16	PEP + CO2 -> OAA	0.0	7.6	0.0	13.0	0.0	0.0	0.0	7.4	0.0	1.7	0.0	4.6
17	OAA + ATP -> PEP + CO2	18.6	5.2	18.3	34.5	9.6	2.7	9.5	19.0	7.0	4.1	6.9	13.1
18	Mal -> Pyr + CO2 + NADPH	28.8	1.0	22.7	34.5	38.7	1.4	35.8	43.8	42.5	5.0	40.7	45.9
19	G6P <-> F6P	-44.4	0.9	-45.8	-43.5	-1.0	0.1	-1.1	-0.9	-1.0	0.1	-1.1	-0.9
20	FBP -> F6P	15.4	0.4	15.1	16.0	1.5	0.1	1.4	1.6	1.7	0.2	1.6	1.8
21	FBP <-> DHAP + GAP	-15.4	0.4	-16.0	-15.1	-1.5	0.1	-1.6	-1.4	-1.7	0.2	-1.8	-1.6
22	DHAP <-> GAP	-15.4	0.4	-16.0	-15.1	-1.5	0.1	-1.6	-1.4	-1.7	0.2	-1.8	-1.6
23	GAP <-> 3PG + ATP + NADH	-16.6	0.4	-17.1	-16.3	-3.4	0.1	-3.5	-3.3	-3.5	0.2	-3.6	-3.4
24	3PG <-> PEP	-17.6	0.5	-18.1	-17.2	-5.4	0.1	-5.5	-5.2	-5.4	0.3	-5.5	-5.2
25	PEP -> Pyr + ATP	0.0	5.2	0.0	15.5	2.5	2.7	0.0	11.9	0.0	4.1	0.0	6.0
26	G6P -> 6PG + NADPH	44.2	0.9	43.3	45.6	0.6	0.1	0.5	0.7	0.6	0.1	0.5	0.8
27	6PG -> Ri5P + CO2 + NADPH	44.1	0.9	43.2	45.5	0.2	0.0	0.1	0.3	0.1	0.1	0.0	0.2
28	Ri5P <-> X5P	29.1	0.6	28.5	30.0	-0.4	0.0	-0.5	-0.4	-0.5	0.0	-0.6	-0.4
29	Ri5P <-> R5P	15.1	0.3	14.8	15.5	0.7	0.0	0.6	0.7	0.6	0.0	0.6	0.6
30	X5P <-> GAP + EC2	29.1	0.6	28.5	30.0	-0.4	0.0	-0.5	-0.4	-0.5	0.0	-0.6	-0.4
31	F6P <-> E4P + EC2	-14.3	0.3	-14.7	-14.0	0.7	0.0	0.6	0.7	0.7	0.0	0.6	0.7
32	S7P <-> R5P + EC2	-14.8	0.3	-15.3	-14.5	-0.2	0.0	-0.3	-0.2	-0.2	0.0	-0.2	-0.1
33	F6P <-> GAP + EC3	-14.8	0.3	-15.3	-14.5	-0.2	0.0	-0.3	-0.2	-0.2	0.0	-0.2	-0.1
34	S7P <-> E4P + EC3	14.8	0.3	14.5	15.3	0.2	0.0	0.2	0.3	0.2	0.0	0.1	0.2

35	6PG -> Pyr + GAP	**0.1**	0.2	0.0	0.2	**0.4**	0.1	0.3	0.5	**0.6**	0.2	0.5	0.7
36	AKG + NADPH + NH3 -> Glu	**8.8**	0.1	8.7	8.8	**14.3**	0.0	14.2	14.3	**13.8**	0.2	13.7	13.9
37	Glu + ATP + NH3 -> Gln	**1.1**	0.0	1.1	1.1	**1.7**	0.0	1.7	1.7	**1.7**	0.0	1.7	1.7
38	Glu + ATP + 2*NADPH -> Pro	**0.3**	0.0	0.3	0.3	**0.6**	0.0	0.6	0.6	**0.5**	0.0	0.5	0.5
39	Glu + CO2 + Gln + Asp + AcCoA + 5*ATP + NADPH -> Arg + AKG + Fum + Ac	**0.5**	0.0	0.5	0.5	**0.8**	0.0	0.8	0.8	**0.7**	0.0	0.7	0.7
40	OAA + Glu -> Asp + AKG	**2.6**	0.3	2.5	2.7	**3.7**	0.0	3.6	3.8	**3.6**	0.5	3.4	3.7
41	Asp + 2*ATP + NH3 -> Asn	**0.2**	0.0	0.2	0.2	**0.3**	0.0	0.3	0.3	**0.3**	0.0	0.3	0.3
42	Pyr + Glu -> Ala + AKG	**0.8**	0.0	0.8	0.8	**1.3**	0.0	1.3	1.3	**1.2**	0.0	1.2	1.2
43	3PG + Glu -> Ser + AKG + NADH	**1.0**	0.1	0.9	1.0	**1.9**	0.0	1.9	2.0	**1.9**	0.2	1.8	1.9
44	Ser <-> Gly + MEETHF	**0.3**	0.1	0.2	0.3	**0.7**	0.0	0.7	0.8	**0.7**	0.2	0.6	0.8
45	Gly <-> CO2 + MEETHF + NADH + NH3	**0.1**	0.1	0.0	0.1	**-0.2**	0.0	-0.3	-0.2	**-0.2**	0.2	-0.3	-0.1
46	Thr <-> Gly + AcCoA + NADH	**0.4**	0.3	0.2	0.4	**0.0**	0.0	-0.1	0.1	**0.0**	0.5	-0.2	0.1
47	Ser + AcCoA + 3*ATP + 4*NADPH + SO4 -> Cys + Ac	**0.2**	0.0	0.2	0.2	**0.4**	0.0	0.4	0.4	**0.4**	0.0	0.4	0.4
48	Asp + Pyr + Glu + SucCoA + ATP + 2*NADPH -> LL_DAP + AKG + Suc	**0.2**	0.0	0.2	0.2	**0.4**	0.0	0.4	0.4	**0.4**	0.0	0.4	0.4
49	LL_DAP -> Lys + CO2	**0.2**	0.0	0.2	0.2	**0.4**	0.0	0.4	0.4	**0.4**	0.0	0.4	0.4
50	Asp + 2*ATP + 2*NADPH -> Thr	**1.0**	0.3	0.9	1.1	**1.1**	0.0	1.0	1.2	**1.0**	0.5	0.9	1.2
51	Asp + METHF + Cys + SucCoA + ATP + 2*NADPH -> Met + Pyr + Suc + NH3	**0.2**	0.0	0.2	0.2	**0.3**	0.0	0.3	0.3	**0.3**	0.0	0.3	0.3
52	Pyr + Pyr + Glu + NADPH -> Val + CO2 + AKG	**0.5**	0.0	0.5	0.5	**0.8**	0.0	0.8	0.8	**0.8**	0.0	0.8	0.8
53	AcCoA + Pyr + Pyr + Glu + NADPH -> Leu + CO2 + CO2 + AKG + NADH	**0.8**	0.0	0.8	0.8	**1.4**	0.0	1.4	1.4	**1.3**	0.0	1.3	1.3
54	Thr + Pyr + Glu + NADPH -> Ile + CO2 + AKG + NH3	**0.3**	0.0	0.3	0.3	**0.5**	0.0	0.5	0.5	**0.5**	0.0	0.5	0.5
55	PEP + PEP + E4P + Glu + ATP + NADPH -> Phe + CO2 + AKG	**0.2**	0.0	0.2	0.2	**0.4**	0.0	0.4	0.4	**0.4**	0.0	0.4	0.4
56	PEP + PEP + E4P + Glu + ATP + NADPH -> Tyr + CO2 + AKG + NADH	**0.2**	0.0	0.2	0.2	**0.3**	0.0	0.3	0.3	**0.3**	0.0	0.3	0.3
57	Ser + R5P + PEP + E4P + PEP + Gln + 3*ATP + NADPH -> Trp + CO2 + GAP + Pyr + Glu	**0.1**	0.0	0.1	0.1	**0.2**	0.0	0.2	0.2	**0.2**	0.0	0.2	0.2
58	R5P + FTHF + Gln + Asp + 5*ATP -> His + AKG + Fum + 2*NADH	**0.2**	0.0	0.2	0.2	**0.3**	0.0	0.3	0.3	**0.3**	0.0	0.3	0.3
59	MEETHF + NADH -> METHF	**0.2**	0.0	0.2	0.2	**0.3**	0.0	0.3	0.3	**0.3**	0.0	0.3	0.3
60	MEETHF -> FTHF + NADPH	**0.2**	0.0	0.2	0.2	**0.3**	0.0	0.3	0.3	**0.3**	0.0	0.3	0.3

61	Biomass	**1.3**	0.0	1.3	1.3	**2.2**	0.0	2.2	2.2	**2.1**	0.0	2.1	2.1
62	CO2_unlabeled <-> CO2	**0.0**	0.0	0.0	0.0	**0.0**	0.0	0.0	0.0	**0.0**	0.0	0.0	0.0
63	NADH <-> NADPH	**30.1**	6.1	22.4	31.0	**56.2**	0.1	50.0	56.4	**57.6**	3.1	54.4	57.8
64	ATP -> ATP.maintenance	**2.7**	0.0	2.7	2.7	**3.6**	0.0	3.6	3.6	**3.9**	0.0	3.9	3.9
65	NADPH -> NADPH.maintenance	**169.2**	4.2	163.6	169.3	**103.1**	1.6	99.8	104.1	**109.4**	1.9	107.3	109.6
66	NADH + O2 -> 3*ATP	**0.0**	6.1	0.0	6.5	**0.0**	0.0	0.0	6.2	**0.0**	3.1	0.0	3.2
67	FADH2 + O2 -> 2*ATP	**145.1**	1.0	139.0	150.7	**155.2**	1.6	148.5	158.4	**153.5**	5.0	150.4	155.6
68	CO2 -> CO2.ext	**158.8**	0.0	158.8	158.8	**131.9**	0.0	131.9	131.9	**134.2**	0.0	134.2	134.2
69	NH3.ext -> NH3	**9.5**	0.0	9.5	9.5	**15.7**	0.0	15.7	15.7	**15.2**	0.0	15.2	15.2
70	SO4.ext -> SO4	**0.2**	0.0	0.2	0.2	**0.4**	0.0	0.4	0.4	**0.4**	0.0	0.4	0.4
71	O2.ext -> O2	**145.1**	4.2	145.0	150.7	**155.2**	1.6	154.1	158.4	**153.5**	1.9	153.3	155.6
Fit		Yes				Yes				Yes			
SSR		210.5				268.3				185.3			
Expected SSR		[185.3-268.4]				[210.8 - 299]				[185.3 - 268.4]			
Normally distributed		Yes				Yes				Yes			

0.174*G6P + 0.068*F6P + 0.107*GAP + 1.882*AcCoA + 0.431*Gly + 0.263*Pro + 0.598*Ala + 0.389*Val + 0.628*Leu + 0.244*Ile + 0.122*Met + 0.055*Cys + 0.191*Phe + 0.135*Tyr + 0.077*Trp + 0.126*His + 0.18*Lys + 0.354*Arg + 0.251*Gln + 0.158*Asn + 0.301*Glu + 0.284*Asp + 0.301*Ser + 0.256*Thr + 46.75*ATP -> Biomass

5.6 References Chapter 5

Aguirre-Plans, J., Meseguer, A., Molina-Fernandez, R., Marín-López, M.A., Jumde, G., Casanova, K., et al. (2021) SPServer: split-statistical potentials for the analysis of protein structures and protein–protein interactions, *BMC Bioinformatics* **22**: 4.

Andrés-Barrao, C., Saad, M.M., Chappuis, M.L., Boffa, M., Perret, X., Ortega Pérez, R., and Barja, F. (2012) Proteome analysis of *Acetobacter pasteurianus* during acetic acid fermentation, *J Proteomics* **75**: 1701-1717.

Antoniewicz, M.R., Kelleher, J.K., and Stephanopoulos, G. (2006) Determination of confidence intervals of metabolic fluxes estimated from stable isotope measurements, *Metabolic engineering* **8**: 324-337.

Bagdasarian, M., Lurz, R., Ruckert, B., Franklin, F.C., Bagdasarian, M.M., Frey, J., and Timmis, K.N. (1981) Specific-purpose plasmid cloning vectors. II. Broad host range, high copy number, RSF1010-derived vectors, and a host-vector system for gene cloning in Pseudomonas, *Gene* **16**: 237-247.

Blank, L.M., Ionidis, G., Ebert, B.E., Bühler, B., and Schmid, A. (2008) Metabolic response of *Pseudomonas putida* during redox biocatalysis in the presence of a second octanol phase, *The FEBS journal* **275**: 5173-5190.

Calero, P., and Nikel, P.I. (2019) Chasing bacterial chassis for metabolic engineering: a perspective review from classical to non-traditional microorganisms, *Microbial biotechnology* **12**: 98-124.

Campanini, B., Benoni, R., Bettati, S., Beck, C.M., Hayes, C.S., and Mozzarelli, A. (2015) Moonlighting O-acetylserine sulfhydrylase: New functions for an old protein, *Biochimica et Biophysica Acta (BBA) - Proteins and Proteomics* **1854**: 1184-1193.

Cavaleiro, A.M., Kim, S.H., Seppala, S., Nielsen, M.T., and Nørholm, M.H. (2015) Accurate DNA assembly and genome engineering with optimized uracil excision cloning, *ACS Synthetic Biology* **4**: 1042-1046.

Chen, J., Li, W., Zhang, Z.-Z., Tan, T.-W., and Li, Z.-J. (2018) Metabolic engineering of *Escherichia coli* for the synthesis of polyhydroxyalkanoates using acetate as a main carbon source, *Microbial Cell Factories* **17**: 102.

Chevalier, S., Bouffartigues, E., Bodilis, J., Maillot, O., Lesouhaitier, O., Feuilloley, M.G.J., et al. (2017) Structure, function and regulation of *Pseudomonas aeruginosa* porins, *FEMS Microbiology Reviews* **41**: 698-722.

Chimiak, A., Hider, R., Liu, A., Neilands, J., Nomoto, K., Sugiura, Y., and Hider, R.C. (1984) Siderophore mediated absorption of iron, *Siderophores from microorganisms and plants*: 25-87.

Couto, N., Wood, J., and Barber, J. (2016) The role of glutathione reductase and related enzymes on cellular redox homoeostasis network, *Free Radical Biology and Medicine* **95**: 27-42.

Crousilles, A., Dolan, S.K., Brear, P., Chirgadze, D.Y., and Welch, M. (2018) Gluconeogenic precursor availability regulates flux through the glyoxylate shunt in *Pseudomonas aeruginosa*, *Journal of Biological Chemistry* **293**: 14260-14269.

Czajka, J.J., Banerjee, D., Eng, T., Menasalvas, J., Yan, C., Munoz, N.M., et al. (2022) Tuning a high performing multiplexed-CRISPRi *Pseudomonas putida* strain to further enhance indigoidine production, *Metabolic Engineering Communications* **15**: e00206.

Deatherage, D.E., and Barrick, J.E. (2014) Identification of mutations in laboratory-evolved microbes from next-generation sequencing data using breseq, *Engineering and analyzing multicellular systems: methods and protocols*: 165-188.

Deeraksa, A., Moonmangmee, S., Toyama, H., Yamada, M., Adachi, O., and Matsushita, K. (2005) Characterization and spontaneous mutation of a novel gene, *polE*, involved in pellicle formation in *Acetobacter tropicalis* SKU1100, *Microbiology (Reading)* **151**: 4111-4120.

Díaz-Guerra, M., Esteban, M., and Martínez, J.L. (2006) Growth of *Escherichia coli* in acetate as a sole carbon source is inhibited by ankyrin-like repeats present in the 2′,5′-linked oligoadenylate-dependent human RNase L enzyme, *FEMS Microbiology Letters* **149**: 107-113.

Dolan, S.K., Kohlstedt, M., Trigg, S., Vallejo Ramirez, P., Kaminski, C.F., Wittmann, C., and Welch, M. (2020) Contextual flexibility in *Pseudomonas aeruginosa* central carbon metabolism during growth in single carbon sources, *MBio* **11**: e02684-02619.

Dragosits, M., and Mattanovich, D. (2013) Adaptive laboratory evolution – principles and applications for biotechnology, *Microbial Cell Factories* **12**: 64.

Duffy, B.K., and Défago, G. (2000) Controlling Instability in *gacS-gacA* regulatory genes during inoculant production of *Pseudomonas fluorescens* biocontrol strains, *Applied and Environmental Microbiology* **66**: 3142-3150.

Dürre, P., and Eikmanns, B.J. (2015) C1-carbon sources for chemical and fuel production by microbial gas fermentation, *Current Opinion in Biotechnology* **35**: 63-72.

Eng, T., Banerjee, D., Lau, A.K., Bowden, E., Herbert, R.A., Trinh, J., et al. (2021) Engineering *Pseudomonas putida* for efficient aromatic conversion to bioproduct using high throughput screening in a bioreactor, *Metabolic Engineering* **66**: 229-238.

Feng, Y., and Cronan, J.E. (2009) *Escherichia coli* unsaturated fatty acid synthesis: complex transcription of the fabA gene and in vivo identification of the essential reaction catalyzed by FabB, *Journal of Biological Chemistry* **284**: 29526-29535.

Flügge, U., and Wessel, D. (1984) Cell-free synthesis of putative precursors for envelope membrane polypeptides of spinach chloroplasts, *FEBS letters* **168**: 255-259.
Fridovich, I. (1974) Superoxide dismutases, *Advances in enzymology and related areas of molecular biology* **41**: 35-97.
Gaddy, J.A., Tomaras, A.P., and Actis, L.A. (2009) The *Acinetobacter baumannii* 19606 OmpA protein plays a role in biofilm formation on abiotic surfaces and in the interaction of this pathogen with eukaryotic cells, *Infection and immunity* **77**: 3150-3160.
Ganne, G., Brillet, K., Basta, B., Roche, B., Hoegy, F., Gasser, V., and Schalk, I.J. (2017) Iron release from the siderophore pyoverdine in *Pseudomonas aeruginosa* involves three new actors: FpvC, FpvG, and FpvH, *ACS Chemical Biology* **12**: 1056-1065.
Genee, H.J., Bonde, M.T., Bagger, F.O., Jespersen, J.B., Sommer, M.O., Wernersson, R., and Olsen, L.R. (2015) Software-supported USER cloning strategies for site-directed mutagenesis and DNA assembly, *ACS Synthetic Biology* **4**: 342-349.
Goedhart, J., and Luijsterburg, M.S. (2020) VolcaNoseR is a web app for creating, exploring, labeling and sharing volcano plots, *Scientific Reports* **10**: 20560.
González Fernández-Niño, S.M., Smith-Moritz, A.M., Chan, L.J.G., Adams, P.D., Heazlewood, J.L., and Petzold, C.J. (2015) Standard flow liquid chromatography for shotgun proteomics in bioenergy research, *Frontiers in bioengineering and biotechnology* **3**: 44.
Griego, A., Douché, T., Gianetto, Q.G., Matondo, M., and Manina, G. (2022) RNase E and HupB dynamics foster mycobacterial cell homeostasis and fitness, *iScience* **25**: 104233.
Gurdo, N., Novelli Poisson, G.F., Juárez, Á., Rios de Molina, M., and Galvagno, M.A. (2018) Improved robustness of an ethanologenic yeast strain through adaptive evolution in acetic acid is associated with its enzymatic antioxidant ability, *Journal of Applied Microbiology* **125**: 766-776.
Gurdo, N., Volke, D.C., and Nikel, P.I. (2022) Merging automation and fundamental discovery into the design–build–test–learn cycle of nontraditional microbes, *Trends in Biotechnology* **40**: 1148-1159.
Hall-Stoodley, L., Costerton, J.W., and Stoodley, P. (2004) Bacterial biofilms: from the natural environment to infectious diseases, *Nature reviews microbiology* **2**: 95-108.
Hassan, K.A., Johnson, A., Shaffer, B.T., Ren, Q., Kidarsa, T.A., Elbourne, L.D.H., et al. (2010) Inactivation of the GacA response regulator in *Pseudomonas fluorescens* Pf-5 has far-reaching transcriptomic consequences, *Environmental Microbiology* **12**: 899-915.
Henstra, A.M., Sipma, J., Rinzema, A., and Stams, A.J.M. (2007) Microbiology of synthesis gas fermentation for biofuel production, *Current Opinion in Biotechnology* **18**: 200-206.

Horinouchi, T., and Furusawa, C. (2020) Understanding metabolic adaptation by using bacterial laboratory evolution and trans-omics analysis, *Biophysical Reviews* **12**: 677-682.

Huang, B., Yang, H., Fang, G., Zhang, X., Wu, H., Li, Z., and Ye, Q. (2018) Central pathway engineering for enhanced succinate biosynthesis from acetate in *Escherichia coli*, *Biotechnology and bioengineering* **115**: 943-954.

Hwang, I.Y., Nguyen, A.D., Nguyen, T.T., Nguyen, L.T., Lee, O.K., and Lee, E.Y. (2018) Biological conversion of methane to chemicals and fuels: technical challenges and issues, *Applied microbiology and biotechnology* **102**: 3071-3080.

Imlay, J.A. (2013) The molecular mechanisms and physiological consequences of oxidative stress: lessons from a model bacterium, *Nature Reviews Microbiology* **11**: 443-454.

Jo, M., Noh, M.H., Lim, H.G., Kang, C.W., Im, D.-K., Oh, M.-K., and Jung, G.Y. (2019) Precise tuning of the glyoxylate cycle in *Escherichia coli* for efficient tyrosine production from acetate, *Microbial Cell Factories* **18**: 57.

Jumper, J., Evans, R., Pritzel, A., Green, T., Figurnov, M., Ronneberger, O., et al. (2021) Highly accurate protein structure prediction with AlphaFold, *Nature* **596**: 583-589.

Kahn, D., and Ditta, G. (1991) Modular structure of FixJ: homology of the transcriptional activator domain with the -35 binding domain of sigma factors, *Mol Microbiol* **5**: 987-997.

Khosravi-Darani, K., Mokhtari, Z.-B., Amai, T., and Tanaka, K. (2013) Microbial production of poly(hydroxybutyrate) from C1 carbon sources, *Applied Microbiology and Biotechnology* **97**: 1407-1424.

Kiefer, D., Merkel, M., Lilge, L., Henkel, M., and Hausmann, R. (2021) From Acetate to Bio-Based Products: Underexploited Potential for Industrial Biotechnology, *Trends Biotechnol* **39**: 397-411.

Kiefer, P., Heinzle, E., Zelder, O., and Wittmann, C. (2004) Comparative metabolic flux analysis of lysine-producing *Corynebacterium glutamicum* cultured on glucose or fructose, *Applied and Environmental Microbiology* **70**: 229-239.

Kim, J., and Park, W. (2014) Oxidative stress response in *Pseudomonas putida*, *Applied Microbiology and Biotechnology* **98**: 6933-6946.

Kim, Y., Lama, S., Agrawal, D., Kumar, V., and Park, S. (2021) Acetate as a potential feedstock for the production of value-added chemicals: Metabolism and applications, *Biotechnology Advances* **49**: 107736.

Klasson, K.T., Ackerson, M.D., Clausen, E.C., and Gaddy, J.L. (1992) Bioconversion of synthesis gas into liquid or gaseous fuels, *Enzyme and Microbial Technology;(United Kingdom)* **14**.

Kohlstedt, M., and Wittmann, C. (2019) GC-MS-based ^{13}C metabolic flux analysis resolves the parallel and cyclic glucose metabolism of *Pseudomonas putida* KT2440 and *Pseudomonas aeruginosa* PAO1, *Metabolic Engineering* **54**: 35-53.

Kulikova, V.V., Revtovich, S.V., Bazhulina, N.P., Anufrieva, N.V., Kotlov, M.I., Koval, V.S., et al. (2019) Identification of O-acetylhomoserine sulfhydrylase, a putative enzyme responsible for methionine biosynthesis in *Clostridioides difficile*: Gene cloning and biochemical characterizations, *IUBMB Life* **71**: 1815-1823.

Lagoa-Costa, B., Abubackar, H.N., Fernández-Romasanta, M., Kennes, C., and Veiga, M.C. (2017) Integrated bioconversion of syngas into bioethanol and biopolymers, *Bioresource technology* **239**: 244-249.

Latif, H., Sahin, M., Tarasova, J., Tarasova, Y., Portnoy, V.A., Nogales, J., and Zengler, K. (2015) Adaptive Evolution of *Thermotoga maritima* Reveals Plasticity of the ABC Transporter Network, *Appl Environ Microbiol* **81**: 5477-5485.

Leone, S., Sannino, F., Tutino, M.L., Parrilli, E., and Picone, D. (2015) Acetate: friend or foe? Efficient production of a sweet protein in *Escherichia coli* BL21 using acetate as a carbon source, *Microbial cell factories* **14**: 1-10.

Leoni, L., Ciervo, A., Orsi, N., and Visca, P. (1996) Iron-regulated transcription of the *pvdA* gene in *Pseudomonas aeruginosa*: effect of Fur and PvdS on promoter activity, *J Bacteriol* **178**: 2299-2313.

Li, Y., Huang, B., Wu, H., Li, Z., Ye, Q., and Zhang, Y.H.P. (2016) Production of succinate from acetate by metabolically engineered *Escherichia coli*, *ACS Synthetic Biology* **5**: 1299-1307.

Long, C.P., Gonzalez, J.E., Feist, A.M., Palsson, B.O., and Antoniewicz, M.R. (2018) Dissecting the genetic and metabolic mechanisms of adaptation to the knockout of a major metabolic enzyme in *Escherichia coli*, *Proc Natl Acad Sci U S A* **115**: 222-227.

Malatesta, F., Antonini, G., Sarti, P., and Brunori, M. (1995) Structure and function of a molecular machine: cytochrome *c* oxidase, *Biophysical chemistry* **54**: 1-33.

Martínez-García, E., Nikel, P.I., Aparicio, T., and de Lorenzo, V. (2014) Pseudomonas 2.0: genetic upgrading of *P. putida* KT2440 as an enhanced host for heterologous gene expression, *Microb Cell Fact* **13**: 159.

Martínez-García, E., and de Lorenzo, V. (2011) Engineering multiple genomic deletions in Gram-negative bacteria: analysis of the multi-resistant antibiotic profile of *Pseudomonas putida* KT2440, *Environmental microbiology* **13**: 2702-2716.

McAnulty, M.J., G. Poosarla, V., Kim, K.-Y., Jasso-Chávez, R., Logan, B.E., and Wood, T.K. (2017) Electricity from methane by reversing methanogenesis, *Nature Communications* **8**: 15419.

McNaught, K.J., Kuatsjah, E., Zahn, M., Prates, É.T., Shao, H., Bentley, G.J., et al. (2023) Initiation of fatty acid biosynthesis in *Pseudomonas putida* KT2440, *Metabolic Engineering* **76**: 193-203.

Melo, A.M., and Teixeira, M. (2016) Supramolecular organization of bacterial aerobic respiratory chains: From cells and back, *Biochimica et Biophysica Acta (BBA)-Bioenergetics* **1857**: 190-197.

Mishra, S., and Imlay, J. (2012) Why do bacteria use so many enzymes to scavenge hydrogen peroxide?, *Arch Biochem Biophys* **525**: 145-160.

Moon, D.C., Choi, C.H., Lee, J.H., Choi, C.-W., Kim, H.-Y., Park, J.S., et al. (2012) *Acinetobacter baumannii* outer membrane protein A modulates the biogenesis of outer membrane vesicles, *The Journal of Microbiology* **50**: 155-160.

Mullins, E.A., Francois, J.A., and Kappock, T.J. (2008) A specialized citric acid cycle requiring succinyl-coenzyme A (CoA):acetate CoA-transferase (AarC) confers acetic acid resistance on the acidophile *Acetobacter aceti*, *J Bacteriol* **190**: 4933-4940.

Nakano, S., Fukaya, M., and Horinouchi, S. (2006) Putative ABC transporter responsible for acetic acid resistance in *Acetobacter aceti*, *Appl Environ Microbiol* **72**: 497-505.

Nguyen, A.D., Hwang, I.Y., Lee, O.K., Kim, D., Kalyuzhnaya, M.G., Mariyana, R., et al. (2018) Systematic metabolic engineering of *Methylomicrobium alcaliphilum* 20Z for 2, 3-butanediol production from methane, *Metabolic engineering* **47**: 323-333.

Nicholson, J.K., and Wilson, I.D. (2003) Understanding 'global' systems biology: metabonomics and the continuum of metabolism, *Nature Reviews Drug Discovery* **2**: 668-676.

Nikel, P.I., Fuhrer, T., Chavarría, M., Sánchez-Pascuala, A., Sauer, U., and de Lorenzo, V. (2021) Reconfiguration of metabolic fluxes in *Pseudomonas putida* as a response to sub-lethal oxidative stress, *The ISME Journal* **15**: 1751-1766.

Nisson, P.E., Rashtchian, A., and Watkins, P.C. (1991) Rapid and efficient cloning of Alu-PCR products using uracil DNA glycosylase, *Genome Research* **1**: 120-123.

Nogales, J., Mueller, J., Gudmundsson, S., Canalejo, F.J., Duque, E., Monk, J., et al. (2020) High-quality genome-scale metabolic modelling of *Pseudomonas putida* highlights its broad metabolic capabilities, *Environmental Microbiology* **22**: 255-269.

Noh, H.J., Woo, J.E., Lee, S.Y., and Jang, Y.-S. (2018) Metabolic engineering of *Clostridium acetobutylicum* for the production of butyl butyrate, *Applied microbiology and biotechnology* **102**: 8319-8327.

Novak, K., and Pflügl, S. (2018) Towards biobased industry: acetate as a promising feedstock to enhance the potential of microbial cell factories, *FEMS Microbiology Letters* **365**.

Paysan-Lafosse, T., Blum, M., Chuguransky, S., Grego, T., Pinto, B.L., Salazar, Gustavo A., et al. (2022) InterPro in 2022, *Nucleic Acids Research* **51**: D418-D427.

Pfeifer, E., Gätgens, C., Polen, T., and Frunzke, J. (2017) Adaptive laboratory evolution of *Corynebacterium glutamicum* towards higher growth rates on glucose minimal medium, *Scientific Reports* **7**: 16780.

Phaneuf, P.V., Gosting, D., Palsson, B.O., and Feist, A.M. (2019) ALEdb 1.0: a database of mutations from adaptive laboratory evolution experimentation, *Nucleic acids research* **47**: D1164-D1171.

Pinhal, S., Ropers, D., Geiselmann, J., and De Jong, H. (2019) Acetate metabolism and the inhibition of bacterial growth by acetate, *Journal of bacteriology* **201**: e00147-00119.

Platt, R., Drescher, C., Park, S.-K., and Phillips, G.J. (2000) Genetic system for reversible integration of DNA constructs and lacZ gene fusions into the *Escherichia coli* chromosome, *Plasmid* **43**: 12-23.

Ringel, M.T., and Brüser, T. (2018) The biosynthesis of pyoverdines, *Microbial cell* **5**: 424.

Roe, A.J., McLaggan, D., Davidson, I., O'Byrne, C., and Booth, I.R. (1998) Perturbation of anion balance during inhibition of growth of *Escherichia coli* by weak acids, *J Bacteriol* **180**: 767-772.

Roe, A.J., O'Byrne, C., McLaggan, D., and Booth, I.R. (2002) Inhibition of *Escherichia coli* growth by acetic acid: a problem with methionine biosynthesis and homocysteine toxicity, *Microbiology* **148**: 2215-2222.

Saeki, A., Matsushita, K., Takeno, S., Taniguchi, M., Toyama, H., THEERAGooL, G., et al. (1999) Enzymes responsible for acetate oxidation by acetic acid bacteria, *Bioscience, biotechnology, and biochemistry* **63**: 2102-2109.

Sainz, T., Pérez, J., Villaseca, J., Hernández, U., Eslava, C., Mendoza, G., and Wacher, C. (2005) Survival to different acid challenges and outer membrane protein profiles of pathogenic *Escherichia coli* strains isolated from pozol, a Mexican typical maize fermented food, *International journal of food microbiology* **105**: 357-367.

Sandberg, T.E., Salazar, M.J., Weng, L.L., Palsson, B.O., and Feist, A.M. (2019) The emergence of adaptive laboratory evolution as an efficient tool for biological discovery and industrial biotechnology, *Metabolic Engineering* **56**: 1-16.

SCHMIDLI-SACHERER, P., KEEL, C., and DÉFAGO, G. (1997) The global regulator GacA of *Pseudomonas fluorescens* CHA0 is required for suppression of root diseases in dicotyledons but not in Gramineae, *Plant Pathology* **46**: 80-90.

Schrader, J., Schilling, M., Holtmann, D., Sell, D., Filho, M.V., Marx, A., and Vorholt, J.A. (2009) Methanol-based industrial biotechnology: current status and future perspectives of methylotrophic bacteria, *Trends in Biotechnology* **27**: 107-115.

Schwechheimer, C., and Kuehn, M.J. (2015) Outer-membrane vesicles from Gram-negative bacteria: biogenesis and functions, *Nature reviews microbiology* **13**: 605-619.
Sitnikov, D.M., Schineller, J.B., and Baldwin, T.O. (1995) Transcriptional regulation of bioluminesence genes from *Vibrio fischeri*, *Mol Microbiol* **17**: 801-812.
Somprasong, N., Jittawuttipoka, T., Duang-Nkern, J., Romsang, A., Chaiyen, P., Schweizer, H.P., et al. (2012) *Pseudomonas aeruginosa* thiol peroxidase protects against hydrogen peroxide toxicity and displays atypical patterns of gene regulation, *J Bacteriol* **194**: 3904-3912.
Son, Y.J., Phue, J.N., Trinh, L.B., Lee, S.J., and Shiloach, J. (2011) The role of Cra in regulating acetate excretion and osmotic tolerance in *E. coli* K-12 and *E. coli* B at high density growth, *Microb Cell Fact* **10**: 52.
Song, H., Li, Y., and Wang, Y. (2023) Two-component system GacS/GacA, a global response regulator of bacterial physiological behaviors, *Engineering Microbiology* **3**: 100051.
Song, H.S., Seo, H.M., Jeon, J.M., Moon, Y.M., Hong, J.W., Hong, Y.G., et al. (2018) Enhanced isobutanol production from acetate by combinatorial overexpression of acetyl-CoA synthetase and anaplerotic enzymes in engineered *Escherichia coli*, *Biotechnology and Bioengineering* **115**: 1971-1978.
Steiner, P., and Sauer, U. (2001) Proteins induced during adaptation of *Acetobacter aceti* to high acetate concentrations, *Appl Environ Microbiol* **67**: 5474-5481.
Thompson, M.G., Incha, M.R., Pearson, A.N., Schmidt, M., Sharpless, W.A., Eiben, C.B., et al. (2020) Fatty Acid and Alcohol Metabolism in *Pseudomonas putida*: Functional Analysis Using Random Barcode Transposon Sequencing, *Applied and environmental microbiology* **86**: e01665-01620.
Touati, D. (2000) Iron and oxidative stress in bacteria, *Archives of biochemistry and biophysics* **373**: 1-6.
Trcek, J., Jernejc, K., and Matsushita, K. (2007) The highly tolerant acetic acid bacterium *Gluconacetobacter europaeus* adapts to the presence of acetic acid by changes in lipid composition, morphological properties and PQQ-dependent ADH expression, *Extremophiles* **11**: 627-635.
Trček, J., Mira, N.P., and Jarboe, L.R. (2015) Adaptation and tolerance of bacteria against acetic acid, *Applied Microbiology and Biotechnology* **99**: 6215-6229.
Valverde, C., Heeb, S., Keel, C., and Haas, D. (2003) RsmY, a small regulatory RNA, is required in concert with RsmZ for GacA-dependent expression of biocontrol traits in *Pseudomonas fluorescens* CHA0, *Molecular Microbiology* **50**: 1361-1379.
Vermeij, P., and Kertesz, M.A. (1999) Pathways of assimilative sulfur metabolism in *Pseudomonas putida*, *Journal of Bacteriology* **181**: 5833-5837.

Vilchez-Vargas, R., Junca, H., and Pieper, D.H. (2010) Metabolic networks, microbial ecology and 'omics' technologies: towards understanding in situ biodegradation processes, *Environmental Microbiology* **12**: 3089-3104.
Visca, P., Ciervo, A., and Orsi, N. (1994) Cloning and nucleotide sequence of the pvdA gene encoding the pyoverdin biosynthetic enzyme L-ornithine N5-oxygenase in *Pseudomonas aeruginosa*, *J Bacteriol* **176**: 1128-1140.
Volke, D.C., Friis, L., Wirth, N.T., Turlin, J., and Nikel, P.I. (2020) Synthetic control of plasmid replication enables target- and self-curing of vectors and expedites genome engineering of *Pseudomonas putida*, *Metabolic Engineering Communications* **10**: e00126.
von Kamp, A., and Klamt, S. (2017) Growth-coupled overproduction is feasible for almost all metabolites in five major production organisms, *Nat Commun* **8**: 15956.
Wallace-Salinas, V., and Gorwa-Grauslund, M.F. (2013) Adaptive evolution of an industrial strain of *Saccharomyces cerevisiae* for combined tolerance to inhibitors and temperature, *Biotechnology for Biofuels* **6**: 151.
Wang, Y. (2002) The Function of OmpA in *Escherichia coli*, *Biochemical and Biophysical Research Communications* **292**: 396-401.
Waterhouse, A.M., Procter, J.B., Martin, D.M.A., Clamp, M., and Barton, G.J. (2009) Jalview Version 2—a multiple sequence alignment editor and analysis workbench, *Bioinformatics* **25**: 1189-1191.
Wendisch, V.F., Brito, L.F., Gil Lopez, M., Hennig, G., Pfeifenschneider, J., Sgobba, E., and Veldmann, K.H. (2016) The flexible feedstock concept in Industrial Biotechnology: Metabolic engineering of *Escherichia coli*, *Corynebacterium glutamicum*, *Pseudomonas*, *Bacillus* and yeast strains for access to alternative carbon sources, *Journal of Biotechnology* **234**: 139-157.
Wiederstein, M., and Sippl, M.J. (2007) ProSA-web: interactive web service for the recognition of errors in three-dimensional structures of proteins, *Nucleic Acids Research* **35**: W407-W410.
Willdigg, J.R., and Helmann, J.D. (2021) Mini Review: Bacterial Membrane Composition and Its Modulation in Response to Stress, *Frontiers in Molecular Biosciences* **8**.
Winsor, G.L., Griffiths, E.J., Lo, R., Dhillon, B.K., Shay, J.A., and Brinkman, F.S. (2016) Enhanced annotations and features for comparing thousands of *Pseudomona*s genomes in the *Pseudomonas* genome database, *Nucleic Acids Res* **44**: D646-653.
Wirth, N.T., Kozaeva, E., and Nikel, P.I. (2020) Accelerated genome engineering of *Pseudomonas putida* by I-SceI-mediated recombination and CRISPR-Cas9 counterselection, *Microbial biotechnology* **13**: 233-249.
Wittmann, C. (2007) Fluxome analysis using GC-MS, *Microbial Cell Factories* **6**: 6.

Worsey, M.J., and Williams, P.A. (1975) Metabolism of toluene and xylenes by *Pseudomonas putida* (*arvilla*) mt-2: evidence for a new function of the TOL plasmid, *Journal of Bacteriology* **124**: 7-13.

Xiao, Y., Ruan, Z., Liu, Z., Wu, S.G., Varman, A.M., Liu, Y., and Tang, Y.J. (2013) Engineering *Escherichia coli* to convert acetic acid to free fatty acids, *Biochemical engineering journal* **76**: 60-69.

Yadrykhins' ky, V., Georgiou, C., and Brenk, R. (2021) Crystal structure of *Pseudomonas aeruginosa* FabB C161A, a template for structure-based design for new antibiotics, *F1000Research* **10**.

Yang, H., Huang, B., Lai, N., Gu, Y., Li, Z., Ye, Q., and Wu, H. (2019) Metabolic engineering of *Escherichia coli* carrying the hybrid acetone-biosynthesis pathway for efficient acetone biosynthesis from acetate, *Microbial Cell Factories* **18**: 1-9.

Yang, S., Li, S., and Jia, X. (2019) Production of medium chain length polyhydroxyalkanoate from acetate by engineered *Pseudomonas putida* KT2440, *Journal of Industrial Microbiology and Biotechnology* **46**: 793-800.

Young, J.D. (2014) INCA: a computational platform for isotopically non-stationary metabolic flux analysis, *Bioinformatics (Oxford, England)* **30**: 1333-1335.

Young, J.D. (2014) INCA: a computational platform for isotopically non-stationary metabolic flux analysis, *Bioinformatics* **30**: 1333-1335.

Yugi, K., Kubota, H., Hatano, A., and Kuroda, S. (2016) Trans-Omics: How To Reconstruct Biochemical Networks Across Multiple 'Omic' Layers, *Trends in Biotechnology* **34**: 276-290.

Yugi, K., and Kuroda, S. (2018) Metabolism as a signal generator across trans-omic networks at distinct time scales, *Current Opinion in Systems Biology* **8**: 59-66.

Zamboni, N., Fendt, S.-M., Rühl, M., and Sauer, U. (2009) ^{13}C-based metabolic flux analysis, *Nature protocols* **4**: 878.

Chapter 6 - System-level analyses of *Pseudomonas putida* strains blocked in sugar phosphorylation and oxidation unveil adaptive mechanisms for restoring systemic equilibrium

Abstract

Glucose phosphorylation and oxidation in the soil bacterium *Pseudomonas putida* has been blocked to generate several mutants with different glucose processing peripheral pathways. The strategy involved the deletion of enzymatic activities in the following steps: i) glucose phosphorylation into glucose-6-phosphate (G6P), ii) glucose oxidation that channel carbon skeletons into gluconate or 2-keto-gluconate (2-KGA) and, iii) glucose phosphorylation and partially oxidation. A set of physiological and multi-omics analysis—metabolomics, proteomics and fluxomics—in the mutant strains, revealed a global metabolic rewiring of the native glucose metabolism components as a consequence of these genetic modifications. In the present study, we showed that pathway-specific metabolites and enzymes, which play a pivotal role in the energy homeostasis, modulate activities in EDEMP and TCA cycles. Time-course metabolomics exhibited substantial changes in hexose phosphates pools in EDEMP (mainly, G6P and F6P) and PP pathway metabolites. Proteomics captured variations in proteins involved in energy homeostasis, such as Gnd, GapA, Icd and Mqo3. Finally, ^{13}C-labelling experiments indicated a significant increase in EMP and ED pathway fluxes as well as TCA cycle. The robust metabolic flexibility allows *P. putida* to cope with the genetic perturbations and preserves stable phenotypes, likely by redirecting metabolic fluxes of key reactions across the cell.

6.1 Introduction

6.1.1 Metabolic control in bacteria under genetic perturbations

Bacteria possess the capacity to adapt to alterations in their environment by modulating their metabolic activities. The central carbon metabolism (CCM) constitutes a range of pathways, such as glycolysis, gluconeogenesis, pentose phosphate (PP) pathway, anaplerosis, tricarboxylic acid cycle (TCA), as well as the glyoxylate shunt (Westfall and Levin, 2018). CCM plays a vital role in maintaining the balance of carbon in the organism, and it can be regulated through gene expression, transcriptional regulation, and enzyme activity modulation. The aforementioned regulation is indispensable for the biological system to occupy a particular ecological niche and withstand adverse growth conditions (Maciąg, et al., 2011). Virtually all bacteria have developed systems to control metabolic fluctuations across the different layers of information—from the genotype to the phenotype. The inherent control of cellular processes operates primarily at the levels of the genome, post-transcriptional and post-translational modifications, allosteric regulation, and metabolites. These regulatory mechanisms work together to maintain balance in the quantities of metabolites and metabolic activity within the cellular metabolism (Gerosa and Sauer, 2011). To provide perspective, one can draw a comparison between an electronic control system and the regulation of global metabolism. In this analogy, the input signal in the electronic device corresponds to the external signal in the biological system, which may consist of a specific metabolite concentration like glucose or environmental factors like temperature, pH, osmolarity or the presence of toxic compounds (Shimizu, 2013, Nijhout, et al., 2019). The external signals can set off a cascade of intracellular reactions that engage multiple cellular components, such as DNA, transcripts, proteins, and metabolites, via diverse biological pathways (**Figure 6.1**). At the same time, internal signals, such as a high concentration of a particular metabolite, can activate or inhibit intracellular targets as part of the inherent biological regulatory system. A master regulator—mimicking a controller in the electronic system—dynamically regulates the biological components by modulating the levels of genes, transcripts, proteins, metabolites, and metabolic fluxes. Ultimately, the metabolic process generates an output signal that determines the final phenotype. However, in order to understand how a biological system re-routes carbon fluxes

against not only external (e.g., physicochemical factors) but also internal fluctuations (e.g., genetic modifications), it is mandatory to analysis several layers of information as well as to understand how they are interconnected (Friedman, et al., 2006, Chavarría, et al., 2012, Soma, et al., 2014, Kobayashi, et al., 2020).

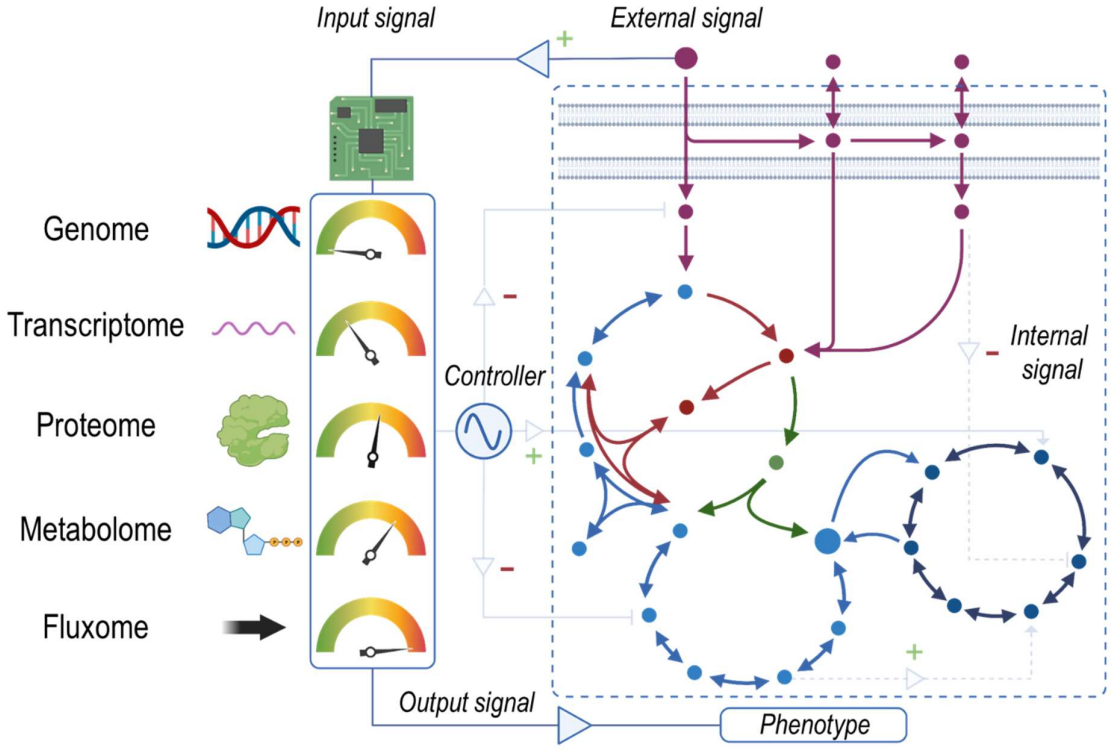

Figure 6.1. Schematic representation of the analogy between an electronic control system and metabolism. An external signal (purple circle) triggers a downstream response into the metabolism (dashed blue square). The controller modulates the fluctuations and controls the entire metabolic network by adjusting the components in the genome, transcriptome, proteome, metabolome and fluxome. Circles represent metabolites and the arrows are the connecting reactions.

Understanding how cells are able to control and regulate metabolic networks can reveal the organization and interactions of cellular networks that enable complex processes such as glucose metabolism in bacteria (Sauer, et al., 2007). Several strategies were exemplified in numerous previous studies. As a first example, authors found that *E. coli*'s intracellular metabolic network is highly stable and resilient when it is subjected to various disturbances (particularly to central carbon metabolism gene knock-out strains). This global stability is vital for efficient cell growth and allows *E.*

coli to respond effectively to changes in the concentration of growth-limiting substances. Fluctuating metabolite levels reflects an active regulation of enzyme expression to maximize growth rates (Kiviet, et al., 2014). This response enables *E. coli* to effectively deal with environmental fluctuations, but it may be costly because it requires additional systems such as sensor proteins, signal mediators, and transcriptional regulators to detect and respond to specific disturbances. The study suggests that this active response to environmental changes at the gene expression level is a common trait of *E. coli*. In addition, *E. coli* does not appear to respond significantly to the disruption of most single metabolic genes by regulating multiple mRNA or protein levels (Ishii, et al., 2007). Another example explores how the perturbations in promoter-ORF regions spread across the *E. coli* transcriptome. The authors used 255 microarrays representing 85 rewired networks and they found a wide range of perturbation with many common patterns of genes differentially expressed between different rewiring (Baumstark, et al., 2015). Finally, a metabolism-centric study exploited the global regulatory network in *Salmonella* virulence under specific *in vitro* mimicking infection conditions. Computational network analysis combined with high-throughput –omics measurements allowed to inferred 168 proteins in *Salmonella* virulence, which were clustered close to SPI-2 (*Salmonella* Pathogenicity Island-2) virulence proteins in the regulatory network. This provided critical insights in the pathogenicity process in this bacterium (Yoon, et al., 2011).

The rapid expansion of more advanced systems biology approaches in the SynBio field allowed exploiting the microbial metabolism in-depth (Gurdo, et al., 2023). As it was previously stated in this thesis, multi-omic methodologies have gained significant attraction in the last decades. A versatile toolbox for a wide system-level analysis was developed not only to support a vast range of SynBio applications—guiding engineering efforts—but also to explore unknown edges of the metabolism. The incorporation of these techniques to studies on metabolism can disentangle the behavior of metabolic networks *per se* or; comprehend how cellular metabolism responds to internal/external changes (Chen, et al., 2013, Donati, et al., 2021).

6.1.2 *Pseudomonas putida* KT2440 bears a model metabolic network to study genetic perturbations

P. putida KT2440 is a bacterium that has been extensively studied for its metabolic capabilities. One of its interesting features is its ability to utilize glucose as a carbon source. Understanding the metabolic network involved in glucose utilization and its regulation can help to gain insights into the bacterium's core architecture. By studying genetic perturbations in the glucose metabolism of *P. putida* KT2440, it is possible to identify key regulatory genes and pathways involved in this process, paving the way for future research in the field of synthetic biology and biotechnology (Weimer, et al., 2020).

A detailed description of the central metabolic design of *P. putida* is explained in **Chapter 1**. In *P. putida* KT2440, glucose diffuses into the periplasm through the outer membrane porin (OprB) (Saravolac, et al., 1991, Wylie and Worobec, 1995, Llamas, et al., 2003). After entering into the periplasm, glucose is either (I) directly imported or (II) oxidized in the periplasm. The direct import (I) into the cytoplasm is orchestrated by the D-glucose ABC-transporter (GtsABCD) and; subsequent phosphorylation mediated by the glucokinase (Glk) into glucose-6-phosphate (G6P). The latter is further converted into 6-phosphogluconate (6PG) by the action of G6P dehydrogenase (G6PDH) and 6-phosphogluconolactonase (Pgl) or; (II) Two-step periplasmic oxidation to yield gluconate and 2-ketogluconate via glucose dehydrogenase (Gcd) and gluconate dehydrogenase (Gad), respectively. Later, gluconate and 2-ketogluconate pass through the cytoplasmic membrane assisted by the GntT and KguT transporters. GnuK phosphorylates gluconate into 6-phosphogluconate. KguK acts over 2-ketogluconate to transform it into 2-ketogluconate-6-P (2-KG6P) which is further converted into 6-phosphogluconate (6PG) by the 2-ketogluconate-6-P reductase (KguD). Both gluconate and 2-ketogluconate can be secreted and retaken in a sequential manner (first gluconate and then 2-ketogluconate). The genes encoding glucokinase/glucose 6-phosphate dehydrogenase, which result in the production of 6-phosphogluconate, are under the control of HexR (del Castillo, et al., 2008). Additionally, the genes responsible for the Entner-Doudoroff (ED) pathway enzymes that produce glyceraldehyde-3-phosphate and pyruvate, as well as *gap-1* that encodes glyceraldehyde-3-phosphate dehydrogenase, are also regulated by HexR.

2-Keto-3-deoxy-6-phosphogluconate (KDPG), an intermediate metabolite in the Entner-Doudoroff (ED) pathway, acts as an effector of HexR causing its dissociation from target operators (*zwf*, *edd*, and *gap-1* genes) (Daddaoua, et al., 2009). At the same time, ED pathway is also necessary for the catabolism of other sugars (*e.g.* fructose) and organic acids like gluconate and 2-ketogluconate. The pathways before described co-exist and act simultaneously in *Pseudomonas putida* KT2440. The upper glucose metabolism is represented in **Figure 6.2**.

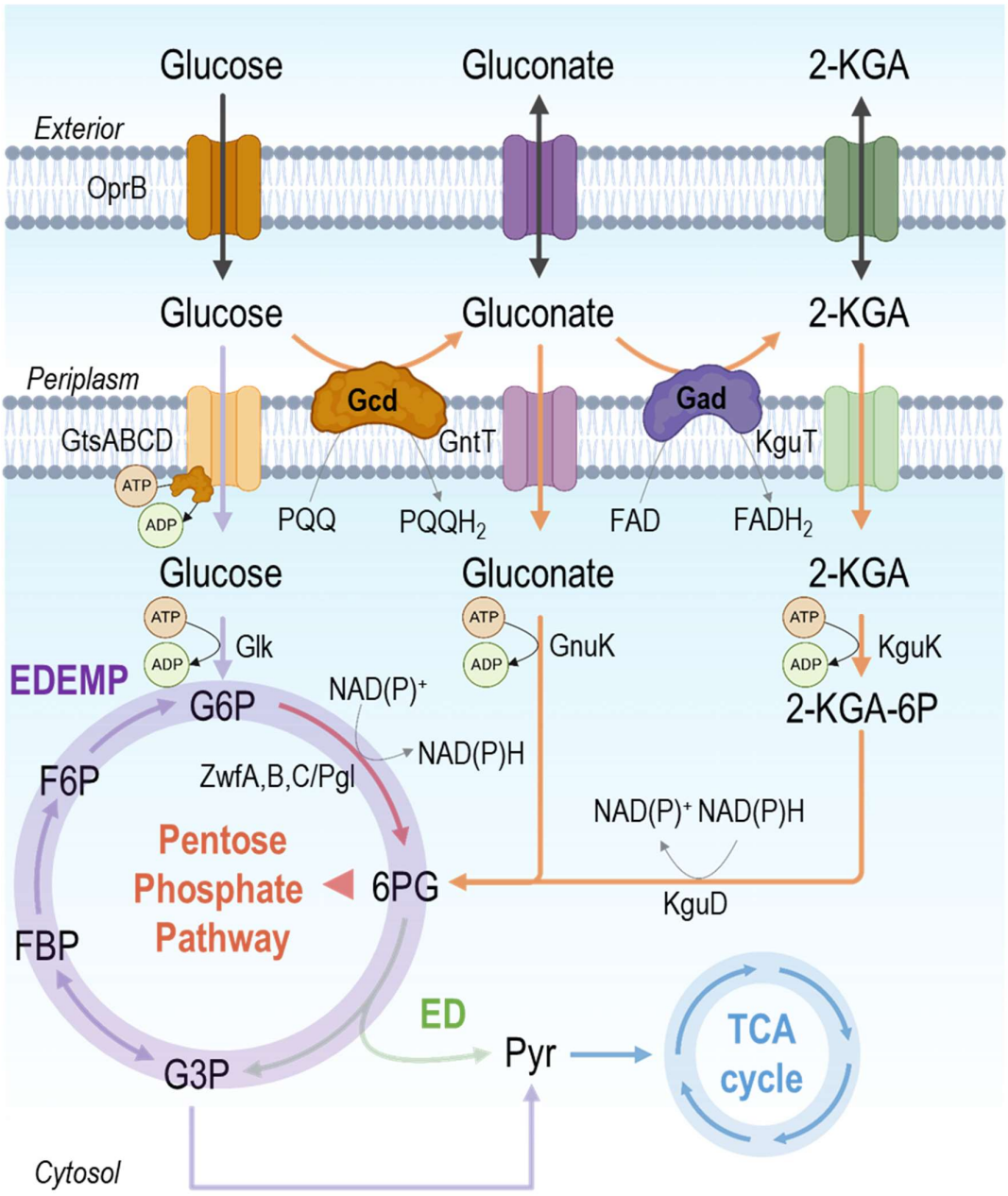

Figure 6.2. Upper glucose metabolism in *Pseudomonas putida* KT2440. The picture shows how glucose enters from the extracellular space (*Exterior*) through the OprB porin into the periplasm. Here, it is either oxidized into gluconate and 2-ketogluconate (2-KGA) or phosphorylated in the cytosol by the action of the glucokinase (Glk). ZwfA,B,C, glucose 6-P dehydrogenase isozymes A, B and C; Pgl, 6-phosphogluconolactonase; Gcd, glucose dehydrogenase; Gad, gluconate oxidase; GntT, gluconate transporter; KguT, 2-ketogluconate transporter; KguK, 2-ketogluconate kinase; KguD, 2-ketogluconate-6-phosphate dehydrogenase; GnuK, gluconate kinase; PQQ, pyrroloquinoline quinone; $PQQH_2$, pyrroloquinoline quinone reduced. 2-KGA-6P, 2-ketogluconate-6-phosphate. G6P, glucose-6-phosphate. 6PG, 6-phosphogluconate. G3P, glyceraldehyde-3-phosphate. FBP, fructose-1,6-bisphosphate. F6P, fructose-6-phosphate. Pyr, pyruvate.

6.1.3 Interplay between peripheral reactions and energy metabolism in *Pseudomonas putida*

The primary steps of glucose uptake take place through a set of three pathways that converge in 6-phosphogluconate (6PG). Each confluent path includes ATP-dependent phosphorylation and oxidation steps. During glucose uptake and phosphorylation, the internalization of glucose requires the utilization of one ATP molecule, while an additional ATP molecule is necessary to phosphorylate glucose to form G6P. Later, glucose-6-phosphate dehydrogenase (Zwf), convert G6P into the central metabolite 6PG yielding one NAD(P)H molecule (Volke, et al., 2021).

In *P. putida*, ATP generation can be partially uncoupled from NADH formation by shifting glucose processing from the phosphorylative branch into a two-step-oxidation reaction via glucose dehydrogenase (Gcd) and gluconate dehydrogenase (Gad). Both enzymes can consecutively oxidize glucose to gluconate and 2-ketogluconate in the periplasm. In this process, the respiratory chain components PQQ (pyrroloquinoline quinone) are reduced into $PQQH_2$ (reduced pyrroloquinoline quinone) by Gcd and FAD into $FADH_2$ by Gad being released two electron equivalents in each oxidation step, while bypassing the NAD(P)H-generating G6P dehydrogenase. Adjacently, gluconate can be directly phosphorylated into 6PG by spending one ATP. In the case of 2-ketogluconate, it is firstly phosphorylated into 2-ketogluconate-6-phosphate and then, it consumes one NAD(P)H to be converted into 6PG (Ebert, et al., 2011).

Besides their role in central carbon metabolism, these reactions are critical in the control of energy homeostasis (Hoek and Rydström, 1988). By disrupting either phosphorylation or oxidative reactions, the cellular energy homeostasis is affected leading to cofactor imbalance and severe effects on bacterial growth (ADACHI, et al., 1979, Olavarria, et al., 2014, Sriherfyna, et al., 2021). To counteract these effects, imbalance-avoiding mechanisms comprise the suitable choice of catabolic pathways, as in *S. cerevisiae* (Blank, et al., 2005), and the differential expression of isoenzymes with different cofactor specificities (Clarke, et al., 1986, Boonstra, et al., 1999, Doan, et al., 2003, Fuhrer and Sauer, 2009). As part of these mechanisms, several biochemical energy cycles are capable of effectively catalyzing reaction of transhydrogenation

without disturbing net catabolic fluxes. There are some examples in literature of those cycles, such as operation of isocitrate dehydrogenase in eukaryotic mitochondria (Sazanov and Jackson, 1994), synergistic process of glyceraldehyde-3-phosphate (GAP) and alcohol dehydrogenases in the yeast *Kluyveromyces lactis* (Overkamp, et al., 2002, Verho, et al., 2002), among others.

6.1.4 Systems biology strategies to study microbial metabolism: the case of *Pseudomonas putida*

The question that comes out from the previous sections is how we can analyze microbial metabolism and the physiological behavior of a living cell under environmental or metabolic perturbations. Bacterial physiology emerged as an important scientific discipline in the early 1900s, offering valuable understanding of the central carbon metabolic pathways. As molecular biology progressed in the 80s and 90s, along with research into growth kinetics and cellular regulation mechanisms, the discipline underwent significant changes (Ideker, et al., 2002). This led to the creation of a sub-discipline called microbial kinetics, which exploit the dynamic of the metabolism using advanced mathematical models (Bailey, 1998). Finally, in the last two decades, the development of more quantitative approaches culminated with the appearance of systems biology, allowing the collection of huge amounts of data with better quality (Edwards, et al., 2001, Wang, et al., 2010, Valgepea, et al., 2013, Klumpp and Hwa, 2014, Scott, et al., 2014). Conventional system biology approaches—aiming to analyse the behavior of a biological system—can capture the entire picture by collecting the information coming from the well-interconnected network between genotype-phenotype (Nielsen, 2017).

This approach can be executed in an integrative manner combining the analysis of individual components in the biological system under study. Likewise, the use of system biology strategies on biological networks has identified spatiotemporal regulation of metabolic pathways, which can enlighten global regulation mechanisms or; decipher how carbon fluxes are distributed in a context of genetic modifications (Munger, et al., 2008, Blaby, et al., 2013, Hackett, et al., 2016).

In this study, systems-level analysis aided by multi-omics strategies was implemented to unwire glucose metabolism at different cellular levels following genetic disruptions. The study was carried out using a collection of *Pseudomonas putida* KT2440 strains having different glucose entry points towards the cytoplasm (**Figure 6.3A**). The strains harbored specific deletions either in the oxidative and/or phosphorylative glucose pathway, which could directly affect cellular and energy homeostasis. Within the strains constructed in this work 1) Δ*gcd*, strain lacking the glucose dehydrogenase, metabolizes glucose via direct phosphorylation while (**Figure 6.3B**); 2) Δ*glk*, is unable to phosphorylate glucose into G6P being forced to oxidized it through the dehydrogenase Gcd as a first step; or mediated by the gluconate dehydrogenase Gad (**Figure 6.3C**). 3) The third strain, Δ*gtsABCD*Δ*glk*Δ*gad*, does not phosphorylate glucose neither can perform a second oxidation step from gluconate into 2-KGA being the entire gluconate pool channeled to 6PG (**Figure 6.3D**). 4) Finally, Δ*gtsABCD*Δ*glk*Δ*gnuK*Δ*gntT* is pushed to double oxidized glucose into 2-KGA and later to 6PG (**Figure 6.3E**). Here, we interrogated whether the physiological interruption in the peripheral reactions of glucose phosphorylation and/or oxidation steps affect central carbon metabolism topology and if those changes can be capture by system-biology approaches. To do so, the mutants were analysed from a physiological point of view by measuring growth, uptake and secretion rates (glucose, gluconate and 2-ketogluconate). Next, the strains were subjected to a time-course targeted metabolomics, semi-quantitative proteomics and ^{13}C metabolic flux analyses to assess how central carbon metabolism metabolites, proteins and fluxes are rewired under glycolytic regime upon genetic perturbations. Finally, this study was intended to: a) shed light on the initial steps of glucose metabolism (phosphorylation and oxidation branches) from a system biology point of view and; b) to propose a metabolic model for regulation of CCM upon genetic perturbations.

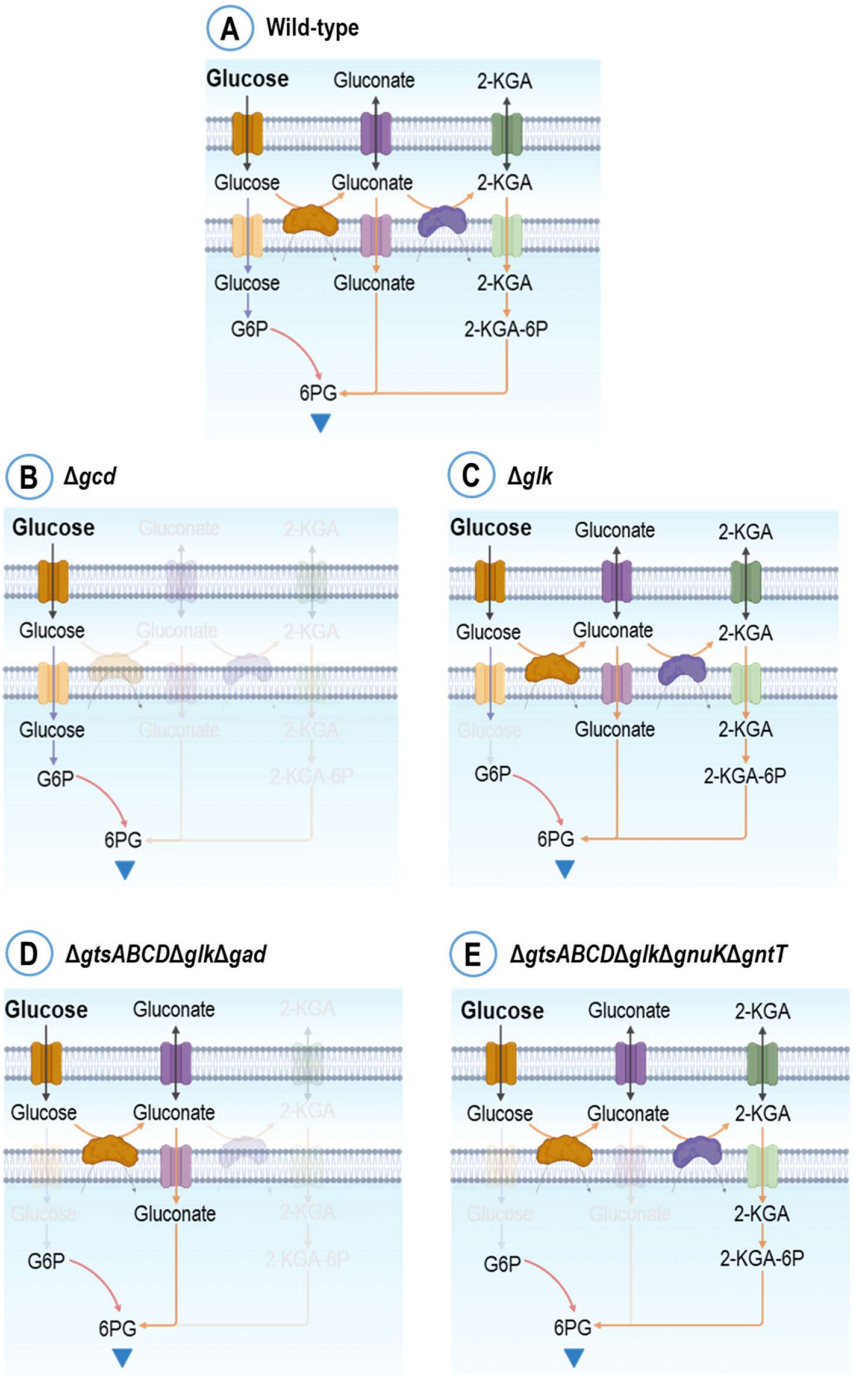

Figure 6.3. Simplified scheme of the different *Pseudomonas putida* KT2440 mutants used in this study. The image illustrates the processes of glucose phosphorylation in the cytosol and glucose oxidation in the periplasm of *P. putida* KT2440. Glucose is transported into the periplasm where it can either be phosphorylated in the cytosol to form G6P or oxidized to gluconate or 2-KGA. Subsequently, the latter two compounds can be phosphorylated and transported back into the cytoplasm. A) Wild-type; B) Δ*gcd*; C) Δ*glk*; D) Δ*gtsABCD*Δ*glk*Δ*gad* and E) Δ*gtsABCD*Δ*glk*Δ*gnuK*Δ*gntT*. The blue down arrowhead indicates reactions toward central carbon metabolism.

6.2 Results

6.2.1 Quantitative physiology of mutant strains with divergent routes for glucose assimilation

Efficient glucose uptake is an important process that many bacteria have optimized through the evolution. Changes in peripheral reactions modify intracellular precursor pools, which affect downstream reactions leading to global rearrangement in the metabolic architecture and rewiring of existing regulatory networks to regain metabolic fitness. To understand the physiology of channeling glucose flux through different entry points into the cytosol, we built different mutants of glucose transporters—oxidation and phosphorylation—by disrupting a combination of peripheral and upper glucose reactions. In order to disentangle the effects of such genetic perturbations at extracellular level, we performed a physiological analysis by measuring glucose and the organic acids gluconate and 2-KGA. To achieve this particular aim, we performed a quantitative physiological characterization of the different *P. putida* KT2440 mutants by: 1) following spectrophotometrically the optical density at 600 nm (OD_{600}) and; 2) measuring glucose, gluconate and 2-KGA concentrations (uptake and secretion rates in mmol g_{CDW}^{-1} h^{-1}) on each strain in de Bont medium containing 15 mM of glucose. Growth curves, glucose consumption as well as gluconate or 2-ketogluconate secretion/consumption are presented in **Figure 6.4**.

The final biomass was similar in all the strains (~4 OD_{600nm}) except for the Δ*glk* mutant, which showed a reduction of 25% (~3 OD_{600nm}). Major differences were observed between the Δ*gcd* mutant and the rest of the strains during the exponential phase. The longer lag-phase, reduced μ_{max} and $Y_{X/S}$ in this strain might be the consequence of the inactivation of the glucose dehydrogenase enzyme, which implies a growth defect in this strain. The specific growth rate for the wild type strain was 0.61 h^{-1} while the mutant growth rates ranged from 0.45 h^{-1} (Δ*gcd*) to 0.64 h^{-1} (Δ*gtsABCD*Δ*glk*Δ*gad*). The quantitative parameters are presented in **Table 6.1**.

Regarding glucose consumption, specific uptake rates ranged between 6 and 7.5 mmol glucose g_{CDW}^{-1} h^{-1}. Glucose uptake rates, on the other hand, increased by 30% in Δ*gcd* and Δ*gtsABCD*Δ*glk*Δ*gnuK*Δ*gntT*, 20% in Δ*gad*, 10% in Δ*glk* and no variations were

observed in Δ*gtsABCD*Δ*glk*Δ*gad* compared to the wild-type strain. These results suggested that significant alterations in respiratory metabolism may be linked to energy imbalance caused by the introduced genetic disruptions.

Table 6.1. Quantitative physiology parameters of mutant strains in de Bont medium with glucose as only carbon source. Maximum exponential growth rates (μ_{max}) were determined via linear regression for growth experiments in 100 mL Erlenmeyer flasks. The average values ± standard deviation were calculated from at least three biological replicates. *q_{ATP} and $q_{NAD(P)H}$ were derived from ^{13}C-metabolic flux analysis. g_{CDW}: grams of cell dry weight.

Strain	Specific growth rate [h^{-1}]	Glucose uptake rate, q_s [mmol $gCDW^{-1}$ h^{-1}]	$Y_{X/S}$ [gCDW g glucose $consumed^{-1}$]	qATP* [mmol $gCDW^{-1}$ h^{-1}]	qNAD(P)H* [mmol $gCDW^{-1}$ h^{-1}]
KT2440	0.61 ± 0.01	5.92 ± 0.20	0.56 ± 0.01	29.0	5.3
Δ*gcd*	0.45 ± 0.02	7.47 ± 0.48	0.39 ± 0.03	21.0	30.2
Δ*glk*	0.53 ± 0.01	6.59 ± 0.24	0.46 ± 0.01	25.5	13.4
Δ*gtsABCD*Δ*glk*Δ*gad*	0.64 ± 0.02	6.02 ± 0.12	0.59 ± 0.02	30.7	7.4
Δ*gtsABCD*Δ*glk*Δ*gnuK*Δ*gntT*	0.53 ± 0.02	7.58 ± 0.47	0.37 ± 0.02	23.5	0.1

The biomass yield showed that *P. putida* KT2440 was more efficient in converting glucose into biomass. Furthermore, Δ*gcd*, Δ*gtsABCD*Δ*glk*Δ*gnuK*Δ*gntT* and Δ*glk* presented lower yields. This can be explained because the double oxidation of glucose through 2-KGA and; later to 6PG, is energetically more expensive for the cell (needing 1 ATP to phosphorylate 2-KGA into 2-KGA-6P and 1 NAD(P)H from 2-KGA-6P into 6PG, see **Table S6.1**) (Volke, et al., 2023). From an energetic point of view, the specific ATP production rates were calculated based on the energy requirement on each step (ATP, NADH, NAD(P)H, $FADH_2$ and UQH_2) considering the reactions in the metabolic network for the ^{13}C parallel labelling experiment. The relative percentages (%) of the reaction contributing to ATP formation and consumption were converted into specific rates. The net specific ATP/NAD(P)H production rates were calculated using **Equation 1**. The values ranged from 21.0 (Δ*gcd*) to 30.7 (Δ*gtsABCD*Δ*glk*Δ*gad*). Here, the cellular ATP supply was higher in the strains that do not use the second oxidation step (2-KGA toward 6PG). The reaction from 2-KGA-6P to 6PG is a sink for NAD(P)H which might indicate that this step is energetically expensive for the cell. Despite the fact that 10% of glucose is redirected towards this reaction in the wild-type strain, it has a negative impact on the overall ATP output because of its lower

efficient compare to glucose oxidation, as reported previously (Kohlstedt and Wittmann, 2019).

Additionally, the NAD(P)H rates also varied between strains. The reason for the elevated $q_{NAD(P)H}$ levels in *Δgcd* can be attributed to the elimination of the glucose oxidation reactions. Consequently, in response to the reduced availability of NAD(P)H, the cell adopts a compensatory mechanism by enhancing the flux through NAD(P)H-producing reactions, such as the conversion of G6P to 6PG, pyruvate to Acetyl-CoA, and isocitrate to *α*-ketoglutarate, which serve as the primary sources of energy. On the other hand, the strain *ΔgtsABCDΔglkΔgnuKΔgntT* showed the lowest NAD(P)H production rate correlating also with its lower flux in the TCA cycle reactions. We know from previous studies that *P. putida* strains possess a great ability to regenerate NAD(P)H and have a low energy demand for cellular maintenance. This is beneficial for NAD(P)H-dependent biocatalysis since it allows for a high net NADH regeneration rate, which is available for biocatalysis due to low NAD(P)H consumption for ATP generation. Moreover, the carbon breakdown process operates without any by-product formation, such as acetate, glycerol, or ethanol, which are commonly observed with other important industrial hosts like *E. coli*, *B. subtilis*, and *S. cerevisiae*, even at high rates (Isken, et al., 1999, Blank, et al., 2008).

Similarly, the findings revealed a connection between the excretion and intake of the organic acids (gluconate and 2-KGA) in relation to the specific genetic deletions that were introduced in these strains. As expected, **t**he wild type strain KT2440 sequentially oxidized glucose into gluconate as a first step and later on into 2-ketogluconate (Pedersen, et al., 2021). The two carboxylic acids were progressively secreted and co-consumed. In the mutant Δ*gcd*, gluconate and 2-ketogluconate were not observed in the supernatant since this strain does not have the glucose dehydrogenase enzyme that converts glucose into gluconate. This strain is forced to directly phosphorylate glucose into glucose-6-phosphate. For the mutant Δ*glk*, gluconate and 2-ketogluconate were detected in the media showing that the deletion of the glucokinase does not have any effect in the organic acid profile. Finally, Δ*gtsABCD*Δ*glk*Δ*gnuK*Δ*gntT* secreted both gluconate and significantly higher 2-ketogluconate concentration (~3 mM) than the rest of the strains in this condition. The

presence of convergent pathways (glucose oxidation and phosphorylation) facilitates glucose utilization by this microorganism, without regards the genetic interruptions, at the different levels in the upper glycolysis. Indeed, this bacteria was able to channel the carbon flux toward the key intermediate 6-phosphogluconate.

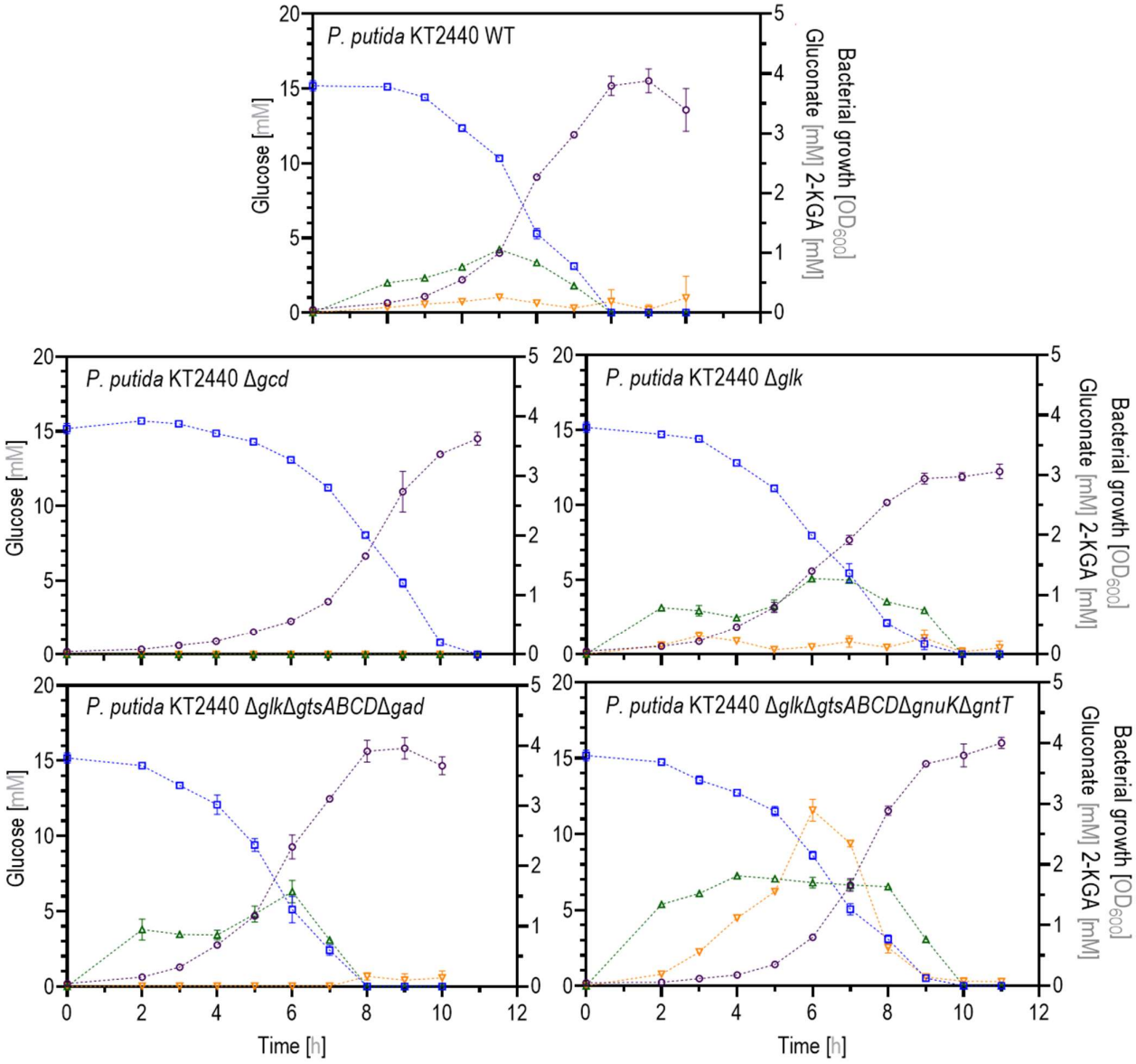

Figure 6.4. Physiological analysis of *Pseudomonas putida* KT2440, Δ*gcd*, Δ*glk*, Δ*gtsABCD*Δ*glk*Δ*gad* and Δ*gtsABCD*Δ*glk*Δ*gnuK*Δ*gntT* in minimal medium supplemented with 15 mM glucose. The strains were cultured in 100 mL flask containing 20 mL of de Bont minimal medium supplemented with 15 mM glucose as the sole source of carbon. The medium with glucose contained an additional 5 g L^{-1} MOPS to buffer the acidifying effect of gluconate and 2-KGA production. Cell density (purple circles), glucose (blue squares), gluconate (green up pointing triangles) and 2-KGA (orange down pointing triangles) concentrations were measured over a period of 10-11 hours. Standard deviation is indicated with error bars calculated from three biological replicates.

6.3 Time-course targeted metabolomics analysis exposes through the central carbon metabolism

To investigate the intracellular changes of key central carbon intermediates, the metabolite content of the strains under study was analysed via LC-MS/MS. Cells were grown in de Bont minimal medium supplemented with 20 mM glucose. Metabolites from EDEMP, PPP and TCA pathways were quantified at four time points along the growth curve OD_{600nm} 0.1 (t1), 0.5 (t2), 1.0-1.2 (t3) and 2.0-2.5 (t4). 16 metabolites were quantified, normalized by cell dry weight (μmol g_{CDW}^{-1}) and represented according the metabolic pathway. Normalized metabolite concentrations and measured metabolites were plotted in the y and x-axis, respectively (**Figure 6.5**).

Within EDEMP metabolites, significant changes in glucose-6-phosphate (G6P) and fructose-6-phosphate (F6P) levels were observed across the cultivation. While the previous intermediates tended to decrease in most of the strains, a substantial increase in G6P was observed for Δ*gcd*. Likewise, F6P was kept at high concentrations suggesting that the cell is producing sugar phosphates for biomass formation. On the other hand, the strains lacking the enzymes glucokinase (Glk): Δ*glk*, Δ*gtsABCD*Δ*glk*Δ*gad* and Δ*gtsABCD*Δ*glk*Δ*gnuK*Δ*gntT*; showed low concentrations of G6P indicating that the cellular metabolite pool shift the glucose incorporation via the oxidative pathways (i.e., glucose oxidation toward gluconate and/or 2-KGA) (Nikel, et al., 2015). As we previously stated, both gluconate and 2-KGA can be funneled into the central carbon metabolism through 6PG and; subsequently, into ED pathway. The 6PG levels in the before mentioned strains were comparable to the wild-type strain KT2440 and, considerably higher than Δ*gcd* strain. In the same direction, the metabolites in the lower EDEMP cycle—DHAP and PEP—significantly decreased in

the early stages (t1 and t2) either to supply biomass precursors or pyruvate to fuel the TCA cycle (Sauer and Eikmanns, 2005, Meza, et al., 2012) (**Figure 6.5A**).

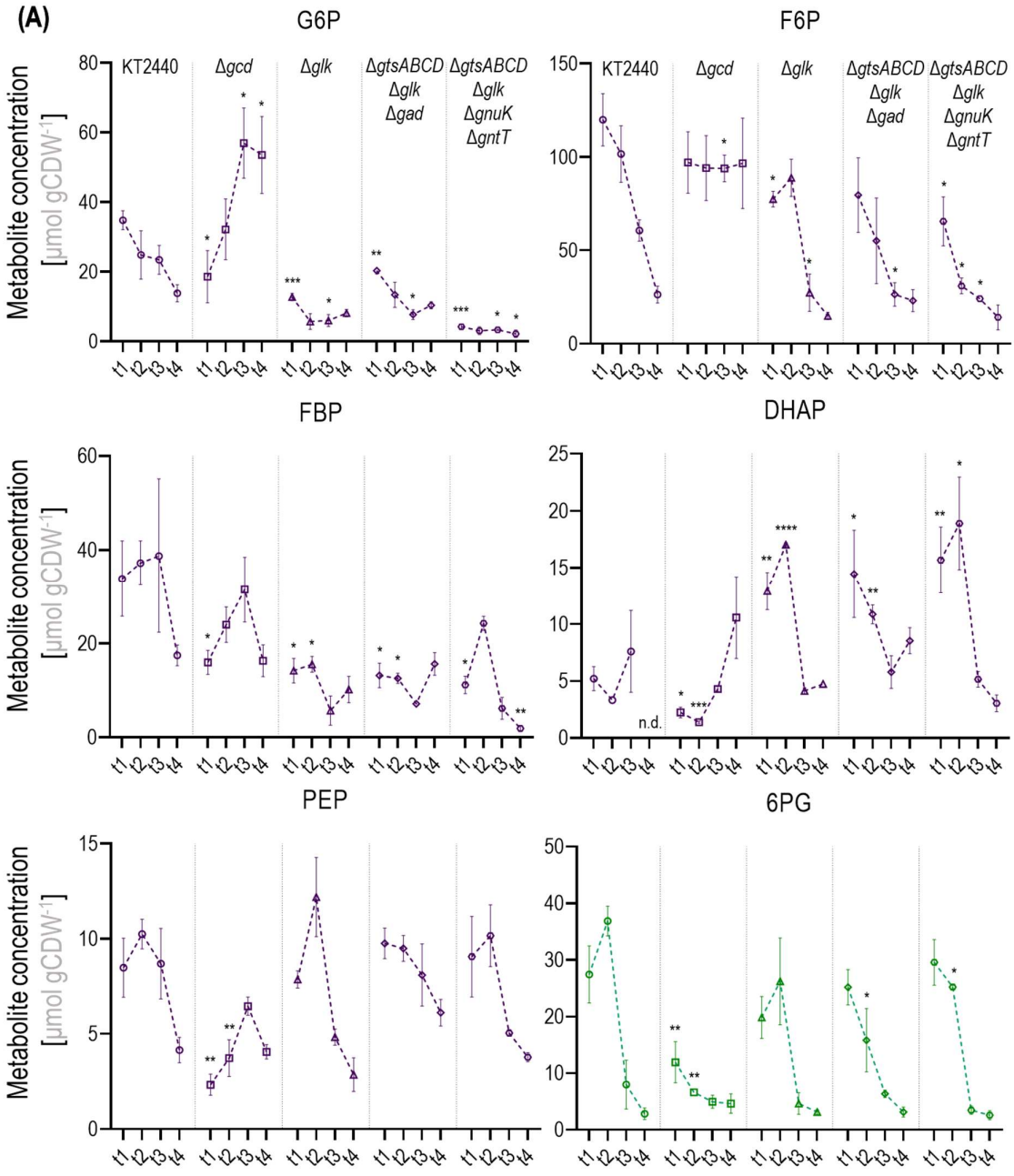

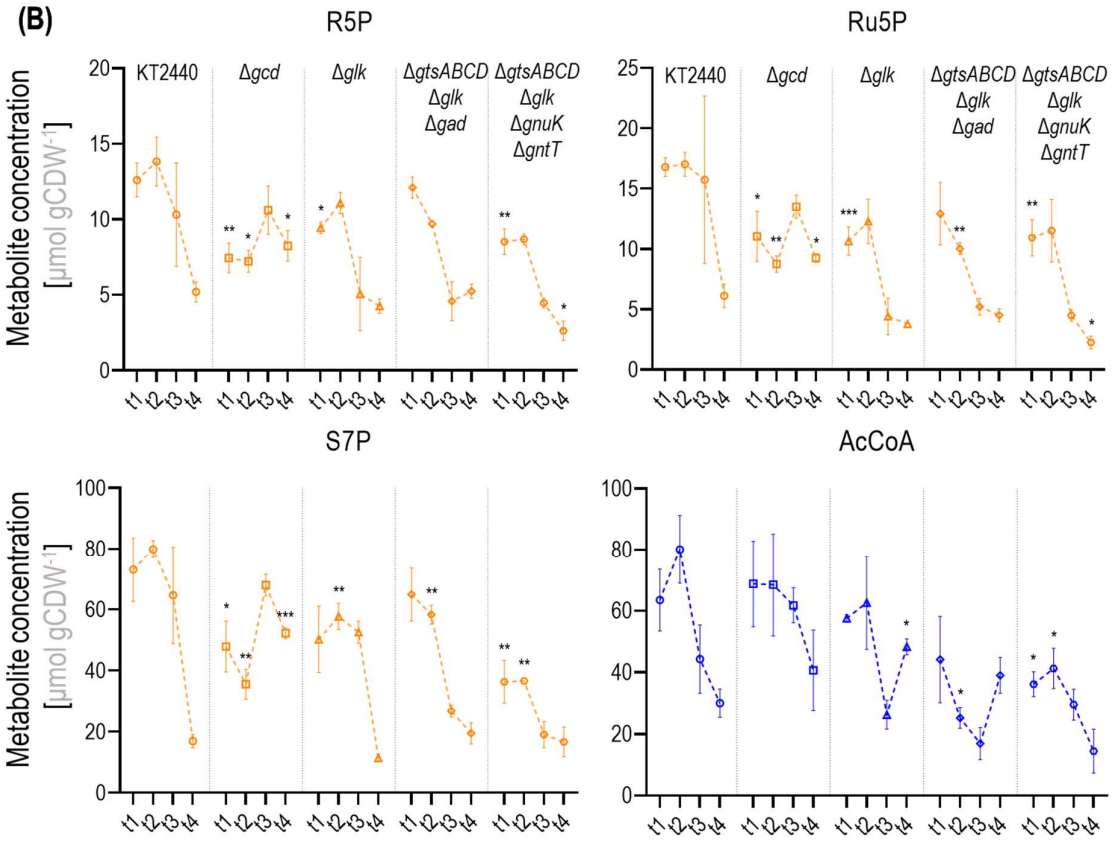
(B)
R5P
Ru5P
S7P
AcCoA
KT2440
Δgcd
Δglk
ΔgtsABCD Δglk Δgad
ΔgtsABCD Δglk ΔgnuK ΔgntT
Metabolite concentration [µmol gCDW-1]
t1 t2 t3 t4

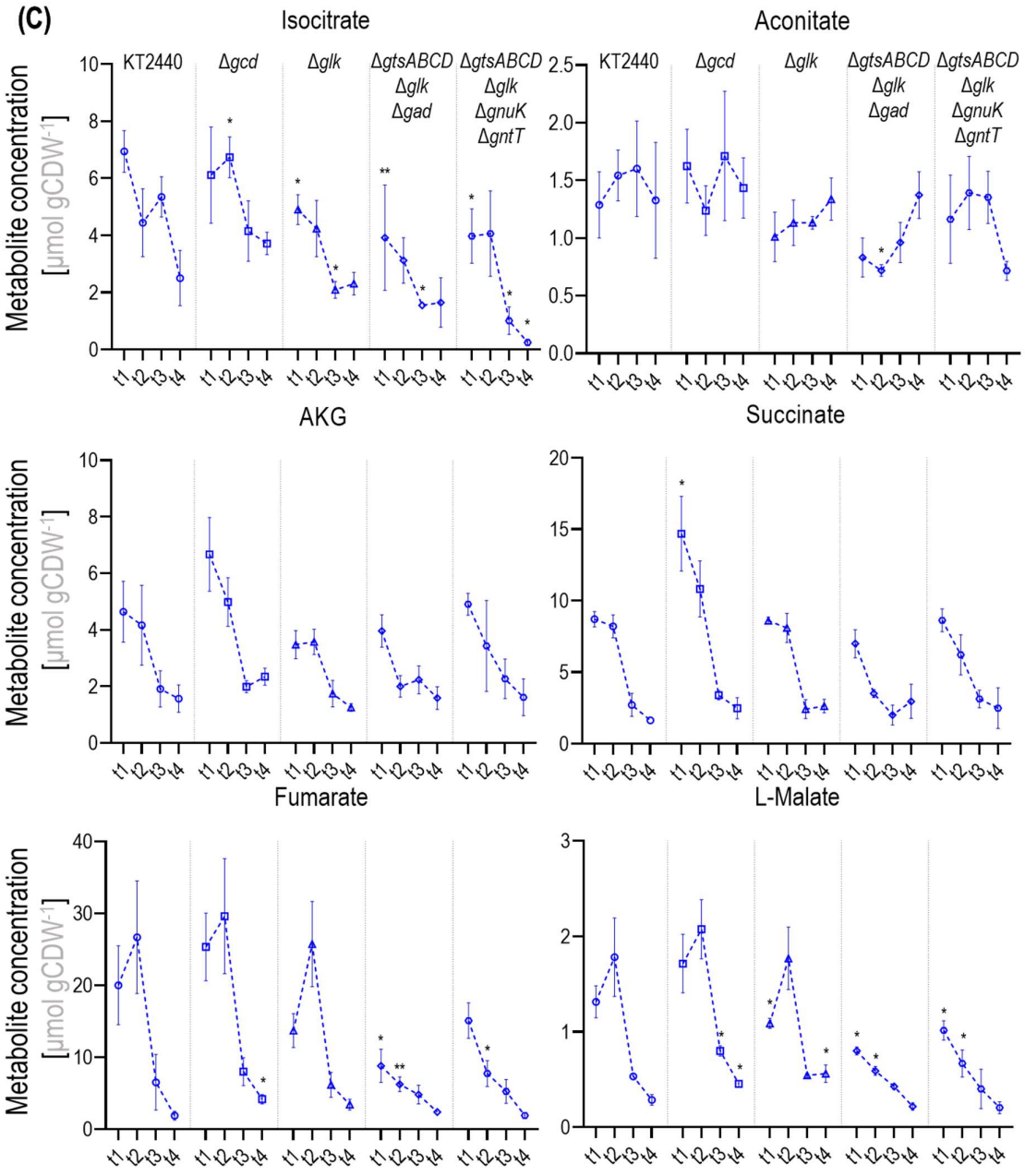

Figure 6.5. Central carbon metabolites concentration in the strains under study grown on de Bont medium at different time points. The strains were cultures in minimal medium supplemented with 15 mM glucose and harvested at different time points (t1, 2, 3 and 4). Metabolites in **A**. EDEMP pathway. **B.** Pentose phosphate pathway and **C.** Tricarboxylic acid cycle. Abbreviations of metabolites are as follows: G6P, glucose-6-P; F6P, fructose-6-P; FBP, fructose-1,6-P_2; DHAP, dihydroxyacetone-P; PEP, phosphoenolpyruvate; 6PG, 6-phosphogluconate; R5P, ribose-5-P; Ru5P, ribulose-5-P; S7P, sedoheptulose-7-P; AcCoA, acetyl-coenzyme A; AKG (2-OG), α-ketoglutarate. The strains are symbolized with circles (KT2440); squares (Δ*gcd*); triangles (Δ*glk*); diamond (Δ*gtsABCD*Δ*glk*Δ*gad*) and hexagon (Δ*gtsABCD*Δ*glk*Δ*gnuK*Δ*gntT*).

Similarly, PPP metabolites R5P, Ru5P and S7P concentrations remained stable in the strain Δ*gcd* at relatively high concentrations during t1-t4. This could be attributed to the cyclic operation of the pentose phosphate pathway aiming to balance the loose of electron equivalents in the glucose oxidative branch (Christodoulou, et al., 2018, Hurbain, et al., 2022). For the other mutants, the concentrations at t1 and t2 were significantly lower and dropping later in mid (t3) and late (t4) stages in comparison to the wild-type strain (**Figure 6.5B**).

Finally, regarding the strains Δ*gcd* and Δ*glk* with respect to TCA cycle metabolites, the products of NADH/$FADH_2$-forming reactions: acetyl-CoA, AKG, succinate and fumarate, exhibited comparable or higher concentrations than the other strains under study at early stages (t1 and t2). Particularly in Δ*gcd* strain, it is worth noting that the absence of glucose dehydrogenase could potentially cause an impairment in the cellular energy status [NADH, NAD(P)H] which is translated in a lower specific growth rate (Volke, et al., 2021). As a response against this energetic imbalance, the cell utilizes specific co-factor-forming reactions to fuel and compensate the amount of electro equivalents not produced in the perisplasmatic oxidation steps (Spaans, et al., 2015). One of this reaction is the production of fumarate from succinate through the succinate dehydrogenase complex (Sdh) yielding $FADH_2$ (Cecchini, et al., 2002). This response could partially supply reducing power for biomass precursor formation. On the other hand, the strains Δ*gtsABCD*Δ*glk*Δ*gad* and Δ*gtsABCD*Δ*glk*Δ*gnuK*Δ*gntT*, showed lower fumarate concentration than the other strains, indicating that co-factors were also obtained in other reactions such as the conversion of G6P into 6PG mediated by ZwfA,B,C and Pgl to give NAD(P)H or; through the action of the pyruvate kinase (Pyk) transforming PEP into pyruvate yielding one ATP (Fuhrer and Sauer, 2009) (**Figure 6.5C**).

6.3.1 Semi-quantitative proteomics analysis exposes changes in reducing power-generating reactions (NADH and NAD(P)H) as a responses to genetic disturbances in glucose peripheral oxidation steps

To study the effects of disturbing the glucose entry points at the protein level, the protein content of the different strains was analysed via mass spectrometry. Cells were grown in de Bont minimal medium supplemented with 15 mM glucose as carbon source and 5 g L^{-1} MOPS. In total, 2517 proteins were detected and; among these, 58 proteins belonging to the central carbon metabolism, were selected to analyse the magnitude of change or $\log_2$(fold change). The wild-type strain KT2440 was taken as reference point and compared against the four strains at different time points (t1-4). The results are shown in **Figure 6.6**. The X-axis represents the selected proteins at t1, t2, t3 and t4 and Y-axis exhibits $\log_2$(fold change). **Table S6.2** shows the $\log_2$(fold change) average and standard deviation for all the proteins analysed in the chapter are listed.

Within the peripheral reactions, in the Δ*gcd* strain, we noted a significant drop in the relative content of proteins involved in glucose oxidation (*PP3383-84*, GnuK, KguE-K and PtxS). Likewise, we observed an upregulation of the glucose transporter GtsA and GtsD, which could indicate that the system increases glucose uptake through the cytoplasm toward G6P by the glucokinase. In Δ*glk* and despite the inactivation of glucokinase, GtsA and D were also upregulated, suggesting the possibility of residual Glk activity. In contrast, Δ*gtsABCD*Δ*glk*Δ*gad* and Δ*gtsABCD*Δ*glk*Δ*gnuK*Δ*gntT* showed no signal after the proteomics analysis, confirming the deletion of the glucose facilitator complex gtsABCD.

In the pentose phosphate pathway, upregulation of ZwfA in Δ*gcd* and Δ*glk* was detected in t1-t2 and t1, t3-t4, respectively. For Δ*gcd*, this could suggest that a greater amount of G6P is transformed into 6PG, while simultaneously producing NAD(P)H with the objective of generating more precursor 6PG—showed a significant decrease in concentration during metabolomics analysis—and providing energy. Although the concentration of G6P was significantly reduced, our results showed that in the case of Δ*glk*, the overregulation of ZwfA facilitated the continuous production of 6PG at levels comparable to those of the wild-type strain. For Δ*gtsABCD*Δ*glk*Δ*gad* and Δ*gtsABCD*Δ*glk*Δ*gnuK*Δ*gntT*, proteomics showed a downregulation of ZwfA. It is

important to mention that the 6PG levels were similar to those of the wild-type strain, which suggests that either GnuK in the first mutant or KguK/KguE proteins in the second one could be responsible for maintaining this pool (**Figure 6.5A**). Going further in the PPP, we also noticed an upregulation of 6-phosphogluconate dehydrogenase (Gnd) in practically all the strains and times along the cultivation. The rise in protein content could imply an increase in the NAD(P)H generation to compensate the potential decline of reducing power produced in the oxidative peripheral branch reactions. Likewise and especially for the Δ*gcd*, the transaldolase Tal (catalyze the conversion of S7P + G3P into E4P + F6P) exhibited an overproduction of up to 100% in t1-t3. This enzyme might contribute to keep the F6P levels constant, as was previously revealed during the metabolomics analysis. In addition, we observed a reduction in the expression of Rpe, RpiA and TktA, which could indicate that the enzymes pool are not directly linked with the energy compensation mechanism in the cell (Rytter, et al., 2021). Regarding the ED pathway, there were significant chances, but they were not of considerable magnitude. This means that this two-step reaction has a comparable activity to the wild-type strain despite the alterations in the glucose peripheral oxidation and phosphorylation pathways. This behavior might explain why environmental bacteria, as *P. putida*, rely on the innate capability to use ED for glucose metabolism (Conway, 1992, Daddaoua, et al., 2009, Nikel, et al., 2015). Relating to the anaplerotic reactions, while Ppc was upregulated in Δ*gcd* and Δ*gtsABCD*Δ*glk*Δ*gnuK*Δ*gntT*, the oxaloacetate decarboxylase (PP1389) was downregulated. Although it was not previously reported in *P. putida*, this might point out that the activity of the Ppc could be positively regulated by the increased of the G6P favoring the reaction toward OAA (Sauer and Eikmanns, 2005) (**Figure 6.6A**). Regarding the EDEMP pathway, there were few notable alterations. Specifically, in the Δ*gcd* mutant, the downregulation of Pgi-1 and Fbp was observed as the primary change. Here, the increase in G6P and F6P concentration in the cytosol could negative control not only Pgi-1 but also Fbp. This relationship has not been previously observed in bacterial cells, but it has been observed in eukaryotic cardiomyocyte cells, which warrants further investigation to better understand the underlying biological processes (Karlstaedt, et al., 2020). In connection with the previous fact, we also argue that the decrease of these two enzymes together with the action of the transaldolase Tal could play a pivotal role in the regulation of F6P levels in the cell.

Moreover, in the lower part of the EDEMP pathway, the glyceraldehyde-3-phosphate dehydrogenase (GapA)—which catalyzes the transformation of GAP to glycerate-1, 3-biphosphate with the production of NADH—was significantly up-regulated in Δ*gcd* but, to a lesser degree in the mutants lacking the glucokinase enzyme (Fillinger, et al., 2000). This follows the same rationale as before where the cell attempts to counterbalance the energy deficit provoked by the inactivation of the glucose oxidative branch. This action mediated by GapA tries to conserve the high energetic efficiency of the EDEMP pathway but also might give rise to a post-translational regulatory checkpoint for the central carbon metabolism. As reported in the literature, the expression of the genes *gapA* and *gapB* are transcriptionally regulated in an opposite manner under glycolytic conditions. Our results indicated that meanwhile the production of GapA was stimulated, GapB was downregulated.

Finally, in the TCA cycle, Acetyl-coenzyme A synthetase 2 (AcsA2) was significantly over-regulated in most time points. This enzyme participates in the conversion of acetate to acetyl coenzyme A (acetyl-CoA) (Zhu, et al., 2022). When comparing our results to previous studies, it must be pointed out that acetate is not produced or secreted during glycolytic regimen in *P. putida*. AcsA2 could have a regulatory function over carbon metabolism genes, as it was previously demonstrated in *P. aeruginosa* (Kretzschmar, et al., 2010). Furthermore, reducing power forming enzymes, such as isocitrate dehydrogenase-NADP dependent (Icd) and malate:quinone oxidoreductase 3 (Mqo3), were significantly overregulated in all the strains and specifically at t3 (mid-exponential). These enzymes might be providing part of the energy in form of NAD(P)H to replenish reducing equivalents (LaPorte, et al., 1984, Kretzschmar, et al., 2002, Molina, et al., 2019). On the other hand, aconitate hydratase I (AcnA-I) and fumarate hydratase class II (FumC) were also up-regulated in Δ*gcd*, suggesting that could push the TCA cycle forward by increasing the pool of metabolites isocitrate, AKG, succinate, fumarate and L-malate (Mhamdi, et al., 2010, Spaans, et al., 2015) (**Figure 6.6C**).

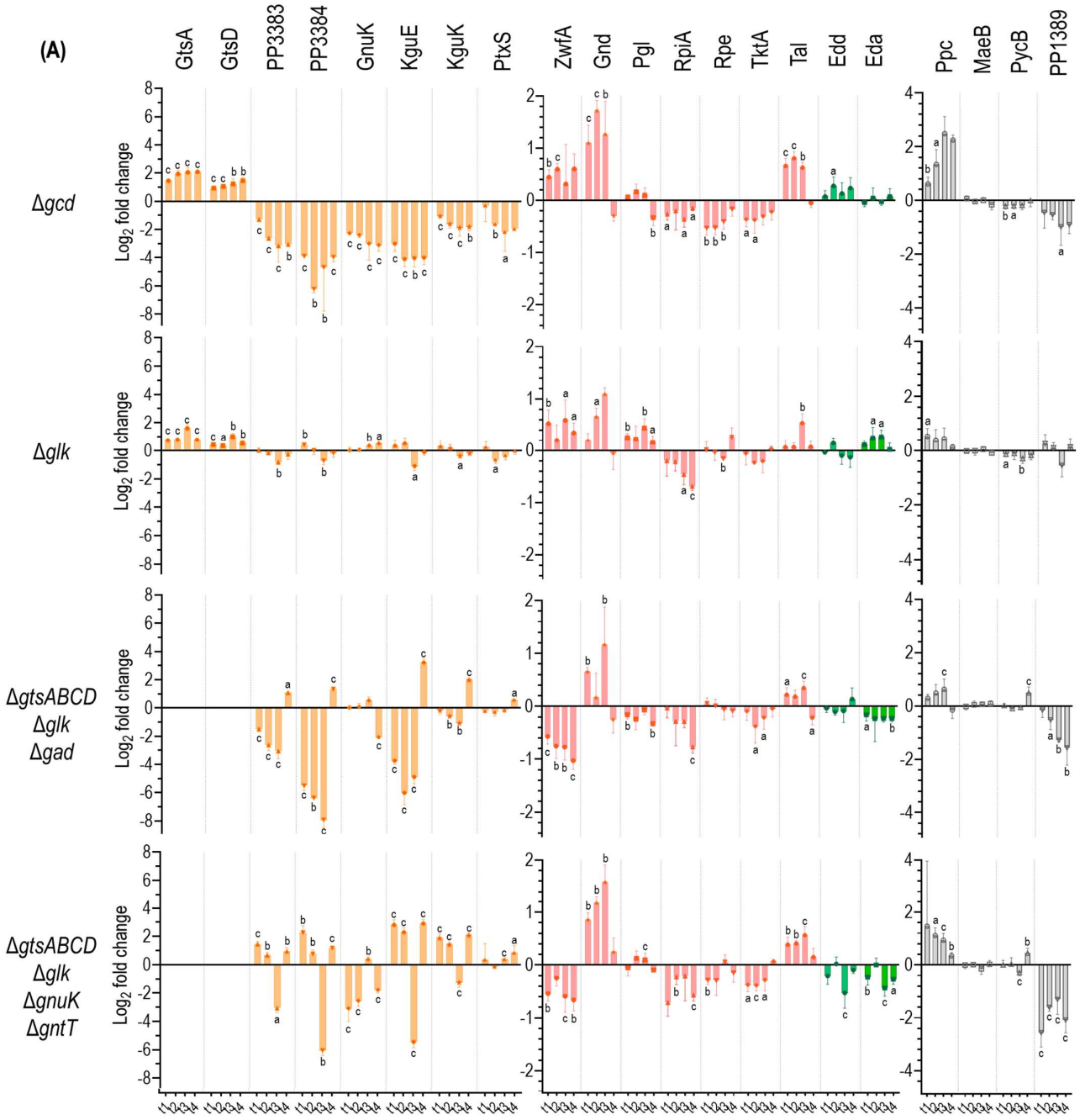
(A)
GtsA
GtsD
PP3383
PP3384
GnuK
KguE
KguK
PtxS
ZwfA
Gnd
Pgl
RpiA
Rpe
TktA
Tal
Edd
Eda
Ppc
MaeB
PycB
PP1389
Δgcd
Δglk
ΔgtsABCD Δglk Δgad
ΔgtsABCD Δglk ΔgnuK ΔgntT
Log2 fold change

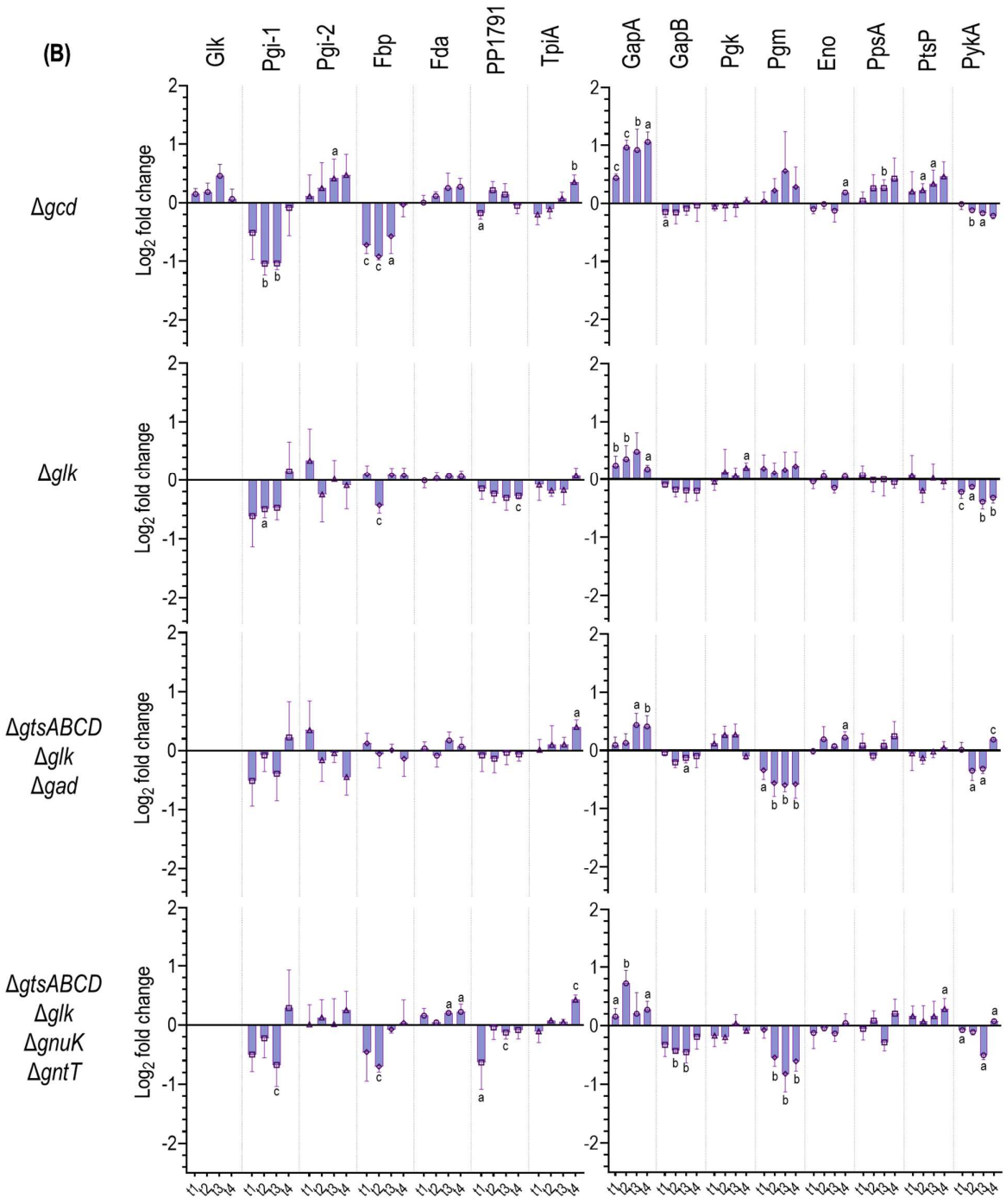
(B)
Glk
Pgi-1
Pgi-2
Fbp
Fda
PP1791
TpiA
GapA
GapB
Pgk
Pgm
Eno
PpsA
PtsP
PykA
Δgcd
Δglk
ΔgtsABCD Δglk Δgad
ΔgtsABCD Δglk ΔgnuK ΔgntT
Log2 fold change
t1 t2 t3 t4

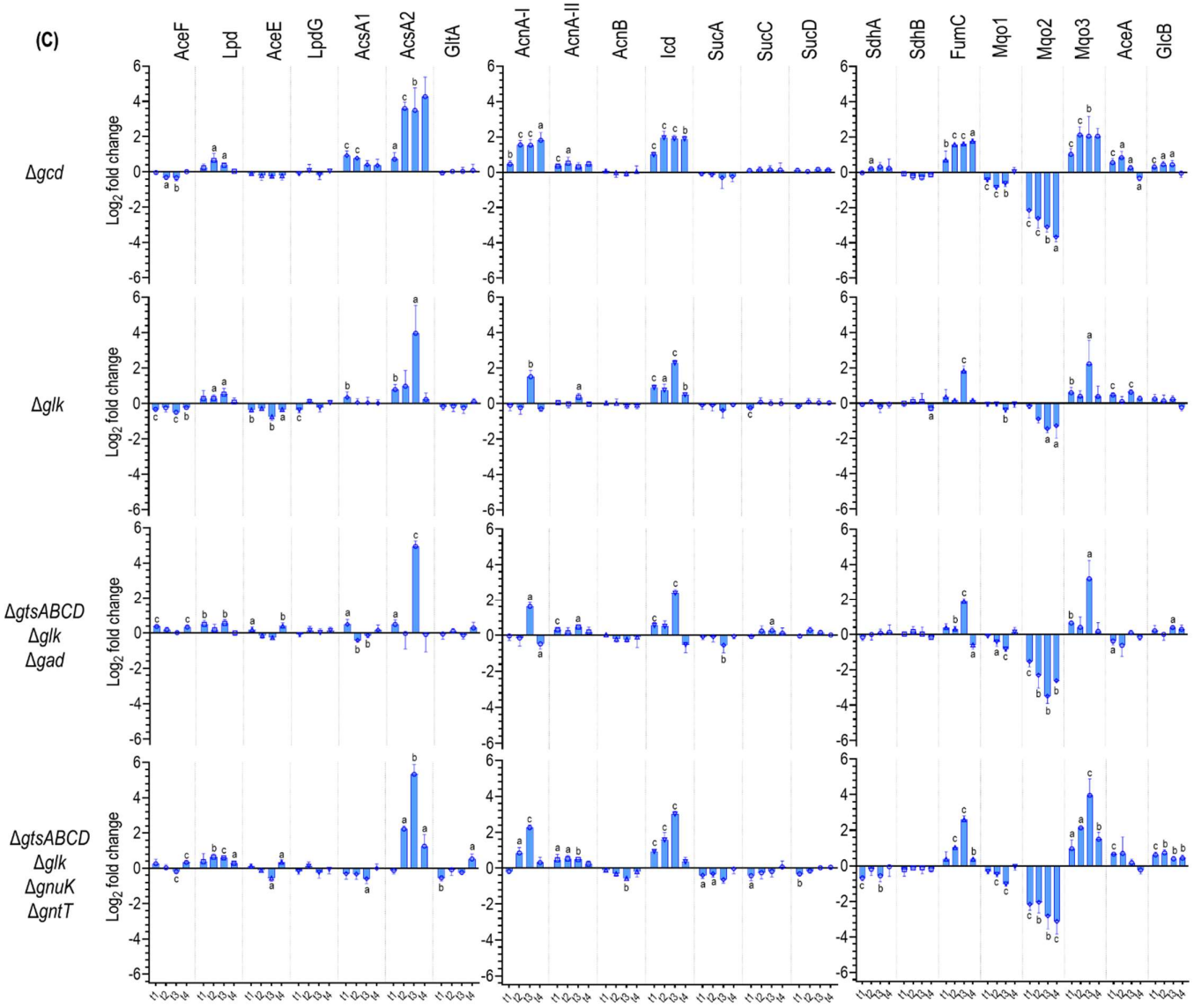

Figure 6.6. Changes in protein expression within central carbon metabolism for strains Δ*gcd*, Δ*glk*, Δ*gtsABCD*Δ*glk* and Δ*gtsABCD*Δ*glk*Δ*gntT* against *Pseudomonas putida* KT2440 wild type. A. Upper glycolysis, PPP, ED and Anaplerosis. Abbreviations of proteins are as follows: GtsA Mannose/glucose subunit A glucose system transporter; GtsD Mannose/glucose subunit D glucose system transporter; PP3383, Gluconate 2-dehydrogenase flavoprotein subunit; PP3384, Gluconate 2-dehydrogenase gamma subunit; GnuK, Gluconokinase; KguE, Epimerase; KguK, Putative 2-ketogluconokinase; PtxS, 2-ketogluconate utilization repressor; ZwfA, Glucose-6-phosphate 1-dehydrogenase A; Gnd, 6-phosphogluconate dehydrogenase; Pgl, 6-phosphogluconolactonase; Rpe, Ribulose-phosphate 3-epimerase; RpiA, Ribose-5-phosphate isomerase; TktA, Transketolase; Tal, Transaldolase; Edd; Phosphogluconate dehydratase; Eda, 2-dehydro-3-deoxy-phosphogluconate aldolase; Ppc, Phosphoenolpyruvate carboxylase; MaeB, Malic enzyme B; PycB, Pyruvate carboxykinase A; PP1389; oxaloacetate decarboxylase. **B. EDEMP and C. TCA.** Glk, glucose-binding periplasmic protein Glucokinase; Pgi-1, Glucose-6-phosphate isomerase 1; Pgi-2, Glucose-6-phosphate isomerase 2; Fbp,

Fructose-1,6-bisphosphatase class 1; Fba, Fructose-1,6-bisphosphate aldolase; PP1791, Putative Aldolase/synthase; TpiA, Triosephosphate isomerase; GapA, Glyceraldehyde-3-phosphate dehydrogenase A; GapB, Glyceraldehyde-3-phosphate dehydrogenase B; Pgk, Phosphoglycerate kinase; Pgm, Phosphoglucomutase; Eno, Enolase; PpsA, Phosphoenolpyruvate synthase; PtsP, Phosphoenolpyruvate-protein phosphotransferase; PykA, Pyruvate kinase; AceF, Acetyltransferase component of pyruvate dehydrogenase complex; Lpd, Dihydrolipoyl dehydrogenase; AceE, Pyruvate dehydrogenase E1 component; LpdG, Dihydrolipoyl dehydrogenase G; AcsA1, Acetyl-coenzyme A synthetase 1; AcsA2, Acetyl-coenzyme A synthetase 2; GltA, Citrate synthase; AcnA-I, Aconitate hydratase I; AcnA-II, Aconitate hydratase II; AcnB, Aconitate hydratase B; Icd, Isocitrate dehydrogenase [NADP]; SucA, Oxoglutarate dehydrogenase (succinyl-transferring); SucC, Succinate-CoA ligase [ADP-forming] subunit beta; SucD, Succinate-CoA ligase [ADP-forming] subunit alpha; SdhA, Succinate dehydrogenase flavoprotein subunit; SdhB, Succinate dehydrogenase iron-sulfur subunit; FumC, Fumarate hydratase class II; Mqo-Malalate:quinone oxidoreductase 1; Mqo-2, Malate:quinone oxidoreductase 2; Mqo-3, Malate:quinone oxidoreductase 3; AceA, Isocitrase; GlcB, Malate synthase.

6.3.2 ^{13}C-Metabolic flux analysis reveals a strong activity of EDEMP and TCA cycle upon metabolic perturbations

Metabolomics and proteomics data served as first step to analyse the dynamics between metabolites and proteins inside the cell (Kell, 2004, Sabidó, et al., 2012). However, the interaction between gene–protein–metabolite cannot be capture by only applying the previous methodologies (Yurkovich and Palsson, 2018). Metabolic flux analysis is a powerful strategy to quantify metabolic fluxes through the different metabolic routes (Sauer, 2006, Heinemann and Sauer, 2010). In order to get a better understanding as well as to characterize the metabolic architecture within the strains, we performed a parallel labelling experiment using [1–$^{13}C_1$]-glucose, [6–$^{13}C_1$]-glucose, and a mixture of each 50% unlabeled and uniformly labelled glucose [U–$^{13}C_6$]-glucose. This particular combination of tracers has been employed previously to generate precise flux maps in *Pseudomonas sp.*, with satisfactory results (Kohlstedt and Wittmann, 2019). The flux distribution maps for all the strains are depicted in **Figure 6.7**, the reactions investigated, atom transitions and the calculated relative fluxes associated to the catabolic pathways are listed in **Table S6.4**. The ^{13}C-MFA analysis of the five strains displayed sum of squared residuals (SSR) values within the given interval.

Our results obtained from the ^{13}C metabolic flux analysis revealed that fluxes in the EDEMP pathway and TCA cycle in the Δ*gcd* mutant strain were 1.5 to 4.0 times greater than those observed in the wild-type strain, respectively (**Figure 6.7A and 6.7B**). It is noteworthy that there was a convergence of net flux towards the G6P node. This was the result of both glucose phosphorylation and F6P isomerization, which then proceeded to 6PG with a relative flux of ~150% (11.2 mmol g_{CDW}^{-1} h^{-1}). This observation was consistent with a higher abundance of Zwf and Gnd proteins detected in the proteomics analysis (**Figure 6.6A**). Additionally, this mutant recycled 80% more of the triose phosphate GAP into to F6P and G6P compared to the wild-type strain (52% versus 29%, respectively). The process of recycling may serve an additional purpose, as it leads to the production of NAD(P)H through the activity of glucose 6-phosphate dehydrogenase (Zwf) (Nikel, et al., 2015). In conjunction with this recycling process, the cell is also able to contribute to the production of E4P and R5P for anabolic purposes, through the reversible reactions in the pentose phosphate pathway (Nikel, et al., 2015). In the lower part of the EDEMP cycle, the split ratio between FBP, DHAP and 3PG was nearly 1:1:1 at the G3P node for all the strains suggesting could work as a key regulator node in the lower glycolysis (Ma and Zeng, 2003, Lee, et al., 2021). Furthermore, the fluxomics results obtained in this experiment, correlated with proteomics analysis where GapA was overregulated during the entire cultivation and the increasing in the concentration of the metabolites DHAP, FBP and G6P from t1 to t3 (**Figure 6.6B**).

The majority of the strains, excluding the mutant strain Δ*gtsABCD*Δ*glk*Δ*gnuK*Δ*gntT*, exhibited negligible flux through the PP pathway. This was because 6PG was largely directed towards the Entner-Doudoroff (ED) pathway, indicating its vital role in glucose catabolism (Chavarría, et al., 2013). In the wild-type strain, 40% of the ED pathway flux was channeled into the TCA cycle while for the strains under study this percentage oscillated between 53-90%. In general, we observed that there was a substantial flux redirection toward the TCA cycle where large amounts of C_3 and C_4 building blocks were interchanged between the EDEMP and TCA cycles (Nikel, et al.,

2015). Also, we noted that the glyoxylate shunt was inactive in all the tested strains, where the remaining flux toward the isocitrate node was mainly converted by the isocitrate dehydrogenase (Icd) through the TCA cycle. Likewise, the anaplerotic reactions were not affected in the conditions tested in this study. With regards to Δ*glk* and Δ*gtsABCD*Δ*glk*Δ*gad*, the metabolic flux map were comparable in terms of flux distribution, with around 50-75% relative flux through TCA cycle and 30-40% in the EDEMP (**Figure 6.7C and 6.7D**).

Regarding the mutant Δ*gtsABCD*Δ*glk*Δ*gnuK*Δ*gntT*, nearly 90% of reduction was observed in the fluxes thought the TCA cycle. Particularly, for this mutant, it is worth mentioning that 60% of the flux was secreted out of the cell in form of 2-KGA and, 30% of the 6PG pool was re-route into the PP pathway. Furthermore, the process of converting 2-ketoglutarate (2-KGA) into 2-ketoglutarate-6-phosphate (2-KGA-6P) through phosphorylation, and then reducing it to 6-phosphogluconate (6PG), is a significant consumer of ATP in this particular strain, leading to a decreased fitness level that contrasts with the results of a physiological analysis. To ensure the energy supply, the strain keeps oxidizing glucose into 2-KGA and deviate a significant fraction of its flux toward PP pathway, attempting to recover reducing power from the reductive decarboxylation of 6-phosphogluconate into ribulose-5-phosphate (Nikel, et al., 2015, Kohlstedt and Wittmann, 2019) (**Figure 6.7E**).

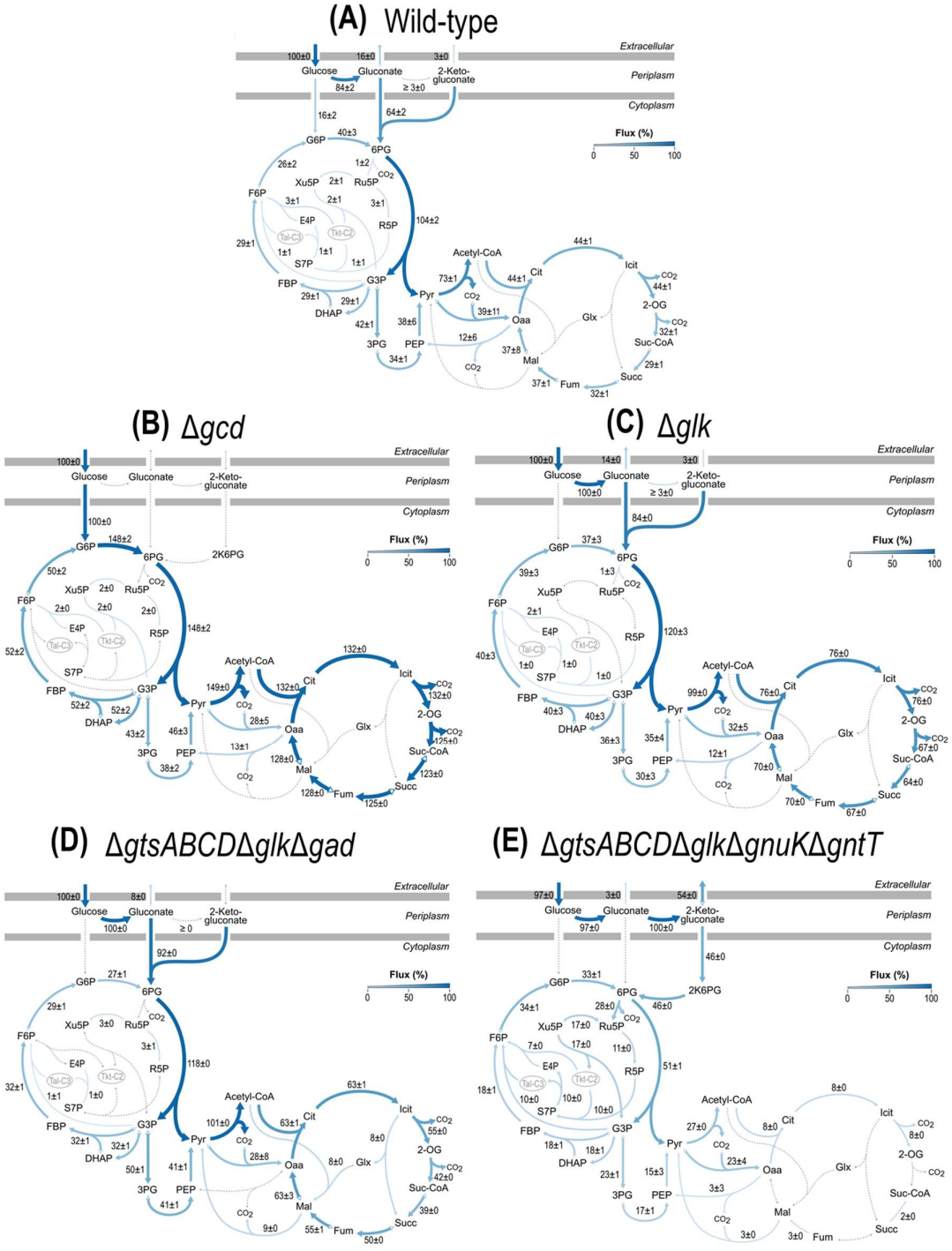

Figure 6.7 Flux distributions of *Pseudomonas putida* KT2440 wild type and their mutants. 1) Wild-type; 2) Δ*gcd*; 3) Δ*glk*; 4) Δ*gtsABCD*Δ*glk*Δ*gad* and 5) Δ*gtsABCD*Δ*glk*ΔgnuKΔ*gntT*. The flux values of the best fit were normalized to the specific glucose uptake rate (refer **Table 6.1** for details) in mmol g_{CDW}^{-1} h^{-1} of 100%. The absolute value for total carbon consumption rate is based in the sum of glucose, gluconate and 2-KGA uptakes. 2-OG represents AKG: 2-oxoglutarate.

6.4 Outlook

6.4.1 Alterations in the peripheral and upper glucose pathway in *Pseudomonas putida* KT2440 channel glucose fluxes through the metabolic 6PG node

Overall, *P. putida* KT2440 strains showed a systematic response upon the different genetic perturbations in the peripheral reactions involved in glucose processing. The genetic deletions exposed changes at different metabolic levels, which were capture by applying metabolism-centric approaches. Interestingly, all the reaction were channeled into the central node 6PG, which acts as one of the most important carbon distributor in the CCM but also potentially as NAD(P)H enhancer formation through Gnd (Udaondo, et al., 2018).

The growth patterns of the various strains were significantly impacted by these alterations. In the strain Δ*gcd*, lacking the glucose dehydrogenase, the process of double oxidation leading to the formation of gluconate and 2-KGA was eliminated, prompting the cell to instead directly undergo glucose phosphorylation. This might compromise the generation of ATP and NADH as a consequence of the absence of the oxidation steps (Ebert, et al., 2011). However, the cell can compensate it by increasing the protein amount in specific reactions across the CCM (Noor, et al., 2010, Pfeuty, et al., 2023). A portion of this energy compensation can be observed through the convergence of metabolic fluxes towards 6PG, coupled with the overproduction of ZwfA and Gnd enzymes.

In contrast, *glk* mutant showed a decrease in the growth rate and reached lower OD_{600nm}, which suggests a shortage in biomass precursors—mainly G6P, and F6P—as reported in the metabolomics study (**Figure 6.5A**) (del Castillo, et al., 2007). Likewise, most of the flux was channeled toward 6PG through Gcd and GnuK enzymes and to a less extent by the second oxidation step though Gad, KguK and KguD. On the other hand, the mutant harboring the deletion Δ*gtsABCD*Δ*glk*Δ*gad* was not affected in terms

of growth. Given that approximately 90% of the glucose undergoes conversion to 6PG via GnuK, it can be inferred that the second oxidation step, leading to 2-KGA, may not be a prerequisite for sustaining cellular energy homeostasis, unlike the initial oxidation step. Moreover, this second step appears to be linked with environmental or energy stresses (Bentley, et al., 2008). Regarding Δ*gtsABCD*Δ*glk*Δ*gnuK*Δ*gntT*, the removal of GnuK beyond what has been previously documented could potentially impact the activation or suppression of specific regulators in genes further downstream (del Castillo, et al., 2008, Daddaoua, et al., 2009, Moreno, et al., 2009, Udaondo, et al., 2018). In this particular strain, the flux was directed towards 6PG via a process involving double oxidation, phosphorylation, and subsequent reduction of 2-KGA-6P to form 6PG.

The time-course targeted metabolomics approach captured the fluctuation in the metabolites levels through the CCM pathways. Notably, the deletion of *gcd* produced an accumulation of G6P while maintaining the F6P and cycling the EDEMP pathway. Consistent with reported knockout of genes in glucose catabolism in *P. putida* strains grown on glucose, we observed a decrease or absence in both protein abundances and metabolic fluxes in the reactions that the genes were knocked out compared to the wild type strain. In the same direction, the CCM metabolome and proteome reacted to meet energetically favorable metabolic fluxes to produce and compensate the reducing power in form of NADH, $FADH_2$ and NAD(P)H. The higher flux in the node glucose-G6P-6PG, could be connected with the overexpression of Glk and ZwfA enzymes together with the increasing concentration of G6P, as well as a possible involvement of HexR and PtsX regulation in *P. putida* (Hamood, et al., 1996, Castillo, et al., 2007, Daddaoua, et al., 2009, Daddaoua, et al., 2012, Udaondo, et al., 2018, Lim, et al., 2022). Furthermore, it could be associated to post-transcriptional regulation mechanisms (gene transcripts stabilization) in upper part of the glycolysis or (Morin, et al., 2016); post-transcriptionally regulated by binding—in close proximity—to the ribosome binding site which, hinders the translation process of the target mRNA,

leading to the inhibition of translation or facilitating mRNA decay (Timmermans and Van Melderen, 2010).

6.4.2 Metabolic versatility model of *Pseudomonas putida* KT2440 upon genetic alterations in the peripheral glucose pathway.

The research findings have prompted the proposal of a metabolic model for *P. putida* that aims to balance energy and metabolic homeostasis within the cell when there is genetic disruption in the peripheral glucose reactions (**Figure 6.8**). The hypothetical model is founded on the findings derived from the multi-omics experiments, which enabled us to pinpoint systemic alterations in the metabolome, proteome, and fluxomes that resulted from the varied genetic modifications. From a metabolomics point of view, metabolite levels of G6P, F6P, PEP, DHAP and 6PG in the EDEMP pathways as well as R5P, Ru5P and S7P in the PPP fluctuate across the cultivation in the different strains. Similarly, we detected a number of key enzymes, associated with energy generation, that we over regulated in the conditions tested. GapA, Icd, and FumC were observed to exhibit variations, as they are responsible for generating NAD(P)H, which is crucial for supplying both redox and energy equivalents to the cell.

Finally, flux distribution maps showed higher activities in the EDEMP and TCA cycle pointing out that both metabolic blocks work in conjunction to regulate energy metabolism by producing ATP and reducing equivalents, such as NADH, NAD(P)H and $FADH_2$, which are subsequently utilized in the electron transport chain to generate energy. Overall, this hypothetical model suggests a complex regulatory network that operates to maintain energy and metabolic homeostasis in *P. putida* (**Figure 6.8**) (Kotte, et al., 2010).

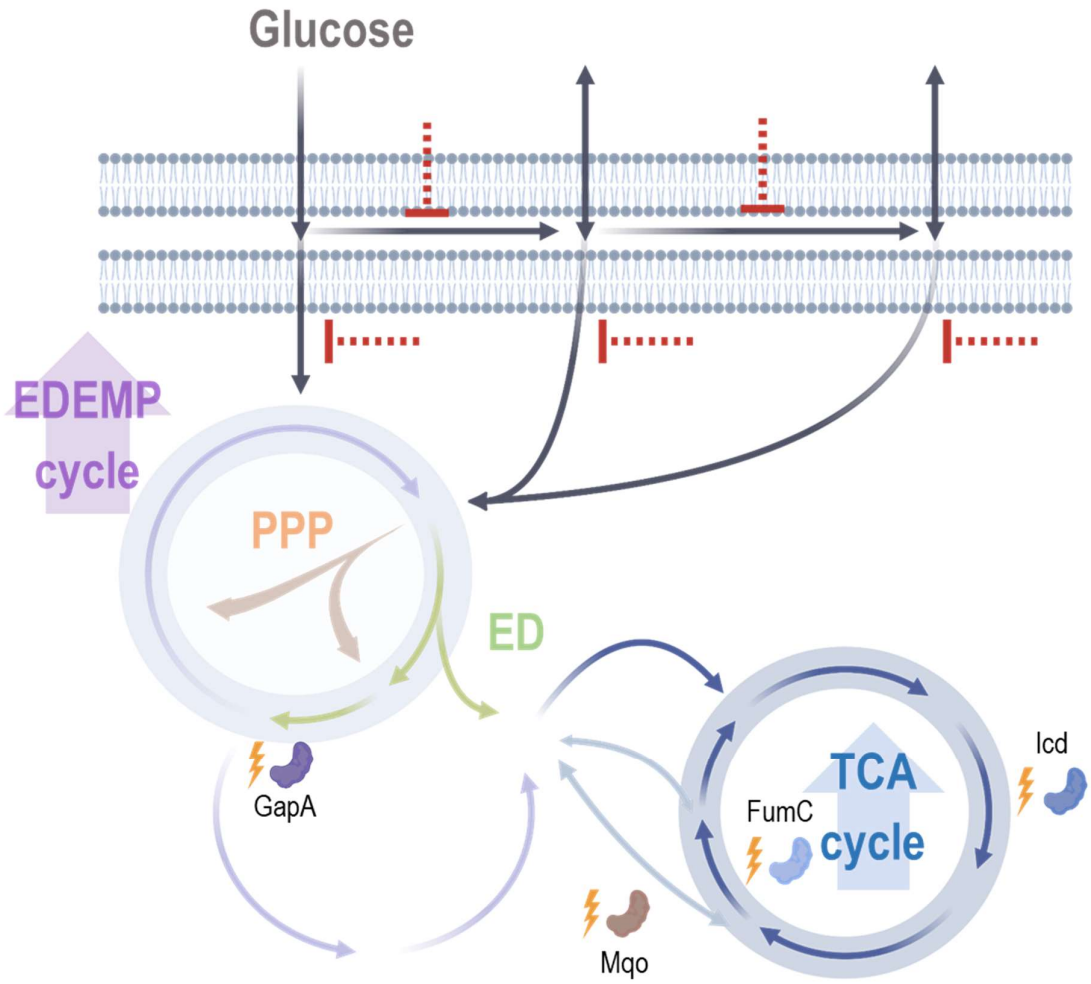

Figure 6.8. Proposed model of metabolic versatility for *Pseudomonas putida* KT2440 subjected to genetic perturbations. EDEMP encompasses the key elements belonging to the Entner-Doudoroff (ED) pathway (in green), the Embden-Meyerhof-Parnas pathway (in purple, operating in the gluconeogenic direction), and the pentose phosphate pathway PPP (in orange). TCA (Tricarboxylic acid) cycle and anaplerotic reactions in grey are also shown. Genetic perturbations in the glucose peripheral reactions are symbolized with red dashed lines. GapA, Icd, Mqo and FumC are enzymes involved in energy homeostasis in this particular model.

6.5 Conclusions

To comprehend the physiological response in the different mutants on glucose, we employed a systems biology approach (quantitative physiology and multi-omics analysis). Aiming to unravel and identify intracellular mechanisms that could tempter the effects of the different genetic modifications, we performed time-course targeted metabolomics, semi-quantitative proteomics and ^{13}C-metabolic flux analysis. By applying these methodologies, we were able to perform an in-depth multi-level analysis of the metabolism in *P. putida* KT2440. In summary, the strong and flexible robustness against energy imbalances makes *P. putida* KT2440 as a suitable microbial host for energy-demanded biocatalysis applications. The system biology analysed presented here, provides useful insights into the physiological and metabolic response of this Gram-negative bacteria to generic perturbations. Overall, while the energy homeostasis model provides a general framework for understanding the regulation of energy metabolism in cells, the specific mechanisms of metabolic regulation can vary widely between different organisms and metabolic pathways. The metabolic regulation in *P. putida* represents an example of how metabolic pathways interact to achieve specific cellular functions.

6.6 Materials and Methods

Table 6.2. Strain used in this study.

Strain	Genotype / Relevant characteristics	Reference or source
P. putida KT2440	Wild-type strain, derived from *P. putida* mt-2 cured of the TOL plasmid pWW0	(Worsey and Williams, 1975, Bagdasarian, et al., 1981)
Δ*gcd*	Deletion of *gcd* gene (*PP1444*) encoding periplasmic glucose dehydrogenase	This study
Δ*glk*	Deletion of *glk* gene (*PP1011*) encoding glucokinase	This study
Δ*gtsABCD*Δ*glk*Δ*gad*	Deletion of *gtsABCD* operon (*PP1015-PP1018*) encoding glucose ABC transporter, glucokinase and *gad* cluster genes	This study
Δ*gtsABCD*Δ*glk*Δ*gnuK*Δ*gnt T*	Deletion of *gtsABCD* operon (*PP1015-PP1018*), glucokinase, *gnuK* gene encoding the gluconate kinase (*PP3416*) and *gntT* gene encoding the citoplasmatic D-gluconate transporter (*PP3417*)	This study

6.6.1 Bacterial strains and culture conditions

The bacterial strains employed in this study are listed in **Table 5.2**. *Pseudomonas putida* strains were incubated at 30°C for all the experiments. Cell propagation and storage, were grown in lysogeny broth (LB) medium (10 g L^{-1} tryptone, 5 g L^{-1} yeast extract, and 10 g L^{-1} NaCl). Liquid pre-cultures were performed using either 50-ml centrifuge Falcon® tubes with a medium volume of 10 mL. Cultures were cultivated in 100-mL flat bottom Erlenmeyer containing 20 mL de Bont medium supplemented with 20 mM glucose as only carbon source. The media was buffered with 5 g L^{-1} 3-(*N*-morpholino)propanesulfonic acid (MOPS) at pH 7.0. Liquid pre-cultures were agitated at 250 rpm (MaxQ™8000 incubator; ThermoFisher Scientific, Waltham, MA, USA). Cultures were incubated at 200 rpm (New Brunswick™ Innova® 42/42R Shaker, sticky pad). Solid culture media contained an additional 15 g L^{-1} agar.

6.6.2 Sampling for multi-omics analysis

Samples were taken according the procedure described in **Chapter 2** with some modifications described as follows: for footprinting analysis, several samples—one per hour—were taken from 2 to 11 hours of cultivation. The bacterial growth was followed by measuring the optical density at 600nm (OD_{600nm}), the samples were centrifuged at 10,000 *g* for 5 min. at 4°C. The supernatant was collected and frozen at -20°C until further characterization. For time-course metabolomics, four samples per flask were taken across the cultivation at different metabolic states: Lag-phase or *t1* (OD_{600nm}~0.1), mid-log(1) or *t2* (OD_{600nm}~0.5), mid-log (2) or *t3* (OD_{600nm}~1.0-1.2) and late or *t4* (OD_{600nm}~2.0-2.5). Each sample was quickly filtrated in MF Millipore™ membrane filter (0.45-μm pore size; Sigma-Aldrich Co.). Later, the filter containing the bacterial biomass was quenched with 1 ml of [40% (vol. $vol.^{-1}$) acetonitrile, 40% (vol. $vol.^{-1}$) methanol and 100 mM formic acid] at −20°C. The resulting solution was transferred into a 2-ml Eppendorf tube; the filter was rinsed with an extra 1-ml of quenching solution and collected in the same tube. Samples were placed in a dry ice bath for 30 min and; after that, the samples were thawed and centrifuged at 13,000 *g* for 5 min. Later, the supernatants were transferred to a new tube to evaporate the solvent in a SpeedVac centrifuge (2 h at 45°C). Finally, the samples were stored at −80°C until prior analysis. Prior to the LC-MS/MS analysis, the samples were resuspended in 100 μl of LC–MS grade water. For proteomics and fluxomics sampling, a total of 1 OD_{600nm} was harvested at phase mid-log (2) or *t3* (OD_{600nm}~1.0-1.2). The samples were centrifuged at 10,000 *g* for 5 minutes and the supernatant was discarded. Next, the biomass was washed twice by adding 1 mL of de Bont minimal media without carbon source. Samples were centrifuged at 10,000 *g* between each wash step and the pellet was frozen at -80°C for further analysis. Three biological replicates were carried out for each experiment.

6.6.3 Determination of physiological parameters

Regression analysis was applied during exponential growth to calculate (i) the maximum specific growth rate (μ_{max}); (ii) the specific rate of glucose (q_s); (iii) biomass yield on substrate ($Y_{X/S}$); (iv) specific ATP production rate (q_{ATP}) and (v) the biomass yield on ATP ($Y_{X/ATP}$). CDW was determined by harvesting 10 mL of cells in independent flasks at different optical densities. The cells were centrifuges at 10,000 *g* for 10 min and washed twice with MQ-water. The biomass was transferred by pipetting into pre-weighed glass and dried at 105 °C until constant weight. q_{ATP} and $q_{NAD(P)H}$ were calculated using the following (**Equation 1**):

$$\sum_{i=0}^{n} r_{i\,ATP/NAD(P)H\ producing\ reactions} - \sum_{i=0}^{n} r_{i\,ATP/NAD(P)H\ consuming\ reactions} \quad \textbf{(Equation 1)}$$

r_i is the specific production or consuming rate for the reaction i and n is the total amount of reactions contributing to ATP or NAD(P)H formation/consumption in the metabolic network of the different *P. putida* strains.

6.6.4 Supernatant analysis via HPLC

Glucose, gluconate and 2-ketogluconate were analyzed using a Dionex Ultimate 3000 HPLC with an Aminex® HPX-87X Ion Exclusion (300×7.8 mm) column (BioRad, Hercules, CA) and RI-150 refractive index and UV (260, 277, 304 and 210 nm) detectors. For analysis, the column was maintained at 30°C and a 5 mM H_2SO_4 solution was used as mobile phase at a flowrate of 0.6 mL min^{-1}. HPLC data were processed using the Chromeleon 7.1.3 software (Thermo Fisher Scientific), and compound concentrations were calculated from peak areas using calibration curves with seven different standard concentrations (Glucose range: 0 – 20 mM. Gluconate: 0 – 10 mM. 2-ketoglucoante: 0 – 10 mM).

6.6.5 Targeted metabolomics analysis via LC-MS/MS

Samples at -80°C were thawed on ice and prepared for injection. Chromatographic separation of metabolites was done with an ACQUITY UPLC™ high-strength silica T3 column (XP, XSelect HSS 2.5 μm, 2.1×150 mm from Waters) in an HPLC apparatus (Shimadzu; Columbia, MD, USA). A gradient of eluent A [5% (vol. vol.$^{-1}$) methanol, 2% (vol. vol.$^{-1}$) 2-propanol, 10 mM tributylamine (TBA) and 10 mM acetic acid in H_2O] and 2-propanol was implemented for metabolite separation (McCloskey, et al., 2018). The flow rate was set to 0.4 ml min^{-1} with a total run time of 33 min.; the autosampler was kept at 10°C and the column oven was set at 40°C with an injection volume of 10 μl. For metabolite identification as well as determination, a mass spectrometer (QTrap™ AB SCIEX mass spectrometer 5500) was operated in negative ion mode with the following settings: ionization set, −4500; temperature, 500°C; curtain gas, 45; collision gas, high; ion source gas, 1; and ion source gas pressure, 250 pound square inch^{-1}. Metabolomics data analysis was carried out in Excel and the analysed data—metabolite fold change (FC)—were used as input to visualize the data in line graphs using GraphPad Prism® 9.5.0.

6.6.6 Semi-quantitative proteomics by mass spectrometry (MS)

For sample processing, the cell pellets were thawed on ice and; later, the tubes were centrifuged at max speed (21,000 *g*) for 10 min. While maintained on ice, two 3-mm zirconium oxide beads (Glen Mills, NJ, USA) were added to the samples. After removing the samples from ice, 100 μl of 95°C 6 M Guanidinium hydrochloride (GuHCl), 5 mM tris(2-carboxyethyl)phosphine (TCEP), 10 mM chloroacetamide (CAA), and 100 mM Tris–HCl pH 8.5) was added to the samples. Cells were lysed using a Mixer Mill (MM 400 Retsch, Haan, Germany) set at 25 Hz for 5 min. at room temperature, followed by 10 min. in a thermal mixer at 95°C and 2000 rpm. The cell debris was removed by centrifugation at 21,000 g for 10 min. Later, 50 μl of supernatant was collected and diluted with 50 μl of 50 mM ammonium bicarbonate. Next, the protein concentration was quantified utilizing Bradford method with BSA

concentration standard. An aliquot containing 100 µg of total protein was collected for tryptic digestion. The enzymatic digestion was performed at 400 rpm for 8 h, after which 10 µl of 10% trifluoroacetic acid (TFA) was added. For peptide purification, enrichment and pre-fractionation, a C18 resin (Empore, 3M, USA) was used as part of the StageTipping process.

The purified peptides were analysed using a CapLC system (Thermo Scientific) coupled to an Orbitrap Q exactive HF-X mass spectrometer (Thermo Scientific). Initially, samples were captured on a pre-column (µ-precolumn C18 Pep-Map 100, 5 µm, 100Å) at a flow rate of 10 µl $min.^{-1}$. Subsequently, the peptides were separated on a 15 cm C18 easy spray column (PepMap RSLC C18 2µm, 100Å, 150 µm×15 cm) at a flow rate of 1.2 µl $min.^{-1}$. A gradient from 4% (v/v) acetonitrile in water to 76% (v/v) was applied over a total of 60 min. While spraying the samples into the mass spectrometer, the instrument operated in data-dependent acquisition (DDA) mode using the following settings: MS-level scans were performed with Orbitrap resolution set to 60,000; AGC Target 3.0e6; maximum injection time 50 ms; intensity threshold 5.0e3; dynamic exclusion 25 s. Data-dependent MS2 selection was performed in Top 20 Speed mode with HCD collision energy set to 28% (AGC target 1.0e4, maximum injection time 22 ms, Isolation window 1.2 m/z). For analysis of the thermo .raw files refer to methodology in **Chapter 2.**

6.6.7 Parallel ^{13}C-labelling cultivations for flux analysis

For parallel labelling tracer experiments, *Pseudomonas putida* strains were grown as indicated in **Bacterial strains and culture conditions** by supplementing the medium with the labeled substrate of preference. In this experiment, three different isotopic tracers combination were used [1–$^{13}C_1$]-glucose, [6–$^{13}C_1$]-glucose, or a mixture of each 50% unlabeled and uniformly labeled glucose [U–$^{13}C_6$]-glucose (Kohlstedt and Wittmann, 2019). All labeled substrates were acquired from Cambridge Isotope Laboratories Inc. (Teddington, Middlesex, United Kingdom). Pre-cultures were

performed in de Bont minimal media with 15 mM unlabeled glucose with 5 g L^{-1} MOPS. The cultures were inoculated at an initial OD_{600nm} of 0.025 in a 100-mL Erlenmeyer flask containing 20 mL of de Bont medium with the specific tracers. For culture inoculation, aliquots were taken from the pre-cultures, centrifuged at 10,000 *g* and 4°C for 5 min, and washed twice using de Bont medium without a carbon source. All experiments were performed in three biological replicates and two technical replicates, and multiple samples were harvested for the analysis of either proteinogenic amino acids or cellular sugars (glucose-6-phosphate and fructose-6-phosphate).

6.6.8 Sample preparation and GC-MS analysis of proteinogenic amino acids and cellular sugar

Please refer to **Chapter 2** for a detailed explanation.

6.6.9 Reaction network and computational design for flux estimation

The metabolic networks of the different *Pseudomonas putida* strains were built based on the most updated genome-scale metabolic model (Nogales, et al., 2020). In total, 79 reactions were included as part of the central carbon metabolism in *Pseudomonas putida* KT2440 Wild-type. In the case of the strains containing the deletions, the following reactions were set to zero (0) form the "core model" of 79 reactions: R3 to R10 for Δ*gcd*; R2 for Δ*glk*; R6 to R9 for Δ*gad*; R2 and R6 to R9 Δ*gtsABCD*Δ*glk*Δ*gad* and; R2 and R5 for Δ*gtsABCD*Δ*glk*Δ*gnuK*Δ*gntT*. All the reactions, as well as the carbon atom transitions, are listed in **Table S6.4** and **Table S6.5**, respectively. The INCA software package was utilized for ^{13}C-metabolic flux analysis (^{13}C-MFA) (Young, 2014). Specific growth rates, uptake and secretion rates for glucose, gluconate and 2-ketogluconate (2-KGA) were used to constrain the MFA model. The general biomass equation was derived from the normalized precursor drainage to calculate experimental growth rates (Ebert, et al., 2011, Kohlstedt and Wittmann, 2019, Czajka, et al., 2022) . The relative fluxes of fixed parameters (glucose, gluconate, 2-KGA, biomass formation, ATP and NAD(P)H)

were calculated and expressed as a percentage based on the uptake rate of glucose (100%) (**Table S6.3**). Intracellular fluxes were estimated by iteratively minimizing the weighted sum-of-squared-residuals (SSR) between simulated and experimental labeling data for proteinogenic amino acids, extracellular sugars and sugar acids, glycogen, and glucosamine [i.e., the mass isotopomer distribution vectors (MDVs) of all analyzed fragments]. To ensure that the global best solution was determined, the flux estimation was iterated 20 times, starting with random initial values. Upon convergence, a $\chi 2$ test was applied to assess the goodness-of-fit. The 95% confidence intervals were calculated by determining the sensitivity of the sum of squared residuals to flux parameter variations (Antoniewicz, et al., 2006). The full set of calculated fluxes, including best fits, standard deviations, upper and lower bounds of the 95% confidence intervals for all fluxes are presented in **Table S6.4**. The flux distributions of the *Pseudomonas putida* strains were visualized by plotting the computed flux values onto custom metabolic maps using the R package *fluctuator*.

6.7 Supplementary Material

Table S6.1. ATP production and consumption for the strains used in this study within the peripheral reactions. ATP estimation from: 1) Glucose to G6P; 2) G6P to 6PG; 3) Glucose to gluconate; 4) Gluconate to 6PG; 5) Gluconate to 2-KGA; and 6) 2-KGA to 6PG. Glnt: Gluconate. G6P: glucose-6-phosphate. 6PG: 6-phosphogluconate. 2-KGA: 2-ketogluconate. ATP: adenosine triphosphate.

Strain	Glucose to G6P	G6P to 6PG	Glucose to Glnt	Glnt to 6PG	Glnt to 2-KGA	2-KGA to 6PG
KT2440	-2 ATP	+1 NADH = 3 ATP	+2 ATP	-1 ATP	+1.5 ATP	-4 ATP (-1ATP - 1NAD(P)H)
Δ*gcd*	-2 ATP	+1 NADH = 3 ATP	0	0	0	0
Δ*glk*	0	0	+2 ATP	-1 ATP	+1.5 ATP	-4 ATP (-1ATP - 1NAD(P)H)
Δ*gtsABCD*Δ*glk*Δ*gad*	0	0	+2 ATP	-1 ATP	0	0
Δ*gtsABCD*Δ*glk*Δ*gnuK*Δ*gntT*	0	0	+2 ATP	0	+1.5 ATP	-4 ATP (-1ATP - 1NAD(P)H)
ATP produced/needed (peripheral reactions toward 6PG)	Phosphorylation to 6PG		First oxidation to 6PG		Second oxidation	
***Pseudomonas putida* KT2440**	+1.0 ATP		+1.0 ATP		-2.5 ATP	

Table S6.2. Changes in protein expression for the strains used in this chapter compared to *P. putida* KT2440. The strains were grown in de Bont media containing 15 mM glucose and 5 g L^{-1} MOPS. Selected proteins from central carbon metabolism were evaluated and abundance changes were calculated with a $\log_2$(fold change). Avg. is the average of four biological replicates at t1 and three biological replicates for t2, t3 and t4. SD represents the standard deviation.

Enzyme name	Protein		*Δgcd*				*Δglk*				*ΔgtsABCD Δglk Δgad*				*ΔgtsABCD Δglk ΔgnuK ΔgntT*			
			t1	t2	t3	t4	t1	t2	t3	t4	t1	t2	t3	t4	t1	t2	t3	t4
Mannose/glucose ABC transporter, glucose-binding periplasmic protein A	GtsA	Avg.	1.46	1.94	2.06	2.09	0.74	0.78	1.60	0.77	-5.79	-5.72	-5.35	-6.40	-4.87	-5.39	-5.57	-6.80
		SD	0.06	0.26	0.32	0.12	0.04	0.12	0.28	0.09	0.27	0.32	0.43	0.09	2.14	0.12	0.42	0.08
Mannose/glucose ABC transporter-ATP binding subunit D	GtsD	Avg.	0.94	1.06	1.23	1.46	0.41	0.32	1.01	0.51	-2.18	-1.35	-2.11	-2.38	-1.88	-2.08	-1.92	-2.55
		SD	0.06	0.13	0.37	0.23	0.13	0.18	0.23	0.24	0.19	0.24	0.30	0.04	0.43	0.24	0.18	0.17
Gluconate 2-dehydrogenase flavoprotein subunit	PP3383	Avg.	-1.29	-2.61	-3.16	-3.04	0.01	-0.17	-0.82	-0.27	-1.48	-2.62	-3.05	1.08	1.45	0.67	-3.06	0.94
		SD	0.10	0.20	1.15	0.19	0.15	0.10	0.20	0.36	0.20	0.42	0.55	0.10	0.19	0.20	0.30	0.28
Gluconate 2-dehydrogenase gamma subunit	PP3384	Avg.	-3.89	-6.23	-4.68	-3.96	0.38	-0.01	-0.73	-0.20	-5.51	-6.38	-7.94	1.32	2.26	0.75	-6.07	1.17
		SD	0.06	0.26	3.10	0.32	0.15	0.28	0.28	0.29	0.35	0.01	0.53	0.16	0.49	0.29	0.35	0.11
Gluconokinase	GnuK	Avg.	-2.25	-2.39	-3.00	-3.10	0.01	0.04	0.34	0.48	0.02	0.08	0.53	-2.06	-3.08	-2.54	0.36	-1.77
		SD	0.11	0.19	1.17	0.44	0.20	0.10	0.04	0.21	0.15	0.24	0.25	0.11	0.92	0.40	0.18	0.23
Putative epimerase	KguE	Avg.	-3.00	-4.09	-4.01	-3.99	0.32	0.49	-1.11	-0.12	-3.73	-6.02	-4.89	3.21	2.80	2.29	-5.45	2.90
		SD	0.54	0.53	0.64	0.50	0.45	0.41	0.32	0.21	0.26	0.83	0.49	0.29	0.37	0.31	0.42	0.29
Putative 2-ketogluconokinase	KguK	Avg.	-1.07	-1.62	-1.88	-1.83	0.25	0.13	-0.40	-0.21	-0.18	-0.59	-1.09	1.96	1.86	1.40	-1.26	2.05
		SD	0.09	0.27	0.59	0.27	0.46	0.29	0.15	0.14	0.26	0.13	0.02	0.14	0.30	0.17	0.33	0.17
2-ketogluconate utilization repressor	PtxS	Avg.	-0.30	-1.60	-2.16	-1.94	0.24	-0.65	-0.35	0.00	-0.20	-0.27	-0.14	0.59	0.35	-0.13	0.39	0.86
		SD	1.14	0.15	1.39	0.07	0.38	0.28	0.32	0.27	0.11	0.31	0.16	0.06	1.13	0.12	0.10	0.48
Glucose-6-phosphate 1-dehydrogenase	ZwfA	Avg.	0.44	0.59	0.31	0.60	0.52	0.20	0.59	0.35	-0.57	-0.75	-0.77	-1.03	-0.54	-0.25	-0.59	-0.66
		SD	0.14	0.11	0.76	0.29	0.27	0.29	0.39	0.19	0.14	0.24	0.25	0.17	0.14	0.15	0.30	0.21
Putative 6-phosphogluconate dehydrogenase	Gnd	Avg.	1.09	1.71	1.26	-0.30	0.20	0.65	1.09	-0.06	0.65	0.16	1.17	-0.25	0.85	1.17	1.58	0.24
		SD	0.34	0.20	0.64	0.10	0.13	0.17	0.13	0.32	0.09	0.46	0.72	0.25	0.14	0.12	0.93	0.27
6-phosphogluconolactonase	Pgl	Avg.	0.06	0.16	0.10	-0.33	0.25	0.22	0.44	0.16	-0.16	-0.24	-0.07	-0.33	-0.05	0.13	0.10	-0.09
		SD	0.02	0.15	0.14	0.15	0.08	0.25	0.18	0.12	0.08	0.20	0.09	0.05	0.15	0.14	0.13	0.02
Ribulose-phosphate 3-epimerase	Rpe	Avg.	-0.27	-0.20	-0.36	-0.15	-0.20	-0.22	-0.46	-0.69	-0.03	-0.28	-0.29	-0.77	-0.71	-0.22	-0.21	-0.57
		SD	0.11	0.37	0.15	0.05	0.30	0.18	0.20	0.08	0.19	0.46	0.12	0.12	0.26	0.15	0.47	0.11
Ribose-5-phosphate isomerase A	RpiA	Avg.	-0.53	-0.53	-0.41	-0.17	0.01	-0.04	-0.16	0.26	0.05	0.01	-0.06	-0.09	-0.29	-0.29	0.06	-0.15
		SD	0.13	0.13	0.14	0.13	0.16	0.15	0.02	0.18	0.10	0.12	0.19	0.11	0.08	0.28	0.13	0.17
Transketolase	TktA	Avg.	-0.37	-0.37	-0.30	-0.22	-0.06	-0.23	-0.21	0.03	-0.09	-0.38	-0.21	-0.04	-0.37	-0.38	-0.28	0.07
		SD	0.14	0.25	0.17	0.16	0.22	0.03	0.22	0.05	0.18	0.32	0.22	0.16	0.13	0.10	0.21	0.03
Transaldolase	Tal	Avg.	0.66	0.81	0.63	-0.06	0.06	0.06	0.53	0.07	0.22	0.18	0.35	-0.21	0.39	0.41	0.56	0.15
		SD	0.14	0.12	0.10	0.08	0.14	0.08	0.18	0.11	0.13	0.12	0.13	0.14	0.14	0.05	0.16	0.16
Phosphogluconate dehydratase	Edd	Avg.	0.07	0.28	0.13	0.23	-0.04	0.14	-0.10	-0.13	-0.03	-0.10	-0.09	0.14	-0.21	0.02	-0.53	-0.09
		SD	0.11	0.17	0.20	0.20	0.04	0.10	0.17	0.19	0.08	0.07	0.22	0.21	0.16	0.13	0.29	0.06
2-dehydro-3-deoxy-phosphogluconate aldolase	Eda	Avg.	-0.04	0.04	-0.03	0.07	0.11	0.25	0.27	0.02	-0.16	-0.23	-0.23	-0.23	-0.23	0.00	-0.43	-0.27
		SD	0.08	0.19	0.07	0.15	0.09	0.20	0.13	0.12	0.12	0.43	0.07	0.06	0.15	0.13	0.16	0.10

Enzyme name	Protein		Δ*gcd*				Δ*glk*				Δ*gtsABCD* Δ*glk* Δ*gad*				Δ*gtsABCD* Δ*glk* Δ*gnuK* Δ*gntT*			
			t1	t2	t3	t4	t1	t2	t3	t4	t1	t2	t3	t4	t1	t2	t3	t4
Phosphoenolpyruvate carboxylase	Ppc	Avg.	0.62	1.34	2.49	2.25	0.53	0.39	0.44	0.12	0.29	0.49	0.63	-0.16	1.47	1.11	0.94	0.35
		SD	0.25	0.55	2.13	0.18	0.29	0.39	0.40	0.09	0.15	0.32	0.38	0.31	2.49	0.29	0.25	0.12
Malic enzyme B	MaeB	Avg.	0.07	-0.04	0.00	-0.17	-0.02	-0.02	0.03	-0.10	-0.02	0.04	0.06	0.08	0.00	0.01	-0.15	0.03
		SD	0.11	0.05	0.11	0.19	0.07	0.16	0.11	0.07	0.13	0.14	0.05	0.11	0.14	0.07	0.20	0.14
Pyruvate carboxylase subunit B	PycB	Avg.	-0.21	-0.20	-0.19	-0.01	-0.14	-0.12	-0.30	-0.19	0.01	-0.10	-0.06	0.49	0.00	0.03	-0.29	0.45
		SD	0.10	0.11	0.16	0.23	0.09	0.23	0.18	0.17	0.08	0.08	0.09	0.22	0.17	0.24	0.12	0.19
Oxaloacetate decarboxylase	PP1389	Avg.	-0.45	-0.54	-0.98	-0.91	0.25	0.09	-0.55	0.12	-0.16	-0.53	-1.28	-1.57	-2.56	-1.60	-1.30	-2.09
		SD	0.58	0.18	0.70	0.33	0.35	0.19	0.43	0.32	0.28	0.36	0.07	0.65	0.54	0.16	0.57	0.48
Glucokinase	Glk	Avg.	0.15	0.18	0.46	0.07	-1.68	-1.56	-1.12	-1.34	-1.22	-0.95	-1.01	-1.33	-0.81	-1.58	-1.35	-1.25
		SD	0.09	0.15	0.40	0.17	0.10	0.07	0.03	0.09	0.27	0.35	0.21	0.20	0.94	0.09	0.02	0.25
Glucose-6-phosphate isomerase 1	Pgi-1	Avg.	-0.51	-1.04	-1.04	-0.09	-0.61	-0.49	-0.47	0.15	-0.51	-0.08	-0.39	0.22	-0.50	-0.22	-0.67	0.29
		SD	0.45	0.19	0.11	0.48	0.52	0.15	0.20	0.50	0.43	0.27	0.46	0.60	0.29	0.33	0.36	0.64
Glucose-6-phosphate isomerase 2	Pgi-2	Avg.	0.11	0.25	0.42	0.48	0.34	-0.24	0.02	-0.09	0.35	-0.16	-0.04	-0.45	0.01	0.13	0.02	0.25
		SD	0.36	0.43	0.33	0.35	0.54	0.47	0.32	0.40	0.49	0.36	0.16	0.31	0.33	0.30	0.43	0.32
Fructose-1,6-bisphosphatase class 1	Fbp	Avg.	-0.72	-0.92	-0.57	-0.03	0.10	-0.43	0.09	0.08	0.12	-0.06	0.01	-0.14	-0.46	-0.70	-0.07	0.04
		SD	0.15	0.06	0.30	0.21	0.15	0.14	0.12	0.13	0.17	0.24	0.10	0.30	0.49	0.10	0.06	0.39
Fructose-1,6-bisphosphate aldolase	Fba	Avg.	0.00	0.11	0.25	0.27	0.00	0.03	0.07	0.07	0.04	-0.09	0.17	0.07	0.16	0.05	0.21	0.22
		SD	0.12	0.07	0.25	0.14	0.13	0.11	0.01	0.10	0.11	0.19	0.14	0.16	0.12	0.04	0.01	0.13
Putative Aldolase/synthase	PP1791	Avg.	-0.18	0.21	0.14	-0.05	-0.14	-0.23	-0.30	-0.27	-0.08	-0.14	-0.04	-0.06	-0.63	-0.04	-0.13	-0.08
		SD	0.11	0.15	0.59	0.14	0.18	0.15	0.21	0.05	0.27	0.24	0.20	0.12	0.46	0.21	0.11	0.15
Triosephosphate isomerase	TpiA	Avg.	-0.20	-0.11	0.07	0.36	-0.08	-0.18	-0.17	0.08	0.01	0.10	0.10	0.40	-0.11	0.08	0.05	0.43
		SD	0.18	0.16	0.11	0.12	0.27	0.10	0.25	0.13	0.17	0.33	0.12	0.12	0.19	0.00	0.05	0.08
Glyceraldehyde-3-phosphate dehydrogenase A	GapA	Avg.	0.44	0.96	0.92	1.06	0.25	0.35	0.48	0.18	0.09	0.13	0.44	0.41	0.16	0.72	0.20	0.27
		SD	0.07	0.13	0.36	0.17	0.16	0.24	0.33	0.07	0.14	0.16	0.20	0.18	0.14	0.22	0.36	0.14
Glyceraldehyde-3-phosphate dehydrogenase B	GapB	Avg.	-0.15	-0.15	-0.09	-0.04	-0.09	-0.18	-0.20	-0.20	-0.04	-0.20	-0.13	-0.10	-0.33	-0.43	-0.45	-0.19
		SD	0.09	0.20	0.11	0.27	0.05	0.13	0.20	0.17	0.06	0.09	0.09	0.20	0.20	0.02	0.19	0.21
Phosphoglycerate kinase	Pgk	Avg.	-0.05	-0.04	-0.03	0.05	-0.04	0.13	0.06	0.20	0.12	0.27	0.27	-0.10	-0.17	-0.20	0.04	-0.09
		SD	0.07	0.26	0.20	0.06	0.15	0.40	0.14	0.08	0.16	0.15	0.18	0.06	0.19	0.10	0.15	0.03
Phosphoglucomutase	Pgm	Avg.	0.03	0.22	0.56	0.71	0.19	0.11	0.17	0.23	-0.34	-0.56	-0.60	-0.58	-0.07	-0.54	-0.82	-0.61
		SD	0.16	0.20	0.68	0.34	0.24	0.17	0.31	0.25	0.16	0.23	0.11	0.24	1.14	0.15	0.31	0.17
Enolase	Eno	Avg.	-0.10	-0.01	-0.13	-0.20	-0.04	0.05	-0.15	0.05	-0.01	0.19	0.08	0.22	-0.12	-0.04	-0.13	0.05
		SD	0.08	0.09	0.19	0.04	0.13	0.11	0.09	0.06	0.06	0.22	0.03	0.10	0.27	0.05	0.14	0.16
Phosphoenolpyruvate synthase	PpsA	Avg.	0.05	0.26	0.27	0.43	0.07	-0.01	0.00	-0.05	0.08	-0.09	0.08	0.24	-0.06	0.08	-0.29	0.21
		SD	0.15	0.24	0.14	0.35	0.17	0.21	0.29	0.10	0.20	0.07	0.10	0.25	0.19	0.17	0.15	0.25
Phosphoenolpyruvate protein phosphotransferase	PtsP	Avg.	0.21	0.23	0.34	0.47	0.07	-0.20	0.02	-0.03	-0.05	-0.13	-0.02	0.05	0.17	0.07	0.16	0.29
		SD	0.34	0.11	0.23	0.25	0.35	0.21	0.25	0.14	0.30	0.10	0.10	0.10	0.17	0.27	0.25	0.18
Pyruvate kinase	PykA	Avg.	-0.01	-0.12	-0.17	-0.21	-0.22	-0.13	-0.39	-0.32	0.01	-0.35	-0.31	0.19	-0.08	-0.11	-0.50	0.08
		SD	0.10	0.04	0.04	0.05	0.11	0.02	0.13	0.09	0.13	0.17	0.08	0.03	0.04	0.05	0.08	0.04

Enzyme name	Protein		Δ*gcd*				Δ*glk*				Δ*gtsABCD* Δ*glk* Δ*gad*				Δ*gtsABCD* Δ*glk* Δ*gnuK* Δ*gntT*			
			t1	t2	t3	t4	t1	t2	t3	t4	t1	t2	t3	t4	t1	t2	t3	t4
Acetyltransferase component of pyruvate dehydrogenase complex	AceF	Avg.	-0.04	-0.31	-0.33	0.01	-0.33	-0.24	-0.49	-0.23	0.36	0.18	0.01	0.33	0.26	0.03	-0.19	0.34
		SD	0.07	0.08	0.17	0.13	0.05	0.24	0.09	0.04	0.06	0.13	0.05	0.05	0.26	0.19	0.07	0.07
Dihydrolipoyl dehydrogenase	Lpd	Avg.	0.23	0.66	0.38	0.03	0.28	0.28	0.53	0.08	0.48	0.18	0.53	0.00	0.38	0.63	0.60	0.29
		SD	0.21	0.38	0.08	0.11	0.45	0.20	0.32	0.23	0.23	0.31	0.21	0.14	0.46	0.17	0.03	0.05
Pyruvate dehydrogenase E1 component	AceE	Avg.	-0.09	-0.21	-0.24	-0.21	-0.36	-0.27	-0.75	-0.34	0.19	-0.14	-0.27	0.39	0.13	-0.11	-0.55	0.35
		SD	0.11	0.28	0.10	0.24	0.13	0.11	0.21	0.08	0.15	0.17	0.05	0.17	0.11	0.08	0.18	0.13
Dihydrolipoyl dehydrogenase	LpdG	Avg.	-0.10	0.07	-0.17	0.04	-0.37	0.10	-0.23	0.04	-0.10	0.14	0.01	0.13	-0.18	0.12	-0.24	-0.06
		SD	0.08	0.35	0.27	0.11	0.15	0.15	0.25	0.15	0.12	0.24	0.22	0.20	0.16	0.23	0.32	0.25
Acetyl-coenzyme A synthetase 1	AcsA1	Avg.	0.93	0.78	0.68	0.63	0.35	0.06	0.05	0.02	0.48	-0.41	-0.14	0.16	-0.31	-0.33	-0.59	0.00
		SD	0.26	0.05	0.23	0.35	0.31	0.22	0.32	0.20	0.28	0.11	0.12	0.29	0.31	0.31	0.27	0.25
Acetyl-coenzyme A synthetase 2	AcsA2	Avg.	0.71	3.60	3.49	4.27	0.79	0.98	3.97	0.23	0.48	-0.03	4.95	-0.09	-0.12	2.23	5.33	1.25
		SD	0.37	0.35	1.27	1.11	0.29	0.89	1.57	0.37	0.25	0.88	0.30	0.98	0.21	0.17	0.65	0.66
Citrate synthase	GltA	Avg.	-0.06	0.03	0.03	0.08	-0.17	-0.15	-0.24	0.11	-0.06	0.10	-0.12	0.28	-0.54	-0.08	-0.23	0.53
		SD	0.13	0.01	0.23	0.36	0.19	0.30	0.33	0.17	0.30	0.16	0.23	0.32	0.19	0.32	0.10	0.28
Aconitate hydratase I	AcnA-I	Avg.	0.45	1.55	1.53	1.80	-0.10	-0.23	1.51	-0.30	-0.02	-0.14	1.63	-0.47	-0.19	0.85	2.26	0.31
		SD	0.19	0.25	0.32	0.44	0.30	0.37	0.35	0.15	0.25	0.45	0.24	0.30	0.08	0.31	0.15	0.30
Aconitate hydratase II	AcnA-II	Avg.	0.35	0.51	0.29	0.45	0.06	-0.02	0.36	-0.04	0.32	0.15	0.48	0.19	0.47	0.51	0.48	0.23
		SD	0.08	0.33	0.25	0.16	0.07	0.21	0.21	0.10	0.07	0.28	0.06	0.28	0.30	0.19	0.12	0.17
Aconitate hydratase B	AcnB	Avg.	0.07	-0.03	-0.07	0.03	0.03	0.02	-0.08	-0.08	0.04	-0.20	-0.21	-0.08	-0.10	-0.31	-0.57	-0.20
		SD	0.10	0.25	0.16	0.32	0.10	0.23	0.21	0.22	0.04	0.18	0.17	0.60	0.09	0.15	0.02	0.29
Isocitrate dehydrogenase [NADP]	Icd	Avg.	0.98	1.95	1.89	1.88	0.90	0.76	2.29	0.49	0.56	0.51	2.40	-0.52	0.93	1.57	3.01	0.35
		SD	0.16	0.37	0.20	0.15	0.16	0.33	0.16	0.12	0.16	0.30	0.19	0.44	0.06	0.42	0.16	0.25
Oxoglutarate dehydrogenase (succinyl-transferring)	SucA	Avg.	-0.10	-0.13	-0.32	-0.25	-0.10	-0.10	-0.38	-0.07	-0.07	-0.07	-0.55	-0.04	-0.40	-0.32	-0.64	-0.04
		SD	0.10	0.14	0.60	0.29	0.21	0.33	0.44	0.08	0.17	0.29	0.42	0.14	0.18	0.19	0.20	0.27
Succinate-CoA ligase [ADP-forming] subunit beta	SucC	Avg.	0.09	0.13	0.13	0.12	-0.24	0.08	0.00	0.00	-0.05	0.25	0.27	0.13	-0.43	-0.26	-0.19	0.06
		SD	0.07	0.17	0.23	0.39	0.05	0.25	0.21	0.27	0.11	0.28	0.19	0.29	0.27	0.34	0.31	0.33
Succinate-CoA ligase [ADP-forming] subunit alpha	SucD	Avg.	0.11	0.04	0.16	0.13	-0.16	0.08	0.04	0.04	-0.03	0.30	0.17	0.03	-0.33	-0.16	0.02	0.05
		SD	0.08	0.04	0.11	0.05	0.07	0.21	0.23	0.09	0.06	0.15	0.10	0.00	0.07	0.11	0.10	0.09
Succinate dehydrogenase flavoprotein subunit	SdhA	Avg.	-0.03	0.20	0.31	0.23	-0.07	0.06	-0.19	-0.06	-0.16	0.00	0.07	0.12	-0.68	-0.20	-0.56	-0.05
		SD	0.04	0.05	0.25	0.53	0.07	0.14	0.34	0.22	0.19	0.32	0.22	0.40	0.16	0.34	0.34	0.54
Succinate dehydrogenase iron-sulfur subunit	SdhB	Avg.	-0.08	-0.20	-0.27	-0.14	0.00	0.08	0.09	-0.28	0.01	0.15	0.01	-0.18	-0.21	-0.12	-0.11	-0.19
		SD	0.13	0.22	0.18	0.09	0.19	0.23	0.46	0.16	0.13	0.29	0.40	0.08	0.38	0.05	0.33	0.16
Fumarate hydratase class II	FumC	Avg.	0.70	1.57	1.61	1.77	0.36	0.15	1.83	0.16	0.38	0.30	1.87	-0.60	0.38	1.03	2.60	0.38
		SD	0.50	0.06	0.11	0.12	0.41	0.08	0.27	0.10	0.21	0.14	0.17	0.26	0.41	0.02	0.21	0.04
Probable malate:quinone oxidoreductase 1	Mqo-1	Avg.	-0.43	-0.86	-0.64	0.03	-0.06	-0.05	-0.39	-0.05	-0.10	-0.43	-0.84	0.13	-0.33	-0.48	-1.03	-0.05
		SD	0.12	0.04	0.18	0.24	0.10	0.10	0.12	0.19	0.06	0.26	0.11	0.25	0.12	0.13	0.11	0.19
Probable malate:quinone oxidoreductase 2	Mqo-2	Avg.	-2.15	-2.62	-3.10	-3.67	-0.18	-0.89	-1.45	-1.28	-1.54	-2.31	-3.50	-2.62	-2.16	-2.05	-2.82	-3.13
		SD	0.45	0.54	0.30	0.28	0.13	0.23	0.23	0.71	0.30	0.73	0.41	0.04	0.34	0.60	0.72	0.70
Probable malate:quinone oxidoreductase 3	Mqo-3	Avg.	1.02	2.12	2.05	2.05	0.59	0.39	2.23	0.38	0.64	0.40	3.19	0.17	0.96	2.13	3.96	1.49
		SD	0.31	0.46	1.11	0.44	0.31	0.31	1.32	0.59	0.08	0.58	1.03	0.49	0.49	0.09	0.92	0.38
Isocitrase	AceA	Avg.	0.55	0.83	0.25	-0.33	0.46	0.09	0.63	0.26	-0.38	-0.63	0.09	-0.16	0.65	0.70	0.17	-0.23
		SD	0.24	0.36	0.14	0.15	0.13	0.28	0.12	0.14	0.22	0.62	0.13	0.18	0.02	0.91	0.19	0.24
Malate synthase G	GlcB	Avg.	0.30	0.43	0.43	0.62	0.24	0.13	0.22	-0.23	0.20	0.00	0.38	0.28	0.61	0.73	0.39	0.43
		SD	0.16	0.19	0.23	0.24	0.26	0.32	0.21	0.20	0.30	0.33	0.07	0.24	0.16	0.17	0.14	0.18

Table S6.3. INCA model constrain parameters in the different *Pseudomonas putida* strains. Normalized uptake, secretion, ATP and NADH maintenance as well as growth rates to the glucose uptake rate (100%) as constrain parameters for ^{13}C-metabolic flux analysis. The relative values can be obtained by dividing the respective specific uptake rates (qs) by glucose uptake rate ($q_{glucose}$) multiplied by 100%.

Strains	Growth rate [h^{-1}]	$q_{Glucose}$ [mmol gCDW^{-1} h^{-1}]	$q_{Gluconate}$ [mmol gCDW^{-1} h^{-1}]	$q_{2\text{-}KGA}$ [mmol gCDW^{-1} h^{-1}]	$q_{ATPmaintenance}$ [mmol gCDW^{-1} h^{-1}]	$q_{NADHmaintenance}$ [mmol gCDW^{-1} h^{-1}]	% Glucose	% Gluconate	% 2-KGA	% Growth rate	%ATP	%NADH
KT2440	0,61	5,92	0,96	0,20	0,92	0,79	100,00	16,28	3,38	10,31	15,55	13,35
Δgad	0,45	7,47	0,00	0,00	0,92	0,79	100,00	0,00	0,00	6,02	12,31	10,57
Δglk	0,53	6,59	0,89	0,18	0,92	0,79	100,00	13,50	2,73	8,04	13,96	11,99
ΔgtsABCDΔglkΔgad	0,64	6,02	0,51	0,00	0,92	0,79	100,00	8,47	0,00	10,63	15,29	13,13
ΔgtsABCDΔglkΔgnuKΔgntT	0,53	7,58	0,21	4,58	0,92	0,79	97,30	2,70	58,83	6,81	11,82	10,15

Table S6.4. Relative net fluxes determined by ^{13}C-MFA in the *Pseudomonas putida* KT2440 model. Relative mean values (%) are net fluxes relative to glucose uptake rate of 100% (uptake rates were estimated for each strain and those mean values are reported in Table S6.3). Mean parameter estimates and 95% confidence bounds using INCA's parameter continuation method are shown below for Wild-type; Δ*gcd*; Δ*glk*; Δ*gad*; Δ*gtsABCD*Δ*glk*Δ*gad* and Δ*gtsABCD*Δ*glk*Δ*gnuK*Δ*gntT*.

Reaction ID	Equation	*Pseudomonas putida* KT2440				*Pseudomonas putida* KT2440 Δ*gcd*			
		Value (%)	SD	Lower bond	Upper bond	Value (%)	SD	Lower bond	Upper bond
R1	Gluc.ext -> Gluc.per	100,0	0,0	100,0	100,0	100,0	0,0	100,0	100,0
R2	Gluc.per + 2*ATP -> G6P	15,9	1,6	13,0	19,3	100,0	0,0	100,0	100,0
R3	Gluc.per -> Gluco.per + UQH2	84,1	1,6	80,7	87,0	0,0	0,0	0,0	0,0
R4	Gluco.per -> Gluco.ext	16,3	0,0	16,3	16,3	0,0	0,0	0,0	0,0
R5	Gluco.per + ATP -> 6PG	64,4	1,6	61,0	67,3	0,0	0,0	0,0	0,0
R6	Gluco.per -> Kgluco.per + FADH2	3,4	0,0	3,4	3,4	0,0	0,0	0,0	0,0
R7	Kgluco.per -> Kgluco.ext	3,4	0,0	3,4	3,4	0,0	0,0	0,0	0,0
R8	Kgluco.per + ATP -> KGluco6P	Sum with R5				0,0	0,0	0,0	0,0
R9	KGluco6P + NADPH -> 6PG					0,0	0,0	0,0	0,0
R10	G6P <-> F6P	-26,2	2,1	-30,8	-23,1	-49,5	1,8	-54,9	-46,4
R11	FBP -> F6P	29,0	1,4	26,6	31,7	51,6	1,8	48,5	56,5
R12	FBP <-> DHAP + GAP	-29,0	1,4	-31,7	-26,6	-51,6	1,8	-56,5	-48,5
R13	DHAP <-> GAP	-29,0	1,4	-31,7	-26,6	-51,6	1,8	-56,5	-48,5
R14	GAP <-> 3PG + ATP + NADH	42,3	1,4	39,5	44,7	43,2	1,8	38,2	46,3
R15	3PG <-> PEP	34,0	1,5	31,3	36,4	38,2	1,8	33,3	41,3
R16	PEP -> Pyr + ATP	37,6	5,7	29,0	41,1	45,9	2,6	0,0	50,8
R17	G6P -> 6PG + NADPH	40,3	3,0	35,4	46,7	148,5	1,8	145,4	153,8
R18	6PG -> Ri5P + CO2 + NADPH	1,0	2,2	0,0	5,8	0,0	0,0	0,0	5,0
R19	Ri5P <-> X5P	-2,1	1,5	-2,8	1,1	-1,6	0,0	-1,6	1,7
R20	Ri5P <-> R5P	3,1	0,7	2,8	4,7	1,6	0,0	1,6	3,3
R21	X5P <-> GAP + EC2	-2,1	1,5	-2,8	1,1	-1,6	0,0	-1,6	1,7
R22	F6P <-> E4P + EC2	3,1	0,7	1,5	3,5	2,0	0,0	0,4	2,0
R23	S7P <-> R5P + EC2	-1,0	0,7	-2,6	-0,7	-0,4	0,0	-2,1	-0,4
R24	F6P <-> GAP + EC3	-1,0	0,7	-2,6	-0,7	-0,4	0,0	-2,1	-0,4
R25	S7P <-> E4P + EC3	1,0	0,7	0,7	2,6	0,4	0,0	0,4	2,1
R26	6PG -> Pyr + GAP	103,7	1,5	101,0	106,6	148,5	1,8	145,4	153,4
R27	Pyr -> AcCoA + CO2 + NADH	73,3	1,0	71,7	74,0	149,2	0,1	147,5	154,4
R28	OAA + AcCoA -> Cit	43,8	1,0	42,2	44,5	131,8	0,1	130,2	132,0
R29	Cit <-> ICit	43,8	1,0	42,2	44,5	131,8	0,1	130,2	132,0
R30	ICit -> Suc + Glyox	0,1	0,0	0,0	0,3	0,0	0,0	0,0	5,2
R31	Glyox + AcCoA -> Mal	0,1	0,0	0,0	0,3	0,0	0,0	0,0	5,2
R32	ICit -> AKG + CO2 + NADPH	43,7	1,0	42,1	44,4	131,8	0,1	126,7	132,0
R33	AKG -> SucCoA + CO2 + NADH	31,6	1,0	30,0	32,4	124,8	0,1	119,6	125,0
R34	SucCoA <-> Suc + ATP	28,5	1,0	26,9	29,3	123,0	0,1	117,8	123,1
R35	Suc -> Fum + FADH2	31,7	1,0	30,1	32,5	124,8	0,1	123,1	125,0

R36	Fum <-> Mal	36,7	1,0	35,1	37,4	127,7	0,1	126,0	127,8
R37	Mal -> OAA + FADH2	36,8	7,5	33,5	37,8	127,7	0,1	104,1	132,8
R38	Pyr + CO2 + ATP -> OAA	181,3	9,2	171,6	187,6	1753,6	3,5	1700,7	2176,8
R39	OAA -> Pyr + CO2	142,7	6,2	135,0	149,1	1725,6	3,1	1715,9	2150,8
R40	PEP + CO2 -> OAA	0,0	6,1	0,0	9,5	0,0	0,0	0,0	51,2
R41	OAA + ATP -> PEP + CO2	11,9	1,3	9,8	14,4	12,5	1,2	10,4	16,6
R42	Mal -> Pyr + CO2 + NADPH	0,0	7,5	0,0	3,1	0,0	0,0	0,0	23,5
R43	AKG + NADPH + NH3 -> Glu	69,3	0,7	68,9	69,9	40,4	0,1	40,2	40,5
R44	Glu + ATP + NH3 -> Gln	8,3	0,0	8,3	8,3	4,9	0,0	4,9	4,9
R45	Glu + ATP + 2*NADPH -> Pro	2,7	0,0	2,7	2,7	1,6	0,0	1,6	1,6
R46	Glu + CO2 + Gln + Asp + AcCoA + 5*ATP + NADPH -> Arg + AKG + Fum + Ac	3,6	0,0	3,6	3,6	2,1	0,0	2,1	2,1
R47	OAA + Glu -> Asp + AKG	19,6	1,5	19,0	21,0	11,3	0,2	10,9	11,6
R48	Asp + 2*ATP + NH3 -> Asn	1,6	0,0	1,6	1,6	1,0	0,0	1,0	1,0
R49	Pyr + Glu -> Ala + AKG	6,2	0,0	6,2	6,2	3,6	0,0	3,6	3,6
R50	3PG + Glu -> Ser + AKG + NADH	8,3	0,7	7,6	8,6	4,9	0,1	4,8	5,1
R51	Ser <-> Gly + MEETHF	2,6	0,7	1,9	2,9	1,6	0,1	1,4	1,8
R52	Gly <-> CO2 + MEETHF + NADH + NH3	0,0	0,7	-0,3	0,7	-0,1	0,1	-0,3	0,1
R53	Thr <-> Gly + AcCoA + NADH	1,9	1,5	1,2	3,2	0,9	0,2	0,6	1,2
R54	Ser + AcCoA + 3*ATP + 4*NADPH + SO4 -> Cys + Ac	1,8	0,0	1,8	1,8	1,1	0,0	1,1	1,1
R55	Asp + Pyr + Glu + SucCoA + ATP + 2*NADPH -> LL_DAP + AKG + Suc	1,9	0,0	1,9	1,9	1,1	0,0	1,1	1,1
R56	LL_DAP -> Lys + CO2	1,9	0,0	1,9	1,9	1,1	0,0	1,1	1,1
R57	Asp + 2*ATP + 2*NADPH -> Thr	7,0	1,5	6,4	8,4	3,9	0,2	3,6	4,2
R58	Asp + METHF + Cys + SucCoA + ATP + 2*NADPH -> Met + Pyr + Suc + NH3	1,3	0,0	1,3	1,3	0,7	0,0	0,7	0,7
R59	Pyr + Pyr + Glu + NADPH -> Val + CO2 + AKG	4,0	0,0	4,0	4,0	2,3	0,0	2,3	2,3
R60	AcCoA + Pyr + Pyr + Glu + NADPH -> Leu + CO2 + CO2 + AKG + NADH	6,5	0,0	6,5	6,5	3,8	0,0	3,8	3,8
R61	Thr + Pyr + Glu + NADPH -> Ile + CO2 + AKG + NH3	2,5	0,0	2,5	2,5	1,5	0,0	1,5	1,5

R62	PEP + PEP + E4P + Glu + ATP + NADPH -> Phe + CO2 + AKG	2,0	0,0	2,0	2,0	1,1	0,0	1,1	1,1
R63	PEP + PEP + E4P + Glu + ATP + NADPH -> Tyr + CO2 + AKG + NADH	1,4	0,0	1,4	1,4	0,8	0,0	0,8	0,8
R64	Ser + R5P + PEP + E4P + PEP + Gln + 3*ATP + NADPH -> Trp + CO2 + GAP + Pyr + Glu	0,8	0,0	0,8	0,8	0,5	0,0	0,5	0,5
R65	R5P + FTHF + Gln + Asp + 5*ATP -> His + AKG + Fum + 2*NADH	1,3	0,0	1,3	1,3	0,8	0,0	0,8	0,8
R66	MEETHF + NADH -> METHF	1,3	0,0	1,3	1,3	0,7	0,0	0,7	0,7
R67	MEETHF -> FTHF + NADPH	1,3	0,0	1,3	1,3	0,8	0,0	0,8	0,8
R68	Biomass formation Refer to*	10,3	0,0	10,3	10,3	6,0	0,0	6,0	6,0
R69	CO2.unlabeled <-> CO2	0,0	0,0	0,0	0,0	0,0	0,0	0,0	0,0
R70	NADH <-> NADPH	50,1	8,9	41,1	55,9	-199,0	1,8	-223,6	-194,2
R71	ATP -> ATP.maintenance	15,6	0,0	15,6	15,6	12,3	0,0	12,3	12,3
R72	NADPH -> NADPH.maintenance	13,4	0,0	13,4	13,4	10,6	0,0	10,6	10,6
R73	NADH + O2 -> 3*ATP	116,4	7,9	112,8	121,7	527,3	0,2	522,1	550,9
R74	FADH2 + O2 -> 2*ATP	71,9	7,7	68,1	73,3	252,5	0,2	228,9	257,7
R75	UQH2 + O2 -> 3*ATP	84,1	1,6	80,7	87,0	0,0	0,0	0,0	144,1
R76	CO2 -> CO2.ext	144,8	0,0	144,8	144,8	403,0	0,0	403,0	403,0
R77	NH3.ext -> NH3	75,4	0,0	75,4	75,4	44,1	0,0	44,1	44,1
R78	SO4.ext -> SO4	1,8	0,0	1,8	1,8	1,1	0,0	1,1	1,1
R79	O2.ext -> O2	272,5	0,0	272,5	272,5	779,8	0,0	779,8	923,8
Fit		Accepted				Accepted			
SSR		214.6				262.1			
Expected SSR		[208.1 - 295.7]				[246.6 - 341.2]			
Normally distribution		Yes				Yes			

Reaction ID	**Equation**	***Pseudomonas putida* KT2440 Δ*glk***			
		Value (%)	**SD**	**Lower bond**	**Upper bond**
R1	Gluc.ext -> Gluc.per	100,0	0,0	100,0	100,0
R2	Gluc.per + 2*ATP -> G6P	0,0	0,0	0,0	0,0
R3	Gluc.per -> Gluco.per + UQH2	100,0	0,0	100,0	100,0
R4	Gluco.per -> Gluco.ext	13,5	0,0	13,5	13,5
R5	Gluco.per + ATP -> 6PG	83,8	0,0	83,8	83,8
R6	Gluco.per -> Kgluco.per + FADH2	2,7	0,0	2,7	2,7
R7	Kgluco.per -> Kgluco.ext	2,7	0,0	2,7	2,7
R8	Kgluco.per + ATP -> KGluco6P	Sum with R5			
R9	KGluco6P + NADPH -> 6PG				
R10	G6P <-> F6P	-38,6	3,1	-43,4	-34,4

R11	FBP -> F6P	40,4	2,8	36,8	44,0
R12	FBP <-> DHAP + GAP	-40,4	2,8	-44,0	-36,8
R13	DHAP <-> GAP	-40,4	2,8	-44,0	-36,8
R14	GAP <-> 3PG + ATP + NADH	36,3	2,8	32,7	39,9
R15	3PG <-> PEP	29,7	2,8	26,0	33,3
R16	PEP -> Pyr + ATP	35,0	3,6	1,0	39,6
R17	G6P -> 6PG + NADPH	37,2	3,1	33,0	42,0
R18	6PG -> Ri5P + CO2 + NADPH	1,4	2,6	0,3	7,3
R19	Ri5P <-> X5P	-0,4	1,7	-2,2	-0,4
R20	Ri5P <-> R5P	-0,4	0,9	2,2	-0,4
R21	X5P <-> GAP + EC2	0,4	1,7	0,4	2,7
R22	F6P <-> E4P + EC2	2,2	0,9	0,9	2,7
R23	S7P <-> R5P + EC2	-0,5	0,1	-3,0	-0,5
R24	F6P <-> GAP + EC3	-0,5	0,1	-3,0	-0,5
R25	S7P <-> E4P + EC3	0,5	0,1	0,5	3,0
R26	6PG -> Pyr + GAP	119,6	3,0	114,8	123,6
R27	Pyr -> AcCoA + CO2 + NADH	99,3	0,2	97,3	104,3
R28	OAA + AcCoA -> Cit	76,0	0,1	74,0	76,7
R29	Cit <-> ICit	76,0	0,1	74,0	76,7
R30	ICit -> Suc + Glyox	0,0	0,1	0,0	4,7
R31	Glyox + AcCoA -> Mal	0,0	0,1	0,0	4,7
R32	ICit -> AKG + CO2 + NADPH	76,0	0,1	71,2	76,7
R33	AKG -> SucCoA + CO2 + NADH	66,6	0,1	61,8	67,3
R34	SucCoA <-> Suc + ATP	64,2	0,2	59,3	64,8
R35	Suc -> Fum + FADH2	66,6	0,2	64,6	67,3
R36	Fum <-> Mal	70,5	0,2	68,5	71,1
R37	Mal -> OAA + FADH2	70,5	0,2	64,5	75,5
R38	Pyr + CO2 + ATP -> OAA	853,7	0,1	819,6	862,3
R39	OAA -> Pyr + CO2	821,3	5,3	812,6	829,3
R40	PEP + CO2 -> OAA	0,0	0,0	0,0	35,6
R41	OAA + ATP -> PEP + CO2	11,8	1,3	9,6	14,1
R42	Mal -> Pyr + CO2 + NADPH	0,0	0,3	0,0	5,8
R43	AKG + NADPH + NH3 -> Glu	1,0	0,0	1,0	1,0
R44	Glu + ATP + NH3 -> Gln	6,5	0,0	6,5	6,5
R45	Glu + ATP + 2*NADPH -> Pro	2,1	0,1	2,1	2,1
R46	Glu + CO2 + Gln + Asp + AcCoA + 5*ATP + NADPH -> Arg + AKG + Fum + Ac	2,8	0,1	2,8	2,8
R47	OAA + Glu -> Asp + AKG	-0,1	0,1	-0,4	0,1
R48	Asp + 2*ATP + NH3 -> Asn	0,9	0,3	0,4	1,3
R49	Pyr + Glu -> Ala + AKG	4,8	0,2	4,8	4,8
R50	3PG + Glu -> Ser + AKG + NADH	6,6	0,2	6,4	6,8
R51	Ser <-> Gly + MEETHF	-0,2	0,2	-0,5	0,1

R52	Gly <-> CO2 + MEETHF + NADH + NH3	-0,2	0,3	0,5	0,1
R53	Thr <-> Gly + AcCoA + NADH	0,7	0,0	0,7	0,7
R54	Ser + AcCoA + 3*ATP + 4*NADPH + SO4 -> Cys + Ac	1,4	0,0	1,4	1,4
R55	Asp + Pyr + Glu + SucCoA + ATP + 2*NADPH -> LL_DAP + AKG + Suc	1,4	0,0	1,4	1,4
R56	LL_DAP -> Lys + CO2	1,4	0,3	1,4	1,4
R57	Asp + 2*ATP + 2*NADPH -> Thr	1,0	0,0	1,0	1,0
R58	Asp + METHF + Cys + SucCoA + ATP + 2*NADPH -> Met + Pyr + Suc + NH3	0,8	0,0	0,8	0,8
R59	Pyr + Pyr + Glu + NADPH -> Val + CO2 + AKG	0,5	0,0	0,5	0,5
R60	AcCoA + Pyr + Pyr + Glu + NADPH -> Leu + CO2 + CO2 + AKG + NADH	0,8	0,0	0,8	0,8
R61	Thr + Pyr + Glu + NADPH -> Ile + CO2 + AKG + NH3	0,7	0,0	0,7	0,7
R62	PEP + PEP + E4P + Glu + ATP + NADPH -> Phe + CO2 + AKG	0,8	0,0	0,8	0,8
R63	PEP + PEP + E4P + Glu + ATP + NADPH -> Tyr + CO2 + AKG + NADH	0,6	0,0	0,6	0,6
R64	Ser + R5P + PEP + E4P + PEP + Gln + 3*ATP + NADPH -> Trp + CO2 + GAP + Pyr + Glu	0,6	0,0	0,6	0,6
R65	R5P + FTHF + Gln + Asp + 5*ATP -> His + AKG + Fum + 2*NADH	1,0	0,0	1,0	1,0
R66	MEETHF + NADH -> METHF	1,0	0,0	1,0	1,0
R67	MEETHF -> FTHF + NADPH	1,0	0,0	1,0	1,0
R68	Biomass formation Refer to *	8,0	0,3	8,0	8,0
R69	CO2.unlabeled <-> CO2	0,0	0,3	0,0	0,0
R70	NADH <-> NADPH	-8,3	4,2	-16,8	-1,4
R71	ATP -> ATP.maintenance	14,0	0,0	14,0	14,0
R72	NADPH -> NADPH.maintenance	12,0	0,3	12,0	12,0
R73	NADH + O2 -> 3*ATP	225,3	0,3	219,8	231,8
R74	FADH2 + O2 -> 2*ATP	139,8	1,7	133,3	145,3
R75	UQH2 + O2 -> 3*ATP	100,0	0,0	100,0	100,0
R76	CO2 -> CO2.ext	239,6	0,0	239,6	239,6
R77	NH3.ext -> NH3	58,9	0,0	58,9	58,9

R78	SO4.ext -> SO4	1,4	0,0	1,4	1,4
R79	O2.ext -> O2	465,1	0,0	465,1	465,1
Fit		Accepted			
SSR		220,3			
Expected SSR		[194,4 - 279,4]			
Normally distribution		Yes			

Reaction ID	**Equation**	***Pseudomonas putida* KT2440 Δ*gtsABCD*Δ*glk*Δ*gad***				***Pseudomonas putida* KT2440 Δ*gtsABCD*Δ*glk*Δ*gntT***			
		Value (%)	**SD**	**Lower bond**	**Upper bond**	**Value (%)**	**SD**	**Lower bond**	**Upper bond**
R1	Gluc.ext -> Gluc.per	100,0	0,0	100,0	100,0	97,3	0,0	97,3	97,3
R2	Gluc.per + 2*ATP -> G6P	0,0	0,0	0,0	0,0	0,0	0,0	0,0	0,0
R3	Gluc.per -> Gluco.per + UQH2	100,0	0,0	100,0	100,0	97,3	0,0	97,3	97,3
R4	Gluco.per -> Gluco.ext	8,5	0,0	8,5	8,5	2,7	0,0	2,7	2,7
R5	Gluco.per + ATP -> 6PG	91,5	0,0	91,5	91,5	0,0	0,0	0,0	0,0
R6	Gluco.per -> Kgluco.per + FADH2	0,0	0,0	0,0	0,0	99,9	0,0	99,9	99,9
R7	Kgluco.per -> Kgluco.ext	0,0	0,0	0,0	0,0	53,8	0,0	53,8	53,8
R8	Kgluco.per + ATP -> KGluco6P	0,0	0,0	0,0	0,0	46,1	0,0	46,1	46,1
R9	KGluco6P + NADPH -> 6PG	0,0	0,0	0,0	0,0	46,1	0,0	46,1	46,1
R10	G6P <-> F6P	-28,7	0,7	-31,1	-27,4	-34,3	0,7	-35,9	-32,8
R11	FBP -> F6P	32,3	0,7	31,0	33,8	17,6	0,7	16,3	19,1
R12	FBP <-> DHAP + GAP	-32,3	0,7	-33,8	-31,0	-17,6	0,7	-19,1	-16,3
R13	DHAP <-> GAP	-32,3	0,7	-33,8	-31,0	-17,6	0,7	-19,1	-16,3
R14	GAP <-> 3PG + ATP + NADH	49,9	0,7	48,4	51,2	22,7	0,7	21,3	24,1
R15	3PG <-> PEP	41,2	0,7	39,8	42,5	17,4	0,7	15,9	18,7
R16	PEP -> Pyr + ATP	41,3	0,8	37,9	42,8	14,6	3,2	8,4	16,2
R17	G6P -> 6PG + NADPH	26,9	0,7	25,5	29,2	33,2	0,7	31,6	34,8
R18	6PG -> Ri5P + CO2 + NADPH	0,0	0,0	0,0	2,6	28,4	0,0	27,6	29,2
R19	Ri5P <-> X5P	-2,9	0,0	-2,9	-1,2	17,2	0,0	16,6	17,7
R20	Ri5P <-> R5P	2,9	0,7	0,3	3,7	11,3	0,0	11,0	11,5
R21	X5P <-> GAP + EC2	-0,4	0,0	-2,9	-0,4	17,2	0,0	16,6	17,7
R22	F6P <-> E4P + EC2	-0,4	0,7	2,7	-0,4	-7,2	0,0	-7,5	-7,0
R23	S7P <-> R5P + EC2	0,4	0,7	0,4	-0,7	-9,9	0,0	-10,2	-9,7
R24	F6P <-> GAP + EC3	-0,7	0,7	-1,6	-0,7	-9,9	0,0	-10,2	-9,7
R25	S7P <-> E4P + EC3	-0,7	0,1	0,7	1,6	9,9	0,0	9,7	10,2
R26	6PG -> Pyr + GAP	118,4	0,1	117,0	119,9	50,9	0,7	49,6	52,3
R27	Pyr -> AcCoA + CO2 + NADH	101,4	0,1	96,9	106,6	26,8	0,0	26,3	27,3
R28	OAA + AcCoA -> Cit	62,7	0,7	61,9	63,0	7,8	0,0	7,8	7,8
R29	Cit <-> ICit	62,7	0,7	61,9	63,0	7,8	0,0	7,8	7,8
R30	ICit -> Suc + Glyox	8,1	0,1	3,6	13,3	0,0	0,0	0,0	0,0
R31	Glyox + AcCoA -> Mal	8,1	0,1	3,6	13,3	0,0	0,0	0,0	0,0
R32	ICit -> AKG + CO2 + NADPH	54,6	0,1	49,5	59,1	7,8	0,0	7,8	7,8

R33	AKG -> SucCoA + CO2 + NADH	42,2	0,1	37,0	46,7	0,0	0,0	0,0	0,0
R34	SucCoA <-> Suc + ATP	39,0	0,1	33,8	43,5	-2,0	0,0	-2,0	-2,0
R35	Suc -> Fum + FADH2	50,3	0,1	49,5	50,5	0,0	0,0	NaN	0,0
R36	Fum <-> Mal	55,4	0,7	54,6	55,6	3,2	0,0	NaN	3,2
R37	Mal -> OAA + FADH2	63,5	2,7	53,2	68,8	0,0	0,0	0,0	0,0
R38	Pyr + CO2 + ATP -> OAA	446,0	6,4	433,7	459,3	112,7	3,3	106,3	115,8
R39	OAA -> Pyr + CO2	418,0	4,0	410,4	425,0	89,8	1,3	86,6	93,0
R40	PEP + CO2 -> OAA	0,0	0,1	0,0	3,5	0,2	3,4	0,0	6,7
R41	OAA + ATP -> PEP + CO2	0,0	0,0	0,0	9,7	2,8	0,2	2,5	3,2
R42	Mal -> Pyr + CO2 + NADPH	8,7	0,3	7,6	9,7	3,2	0,0	3,2	3,2
R43	AKG + NADPH + NH3 -> Glu	71,4	0,1	71,1	71,6	44,6	0,0	44,3	44,8
R44	Glu + ATP + NH3 -> Gln	8,6	0,3	8,6	8,6	5,4	0,0	5,4	5,4
R45	Glu + ATP + 2*NADPH -> Pro	1,0	0,0	1,0	1,0	1,7	0,0	1,7	1,7
R46	Glu + CO2 + Gln + Asp + AcCoA + 5*ATP + NADPH -> Arg + AKG + Fum + Ac	3,8	0,6	3,8	3,8	2,3	0,0	2,3	2,3
R47	OAA + Glu -> Asp + AKG	20,0	0,1	19,5	20,5	12,6	0,0	12,0	13,1
R48	Asp + 2*ATP + NH3 -> Asn	1,7	0,1	1,7	1,7	1,0	0,0	1,0	1,0
R49	Pyr + Glu -> Ala + AKG	-0,1	0,1	-0,4	0,1	4,0	0,0	4,0	4,0
R50	3PG + Glu -> Ser + AKG + NADH	0,9	0,3	0,4	8,9	5,4	0,0	5,1	5,6
R51	Ser <-> Gly + MEETHF	-0,3	0,3	-0,7	0,0	1,7	0,0	1,4	1,9
R52	Gly <-> CO2 + MEETHF + NADH + NH3	-0,1	0,6	0,5	0,1	0,0	0,0	-0,3	0,2
R53	Thr <-> Gly + AcCoA + NADH	1,7	0,3	1,2	2,2	1,1	0,0	0,6	1,7
R54	Ser + AcCoA + 3*ATP + 4*NADPH + SO4 -> Cys + Ac	1,9	0,3	1,9	1,9	1,2	0,0	1,2	1,2
R55	Asp + Pyr + Glu + SucCoA + ATP + 2*NADPH -> LL_DAP + AKG + Suc	0,7	0,0	0,7	0,7	1,2	0,0	1,2	1,2
R56	LL_DAP -> Lys + CO2	1,9	0,6	1,9	1,9	1,2	0,0	1,2	1,2
R57	Asp + 2*ATP + 2*NADPH -> Thr	7,0	0,3	6,5	7,5	4,5	0,0	3,9	5,0
R58	Asp + METHF + Cys + SucCoA + ATP + 2*NADPH -> Met + Pyr + Suc + NH3	1,3	0,0	1,3	1,3	0,8	0,0	0,8	0,8
R59	Pyr + Pyr + Glu + NADPH -> Val + CO2 + AKG	4,1	0,0	4,1	4,1	2,6	0,0	2,6	2,6
R60	AcCoA + Pyr + Pyr + Glu + NADPH -> Leu + CO2 + CO2 + AKG + NADH	0,8	0,0	0,8	0,8	4,2	0,0	4,2	4,2

R61	Thr + Pyr + Glu + NADPH -> Ile + CO2 + AKG + NH3	0,5	0,0	0,5	0,5	1,6	0,0	1,6	1,6
R62	PEP + PEP + E4P + Glu + ATP + NADPH -> Phe + CO2 + AKG	0,8	0,0	0,8	0,8	1,3	0,0	1,3	1,3
R63	PEP + PEP + E4P + Glu + ATP + NADPH -> Tyr + CO2 + AKG + NADH	0,7	0,0	0,7	0,7	0,9	0,0	0,9	0,9
R64	Ser + R5P + PEP + E4P + PEP + Gln + 3*ATP + NADPH -> Trp + CO2 + GAP + Pyr + Glu	0,8	0,0	0,8	0,8	0,5	0,0	0,5	0,5
R65	R5P + FTHF + Gln + Asp + 5*ATP -> His + AKG + Fum + 2*NADH	1,3	0,0	1,3	1,3	0,8	0,0	0,8	0,8
R66	MEETHF + NADH -> METHF	1,3	0,0	1,3	1,3	0,8	0,0	0,8	0,8
R67	MEETHF -> FTHF + NADPH	1,3	0,0	1,3	1,3	0,8	0,0	0,8	0,8
R68	Biomass formation Refer to *	10,6	0,0	10,6	10,6	6,6	0,0	6,6	6,6
R69	CO2.unlabeled <-> CO2	0,0	0,0	0,0	0,0	0,0	0,0	0,0	0,0
R70	NADH <-> NADPH	56,7	0,3	46,3	61,6	61,9	0,7	60,5	63,3
R71	ATP -> ATP.maintenance	15,3	0,0	15,3	15,3	11,8	0,0	11,8	11,8
R72	NADPH -> NADPH.maintenance	13,1	0,0	13,1	13,1	10,2	0,0	10,2	10,2
R73	NADH + O2 -> 3*ATP	156,6	2,8	151,2	167,0	0,0	0,0	0,0	NaN
R74	FADH2 + O2 -> 2*ATP	113,8	2,8	103,4	119,1	99,9	0,0	99,9	99,9
R75	UQH2 + O2 -> 3*ATP	100,0	0,0	100,0	100,0	97,3	0,0	97,3	97,3
R76	CO2 -> CO2.ext	201,4	0,0	201,4	201,4	59,9	0,0	59,9	59,9
R77	NH3.ext -> NH3	77,9	0,0	77,9	77,9	48,6	0,0	48,6	48,6
R78	SO4.ext -> SO4	1,9	0,0	1,9	1,9	1,2	0,0	1,2	1,2
R79	O2.ext -> O2	370,3	0,0	370,3	370,3	197,2	0,0	197,2	197,2
Fit		Accepted				Accepted			
SSR		183,1				159,1			
Expected SSR		[180,8 - 263,0]				[149,2 - 224,6]			
Normally distribution		Yes				Yes			

Biomass equation: 0.174*G6P + 0.068*F6P + 0.107*GAP + 1.882*AcCoA + 0.431*Gly + 0.263*Pro + 0.598*Ala + 0.389*Val + 0.628*Leu + 0.244*Ile + 0.122*Met + 0.055*Cys + 0.191*Phe + 0.135*Tyr + 0.077*Trp + 0.126*His + 0.18*Lys + 0.354*Arg + 0.251*Gln + 0.158*Asn + 0.301*Glu + 0.284*Asp + 0.301*Ser + 0.256*Thr + 46.75*ATP -> Biomass.

Table 6.S5. Atom transition list from the reactions in Table 6.S5. Reaction IDs are on the left column while the corresponding reactions on the right column. Letters in parenthesis symbolizes the carbon position in the molecule.

Reaction ID	Atom Transitions
R1	Gluc.ext (abcdef) -> Gluc.per (abcdef)
R2	Gluc.per (abcdef) + 2*ATP -> G6P (abcdef)
R3	Gluc.per (abcdef) -> Gluco.per (abcdef) + UQH2
R4	Gluco.per (abcdef) -> Gluco.ext (abcdef)
R5	Gluco.per (abcdef) + ATP -> 6PG (abcdef)
R6	Gluco.per (abcdef) -> Kgluco.per (abcdef) + FADH2
R7	Kgluco.per (abcdef) -> Kgluco.ext (abcdef)
R8	Kgluco.per (abcdef)+ ATP -> KGluco6P (abcdef)
R9	KGluco6P (abcdef) + NADPH -> 6PG (abcdef)
R10	G6P (abcdef) <-> F6P (abcdef)
R11	FBP (abcdef) -> F6P (abcdef)
R12	FBP (abcdef) <-> DHAP (cba) + GAP (def)
R13	DHAP (abc) <-> GAP (abc)
R14	GAP (abc) <-> 3PG (abc) + ATP + NADH
R15	3PG (abc) <-> PEP (abc)
R16	PEP (abc) -> Pyr (abc) + ATP
R17	G6P (abcdef) -> 6PG (abcdef) + NADPH
R18	6PG (abcdef) -> Ri5P (bcdef) + CO2 (a) + NADPH
R19	Ri5P (abcde) <-> X5P (abcde)
R20	Ri5P (abcde) <-> R5P (abcde)
R21	X5P (abcde) <-> GAP (cde) + EC2 (ab)
R22	F6P (abcdef) <-> E4P (cdef) + EC2 (ab)
R23	S7P (abcdefg) <-> R5P (cdefg) + EC2 (ab)
R24	F6P (abcdef) <-> GAP (def) + EC3 (abc)
R25	S7P (abcdefg) <-> E4P (defg) + EC3 (abc)
R26	6PG (abcdef) -> Pyr (abc) + GAP (def)
R27	Pyr (abc) -> AcCoA (bc) + CO2 (a) + NADH
R28	OAA (abcd) + AcCoA (ef) -> Cit (dcbfea)
R29	Cit (abcdef) <-> ICit (abcdef)
R30	ICit (abcdef) -> Suc (edcf) + Glyox (ab)
R31	Glyox (ab) + AcCoA (cd) -> Mal (abdc)
R32	ICit (abcdef) -> AKG (abcde) + CO2 (f) + NADPH
R33	AKG (abcde) -> SucCoA (bcde) + CO2 (a) + NADH
R34	SucCoA (abcd) <-> Suc (abcd) + ATP
R35	Suc (abcd) -> Fum (abcd) + FADH2
R36	Fum (abcd) <-> Mal (abcd)
R37	Mal (abcd) -> OAA (abcd) + FADH2
R38	Pyr (abc) + CO2 (d) + ATP -> OAA (abcd)

R39	OAA (abcd) -> Pyr (abc) + CO2 (d)
R40	PEP (abc) + CO2 (d) -> OAA (abcd)
R41	OAA (abcd) + ATP -> PEP (abc) + CO2 (d)
R42	Mal (abcd) -> Pyr (abc) + CO2 (d) + NADPH
R43	AKG (abcde) + NADPH + NH3 -> Glu (abcde)
R44	Glu (abcde) + ATP + NH3 -> Gln (abcde)
R45	Glu (abcde) + ATP + 2*NADPH -> Pro (abcde)
R46	Glu (abcde) + CO2 (f) + Gln (ghijk) + Asp (lmno) + AcCoA (pq) + 5*ATP + NADPH -> Arg (abcdef) + AKG (ghijk) + Fum (lmno) + Ac (pq)
R47	OAA (abcd) + Glu (efghi) -> Asp (abcd) + AKG (efghi)
R48	Asp (abcd) + 2*ATP + NH3 -> Asn (abcd)
R49	Pyr (abc) + Glu (defgh) -> Ala (abc) + AKG (defgh)
R50	3PG (abc) + Glu (defgh) -> Ser (abc) + AKG (defgh) + NADH
R51	Ser (abc) <-> Gly (ab) + MEETHF (c)
R52	Gly (ab) <-> CO2 (a) + MEETHF (b) + NADH + NH3
R53	Thr (abcd) <-> Gly (ab) + AcCoA (cd) + NADH
R54	Ser (abc) + AcCoA (de) + 3*ATP + 4*NADPH + SO4 -> Cys (abc) + Ac (de)
R55	Asp (abcd) + Pyr (efg) + Glu (hijkl) + SucCoA (mnop) + ATP + 2*NADPH -> LL_DAP (abcdgfe) + AKG (hijkl) + Suc (mnop)
R56	LL_DAP (abcdefg) -> Lys (abcdef) + CO2 (g)
R57	Asp (abcd) + 2*ATP + 2*NADPH -> Thr (abcd)
R58	Asp (abcd) + METHF (e) + Cys (fgh) + SucCoA (ijkl) + ATP + 2*NADPH -> Met (abcde) + Pyr (fgh) + Suc (ijkl) + NH3
R59	Pyr (abc) + Pyr (def) + Glu (ghijk) + NADPH -> Val (abcef) + CO2 (d) + AKG (ghijk)
R60	AcCoA (ab) + Pyr (cde) + Pyr (fgh) + Glu (ijklm) + NADPH -> Leu (abdghe) + CO2 (c) + CO2 (f) + AKG (ijklm) + NADH
R61	Thr (abcd) + Pyr (efg) + Glu (hijkl) + NADPH -> Ile (abfcdg) + CO2 (e) + AKG (hijkl) + NH3
R62	PEP (abc) + PEP (def) + E4P (ghij) + Glu (klmno) + ATP + NADPH -> Phe (abcefghij) + CO2 (d) + AKG (klmno)
R63	PEP (abc) + PEP (def) + E4P (ghij) + Glu (klmno) + ATP + NADPH -> Tyr (abcefghij) + CO2 (d) + AKG (klmno) + NADH
R64	Ser (abc) + R5P (defgh) + PEP (ijk) + E4P (lmno) + PEP (pqr) + Gln (stuvw) + 3*ATP + NADPH -> Trp (abcedklmnoj) + CO2 (i) + GAP (fgh) + Pyr (pqr) + Glu (stuvw)
R65	R5P (abcde) + FTHF (f) + Gln (ghijk) + Asp (lmno) + 5*ATP -> His (edcbaf) + AKG (ghijk) + Fum (lmno) + 2*NADH
R66	MEETHF (a) + NADH -> METHF (a)
R67	MEETHF (a) -> FTHF (a) + NADPH
R68	0.174*G6P + 0.068*F6P + 0.107*GAP + 1.882*AcCoA + 0.431*Gly + 0.263*Pro + 0.598*Ala + 0.389*Val + 0.628*Leu + 0.244*Ile + 0.122*Met + 0.055*Cys + 0.191*Phe + 0.135*Tyr + 0.077*Trp + 0.126*His + 0.18*Lys + 0.354*Arg + 0.251*Gln + 0.158*Asn + 0.301*Glu + 0.284*Asp + 0.301*Ser + 0.256*Thr + 46.75*ATP -> Biomass
R69	CO2.unlabeled (a) <-> CO2 (a)
R70	NADH <-> NADPH
R71	ATP -> ATP.maintenance
R72	NADPH -> NADPH.maintenance
R73	NADH + O2 -> 3*ATP
R74	FADH2 + O2 -> 2*ATP
R75	UQH2 + O2 -> 3*ATP
R76	CO2 (a) -> CO2.ext (a)
R77	NH3.ext -> NH3
R78	SO4.ext -> SO4
R79	O2.ext -> O2

Reference Chapter 6

ADACHI, O., MATSUSHITA, K., SHINAGAWA, E., and AMEYAMA, M. (1979) Occurrence of old yellow enzyme in *Gluconobacter suboxydans*, and the cyclic regeneration of NADP, *The Journal of Biochemistry* **86**: 699-709.

Antoniewicz, M.R., Kelleher, J.K., and Stephanopoulos, G. (2006) Determination of confidence intervals of metabolic fluxes estimated from stable isotope measurements, *Metabolic engineering* **8**: 324-337.

Bagdasarian, M., Lurz, R., Ruckert, B., Franklin, F.C., Bagdasarian, M.M., Frey, J., and Timmis, K.N. (1981) Specific-purpose plasmid cloning vectors. II. Broad host range, high copy number, RSF1010-derived vectors, and a host-vector system for gene cloning in Pseudomonas, *Gene* **16**: 237-247.

Bailey, J.E. (1998) Mathematical Modeling and Analysis in Biochemical Engineering: Past Accomplishments and Future Opportunities, *Biotechnology Progress* **14**: 8-20.

Baumstark, R., Hänzelmann, S., Tsuru, S., Schaerli, Y., Francesconi, M., Mancuso, F.M., et al. (2015) The propagation of perturbations in rewired bacterial gene networks, *Nature Communications* **6**: 10105.

Bentley, D.R., Balasubramanian, S., Swerdlow, H.P., Smith, G.P., Milton, J., Brown, C.G., et al. (2008) Accurate whole human genome sequencing using reversible terminator chemistry, *Nature* **456**: 53-59.

Blaby, I.K., Glaesener, A.G., Mettler, T., Fitz-Gibbon, S.T., Gallaher, S.D., Liu, B., et al. (2013) Systems-level analysis of nitrogen starvation–Induced modifications of carbon metabolism in a *Chlamydomonas reinhardtii* starchless mutant, *The Plant Cell* **25**: 4305-4323.

Blank, L.M., Ionidis, G., Ebert, B.E., Bühler, B., and Schmid, A. (2008) Metabolic response of *Pseudomonas putida* during redox biocatalysis in the presence of a second octanol phase, *The FEBS journal* **275**: 5173-5190.

Blank, L.M., Lehmbeck, F., and Sauer, U. (2005) Metabolic-flux and network analysis in fourteen hemiascomycetous yeasts, *FEMS Yeast Res* **5**: 545-558.

Boonstra, B., French, C.E., Wainwright, I., and Bruce, N.C. (1999) The *udhA* gene of E*scherichia coli* encodes a soluble pyridine nucleotide transhydrogenase, *J Bacteriol* **181**: 1030-1034.

Castillo, T.d., Ramos, J.L., Rodríguez-Herva, J.J., Fuhrer, T., Sauer, U., and Duque, E. (2007) Convergent Peripheral Pathways Catalyze Initial Glucose Catabolism in *Pseudomonas putida*: Genomic and Flux Analysis, *Journal of Bacteriology* **189**: 5142-5152.

Cecchini, G., Schröder, I., Gunsalus, R.P., and Maklashina, E. (2002) Succinate dehydrogenase and fumarate reductase from *Escherichia coli*, *Biochimica et Biophysica Acta (BBA) - Bioenergetics* **1553**: 140-157.

Chavarría, M., Kleijn, R.J., Sauer, U., Pflüger-Grau, K., and Lorenzo, V.d. (2012) Regulatory Tasks of the Phosphoenolpyruvate-Phosphotransferase System of Pseudomonas putida in Central Carbon Metabolism, *mBio* **3**: e00028-00012.

Chavarría, M., Nikel, P.I., Pérez-Pantoja, D., and de Lorenzo, V. (2013) The Entner–Doudoroff pathway empowers *Pseudomonas putida* KT2440 with a high tolerance to oxidative stress, *Environmental Microbiology* **15**: 1772-1785.

Chen, Y., Ding, Y., Yang, L., Yu, J., Liu, G., Wang, X., et al. (2013) Integrated omics study delineates the dynamics of lipid droplets in *Rhodococcus opacus* PD630, *Nucleic Acids Research* **42**: 1052-1064.

Christodoulou, D., Link, H., Fuhrer, T., Kochanowski, K., Gerosa, L., and Sauer, U. (2018) Reserve Flux Capacity in the Pentose Phosphate Pathway Enables *Escherichia coli*'s Rapid Response to Oxidative Stress, *Cell Systems* **6**: 569-578.e567.

Clarke, D.M., Loo, T.W., Gillam, S., and Bragg, P.D. (1986) Nucleotide sequence of the *pntA* and *pntB* genes encoding the pyridine nucleotide transhydrogenase of *Escherichia coli*, *Eur J Biochem* **158**: 647-653.

Conway, T. (1992) The Entner-Doudoroff pathway: history, physiology and molecular biology, *FEMS Microbiology Reviews* **9**: 1-27.

Czajka, J.J., Banerjee, D., Eng, T., Menasalvas, J., Yan, C., Munoz, N.M., et al. (2022) Tuning a high performing multiplexed-CRISPRi *Pseudomonas putida* strain to further enhance indigoidine production, *Metabolic Engineering Communications* **15**: e00206.

Daddaoua, A., Fillet, S., Fernández, M., Udaondo, Z., Krell, T., and Ramos, J.L. (2012) Genes for carbon metabolism and the ToxA virulence factor in *Pseudomonas aeruginosa* are regulated through molecular interactions of PtxR and PtxS, *PLoS One* **7**: e39390.

Daddaoua, A., Krell, T., and Ramos, J.-L. (2009) Regulation of glucose metabolism in *Pseudomonas*: the phosphorylative branch and Entner-Doudoroff enzymes are regulated by a repressor containing a sugar isomerase domain, *Journal of Biological Chemistry* **284**: 21360-21368.

del Castillo, T., Duque, E., and Ramos, J.L. (2008) A set of activators and repressors control peripheral glucose pathways in *Pseudomonas putida* to yield a common central intermediate, *Journal of bacteriology* **190**: 2331-2339.

del Castillo, T., Ramos, J.L., Rodríguez-Herva, J.J., Fuhrer, T., Sauer, U., and Duque, E. (2007) Convergent peripheral pathways catalyze initial glucose catabolism in *Pseudomonas putida*: genomic and flux analysis, *J Bacteriol* **189**: 5142-5152.

Doan, T., Servant, P., Tojo, S., Yamaguchi, H., Lerondel, G., Yoshida, K.I., et al. (2003) The *Bacillus subtilis ywkA* gene encodes a malic enzyme and its transcription is activated by the YufL/YufM two-component system in response to malate, *Microbiology (Reading)* **149**: 2331-2343.

Donati, S., Kuntz, M., Pahl, V., Farke, N., Beuter, D., Glatter, T., et al. (2021) Multi-omics analysis of CRISPRi-knockdowns identifies mechanisms that buffer decreases of enzymes in *E. coli* metabolism, *Cell Systems* **12**: 56-67.e56.

Ebert, B.E., Kurth, F., Grund, M., Blank, L.M., and Schmid, A. (2011) Response of *Pseudomonas putida* KT2440 to increased NADH and ATP demand, *Appl Environ Microbiol* **77**: 6597-6605.

Edwards, J.S., Ibarra, R.U., and Palsson, B.O. (2001) *In silico* predictions of *Escherichia coli* metabolic capabilities are consistent with experimental data, *Nature Biotechnology* **19**: 125-130.

Fillinger, S., Boschi-Muller, S., Azza, S., Dervyn, E., Branlant, G., and Aymerich, S. (2000) Two glyceraldehyde-3-phosphate dehydrogenases with opposite physiological roles in a nonphotosynthetic bacterium, *J Biol Chem* **275**: 14031-14037.

Friedman, D.B., Stauff, D.L., Pishchany, G., Whitwell, C.W., Torres, V.J., and Skaar, E.P. (2006) *Staphylococcus aureus* redirects central metabolism to increase iron availability, *PLoS pathogens* **2**: e87.

Fuhrer, T., and Sauer, U. (2009) Different biochemical mechanisms ensure network-wide balancing of reducing equivalents in microbial metabolism, *Journal of bacteriology* **191**: 2112-2121.

Fuhrer, T., and Sauer, U. (2009) Different biochemical mechanisms ensure network-wide balancing of reducing equivalents in microbial metabolism, *J Bacteriol* **191**: 2112-2121.

Gerosa, L., and Sauer, U. (2011) Regulation and control of metabolic fluxes in microbes, *Current Opinion in Biotechnology* **22**: 566-575.

Gurdo, N., Volke, D.C., McCloskey, D., and Nikel, P.I. (2023) Automating the design-build-test-learn cycle towards next-generation bacterial cell factories, *New Biotechnology* **74**: 1-15.

Hackett, S.R., Zanotelli, V.R.T., Xu, W., Goya, J., Park, J.O., Perlman, D.H., et al. (2016) Systems-level analysis of mechanisms regulating yeast metabolic flux, *Science* **354**: aaf2786.

Hamood, A.N., Colmer, J.A., Ochsner, U.A., and Vasil, M.L. (1996) Isolation and characterization of a *Pseudomonas aeruginosa* gene, *ptxR*, which positively regulates exotoxin A production, *Mol Microbiol* **21**: 97-110.

Heinemann, M., and Sauer, U. (2010) Systems biology of microbial metabolism, *Current Opinion in Microbiology* **13**: 337-343.
Hoek, J.B., and Rydström, J. (1988) Physiological roles of nicotinamide nucleotide transhydrogenase, *Biochem J* **254**: 1-10.
Hurbain, J., Thommen, Q., Anquez, F., and Pfeuty, B. (2022) Quantitative modeling of pentose phosphate pathway response to oxidative stress reveals a cooperative regulatory strategy, *iScience* **25**: 104681.
Ideker, T., Ozier, O., Schwikowski, B., and Siegel, A.F. (2002) Discovering regulatory and signalling circuits in molecular interaction networks, *Bioinformatics* **18**: S233-S240.
Ishii, N., Nakahigashi, K., Baba, T., Robert, M., Soga, T., Kanai, A., et al. (2007) Multiple high-throughput analyses monitor the response of *E. coli* to perturbations, *Science* **316**: 593-597.
Isken, S., Derks, A., Wolffs, P.F., and de Bont, J.A. (1999) Effect of organic solvents on the yield of solvent-tolerant *Pseudomonas putida* S12, *Applied and Environmental Microbiology* **65**: 2631-2635.
Karlstaedt, A., Khanna, R., Thangam, M., and Taegtmeyer, H. (2020) Glucose 6-Phosphate Accumulates via Phosphoglucose Isomerase Inhibition in Heart Muscle, *Circ Res* **126**: 60-74.
Kell, D.B. (2004) Metabolomics and systems biology: making sense of the soup, *Current opinion in microbiology* **7**: 296-307.
Kiviet, D.J., Nghe, P., Walker, N., Boulineau, S., Sunderlikova, V., and Tans, S.J. (2014) Stochasticity of metabolism and growth at the single-cell level, *Nature* **514**: 376-379.
Klumpp, S., and Hwa, T. (2014) Bacterial growth: global effects on gene expression, growth feedback and proteome partition, *Current Opinion in Biotechnology* **28**: 96-102.
Kobayashi, S., Kawaguchi, H., Shirai, T., Ninomiya, K., Takahashi, K., Kondo, A., and Tsuge, Y. (2020) Automatic redirection of carbon flux between glycolysis and pentose phosphate pathway using an oxygen-responsive metabolic switch in *Corynebacterium glutamicum*, *ACS Synthetic Biology* **9**: 814-826.
Kohlstedt, M., and Wittmann, C. (2019) GC-MS-based ^{13}C metabolic flux analysis resolves the parallel and cyclic glucose metabolism of *Pseudomonas putida* KT2440 and *Pseudomonas aeruginosa* PAO1, *Metabolic Engineering* **54**: 35-53.
Kotte, O., Zaugg, J.B., and Heinemann, M. (2010) Bacterial adaptation through distributed sensing of metabolic fluxes, *Molecular Systems Biology* **6**: 355.
Kretzschmar, U., Khodaverdi, V., and Adrian, L. (2010) Transcriptional regulation of the acetyl-CoA synthetase gene acsA in Pseudomonas aeruginosa, *Archives of Microbiology* **192**: 685-690.

Kretzschmar, U., Rückert, A., Jeoung, J.-H., and Görisch, H. (2002) Malate:quinone oxidoreductase is essential for growth on ethanol or acetate in *Pseudomonas aeruginosa* The GenBank accession number for the *Pseudomonas aeruginosa* ATCC 17933 *mqo* sequence reported in this work is AY129296, *Microbiology* **148**: 3839-3847.

LaPorte, D.C., Walsh, K., and Koshland, D.E., Jr. (1984) The branch point effect. Ultrasensitivity and subsensitivity to metabolic control, *J Biol Chem* **259**: 14068-14075.

Lee, J.Y., Cha, S., Lee, J.H., Lim, H.G., Noh, M.H., Kang, C.W., and Jung, G.Y. (2021) Plug-in repressor library for precise regulation of metabolic flux in *Escherichia coli*, *Metabolic Engineering* **67**: 365-372.

Lim, H.G., Rychel, K., Sastry, A.V., Bentley, G.J., Mueller, J., Schindel, H.S., et al. (2022) Machine-learning from *Pseudomonas putida* KT2440 transcriptomes reveals its transcriptional regulatory network, *Metabolic Engineering* **72**: 297-310.

Llamas, M.A., Rodríguez-Herva, J.J., Hancock, R.E.W., Bitter, W., Tommassen, J., and Ramos, J.L. (2003) Role of *Pseudomonas putida* tol-oprL gene products in uptake of solutes through the cytoplasmic membrane, *Journal of Bacteriology* **185**: 4707-4716.

Ma, H.-W., and Zeng, A.-P. (2003) The connectivity structure, giant strong component and centrality of metabolic networks, *Bioinformatics* **19**: 1423-1430.

Maciąg, M., Nowicki, D., Janniere, L., Szalewska-Pałasz, A., and Węgrzyn, G. (2011) Genetic response to metabolic fluctuations: correlation between central carbon metabolism and DNA replication in *Escherichia coli*, *Microbial Cell Factories* **10**: 19.

McCloskey, D., Xu, J., Schrübbers, L., Christensen, H.B., and Herrgård, M.J. (2018) RapidRIP quantifies the intracellular metabolome of 7 industrial strains of *E. coli*, *Metabolic Engineering* **47**: 383-392.

Meza, E., Becker, J., Bolivar, F., Gosset, G., and Wittmann, C. (2012) Consequences of phosphoenolpyruvate:sugar phosphotranferase system and pyruvate kinase isozymes inactivation in central carbon metabolism flux distribution in *Escherichia coli*, *Microbial Cell Factories* **11**: 127.

Mhamdi, A., Mauve, C., Gouia, H., Saindrenan, P., Hodges, M., and Noctor, G. (2010) Cytosolic NADP-dependent isocitrate dehydrogenase contributes to redox homeostasis and the regulation of pathogen responses in *Arabidopsis* leaves, *Plant, cell & environment* **33**: 1112-1123.

Molina, L., Rosa, R.L., Nogales, J., and Rojo, F. (2019) *Pseudomonas putida* KT2440 metabolism undergoes sequential modifications during exponential growth in a complete medium as compounds are gradually consumed, *Environmental Microbiology* **21**: 2375-2390.

Moreno, R., Martínez-Gomariz, M., Yuste, L., Gil, C., and Rojo, F. (2009) The *Pseudomonas putida* Crc global regulator controls the hierarchical assimilation of amino

acids in a complete medium: Evidence from proteomic and genomic analyses, *PROTEOMICS* **9**: 2910-2928.

Morin, M., Ropers, D., Letisse, F., Laguerre, S., Portais, J.-C., Cocaign-Bousquet, M., and Enjalbert, B. (2016) The post-transcriptional regulatory system CSR controls the balance of metabolic pools in upper glycolysis of *Escherichia coli*, *Molecular Microbiology* **100**: 686-700.

Munger, J., Bennett, B.D., Parikh, A., Feng, X.-J., McArdle, J., Rabitz, H.A., et al. (2008) Systems-level metabolic flux profiling identifies fatty acid synthesis as a target for antiviral therapy, *Nature Biotechnology* **26**: 1179-1186.

Nielsen, J. (2017) Systems Biology of Metabolism, *Annu Rev Biochem* **86**: 245-275.

Nijhout, H.F., Best, J.A., and Reed, M.C. (2019) Systems biology of robustness and homeostatic mechanisms, *Wiley Interdisciplinary Reviews: Systems Biology and Medicine* **11**: e1440.

Nikel, P.I., Chavarría, M., Fuhrer, T., Sauer, U., and de Lorenzo, V. (2015) *Pseudomonas putida* KT2440 Strain Metabolizes Glucose through a Cycle Formed by Enzymes of the Entner-Doudoroff, Embden-Meyerhof-Parnas, and Pentose Phosphate Pathways, *J Biol Chem* **290**: 25920-25932.

Nogales, J., Mueller, J., Gudmundsson, S., Canalejo, F.J., Duque, E., Monk, J., et al. (2020) High-quality genome-scale metabolic modelling of *Pseudomonas putida* highlights its broad metabolic capabilities, *Environmental Microbiology* **22**: 255-269.

Noor, E., Eden, E., Milo, R., and Alon, U. (2010) Central Carbon Metabolism as a Minimal Biochemical Walk between Precursors for Biomass and Energy, *Molecular Cell* **39**: 809-820.

Olavarria, K., De Ingeniis, J., Zielinski, D.C., Fuentealba, M., Muñoz, R., McCloskey, D., et al. (2014) Metabolic impact of an NADH-producing glucose-6-phosphate dehydrogenase in *Escherichia coli*, *Microbiology* **160**: 2780-2793.

Overkamp, K.M., Bakker, B.M., Steensma, H.Y., van Dijken, J.P., and Pronk, J.T. (2002) Two mechanisms for oxidation of cytosolic NADPH by *Kluyveromyces lactis* mitochondria, *Yeast* **19**: 813-824.

Pedersen, B.H., Gurdo, N., Johansen, H.K., Molin, S., Nikel, P.I., and La Rosa, R. (2021) High-throughput dilution-based growth method enables time-resolved exo-metabolomics of *Pseudomonas putida* and *Pseudomonas aeruginosa*, *Microbial Biotechnology* **14**: 2214-2226.

Pfeuty, B., Hurbain, J., and Thommen, Q. (2023) Control Analysis of Cooperativity and Complementarity in Metabolic Regulations: The Case of NADPH Homeostasis, *Metabolites* **13**: 485.

Rytter, H., Jamet, A., Ziveri, J., Ramond, E., Coureuil, M., Lagouge-Roussey, P., et al. (2021) The pentose phosphate pathway constitutes a major metabolic hub in pathogenic Francisella, *PLoS Pathog* **17**: e1009326.
Sabidó, E., Selevsek, N., and Aebersold, R. (2012) Mass spectrometry-based proteomics for systems biology, *Current opinion in biotechnology* **23**: 591-597.
Saravolac, E.G., Taylor, N.F., Benz, R., and Hancock, R.E. (1991) Purification of glucose-inducible outer membrane protein OprB of *Pseudomonas putida* and reconstitution of glucose-specific pores, *Journal of Bacteriology* **173**: 4970-4976.
Sauer, U. (2006) Metabolic networks in motion: ^{13}C-based flux analysis, *Molecular Systems Biology* **2**: 62.
Sauer, U., and Eikmanns, B.J. (2005) The PEP—pyruvate—oxaloacetate node as the switch point for carbon flux distribution in bacteria: We dedicate this paper to Rudolf K. Thauer, Director of the Max-Planck-Institute for Terrestrial Microbiology in Marburg, Germany, on the occasion of his 65th birthday, *FEMS Microbiology Reviews* **29**: 765-794.
Sauer, U., Heinemann, M., and Zamboni, N. (2007) Getting Closer to the Whole Picture, *Science* **316**: 550-551.
Sazanov, L.A., and Jackson, J.B. (1994) Proton-translocating transhydrogenase and NAD- and NADP-linked isocitrate dehydrogenases operate in a substrate cycle which contributes to fine regulation of the tricarboxylic acid cycle activity in mitochondria, *FEBS Lett* **344**: 109-116.
Scott, M., Klumpp, S., Mateescu, E.M., and Hwa, T. (2014) Emergence of robust growth laws from optimal regulation of ribosome synthesis, *Molecular Systems Biology* **10**: 747.
Shimizu, K. (2013) Regulation systems of bacteria such as *Escherichia coli* in response to nutrient limitation and environmental stresses, *Metabolites* **4**: 1-35.
Soma, Y., Tsuruno, K., Wada, M., Yokota, A., and Hanai, T. (2014) Metabolic flux redirection from a central metabolic pathway toward a synthetic pathway using a metabolic toggle switch, *Metabolic Engineering* **23**: 175-184.
Spaans, S., Weusthuis, R., Van Der Oost, J., and Kengen, S. (2015) NADPH-generating systems in bacteria and archaea, *Frontiers in Microbiology* **6**.
Sriherfyna, F.H., Matsutani, M., Hirano, K., Koike, H., Kataoka, N., Yamashita, T., et al. (2021) The auxiliary NADH dehydrogenase plays a crucial role in redox homeostasis of nicotinamide cofactors in the absence of the periplasmic oxidation system in *Gluconobacter oxydans* NBRC3293, *Applied and Environmental Microbiology* **87**: e02155-02120.
Timmermans, J., and Van Melderen, L. (2010) Post-transcriptional global regulation by CsrA in bacteria, *Cell Mol Life Sci* **67**: 2897-2908.

Udaondo, Z., Ramos, J.-L., Segura, A., Krell, T., and Daddaoua, A. (2018) Regulation of carbohydrate degradation pathways in *Pseudomonas* involves a versatile set of transcriptional regulators, *Microbial Biotechnology* **11**: 442-454.

Valgepea, K., Adamberg, K., Seiman, A., and Vilu, R. (2013) *Escherichia coli* achieves faster growth by increasing catalytic and translation rates of proteins, *Molecular BioSystems* **9**: 2344-2358.

Verho, R., Richard, P., Jonson, P.H., Sundqvist, L., Londesborough, J., and Penttilä, M. (2002) Identification of the first fungal NADP-GAPDH from *Kluyveromyces lactis*, *Biochemistry* **41**: 13833-13838.

Volke, D.C., Gurdo, N., Milanesi, R., and Nikel, P.I. (2023) Time-resolved, deuterium-based fluxomics uncovers the hierarchy and dynamics of sugar processing by *Pseudomonas putida*, *Metabolic Engineering*.

Volke, D.C., Olavarría, K., and Nikel, P.I. (2021) Cofactor Specificity of Glucose-6-Phosphate Dehydrogenase Isozymes in *Pseudomonas putida* Reveals a General Principle Underlying Glycolytic Strategies in Bacteria, *mSystems* **6**: e00014-00021.

Wang, P., Robert, L., Pelletier, J., Dang, W.L., Taddei, F., Wright, A., and Jun, S. (2010) Robust Growth of *Escherichia coli*, *Current Biology* **20**: 1099-1103.

Weimer, A., Kohlstedt, M., Volke, D.C., Nikel, P.I., and Wittmann, C. (2020) Industrial biotechnology of *Pseudomonas putida*: advances and prospects, *Applied Microbiology and Biotechnology* **104**: 7745-7766.

Westfall, C.S., and Levin, P.A. (2018) Comprehensive analysis of central carbon metabolism illuminates connections between nutrient availability, growth rate, and cell morphology in *Escherichia coli*, *PLoS genetics* **14**: e1007205.

Worsey, M.J., and Williams, P.A. (1975) Metabolism of toluene and xylenes by *Pseudomonas putida* (*arvilla*) mt-2: evidence for a new function of the TOL plasmid, *Journal of Bacteriology* **124**: 7-13.

Wylie, J.L., and Worobec, E.A. (1995) The OprB porin plays a central role in carbohydrate uptake in *Pseudomonas aeruginosa*, *Journal of Bacteriology* **177**: 3021-3026.

Yoon, H., Ansong, C., McDermott, J.E., Gritsenko, M., Smith, R.D., Heffron, F., and Adkins, J.N. (2011) Systems analysis of multiple regulator perturbations allows discovery of virulence factors in *Salmonella*, *BMC Syst Biol* **5**: 100.

Young, J.D. (2014) INCA: a computational platform for isotopically non-stationary metabolic flux analysis, *Bioinformatics (Oxford, England)* **30**: 1333-1335.

Yurkovich, J.T., and Palsson, B.O. (2018) Quantitative -omic data empowers bottom-up systems biology, *Current Opinion in Biotechnology* **51**: 130-136.

Zhu, L., Zhang, J., Yang, J., Jiang, Y., and Yang, S. (2022) Strategies for optimizing acetyl-CoA formation from glucose in bacteria, *Trends in Biotechnology* **40**: 149-165.

Chapter 7 - Systems-level analysis of an engineered *Pseudomonas putida* strain carrying a synthetic glycolysis

Alberto Sánchez-Pascuala[a]†, Nicolás Gurdo[b]†, Lorena Fernandez-Cabezón[b]†, Justine Turlin[b], V, Nicolas Wirth[b], Josefin Johnsen[b], Elsayed T.Mohamed[b], Ana Catarina Sobral da Rocha[b], Stefano Donati[b], Shannara Kayleigh Taylor Parkins[b], Marie Vestergaard Lukassen[c], Lars Nielsen[b,d], Tobias Fuhrer[e], Adam M. Feist[b,f], Uwe Sauer[e], Victor de Lorenzo[g], & Pablo I. Nikel[b]*.

a Department of Biochemistry and Synthetic Metabolism, Max Planck Institute for Terrestrial Microbiology, 35043, Marburg, Germany.
b The Novo Nordisk Foundation Center for Biosustainability, Technical University of Denmark, 2800 Kongens Lyngby, Denmark.
c DTU Proteomics Core Facility, Department of Biotechnology and Biomedicine Section for Protein Science and Biotherapeutics, Technical University of Denmark, 2800 Kongens Lyngby, Denmark.
d Australian Institute for Bioengineering and Nanotechnology, The University of Queensland, Brisbane, QLD 4072, Australia.
e Institute of Molecular Systems Biology, ETH Zurich, Zurich, Switzerland.
f Department of Bioengineering, University of California, San Diego, La Jolla, California 92093, United States.
g Systems Biology Department, Centro Nacional de Biotecnología-CSIC, Campus de Cantoblanco, 28049, Madrid, Spain.

* Correspondence to:
Pablo I. Nikel (pabnik@biosustain.dtu.dk)
The Novo Nordisk Foundation Center for Biosustainability,
Technical University of Denmark
Lyngby, Denmark
Tel: (+45 93) 51 19 18

Summary

Synthetic circuits can be introduced into host microorganisms to enhance specific physiological traits and provide new functionalities for bioproduction. This study focuses on modifying the metabolic identity of *Pseudomonas putida* and transitioning it to a new lifestyle by reshaping its central carbon metabolism (CCM). Previous research successfully incorporated a glycolytic module from *E. coli*, converting the native cyclic Entner-Doudoroff (ED) pathway to a linear Embden-Meyerhof-Parnas (EMP) glycolysis. However, the engineered strain did not exhibit optimal growth performance under glucose conditions. In this work, we employed adaptive laboratory evolution (ALE) to improve the overall fitness of the bacterium and utilized a systems biology approach to investigate the impact of the *E. coli* glycolytic module in *P. putida*. Through evolution, a point mutation in the topoisomerase A gene (*topA*) was identified, leading to global rewiring at the proteome and fluxome levels, resulting in enhanced fitness and performance of the engineered strain. Additionally, network-wide proteomics and metabolic flux analysis revealed adjustments in protein levels within the introduced glycolytic enzymes and significant rerouting of flux in the Embden-Meyerhof-Parnas (EMP) glycolytic pathway and Tricarboxylic Acid cycle (TCA). Overall, our findings highlight the potential of strategically modifying metabolic characteristics in a versatile bacterium to enhance physiological traits.

7.1 Introduction

Synthetic metabolism has been widely implemented to build novel biosynthetic pathways into different microbial *chassis.* Plugging -in and –out biological components as part of the central metabolism core, can provide unique properties to be exploited from a biotechnological point of view (Medema, et al., 2011). For example, the incorporation of metabolic modules allows reprogramming central carbon metabolism by rationally redirecting the fluxes toward the desired final product. Even though there are several evidences showing that specific metabolic features can be incorporated into metabolic networks (Gassler, et al., 2020, Moon, et al., 2023), transforming the metabolic *identity* of central carbon metabolism is one of the hardest task in synthetic biology and metabolic engineering to date. This requires different approaches involving rational rewiring of the native biochemical network together with tightly-controlled expression of genetic elements which encodes the intended catabolic route. Particularly for glucose metabolism, systematic strategies that target central carbon metabolism–to obtain energy and precursors needed for growth and bioproduction–are relatively limited.

One partial but successful example is given by Sánchez-Pascuala et al. (2019) where two GlucoBrick (GBI and GBII), containing the linear Embden-Meyerhof-Parnas (EMP) glycolysis from *Escherichia coli*, were implemented in *Pseudomonas putida* KT2440. The first part of the glycolytic process in *E. coli* encompasses a series of ten reaction steps that convert glucose into pyruvate. This widely investigated process is known as the Embden-Meyerhof-Parnas (EMP) pathway, which involves the successive action of ten distinct enzymes (Romano and Conway, 1996). Concerning the GlucoBrick introduced in *P. putida*, the first operon (GBI) encodes the genes for the upper catabolic block of the glycolysis pathway, which comprises the *preparatory phase*. The second operon (GBII) encodes the genes for the lower catabolic block of the glycolytic pathway, which comprises the *pay-off phase*. The first module encompasses Glk (Glucokinase), Pgi (Phosphoglucose isomerase), PfkA (6-phosphofructo-1-kinase), FbaA (Fructose-1,6-bisphosphate aldolase) and TpiA (Triose phosphate

isomerase). The second module contains genes encoding for GapA (Glyceraldehyde-3-*P*-dehydrogenase), Pgk (Phosphoglycerate kinase), GpmA (Phosphoglycerate mutase A), Eno (Enolase) and PykF (Pyruvate kinase). In that work, the approach consisted on eliminating the enzymatic activities of the Entner-Doudoroff (ED) pathway as well as the peripheral reactions for glucose oxidation in order to avoid carbon loss in form of organic acids (gluconate and 2-ketogluconate). Then, *E. coli* glycolytic enzymes from the EMP pathway–that convert glucose into pyruvate–were introduced into the mutant strain with the aim of filling the metabolic gaps for the complete metabolism of glucose toward TCA cycle. The previous study demonstrated that by precisely rewiring *P. putida* native metabolism with the corresponding genetic graft containing the artificial glycolytic module empowers glucose-dependent growth through a linear glycolytic pathway for sugar catabolism. The EMP metabolic pathway plays a crucial role in generating various precursor molecules, serving as the primary route leading to the central hub pyruvate—acetyl-CoA. Achieving an optimal growth necessitates the presence of an effective mechanism that governs protein allocation, ensuring its efficient utilization (Li, et al., 2014, Grigaitis, et al., 2021).

Even though the strategy was successfully implemented, the previous grafted prototype obtained in Sánchez-Pascuala et al. (2019) presented a slow specific growth rate of 0.05 h^{-1} and a prolonged lag phase of approximately 24-36 h. It is important to note that while the glycolytic module was originally introduced into a plasmid-based structure, specifically induced by 3-methylbenzoate, for the current investigation, the module was integrated into the genome using transposon vectors.

In pursuit of optimal titers and productivity, effective biocatalysts are strategically designed to yield desirable outcomes. In addition, to optimize the efficiency of the relevant metabolic pathway and further enhance its performance, the implementation of additional improvements become a viable approach. For instance, adaptive laboratory evolution has proven to be a powerful approach that has been widely utilized to acquire strains with superior metabolic performance (Dragosits and Mattanovich, 2013). Additionally, systematic approaches such as multi-omics analysis

have enabled a systems-level understanding of microbial metabolism – guiding engineering efforts as an essential element of the design–build–test–learn (DBTL) cycle (Carbonell, et al., 2018). The recent advances made not only provide new opportunities for modifying bacterial *chassis* to generate innovative whole-cell biocatalysts, but also give rise to intriguing inquiries on how species *identity* is determined by core metabolism. Enlarging the application of synthetic metabolism would significantly increase the understanding of the biological system and provide innovative biosynthetic pathways for the production of novel and high-value chemicals.

P. putida KT2440 is recognized for its versatile metabolism and amenability to rewiring its metabolic pathways upon genetic disturbances or stressful environmental conditions (Belda, et al., 2016, Calero, et al., 2022). In this study, we employed the grafted *chassis* created by Sánchez-Pascuala et al. (2019), which incorporates the GlucoBrick platform that consists of two modules, each with five individual bricks. Module I (GBI) encodes the enzymes necessary for the *preparatory phase*, which employs ATP to convert hexoses into trioses-P [in this case, glucose → glyceraldehyde-3-P (G3P)]. Module II (GBII) encodes the enzymes required for the *pay-off phase*, the latter half of the EMP pathway, and changes trioses phosphate to pyruvate (Pyr) (i.e. G3P → Pyr). Given this context, we implemented an ALE strategy on glucose to enhance the catalytic efficiency of the EMP pathway towards pyruvate in the grafted *P. putida* KT2440. The ALE strategy enhanced growth on glucose compared to the non-evolved strains, and we identified a point mutation in topoisomerase I (Top^{A299P}) that had a positive effect on the final phenotype achieved in this study. To gain a comprehensive understanding of the dynamic interplay between the different layers of information, we carried out multi-omics analyses, encompassing genomics, metabolic flux analysis, and quantitative proteomics. The system-level analyses confirmed a higher carbon flux via the EMP pathway and a wide-proteome rewiring of key proteins in the synthetic GlucoBrick graft using glucose as the carbon source. Overall, this study demonstrated the plasticity of central

carbon metabolism in *P. putida* KT2440 and highlighted the potential of synthetic metabolism as a tool for future biotechnological applications.

7.2 Results

7.2.1 Adaptive laboratory evolution enhances glucose assimilation in two populations of *Pseudomonas putida* SG2.

In *P. putida* KT2440, there are two ways of processing glucose: (i) direct phosphorylation through the cytoplasmatic enzyme glucokinase (Glk) which converts glucose into glucose-6-phosphate (G6P), and (ii) through oxidation mediated by the periplasmatic glucose dehydrogenase (Gcd), which involves glucose oxidation into gluconate. In a second oxidation phase, gluconate is re-oxidized into 2-ketogluconate (2-KGA) by gluconate 2-dehydrogenase (Gad) (del Castillo, et al., 2007). Sánchez-Pascuala et al. (2019) generated a *P. putida* strain, named SG2, with a different metabolic lifestyle where the native glucose metabolism was transformed by incorporating the conventional linear glycolytic pathway—i.e. by plugging the corresponding GlucoBrick device—from *E. coli* (**Figure 7.1A, 1B**).

Results showed that the glycolytic module was successfully implanted in *P. putida*; however, the activity and fluxes through the components were not optimal due to its deficient and impaired growth on glucose. This observation prompted the question whether we could boost the pathway activity *in vivo* through direct adaptive evolution. To address this point, we started to improve the glucose assimilation of the engineered strain *P. putida* SG2 harboring the full lineal glycolytic route. As the previous initial growth rate of SG2 after the implementation of the GlucoBrick was 0.05 h^{-1}, we decided to evolve the strain in M9 minimal medium supplemented with 40 mM glucose as the only carbon and energy source. Two independent populations of the SG2 strain (i.e. population A and population B) were evolved in parallel batches under the strict selection pressure of continuous exponential growth on glucose (**Figure 7.1C** and **Figure S7.1**).

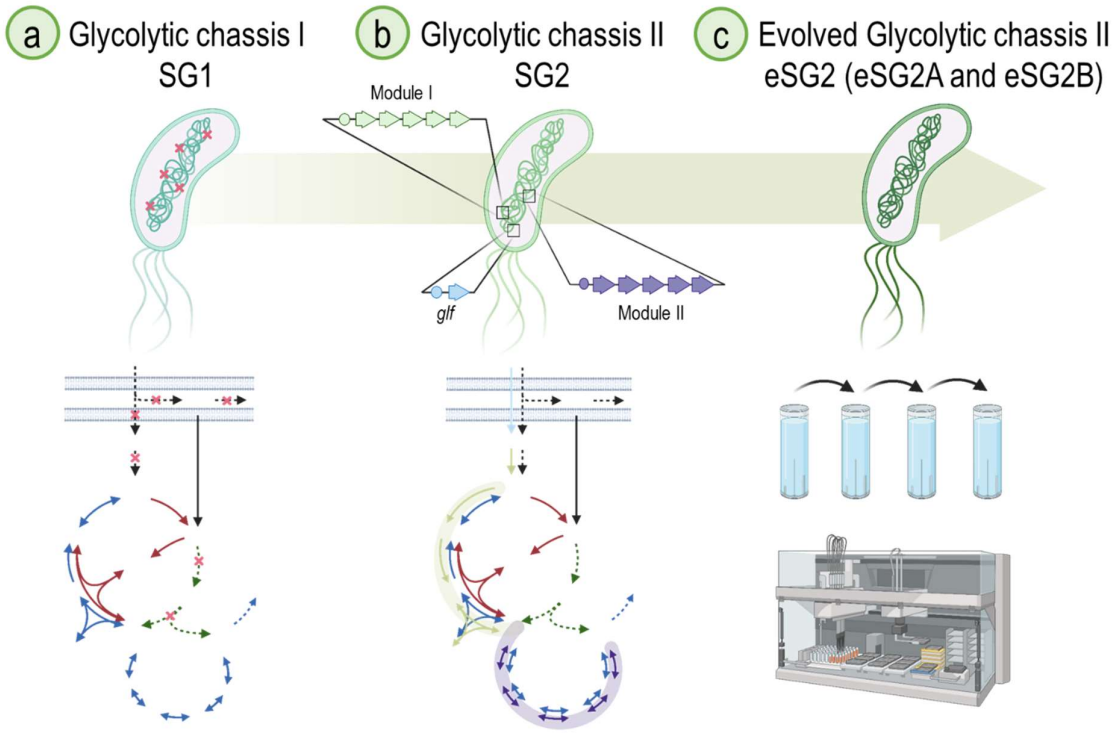

Figure 7.1. Construction of evolved grafted glycolytic chassis eSG2 used in this work. A. Glycolytic chassis 1–SG1– contains in-frame deletions of the genes Δ*glk*, Δ*gcd*, Δ*edd*, Δ*gad*, Δ*PP3382*, Δ*PP3383*, Δ*PP3384*, Δ*PP3623*, and Δ*PP4232* **B.** Glycolytic chassis 2–SG2–harbors Module I from the GlucoBrick system (i.e., genes encoding the enzymes needed for the conversion of glucose into glyceraldehyde-3-P: *glk* (b2388), *pgi* (b4025), *pfkA* (b3916), *fbaA* (b2925) and *tpiA* (b3919). Module II contains *gapA* (b1779), *pgk* (b2926), *gpmA* (b0755), *eno* (b2779), and *pykF* (b1676) and the glucose facilitator (*glf*) from *Zymomonas mobilis* as an alternative transport system. **C.** Evolved SG2 or eSG2 strain evolved in glucose implemented in this study.

The evolution experiments were conducted for about 80 days, or 42-46 passages, until there was no further increase in the specific growth rate in both evolutionary lineages (LaCroix, et al., 2015, Mohamed, et al., 2019). At the end of the experiment, populations A and B exhibited growth rates on glucose of 0.17 h^{-1} and 0.27 h^{-1}, respectively. This represents a 3.3-fold and 5.5-fold increase in relative fitness compared to the original strain SG2. The growth rate trajectories during the ALE experiments for both evolved populations are presented in Supplementary **Figure S7.1A** and **S7.1B**. Both replicate experiments resulted in approximately 9.50-9.60 x 10^{11} cumulative cell divisions (CCD). CCD is used as an alternative way to measure the

timescale of ALE, as it accounts for variability during the passaging process (Lee, et al., 2011). Although both evolved populations demonstrated an enhancement in fitness, there were notable disparities in terms of their fitness relative to the initial strain and the dynamics of the ALE process. These discrepancies could potentially be attributed to distinct mutations that were responsible for the observed improvement in glucose growth. Samples from both final populations, eSG2A and eSG2B, were collected and stored in 25% (v v^{-1}) glycerol stocks at -80°C for later whole-genome sequencing (WGS) analysis.

7.2.2 Screening of evolved clones in 96-well microtiter plates and physiological candidates characterization in shaken-flask cultivations.

Individual clones from the two endpoint populations, eSG2A and eSG2B, were isolated on M9 agar minimal medium supplemented with 40 mM glucose. Specifically, five clones designated as eSG2 clones 1-5 from population A, and five clones designated as eSG2 clones 6-10 from population B, were chosen for the purpose of examining their specific growth rate. This analysis was performed on M9 minimal medium, which was supplemented with 40 mM glucose, and the growth evaluation was carried out using 96-well microtiter plates. The wild-type strain KT2440 and non-evolved parental strain SG2 were used as controls. Specific growth rates ranged between 0.13-0.15 h^{-1} for the clones selected in population A and 0.18-0.33 h^{-1} for population B, representing a 2.0 to 5.0-fold increase in comparison to the non-evolved SG2 (**Figure 7.2A**). These results were comparable to those obtained from the populations that underwent evolution on glucose. Also, the growth curves indicated that the clones derived from population A had a shorter or absent lag phase, but a slower growth rate than the clones originally from population B (**Figure 7.2B** and **7.2C**). Between the two populations, clones $eSG2A^{3}$ (Clone 3) and $eSG2B^{9}$ (Clone 9) presented the highest growth rates and were selected for further physiological characterization in shaken flasks. Thus, the use of the ALE strategy showcases that through extended periods of evolution, microorganisms can adapt to particular

conditions and consequently achieve an improvement in fitness (Long and Antoniewicz, 2018).

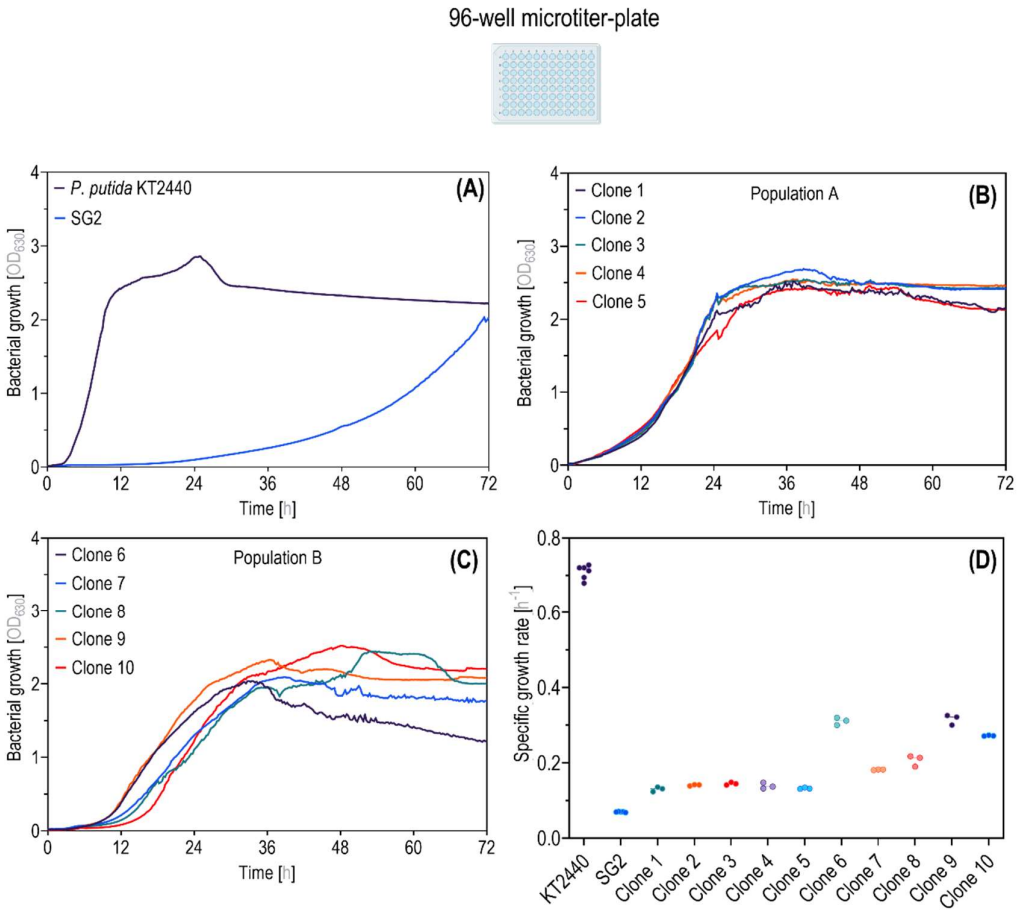

Figure 7.2. Evaluation of selected populations and its respective clones in 96 well microtiter plate. Growth profiles at OD_{630} of **(A)** *Pseudomonas putida* KT2440 and SG2, **(B)** clones obtained from population A and **(C)** clones obtained from population B. **(D)** Specific growth rate of *Pseudomonas putida* KT2440, SG2 and ten evolved clones from population A and B. Lines correspond to the average of six biological replicates in the case of KT2440, five biological replicates for SG2 and three biological replicates. The strains were cultivated at 30°C in M9 minimal medium containing 40 mM glucose as sole carbon source.

To better characterize growth on glucose, we performed growth experiments in shaken flasks and subsequently analyzed the metabolites consumed and secreted in the supernatant. Again, wild-type *Pseudomonas putida* KT2440 strain was used as reference. After estimating the physiological parameters, we found that both specific growth and uptake rates were considerably enhanced (0.24 h^{-1} and 3.18 mmol glucose

g_{CDW}^{-1} h^{-1} and 0.28 h^{-1} and 2.57 mmol glucose g_{CDW}^{-1} h^{-1} for eSG2A^{3} and eSG2B^{9}, respectively) by 5.0-fold for both clones in comparison with SG2 strain (0.056 h^{-1} and 0.59 mmol glucose g_{CDW}^{-1} h^{-1}) (**Table 7.1**). Beneficial mutations gathered during the adaption on glucose probably explain the increase in growth performance and glucose assimilation (Mohamed, et al., 2020). The observed biomass yields in both evolved clones eSG2A^{3} and eSG2B^{9} were almost identical to the one obtained in KT2440, but the SG2 strain showed a higher yield.

Again, these results—growth and glucose uptake rate—are consistent with the previous data obtained after the evolution and in 96-well microtiter plate. In addition, growth curves reflected the data calculated in **Table 7.1** where lag phases were significantly shorter in eSG2A^{3} and eSG2B^{9} than SG2, 12 and 36 hours, respectively. Along the same line, glucose consumption was faster in the two evolved clones in comparison to the parental strain. However, while the final optical density was greater in cultures of strain SG2 than in the evolved clones, lactate was unexpectedly detected at later stages, leading to a loss of carbon that could have potentially been used for biomass production (**Figure 7.3B, 7.3C** and **7.3D**). Finally, as part of the sequential glucose oxidation in *P. putida* KT2440, gluconate and subsequently 2-KGA were observed in the supernatant. Both of these organic acids can be retaken and used as a carbon source by the bacterium (**Figure 7.3A**). For the evolved clones, the two organic acids were not detected due to the fact the peripheral reactions were previously removed when building the SG2 strain.

Table 7.1. Determination of physiological parameters of *Pseudomonas putida* KT2440, SG2 and the two selected evolved clones eSGSA and eSG2B. Specific growth rates (μ), glucose uptake rates (q_S) and biomass yield ($Y_{X/S}$) were estimated from experiment carried out in **Figure 3**. The values represent the average of three biological replicates ± standard deviation. g_{CDW}, grams of cell dry weight.

Pseudomonas putida	Specific growth rate μ [h^{-1}]	Glucose uptake rate q_S [mmol glucose $gCDW^{-1}$ h^{-1}]	Biomass yield $Y_{X/S}$ [g glucose g CDW^{-1}]
KT2440	0.75 ± 0.02	8.51 ± 0.41	0.44 ± 0.01
SG2	0.06 ± 0.01	0.59 ± 0.01	0.56 ± 0.03
eSG2A	0.24 ± 0.01	3.18 ± 0.17	0.46 ± 0.01
eSG2B	0.28 ± 0.06	2.57 ± 0.19	0.46 ± 0.03

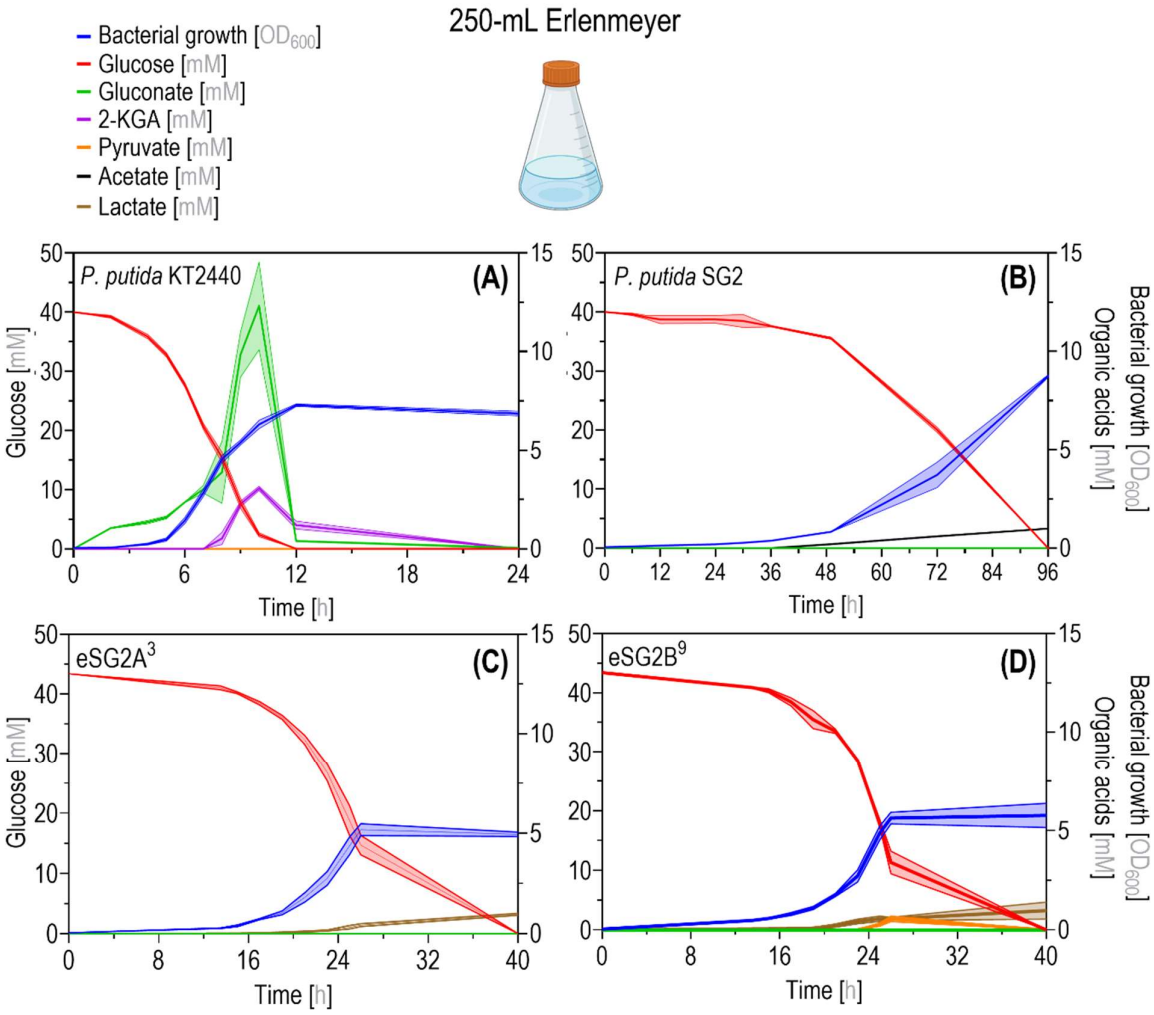

Figure 7.3. Physiological characterization of evolved strain shows improvement of specific growth and glucose consumption rates on glucose. (A) *P. putida* KT2440 as control condition. **(B)** SG2 strain. **(C)** eSG2A and **(D)** eSG2B. Experiments were conducted using M9 minimal medium containing 40 mM glucose. Solid lines represent the average and shaded areas correspond to the standard deviation of three biological replicates. Consumption or secretion of different metabolites were measured by HPLC and plotted using colored lines: glucose (red), gluconate (green), 2-KGA (purple), orange (pyruvate), black (acetate) and brown (lactate). Bacterial growth is represented by the blue line.

7.2.3 Whole genome sequencing and mutation analysis

In order to proceed with the analysis of the two strains, we analyzed the genetic modifications of the enhanced final phenotype on glucose minimal medium. This was achieved through whole genome sequencing (WGS) that enables the identification of

genetic mutations and variations in the entire genome of the strains under study (Giani, et al., 2020). The two isolated clones eSG2A^{3} and eSG2B^{9} were sequenced along with the corresponding endpoint populations from which they were isolated (i.e. eSG2A and eSG2B, respectively). The full list of mutations identified in both fast-growing clones is shown in **Table 7.2**. To determine the specific mutations that contributed to the improved fitness, the genome sequence of every individual clone was compared to the genome sequence of its corresponding population. By examining the open reading frames and intragenic regions, we were able to identify mutations that were present in multiple individuals and likely played a role in enhancing their fitness. Interestingly, no shared key mutations were found between the two replicate evolution experiments. The most relevant key mutations of the two evolved clones are described below.

In the clone eSG2A^{3}, a point mutation was detected in the *topA* gene (*PP2139*), specifically the mutation A299P (GCC→CCC), hereafter referred to as Top^{A299P}, which was also present in the endpoint population eSG2A (**Table 7.2**). The *topA* gene encodes a DNA topoisomerase I protein that prevents hyper-negative supercoiling of DNA during transcription and, together with the antagonistic activity of DNA gyrases, directly controls the level of DNA supercoiling (Vos, et al., 2011, Dorman and Dorman, 2016, Ferrándiz, et al., 2016). The topological changes in DNA (i.e. DNA supercoiling) have been shown to be a fundamental regulatory principle in the control of bacterial gene expression, allowing bacteria to adapt to environmental changes and competition from neighboring microorganisms. Interestingly, mutations in *E. coli topA* gene have been observed to provide a substantial improvement in fitness and thus a selective growth advantage (Crozat, et al., 2005, Crozat, et al., 2010, Deatherage and Barrick, 2021). Several point mutations described in the *topA* gene have also shown to affect global gene expression (and thus, metabolism) in many bacteria and eukaryotic organisms (Hatfield and Benham, 2002, Durand-Dubief, et al., 2010, Yan, et al., 2019). To provide an example, a mutated form of topoisomerase I led to widespread modifications in the pattern of gene expression in a particular strain of *B. subtilis*.

These changes included an increase in the activity of glycolytic genes and a decline in the activity of gluconeogenic genes (Reuß, et al., 2018). The A299 amino acid residue found in the TopA protein of *P. putida* seems to be a conserved component among the TopA proteins of various bacterial species (*S. coelicolor*, *E. coli* and *P. aeruginosa*) (**Figure 7.4**). Therefore, the A299P mutation could be altering the enzymatic activity of TopA and affecting global gene expression in the clone eSG2A^{3} because of changes in the DNA topology, which could ultimately lead to the observed increase in fitness in glucose cultures. TopA appears to be essential for cell viability in several bacteria, including *P. aeruginosa*, so it is unlikely that the Top^{A299P} variants encode a fully inactive topoisomerase protein in *P. putida* (Sandhaus, et al., 2018, Leela, et al., 2021). Alternative functional roles of the TopA protein in *P. putida* should also be considered. For example, specific point mutations in the *topA* gene of *E. coli* lead to the emergence of mutator phenotypes, characterized by a distinct pattern of mutations that is notably enriched with deletions and tandem duplications (Bachar, et al., 2020). Another study showed that the TopA protein interacts with the RNA polymerase in *B. subtilis*, and therefore, can directly affect its activity and promoter preference (Delumeau, et al., 2011).

Figure 7.4. Protein sequence alignment of the internal region of TopA proteins from different bacteria. Protein identity percentages of the different TopA proteins and the TopA protein from *Pseudomonas putida* KT2440 are indicated in parenthesis. Protein sequences (UniProt database): *Streptomyces coelicolor* A3(2) (Q9X909), *Escherichia coli* K-12 (P06612), *Pseudomonas putida* KT2440 (Q88KZ9) and *Pseudomonas aeruginosa* PAO1 (Q9HZJ5). Number on the left and right correspond to the aminoacids coordinates in the sequence.

In the clone eSG2B^{9}, we identified a point mutation in the heterologous *pykF* gene (GlucoBrick II), the mutation H43L (CAC→CTC), which was also present in the endpoint population eSG2B (**Table 7.2**). The *pykF* gene encoding the pyruvate kinase

I of *Escherichia coli* catalyzes the formation of pyruvate in the last irreversible enzymatic step of glycolysis, a critical reaction for the control of metabolic flux in the second part of glycolysis towards TCA cycle (Mattevi, et al., 1995). Several mutations in the *pykF* gene have been shown to provide a substantial improvement in fitness of *Escherichia coli* during long-term evolution experiments, including mutations that completely abrogate the PykF function (Peng, et al., 2018, Deatherage and Barrick, 2021). Earlier ALE experiments aimed at enhancing growth rate in minimal media have detected mutations in *pykF* or adjacent intergenic regions (LaCroix, et al., 2015). These mutations have been found to cause a reduction in the expression of PykF (Sandberg, et al., 2014).

Additionally, some studies have revealed that deleting *pykF* results in a downregulation of glycolysis and an upregulation of the pentose phosphate pathway (Al Zaid Siddiquee, et al., 2004, Siddiquee, et al., 2004). We also found a second point mutation in the *oxyR* gene (*PP5309*) in the clone eSG2B^{9}, the mutation F106I (TTC→ATC). The *oxyR* gene encodes a peroxide-sensing transcriptional regulator that has been found previously mutated in populations of *Pseudomonas putida* grown on glucose during ALE experiments (Mohamed, et al., 2020). Other mutations in *oxyR* gene has also been identified in laboratory evolution experiments with other bacterial species and might be associated with a reduction of DNA damage from reactive oxygen species (Anand, et al., 2020).

Table 7.2. Most relevant mutations found in the ALE-evolved clones isolated for further physiological characterization studies. The presence or absence of the identified mutations in the whole populations is also represented by percentage of frequencies in re-sequencing reads. Abbreviation: SNP, single-nucleotide polymorphism; INS, insertion; DEL, deletion.

Position*	Mutation	Gene	Product	Details	Population A		Population B	
					Population	Clone eSG2A	Population	Clone eSG2B
2,440,892	SNP (G→C)	*topA (PP_2139)*	DNA topoisomerase I	A299P (GCC→CCC)	1	1		
3,442,664	SNP (T→G)	*PP_3062*	Phage tail tape measure protein	F763C (TTT→TGT)		1		
4,636,691	SNP (G→T)	*gcvA (PP_4107)*	GcvA family transcriptional regulator	S213I (AGC→ATC)		1		
4,735,298	INS (+T)	*PP_4194, PP_4195*	-	Intergenic (+535/+217)		1		
5,329,883	SNP (G→C)	*PP_4696*	Sigma-54-dependent Fis family transcriptional regulator	G183R (GGC→CGC)		1		
945,036	SNP (T→A)	*pykF**	Pyruvate kinase I (*E. coli*)	H43L (CAC→CTC)			0.6	1
2,836,198	DEL (Δ24 pb)	*PP_2488, PP_2489*	-	Intergenic (-14/+167)				1
3,775,508	SNP (T→G)	*PP_3338, PP_3339*	-	Intergenic (+54/-87)				1
4,430,964	INS (+T)	*PP_3931, PP_3932*	-	Intergenic (+262/-89)				1
4,735,122	SNP (C→T)	*PP_4194, PP_4195*	-	Intergenic (+360/+393)				1
5,674,195	INS (+GGGGC)	*PP_4986, PP_4987*	-	Intergenic (-132/+70)				1
6,055,711	SNP (T→A)	*oxyR (PP_5309)*	Hydrogen peroxide-sensing transcriptional regulator	F106I (TTC→ATC)				1

7.2.4 Metabolic flux analysis reveals higher flux through the EMP route on evolved strains eSG2A^{3} and eSG2A^{9}

In order to gain an understanding about the *in vivo* absolute metabolic fluxes distribution of the refactoring and evolved *P. putida* strains on glucose, we conducted a ^{13}C fluxome analysis. This analysis involved examining the distribution of mass isotopomer in both proteinogenic amino acids and cell carbohydrates (glycogen and glucosamine), using three different tracers as outlined in the Materials and Methods section. The calculated relative fluxes for SG2, eSG2A^{3}, eSG2B^{9} and KT2440 (as control) strains cultured on labeled glucose are visualized in **Figure 7.5** and the absolute values ± standard deviation as well as upper and lower bound are detailed in **Table S7.3**. As the modified strains do not contain the peripheral and ED reactions, the fluxes into gluconate and KDPG were set up to zero. We employed this experimental approach to gain insights into the extent to which the *chassis* could tolerate manipulation with respect to redirecting its central carbon metabolism. Under this condition, glucose was fully processed via the glucokinase enzyme (Glk), resulting in the formation of G6P. At this node, the flux was divided into F6P and 6PG in a strain-specific manner.

Our findings indicate that adapted strains eSG2A^{3} and eSG2B^{9} displayed a significant increase in the flux through F6P, with percentages of 88.5% and 86.3%, respectively, compared to SG2 (68.3%). Relative fluxes through PPP were 3 times higher in the parental strain than the evolved strains. Also, SG2 redirected 30% of the G6P absolute flux into 6PG and Ri5P, while the evolved strains redirected only 10%. Regarding EMP, fluxes through PfkA until Eno were practically identical in all the strains. In the EMP pathway, the final step relies deeply on the pyruvate kinase (PykF), which is a critical allosteric enzyme. PykF is responsible for carrying out one of the two substrate-level phosphorylation reactions that produce ATP, making it a crucial mediator of an important metabolic step in *P. putida* (Emmerling, et al., 2002, Zhao, et al., 2017). We found a partial re-routing of the metabolic flux from PEP to pyruvate (63% for SG2 and 110-120% for the evolved strains) into PEP to OAA (100% for SG2 and 50-60% for the evolved strains). Furthermore, in *E. coli* and *P. putida*, glucose is directed towards the production of PEP and pyruvate, and later to Acetyl-CoA, which serve as the main precursor for TCA cycle. The primary roles of this central pathway are to produce

precursor metabolites for biosynthesis, as well as NAD(P)H for biosynthesis and NADH for energy production (Puchałka, et al., 2008).

When analyzing the carbon fluxes in the TCA cycle, it was discovered that a significant redirection of the metabolic flux occurred at the level of the isocitrate node. In this scenario, the TCA cycle enzyme isocitrate dehydrogenase encoded by *icd* (*PP4011*), and the glyoxylate shunt enzyme isocitrate lyase (Icl) encoded by *aceA* (*PP4116*), both strive to utilize the available isocitrate. Icd has a much lower affinity for isocitrate [Km = 8 μm] (LaPorte, et al., 1984) than ICL [Km = 604 μm] (Crousilles, et al., 2018). Hence, to achieve a substantial flux through the glyoxylate shunt, Icd should be deactivated which seems to be the case for the evolved strains. The evolved strains displayed a much larger flux through the glyoxylate shunt at this point, with a relative flux of 60% and 40% for eSG2A^{3} and eSG2B^{9}, respectively, compared to just 15% in the SG2 strain. Idh can be either enhanced or inhibited by elevated or reduced levels of OAA. The division of flux at the intersection between the TCA cycle and the glyoxylate shunt could also impact the delivery of NAD(P)H to the cell, prompting the activation of compensatory mechanisms.

Ultimately, there was no observable flux toward pyruvate from malate produced via the TCA cycle through the operation of malic enzyme, contributing to the so-called *pyruvate shunt*. The pyruvate shunt, a loop of reactions that transforms malate → pyruvate → oxaloacetate → malate, produces NAD(P)H for anabolism, but consumes 1 ATP equivalent in the process. Consequently, this pathway has the potential to serve as an additional source of NAD(P)H. In general, the strains examined here appear to feature a robust utilization of the EMP pathway as well as an active TCA cycle and glyoxylate shunt in these glucose conditions.

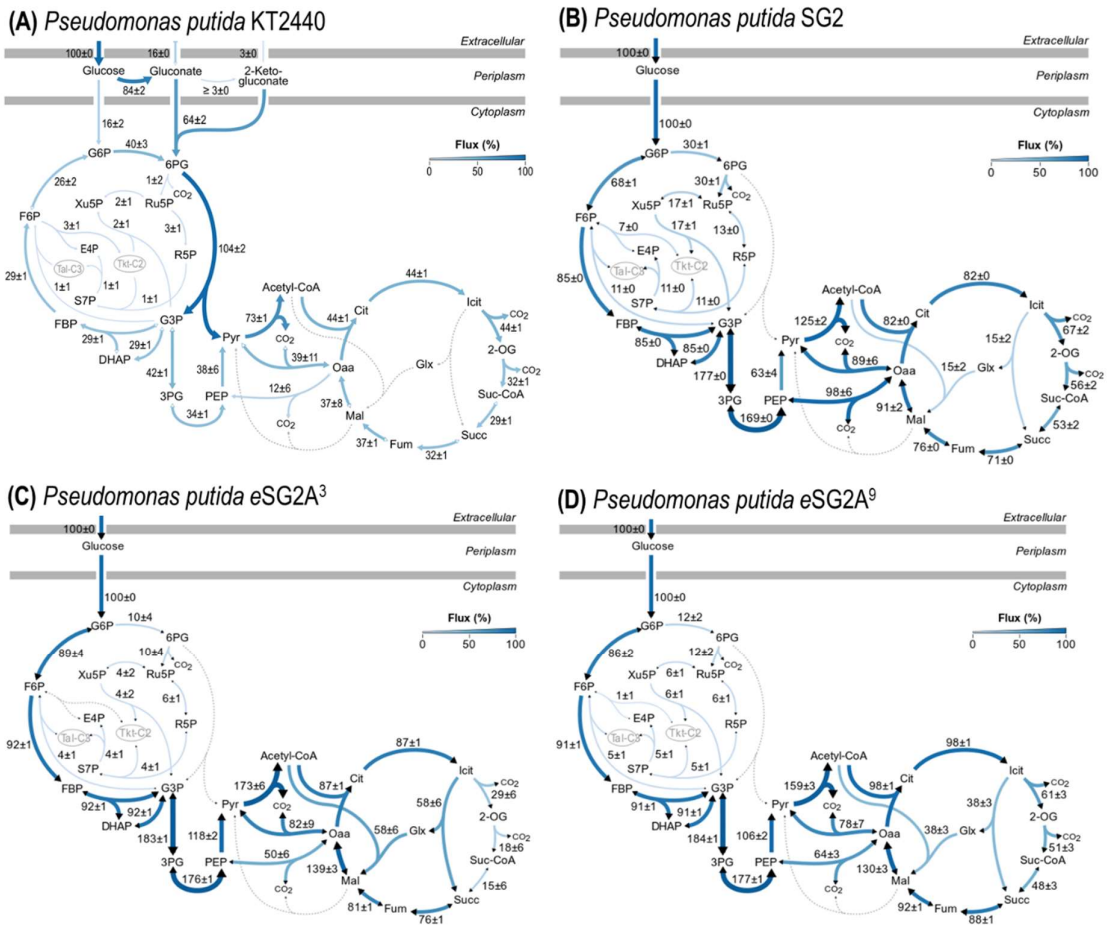

Figure 7.5. Intracellular carbon fluxes of glucose-grown *P. putida* KT2440 **(A)**, SG2 **(B)**, eSG2A[3] **(C)** and eSG2[9] **(D)** as determined by ^{13}C metabolic flux analysis. All fluxes are given as a molar percentage of the mean specific glucose uptake rate of qs^{KT2440}=8.51 mmol g_{CDW}^{-1} h^{-1}, qs^{SG2}= 0.591 mmol g_{CDW}^{-1} h^{-1}, qs^{eSG2A3}= 3.178 mmol g_{CDW}^{-1} h^{-1} and qs^{eSG2A9}= 2.572 mmol g_{CDW}^{-1} h^{-1} which was set to 100%.

7.2.5 Reverse engineering of Top^{A299P} into refactoring SG2 enhances growth on glucose

As it was previously stated, the mutation in topoisomerase I leads to significant rearrangements at systems level (e.g. central carbon metabolism) due to its vital role in regulating the DNA topology and replication. The interconnection between the metabolic state of a cell and crucial processes such as DNA replication, initiation, and elongation is of utmost importance. This implies a critical relationship between these

events and the overall process of cellular duplication (Jannière, et al., 2007). With this background, we hypothesized that the mutation in Top^{A299P} can improve the SG2 phenotype as shown in the evolved strain eSG2A^{3}. Supported by physiological data, we decided to reverse engineer SG2 with the point mutation Top^{A299P} to evaluate the effect at growth level. A growth assessment was conducted using a 96-well microtiter plate to compare the growth in the engineered SG2, the evolved clone eSG2A^{3}, and the single mutant SG2 Top^{A299P}. The results showed that the point mutation in the SG2 Top^{A299P} mutant had a significant impact on glucose growth, increasing the specific growth rate by 50%. Specifically, the growth rate improved from 0.063 h^{-1} in the case of SG2 to 0.094 h^{-1} for the single mutant. These findings raised the question of whether this specific mutation in the topoisomerase I could potentially influence other aspects of cellular metabolism and what kind of effects it may have at proteome level.

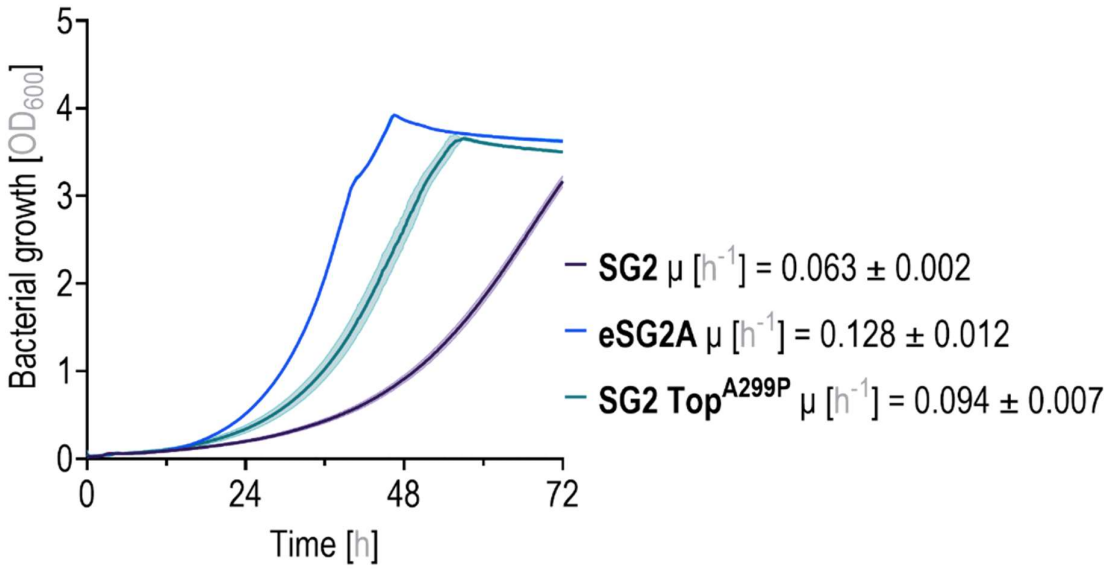

Figure 7.6. Assessing growth of reverse engineered strain SG2. Cultivation of the different strains on glucose as a sole carbon source within a 96-well plate. Plate reader experiments were performed in triplicates, average is shown with solid lines and standard deviation is pointed with shaded area around the main line. Values OD_{600} were previously converted from OD_{630} by using the corresponding calibration curve.

7.2.6 Network-wide proteome analysis exposed protein redistribution across EMP as a strategy to optimize enzyme levels

Building upon our previous findings, we decided to further explored system level variations causes by Top^{A299P} mutation. First, we analyzed the proteome changes on *Pseudomonas putida* SG2, $eSG2A^{3}$, Top^{A299P} and *P. putida* KT2440 as control condition. The strains were cultivated in the presence of 40 mM glucose and harvested in mid-log phase (corresponding to OD_{600} ~1.0). Then, a network-wide absolute quantification proteomics analysis was carried out focusing the analysis on central carbon metabolism enzymes.

We observed an upregulation of the enzyme PfkA and TpiA associated with the initial segment or *preparatory phase* of the EMP pathway (specifically, from G6P to G3P) in both the evolved strain and the single mutant when compared to SG2. Initially, we investigated the *E. coli* proteins that were plugged in as part of the glycolytic module (corresponding to the EMP pathway). We found that the abundance of proteins involved in this pathway changed significantly along the metabolic pathway from glucose toward pyruvate. No significant differences were observed in Glk and Pgi-1. Despite confirming the deletion of the native Glk and Pgi-1 genes, there was still presence of residual protein levels in the crude extract at very low levels, which could potentially be due to technical issues with the detection.

Significantly, the protein levels of the enzyme PfkA were notably elevated, demonstrating an increase ranging from 7- to 4-fold for $eSG2^{3}$ and Top^{A299P}, respectively. These levels approached those observed for the Fbp in the native and control wild-type strain KT2440 (**Figure 7.7**). Regarding the TpiA protein, it is noteworthy that Top^{A299P} exhibited a higher protein content compared to SG2 and the evolved strain, $eSG2^{3}$. Contrarily, by analysing the route from G3P to pyruvate, there was a downregulation of GapA, Pgk, GpmA, Eno and PykF ranging from 2- to 5-fold in the evolved and single mutant strains compared to SG2. Furthermore, the presence of the Top^{A299P} mutation showed a strong correlation with the protein levels observed in the $eSG2A^{3}$ strains during the *pay-off phase*. This indicates that the mutation could potentially be affecting the transcription of the genes involved in the pathway and, consequently, the protein levels. Additionally, the quantity of protein generated

during the *pay-off phase* was significantly greater in the SG2 strain than in the evolved and single mutant strains, estimated to be in the range of several hundred femtomoles per ug of crude extract. Conversely, the rise in protein levels during the initial stage was not as substantial as in the *pay-off phase* (**Figure 7.7**).

In connection to this, various bacterial growth models have proposed that protein synthesis can act as a limiting factor for growth under certain conditions (Molenaar, et al., 2009, Scott, et al., 2010). The results obtained in this section may suggest that heightened protein expression in the SG2 strain could have negative effects on growth by increasing misfolding and causing toxic promiscuous activity (Eames and Kortemme, 2012). Since glycolytic enzymes make up a significant portion of microbial proteomes, reducing their levels (e.g., by regulating gene expression) could enable cells to increase their growth rate. Consequently, the cellular growth and adaptation to the introduced glycolytic synthetic pathway are significantly influenced by the efficient allocation of resources, emphasizing its critical role (Peebo, et al., 2015).

On the other hand, the PP pathway exhibited a notable downregulation of ZwfA and Pgl (approaching negligible levels) in the evolved strains. In contrast, there was an upregulation observed in the Tal enzyme. These findings indicate that the evolved strains do not heavily rely on the PPP metabolic block, confirming earlier observations from the metabolic flux analysis experiment. However, the higher protein levels of Tal protein suggests that the cells aim to enhance the pool of G3P, thereby facilitating the progression towards the *pay-off phase*. In addition to the conducted analysis, Top^{A299P} does not appear to significantly impact the protein changes in the PP pathway, as the concentrations of proteins in the TopA mutant were found to be similar to those observed in SG2 and the control condition (**Figure S7.2**). This indicates that the presence of a different mutation in the evolved strain, such as in the transcriptional regulator GcvA, can result protein level changes within the PP pathway (**Table 7.2**) (Leyn, et al., 2011).

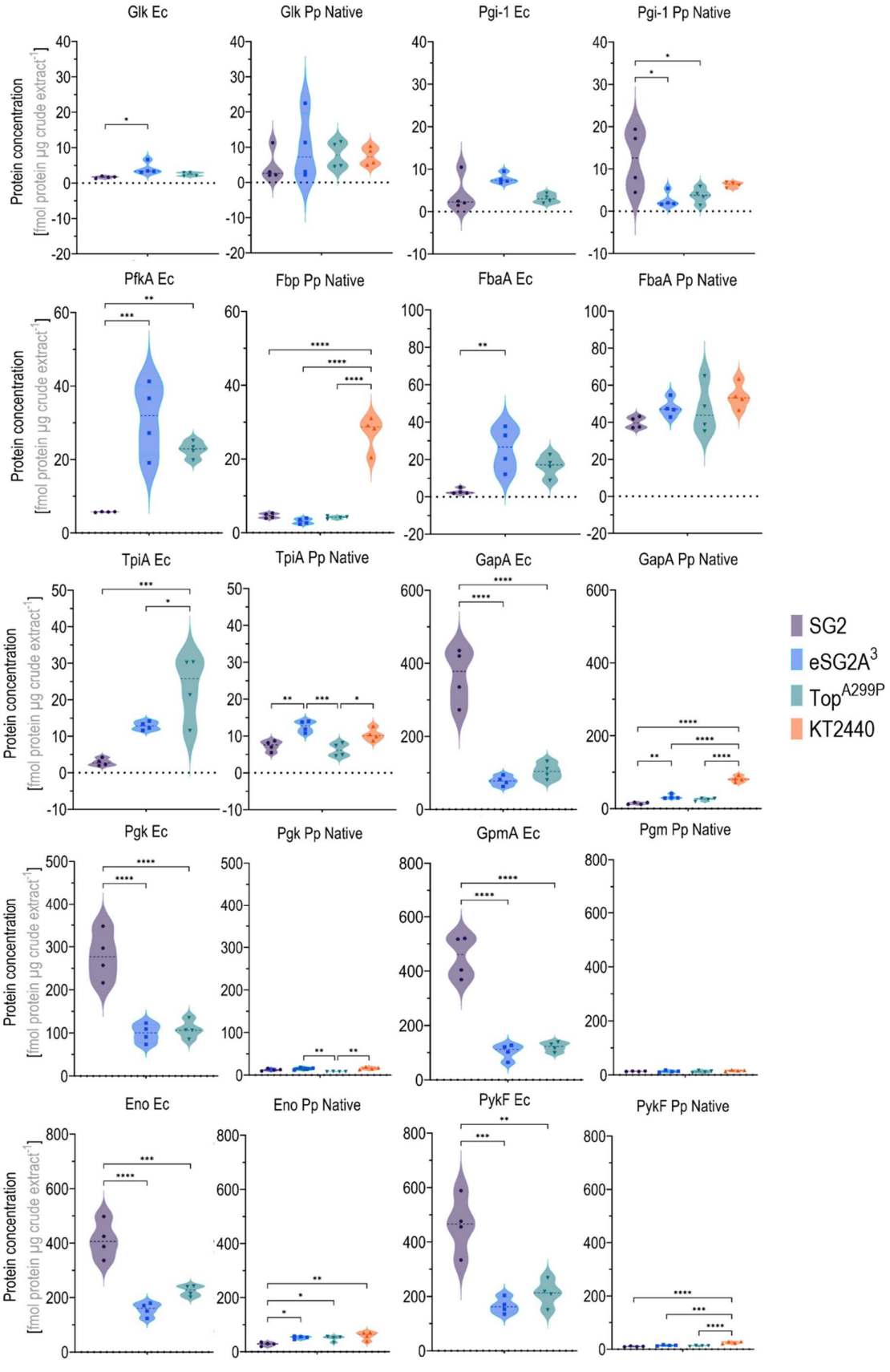
Glk Ec
Glk Pp Native
Pgi-1 Ec
Pgi-1 Pp Native
PfkA Ec
Fbp Pp Native
FbaA Ec
FbaA Pp Native
TpiA Ec
TpiA Pp Native
GapA Ec
GapA Pp Native
Pgk Ec
Pgk Pp Native
GpmA Ec
Pgm Pp Native
Eno Ec
Eno Pp Native
PykF Ec
PykF Pp Native
Protein concentration
[fmol protein µg crude extract-1]
SG2
eSG2A3
TopA299P
KT2440

Figure 7.7 Comparison in protein concentration within EMP of the different glycolytic strains SG2, eSG2A^{3}, Top^{A299P} and the control wild-type strain KT2440. The strains were grown in M9 minimal medium containing 40 mM glucose. Concentrations are given in fmol protein μg crude extract^{-1} from four biological replicates. One-way ANOVA was carried out to perform the statistical analysis. * $p<0.05$, **$p<0.01$, ***$p<0.001$ and *$p<0.0001$. Glk, glucokinase; Pgi-1, glucose-6-phosphate isomerase; PfkA, 6-phosphofructokinase I; FbaA, fructose 1,6-bisphosphate aldolase; TpiA, triosephosphate isomerase; GapA, glyceraldehyde 3-phosphate dehydrogenase; Pgk, phosphoglycerate kinase; GpmA, 2,3-bisphosphoglycerate-dependent phosphoglycerate mutase ; Eno, enolase; PykF, pyruvate kinase.

7.2.7 Quantitative proteomics detects proteome changes at the isocitrate node leading to flux reconfiguration through the glyoxylate shunt

The glyoxylate shunt is a non-reversible process that allows for the preservation of carbon skeletons necessary for gluconeogenesis and biomass production by circumventing the oxidative decarboxylation phases of the TCA cycle (Kornberg, 1966). In the 1980s, the mechanisms that govern the allocation of carbon flux between the TCA cycle and glyoxylate shunt were studied in *E. coli* (Maloy and Nunn, 1982). Here, the enzymes isocitrate dehydrogenase (Icd) from the TCA cycle and isocitrate lyase (AceA) from the glyoxylate shunt compete for the same pool of isocitrate. Icd has a lower affinity for isocitrate with a Km of 8 μm, while AceA has a higher Km of 604 μm (LaPorte, et al., 1984, Walsh and Koshland, 1984). Therefore, to achieve a substantial carbon flux through the glyoxylate shunt, Icd must be inactivated, which can be accomplished through reversible phosphorylation by the enzyme AceK. However, not all the bacteria follow the same enzymatic pathway at the branch point between the TCA cycle and the glyoxylate shunt, and may possess a secondary isozyme of isocitrate dehydrogenase that is not affected by AceK, as for example the AceK-insensitive isocitrate dehydrogenase isozyme (Idh) (Crousilles, et al., 2018).

In the case of environmental bacteria *P. putida* and human pathogen *P. aeruginosa*, there is an extra level of complexity. Three enzymes, namely Icd, Idh, and AceA (Icl), are in competition for isocitrate. Moreover, these bacteria harbor the Icd kinase/phosphatase, AceK, which exerts regulatory control over Icd by phosphorylation and subsequent inhibition of its enzymatic activity. To better understand the protein changes at the isocitrate node, and building upon our previous fluxomics data (**Figure 7.5**), we examined the protein concentrations of enzymes

involved in the TCA cycle (as illustrated in **Figure 7.8**). Our analysis revealed significant alterations in the levels of Icd, Idh, and AceA proteins during glucose growth. SG2 and Top^{A299P} were found to have an opposite relationship in comparison with the evolved strains eSG2A^{3}. Surprisingly, Top^{A299P} did not follow the same trend as the evolved strain suggesting that the mechanisms leading to this outcome do not operate through the isocitrate node. The protein level of Icd was higher in SG2/Top^{A299P}, reaching 100 fmol μg crude extract^{-1} in both cases. However, in eSG2A^{3}, there was a 50% decrease in Icd protein level. On the other hand, Idh and AceA exhibited a significant increase in protein levels (up to three times higher) in eSG2A^{3}, as compared to both the single mutant and SG2 strains. This observation could indicate that the evolved strain redirected the carbon flux through the glyoxylate shunt by regulating not only AceA but also GlcB. The latter was likewise found to follow a similar trend as for AceA. It appears that AceA-GlcB play a vital role in the growth and carbon preservation in the evolved strain (Crousilles, et al., 2018). This finding is consistent with previous studies suggesting that there is a considerable carbon flux through the glyoxylate shunt even when glucose is used as the primary source of energy (Dolan, et al., 2020).

Upon examining the remaining steps of the TCA cycle, we noted that SucA and SucDC maintained consistent levels among the three investigated strains and were present in lower concentrations compared to the control strain KT2440. We observed a unique pattern in the production of fumarase isozymes in the different strains. Fumarate hydratase (Fum) was produced in similar amounts in the evolved and single mutant strains while the SG2 strain presented lower concentrations than KT2440. FumC-I was overproduced in eSG2^{3} and almost completely absent in SG2 as well as in the control condition. Lastly, FumC-II concentrations were higher in SG2 (25 fmol μg crude extract^{-1} in average) than eSG2A^{3} and Top^{A299P}. While there is no currently information regarding a compensation system, it is possible that such isozyme system could help control the flux at this point in the TCA cycle. However, it should be noted that in *E. coli*, the actions of these isozymes have been linked to DNA damage (Silas, et al., 2021). Concerning the other proteins involved in the TCA cycle, we noticed a decrease in the levels of AceE and AceF proteins in the evolved, single mutant and KT2440 strains when compared to SG2. These proteins, namely the pyruvate dehydrogenase E1 and

acetyltransferase component of the pyruvate dehydrogenase complex, respectively, exhibited comparable behavior to the proteins in the *pay-off phase* (Jeyaseelan and Guest, 1980). In addition, we observed a significant increase in the levels of citrate synthase (GltA) in the evolved strain, as compared to SG2. This particular enzyme is responsible for catalyzing the condensation of oxaloacetate and acetyl-CoA to produce citrate, which is then utilized to fuel the TCA cycle (Gerike, et al., 1998). In the subsequent step, the conversion of citrate to isocitrate via cis-aconitate is mainly facilitated by the aconitase hydratase. AcnB is primarily responsible for carrying out this process. In the evolved strain and KT2440, the protein levels were three time higher than in SG2 and Top^{A299P}. Overall, we could

Regarding the anaplerotic reactions, we observed a higher protein concentration for the phosphoenolpyruvate carboxylate enzyme (Ppc) and malic enzyme (MaeB) in the evolved strain eSG2^{3} in comparison to SG2, Top^{A299P} and KT2440. Pyruvate carboxylase complex [PycB/AccC-2] exhibited lower concentrations in SG2, eSG2^{3} and Top^{A299P} in comparison to KT2440. These findings potentially indicate a level of adaptability in the anaplerotic reactions, which may be governed by the regulation at pyruvate shunt level (Lien, et al., 2015). Notably, despite the elevated abundance of the MaeB enzyme observed in the proteomics investigations, there exists no apparent association with the fluxomics data, which indicates negligible flux from malate to OAA. This observation could potentially indicates the occurrence of a post-translational modification (PTM), such as acetylation at one of the lysine residues, which could impede the catalytic activity of this essential enzyme in the anaplerotic reactions (Pisithkul, et al., 2015). Finally, further investigations are warranted to fully understand the implications of these observed changes.

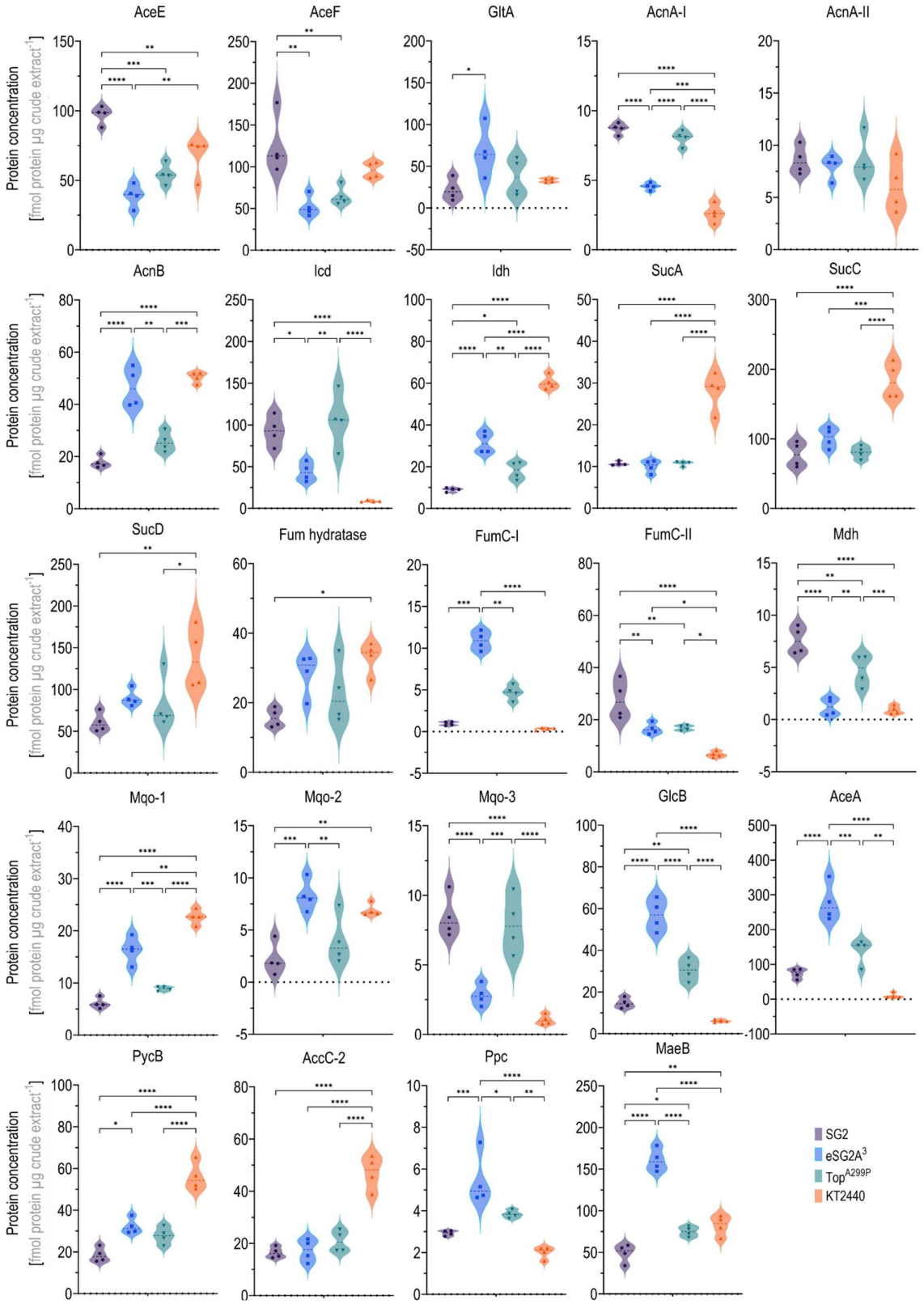
AceE
AceF
GltA
AcnA-I
AcnA-II
AcnB
Icd
Idh
SucA
SucC
SucD
Fum hydratase
FumC-I
FumC-II
Mdh
Mqo-1
Mqo-2
Mqo-3
GlcB
AceA
PycB
AccC-2
Ppc
MaeB
Protein concentration
[fmol protein µg crude extract-1]
SG2
eSG2A3
TopA299P
KT2440

Figure 7.8 Comparison in protein concentration within TCA cycle of the different glycolytic strains SG2, eSG2A^{3}, Top^{A299P} and the control strain KT2440. The strains were grown in M9 minimal medium containing 40 mM glucose. Concentrations are given in fmol protein μg crude extract-1 from four biological replicates. One-way ANOVA was carried out to perform the statistical analysis. * $p<0.05$, ** $p<0.01$, *** $p<0.001$ and * $p<0.0001$. AceF, Acetyltransferase component of pyruvate dehydrogenase complex; AceE, Pyruvate dehydrogenase E1 component; GltA, Citrate synthase; AcnA-I, Aconitate hydratase A I ; AcnA-II, Aconitate hydratase A II; AcnB, Aconitate hydratase B; Icd, Isocitrate dehydrogenase [NADP]; Idh, Isocitrate dehydrogenase [NADP]; SucA, Oxoglutarate dehydrogenase A; SucD, Succinate--CoA ligase [ADP-forming] subunit alpha; SucC, Succinate--CoA ligase [ADP-forming] subunit beta ; Fum, Fumarate hydratase class I; FumC-I, Fumarate hydratase class II; FumC-II, Fumarate hydratase class II; Mdh, Malate dehydrogenase; Mqo-1, Malate:quinone oxidoreductase 1; Mqo-2, Malate:quinone oxidoreductase 2; Mqo-3, Malate:quinone oxidoreductase 3; AceA, Isocitrase; GlcB, Malate synthase G.

7.3 Outlook

In this work, we aimed to investigate the consequences of incorporating a glycolytic graft derived from GlucoBrick I and II in *E. coli* into the chassis *P. putida*. The analysis focused on the system level to obtain a deeper understanding of how the integration of synthetic modules can potentially alter the metabolic identity of the microorganism. Although successful implantation of the glycolytic module was achieved, the activity and fluxes through the components were suboptimal, resulting in deficient growth on glucose. To address this, we conducted direct ALE experiments using M9 minimal medium supplemented with glucose as the sole carbon and energy source. SG2 strain was evolved under strict selection pressure for continuous exponential growth on glucose. Two evolved populations were obtained and from each population, the most promising candidate was chosen for subsequent physiological analysis (eSG2A^{3} and eSG2A^{9}). The results showed a significant improvement in fitness, with evolved populations exhibiting growth rates of 0.17-0.27 h^{-1}, representing a 3.3-fold to 5.5-fold increase compared to the original strain SG2.

To analyze the genetic modifications underlying the enhanced phenotypes of the two strains, whole genome sequencing (WGS) was performed on the isolated clones eSG2A^{3} and eSG2B^{9}, as well as their respective endpoint populations (eSG2A and eSG2B). In the clone eSG2A^{3}, a point mutation was detected in the *topA* gene (*PP2139*),

namely A299P (GCC→CCC), referred to as Top^{A299P}. Mutations in *topA* have been associated with improved fitness in other bacteria, affecting gene expression and metabolic pathways. In the clone eSG2B^{9}, a point mutation was identified in the heterologous *pykF* gene (GlucoBrick II), resulting in H43L (CAC→CTC). PykF is involved in the final step of glycolysis and mutations in this gene have been observed to enhance fitness in *E. coli*. A second point mutation was found in the *oxyR* gene (PP5309), F106I (TTC→ATC), which encodes a peroxide-sensing transcriptional regulator. It has been previously detected in *P. putida* populations grown on glucose during evolution experiments, potentially associated with DNA damage reduction causes by reactive oxygen species (ROS) (Anand, et al., 2020, Mohamed, et al., 2020). Further studies are needed to elucidate the regulatory mechanisms and functional roles of these mutations in *P. putida*'s improved phenotypes.

The *in vivo* metabolic flux distribution in *P. putida* strains revealed significant changes. Specifically, the evolved strains eSG2A^{3} and eSG2B^{9} exhibited a substantial increase in the flux through F6P compared to the original strain SG2. Along the same line, there was a decrease in the relative fluxes through the PP pathway in the evolved strains compared to SG2. Flux redirection from G6P to 6PG and Ri5P was reduced in the evolved strains compared to SG2. Also, fluxes through the EMP pathway were similar among all strains. The metabolic flux from PEP to pyruvate was partially rerouted toward OAA in the evolved strains. Notably, the TCA cycle flux was redirected at the isocitrate node, favoring the glyoxylate shunt in the evolved strains. Both evolved strains exhibited a larger flux through the glyoxylate shunt. Overall, the examined strains demonstrated robust utilization of the EMP pathway, an active TCA cycle, and glyoxylate shunt under glucose conditions.

At proteome level, *P. putida* strains were analyzed, focusing on enzymes related to central carbon metabolism. The initial segment of the EMP pathway showed upregulation of enzymes in both the evolved and single mutant strains compared to SG2. However, there were no significant differences in Glk and Pgi-1 proteins except

for a slight upregulation in Glk for the evolved strain. PfkA protein levels increased similar to the control strain, while FbaA levels were comparable among all strains. Downregulation of GapA, Pgk, GpmA, Eno, and PykF was observed from G3P to pyruvate in the evolved and single mutant strains. In general, the protein levels of the Top^{A299P} strain correlated with $eSG2A^{3}$ in the *preparative* and *pay-off phase* of the glycolysis. Protein synthesis, particularly of glycolytic enzymes, can influence growth, and resource allocation, which are crucial for cellular growth and adaptation. The evolved strains exhibited downregulation of ZwfA and Pgl in the PP pathway, indicating reduced reliance on this metabolic block, while Tal enzyme levels were upregulated to potentially enhance the G3P pool.

Regarding protein changes at the isocitrate and glyoxylate levels, we observed significant alterations in the protein levels of enzymes involved in these metabolic pathways. Notably, Icd protein levels were higher in SG2 and Top^{A299P}, while $eSG2A^{3}$ exhibited a decrease. On the other hand, Idh and AceA proteins had significantly increased levels in $eSG2A^{3}$ compared to the other strains. This suggests a redirection of carbon flux through the glyoxylate shunt in the evolved strain. The TCA cycle enzymes SucA and SucDC maintained consistent levels, while fumarase isozymes exhibited varying concentrations among the strains. The levels of AceE and AceF proteins decreased in the evolved strain, and GltA protein levels were significantly higher. Additionally, anaplerotic reactions showed differences in MaeB and Ppc protein concentrations, indicating potential adaptability in these pathways. Further investigations are needed to fully understand the implications of these observed changes.

7.4 Materials and Methods

7.4.1 Culture conditions

Pseudomonas putida cultures were incubated at 30°C. For physiological experiments, bacterial cells were grown in a rotatory shaker at 200 rpm. in 250-ml Erlenmeyer flasks filled with 50 ml of M9 minimal medium, containing 6 g l^{-1} Na_2HPO_4, 3 g l^{-1} KH_2PO_4, 1.4 g l^{-1} $(NH_4)_2SO_4$, 0.5 g l^{-1} NaCl, 0.2 g l^{-1} $MgSO_4 \cdot 7H_2O$, and 2.5 ml l^{-1} of a trace elements solution (Nikel and de Lorenzo, 2013). Unless otherwise indicated, minimal medium cultures were added with glucose at 40 mM.

7.4.2 Bacterial transformation

Electrocompetent *P. putida* cells were obtained by subsequent washings at room temperature with 300 mM sucrose (Choi, et al., 2006). For all strains, when appropriate, the electroporation was performed in a Gene Pulser/Pulse Controller (Bio-Rad) system configured as follows: 2.5 kV, 25 μF, 200 W.

7.4.3 DNA manipulation and sequencing

DNA manipulations were carried out following routine laboratory techniques (Green and Sambrook, 2012). Plasmid DNA purification was accomplished with the QIAprep Spin Miniprep kit (Qiagen Inc., Valencia, CA, USA) according to the manufacturer's instructions. Restriction and DNA modification enzymes employed in this study were purchased from New England Biolabs (Ipswich, MA, USA). Isolate colonies from fresh LB plates were the starting material for colony polymerase chain reaction (PCR) amplification in order to check the presence of plasmid or gene deletions/insertion. PCR products were purified with the NucleoSpin Extract II kit (Macherey-Nagel, Düren, Germany). Agarose gel visualization was possible with the use of VersaDoc™ apparatus (Bio-Rad Corp., Hercules, CA, USA). Sanger sequencing (Secugen SL, Madrid, Spain) was used in order to check the accuracy of all the DNA constructs.

7.4.4 Design of oligonucleotides

Oligonucleotides employed in PCR reactions were designed from the DNA sequence of interest using the software DNASTAR Lasergene Suite v14 (DNASTAR, Inc. Madison, WI, USA). The oligonucleotides used in this study were obtained from Sigma-Aldrich Co. (St. Louis, MO, USA).

7.4.5 Construction of *Pseudomonas putida* Top^{A299P} mutant strains

Plasmid pGNW2·*topA*::A299P was constructed using uracil-excision (USER) cloning by amplifying the 1,000 bp upstream and downstream of the *topA*::A299P mutation with Phusion U Hot StartTM DNA polymerase (ThermoFisher Scientific Co., Waltham, MA, USA) according to the manufacturer's recommendations using uracil-containing primers. Plasmid pGNW2 was further digested with *DpnI* prior to mixing 1 μL of *DpnI*-treated plasmid with 100 ng of each PCR fragment and 1 μL of USERTM enzyme (New England BioLabs, Ipswich, MA, USA) in a final volume of 10 μL. The reaction was incubated for 30 min at 37°C, followed by a temperature decrease during 3 min (from 28°C to 20°C, 2°C per step), and incubation at 10°C for at least 10 min. Finally, 50 μL of chemically-competent *E. coli* DH5α λpir cells were transformed with 5 μL of the USER.

The suicide pGNW2-derivative plasmid harboring homologous regions was delivered by electroporating 50 μL of freshly-prepared *P. putida* EM42 electrocompetent cells, washed three times with 300 mM sucrose with 500 ng of DNA (Wirth, et al., 2020). Electroporation was performed with a Gene Pulser XCell (Bio-Rad, Hercules, CA, USA) set to 2.5 kV, 25 μF capacitance and 200 Ω resistance in a 2-mm gap cuvette. Positive co-integrants were further transformed via electroporation with a plasmid encoding the meganuclease *I-SceI*, which cuts pGNW2 within the chromosome forcing a second homologous recombination event. Cells were recovered in 1 mL of LB medium supplemented with 2 mM of 3-methylbenzoate (3-*m*Bz) for at least 3 h at 30°C, and plated onto LB medium agar containing the corresponding antibiotic(s) and 1 mM 3-*m*Bz to induce *I-SceI* expression. Positive clones were identified by colony

PCR, verified by DNA sequencing and cured from the resolving plasmid by serial dilution under non-selective conditions.

7.4.6 Bacterial strains and growth conditions

All bacterial strains and plasmids used in this work are listed in **Table S7.1**. *E. coli* DH5α was used for cloning and plasmid maintenance. *E. coli* and *P. putida* strains were routinely grown in lysogeny broth (LB) medium (10 g L^{-1} tryptone, 5 g L^{-1} yeast extract and 5 g L^{-1} NaCl) at 37°C and 30°C, respectively, in an orbital shaker at 200 rpm. For all physiological experiments, *P. putida* was grown in M9 minimal medium supplemented with different concentrations of glucose (20-40 mM) as sole carbon source. Bacterial growth was estimated by measuring the optical density at 600 nm (OD_{600}).

7.4.7 Adaptive Laboratory Evolution (ALE)

Two adaptive laboratory evolution experiments of the engineered strain *P. putida* SG2 were carried out in parallel on a custom-designed liquid handling platform (Sandberg, et al., 2014, LaCroix, et al., 2015, Mohamed, et al., 2019). Briefly, the SG2 strain was streaked on an LB agar plate overnight, and two single colonies were picked as starters of the evolution experiments. The cells were cultured on 15 mL of magnetically stirred 40 mM glucose M9 minimal medium supplemented with trace elements and vitamins (Mohamed, et al., 2017) under full aeration conditions and an incubation temperature of 30°C. When the cultures reached the late-exponential growth phase (i.e. an OD600 of 0.30), a 900 μL culture volume was transferred into a new tube with 15 mL of fresh M9 medium. The exponential growth phase of the cultures took place from the moment of inoculation until the cultures reached an OD600 of 0.30, and the maximum final OD600 observed was approximately 0.50. The OD600 was measured by a Sunrise Plate Reader (Tecan Inc., Switzerland), and the correction factor between the plate reader OD600 and a benchtop spectrophotometer with a 1-cm path length was 4.29. Growth rate was calculated for each flask by calculating the slope of a least-squares linear regression fit to the natural logarithm of the OD600 measurements versus time.

Each population lineage was periodically validated by PCR, using the oligonucleotides *rpoD*-F and *rpoD*-R (Supplementary Information **Table S7.2**). Samples of the populations were also periodically taken and stored in 25% glycerol stocks at −80°C for reference and for later sequencing analysis. The evolution experiments were concluded once increases in the growth rate were no longer observed during several passages (LaCroix, et al., 2015, Mohamed, et al., 2019).

7.4.8 Initial clonal screening of evolved populations in microtiter

Three independent pre-cultures of *P. putida* KT2440, SG2 and the 10 clones selected were grown for 16, 48 and 24 h, respectively in 10 ml of M9 media with 40 mM glucose in 50 ml Falcon tubes. The pre-cultures were incubated in an orbital shaker at 250 rpm and 30°C. Once the pre-cultures reached exponential phase, the tubes were centrifuged at 10,000 *g* for 5 min, washed twice with 10 ml of M9 media without carbon source. The initial optical density was 0.05 OD600 ml^{-1} on each well and the bacterial growth was followed by measuring the OD630 every 15 minutes in a BioTek ELx808 Absorbance Microtiter Reader (BioTek Instruments Inc., Winooski, VT, USA) where the agitation and temperature were set up at 1080 rpm and 30°C, respectively.

7.4.9 Physiological characterization of ALE-evolved clones in shaken flasks

Three biological replicates of *P. putida* KT2440, SG2 and the 2 well-performed clones were inoculated as pre-cultures using the same conditions as it was described before (See "Initial clonal screening of evolved populations in microtiter"). The pre-cultures were used to inoculate 250 ml baffled bottom shaking flask containing 50 ml of M9 media with 40 mM glucose with an initial OD_{600} of 0.05. The flasks were incubated in an orbital shaker at 200 rpm and 30°C. Different aliquots of 700 µl were withdrawn along the growth curves to measure glucose consumption and metabolites secretion into the media. Samples were centrifuged at 10,000 *g* for 5 min at 4°C; the supernatants were collected in Eppendorf tubes and were stored at -20°C until further analysis.

7.4.10 Glucose and organic acids quantification by high-performance liquid chromatography (HPLC)

For glucose and organic acid -gluconate, 2-ketogluconate, succinate, lactate, formate, acetate and pyruvate- analyses, frozen samples were thawed at 4°C and further processed for high-performance liquid chromatography (HPLC). The quantification was performed on a Dionex Ultimate 3000 system (Thermo Scientific, Waltham, USA) with a HPx87H ion exclusion column (125-0140, Aminex, Dublin, Ireland), equipped with a guard column holder (125-0131, Bio-Rad, Hercules, California, USA) and guard column (125-0129, Bio-Rad, Hercules, California, USA) and eluted with 5 mM H_2SO_4 at an isocratic flow of 0.6 ml min^{-1} at 30°C for 30 min. Glucose, 2-ketogluconate, succinate, lactate, formate and acetate were analysed by RI detection using a Smartline RI detector 2300 (KNAUER Wissenschaftliche Geräte, Berlin, Germany), whereas gluconate and pyruvate were analysed by UV detection at a wavelength of 210 nm using a System Gold 166 UV detector (Beckman Coulter, Brea, USA) (Pedersen, et al., 2021).

7.4.11 Genomic DNA purification, library construction, and whole genome sequencing (WGS)

DNA was purified using the PureLinkTM Genomic DNA purification kit (Invitrogen, Waltham, MA, USA) from 2 mL of overnight cultures inoculated from cryostocks. The genomic DNA of each sample was randomly sheared into short fragments of about 350 bp using ultrasonic interruption. Short and large DNA fragments were removed using magnetic bead size selection and subsequently verified by capillary gel electrophoresis. The obtained DNA fragments were subjected to library construction using the NEBNextTM DNA Library Prep Kit (NEB), following the supplier's specifications. Libraries quality control was performed with a Qubit® 2.0 fluorometer and an AgilentTM 2100 BioAnalyzer. Subsequent sequencing was performed using the Illumina NovaSeqTM 6000 PE150 platform. For quality-control purposes, paired reads were discarded when: (i) either read contains adapter contamination, (ii) uncertain nucleotides (N) constitute >10% of either read, or (iii) low quality nucleotides (base quality less than 5, $Q \leq 5$) constitute >50% of either read. The effective

sequencing data were aligned with the reference sequence (NCBI Reference Sequence: X) through Burrows-Wheeler Aligner (BWA) software (Li and Durbin, 2009), and the mapping rate and coverage were counted according to the alignment results. The duplicates were removed by means of the SAMtools package (Danecek, et al., 2021). Single nucleotide polymorphisms (SNPs) and InDels were detected using SAMtools and followed by annotation using ANNOVAR (Wang, et al., 2010). Libraries construction, sequencing and subsequent data quality control was performed by Novogene Co. Ltd. (Cambridge, United Kingdom).

7.4.12 Parallel labelling experiment: flux distribution analysis of SG2, evolved clones and Topoisomerase mutant

For parallel isotopic labeling experiment, *P. putida* KT2440 was pre-grown in M9 with 40 mM unlabeled $^{12}C_6$ glucose. The pre-cultures were started from a fresh LB agar plate (<5 days old) in 10 mL conical tubes with 2 ml of M9 media containing the corresponding labelled tracer in (*P. putida* KT2440, SG2 and the 2 selected clones were cultivated–in biological triplicates–for fluxomic analyses at 30°C and 250 rpm. The parallel labelling experiment was carried out using 3 different tracers: (i) 99% [1–^{13}C] glucose, (ii) 99% [6–^{13}C] glucose, and (iii) an 50:50% mixture of naturally labelled ^{12}C and 99% [U-$^{13}C_6$] glucose (Cambridge Isotopes Laboratories Inc., MA and Omicron Biochemicals, IN). An atom transition map containing 82 reactions of *P. putida* KT2440 core metabolism was constructed using previous published resources with slightly modifications representing the metabolic network of the four different strains. The INCA software package was used to analyze the metabolic network for parallel tracer experiments (Young, 2014).

7.4.13 Proteomics: Sample preparation and LC-MS/MS parameters

Sample preparation for proteomic analysis was performed as described previously by (Gurdo, et al., 2023). Briefly, cell pellets of *P. putida* strains were lysed in 6 M Gu·HCl [guanidinium hydrochloride], 5 mM TCEP [tris(2-carboxyethyl)phosphine], 10 mM CAA [2-chloroacetamide] and 100 mM Tris·HCl, pH = 8.5, disrupted mechanically and heated to 99°C. After centrifugation, the cell-free lysates were diluted with 50 mM

ammonium bicarbonate and subjected to bicinchoninic acid (BCA) assay to estimate protein concentrations. Trypsin and LysC digestion mix (Promega) was added to 20 μg protein of each sample and incubated for 8 hours. Trifluoroacetic acid was added to halt digestion and the samples were desalted using C18 resin (Empore, 3M) before HPLC-MS analysis. HPLC-MS analysis of the samples was performed on the Orbitrap Exploris 480 instrument (Thermo Fisher Scientific) prefaced by the EASY-nLC 1200 HPLC system (Thermo Fisher Scientific). For each sample, 500 ng of peptides was captured on a 2cm C18 trap column (Thermo Fisher 164946) and subsequently separated using a 70 minute gradient from 8% v v^{-1} to 48% v v^{-1} of acetonitrile in 0.1% v v^{-1} formic acid on a 15cm C18 reverse-phase analytical column (Thermo EasySpray ES904) at a flow rate of 250 nL min^{-1}. The mass spectrometer was operated in data-independent acquisition mode with the specific settings listed below.

7.4.14 DIA method and data analysis

For data-independent acquisition, the mass spectrometer was run with the HRMS1 method as previously described (Xuan, et al., 2020). It was preceded by the FAIMS Pro Interface (Thermo Fisher Scientific) with a compensation voltage (CV) of -45 V, and any modifications are mentioned below. Full MS1 spectra were collected at a resolution of 120,000 and scan range of 400-1,000 m/z, with an AGC target of 300 or the maximum injection time set to auto. MS2 spectra were obtained at a resolution of 60,000, with an AGC target of 1000 or the maximum injection time set to auto, and the collision energy set to 32. Each cycle consisted of three DIA experiments each covering a range of 200 m/z with a window size of 6 m/z and a 1 m/z overlap, while a full MS scan was obtained in between experiments.

For the data analysis of raw files from the DIA method, DIA-NN was used with library free approach (Demichev, et al., 2020). DIA-NN was used for library-free analyses with the following settings: the smart profiling and the heuristic protein inference activated and the FDR cut-off set at 1%. For the additional in silico digest feature, acetylation of the protein N-term and oxidation of methionine residues were set as variable modifications, and the cleavage specificity was set to ”K*,R*” (Trypsin/P). Also, the following incorporations were added: generate spectral library, predictor,

FASTA search and match-between-runs (MBR) enabled, minimum 200 and maximum 1,800 m/z for fragment exclusion, minimum 7 and maximum 30 for peptide length, minimum 300 and maximum 1,800 m/z for precursor exclusion, minimum 1 and maximum 4 for precursor charge, and the maximum missed cleavages set to 1.

7.4.15 Protein intensity inference

Before protein inference using the LFAQ algorithm (Chang, et al., 2018), precursor intensities were summed based on identical sequence to obtain peptide intensities and filtered with an FDR cut-off of 1%, similarly to the aLFQ R package import functionality. A tailored Python script was created to facilitate communication with the LFAQ algorithm through the command line. The input data for the LFAQ algorithm was divided on a per-sample basis, and the corresponding output was subsequently merged. This was necessary as the LFAQ algorithm exclusively conducts protein inference for individual samples. For subsequent analyses, only protein intensities were employed; nonetheless, the LFAQ algorithm requires protein concentrations to be calculated. To address this challenge, a supplementary input file was generated, consisting of randomly selected protein identifiers from the protein database and associated random concentrations. This additional input was incorporated without influencing the calculated protein intensities.

7.4.16 Protein identification and absolute quantification

For the analysis, sequence identification was performed using a protein database consisting of either the *E. coli* (UP000000625) or the *P. putida* (UP000000556) reference proteome. Proteome-wide absolute quantification was carried out using standard-free TPA method (Wiśniewski, et al., 2014). A custom Python script was developed to carry out all the quantification approach. The calculated protein intensities from the inference algorithm was used as input, together with a table recording total protein mass per sample.

7.4.17 Statistical Analysis

All the experiments reported were independently repeated at least twice (as indicated in the corresponding figure or table legend), and the mean value of the corresponding parameter ± standard deviation is presented. In some cases, the level of significance of the differences when comparing results was evaluated by means of the Student's t test with α = 0.05. For proteomics analysis, one-way ANOVA was applied for determining differences in normalized protein concentrations. For the statistical analysis, we exclusively employed the proteins that were consistently identified in all replicate data sets pertaining to a specific comparison.

References Chapter 7

Al Zaid Siddiquee, K., Arauzo-Bravo, M., and Shimizu, K. (2004) Metabolic flux analysis of *pykF* gene knockout *Escherichia coli* based on ^{13}C-labeling experiments together with measurements of enzyme activities and intracellular metabolite concentrations, *Applied microbiology and biotechnology* **63**: 407-417.

Anand, A., Chen, K., Catoiu, E., Sastry, A.V., Olson, C.A., Sandberg, T.E., et al. (2020) OxyR is a convergent target for mutations acquired during adaptation to oxidative stress-prone metabolic states, *Molecular Biology and Evolution* **37**: 660-667.

Bachar, A., Itzhaki, E., Gleizer, S., Shamshoom, M., Milo, R., and Antonovsky, N. (2020) Point mutations in topoisomerase I alter the mutation spectrum in *E. coli* and impact the emergence of drug resistance genotypes, *Nucleic acids research* **48**: 761-769.

Bagdasarian, M., Lurz, R., Ruckert, B., Franklin, F.C., Bagdasarian, M.M., Frey, J., and Timmis, K.N. (1981) Specific-purpose plasmid cloning vectors. II. Broad host range, high copy number, RSF1010-derived vectors, and a host-vector system for gene cloning in Pseudomonas, *Gene* **16**: 237-247.

Belda, E., van Heck, R.G.A., José Lopez-Sanchez, M., Cruveiller, S., Barbe, V., Fraser, C., et al. (2016) The revisited genome of *Pseudomonas putida* KT2440 enlightens its value as a robust metabolic chassis, *Environmental Microbiology* **18**: 3403-3424.

Calero, P., Gurdo, N., and Nikel, P.I. (2022) Role of the CrcB transporter of *Pseudomonas putida* in the multi-level stress response elicited by mineral fluoride, *Environmental Microbiology* **24**: 5082-5104.

Carbonell, P., Jervis, A.J., Robinson, C.J., Yan, C., Dunstan, M., Swainston, N., et al. (2018) An automated Design-Build-Test-Learn pipeline for enhanced microbial production of fine chemicals, *Communications Biology* **1**: 66-66.

Chang, C., Gao, Z., Ying, W., Fu, Y., Zhao, Y., Wu, S., et al. (2018) LFAQ: Toward unbiased label-free absolute protein quantification by predicting peptide quantitative factors, *Analytical chemistry* **91**: 1335-1343.

Choi, K.-H., Kumar, A., and Schweizer, H.P. (2006) A 10-min method for preparation of highly electrocompetent Pseudomonas aeruginosa cells: application for DNA fragment transfer between chromosomes and plasmid transformation, *Journal of microbiological methods* **64**: 391-397.

Crousilles, A., Dolan, S.K., Brear, P., Chirgadze, D.Y., and Welch, M. (2018) Gluconeogenic precursor availability regulates flux through the glyoxylate shunt in *Pseudomonas aeruginosa*, *Journal of Biological Chemistry* **293**: 14260-14269.

Crozat, E., Philippe, N., Lenski, R.E., Geiselmann, J., and Schneider, D. (2005) Long-term experimental evolution in *Escherichia coli*. XII. DNA topology as a key target of selection, *Genetics* **169**: 523-532.

Crozat, E., Winkworth, C., Gaffé, J., Hallin, P.F., Riley, M.A., Lenski, R.E., and Schneider, D. (2010) Parallel genetic and phenotypic evolution of DNA superhelicity in experimental populations of *Escherichia coli*, *Molecular Biology and Evolution* **27**: 2113-2128.

Danecek, P., Bonfield, J.K., Liddle, J., Marshall, J., Ohan, V., Pollard, M.O., et al. (2021) Twelve years of SAMtools and BCFtools, *Gigascience* **10**: giab008.

Deatherage, D.E., and Barrick, J.E. (2021) High-throughput characterization of mutations in genes that drive clonal evolution using multiplex adaptome capture sequencing, *Cell Systems* **12**: 1187-1200. e1184.

del Castillo, T., Ramos, J.L., Rodríguez-Herva, J.J., Fuhrer, T., Sauer, U., and Duque, E. (2007) Convergent peripheral pathways catalyze initial glucose catabolism in *Pseudomonas putida*: genomic and flux analysis, *J Bacteriol* **189**: 5142-5152.

Delumeau, O., Lecointe, F., Muntel, J., Guillot, A., Guédon, E., Monnet, V., et al. (2011) The dynamic protein partnership of RNA polymerase in *Bacillus subtilis*, *Proteomics* **11**: 2992-3001.

Demichev, V., Messner, C.B., Vernardis, S.I., Lilley, K.S., and Ralser, M. (2020) DIA-NN: neural networks and interference correction enable deep proteome coverage in high throughput, *Nature Methods* **17**: 41-44.

Dolan, S.K., Kohlstedt, M., Trigg, S., Vallejo Ramirez, P., Kaminski, C.F., Wittmann, C., and Welch, M. (2020) Contextual flexibility in *Pseudomonas aeruginosa* central carbon metabolism during growth in single carbon sources, *MBio* **11**: e02684-02619.

Dorman, C.J., and Dorman, M.J. (2016) DNA supercoiling is a fundamental regulatory principle in the control of bacterial gene expression, *Biophysical reviews* **8**: 209-220.

Dragosits, M., and Mattanovich, D. (2013) Adaptive laboratory evolution – principles and applications for biotechnology, *Microbial Cell Factories* **12**: 64.

Durand-Dubief, M., Persson, J., Norman, U., Hartsuiker, E., and Ekwall, K. (2010) Topoisomerase I regulates open chromatin and controls gene expression *in vivo*, *The EMBO journal* **29**: 2126-2134.

Eames, M., and Kortemme, T. (2012) Cost-benefit tradeoffs in engineered lac operons, *Science* **336**: 911-915.

Emmerling, M., Dauner, M., Ponti, A., Fiaux, J., Hochuli, M., Szyperski, T., et al. (2002) Metabolic flux responses to pyruvate kinase knockout in *Escherichia coli*, *Journal of bacteriology* **184**: 152-164.

Ferrándiz, M.-J., Martín-Galiano, A.J., Arnanz, C., Camacho-Soguero, I., Tirado-Vélez, J.-M., and de la Campa, A.G. (2016) An increase in negative supercoiling in bacteria reveals topology-reacting gene clusters and a homeostatic response mediated by the DNA topoisomerase I gene, *Nucleic Acids Research* **44**: 7292-7303.

Gassler, T., Sauer, M., Gasser, B., Egermeier, M., Troyer, C., Causon, T., et al. (2020) The industrial yeast *Pichia pastoris* is converted from a heterotroph into an autotroph capable of growth on CO_2, *Nature Biotechnology* **38**: 210-216.

Gerike, U., Hough, D.W., Russell, N.J., Dyall-Smith, M.L., and Danson, M.J. (1998) Citrate synthase and 2-methylcitrate synthase: structural, functional and evolutionary relationships, *Microbiology* **144**: 929-935.

Giani, A.M., Gallo, G.R., Gianfranceschi, L., and Formenti, G. (2020) Long walk to genomics: History and current approaches to genome sequencing and assembly, *Computational and Structural Biotechnology Journal* **18**: 9-19.

Green, M.R., and Sambrook, J. (2012) Molecular cloning, *A Laboratory Manual 4th*.

Gurdo, N., Taylor Parkins, S.K., Fricano, M., Wulff, T., Nielsen, L.K., and Nikel, P.I. (2023) Protocol for absolute quantification of proteins in Gram-negative bacteria based on QconCAT-based labeled peptides, *STAR Protocols* **4**: 102060.

Hatfield, G.W., and Benham, C.J. (2002) DNA topology-mediated control of global gene expression in *Escherichia coli*, *Annual review of genetics* **36**: 175-203.

Jannière, L., Canceill, D., Suski, C., Kanga, S., Dalmais, B., Lestini, R., et al. (2007) Genetic evidence for a link between glycolysis and DNA replication, *PLoS One* **2**: e447.

Jeyaseelan, K., and Guest, J.R. (1980) Isolation and properties of pyruvate dehydrogenase complex mutants of *Pseudomonas aeruginosa* PAO, *Microbiology* **120**: 385-392.

Kornberg, H.L. (1966) The role and control of the glyoxylate cycle in *Escherichia coli*, *Biochem J* **99**: 1-11.

LaCroix, R.A., Sandberg, T.E., O'Brien, E.J., Utrilla, J., Ebrahim, A., Guzman, G.I., et al. (2015) Use of adaptive laboratory evolution to discover key mutations enabling rapid growth of *Escherichia coli* K-12 MG1655 on glucose minimal medium, *Applied and environmental microbiology* **81**: 17-30.

LaPorte, D.C., Walsh, K., and Koshland, D.E., Jr. (1984) The branch point effect. Ultrasensitivity and subsensitivity to metabolic control, *J Biol Chem* **259**: 14068-14075.

Lee, D.-H., Feist, A.M., Barrett, C.L., and Palsson, B.Ø. (2011) Cumulative number of cell divisions as a meaningful timescale for adaptive laboratory evolution of *Escherichia coli*, *PloS one* **6**: e26172.

Leela, J.K., Raghunathan, N., and Gowrishankar, J. (2021) Topoisomerase I essentiality, DnaA-independent chromosomal replication, and transcription-replication conflict in *Escherichia coli*, *Journal of Bacteriology* **203**: e00195-00121.

Leyn, S.A., Li, X., Zheng, Q., Novichkov, P.S., Reed, S., Romine, M.F., et al. (2011) Control of proteobacterial central carbon metabolism by the HexR transcriptional regulator: a case study in *Shewanella oneidensis*, *J Biol Chem* **286**: 35782-35794.

Li, H., and Durbin, R. (2009) Fast and accurate short read alignment with Burrows–Wheeler transform, *bioinformatics* **25**: 1754-1760.

Lien, S.K., Niedenführ, S., Sletta, H., Nöh, K., and Bruheim, P. (2015) Fluxome study of *Pseudomonas fluorescens* reveals major reorganisation of carbon flux through central metabolic pathways in response to inactivation of the anti-sigma factor MucA, *BMC Systems Biology* **9**: 6.

Long, C.P., and Antoniewicz, M.R. (2018) How adaptive evolution reshapes metabolism to improve fitness: recent advances and future outlook, *Current opinion in chemical engineering* **22**: 209-215.

Maloy, S.R., and Nunn, W.D. (1982) Genetic regulation of the glyoxylate shunt in *Escherichia coli* K-12, *Journal of bacteriology* **149**: 173-180.

Mattevi, A., Valentini, G., Rizzi, M., Speranza, M.L., Bolognesi, M., and Coda, A. (1995) Crystal structure of *Escherichia coli* pyruvate kinase type I: molecular basis of the allosteric transition, *Structure* **3**: 729-741.

Medema, M.H., Breitling, R., Bovenberg, R., and Takano, E. (2011) Exploiting plug-and-play synthetic biology for drug discovery and production in microorganisms, *Nature Reviews Microbiology* **9**: 131-137.

Meselson, M., and Yuan, R. (1968) DNA Restriction Enzyme from *E. coli*, *Nature* **217**: 1110-1114.

Mohamed, E.T., Mundhada, H., Landberg, J., Cann, I., Mackie, R.I., Nielsen, A.T., et al. (2019) Generation of an *E. coli* platform strain for improved sucrose utilization using adaptive laboratory evolution, *Microbial Cell Factories* **18**: 116.

Mohamed, E.T., Wang, S., Lennen, R.M., Herrgård, M.J., Simmons, B.A., Singer, S.W., and Feist, A.M. (2017) Generation of a platform strain for ionic liquid tolerance using adaptive laboratory evolution, *Microbial cell factories* **16**: 1-15.

Mohamed, E.T., Werner, A.Z., Salvachúa, D., Singer, C.A., Szostkiewicz, K., Jiménez-Díaz, M.R., et al. (2020) Adaptive laboratory evolution of *Pseudomonas putida* KT2440 improves p-coumaric and ferulic acid catabolism and tolerance, *Metabolic engineering communications* **11**: e00143.

Molenaar, D., van Berlo, R., de Ridder, D., and Teusink, B. (2009) Shifts in growth strategies reflect tradeoffs in cellular economics, *Mol Syst Biol* **5**: 323.

Moon, J., Schubert, A., Waschinger, L.M., and Müller, V. (2023) Reprogramming the metabolism of an acetogenic bacterium to homoformatogenesis, *The ISME Journal*.

Nikel, P.I., and de Lorenzo, V. (2013) Implantation of unmarked regulatory and metabolic modules in Gram-negative bacteria with specialised mini-transposon delivery vectors, *Journal of biotechnology* **163**: 143-154.

Pedersen, B.H., Gurdo, N., Johansen, H.K., Molin, S., Nikel, P.I., and La Rosa, R. (2021) High-throughput dilution-based growth method enables time-resolved exo-metabolomics of *Pseudomonas putida* and *Pseudomonas aeruginosa*, *Microbial Biotechnology* **14**: 2214-2226.

Peebo, K., Valgepea, K., Maser, A., Nahku, R., Adamberg, K., and Vilu, R. (2015) Proteome reallocation in *Escherichia coli* with increasing specific growth rate, *Molecular BioSystems* **11**: 1184-1193.

Peng, F., Widmann, S., Wünsche, A., Duan, K., Donovan, K.A., Dobson, R.C., et al. (2018) Effects of beneficial mutations in *pykF* gene vary over time and across replicate populations in a long-term experiment with bacteria, *Molecular biology and evolution* **35**: 202-210.

Pisithkul, T., Patel, N.M., and Amador-Noguez, D. (2015) Post-translational modifications as key regulators of bacterial metabolic fluxes, *Current Opinion in Microbiology* **24**: 29-37.

Puchałka, J., Oberhardt, M.A., Godinho, M., Bielecka, A., Regenhardt, D., Timmis, K.N., et al. (2008) Genome-scale reconstruction and analysis of the *Pseudomonas putida* KT2440 metabolic network facilitates applications in biotechnology, *PLoS Comput Biol* **4**: e1000210.

Reuß, D.R., Rath, H., Thürmer, A., Benda, M., Daniel, R., Völker, U., et al. (2018) Changes of DNA topology affect the global transcription landscape and allow rapid growth of a *Bacillus subtilis* mutant lacking carbon catabolite repression, *Metabolic engineering* **45**: 171-179.

Sánchez-Pascuala, A., Fernández-Cabezón, L., de Lorenzo, V., and Nikel, P.I. (2019) Functional implementation of a linear glycolysis for sugar catabolism in *Pseudomonas putida*, *Metabolic engineering* **54**: 200-211.

Sandberg, T.E., Pedersen, M., LaCroix, R.A., Ebrahim, A., Bonde, M., Herrgard, M.J., et al. (2014) Evolution of *Escherichia coli* to 42 C and subsequent genetic engineering reveals adaptive mechanisms and novel mutations, *Molecular biology and evolution* **31**: 2647-2662.

Sandhaus, S., Chapagain, P.P., and Tse-Dinh, Y.-C. (2018) Discovery of novel bacterial topoisomerase I inhibitors by use of in silico docking and in vitro assays, *Scientific reports* **8**: 1-9.

Scott, M., Gunderson, C.W., Mateescu, E.M., Zhang, Z., and Hwa, T. (2010) Interdependence of cell growth and gene expression: origins and consequences, *Science* **330**: 1099-1102.

Siddiquee, K.A.Z., Arauzo-Bravo, M.J., and Shimizu, K. (2004) Effect of a pyruvate kinase (*pykF*-gene) knockout mutation on the control of gene expression and metabolic fluxes in *Escherichia coli*, *FEMS microbiology letters* **235**: 25-33.

Silas, Y., Singer, E., Das, K., Lehming, N., and Pines, O. (2021) A combination of Class-I fumarases and metabolites (alpha-ketoglutarate and fumarate) signal the DNA damage response in *Escherichia coli*, *Proceedings of the National Academy of Sciences* **118**: e2026595118.

Vos, S.M., Tretter, E.M., Schmidt, B.H., and Berger, J.M. (2011) All tangled up: how cells direct, manage and exploit topoisomerase function, *Nature reviews Molecular cell biology* **12**: 827-841.

Walsh, K., and Koshland, D.E. (1984) Determination of flux through the branch point of two metabolic cycles. The tricarboxylic acid cycle and the glyoxylate shunt, *Journal of Biological Chemistry* **259**: 9646-9654.

Wang, K., Li, M., and Hakonarson, H. (2010) ANNOVAR: functional annotation of genetic variants from high-throughput sequencing data, *Nucleic acids research* **38**: e164-e164.

Wirth, N.T., Kozaeva, E., and Nikel, P.I. (2020) Accelerated genome engineering of *Pseudomonas putida* by I-SceI-mediated recombination and CRISPR-Cas9 counterselection, *Microbial biotechnology* **13**: 233-249.

Wiśniewski, J.R., Hein, M.Y., Cox, J., and Mann, M. (2014) A "proteomic ruler" for protein copy number and concentration estimation without spike-in standards, *Molecular & cellular proteomics* **13**: 3497-3506.

Xuan, Y., Bateman, N.W., Gallien, S., Goetze, S., Zhou, Y., Navarro, P., et al. (2020) Standardization and harmonization of distributed multi-center proteotype analysis supporting precision medicine studies, *Nature Communications* **11**: 5248.

Yan, R., Hu, S., Ma, N., Song, P., Liang, Q., Zhang, H., et al. (2019) Regulatory effect of DNA topoisomerase I on T3SS activity, antibiotic susceptibility and quorum-sensing-independent pyocyanin synthesis in *Pseudomonas aeruginosa*, *International journal of molecular sciences* **20**: 1116.

Young, J.D. (2014) INCA: a computational platform for isotopically non-stationary metabolic flux analysis, *Bioinformatics (Oxford, England)* **30**: 1333-1335.

Zhao, C., Lin, Z., Dong, H., Zhang, Y., and Li, Y. (2017) Reexamination of the physiological role of PykA in *Escherichia coli* revealed that it negatively regulates the

intracellular ATP levels under anaerobic conditions, *Applied and Environmental Microbiology* **83**: e00316-00317.

7.5 Supplementary Information

Table S7.1. Bacterial strains used in this Chapter.

	Relevant characteristics	Reference
Bacterial strains		
Escherichia coli		
DH5α	*Cloning host; F⁻ λ⁻ endA1 glnX44(AS) thiE1 recA1 relA1 spoT1 gyrA96(NalR) rfbC1 deoR nupG Φ80(lacZΔM15) Δ(argF-lac)U169 hsdR17(rK7(r⁻K⁻ m⁺K)*	(Meselson and Yuan, 1968)
Pseudomonas putida		
KT2440	Wild-type strain, derived from *P. putida* mt-2 cured of the TOL plasmid pWW0	(Bagdasarian, et al., 1981)
SG2	Glycolytic *chassis*, derivative of *P. putida* KT2440 with the deletions Δ*glk*, Δ*gcd*, Δ*gad*, Δ*edd*, Δ*eda*, Δ*gts* and chromosomal insertion of the gene encoding the *Glf* glucose transporter from *Zymomonas mobilis*, and GlucoBricks containing Module I and II.	(Sánchez-Pascuala, et al., 2019)
eSG2A	ALE-evolved population with higher growth rate on glucose derived from the starting strain SG2 (flask 46; population A)	This work
eSG2B	ALE-evolved population with higher growth rate on glucose derived from the starting strain SG2 (flask 42; population B)	This work
eSG2A (Clone 1)	Evolved clone with higher growth rate on glucose isolated from the endpoint of the ALE-evolved population eSG2 #A	This work
eSG2A (Clone 2)	Evolved clone with higher growth rate on glucose isolated from the endpoint of the ALE-evolved population eSG2 #A	This work
eSG2A (Clone 3)	Evolved clone with higher growth rate on glucose isolated from the endpoint of the ALE-evolved population eSG2 #A	This work
eSG2A (Clone 4)	Evolved clone with higher growth rate on glucose isolated from the endpoint of the ALE-evolved population eSG2 #A	This work
eSG2A (Clone 5)	Evolved clone with higher growth rate on glucose isolated from the endpoint of the ALE-evolved population eSG2 #B	This work
eSG2B (Clone 1)	Evolved clone with higher growth rate on glucose isolated from the endpoint of the ALE-evolved population eSG2 #B	This work
eSG2B (Clone 2)	Evolved clone with higher growth rate on glucose isolated from the endpoint of the ALE-evolved population eSG2 #B	This work
eSG2B (Clone 3)	Evolved clone with higher growth rate on glucose isolated from the endpoint of the ALE-evolved population eSG2 #B	This work
eSG2B (Clone 4)	Evolved clone with higher growth rate on glucose isolated from the endpoint of the ALE-evolved population eSG2 #B	This work
eSG2B (Clone 5)	Evolved clone with higher growth rate on glucose isolated from the endpoint of the ALE-evolved population eSG2 #B	This work

Table S7.2. Oligonucleotides used in this chapter.

Oligonucleotides	Sequence (5'→ 3')	Uses
rpoD-F	ATCCGATCAGCTTCAGGCAACCTC	Validation of lineage during ALE
rpoD-R	ATGCGGATGGTGCGTGCCTG	

Table S7.3. Relative net fluxes determined by ^{13}C-MFA in *Pseudomonas putida* strains. Best fit represents the relative mean values (%) related to glucose uptake rate of 100%. Mean parameter estimates and 95% confidence bounds using INCA's parameter continuation method for SG2, eSG2A[3] and eSG2B[9] are shown.

Reaction ID	Equations (Carbon atom transition)	SG2				eSG2A[3]				eSG2A[9]			
		Best fit	SD	LB	UP	Best fit	SD	LB	UP	Best fit	SD	LB	UP
R1	Gluc.ext -> Gluc.per	100.0	0.0	100.0	100.0	100.0	0.0	100.0	100.0	100.0	0.0	100.0	100.0
R2	Gluc.per + 2*ATP -> G6P	100.0	0.0	100.0	100.0	100.0	0.0	100.0	100.0	100.0	0.0	100.0	100.0
R3	G6P <-> F6P	69.6	2.6	67.9	71.8	88.5	3.7	86.2	91.6	86.3	2.1	84.4	88.0
R4	F6P + ATP -> FBP	78.4	1.8	76.1	80.7	91.8	1.2	90.3	92.8	91.3	1.1	89.6	92.1
R5	FBP <-> DHAP + GAP	78.4	1.8	76.1	80.7	91.8	1.2	90.3	92.8	91.3	1.1	89.6	92.1
R6	DHAP <-> GAP	78.4	1.8	76.1	80.7	91.8	1.2	90.3	92.8	91.3	1.1	89.6	92.1
R7	GAP <-> 3PG + ATP + NADH	170.0	1.8	167.7	172.4	183.3	1.2	181.8	184.3	183.7	1.1	182.0	184.4
R8	3PG <-> PEP	163.5	1.9	161.2	165.8	175.9	1.2	173.2	178.4	177.4	1.1	175.7	178.2
R9	PEP -> Pyr + ATP	87.4	2.5	83.8	92.3	117.9	2.3	86.6	148.0	106.1	2.3	100.2	113.3
R10	G6P -> 6PG + NADPH	28.8	2.6	26.5	30.5	9.8	3.7	6.7	12.2	12.2	2.1	10.4	14.1
R11	6PG -> Ri5P + CO2 + NADPH	18.0	2.5	14.2	21.2	9.8	3.7	6.6	12.2	11.9	1.9	9.7	13.8
R12	Ri5P <-> X5P	9.4	1.7	6.9	11.5	3.9	2.5	1.8	5.5	5.6	1.3	4.1	6.9
R13	Ri5P <-> R5P	8.6	0.8	7.3	9.6	5.9	1.2	4.8	6.7	6.3	0.6	5.6	7.0
R14	X5P <-> GAP + EC2	9.4	1.7	6.9	11.5	3.9	2.5	1.8	5.5	5.6	1.3	4.1	6.9
R15	F6P <-> E4P + EC2	-2.8	0.8	-3.9	-1.5	0.0	1.2	-0.8	1.1	-1.0	0.6	-1.7	-0.3
R16	S7P <-> R5P + EC2	-6.6	0.8	-7.7	-5.4	-3.9	1.2	-4.7	-2.8	-4.5	0.6	-5.2	-3.8
R17	F6P <-> GAP + EC3	-6.6	0.8	-7.7	-5.4	-3.9	1.2	-4.7	-2.8	-4.5	0.6	-5.2	-3.8
R18	S7P <-> E4P + EC3	6.6	0.8	5.4	7.7	3.9	1.2	2.8	4.7	4.5	0.6	3.8	5.2
R19	6PG -> Pyr + GAP	10.8	1.9	7.7	14.0	0.0	0.0	0.0	1.8	0.3	0.9	0.0	2.1
R20	Pyr -> AcCoA + CO2 + NADH	133.7	3.2	128.3	140.8	172.6	5.8	162.5	185.2	159.4	2.7	154.5	164.1
R21	OAA + AcCoA -> Cit	87.6	1.0	86.4	89.0	87.5	1.2	86.4	88.5	98.3	0.6	97.6	99.1
R22	Cit <-> ICit	87.6	1.0	86.4	89.0	87.5	1.2	86.4	88.5	98.3	0.6	97.6	99.1
R23	ICit -> Suc + Glyox	21.1	3.0	16.1	27.6	58.3	5.8	48.1	71.1	37.6	2.6	32.8	42.1
R24	Glyox + AcCoA -> Mal	21.1	3.0	16.1	27.6	58.3	5.8	48.1	71.1	37.6	2.6	32.8	42.1
R25	ICit -> AKG + CO2 + NADPH	66.5	2.7	60.4	71.1	29.2	6.1	16.2	39.6	60.7	2.6	56.3	65.5
R26	AKG -> SucCoA + CO2 + NADH	55.4	2.7	49.3	60.0	17.8	6.1	4.8	28.2	50.6	2.6	46.1	55.3
R27	SucCoA <-> Suc + ATP	52.6	2.7	46.5	57.1	14.9	6.1	1.9	25.3	47.9	2.6	43.5	52.7
R28	Suc -> Fum + FADH2	76.5	1.0	75.3	77.9	76.1	1.2	75.1	77.2	88.2	0.6	87.4	88.9
R29	Fum <-> Mal	81.1	1.0	79.9	82.5	80.8	1.2	79.7	81.9	92.3	0.6	91.6	93.1
R30	Mal -> OAA + FADH2	102.2	2.5	82.2	109.3	139.1	2.6	133.7	151.7	129.9	3.2	121.5	134.6
R31	Pyr + CO2 + ATP -> OAA	254.3	6.1	208.5	360.1	34.5	6.5	20.4	46.3	71.7	1.7	66.9	73.6
R32	OAA -> Pyr + CO2	317.1	11.0	212.0	465.1	117.0	5.5	109.6	127.5	149.5	7.2	140.6	152.5
R33	PEP + CO2 -> OAA	103.6	2.5	91.1	121.0	121.9	2.3	116.5	126.5	93.8	2.3	87.5	99.6
R34	OAA + ATP -> PEP + CO2	35.1	4.3	28.2	41.8	71.7	5.6	60.9	82.5	29.5	2.3	25.3	34.0
R35	Mal -> Pyr + CO2 + NADPH	0.0	2.5	0.0	51.0	0.0	2.6	0.0	4.4	0.0	3.2	-4.0	9.2

Reaction ID	Equations (Carbon atom transition)	SG2				eSG2A[3]				eSG2A[9]			
		Best fit	SD	LB	UB	Best fit	SD	LB	UB	Best fit	SD	LB	UB
R36	AKG + NADPH + NH3 -> Glu	64.9	0.6	64.5	65.3	65.7	0.1	65.0	65.8	59.2	0.0	58.9	59.3
R37	Glu + ATP + NH3 -> Gln	7.7	0.0	7.7	7.7	7.8	0.0	7.8	7.8	7.0	0.0	7.0	7.0
R38	Glu + ATP + 2*NADPH -> Pro	2.5	0.0	2.5	2.5	2.6	0.0	2.6	2.6	2.3	0.0	2.3	2.3
R39	Glu + CO2 + Gln + Asp + AcCoA + 5*ATP + NADPH -> Arg + AKG + Fum + Ac	3.4	0.0	3.4	3.4	3.4	0.0	3.4	3.4	3.1	0.0	3.1	3.1
R40	OAA + Glu -> Asp + AKG	20.2	1.2	19.4	21.0	19.4	0.1	18.0	19.6	18.0	0.1	17.4	18.2
R41	Asp + 2*ATP + NH3 -> Asn	1.5	0.0	1.5	1.5	1.5	0.0	1.5	1.5	1.4	0.0	1.4	1.4
R42	Pyr + Glu -> Ala + AKG	5.7	0.0	5.7	5.7	5.8	0.0	5.8	5.8	5.2	0.0	5.2	5.2
R43	3PG + Glu -> Ser + AKG + NADH	6.6	0.6	6.2	7.0	7.4	0.1	7.2	8.0	6.3	0.0	6.2	6.6
R44	Ser <-> Gly + MEETHF	1.3	0.6	0.9	1.7	2.0	0.1	1.8	2.6	1.5	0.0	1.4	1.8
R45	Gly <-> CO2 + MEETHF + NADH + NH3	1.1	0.6	0.6	1.5	0.4	0.1	-0.2	0.6	0.7	0.0	0.4	0.8
R46	Thr <-> Gly + AcCoA + NADH	3.9	1.2	3.0	4.7	2.6	0.1	1.3	2.9	3.0	0.1	2.4	3.2
R47	Ser + AcCoA + 3*ATP + 4*NADPH + SO4 -> Cys + Ac	1.7	0.0	1.7	1.7	1.7	0.0	1.7	1.7	1.5	0.0	1.5	1.5
R48	Asp + Pyr + Glu + SucCoA + ATP + 2*NADPH -> LL_DAP + AKG + Suc	1.7	0.0	1.7	1.7	1.7	0.0	1.7	1.7	1.6	0.0	1.6	1.6
R49	LL_DAP -> Lys + CO2	1.7	0.0	1.7	1.7	1.7	0.0	1.7	1.7	1.6	0.0	1.6	1.6
R50	Asp + 2*ATP + 2*NADPH -> Thr	8.6	1.2	7.8	9.4	7.5	0.1	6.2	7.8	7.3	0.1	6.7	7.5
R51	Asp + METHF + Cys + SucCoA + ATP + 2*NADPH -> Met + Pyr + Suc + NH3	1.2	0.0	1.2	1.2	1.2	0.0	1.2	1.2	1.1	0.0	1.1	1.1
R52	Pyr + Pyr + Glu + NADPH -> Val + CO2 + AKG	3.7	0.0	3.7	3.7	3.8	0.0	3.8	3.8	3.4	0.0	3.4	3.4
R53	AcCoA + Pyr + Pyr + Glu + NADPH -> Leu + CO2 + CO2 + AKG + NADH	6.0	0.0	6.0	6.0	6.1	0.0	6.1	6.1	5.5	0.0	5.5	5.5
R54	Thr + Pyr + Glu + NADPH -> Ile + CO2 + AKG + NH3	2.3	0.0	2.3	2.3	2.4	0.0	2.4	2.4	2.1	0.0	2.1	2.1
R55	PEP + PEP + E4P + Glu + ATP + NADPH -> Phe + CO2 + AKG	1.8	0.0	1.8	1.8	1.9	0.0	1.9	1.9	1.7	0.0	1.7	1.7
R56	PEP + PEP + E4P + Glu + ATP + NADPH -> Tyr + CO2 + AKG + NADH	1.3	0.0	1.3	1.3	1.3	0.0	1.3	1.3	1.2	0.0	1.2	1.2
R57	Ser + R5P + PEP + E4P + PEP + Gln + 3*ATP + NADPH -> Trp + CO2 + GAP + Pyr + Glu	0.7	0.0	0.7	0.7	0.7	0.0	0.7	0.7	0.7	0.0	0.7	0.7
R58	R5P + FTHF + Gln + Asp + 5*ATP -> His + AKG + Fum + 2*NADH	1.2	0.0	1.2	1.2	1.2	0.0	1.2	1.2	1.1	0.0	1.1	1.1
R59	MEETHF + NADH -> METHF	1.2	0.0	1.2	1.2	1.2	0.0	1.2	1.2	1.1	0.0	1.1	1.1
R60	MEETHF -> FTHF + NADPH	1.2	0.0	1.2	1.2	1.2	0.0	1.2	1.2	1.1	0.0	1.1	1.1
R61	0.174*G6P + 0.068*F6P + 0.107*GAP + 1.882*AcCoA + 0.431*Gly + 0.263*Pro + 0.598*Ala + 0.389*Val + 0.628*Leu + 0.244*Ile + 0.122*Met + 0.055*Cys + 0.191*Phe + 0.135*Tyr + 0.077*Trp + 0.126*His + 0.18*Lys + 0.354*Arg + 0.251*Gln + 0.158*Asn + 0.301*Glu + 0.284*Asp + 0.301*Ser + 0.256*Thr + 46.75*ATP -> Biomass	9.5	0.0	9.5	9.5	9.7	0.0	9.7	9.7	8.7	0.0	8.7	8.7
R62	CO2.unlabeled <-> CO2	0.0	0.0	0.0	0.0	0.0	0.0	0.0	0.0	0.0	0.0	0.0	0.0
R63	NADH <-> NADPH	190.3	1.7	140.3	222.7	319.4	7.8	269.9	361.3	365.0	7.7	339.9	283.2
R64	ATP -> ATP.maintenance	156.0	0.0	156.0	156.0	50.0	0.0	50.0	50.0	54.0	0.0	54.0	54.0
R65	NADPH -> NADPH.maintenance	186.0	1.7	165.8	196.5	251.3	1.8	248.2	256.7	343.5	2.4	334.9	351.7
R66	NADH + O2 -> 3*ATP	188.9	1.7	0.0	338.2	73.4	7.8	50.3	82.5	46.4	7.7	34.5	54.1
R67	FADH2 + O2 -> 2*ATP	178.7	2.5	128.3	186.7	215.2	2.6	209.8	227.7	218.1	3.2	209.8	225.2
R68	UQH2 + O2 -> 3*ATP	0.1	1.7	0.0	149.5	0.0	0.0	0.0	58.1	0.0	0.0	0.0	101.6
R69	CO2 -> CO2.ext	289.2	0.0	289.2	289.2	282.6	0.0	282.6	282.6	315.4	0.0	315.4	315.4
R70	NH3.ext -> NH3	69.6	0.0	69.6	69.6	71.0	0.0	71.0	71.0	63.7	0.0	63.7	63.7
R71	SO4.ext -> SO4	1.7	0.0	1.7	1.7	1.7	0.0	1.7	1.7	1.5	0.0	1.5	1.5
R72	O2.ext -> O2	367.7	3.7	364.0	517.7	288.6	1.8	283.5	291.7	264.4	2.4	262.1	666.7

Parameter continuation INCA	**SG2**	**eSG2A^{3}**	**eSG2A^{9}**
Fit	Yes	Yes	Yes
SSR	284.7	259.6	295.5
Expected SSR	[232.8-325.0]	[236.5-329.5]	[243.8-338.0]

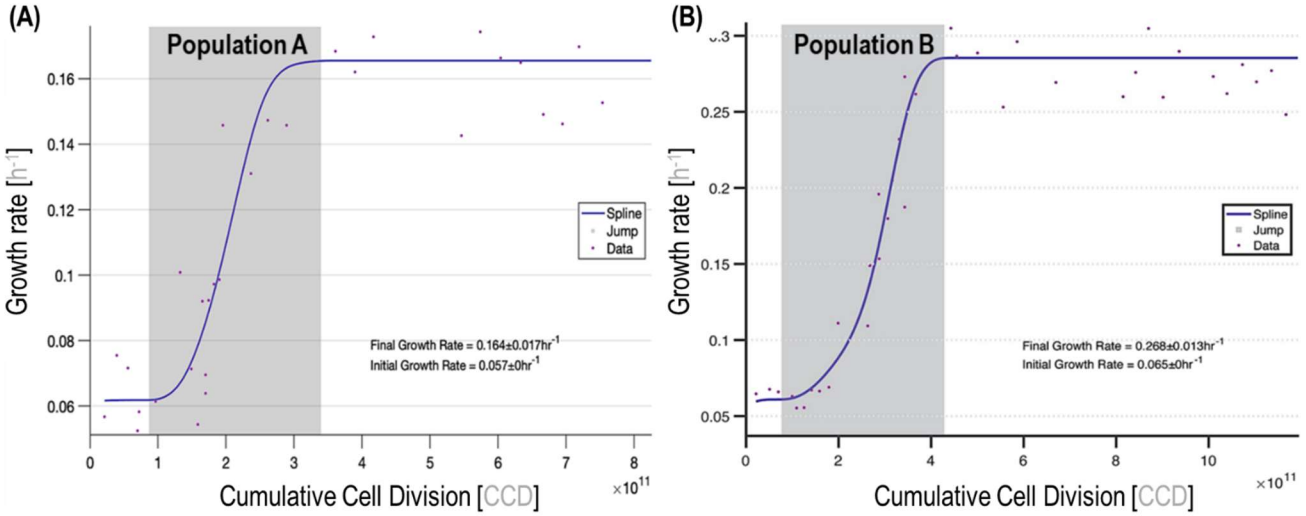

(C)

ALE experiment	Start strain growth rate [h^{-1}]	Strain population	Total CCD x10^{11}	Average achieved growth rate [h^{-1}]	Number of flasks achieved	Ratio of fitness increase compared to initial strain
P. putida SG2	0.05	A	9.6	0.17 ± 0.017	46	3.3
		B	9.5	0.27 ± 0.013	42	5.4

Figure S7.1. Trajectories of populations A and B during adaptive laboratory evolution. Cells were grown in M9 containing 40 mM glucose as only carbon source. **A, B**. Serial batches were run until no growth rate improvement was observed. X-axis represents Cumulative Cell Division [CCD] and Y-axis growth rate [h^{-1}]. **C**. Parameters obtained after the evolution.

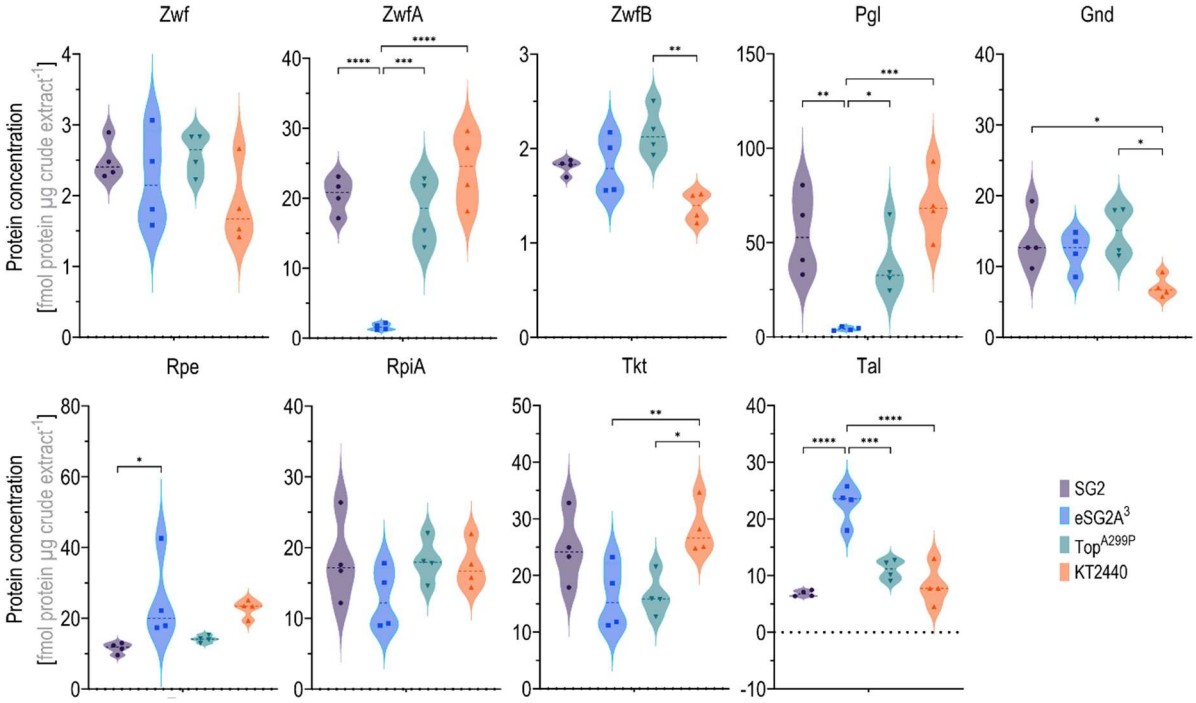

Figure S7.2. Comparison in protein concentration within Pentose Phosphate Pathway (PPP) of the different glycolytic strains SG2, eSG2A^3, Top^{A299P} and the control wild-type strain KT2440. The strains were grown in M9 minimal medium containing 40 mM glucose. Concentrations are given in fmol protein µg crude extract^{-1} from four biological replicates. One-way ANOVA was carried out to perform the statistical analysis. * $p<0.05$, ** $p<0.01$, *** $p<0.001$ and * $p<0.0001$. Zwf, Glucose-6-phosphate 1-dehydrogenase; ZwfA, Glucose-6-phosphate 1-dehydrogenase A; ZwfB, Glucose-6-phosphate 1-dehydrogenase B; Pgl, 6-phosphogluconolactonase; Gnd, 6-phosphogluconate dehydrogenase; RpiA, Ribose-5-phosphate isomerase; Rpe, Ribulose-phosphate 3-epimerase; Tal, Transaldolase; Tkt; Transketolase.

Chapter 8 - Conclusions and future perspectives

In conclusion, this Ph.D. thesis has explored the metabolism of the soil bacterium *Pseudomonas putida* from a systems biology point of view shedding light on the potential of this versatile bacterium for basic research and sustainable biotechnological applications. By employing systems biology approaches, we have gained valuable insights into the complex cellular networks of *P. putida*, elucidating even more metabolic capabilities and regulatory mechanisms under different conditions.

Through the comprehensive analysis of *P. putida*'s genome, fluxome, proteome, and metabolome, we have identified key genetic targets and metabolic bottlenecks that influence its performance as a microbial cell factory. Furthermore, this research has highlighted the importance of a holistic and multidisciplinary approach for a successful implementation of *P. putida*-based bioeconomy. Merging systems and synthetic biology principles has proven to be crucial in bridging the gap between fundamental research and industrial applications. The integration into the bioeconomy framework has the potential to revolutionize the way we produce and utilize valuable bio-based products, contributing to a more sustainable and environmentally friendly society.

This research opens up several exciting possibilities. Firstly, there is the potential for further development and refinement of the multi-omic platform introduced in **Chapter 2** and **Chapter 3**. This could involve integrating the various methodologies into a more robust and standardized process, which could be accomplished by leveraging the concept of a Biofoundry. For example, the implementation of high-throughput screening methods and directed evolution strategies will allow for the rapid development of *P. putida* strains with improved performance, stability, and tolerance to diverse environmental conditions. The integration of omics data and computational modeling can be further refined, enabling more accurate predictions and rational design of microbial cell factories.

By studying multi-substrate conditions, as in **Chapter 4,** we gained insights into the regulatory mechanisms and metabolic adaptations of *P. putida* in response to two carbon

sources (glucose and citrate). This knowledge provided a deeper understanding of how *P. putida* efficiently switches between different substrates and optimizes its metabolic pathways in order to adapt to different conditions. In this way, we acknowledged that exploring multi substrate conditions in *P. putida* could have significant implications for biotechnological applications.

In **Chapter 5**, we studied acetate metabolism in *P. putida* which is of significant importance in the context of acetate-based bioeconomy. Acetate is a valuable carbon source that can be utilized for the production of various bio-based chemicals and fuels. However, the toxic effects of acetate can limit microbial growth and productivity, posing challenges to its efficient utilization. Understanding how the bacterium responds to toxic acetate conditions is crucial for the development of acetate-based bioprocesses. By investigating the mechanisms underlying acetate tolerance and metabolism from a genetic, proteomics and metabolomics perspective, we identified genetic targets and metabolic bottlenecks that enhanced acetate utilization. This knowledge can guide the design of engineered *P. putida* strains towards a more robust and efficient platform to utilize acetate as a carbon source. In addition to its adaptability and tolerance to high acetate concentrations, the abilities of *P. putida* hold significant implications for bioremediation practices.

In **Chapter 6** and **Chapter 7**, we explored a) glucose catabolism in *P. putida* upon genetic perturbations and; b) the incorporation of a glycolytic module from *E. coli*. In the first case of study, blocking glucose phosphorylation or oxidation pathways revealed compensatory mechanisms that the bacterium employs to sustain its growth and energy homeostasis. This information can be used to elucidate the metabolic networks interconnectivity and can help to identify alternative routes and metabolic engineering targets for manipulating glucose metabolism in *P. putida*. In the second case, we highlighted the potential to modify conserved metabolic characteristics to improve desired physiological traits. Thus, the refactoring of the glycolytic pathway emerged as an appealing objective in the domain of metabolic engineering for industrial microorganisms. Numerous approaches in metabolic engineering have been devised to

redirect carbon flux towards desired compounds. Within these various strategies, the modification of the glycolytic pathway emerges as a highly promising approach due to its potential to significantly enhance the efficiency of sugar uptake. By enhancing the efficiency of this crucial metabolic route, the productivity of microbial catalysts can be directly augmented, paving the way for enhanced industrial bioprocesses.

As a final statement, this Ph.D. thesis has provided a foundation for the exploration and exploitation of *Pseudomonas putida* in the context of systems biology. By unraveling the complex interplay between cellular processes and engineering principles, we have laid the groundwork for a sustainable and efficient bio-based industry. Advances in synthetic biology techniques, such as genome editing and pathway optimization, will undoubtedly play a pivotal role in expanding the capabilities of *P. putida* as a cell factory. Consequently, we postulate that the integration of a metabolism-centric approaches into the DBTL cycle will serve as a catalyst for the advancement of industrial biotechnology in the foreseeable future. This integration will facilitate the biosynthesis of *new-to-nature* compounds that are currently beyond the biological scope of commonly utilized cell factories. Despite the existence of several unresolved challenges such as: i) the immense landscape of complex cellular traits in non-traditional hosts; ii) selection of the correct cell platform and, iii) automation of these metabolism-centric approaches; we believe that the methodologies presented in this thesis offer potential solutions that could effectively be applied to enhance the design of microbial cell factories to consolidate the bioeconomy. This becomes especially pertinent in a time where there is an urgent and imperative need for viable alternatives to oil-based production, which is highly susceptible to geopolitical and socioeconomic influences. The future prospects are promising, and continued research and collaboration in this field will undoubtedly lead to remarkable advancements and the realization of a bioeconomy driven by *P. putida*'s potential.